Noble-metal free carbon-based materials for energy conversion

Rafael Gomes Morais

Thesis presented to obtain the Doctor of Philosophy (PhD) degree in Chemical and Biological Engineering

Laboratory of Separation and Reaction Engineering - Laboratory of Catalysis and Materials (LSRE-LCM) – Associated Laboratory in Chemical Engineering (ALiCE), Department of Chemical Engineering, Faculty of Engineering, University of Oporto, Portugal

Supervisors

Professor Manuel Fernando Ribeiro Pereira

Doctor Natalia Rey Raap







2023

Assinado por : **MANUEL FERNANDO RIBEIRO PEREIRA**
Num. de Identificação: BI09493432

This work was financially supported by Fundação para a Ciência e Tecnologia (FCT) through the PhD grant BD.2020.06422.BD

Additional funding was provided by: Project "BiCat4Energy" with reference PTDC/EQU-EQU/1707/2020 and LA/P/0045/2020 (ALiCE), UIDB/50020/2020 and UIDP/50020/2020 (LSRE-LCM), funded by national funds through FCT/MCTES (PIDDAC).





“In this journey, there's no final destination. There's only the next one. In the pursuit of perfection, the only thing that counts is the journey itself, the pursuit itself … because there is no such thing as perfect, there is only the relentless pursuit of perfection.” – Thomas Edward Patrick Brady, Jr.

Preface

This PhD thesis presented herein is submitted for the degree of Doctor in Chemical and Biological Engineering. This work was written based on the experiments carried out in the research unit LSRE-LCM (Laboratory of Separation and Reaction Engineering – Laboratory of Catalysis and Materials), member of ALiCE (Associate Laboratory in Chemical Engineering), hosted in the Department of Chemical Engineering, Faculty of Engineering of the University of Porto. The research herein reported was supervised by Professor M. Fernando. R. Pereira and by Doctor Natalia Rey Raap. Furthermore, one Erasmus research internship was accomplished at the Technische Universität Darmstadt (TU Darmstadt, Germany), under the supervision of Professor Bastian Etzold.

The journey started after my interest in continuing to increase my knowledge in globally relevant topics after a brief introduction to research in the energy field during my early years as an undergraduate student. This thesis represents my first contact with the world of carbon materials and the electrochemistry field. It describes the importance of properly designing carbon electrocatalysts to achieve high electrocatalytic activities towards oxygen reactions, and the main results obtained during this journey are organized into ten chapters.

Chapter 1 describes the necessity to optimize the unitized regenerative fuel cell system, the state-of-the-art of bifunctional oxygen electrocatalysts, the motivation and objectives of this work, and the thesis outline. *Chapter 2* thoroughly describes all reagents, synthesis procures, and characterization techniques used throughout the completion of the thesis. *Chapters 3 to 9* present the main core of this research resulting from a compilation of 7 scientific publications, 5 of which are already published, 1 currently under review, and another under preparation. *Chapter 10* summarizes the main conclusions of this work and provides suggestions for future works.

Acknowledgments

The elaboration of this thesis is the culmination of the cooperation and aid of several people, to whom I would like to express my sincere gratitude:

To Professor Manuel Fernando Ribeiro Pereira for allowing me the opportunity to pursue a PhD under his supervision, and for the continuous support and freedom to create my own investigation path during this research journey. I am grateful for the availability and the discussions surrounding carbon materials that were important to expand my knowledge.

To my co-supervisor Doctor Natalia Rey Raap for her enormous patience to introduce me to a whole new field that I was not familiar with and for her relentless pursuit to improve my scientific writing skills. I am also grateful for the daily support and teachings provided, which greatly helped me understand what was being done and the reasons for it, and for pushing me to improve everything that I did. Without her, it would have not been possible to accomplish this work and for me to be the researcher that I am today.

I am grateful to Fundação para a Ciência e a Tecnologia (FCT), for its financial support through the PhD scholarship received (2020.06422.BD).

I would like to thank Professor José Luís Figueiredo for all the wisdom and knowledge passed to me over the years and for contributing to all the work presented in this thesis.

To Professor Madalena Dias, as Director and scientific coordinator of the Associate Laboratory LSRE-LCM, for the words of wisdom during my 5 years as a student before starting this PhD project and for promptly accepting my request to pursue my thesis within LSRE-LCM.

To the Department of Chemical Engineering, for providing access to the technical means necessary to accomplish this work.

To Professor Bastian Etzold for the opportunity to join his research group at Technische Universität Darmstadt for the development of part of this work.

To Nicolai Schmitt and my other colleagues at TU Darmstadt for their warm reception, friendship, availability, and teachings during my work with their group. I am also grateful

for all the good times during and after work, especially the Champions League nights, and for making me a fan of Darmstadt FC.

To TU Darmstadt, for accepting my application and providing the necessary means to carry out my research.

My sincere thanks to Professor José Inácio Martins for all the important electrochemistry insight provided and stimulating discussion on that area, as well as for pushing me to develop other skills beyond the scope of my work.

To Doctor Luís Carlos Matos, I would like to express my sincere gratitude for more than a decade of friendship and for providing a solution to every technical problem that I faced during this project. I would also like to thank you for all the conversations and fun during this journey.

To all my current and former laboratory colleagues for their support, availability, and cooperation. To Raquel and Patrícia, for all the help and support provided whenever needed. To my former 306 colleagues: Miguel, Gabriela and Luísa for all the conversations and fun we had in the laboratory.

To my friends for their friendship, concern, advice and all the good moments over the years.

To my family, especially my parents, for their continuous support and love during my life.

To Filipa, I am profoundly grateful for her unwavering support during this journey and for making this such a wonderful ride. Thank you for always believing in my abilities and being the driving force to endure the pressures and demands of academia. I am grateful for all the adventures and laughs together, and for your presence in my life that propelled my personal growth and helped me reach new heights in my life journey.

To Scooby, for everything.

Abstract

The rising global energy demand and the harmful effects of fossil fuels on the environment have led to an intense focus by the scientific community on technologies that could replace those fuels using renewable sources. Thus, a surge of interest in hydrogen as an energy vector has been arising with the intervention of the European Commission, which proposes using this element as one of the tools to achieve climate neutrality. Hydrogen can be used in a unitized regenerative fuel cell (URFC), which is an environmentally friendly device that operates in two modes: electrolyzer (EL) and fuel cell (FC). In the former mode, water splitting takes place producing the necessary reactants to fuel the FC (H_2 and O_2), whereas the latter generates H_2O and energy. Thus, no polluting products are formed during the URFC's operation. Nonetheless, the oxygen reduction and evolution reactions (ORR and OER, respectively) are sluggish and require bifunctional oxygen catalysts (BOCs) capable of properly catalyzing both reactions. Nowadays, the benchmark catalysts for the oxygen reactions are based on noble metals (Pt/C, RuO_2 and IrO_2) which are scarce and expensive, hence the need to find cheaper suitable replacements. In this context, this PhD thesis focuses on the preparation of highly electroactive BOCs able to replace the current noble metal-based electrocatalysts.

To achieve the aim of this thesis, three different sets of carbon supports (glucose-derived carbons, commercial carbon nanotubes – CNT, and glucose-derived carbon/CNT composites) were successfully employed to prepare ORR/OER electrocatalysts. Their performance towards ORR and/or OER was studied at a laboratory scale and the topmost promising ones were evaluated as realistic FC electrocatalyst layers. The materials were extensively characterized to establish the effect of each property on the materials' electroactivity for each reaction. Twelve different techniques were used to determine the textural (N_2 adsorption-desorption isotherms), physical (electrical conductivity), morphological (Raman spectroscopy, transmission electron microscopy – TEM, scanning electron microscopy – SEM) and chemical (energy-dispersive spectroscopy – EDS, elemental analysis, X-ray photoelectron spectroscopy – XPS, temperature-programmed desorption – TPD, Fourier transform infrared spectroscopy – FTIR, inductively coupled plasma optical emission spectrometry – ICP-OES, X-ray diffraction

– XRD) properties. The insightful knowledge gathered from these techniques was then used to understand the electrocatalysts' electrochemical performance.

The research started by evaluating the influence of the textural properties, specifically microporosity, on its performance towards the ORR. For that, glucose-derived materials were prepared by hydrothermal carbonization (HTC) followed by physical activation using CO_2 atmosphere (activated glucose - AG) for different times or by carbonization (carbonized glucose - CG) under N_2 atmosphere. A direct relationship between the microporosity of the porous carbons and the limiting current density (J_L) was found. Moreover, nitrogen functionalities were incorporated using melamine via ball milling (BM) or via the physical mixture of the carbon support and the melamine. The methodology chosen to functionalize the carbon structures did not seem to influence the amount of nitrogen incorporated but the type of nitrogen functionalities. BM favored the formation of quaternary and oxidized nitrogen groups (N-Q and N-X, respectively), whereas the mixing approach favored the incorporation of pyridinic and pyrrolic groups (N-6 and N-5, respectively). The presence of nitrogen improved the onset potential (E_{onset}) and shifted the reaction mechanism from the two-electron to a closer to the four-electron mechanism. It was also observed that a high N-6/N-5 ratio improved the E_{onset}, whereas a lower N-Q/N-5 ratio favored a more direct reaction mechanism.

Based on these initial results, glucose-derived carbons were prepared by HTC in the presence of CNT or oxidized CNT (CNT_O) to evaluate their influence on the properties of these composites. Additionally, nitrogen functionalities were incorporated by ball-milling the composite and melamine together. The oxygen functionalities on the CNT favored the formation of a more homogenous carbon matrix with enhanced mechanical strength. This improvement partially avoided the crushing of CNT and carbon spheres during the BM process and improved the electrical conductivity of the composite. The synthesized materials with or without nitrogen functionalities were then tested towards the ORR. The presence of CNT and nitrogen on the composites increased the number of active centers on the carbon matrix and improved its chemical reactivity. Thus, the E_{onset} and the J_L increased by 20% and 47%, respectively, in comparison to the CG electrocatalyst due to the N-doped composite's higher electrical conductivity.

Taking these results into consideration, iron and nitrogen functionalities were added to the glucose-derived carbon/CNT_O composite using different approaches. The incorporation of Fe and N in a one-step procedure under H_2 atmosphere led to a larger formation of N-Q and N-X functionalities, whereas the incorporation of nitrogen under N_2 atmosphere after the incorporation of iron mainly generated N-6. The Fe,N-doped composite using the two-step approach exhibited an increase of E_{onset} of 130 mV, compared to CG, with the N-Q surface groups favoring the direct oxygen reduction. However, the Fe,N-doped composite using the one-step technique improved the long-term performance of the electrocatalyst, which may be related to its higher relative amount of N-Q.

To further optimize the ORR performance of the electrocatalysts, iron(II) phthalocyanine (FePc) was incorporated into CG, AG and CNT and their N-doped counterparts. The use of three different supports with different porosities allowed the evaluation of the effect of microporosity on the incorporation of FePc and, consequently, on the ORR performance. FePc was preferentially incorporated inside the porous structure, especially in samples with a more developed microporosity. Nonetheless, the decomposition of melamine to introduce nitrogen functionalities (N-doped carbons) appeared to block some of that microporosity, which then favored the incorporation of FePc nearer the carbons' surface. Regardless of the carbon support employed, the Fe-N_4 complex was the main ORR active site displaying a very high electroactivity. The presence of FePc on the porous carbons led to an E_{onset} of 0.88 V and a direct oxygen reduction mechanism, which greatly approaches the electrocatalysts' ORR performance to that of the commercial Pt/C. On the other hand, the incorporation of FePc on CNT or N-CNT led to an E_{onset} very similar to Pt/C in addition to a four-electron mechanism with < 1% by-product formation and to a half-wave potential ($E_{1/2}$) 40-50 mV higher than that of Pt/C. Moreover, the current density generated is 17% higher than that of Pt/C due to the presence of FePc on CNT's carbon matrix.

In the quest to develop efficient BOCs able to catalyze the ORR and the OER, CNT were further modified by incorporating FePc and/or cobalt(II) phthalocyanine (CoPc). In this study, monometallic samples were prepared with each precursor and mixed in different mass ratios to investigate the importance of each phthalocyanine. The ORR performance

of the synthesized materials was controlled by the relative FePc contribution to the total FePc/CoPc active sites, especially the J_L and reaction mechanism. In fact, two relationships were found, one between J_L and the FePc:CoPc mass ratio and the other one between the reaction mechanism and the metallic active centers' ratios. Interestingly, samples that presented a FePc:CoPc mass ratio ≥ 1 surpassed the ORR performance of the Pt/C catalyst and exhibited similar long-term stability. The presence of both metallic complexes led to a synergetic effect towards the OER. A 1:1 CoPc:FePc mass ratio displayed the lowest OER potential at 10 mA cm^{-2} (E_{10}, 1.67 V) of all prepared samples and produced the lowest potential gap between oxygen reactions (ΔE = 0.81 V), which is much lower than the commercial Pt/C (1.04 V) and RuO_2 (0.98 V), demonstrating the high potential of these electrocatalysts to replace noble metals.

To further improve the bifunctional oxygen electroactivity of the CNT, a different cobalt precursor was incorporated: cobalt(II) nitrate hexahydrate. Several Co-doped CNT catalysts were prepared using different thermal treatment temperatures and/or atmospheres. It was observed that increasing temperatures and employing an H_2 atmosphere favored the formation of Co^{2+}, which enhanced the oxygen evolution reaction. The optimized Co-doped CNT was then physically mixed with the FePc-doped CNT. A sample with 1:1 mass ratio produced an OER electroactivity (E_{10} = 1.64 V) close to the Co-doped CNT, using only half of the cobalt content of the monometallic sample, and a higher $E_{1/2}$ (0.88 V) than Pt/C (0.83 V). Furthermore, this sample also provided the lowest ΔE (0.76 V) of the synthesized samples and commercial electrocatalysts, even surpassing most state-of-the-art carbon-supported electrocatalysts.

The materials' bifunctional oxygen electroactivity was finally assessed at a larger scale. The most promising electrocatalysts evaluated at a laboratory scale, prepared by incorporation of FePc and cobalt nitrate on CNT, were tested as realistic fuel cell electrocatalyst layers at relevant current densities. The evaluation of the electrochemical ORR and OER confirmed the activity trends previously observed for both reactions, in which FePc excels at ORR, whereas cobalt primarily catalyzes the OER. Interestingly, the monometallic FePc-doped CNT displayed higher ORR electroactivities than state-of-the-art Fe-N-C electrodes. However, this catalyst's performance sharply decreased after stability measurements, which makes unfeasible its commercialization. Nonetheless, the

incorporation of FePc on the Co-doped CNT was crucial in achieving the highest ORR long-term stability and generating high current densities (-2000 mA cm^{-2}) at potentials similar to those used at the fuel cell scale (0.6 V). The synergy between FePc and the cobalt species made it viable to continue the scale-up pursuit of this electrocatalyst as it presented very interesting ORR performances. This sample also achieved the highest OER performance (before and after stability measurements); hence, it is the most electroactive bifunctional oxygen electrocatalyst of the evaluated carbons, demonstrating its high potential to replace noble metal materials.

Overall, the synthesized material presented high electroactivities towards both ORR and OER, surpassing those of the benchmark catalysts (Pt/C and RuO_2) at the laboratory scale. Moreover, at the catalyst layer scale, ORR and OER electroactivities similar to those of Pt/C and RuO_2, respectively, were achieved. Therefore, the main objective of designing highly electroactive bifunctional oxygen catalysts was achieved.

Resumo

O aumento da procura global de energia e os efeitos prejudiciais dos combustíveis fósseis sobre o ambiente levaram a que a comunidade científica se concentrasse intensamente nas tecnologias que poderiam substituir esses combustíveis utilizando fontes renováveis. Assim, surgiu um grande interesse pelo hidrogénio como vetor energético, alavancado pela Comissão Europeia, que propõe a utilização deste elemento como um dos instrumentos para alcançar a neutralidade climática. O hidrogénio pode ser utilizado numa célula de combustível unitária regenerativa (URFC), que é um dispositivo ambientalmente mais sustentável que funciona em dois modos: eletrolisador (EL) e célula de combustível (FC). No primeiro, ocorre a eletrólise da água e geram-se os reagentes necessários para a FC (H_2 e O_2), enquanto que no segundo se obtém H_2O e energia. Assim, não há formação de produtos poluentes durante o funcionamento da URFC. No entanto, as reações de redução e evolução do oxigénio (ORR e OER, respetivamente) são lentas e requerem catalisadores de oxigénio bifuncionais (BOC) capazes de catalisar adequadamente ambas as reações. Hoje em dia, os catalisadores de referência para as reações de oxigénio são à base de metais nobres (Pt/C, RuO_2 and IrO_2), que são escassos e caros, daí a necessidade de encontrar substitutos adequados mais baratos. Neste contexto, esta tese de doutoramento foca-se na preparação de BOC altamente eletroativos capazes de substituir os atuais eletrocatalisadores à base de metais nobres.

Para atingir o objetivo desta tese, três conjuntos diferentes de suportes de carbono (materiais de carbono derivados de glucose, nanotubos de carbono comerciais - CNT, e compósitos destes dois materiais) foram utilizados com sucesso na preparação de eletrocatalisadores para ORR/OER. Os seus desempenhos na ORR e/ou OER foram estudados à escala laboratorial e os mais promissores foram avaliados numa configuração de meia-célula de elétrodo de difusão de gás. Os materiais foram extensivamente caracterizados para avaliar o efeito de cada propriedade na eletroatividade dos materiais para cada reação. Foram utilizadas doze técnicas diferentes para determinar: propriedades texturais (isotérmicas de adsorção-dessorção de N_2), físicas (condutividade elétrica); morfológicas (espectroscopia Raman, microscopia eletrónica de transmissão - TEM, microscopia eletrónica de varrimento - SEM); e químicas (espectroscopia dispersiva de

energia - EDS, análise elementar, espectroscopia de fotoeletrões de raios X - XPS, dessorção programada por temperatura - TPD, espectroscopia de infravermelhos por transformada de Fourier - FTIR, espectrometria de emissão ótica com plasma indutivamente acoplado - ICP-OES, difração de raios X - XRD). O conhecimento detalhado obtido a partir destas técnicas foi então utilizado para compreender o desempenho eletroquímico dos eletrocatalisadores.

O estudo começou por avaliar a influência das propriedades texturais dos materiais, particularmente o efeito da microporosidade, na ORR. Para tal, materiais de carbono derivados de glucose foram preparados por síntese hidrotérmica (HTC), seguindo-se uma ativação física em atmosfera de CO_2 (glucose ativada – AG) para diferentes tempos ou uma carbonização (glucose carbonizada – CG) em atmosfera de N_2. Foi encontrada uma relação direta entre a microporosidade dos carvões porosos e a densidade de corrente limite (J_L). Além disso, foram incorporadas funcionalidades de azoto por mistura física dos suportes de carbono e da melamina ou através da respetiva moagem num moinho de bolas (BM). A metodologia escolhida para funcionalizar as estruturas de carbono não pareceu influenciar a quantidade, mas sim o tipo de funcionalidades de azoto incorporado. A utilização do BM favoreceu a formação de grupos de azoto quaternário e oxidado (N-Q e N-X, respetivamente), enquanto a mistura física favoreceu a incorporação de grupos piridínicos e pirrólicos (N-6 e N-5, respetivamente). A presença de azoto melhorou o potencial de início (E_{onset}) e deslocou o mecanismo de reação de um mecanismo de dois-eletrões para um mecanismo mais próximo de quatro-eletrões. Observou-se também que um rácio N-6/N-5 elevado melhorou o E_{onset} enquanto um rácio N-Q/N-5 mais baixo favoreceu um mecanismo de reação mais direto.

Considerando estes resultados iniciais, os materiais de carbono derivados da glucose foram preparados por HTC na presença de CNT ou CNT oxidados (CNT_O) para avaliar a sua influência nas propriedades destes compósitos. Adicionalmente, foram incorporadas funcionalidades de azoto por moagem de bolas do compósito e da melamina em conjunto. As funcionalidades de oxigénio nos CNT favoreceram a formação de uma matriz de carbono mais homogénea com maior resistência mecânica. Esta melhoria evitou parcialmente a trituração dos CNT e das esferas de carbono durante o processo de BM e melhorou a condutividade elétrica do compósito. Os materiais sintetizados com ou

sem funcionalidades de azoto foram então testados na ORR. A presença de CNT e azoto nos compósitos aumentou o número de centros ativos na matriz de carbono e melhorou a sua atividade. Assim, o E_{onset} e a J_L aumentaram 20% e 47%, respetivamente, em comparação com o eletrocatalisador de glucose carbonizada (CG) devido à maior condutividade elétrica do compósito dopado com azoto.

Tendo estes resultados em consideração, foram adicionadas funcionalidades de ferro e azoto ao compósito de carbono derivado da glucose/CNT_O utilizando diferentes abordagens. A incorporação de Fe e N num procedimento de um único passo sob atmosfera de H_2 levou a uma maior formação de funcionalidades N-Q e N-X, enquanto a incorporação de azoto sob atmosfera N_2 após a incorporação de ferro gerou principalmente N-6. O compósito dopado com Fe e N preparado através da abordagem de dois passos exibiu um aumento do E_{onset} de 130 mV, em comparação com a amostra CG, com os grupos de superfície N-Q a favorecerem a redução direta do oxigénio. Contudo, o compósito dopado com Fe e N usando a técnica de um único passo melhorou o desempenho a longo prazo dos eletrocatalisadores, o que pode estar relacionado com a sua maior quantidade relativa de N-Q.

Para otimizar ainda mais o desempenho dos eletrocatalisadores na ORR, foi incorporada ftalocianina de ferro (II) (FePc) nos suportes CG, AG e CNT e nos seus homólogos dopados com azoto. A utilização de três suportes diferentes com porosidades distintas permitiu a avaliação do efeito da microporosidade na incorporação da FePc e, consequentemente, no desempenho na ORR. A FePc foi preferencialmente incorporada dentro da estrutura porosa, especialmente em amostras com uma microporosidade mais desenvolvida. No entanto, a decomposição da melamina para introduzir funcionalidades de azoto (materiais de carbono dopados com azoto) pareceu bloquear alguma dessa microporosidade, o que favoreceu então a incorporação da FePc mais próximo da superfície dos materiais. Independentemente do suporte de carbono utilizado, o complexo $Fe\text{-}N_4$ foi o principal centro ativo na ORR, com uma eletroatividade muito elevada. A presença da FePc nos materiais de carbono porosos levou a um E_{onset} de 0.88 V e a um mecanismo direto de redução de oxigénio, que se aproxima muito do desempenho do eletrocatalisador comercial de Pt/C na ORR. Por outro lado, a incorporação da FePc em CNT ou N-CNT levou a um E_{onset} muito semelhante ao da Pt/C, para além de um

mecanismo de quatro eletrões com formação de subprodutos < 1% e a um $E_{1/2}$ 40-50 mV superior ao da Pt/C. Além disso, a densidade de corrente gerada é 17% superior à da Pt/C devido à presença da FePc na matriz de carbono dos CNT.

Na procura do desenvolvimento de BOC eficientes capazes de catalisar a ORR e a OER, foram adicionalmente modificados CNT incorporando FePc e/ou ftalocianina de cobalto (II) (CoPc). Neste estudo, foram preparadas amostras monometálicas com cada precursor e misturadas em diferentes rácios de massa para investigar a importância de cada ftalocianina. O desempenho na ORR dos materiais sintetizados foi controlado pela contribuição relativa da FePc para o total de centros ativos de FePc/CoPc, especialmente a J_L e o mecanismo de reação. De facto, foram encontradas duas relações entre a J_L e o rácio mássico FePc:CoPc e entre o mecanismo de reação e os rácios dos centros ativos metálicos. Curiosamente, amostras que apresentavam um rácio de massa FePc:CoPc ≥ 1 superaram o desempenho do catalisador Pt/C na ORR e exibiram uma estabilidade semelhante em ensaios de longa duração. A presença de ambos os complexos metálicos levou a um efeito sinergético em relação à OER. Uma relação de massa CoPc:FePc de 1:1 mostrou o menor potencial para a OER a 10 mA cm^{-2} (E_{10}, 1.67 V) de todas as amostras preparadas e apresentou o menor intervalo de potencial entre as reações de oxigénio (ΔE = 0.81 V), que é muito inferior ao do Pt/C comercial (1.20 V) e RuO_2 (1.41 V), demonstrando o elevado potencial destes eletrocatalisadores para substituir metais nobres.

Para melhorar ainda mais a eletroatividade bifuncional dos CNT para as reações de oxigénio, foi incorporado um precursor de cobalto diferente: o nitrato de cobalto (II) hexahidratado. Vários catalisadores de CNT dopados com Co foram preparados utilizando diferentes temperaturas e/ou atmosferas durante o tratamento térmico. Observou-se que o aumento das temperaturas e a utilização de uma atmosfera de H_2 favoreceu a formação de Co^{2+}, o que melhorou a reação de evolução do oxigénio. Os CNT otimizados dopados com Co foram então fisicamente misturados com os CNT dopados com FePc. Uma amostra com rácio mássico de 1:1 produziu uma eletroatividade para a OER (E_{10} = 1.64 V) próxima dos CNT dopados com Co, utilizando apenas metade do conteúdo de cobalto da amostra monometálica, e um $E_{1/2}$ (0.88 V) superior à Pt/C (0.83 V). Além disso, esta amostra também produziu a mais baixa ΔE (0.76 V) das

amostras sintetizadas e eletrocatalisadores comerciais, ultrapassando mesmo a maioria dos eletrocatalisadores suportados em materiais de carbono do estado-da-arte.

A eletroatividade bifuncional para as reações de oxigénio dos materiais foi finalmente avaliada numa escala maior. Os eletrocatalisadores mais promissores a nível laboratorial, preparados através da incorporação da FePc e nitrato de cobalto nos CNT, foram testados numa configuração de meia-célula de elétrodo de difusão de gás a densidades de corrente relevantes. A avaliação da eletroatividade na ORR e OER confirmou as tendências de atividade previamente observadas para ambas as reações, nas quais a FePc se sobressai na ORR, enquanto o cobalto catalisa principalmente a OER. Curiosamente, a amostra monometálica de CNT dopados com FePc mostrou eletroatividades na ORR mais elevadas do que os elétrodos Fe-N-C de última geração. Contudo, a incorporação da FePc nos CNT dopados com Co foi crucial para alcançar a maior estabilidade de longa duração na ORR e gerar densidades de corrente elevadas (-2000 mA cm^{-2}) a potenciais semelhantes àqueles usados à escala da célula de combustível (0.6 V). A sinergia entre FePc e espécies de cobalto tornou viável continuar na busca de aumentar a escala deste eletrocatalisador dado que apresentou desempenhos na ORR muito interessantes. Esta amostra também alcançou o desempenho mais elevado na OER (antes e após medições de estabilidade); por conseguinte, é o eletrocatalisador bifuncional de oxigénio mais promissor dos materiais de carbono avaliados, demonstrando o seu elevado potencial para substituir os eletrocatalisadores de metais nobres.

No geral, o material sintetizado apresentou elevadas eletroatividades tanto para a ORR como para a OER, superando as dos catalisadores de referência (Pt/C e RuO_2) na escala laboratorial. Além disso, à escala de meia-célula de elétrodo de difusão de gás, foram alcançadas eletroatividades na ORR e OER semelhantes às da Pt/C e RuO_2, respetivamente. Como tal, o objetivo principal de desenhar catalisadores de oxigénio bifuncionais altamente eletroativos foi alcançado.

Table of Contents

Preface i

Acknowledgments iii

Abstract v

Resumo xi

Table of Contents xvii

List of Figures xxv

List of Tables xxxvii

List of Abbreviations and Variables xli

Chapter 1 - *State-of-the-art, Motivation, Objectives and Thesis Outline* 1

1.1. Unitized Regenerative Fuel Cell (URFC) 2

1.1.1. Oxygen Reduction Reaction 5

1.1.2. Oxygen Evolution Reaction 8

1.1.3. Electrocatalysts 10

1.2. Carbon materials 11

1.2.1. Textural properties 12

1.2.2. Surface chemistry 15

1.3. Motivation and objectives 29

1.4. Thesis outline 32

1.5. References 35

Chapter 2 - *Materials and Methods* 45

2.1. Reagents 46

2.2. Electrocatalysts preparation 47

2.2.1. Carbon supports 47

2.2.2. Nitrogen functionalization 50
2.2.3. Incorporation of transition metals 51
2.2.4. Incorporation of nitrogen and transition metals 53
2.3. Physicochemical characterization 58
2.3.1. Textural properties 58
2.3.2. Physical properties 60
2.3.3. Morphological properties 61
2.3.4. Chemical properties 64
2.4. Electrochemical characterization 72
2.4.1. Electrochemical setup 72
2.4.2. Working electrodes 73
2.4.2.1. Rotating disk electrode (RDE) 73
2.4.2.2. Rotating ring-disk electrode (RRDE) 74
2.4.3. Electrode preparation 75
2.4.4. Oxygen Reduction Reaction (ORR) and Oxygen Evolution Reaction (OER) 76
2.4.5. Oxygen bifunctionality 81
2.4.6. Additional electrochemical characterizations 81
2.5. Electrochemical application 83
2.6. References 90
Chapter 3 - *Glucose-derived carbons with tailored properties as electrocatalysts for the oxygen reduction reaction* 93
Abstract 94
3.1. Introduction 95
3.2. Experimental 97

3.2.1. Preparation of carbon materials 97
3.2.2. Materials characterization 98
3.2.3. Electrochemical characterization 99
3.3. Results and discussion 100
3.3.1. Effect of microporosity 100
3.3.2. Effect of the surface chemistry 104
3.3.3. Electrochemical measurements 111
3.4. Conclusions 116
3.5. Supporting Information 117
3.5.1. Effect of microporosity 117
3.5.2. Effect of the surface chemistry 119
3.6. References 126
Chapter 4 - *Hydrothermal carbon/carbon nanotube composites as electrocatalysts for the oxygen reduction reaction* 129
Abstract 130
4.1. Introduction 131
4.2. Materials and methods 133
4.2.1. Chemicals and materials 133
4.2.2. Materials preparation 133
4.2.3. Physicochemical characterization 134
4.2.4. Electrode preparation 135
4.2.5. Electrochemical measurements 135
4.3. Results and discussion 136
4.3.1. Textural, morphological and chemical properties 136

4.3.2. Electrochemical measurements 144
4.4. Conclusions 148
4.5. Supplementary Information 149
4.5.1. Electrocatalyst's properties 149
4.5.2. Electrochemical measurements 151
4.5.3. Equations 152
4.6. References 155
Chapter 5 - *Improving the electrocatalytic activity of glucose/carbon nanotube composites for the oxygen reduction reaction by doping with nitrogen and iron* 159
Abstract 160
5.1. Introduction 161
5.2. Experimental 163
5.2.1. Preparation of electrocatalysts 163
5.2.2. Chemical and textural characterization 164
5.2.3. Electrochemical characterization 165
5.3. Results and discussion 167
5.3.1. Chemical properties 167
5.3.2. Electrochemical assessments 174
5.4. Conclusions 179
5.5. Supplementary Information 181
5.6. References 187
Chapter 6 - *Highly electroactive N–Fe hydrothermal carbons and carbon nanotubes for the oxygen reduction reaction* 191
Abstract 192
6.1. Introduction 193

6.2. Experimental 195
6.2.1. Preparation of electrocatalysts 195
6.2.2. Textural and chemical characterization 196
6.2.3. Electrochemical characterization 197
6.3. Results and discussion 199
6.3.1. Textural and morphological properties 199
6.3.2. Chemical properties 202
6.3.3. Electrochemical assessments 207
6.4. Conclusions 218
6.5. Supplementary Information 219
6.5.1. Experimental 219
6.5.2. Results and discussion 221
6.5.2.1. Textural properties 221
6.5.2.2. Chemical properties 222
6.5.2.3. Electrochemical assessment 227
6.6. References 229
Chapter 7 - *Fe, Co, N-doped carbon nanotubes as bifunctional oxygen electrocatalysts* 233
Abstract 234
7.1. Introduction 235
7.2. Experimental 237
7.2.1. Preparation of electrocatalysts 237
7.2.2. Textural and chemical characterization 238
7.2.3. Electrochemical characterization 239

7.3. Results and discussion 243
7.3.1. Chemical properties 243
7.3.2. Morphological and textural properties 245
7.3.3. Electrochemical assessments 248
7.4. Conclusions 265
7.5. Supplementary Information 266
7.5.1. Electrocatalysts preparation 266
7.5.2. Electrocatalysts characterization 269
7.6. References 276
Chapter 8 - *Optimization of cobalt on CNT towards the oxygen evolution reaction and its synergy with iron (II) phthalocyanine as bifunctional oxygen electrocatalyst* 281
Abstract 282
8.1. Introduction 283
8.2. Experimental 285
8.2.1. Preparation of electrocatalysts 285
8.2.2. Chemical and textural characterization 285
8.2.3. Electrochemical characterization 286
8.3. Results and discussion 289
8.3.1. Chemical properties 289
8.3.2. Electrochemical assessments 295
8.3.2.1. Oxygen Evolution Reaction 295
8.3.2.2. Oxygen Reduction Reaction 300
8.3.2.3. Bifunctional oxygen electrocatalysis 304
8.4. Conclusions 306

8.5. Supplementary Information 307
8.5.1. Electrocatalysts characterization 307
8.5.2. Electrochemical assessments 313
8.6. References 315
Chapter 9 - *Gas diffusion electrode evaluation* 319
Abstract 320
9.1. Introduction 321
9.2. Experimental 322
9.2.1. Catalyst ink and electrode preparation 322
9.2.2. GDE half-cell measurements 323
9.3. Results and discussion 324
9.3.1. Oxygen Reduction Reaction 324
9.3.2. Oxygen Evolution Reaction 328
9.3.3. Bifunctional Oxygen Electrocatalysis 333
9.4. Conclusions 333
9.5. References 335
Chapter 10 *Conclusions and Future Work* 337
10.1. Main Conclusions 338
10.1.1. Oxygen Reduction Reaction electrocatalysts 338
10.1.2. Bifunctional oxygen electrocatalysts 342
10.2. Future work 348
Appendixes 351
Appendix A – Method's equations 352

Appendix B – Full agreement of the co-authors on the inclusion of the manuscripts 358

Appendix C – Published articles 363

List of Figures

Figure 1.1 - Unitized regenerative fuel cell operation schematics (adapted from [17])... 4

Figure 1.2 - Scheme of the reaction losses in a fuel cell and an electrolyzer (adapted from [17]). 4

Figure 1.3 - The direct ORR mechanism for acid (blue line) and alkaline (red line) conditions, in which the black line indicates the formation of intermediates in both reactions. The green line indicates the indirect ORR mechanism formation of by-products for both acidic (blue line) and alkaline conditions (red line). 6

Figure 1.4 – The commonly accepted OER mechanism for acid (blue line) and alkaline (red line) conditions, and an alternative OER route (green line). (adapted from [29]). ... 9

Figure 1.5 – Oxygen, nitrogen and sulfur surface groups and techniques for their identification/quantification [58]..... 15

Figure 1.6 - Porphyrin and phthalocyanine structures. Grey – carbon, white – hydrogen, blue – nitrogen.……..……25

Figure 1.7 – Materials synthesized and their respective target oxygen reaction(s) to accomplish the objectives proposed. 30

Figure 2.1 - Scheme of the synthesis methodologies employed to prepare carbonized and activated glucose-derived carbons..... 48

Figure 2.2 - Scheme of the synthesis methodologies employed to prepare glucose-derived carbon/CNT composites. 50

Figure 2.3 - Scheme of the synthesis methodologies employed to prepare N-doped carbons. 51

Figure 2.4 - Scheme of the synthesis methodologies employed to prepare Fe-doped carbon composites. 52

Figure 2.5 - Scheme of the synthesis methodologies employed to prepare Fe-doped carbon composites. 53

Figure 2.6 - Scheme of the synthesis methodologies employed to prepare Fe,N-doped carbon composites. 54

Figure 2.7 - Scheme of the synthesis methodologies employed to prepare Fe,N-doped carbon electrocatalysts.....55

Figure 2.8 - Scheme of the synthesis methodologies employed to prepare CoPc,FePc-doped carbons. 56

Figure 2.9 - Scheme of the synthesis methodologies employed to prepare Co,Fe,N-doped carbons.....58

Figure 2.10 - Three-electrode cell used for oxygen reduction and evolution reactions electrochemical characterization (a), rotating disc electrode (b) and rotating ring-disc electrode (c). 73

Figure 2.11 - A typical ORR linear sweep voltammetry curve with different reaction regions and main ORR parameters…….…….77

Figure 2.12 - Mechanisms of the oxygen reduction reaction……..……79

Figure 2.13 - Electrochemical impedance spectroscopy Nyquist plot regions (Reprinted with permission from [31])……..……....82

Figure 2.14 - a) Photograph of the assembled half-cell gas diffusion electrode setup. b) Cross-section of the cell showing the position of working (WE), counter (CE), and reference electrode (RE) and the connection of the reference electrode via a lugging capillary. c) Function principle of the characterization technique (Reprinted with permission from [32])……..……83

Figure 2.15 - Comparison of different levels of electrochemical catalyst (layer) evaluation. Reprinted with permission from [17]. Copyright 2022 American Chemical Society……...……..85

Figure 3.1 - N_2 adsorption/desorption isotherms (a) and pore size distributions (b) of the activated carbons. 101

Figure 3.2 - Linear sweep voltammetry recorded in an O_2-saturated 0.1 mol L^{-1} KOH electrolyte at 1600 rpm (a) and Nyquist plot obtained from electrochemical impedance spectroscopy (b). 102

Figure 3.3 - Relation between BET surface area and the limiting current density of the activated samples..... 103

Figure 3.4 - Deconvolution of the XPS N 1s spectra for N-AG_{BM} (a) N-AG_C (b), N-CG_{BM} (c) and N-CG_C (d)..... 107

Figure 3.5 - TPD profiles of CO_2 for activated samples (a) and carbonized samples (b) and CO profiles of activated samples (c) and carbonized samples (d)..... 108

Figure 3.6 - N_2 adsorption/desorption isotherms at -196 ºC for activated carbons (a) and carbonized carbons (b). 109

Figure 3.7 - Linear sweep voltammetry recorded in an O_2-saturated 0.1 mol L^{-1} KOH electrolyte at 1600 rpm for activated (a) and carbonized (b) samples..... 111

Figure 3.8 - Relation between BET surface area and limiting current density of undoped samples and doped samples..... 114

Figure 3S.1 - TPD profiles of CO_2 (a) and CO (b) for AG_{6h} and AG_{1h}..... 118

Figure 3S.2 - Hydrogen peroxide production for sample AG_{6h}..... 118

Figure 3S.3 - C 1s spectra deconvolution of AG (a), AG_{BM} (b), N-AG_{BM} (c), N-AG_C (d), CG (e), CG_{BM} (f), N-CG_{BM} (g), N-CG_C (h). 119

Figure 3S.4 - O 1s spectra deconvolution of AG (a), AG_{BM} (b), N-AG_{BM} (c), N-AG_C (d), CG (e), CG_{BM} (f), N-CG_{BM} (g), N-CG_C (h). 120

Figure 3S.5 - TPD profile deconvolution of AG for CO_2 (a) and CO (b). 121

Figure 3S.6 - TPD profile deconvolution of AG_{BM} for CO_2 (a) and CO (b). 121

Figure 3S.7 - TPD profile deconvolution of CG for CO_2 (a) and CO (b). 121

Figure 3S.8 - TPD profile deconvolution of CG_{BM} for CO_2 (a) and CO (b). 122

Figure 3S.9 - Pore size distributions for activated samples (a) and carbonized samples (b). 122

Figure 3S.10 - O_2-saturated cyclic voltammograms for activated samples (a) and carbonized samples (b) and N_2-saturated cyclic voltammograms for activated samples (c) and carbonized samples (d). 124

Figure 3S.11 - Number of electrons exchanged for activated samples (a) and carbonized samples (b) at different potentials. 125

Figure 3S.12 - Hydrogen peroxide production for activated samples. 125

Figure 4.1 - N_2 adsorption-desorption isotherms of carbonized glucose and undoped and N-doped carbon composites prepared by introducing CNT (a) and oxidized CNT (b). Filled symbols: adsorption; open symbols: desorption. 137

Figure 4.2 - SEM micrographs of carbonized glucose (a) and carbon composites prepared by introducing CNT (b) and oxidized CNT (c). 138

Figure 4.3 - (a) FTIR spectra of hydrothermal glucose prepared without CNT (G) and in the presence of CNT (G/CNT) and CNT_{oxi} (G/CNT_{oxi}) and (b) Raman spectra of carbonized glucose and undoped and N-doped carbon composites prepared by introducing CNT and oxidized CNT. 140

Figure 4.4 - XPS spectra of N 1s for N-doped composites N-CG/CNT (a) and N-CG/CNT_{oxi} (b). 143

Figure 4.5 - Linear sweep voltammograms (LSV) and the number of electrons transferred measured at 1600 rpm for the carbonized glucose and the undoped and N-doped carbon composites prepared by introducing CNT (a and c) and oxidized CNT (b and d). 145

Figure 4.6 - Chronoamperometry experiments measured at 0.4 V vs RHE for 10000 seconds for the carbonized glucose and the undoped and N-doped carbon composites prepared by introducing CNT (a) and oxidized CNT (b). 147

Figure 4S.1 - N_2 adsorption-desorption isotherms of carbon nanotubes and oxidized carbon nanotubes. 149

Figure 4S.2 - SEM micrographs of N-doped composites with carbon nanotubes and with oxidized carbon nanotubes. 150

Figure 4S.3 - Cyclic Voltammograms measured at a scan rate of 5 mV s^{-1} in an electrolyte saturated with N_2 and O_2 for carbonized glucose (a), composite CG/CNT (b) and composite CG/CNT_{oxi} (c). 151

Figure 4S.4 - Cyclic Voltammograms measured at a scan rate of 5 mV s^{-1} in an electrolyte saturated with N_2 and O_2 for N-doped composites prepared with CNT (a) and CNT_{oxi} (b). 151

Figure 4S.5 - Relationship between the limiting current density and electrical conductivity. 152

Figure 5.1 - Scheme of the synthesis methodologies employed to prepare Fe,N-doped carbon electrocatalysts. 164

Figure 5.2 - Deconvolution of the N 1s X-ray photoelectron spectra of $N\text{-}CG_{5Fe}$ (a), $CG_{5Fe,N}$ (b) $N\text{-}CG/CNT_{O,5Fe}$ (c) and $CG/CNT_{O,5Fe,N}$ (d) electrocatalysts…….. 170

Figure 5.3 - SEM micrographs of CG (a), CG/CNT_O (b), CG_{5Fe} (c), $N\text{-}CG_{5Fe}$ (d), $CG_{5Fe,N}$ (e), $CG/CNT_{O,5Fe}$ (f), $N\text{-}CG/CNT_{O,5Fe}$ (g) and $CG/CNT_{O,5Fe,N}$ (h) electrocatalysts…….….172

Figure 5.4 - Disk current density produced by undoped and Fe-doped (a) and Fe,N-doped (b) electrocatalysts at 1600 rpm in O_2-saturated electrolyte (0.1 mol L^{-1} KOH) and number of electrons exchanged during the oxygen reduction reaction for undoped and Fe-doped (c) and Fe,N-doped (d) electrocatalysts……175

Figure 5.5 - Chronoamperometry measurements (0.4 V for 10000 s) for undoped and Fe-doped electrocatalysts (a), and Fe,N-doped electrocatalysts (b) in an O_2-saturated 0.1 mol L^{-1} KOH electrolyte at 1600 rpm..... 178

Figure 5S.1 - XPS survey spectra of the prepared Fe,N-doped CG (a,b) and CG/CNT composites (c,d) electrocatalysts, in which $N\text{-}CG_{5Fe}$ and $N\text{-}CG/CNT_{O,5Fe}$ were prepared using a two-step method and $CG_{5Fe,N}$ and CG/CNT_O were prepared using a one-step method. 181

Figure 5S.2 - N_2 adsorption-desorption isotherms at -196 ºC of undoped, CG_{XFe} and $CG/CNT_{O,5Fe}$ (a), and $N\text{-}CG_{5Fe}$, $N\text{-}CG/CNT_{O,5Fe}$, $CG_{5Fe,N}$ and $CG/CNT_{O,5Fe,N}$ (b) electrocatalysts. 182

Figure 5S.3 - Elemental mapping of N-CG/$CNT_{O,5Fe}$ (a) and CG/$CNT_{O,5Fe,N}$ (b). Red – Carbon, Yellow – Iron. 182

Figure 5S.4 - Raman spectra of undoped and Fe-doped electrocatalysts (a), and Fe,N-doped electrocatalysts (b). 183

Figure 5S.5 - Cyclic voltammograms recorded at 5 mV s^{-1} in N_2- and O_2-saturated 0.1 mol L^{-1} KOH electrolyte from 1.15 V to -0.05 V. 184

Figure 5S.6 - Disk current density produced (a) at 1600 rpm in O_2-saturated electrolyte (0.1 mol L^{-1} KOH) and number of electrons exchanged during the oxygen reduction reaction for Pt/C. 185

Figure 5S.7 - Nyquist plots for CG and CG/CNT_O obtained by electrochemical impedance spectroscopy. 185

Figure 5S.8 - Onset potential (a) and current density at a potential of 0.4 V (b) obtained from the linear sweep voltammetry curves of Figure 5a (a) for the CG_{XFe} samples versus the percentage of Fe calculated by ICP. 186

Figure 6.1 - N_2 adsorption-desorption isotherms of carbonized samples (a), activated samples (b) and carbon nanotubes (c). 199

Figure 6.2 - Schematic illustration of the pore blockage and the effect on the incorporation of FePc. 200

Figure 6.3 - SEM micrographs of CG_{FePc} (a), AG_{FePc} (b), CNT_{FePc} (c), N-CG_{FePc} (d), N-AG_{FePc} (e) and N-CNT_{FePc} (f). 201

Figure 6.4 - Relative content of each nitrogen functionality in each carbon sample functionalized with melamine and/or that incorporated FePc. 206

Figure 6.5 - N_2-saturated cyclic voltammograms for carbonized samples (a), activated samples (b) and CNTs (c) in 0.1 mol L^{-1} KOH electrolyte at 5 mV s^{-1}. 208

Figure 6.6 - Linear sweep voltammetry recorded in an O_2-saturated 0.1 mol L^{-1} KOH electrolyte at 1600 rpm for carbonized samples (a), activated samples (b) and CNTs (c) and the production of hydrogen peroxide for carbonized samples (d), activated samples (e) and CNTs (f). 210

Figure 6.7 - Chronoamperometry measurements for carbonized samples (a), activated samples (b) and CNTs (c) applying 0.4 V during 10000 s at 1600 rpm in 0.1 mol L^{-1} KOH electrolyte. 216

Figure 6S.1 - Linear sweep voltammogram of samples CG_{FePc}, $CG_{2x\text{-}FePc}$ and 800-CG_{FePc} at 5 mV s^{-1} and 1600 rpm in 0.1 mol L^{-1} KOH. 220

Figure 6S.2 - Pore size distribution of CG and AG. 221

Figure 6S.3 - Deconvolution of the C 1s spectrum for all the prepared samples. 223

Figure 6S.4 - Deconvolution of the N 1s spectrum for the functionalized carbon materials. 224

Figure 6S.5 - Deconvolution of the Fe 2p spectrum for samples CG_{FePc}, N-CG_{FePc}, CNT_{FePc} and N-CNT_{FePc}. 225

Figure 6S.6 - Deconvolution of the N 1s spectrum of FePc. 225

Figure 6S.7 - Elemental mapping analysis of N-CG_{FePc} (a) and N-CNT_{FePc} (b). Yellow – Carbon, Blue – Oxygen, Green – Nitrogen, Red – Iron. 226

Figure 6S.8 - Cyclic voltammogram of CG_{FePc}, AG_{FePc} and CNT_{FePc} at 100 mV s^{-1} in N_2-saturated 0.1 mol L^{-1} KOH. 227

Figure 6S.9 - Cyclic voltammogram of the prepared electrocatalysts at 100 mV s^{-1} in 0.1 mol L^{-1} KOH. 228

Figure 7.1 - SEM micrographs of CNT_{Fe} (a) and $50CNT_{Co}/50CNT_{Fe}$ (b). 246

Figure 7.2 - Raman spectra of CNT and the monometallic electrocatalysts (a) and bimetallic electrocatalysts (b). 247

Figure 7.3 - N_2 adsorption-desorption isotherms at -196 ºC of CNT, and the monometallic and bimetallic electrocatalysts. 248

Figure 7.4 - Cyclic voltammograms recorded at 100 mV s^{-1} in N_2-saturated 0.1 mol L^{-1} KOH electrolyte from 1.10 to -0.05 V using a rotating ring-disk glassy carbon electrode with a Pt ring. 249

Figure 7.5 - Cyclic voltammograms recorded at 5 mV s^{-1} in N_2 (black) and O_2-saturated (orange) 0.1 mol L^{-1} KOH electrolytes from 1.10 to -0.05 V of CNT (a), CNT_{Co} (b), CNT_{Fe} (c), $75CNT_{Co}/25CNT_{Fe}$ (d), $50CNT_{Co}/50CNT_{Fe}$ (e) and $25CNT_{Co}/75CNT_{Fe}$ (f) using a rotating ring-disk glassy carbon electrode with a Pt ring. 251

Figure 7.6 - Disk current density (a) and ring current (b) of the linear sweep voltammetry curves recorded at 5 mV s^{-1} in O_2-saturated 0.1 mol L^{-1} KOH electrolyte at 1600 rpm from 1.10 V to 0.15 V using a rotating ring-disk glassy carbon electrode with a Pt ring, production of hydrogen peroxide (c) and number of electrons exchanged (d) for the prepared samples. 253

Figure 7.7 - Schematic illustration of H_2O_2 adsorption on iron and cobalt phthalocyanines and their respective reaction mechanisms. 255

Figure 7.8 - Current density obtained from the linear sweep voltammetry curves of Figure 7.6a (a) and the number of electrons exchanged obtained from Figure 7.6d (b) at a potential of 0.4 V for the prepared samples versus the percentage of FePc against the total Pcs content calculated by ICP. 256

Figure 7.9 - Chronoamperometry measurements for the prepared samples (a) and methanol resistance of sample $50CNT_{Co}/50CNT_{Fe}$ (b) applying 0.4 V during 10000 s at 5 mV s^{-1} and 1600 rpm in an O_2-saturated 0.1 mol L^{-1} KOH electrolyte using a rotating disk glassy carbon electrode. 257

Figure 7.10 - Linear sweep voltammetry curves recorded at 5 mV s^{-1} in an N_2-saturated 0.1 mol L^{-1} KOH electrolyte at 1600 rpm from 1.00 to 1.85 V (a) and their corresponding Tafel plots (b) using a rotating disk glassy carbon electrode. 259

Figure 7.11 - Linear sweep voltammetry curves of $50CNT_{Co}/50CNT_{Fe}$ before and after the stability test. 263

Figure 7S.1 - Linear sweep voltammograms of the prepared samples recorded at 5 mv s^{-1} and 1600 rpm in (a) O_2-saturated 0.1 mol L^{-1} KOH electrolyte from 1.10 to 0.15 V to evaluate the performance towards the ORR using a rotating ring-disk glassy carbon electrode with a Pt ring and (b) N_2-saturated 0.1 mol L^{-1} KOH electrolyte from 1.00 to

1.85 V to evaluate the performance towards the OER using a rotating disk glassy carbon electrode. 266

Figure 7S.2 - Linear sweep voltammograms of the physically mixed samples recorded at 5 mv s^{-1} and 1600 rpm in (a) O_2-saturated 0.1 mol L^{-1} KOH electrolyte from 1.10 to 0.15 V to evaluate the performance towards the ORR using a rotating ring-disk glassy carbon electrode with a Pt ring and (b) N_2-saturated 0.1 mol L^{-1} KOH electrolyte from 1.00 to 1.85 V to evaluate the performance towards the OER using a rotating disk glassy carbon electrode. 267

Figure 7S.3 - Linear sweep voltammogram of sample $25CNT_{Co}/75CNT_{Fe}$ recorded at 5 mv s^{-1} and 1600 rpm in N_2-saturated (red) and O_2-saturated (green) 0.1 mol L^{-1} KOH electrolyte from 1.00 to 1.85 V to evaluate the performance towards the OER using a rotating disk glassy carbon electrode. 268

Figure 7S.4 - Survey spectra of the prepared monometallic and bimetallic electrocatalysts. 270

Figure 7S.5 - Deconvolution of the N 1s X-ray photoelectron spectra of the prepared monometallic and bimetallic electrocatalysts and FePc. 271

Figure 7S.6 - Deconvolution of the Co 2p (top row) and the Fe 2p (bottom row) X-ray photoelectron spectra of the prepared monometallic and bimetallic electrocatalysts. . 272

Figure 7S.7 - SEM micrographs of CNT_{Co}, CNT_{Fe} and $50CNT_{Co}/50CNT_{Fe}$. 273

Figure 7S.8 - TEM micrograph of CNT_{Co} and $50CNT_{Co}/50CNT_{Fe}$ 273

Figure 7S.9 - SEM micrographs and respective elemental mapping analysis of CNT_{Co} (a and b), CNT_{Fe} (c and d) and $50CNT_{Co}/50CNT_{Fe}$ (e, f and g). Purple – Cobalt (b and f), Yellow – Iron (d and g). 274

Figure 7S.10 - Linear fitting of capacitive currents at 1.13 V vs RHE plotted against the scan rate obtained from cyclic voltammograms recorded at a scan rate range between 5 mV s^{-1} and 220 mV s^{-1} in N_2-saturated 0.1 mol L^{-1} KOH electrolyte. 275

Figure 8.1 - Raman spectra of the Co-doped (a) and Co,Fe-doped electrocatalysts (b). 294

Figure 8.2 - Co-doped samples' (a) OER LSV curves recorded at 1600 rpm using a scan rate of 5 mV s^{-1} in a N_2-saturated 0.1 mol L^{-1} KOH electrolyte, and respective Tafel plots (b). 296

Figure 8.3 - Co,Fe-doped samples' (a) OER LSV curves recorded at 1600 rpm using a scan rate of 5 mV s^{-1} in a N_2-saturated 0.1 mol L^{-1} KOH electrolyte, and respective Tafel plots (b).....297

Figure 8.4 - 1st and 1000th OER LSV curves of bimetallic samples obtained in the stability test. 299

Figure 8.5 - Disk current density of the oxygen reduction reaction curves recorded at 1600 rpm and 5 mV s^{-1} in O_2-saturated 0.1 mol L^{-1} KOH electrolyte (a) and number of electrons exchanged (b).....300

Figure 8.6 - Chronoamperometry assessments for the synthesized samples and Pt/C (a) and methanol resistance of samples CNT_{Fe}, CNT_{Fe}/CNT_{Co_185H2} and Pt/C (b) applying 0.4 V during 10000 s at 1600 rpm in an O_2-saturated 0.1 mol L^{-1} KOH electrolyte. 303

Figure 8S.1 - Survey spectra of the prepared electrocatalysts.....309

Figure 8S.2 - Deconvolution of the Co 2p X-ray photoelectron spectra of the prepared electrocatalysts. 310

Figure 8S.3 - N_2 adsorption-desorption isotherms at -196 ºC of the monometallic (a) and bimetallic electrocatalysts (b).....310

Figure 8S.4 - XRD patterns of the monometallic electrocatalysts. 311

Figure 8S.5 - Linear sweep voltammetry curves recorded at 5 mV s^{-1} in a N_2-saturated 0.1 mol L^{-1} KOH electrolyte at 1600 rpm from 1.00 to 1.85 V for CNT_{Fe}.....313

Figure 8S.6 - Linear sweep voltammetry curves recorded at 5 mV s^{-1} in a N_2-saturated 0.1 mol L^{-1} KOH electrolyte at 1600 rpm from 1.00 to 1.85 V for $CNT_{0.5Co_185H2}$.....313

Figure 8S.7 - Linear fitting of capacitive currents at 0.75 V vs RHE plotted against the scan rate obtained from cyclic voltammograms of monometallic (a) and bimetallic (b) samples recorded at a scan rate range between 5 mV s^{-1} and 220 mV s^{-1} in N_2-saturated 0.1 mol L^{-1} KOH electrolyte.....314

Figure 9.1 - ORR polarization curves of CNT and monometallic samples (a) and bimetallic samples (b) and Pt/C recorded in an O_2-saturated 2 mol L^{-1} KOH electrolyte. 324

Figure 9.2 - ORR polarization curves before and after accelerated stability testing of the monometallic (a) and bimetallic samples (b) and Pt/C recorded in an O_2-saturated 2 mol L^{-1} KOH electrolyte. 327

Figure 9.3 - OER polarization curves of the monometallic (a) and bimetallic samples (b) and RuO_2 recorded in an N_2-saturated 2 mol L^{-1} KOH electrolyte. 329

Figure 9.4 - Chronopotentiometry assessments for the synthesized samples and RuO_2 by applying 10 mA cm^{-2} for 1 h in an N_2-saturated 2 mol L^{-1} KOH electrolyte. 332

List of Tables

Table 1.1 - E_{10}, $E_{1/2}$ and ΔE of some state-of-the-art electrocatalysts (adapted from [115]). 28

Table 1.2 - Published or submitted peer-reviewed articles 33

Table 2.1 - Decomposition temperature ranges of different oxygen functional groups [9]. 69

Table 3.1 - Chemical composition determined by elemental analysis. 104

Table 3.2 - Electrochemical results of the synthesized samples..... 112

Table 3S.1 - Textural characterization of samples activated during different times. ... 117

Table 3S.2 - Elemental analysis of samples activated during different times. 117

Table 3S.3 - CO and CO_2 amounts obtained from TPD measurements of AG_{1h} and AG_{6h} 117

Table 3S.4 - Onset potential of samples activated during different times..... 118

Table 3S.5 - Textural characterization of activated and carbonized samples..... 123

Table 4.1 - Textural properties of carbonized glucose and undoped and N-doped carbon composites. 138

Table 4.2 - Chemical composition and electrical conductivity of carbonized glucose, undoped and N-doped carbon composites, carbon nanotubes, and oxidized carbon nanotubes..... 142

Table 4.3 - Electrochemical parameters obtained from linear sweep voltammetry measurements. 146

Table 4S.1 - Textural properties of carbon nanotubes and oxidized carbon nanotubes. 149

Table 4S.2 - Integrated areas of the peaks D and G obtained by Raman spectroscopy. 150

Table 5.1 - Chemical composition determined by elemental analysis and ICP. 167

Table 5.2 - Textural properties determined by N_2 adsorption/desorption isotherms at -196 ºC. 171

Table 5.3 - Main electrochemical parameters: onset potential (E_{onset}), current density ($J_{0.4}$), hydrogen peroxide (H_2O_2) formation, and the number of electrons exchanged (n_e) for the synthesized materials and commercial Pt/C. 176

Table 5S.1 - Surface chemical composition determined by XPS. 181

Table 5S.2 - Ratio of the integrated D and G peaks obtained by Raman spectroscopy. 183

Table 6.1 - Chemical composition determined by Elemental Analysis, ICP and XPS. 203

Table 6.2 - Onset potential (E_{onset}), half-wave potential ($E_{1/2}$), limiting current density (J_L), kinetic current density (J_K), hydrogen peroxide (H_2O_2) formation and the number of electrons exchanged (n_e) for the prepared electrocatalysts and the commercial Pt/C catalyst. 211

Table 6S.1 - Textural properties of the prepared carbon materials determined by N_2 adsorption/desorption isotherms at -196 ºC. 221

Table 7.1 - Chemical composition determined by elemental analyzes and ICP. 243

Table 7.2 - Onset potential (E_{onset}), half-wave potential ($E_{1/2}$), the potential at which a current density of 3 mA cm^{-2} is achieved (E_3), limiting current density (J_L), hydrogen peroxide (H_2O_2) formation, and the number of electrons exchanged (n_e) for the prepared electrocatalysts and the commercial Pt/C catalyst. 254

Table 7.3 - $E_{1/2}$, E_3, E_{10} and ΔE for the prepared samples and benchmark catalysts. ... 264

Table 7S.1 - Surface chemical composition determined by XPS. 269

Table 7S.2 - Ratio of the integrated D and G peaks obtained by Raman spectroscopy. 274

Table 7S.3 - Textural properties determined by N_2 adsorption/desorption isotherms at -196 ºC. 275

Table 8.1 - Chemical composition determined by elemental analyzes and ICP, and values of S_{BET} obtained from the N_2 adsorption-desorption isotherms. 290

Table 8.2 - Main electrochemical ORR parameters: Onset potential (E_{onset}), half-wave potential ($E_{1/2}$), limiting current density (J_L), by-product (H_2O_2) production, and the number of electrons exchanged (n_e) for the synthesized electrocatalysts and Pt/C catalyst. 301

Table 8.3 - $E_{1/2}$, $E_{10,}$ and ΔE for the prepared samples and benchmark electrocatalysts. 305

Table 8.4 - ΔE of the most electroactive sample prepared and some state-of-the-art electrocatalysts. 306

Table 8S.1 - Surface chemical composition determined by XPS. 308

Table 8S.2 - Ratio of the integrated D and G peaks obtained by Raman spectroscopy. 311

Table 9.1 - Potentials required to achieve a determined current density during ORR assessments for the synthesized materials and Pt/C in an O_2-saturated 2 mol L^{-1} KOH electrolyte. 325

Table 9.2 - Potential losses at different current densities during accelerated stability testing measurements for the synthesized materials and Pt/C in an O_2-saturated 2 mol L^{-1} KOH electrolyte. 327

Table 9.3 - Potentials required to achieve a determined current density during OER assessments for the synthesized materials and RuO_2 in an N_2-saturated 2 mol L^{-1} KOH electrolyte. 330

Table 10.1 - $E_{1/2}$, E_{10} and ΔE of the most promising prepared samples and benchmark electrocatalysts..... 345

List of Abbreviations and Variables

ΔE – potential gap

η – overpotential

θ – Bragg angle

λ – wavelength

δ – diffusion layer thickness

α – slope value

β – affinity coefficient

T - crystallite size

ν – kinematic viscosity

ω – rotation speed

ω – frequency

σ – Warburg coefficient

A – area

AC – alternate current

A_D – disk area

AEMFC – anion-exchange membrane fuel cell

AG – activated glucose

a_m – area occupied by each adsorbed molecule

A_R – ring area

AST – accelerated stability testing

ATR – attenuated total reflection

BE – binding energy

BET – Brunauer-Emmett-Teller

BOC – bifunctional oxygen catalyst

BSE – backscattered electron

c – BET constant

C - capacitance

C_0^* - bulk concentration of saturated O_2 in the electrolyte

C_{dl} – double-layer capacitance

CE – counter electrode

CG – carbonized glucose

CL – catalyst layer

CNT – carbon nanotubes

CNT_O – oxidized carbon nanotubes

CoPc – cobalt(II) phthalocyanine

C_S – specific capacitance

CV – cyclic voltammetry

CVD – chemical vapor deposition

d – distance

D – diffusion coefficient

DC – direct current

DR - Dubinin-Radushkevich

E_{-500} – potential required to achieve a current density of -500 mA cm^{-2}

E_{-1000} – potential required to achieve a current density of -500 mA cm^{-2}

E_{-1500} – potential required to achieve a current density of -500 mA cm^{-2}

E_{-2000} – potential required to achieve a current density of -500 mA cm^{-2}

E_0 – characteristic energy

E_1 – adsorption energy of the first layer

$E_{1/2}$ – half-wave potential

E_{10} – potential required to achieve a current density of 10 mA cm^{-2}

E_{500} – potential required to achieve a current density of 500 mA cm^{-2}

E_{1000} – potential required to achieve a current density of 1000 mA cm^{-2}

E_{1500} – potential required to achieve a current density of 1500 mA cm^{-2}

E_3 – potential required to achieve a current density of 3 mA cm^{-2}

EA – elemental analysis

ECSA – electrochemical active surface area

EDS – energy-dispersive spectroscopy

EIS – electrochemical impedance spectroscopy

E_L – condensation heat

E_{onset} – onset potential

ETD – Everhart-Thornley detector

EL - electrolyzer

F – Faraday constant

FAT – fixed analyzer transmission

FC – fuel cell

FePc – iron(II) phthalocyanine

FTIR – Fourier transform infrared spectroscopy

GDE – gas diffusion electrode

GDL – gas diffusion layer

HER – hydrogen evolution reaction

HOR – hydrogen oxidation reaction

HTC – hydrothermal carbonization

I – current

$I_{2e}/I_{2e'}$ – Faradaic current related to the oxygen reduction reaction indirect mechanism

I_{4e} - Faradaic current related to the oxygen reduction reaction direct mechanism

I_D – Faradaic current at the disk

iR – ionic electrolyte resistance

I_R – Faradaic current at the ring

ICP – inductively coupled plasma

ICP-OES – inductively coupled plasma optical emission spectrometry

IR - infrared

IWI – incipient wetness impregnation

J – current density

J_K – kinetic current density

J_L – diffusion limiting current density

K – shape factor

KE – kinetic energy

KL – Koutecký-Levich

LF – Lorentzian finite

LSV – linear sweep voltammetry

MEA – membrane exchange assembly

MPL – microporous layer

n – number of moles / diffraction order

N – collection coefficient at the ring

N-6 – pyridinic nitrogen

N-5 – pyrrolic nitrogen

N-Q – quaternary nitrogen

N-X – oxidized nitrogen

n^a – total amount of adsorbed gas

N_A – Avogadro's number

n_m^a – monolayer adsorbed gas quantity

n_e – number of electrons exchanged

N_e – total number of electrons transferred

N_{H2O2} – total number of hydrogen peroxide molecules

N_{O2} – total number of oxygen molecules participating in the oxygen reduction reaction

OER – oxygen evolution reaction

ORR – oxygen reduction reaction

P – equilibrium pressure

P_0 – saturation pressure

Pc - phthalocyanine

PEMFC – proton exchange membrane fuel cell

QSDFT – Quenched Solid Density Functional Theory

RDE – rotating disk electrode

RE – reference electrode

RHE – reversible hydrogen electrode

RRDE – rotating ring-disk electrode

R – gas constant / resistance

R_s –electrolyte resistance

R_u – uncompensated electrolyte ohmic resistance

S_{BET} – specific surface area

SE – secondary electron

SEM – scanning electron microscopy

S_{ext} – external surface area

SUTW – super ultra-thin window

t – thickness / time

T - temperature

TCD – thermal conductivity detector

TEM – transmission electron microscopy

TOF – turnover frequency

TPD – temperature-programmed desorption

URFC – unitized regenerative fuel cell

V - voltage

V_p – total pore volume – volume of nitrogen adsorbed at the saturation point

V_{DR} – volume of micropores calculated by the Dubinin-Radushkevich method

V_{micro} – volume of micropores calculated by the t-plot method

W – volume filled at a certain relative pressure

WE – working electrode

XPS – X-ray photoelectron spectroscopy

XRD – X-ray diffraction

XRF - X-ray fluorescence spectrometry

Z - impedance

Z_C – capacitor impedance

Z_R – Resistor impedance

Z_W – Warburg impedance

Chapter 1

State-of-the-art, Motivation, Objectives and Thesis Outline

1.1. Unitized Regenerative Fuel Cell (URFC)

The escalating world industrialization, population growth, and increasing use of portable electronic devices are leading to a significant rise in global energy demand. The percentual growth of global energy demand in 2021, 6% [1], widely surpassed the increment of 2018 (2.9%), which at the time was the fastest growth since 2010 and almost double of the past decade [2]. According to the United States Energy Information Administration, the historical analysis of the world's energy consumption led to a projection of a 28% increase from 2015 to 2040. Interestingly, this projection remarks the importance of renewable energy in the future, representing one of the fastest-growing energy sources in percentual terms, with an average yearly increase of 2.3%. Besides, regardless of the decrease in the overall global energy demand that took place in 2020 due to the recent COVID-19 pandemic, the importance and use of renewable energies have not been affected [3]. In fact, these energies are estimated to account for 80% of the increase in global electricity demand until the end of this decade [3]. In this context, over the last decades, the scientific community has been intensely focused on technologies that could replace fossil fuels due to their high gas emissions and limited availability, specifically on technologies based on renewable sources. However, the consumption of renewable sources is still far from being the most important energy source. Furthermore, countries require energy sources that are constantly available at an affordable price to guarantee energy security, which involves lower dependence on imported energy sources, commonly fossil fuels, and taking more advantage of the renewable ones available in each territory [4]. Considering the forecast for renewable electricity generation an important challenge arises: the development of new conversion systems or modification of current devices to generate energy in a continuous and sustainable mode.

Fuel cells are one of the most environmentally friendly technologies to produce energy. The main concept of this device involves the use of fuels, mainly hydrogen, which are transformed by electrochemical reactions only into energy and water, so no pollutants are generated [5, 6]. Based on this idea, fuel cells (FCs) seem to have the potential to play a major role in the future of the global energy scenario as the reactants required (oxygen and hydrogen) are the major components of water, and hence, abundant on the planet.

Since hydrogen is one of the hottest topics towards renewable energies and the European Commission has already proposed its use to achieve a climate-neutral continent [7], this type of device continues to gain momentum on the energy world stage. [3]. Furthermore, a recent report suggests that by 2050 the hydrogen demand will grow by 50% [8]. On the other hand, to further enhance the efficiency and commercial competitiveness of this technology, it can be coupled with an electrolyzer (EL) that can split water and produce the reactants that will be reused in the fuel cell [9]. This system is called the unitized regenerative fuel cell (URFC). The URFC combines an H_2/O_2 generation device – an electrolyzer - and an energy conversion device – a fuel cell - in a single device to achieve maximum efficiency and lower manufacturing costs [7, 10-12]. The URFC is environmentally friendly, as the electrolyzer mode simply leads to water splitting (H_2O) to generate the necessary reactants for the fuel cell (H_2 and O_2), whereas the conversion mode does not generate polluting products, only H_2O and energy [5, 6, 11]. This device not only complies with the European strategy on adaptation to climate change but is also one of the most promising devices for the short and long-term future of green energy as it is capable to handle the intermittency of renewable energies. The URFC involves four different electrochemical reactions (Figure 1.1): two reactions that take place while operating in the electrolyzer mode – the oxygen evolution reaction (OER) and the hydrogen evolution reaction (HER) - and another pair of reactions that take place in the fuel cell mode – the oxygen reduction reaction (ORR) and the hydrogen oxidation reaction (HOR) [13]. So, the URFC is compartmentalized in two separate electrodes: one for the oxygen pair of reactions (ORR and OER) and another for the hydrogen reactions (HER and HOR). Therefore, the electrode containing the oxygen reaction pair uses one electrocatalyst to properly catalyze both ORR and OER, whereas the electrode containing the hydrogen reaction pair uses another electrocatalyst for the HER and HOR.

Consequently, the design of efficient bifunctional electrocatalysts is essential for the development of the URFC, which is currently one of the main challenges the scientific community is facing. As the URFC works alternatively, the reactions that are taking place at each electrode (ORR/OER and HOR/HER) depend on the URFC mode at the time of operation [14-16]. A schematic of the system operation is displayed in Figure 1.1.

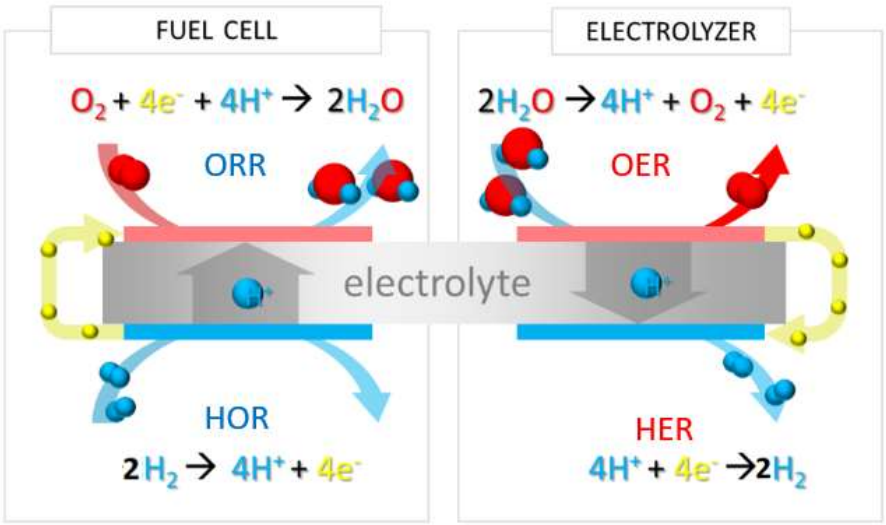


Figure 1.1 - Unitized regenerative fuel cell operation schematics (adapted from [17]).

One of the most important parameters towards the commercialization of URFCs is the optimization of their efficiency by decreasing the losses occurring due to the four electrochemical reactions. A scheme of the reaction losses during operation is presented in Figure 1.2.

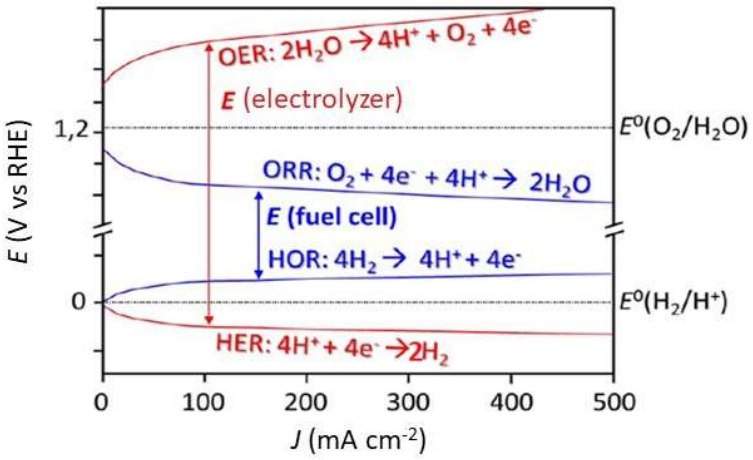


Figure 1.2 - Scheme of the reaction losses in a fuel cell and an electrolyzer (adapted from [17]).

Firstly, it should be noted that this scheme represents a general overview of the reaction losses in acidic conditions as proton-exchange membrane fuel cells (PEMFCs) and

electrolyzers are the most mature technologies in comparison to their alkaline counterparts [9, 14, 17-19]. Additionally, it is possible to observe the standard potentials for each reaction pair if they had maximum efficiency, in this case, 1.23 V and 0 V (vs RHE) for the oxygen and hydrogen pair of reactions, respectively. The losses of each reaction pair, observed in Figure 1.2, are the difference between the reactions' standard potentials and the potential required to achieve a certain current density. The difference between these two potentials is called overpotential and is commonly used to assess the suitability of an electrocatalyst for the electrochemical reaction. Further analyzing the figure, it is possible to observe small losses for the HOR/HER pair in comparison to the ORR/OER pair, which presents very high overpotentials even at very low current densities. Thus, the sluggish reaction kinetics of ORR and OER hinder the overall performance of the URFC and require further optimization before large-scale commercialization. Hence, the current works' prime focus is improving the performance of both oxygen reactions. In order to attain these improvements, a deep understanding of the reaction mechanism is needed.

1.1.1. Oxygen Reduction Reaction

Two different processes can express the ORR mechanism. The first is a highly efficient one-step mechanism of four-electrons (known as the direct mechanism), which does not produce secondary products and diminishes the energy loss during the reaction [20]. This mechanism is commonly observed with a Pt-based electrocatalyst [21, 22]. The ORR direct mechanism in acidic or alkaline electrolytes can be expressed by Eq. 1.1 and 1.2, respectively [23, 24]:

$$O_2 + 4H^+ + 4e^- \leftrightarrow 2H_2O \text{ (1.23 V vs RHE)} \quad (1.1)$$

$$O_2 + 2H_2O + 4e^- \leftrightarrow 4\,OH^- \text{ (0.40 V vs RHE)} \quad (1.2)$$

The direct mechanism can follow two different paths: i) an associative mechanism in which O_2 is adsorbed and accepts 4 protons and electrons (acidic conditions) or 4 electrons (alkaline conditions) resulting in 2 H_2O (acidic electrolyte) or 4 OH^- (alkaline electrolyte) or, ii) adsorbed O_2 dissociates into two adsorbed O and each oxygen atom accepts 2 protons and electrons (acidic conditions) or 2 electrons (alkaline conditions) to produce 1 H_2O (acidic medium) or 2 OH^- (alkaline medium). Nonetheless, several

intermediate and elementary steps occur during the ORR (Figure 1.3). Initially, the active site (*) adsorbs an O_2 molecule which can then be dissociated (*-O) or maintained (*-O_2) as abovementioned. In the latter case, the oxygen molecule reacts and forms an intermediate species on the active center (*-OOH), which further reacts and results in an *-O species, which is equivalent to that formed during the dissociative process. Therefore, the reaction mechanism after this point is the same for both associative and dissociative processes: another electron is accepted and another intermediate is formed on the active site (*-OH), which is then further reduced to the final reaction product (H_2O and OH^-, in acidic and alkaline electrolyte, respectively) and liberates the active center (*) which is then available to reduce another O_2 molecule.

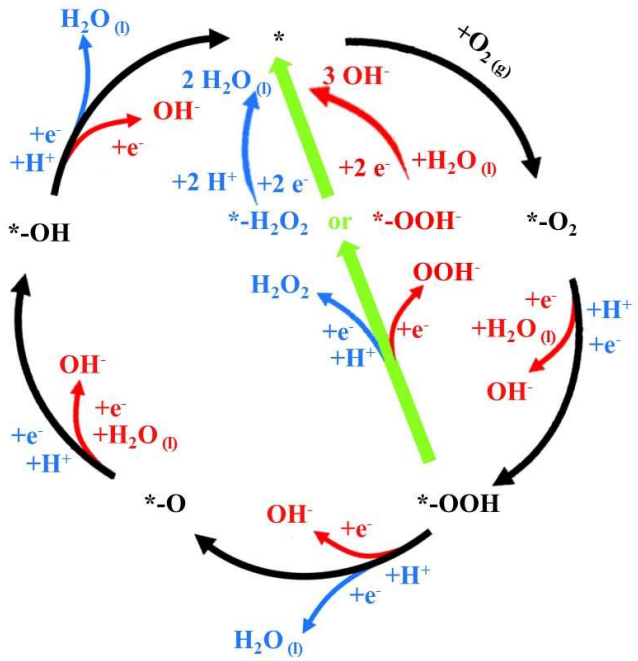


Figure 1.3 - The direct ORR mechanism for acid (blue line) and alkaline (red line) conditions, in which the black line indicates the formation of intermediates in both reactions. The green line indicates the indirect ORR mechanism formation of by-products for both acidic (blue line) and alkaline conditions (red line).

Nonetheless, a sluggish two-step mechanism can also take place during the ORR. This second process is related to a mechanism of two-electrons (known as the indirect mechanism), in which the formation of by-products is observed [25]. The ORR indirect mechanism in acidic or alkaline electrolytes can be expressed by Eq. 1.3-1.4 and 1.5-1.6, respectively [23]:

$$O_2 + 2H^+ + 2e^- \leftrightarrow H_2O_2 \text{ (0.70 V vs RHE)} \quad (1.3)$$

$$H_2O_2 + 2H^+ + 2e^- \leftrightarrow 2H_2O \text{ (1.78 V vs RHE)} \quad (1.4)$$

$$O_2 + H_2O + 2e^- \leftrightarrow HO_2^- + OH^- \text{ (}-0.08 \text{ V vs RHE)} \quad (1.5)$$

$$HO_2^- + H_2O + 2e^- \leftrightarrow 3OH^- \text{ (0.88 V vs RHE)} \quad (1.6)$$

Figure 1.3 displays each step of both direct (black line) and indirect (green line) ORR mechanisms in acidic (blue line) and alkaline (red line) electrolytes, in which "*" represents the electrocatalyst's active center. The formation of an undesired reaction by-product (H_2O_2 or HO_2^-, in acidic and alkaline electrolytes, respectively) can be desorbed into the electrolyte (blue and red lines on the indirect mechanism shown in Figure 1.3) or continue adsorbed on the active center. Nonetheless, the remain adsorbed by-products can be further reduced to H_2O (acidic medium) or OH^- (alkaline medium), although it still hinders the overall reaction due to its sluggish kinetics.

The reaction mechanism is closely related to the chosen electrocatalyst, which efficiency is commonly studied by analyzing the following parameters: i) the onset potential, ii) half-wave potential ($E_{1/2}$), iii) the limiting current density, iv) the number of electrons transferred, v) the formation of by-products, vi) the stability during operation and vii) poisoning resistance. An efficient electrocatalyst should give rise to an ORR onset potential as high as possible to ensure that the reaction's overpotential is low. The $E_{1/2}$ is related to the potential at which half the limiting current density is achieved and should be as close as possible to the onset potential so that a low increase of overpotential is required to produce higher current densities. Regarding the limiting current density, electrocatalysts that, for the same applied potential, originate a higher absolute current density display better electrochemical performance. The number of electrons transferred is related to the reaction mechanism in which, preferentially, four electrons should be transferred to avoid the formation of by-products and energy losses. Furthermore, an

electrocatalyst should have high stability; in other words, the generated current density should be maintained close to the value produced by the fresh electrocatalyst, which would result in a higher lifetime of the material. Lastly, the electrocatalyst should be able to preserve its active sites to avoid poisoning; molecules other than O_2 should not be adsorbed by the electrocatalyst and hinder its electrochemical performance. The experimental procedures employed and calculations made to determine each of these parameters are thoroughly explained in *Chapter 2 - Materials and Methods*.

1.1.2. Oxygen Evolution Reaction

Unlike ORR, the OER mechanism is generally accepted as a four-electron associative mechanism in both acidic and alkaline media [26-28], even though the reaction is different. In acidic media, water is separated into molecular oxygen and hydrogen protons (reaction 1.7); whereas in a basic electrolyte, hydroxide ions liberated from the electrolyte are converted into molecular oxygen and water (reaction 1.8) [27].

$$2H_2O \leftrightarrow 4H^+ + 4e^- + O_2 \quad (1.23\ \text{V vs RHE}) \tag{1.7}$$

$$4OH^- \leftrightarrow O_2 + 2H_2O + 4e^- \quad (-0.40\ \text{V vs RHE}) \tag{1.8}$$

The OER mechanism and respective our-electron/proton transfer steps are presented in Figure 1.4. Initially, in an acidic medium (red line), the active site (*) adsorbs an H_2O molecule, in which a proton and an electron are released, leading to an *-OH bond. Subsequently, three extra individual steps involving the release of H^+ and an electron. The subsequent step results in the formation of the intermediate adsorbed species *-O, which will subsequently react with an H_2O molecule and lead to an *-OOH bond. This latter bond will then form the O_2 molecule (OER product) and release the abovementioned species. Regarding the basic medium (blue line), similar steps to those occurring in an acidic medium take place. Firstly, OH^- is adsorbed by the active site (*-OH) and an electron is released, followed by a reaction with another OH^- that results in the release of H_2O and another electron, and the formation of the *-O intermediate. Next, the active center reacts with another OH^- and an electron is released leading to the *-OOH intermediate. Lastly, the adsorbed species reacts with OH^- to generate the reaction product (O_2) and release a water molecule and an electron. Additionally, another route

for the direct reaction of two adjacent oxo (M–O) intermediates (green) to produce oxygen is possible as well [29].

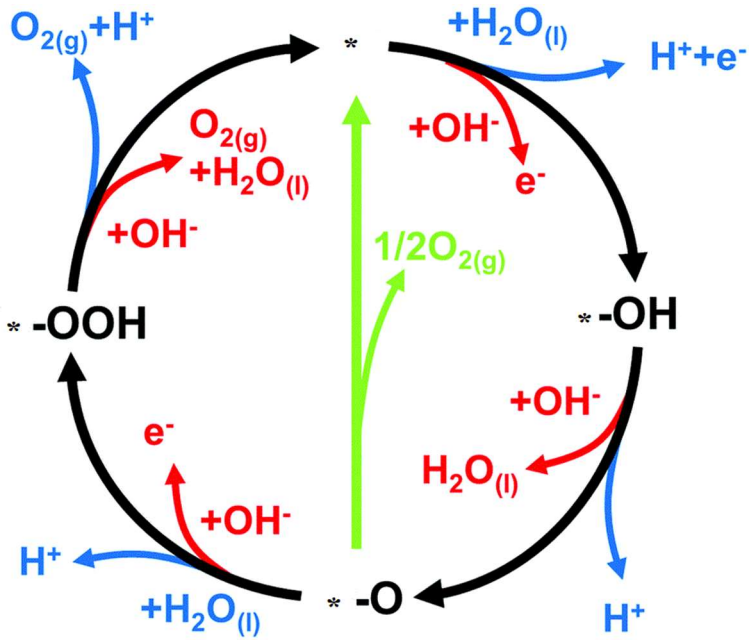


Figure 1.4 – The commonly accepted OER mechanism for acid (blue line) and alkaline (red line) conditions, and an alternative OER route (green line). (adapted from [29]).

The electrocatalysts' efficiency towards the OER is mainly determined by the overpotential required to achieve a current density of 10 mA cm^{-2} (E_{10}), which is directly correlated to the reaction kinetics. The lower the energy required to overcome the kinetic barrier (lower overpotential), the superior the catalysts' electrocatalytic ability [29-31]. Nonetheless, three other parameters are also usually assessed to provide a full insight into the electrocatalysts' performance [30]: i) the exchanged current density, ii) the Tafel slope value, and iii) the turnover frequency (TOF). The current density is a good indicator of the interactions (charge transferring and intrinsic bonding) between reactants and electrocatalysts. An increase in current density indicates a higher affinity of the material toward the electrocatalytic reaction. The Tafel slope correlates the increase of current density with a variation of overpotential. In this case, the lowest possible value is desired, indicating a faster reaction rate constant and good electrocatalytic kinetics. The TOF

assesses the intrinsic activity of an electrocatalyst by correlating the current density with the amount of catalyst used. A high TOF value is an indicator of good intrinsic electrocatalyst activity. The experimental procedures employed and calculations made to determine each of these parameters are thoroughly explained in *Chapter 2 - Materials and Methods.*

1.1.3. Electrocatalysts

One of the most important features of a URFC is the materials used as electrocatalysts that mostly define the overall device price and the environmental friendliness of the energy conversion approach [32]. The current benchmark electrocatalysts used to catalyze the oxygen reactions properly are Pt/C, IrO_2 or RuO_2, which are scarce and very expensive, increasing the overall cost of the device and limiting their commercialization [12]. Therefore, the oxygen reaction kinetics should be improved using different materials that reduce the costs of the electrocatalysts [12, 13, 33-35]. Furthermore, the most developed URFC technology is based on the proton-exchange membrane fuel cell (PEMFC), which operates in acidic conditions [7, 9, 12, 14, 17, 18]. Nonetheless, using basic media operating conditions, by employing an anion-exchange membrane fuel cell (AEMFC), enables the use of a wider range of materials than those applicable in PEMFCs [17]. The electrocatalysis of the oxygen reactions in acidic media is mostly favored by noble metals and their oxides [14, 17], whereas alkaline media provides conditions for a wider range of materials to excel, such as carbon materials and transition metals.

Using catalysts such as noble metal-free carbon materials helps achieve a much cost-efficient large-scale in comparison to the Pt/C benchmark catalyst (20% Pt on carbon) production of the alkaline URFC [17, 36]. Additionally, it is possible to achieve faster kinetics in an alkaline than in acidic media, improving the ever-problematic sluggish kinetics of the oxygen reactions, due to the multi-electron transfer processes and strong reaction irreversibility of oxygen [17, 36]. Therefore, the synthesis of materials capable of diminishing the losses of ORR and OER would greatly improve the URFC's performance. The OER takes place over the same electrocatalysts as the ORR, so bifunctional oxygen catalysts (BOCs) should be developed to give rise to outstanding performances towards OER and properly catalyze the ORR. BOCs should present high

electrocatalytic activity towards the ORR and OER, high electrical conductivity, high chemical, electrochemical and catalytic stability, high long-term stability under harsh operating conditions, high interaction between the catalyst particles and the support surface, and should not dissolve in the electrolyte [37-39]. The benchmark BOCs are based on noble-metals, which, as previously explained, require suitable replacements to facilitate the commercialization of the URFC. To properly design BOCs, the use of carbon materials is scientifically attractive due to their high versatility, abundance, catalytic activity, electronic conductivity, cost, and surface area.

1.2. Carbon materials

Carbon materials have been used as electrocatalysts for several electrochemical reactions for more than a decade, demonstrating multifunctional electrocatalytic activities, in particular towards the ORR and OER [23, 40, 41]. Carbon presents a wide variety of structures, such as amorphous carbons (carbon black and activated carbon) and crystalline carbons (graphite and diamond), each with their respective set of characteristics derived from their structures [42]. Moreover, some carbon-based materials present intrinsic characteristics that enhance the mass diffusion and electron transfer for the oxygen reactions, which is crucial to achieving competitive electrocatalytic performances [41]. However, carbon materials alone are unable to properly catalyze both the ORR and OER. Therefore, considering that the electroactivity of carbon materials depends on their physico-chemical properties, great efforts have been made to tailor their textural and chemical properties to improve their electrochemical performance. The use of carbon materials functionalized with heteroatoms or as carbon supports for metals are two of the most common methodologies to design BOCs. To achieve an optimal energy scenario, the carbon support should be prepared using green sources and synthesis techniques. In this regard, hydrothermal carbonization (HTC) is a commonly used environmentally friendly method to transform biomass into carbon materials under mild synthesis conditions at low cost [43]. Regardless of the starting material, three main steps are usually observed during an HTC procedure: i) dehydration of the carbohydrate to (hydroxymethyl)furfural; ii) polymerization towards polyfurans and iii) carbonization/aromatization via further intermolecular dehydration [43, 44]. This process usually presents a yield between 30 and 40% and a final carbonaceous material with

carbon as the majority element (C > 60%) [44]. Despite the great interest of the HTC-derived carbonaceous materials, they present a drawback to consider which is the lack of porosity and the low surface areas, which hinder their capability to be properly applied in energy conversion technologies [42, 44]. Hence, further modifications to textural and chemical properties are required to achieve oxygen bifunctionality.

1.2.1. Textural properties

The textural properties play an important role in the performance of the electrocatalysts towards the ORR and OER. Macropores (> 50 nm) facilitate gas transportation, whereas mesopores (between 2 and 50 nm) provide active centers towards the ORR and OER and enhance the mass transfer of the electrolyte with dissolved oxygen. Regarding microporosity, although its importance has been suggested [45, 46], only recent research has been focused on its relationship with the catalysts' electroactivity. More specifically, it has been reported that ultramicropores (< 0.7 nm) are good active sites for oxygen adsorption [47, 48], which enhances the material's electroactivity. Moreover, a proper wetting of the electrocatalyst's surface is required to minimize the mass transfer process loss in the micropores (< 2 nm) [47]. The design of carbon's textural properties is important to ensure that the majority of the active centers are exposed to the electrolyte and oxygen feedstocks [48]. According to the initial carbon material and the necessity for a certain level of porosity, carbonization, physical activation or chemical activation can be performed to properly tailor the textural properties.

Carbonization is one of the most common processes used to obtain carbon materials from organic precursors. This process involves heating the carbon precursor under an inert atmosphere, being temperature, time and heating rate the most important parameters to control the final textural properties. During pyrolysis, moisture and volatile matter of the carbon source are removed, remaining the solid char [42]. The carbonization temperature ranges from 400 °C to 800 °C [49, 50]. Due to the effect of temperature, the scission of chemical bonds and the depolymerization of polymeric carbon materials take place, leading to the formation of new bonds that stabilize the carbon atoms, which in turn, results in a non-volatile and stable carbon framework [49, 51]. The heating rate also plays an important role during carbonization. A slow heating rate (10 °C min^{-1}) favors the

production of solid char residues, whereas high heating rates (up to 1000 °C s^{-1}) minimize thermal decomposition and, predominantly, generate liquid products [50]. In addition to stabilizing the carbon structure, carbonization also gives rise to an increase in the micropore volume and surface area and also may widen the pores [52]. Nonetheless, carbonization leads to surface areas smaller than 1000 m^2 g^{-1}, and hence, carbons may require further treatments, such as activation, if higher surface areas are required for their application.

Activation is a well-known method to modify the textural properties of carbon materials. It can be carried out either during or after carbonization, resulting in materials with different properties. There are two main methods to activate carbon materials: physical activation and chemical activation [53].

Physical activation is performed by subjecting the carbon material to a carbon gasification reactant known as activating agent. Some of the most common activation agents are CO_2 and steam or a mixture of them, which are clean compounds and easy to handle [42, 51, 54, 55], and the temperature ranges between 700 and 1000 °C [54, 55]. In this process, three different stages take place: i) a fast weight loss up to 200 °C, corresponding to the removal of water, ii) a slow weight loss until 500 °C derived from the initial pyrolysis and iii) a small weight loss at higher temperatures attributed to the consolidation of the char structure [42]. During this reaction, some of the carbon atoms react with the oxidation gas being removed, leaving gaps in the carbon structure and, consequently, developing porosity [54]. This reaction is favored at higher temperatures. Similarly, increasing the holding time prolongs the contact between the carbon material and the oxidizing gas, thus increasing the number of carbon atoms removed from the surface, culminating in a more developed porosity. Steam activations usually use holding times of 1 or 2 hours, whereas CO_2 activations are typically performed with higher holding times due to the slower oxidation rate [55]. Additionally, employing higher flow rates of oxidizing gas also increases the contact of gas/carbon structure, which also favors the removal of carbon atoms due to the higher contact between the oxidizing gas and the carbon material. The heating rate is also a crucial parameter. An optimal rate of 10 °C min^{-1} has been reported to lead to the highest surface areas [56].

Regarding chemical activation, the carbon material undergoes a thermal treatment in the presence of a chemical agent. Generally, these chemical precursors are acids, compounds containing alkaline earth metals or even transition metal salts. Some of the most common precursors are $ZnCl_2$, NaOH, KOH, H_3PO_4 and Na_2CO_3 [51, 55, 57]. These reagents act as dehydrating agents removing oxygen and hydrogen atoms from the carbon matrix, and hence, generating porosity [51, 57]. The temperature for chemical activation ranges from 400 to 700 °C but it depends on the chemical agent selected [55, 57]. For instance, KOH, which is the most common agent, needs temperatures higher than the normal range of chemical activation (> 700 °C) [55]. Besides, the type of porosity generated also depends on the chemical agent employed. $ZnCl_2$ reacts with the carbon structure and is posteriorly removed; therefore, the porosity is originated from the spaces created by $ZnCl_2$, instead of the traditional dehydration strategy [55]. In the case of alkaline metals, the choice of the appropriate cation is crucial, as a larger cationic size gives rise to carbons with larger surface areas. The ratio between the chemical agent and the carbon material is also an important parameter. $ZnCl_2$ is a prime example of a precursor in which the impregnation ratio of $ZnCl_2$/carbon is the most critical parameter to develop porosity, as a high $ZnCl_2$/carbon ratio can lead to the deposition of $ZnCl_2$ on the external surface of the carbon material, resulting in the decomposition of the organic matter leading to wider and larger pores [51]. Hence, the treatment's temperature must be chosen according to the precursor used, as each one reacts differently at high temperatures [51, 55]. Chemical activation requires inferior temperatures than physical activation and inhibits the formation of tar, which results in higher yields of carbon material [51, 57]. However, chemical activation also has important drawbacks due to residual inorganic material remaining inside the carbon structure, which needs to be posteriorly removed by washing, increasing the process cost. Additionally, the chemical activation agents also must be properly disposed, as most of them represent an environmental hazard.

1.2.2. Surface chemistry

The chemical properties can be tailored using multiple techniques and precursors, culminating in a wide range of surface functionalities. The chemical properties of carbon materials can be modified by incorporating heteroatoms and metals in their structure. Therefore, understanding the role of heteroatoms and transition metals towards ORR/OER is essential to properly develop new BOCs. The most common heteroatoms used to modify the surface chemistry of carbon materials are oxygen, nitrogen, sulfur, whose main functional groups are shown in Figure 1.5, whereas the most common metals are iron, cobalt, nickel, manganese, and copper. Functionalization methods may be divided into two different categories, those performed using post-treatments (*ex-situ*) and those performed during the synthesis of the carbon material (*in-situ*).

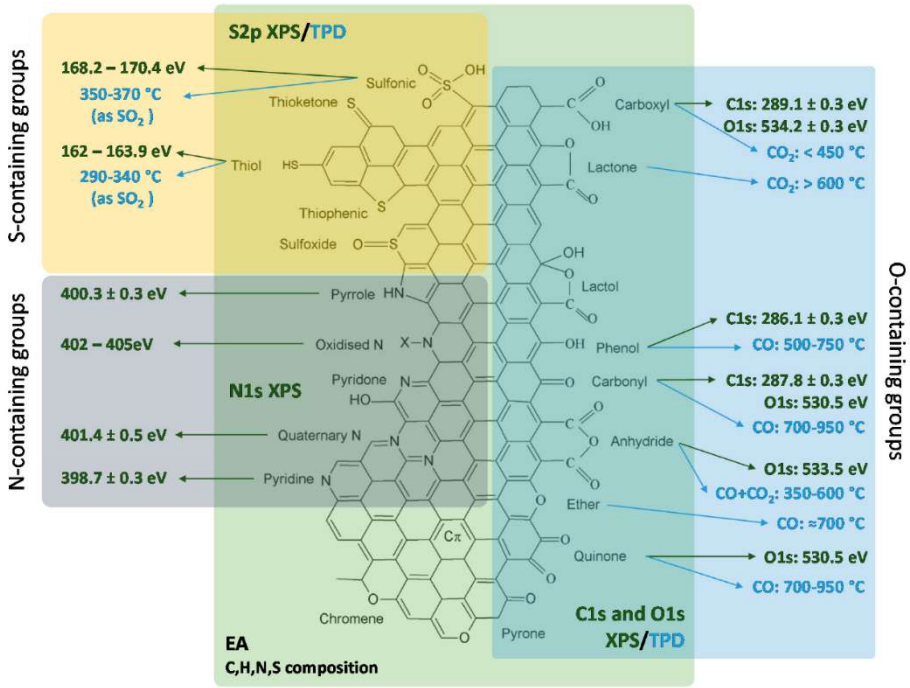


Figure 1.5 - Oxygen, nitrogen and sulfur surface groups and techniques for their identification/quantification [58].

The functionalization of carbon materials by *ex-situ* methods may be performed following different approaches, according to the type of heteroatom precursor used: solid, liquid or gaseous. Carbon materials can be manually mixed, stirred or ball-milled with a

solid or liquid precursor. Once mixed properly, a posterior thermal treatment under an inert atmosphere allows the decomposition of the precursor, resulting in the functionalization of the surface. It should be highlighted that ball-milling, besides mixing the carbon and the heteroatom precursor, can also introduce oxygen functionalities due to the contact with air; and it can also modify the carbon structure and create defects, which could favor simultaneous or posterior functionalization [59, 60]. Gaseous precursors are frequently used in post-synthesis methods and allow to functionalize carbon materials with different heteroatoms, according to the functionalization precursor used [61-63]. Gaseous treatments are performed by subjecting the carbon material to a certain temperature under a gas flow containing the precursor of the heteroatom that is going to be incorporated. Temperature and time are two important parameters that should be properly selected. Temperature can be used to modulate the heteroatom's functionalities being formed or released, whereas an increase in the time of functionalization results in the incorporation of a higher amount of heteroatoms [61]. Regarding the incorporation of metals, the impregnation process is a common method employed to introduce metal phases on carbon materials using liquid precursors [53, 64]. Generally, the precursor is dissolved in a solvent (normally water or ethanol) and added one drop at a time into the carbon material. Two types of impregnation are usually performed: i) wet impregnation, in which an excess of solvent is used or ii) pore volume impregnation, in which the quantity of solvent used is just enough to fill the pore volume of the carbon support [65, 66].

In-situ methods may simplify the overall preparation of functionalized carbon materials as synthesis and functionalization occur in one single step. This offers an advantage over the *ex-situ* methods due to the lower consumption of time and energy required. Hydrothermal functionalization is one of the greenest *in-situ* techniques, in which the carbon material and heteroatom precursor(s) are enclosed in a Teflon-lined autoclave. Subsequently, the mixture undergoes a heat treatment at low temperatures (< 250 °C) with self-generated pressures for long periods (several hours or even days) [67, 68]. Additionally, less-mentioned but also environmentally-friendly techniques such as arc-discharge or chemical vapor deposition (CVD) are often used to synthesize and functionalize carbon materials [69-71]. The former method requires a direct current

between a pair of electrodes under an inert gas or air at about 500 torr [72], giving rise to doped carbons without any metal catalyst and with high structural perfection [72]. On the other hand, CVD requires templates for the synthesis [73], in which volatile precursors easily penetrate the pores of the templates, resulting in mater[53].

The incorporation of heteroatoms into carbon materials is one of the most important modifications that can be performed to tailor the electrocatalyst's properties and achieve higher electroactivities. Although the electrochemical performance towards the ORR and OER of several heteroatoms such as boron, sulfur and phosphorus have been studied, they do not provide catalytic enhancements as promising as those observed for nitrogen, which is, in fact, the most studied heteroatom. On the other hand, it has been reported that oxygen may play a key role in enhancing the material's electroactivity. The understanding of the effect of this heteroatom is essential, as oxygen is intrinsically found in most carbon materials.

Oxygen

Oxygen is a heteroatom that positively influences the electroactivity of carbon materials towards the ORR and OER. This heteroatom is found in small amounts in many carbon structures, but it can also be introduced through oxidation processes, incorporating a wide range of oxygen functionalities. The most common oxygenated groups are carboxylic acids and anhydrides, lactones, phenols, carbonyl/quinones, ethers, and pyrones (Figure 1.5). The nature and amount of oxygen functionalities incorporated into the carbon structure will depend on the precursor selected and the chemical and thermal treatment applied, which can be performed in the liquid- or gas-phase. The most common oxidizing agents used in liquid-phase treatments are HNO_3, H_2SO_4, and H_2O_2 [74-76]. The liquid oxidizing agent is put in contact with the carbon material at a selected concentration, contact time, and temperature. Then, the material is washed and dried. Some of these oxidation agents possess another heteroatom besides oxygen (such as nitrogen and sulfur), leading to the incorporation of more than one heteroatom. The temperature and time employed in the liquid-phase treatment depend on the nature of the oxidizing agent and the carbon material to be functionalized. Liquid-phase oxidation usually results in carbons with a more acidic surface due to the formation of carboxylic acids [61-63, 77]. The stronger the acid/oxidant is, the more favorable the formation of carboxylic acid

groups will be. On the other hand, gas-phase oxidation involves a thermal treatment in which the carbon material is subjected to a certain temperature, generally between 350 and 450 °C, under an oxidation agent flow [61]. The most common precursor for this type of treatment is diluted oxygen. Nonetheless, exposing a carbon material to ozone or CO_2 has also resulted in an efficient method to functionalize carbon materials. Besides, these carbons develop hydrophilicity as a result of the transformation of C=C bonds into out-of-plane C-C, due to the formation of the oxygen functionalities [61, 77-79]. Gas-phase oxidation is more effective in incorporating oxygen than the liquid-phase treatment and mainly develops anhydrides, lactones, phenols, and carbonyl/quinone groups [61]. Regardless of the oxygen functional groups incorporated by liquid-phase or gas-phase treatments, some of these oxygen surface functionalities may be removed by applying a thermal treatment under an inert atmosphere. Temperatures above 600 °C will remove the carboxylic anhydrides, a significant quantity of lactone, and some phenols; the remaining lactones and phenols are removed above 750 °C; and the carbonyl and ether functionalities may be eliminated at temperatures above 1100 °C [61].

In general, oxygen atoms in the carbon matrix lead to the creation of more structural defects, which improves oxygen adsorption by changing the charge distribution of adjacent carbon atoms; may improve the wettability of the material, which benefits the electrolyte diffusion [75, 80]; enhances the activation of O_2 molecules to efficiently reduce them at low overpotential and facilitates the reduction of by-products at sufficiently high overpotentials [81]. However, specific functionalities such as quinones and pyrones have been reported to change the electronic density of a carbon's surface, which favors the oxygen adsorption at those functionalities [75], demonstrating the importance of controlling the oxygen functionalities to enhance the performance of carbon electrocatalysts towards the ORR. Regarding OER, oxidized carbons have also been reported to enhance electroactivity. The incorporation of oxygen can lead to the formation of a positively charged carbon, which will be able to adsorb OH^- and H_2O via attractive electrostatic forces, promoting the electron transfer, and hence, the electroactivity [82]. Furthermore, altering the electronic distribution of the surrounding carbons due to oxygen atoms facilitates the adsorption of intermediate species, further enhancing the reaction mechanism [82, 83]. Nonetheless, this effect seems to be more

related to the presence of ketonic C=O functional groups than the other oxygen functionalities [83].

Nitrogen

The incorporation of nitrogen atoms into the carbon structure is one of the most studied functionalization techniques, as nitrogen functionalities have been shown to provide crucial improvements to the carbon materials' electroactivities towards the ORR and OER. There are three main nitrogen functionalities (Figure 1.5): pyridinic-nitrogen (N-6), pyrrolic-nitrogen (N-5), and quaternary-nitrogen (N-Q). Nitrogen atoms can be incorporated into a carbon structure by using thermal treatments with gaseous, liquid or solid precursors, by ball-milling followed by a thermal treatment, or by hydrothermal functionalization, among others. Besides, different precursors such as pyrrole, aniline, ammonia, and melamine can be used to incorporate different nitrogen functionalities [61, 84-87]. Aniline preferentially forms N-6 functionalities, whereas pyrrole favors the incorporation of pyrrolic-nitrogen. On the other hand, ammonia favors the formation of pyridinic groups at low temperatures and quaternary nitrogen at high temperatures (1000 °C) [88]. Functionalization with melamine may also result in materials with different functional groups. An increase of melamine:carbon ratio results mainly in a significant increase of N-6 functionalities and a decrease of N-Q groups [87]. The temperature of the treatment also plays an important role. For solid precursors, temperatures lower than 500 °C may form lactam, imides, and amines, whereas at temperatures above 600 °C, the three main nitrogen functionalities (N-6, N-5 and N-Q) are formed [61]. In the case of using gaseous precursors, temperatures in the range of 400-700 °C and prolonged holding times are needed to successfully functionalize the carbon material in terms of total nitrogen functionalization. Additionally, quaternary and oxide functionalities are only observed at high temperatures (700 °C) [61]. Generally, higher temperatures are reported to convert the pyridinic functionalities into N-Q, regardless of the nature of the precursor [61, 88], whereas N-5 is thermally unstable and may convert into N-Q at temperatures above 800 °C [70].

The functionalization with nitrogen is one of the most interesting strategies to enhance the reaction mechanism to a four-electron pathway in the ORR [29, 70, 88-90]. The similarity of C and N atomic size, complemented by nitrogen's five valence electrons,

allows a very strong covalent bond of the N-C material, thus increasing the electrocatalyst stability [70]. Furthermore, oxygen adsorption, which is crucial for oxygen reactions, may occur at defect sites resulting from nitrogen doping, favoring a four-electron mechanism [70]. Theoretically, each nitrogen functionality may give different benefits to the electrochemical performance of the electrocatalysts. The presence of N-Q in a basal plane results in an electron density movement, which favors oxygen dissociation [91]. N-6 is present in the plane of the carbon matrix and possesses a lone electron pair, which favors the bonding of oxygen to the neighboring carbon and, consequently, increases the ability to donate electrons and adsorb oxygen [92]. N-5 can modify the band structure of the carbons offering two *p*-electrons to the aromatic system. However, N-5 groups have also been reported to lead to an undesirable indirect reaction mechanism towards the ORR, requiring a subsequent thermal treatment at higher temperatures (800 °C) to convert it into N-Q functionalities [70]. All three nitrogen groups present very interesting characteristics to improve carbon material's electroactivity. Nonetheless, there is some controversy in the existing literature about which functionality results in higher performance. Some studies point out that the ORR is promoted by pyridinic groups [93, 94], while others suggest that the catalytic enhancement is due to N-Q [41, 95-97], to both N-6 and N-Q [88, 98, 99] or even to the synergies between pyridinic and pyrrolic groups [93, 100]. Recently, it has also been reported that the ratios between the nitrogen functionalities are the parameters playing the major role towards the ORR [91]. Furthermore, an excessive incorporation of nitrogen functionalities seems to result in lackluster performance towards the ORR [70]. This lack of unanimity may be probably due to the nature of the carbon material, which can have different synergies towards the nitrogen functionalities.

The nitrogen-doping towards OER seems to be as controversial as in the ORR, even though the OER is commonly studied using transition metals and, hence, there are fewer reports of metal-free N-doped carbons as OER electrocatalysts than for the ORR. The incorporation of nitrogen functionalities withdraws electronic charge from carbon atoms in their proximity, which transforms the carbon atom into an active center [101, 102]. These carbon active sites can then promote the electron transfer between the oxygen species and the catalyst surface by adsorbing OH^- through electrostatic forces and,

consequently, enhance the OER activity. Some authors claim that N-6 functionalities are the main responsible for improving the electroactivity in carbon materials towards the oxygen evolution reaction [41, 94, 97, 103]. Nonetheless, there are reports that state that both N-6 and N-5 enhance the OER activity [100], while others suggest that N-Q is the main OER promoter [101]. However, regardless of the type of nitrogen functionality, most published studies seem to agree that the existence of electron-deficient centers in electrocatalysts is the key reason for achieving higher OER electroactivities [102, 104, 105]. Moreover, the presence of a specific type of nitrogen functionality does not necessarily guarantee an improvement in the reaction's activity. Alike in the ORR, these discrepancies can be attributed to the carbon support employed. In fact, it has been reported that the presence of N-Q in carbon nanotubes decreases the OER overpotential more than N-6 and N-5, while this effect is not observed in graphene-based supports [100]. Therefore, the incorporation of nitrogen functionalities must be carefully considered alongside the properties of the carbon supports.

Transition metals

The incorporation of metals can also be an interesting methodology to modify the chemical properties of carbon materials. Noble and transition metals are usually introduced into carbons, as both groups have interesting properties for several applications. Nonetheless, noble metals are scarce and costly; hence, using transition metals is preferable to achieve an economic and environmentally sustainable future. The most frequently used transition metals are iron, cobalt, nickel, magnesium, and copper [106-113]. These transition metals are commonly incorporated via impregnation methods using different types of precursors, such as metal oxides or salts [66], which usually requires reducing the metal to its metallic form after the impregnation process. This process involves a two-step thermal treatment, named annealing and reduction, which are performed at the reduction temperature of the selected metal and under an inert atmosphere (N_2 or Ar) and a reducing atmosphere (H_2), respectively. Studies focused on the use of transition metal oxides have demonstrated that they can catalyze the ORR/OER with high electrocatalytic activities [114, 115]. Overall, the use of transition metal double oxides (spinels) has provided interesting bifunctional oxygen electroactivities. Among these materials, the combination of Co and Fe has outperformed the combination of Ni/Fe

and Mn/Fe, suggesting that the Co/Fe synergy is ideal for achieving oxygen bifunctionality [115]. Therefore, the combination of Fe and Co is one of the best representatives of the incorporation of dual metal active sites due to their low costs and bifunctional oxygen electroactivities [70, 116]. Therefore, this thesis will focus on these two metals; hence, more relevance will be given to what is published in the literature regarding Co and Fe. Transition metals exhibit low intrinsic electrical conductivity and low surface areas, and hence, need to be supported in a high-electrical conductive material such as carbon supports to give rise to high performances [114, 116]. The supported transition metal should display high activity, stability, and selectivity towards ORR and OER and should be sustainable and low-cost to be commercially attractive [116]. The electrochemical performance of the transition metal may be optimized by modifying its structure, morphology, composition, facet, and defects, whereas its sustainability can be accessed by its reliability and non-toxicity, as well as by its preparation process, which should be as green and environmentally friendly as possible [116]. Regarding the carbon support, it needs to present: i) high stability to prevent the electrocatalysts' degradation, ii) a large surface area to promote the dispersion of the metal and expose the active centers to the electrolyte, iii) a good coupling effect with the transition metal so that their synergy can enhance the electrocatalytic activity and the electrocatalyst's stability, and iv) high electrical conductivity to dimmish the ohmic resistance [116].

One of the main parameters of transition metals that play an important role in their electroactivity towards the ORR and the OER is their electronic state. Transition metals present two main electronic states on their surface: the *sp*-bands and the *d*-bands. The *sp*-bands are very similar for all transition metals, hence their contribution to the adsorption energy of the oxygen molecules for different metals will not present significant variations [117]. Therefore, the adsorption step will be controlled by the different *d*-bands that couple with the different adsorbate's valence states producing bonding and antibonding states [117]. From these two states, the antibonding is closer to the Fermi level and will govern the adsorption stage [117]. An up-shift of the *d*-states energy increases the antibonding states and decreases the antibonding filling, which results in stronger adsorption [31, 117]. The ORR active sites of transition metal oxides are usually the

metallic center whose catalytic activity is heavily influenced by the metal-oxygen coordination and the surface's electronegativity [102]. A study was published containing very important and interesting findings of the five transition metals abovementioned and their effect on the ORR [110]. The study reported two main conclusions that should be considered for the future design of electrocatalysts: i) pyrolysis of the carbon support with different transition metals significantly improves the catalytic activity towards the ORR in the following order Co >> Fe > Cu >Mn >> Ni and ii) Fe has the best selectivity for the ORR giving rise to the lowest by-product formation (Fe > Mn > Co >> Cu > Ni). The ORR activity in Fe sites has been attributed to the Fe^{2+} oxidation state rather than the Fe^{3+} specie [118]. Altough Fe species seems to present higher intrinsic activities towards the ORR than the Co species as well as faster charge transfer kinetics [118], the effect of Co has been also studied. The presence of Co^{2+} seems to be more influential than Co^{3+} towards the ORR due to Co^{2+}'s electron transferred to $O_{2(ads)}$ and the assistance in weakening or breaking the oxygen bonds, which results in the cobalt specie oxidation to Co^{3+} [116, 118]. Nonetheless, Co^{3+} cations are donor-acceptor reduction sites that can also be efficiently used in the ORR [116].

Transition metals supported on carbon materials also have important effects on the OER. An increase in the oxidation state of a transition metal ion can increase its electronegativity to a level closer to that of the O 2p energy level, leading to a higher metal-oxygen hybridization and, consequently, a more favorable electroactivity towards the OER [102]. Metals such as Co, Mn, Fe and Ni are the most commonly used transition metals to achieve high electrocatalytic performances [30]. The increase of element electronegativity (Mn < Fe < Co < Ni) reduces the energy required to bond oxygen atoms and may lead to the incorporation of moderately charged O anions that may balance the binding energy of OER intermediates (*-O, *-OH and *-OOH) and, consequently, the reaction's overpotential is reduced [28]. There is some controversy in the literature regarding Fe as an OER active center, as some authors report that iron species is, in fact, an active site for the OER [119-121], whereas other authors indicate that iron only enhances the electrode's conductivity [122, 123] or promotes electrons transfer [124] rather than acting as an active center. Regarding cobalt, the Co_3O_4's octahedron geometry has been reported to outperform the cubic geometry in cycling studies, capacities and rate

capabilities [125]. Moreover, the theoretical study of these geometries also demonstrated that the octahedral geometry has a lower O_2 desorption activation barrier than the cubic geometry, which enhances the active centers' refreshing and, consequently, their exposure resulting in higher ORR and OER electroactivities [125]. The oxidation state of Co is also involved in some controversy regarding which of them (Co^{2+} [126, 127], Co^{3+} [128, 129], Co^{4+} [122, 130, 131], or both Co^{2+} and Co^{3+} [132]) is the most electroactive towards the OER.

Synergy between transition metals and heteroatoms

The incorporation of heteroatoms and transition metals in a single carbon material can be interesting to tailor the properties of carbon materials. Studies using heteroatoms and transition metals on a carbon material have been reported to enhance its activity towards energy conversion applications [92, 133]. They can be incorporated in different steps, one heteroatom/metal per step [134, 135] or, in a single step with precursors containing the desired heteroatom/metal [107]. It can be used one transition metal and one heteroatom [107] or more of each type [136]. The appropriate methodology described for the functionalization with heteroatoms and the incorporation of transition metal may be combined to obtain these types of materials.

As already mentioned, both heteroatoms and transition metals have interesting properties towards the ORR and OER. Therefore, the appropriate combination between them is expected to further enhance the catalyst's performance, which is crucial for replacing commercial catalysts. The incorporation of nitrogen and transition metals is the most common combination studied for oxygen reactions [137-140]. The synergy between nitrogen and Fe or Co (Fe/N and Co/N) results in higher electroactivities towards both oxygen reactions than the combination of nitrogen with Ni (Ni/N) [140]. The N-Q functionality dramatically increases the charge, spin density and binding energy of Fe atoms, leading to higher activities and stabilities [141]. Furthermore, adding Co or Fe can be pivotal to achieving certain nitrogen functionalities. Cobalt catalyzes the incorporation of N-6 at the edge of graphene planes and, conversely, Fe favors the nitrogen functionalization at the center of the graphene layer resulting in N-Q [70]. Nonetheless, the pyrolysis temperature applied to bond the transition metal to the N-carbon structures is very important as it can completely modify the type of resulting bonds in the structures.

For example, employing temperatures higher than 800 °C can result in the severance of the Co-N bonds and the formation of metallic Co-Co bonds [70].

An interesting strategy to incorporate a transition metal and nitrogen is using MN_4 (M=metal) complexes as precursors. These complexes have been reported as excellent oxygen electrocatalysts and can be incorporated into carbon materials with an impregnation step, followed by a thermal treatment [35, 107]. The most common types of MN_4 complexes are porphyrin complexes and phthalocyanines (Pcs). The base structures of these complexes are presented in Figure 1.6, in which the transition metal is located in the center of the complex. Besides MN_x complexes, MS_y complexes can also be found in literature as efficient oxygen electrocatalysts, although they are not as used as nitrogen-containing complexes.

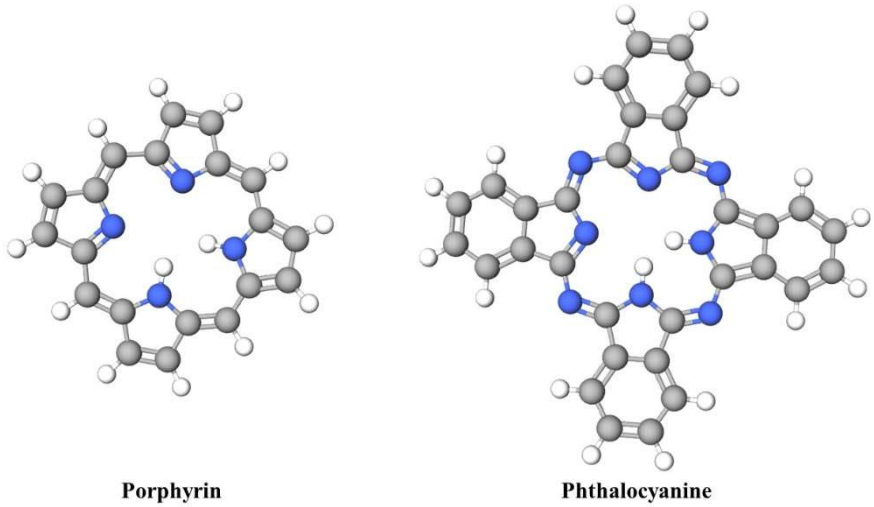


Figure 1.6 - Porphyrin and phthalocyanine structures. Grey – carbon, white – hydrogen, blue – nitrogen.

The most common transition metals that can be found inside porphyrin and Pc structures are Fe, Co, Mn, Cu, and Ni. The ORR electrochemical activity of Pcs with different central chelated metal ions has been widely studied and the following conclusions have been reported: i) the electrochemical performance follows the trend Fe(II) > Co(II) > Ni(II) > Cu(II), ii) M-N_x groups provide superior catalytic activity towards the ORR when compared to M-S_y groups, iii) pyridinic-N and metal are necessary to compose an active site towards the ORR and iv) Fe-N_x are the active sites with higher activities for the ORR

[110, 112, 142, 143]. Considering these results, the synergy between nitrogen and Co/Fe appears to be the most interesting combination to modify the surface chemistry of carbon materials.

The Fe-N_x active centers are considered the most energetically favored sites to reduce O_2 using a 4-electron pathway, whereas N-Q and hydrogenated nitrogen sites present in the neighboring favor the formation of by-products [35]. Moreover, Fe-N_4 is theoretically more stable than Fe-N_2 [144]. Therefore, the Fe-N_4 complex is the most studied combination in Fe-N_x-C electrocatalysts. Experiments and theoretical studies suggest that an increase of N-Q content in Fe-N_4 centers gives rise to an enhanced intrinsic active of the active sites towards the ORR [145]. Theoretical studies demonstrate that, similarly to Fe-N_x structures, the Co-N_4 active sites are more stable than the Co-N_2 centers and are more important towards the ORR, although they present a weak interaction with the by-product and, consequently, only perform a two-electron reduction [146]. Overall, the most studied bimetallic N-doped structures for the ORR are those that present the synergistic effect of dual active sites involving Fe and other transition metals, as Fe is widely considered the optimal transition metal towards the ORR. The combination of Fe-Co sites in Fe,Co,N-doped carbons can enhance the ORR activity by lowering the cleavage barrier of the oxygen molecule bond regardless of their porphyrin or Pc-like structure [145]. Furthermore, the dissociation barrier of O_2 and OOH using Fe-Co sites is also significantly lower than their monometallic counterparts. Moreover, the combination of FePc and CoPc has been reported to display impressive high electrocatalytic activity towards the ORR due to the synergy between the MN_x sites and the N-6 species [147].

The combination of N-Q functionalities with iron species has also been reported as the main N-Fe synergy to achieve superior OER electroactivities. The incorporation of N-Q allows the formation of more stable Fe/N configurations than the addition of N-6 or N-5 and also increases the charge and spin densities of the Fe atom, which improves the OER and the stability of the iron active sites [141]. The incorporation of nitrogen atoms can help increase the stability of high oxidation state of metals due to their electron donor properties [148]. Theoretical calculations demonstrate that introducing nitrogen ligands and cobalt species can form active sites (Co-N_4 and Co-N_2) that are highly electroactive

towards the OER [148]. Moreover, the Co-N_3 species seems to have a much worse OER performance than its Co-N_X counterparts due to a too strong adsorption of OH^*; hence, the OER performance of Co-N_X is as follows: Co-N_4 > Co-N_2 > Co-N_3 [148]. The coexistence of Fe and Co sites on N-doped carbons has also been reported to enhance the OER electroactivity. The formation of Fe-N_4 species favors the adsorption of the first intermediate (OOH*), whereas the cobalt active center adsorbs O* and can help stabilize the intermediate on the iron site through hydrogen bond interaction [149]. Regarding the combination of FePc and CoPc towards OER, high OER electroactivities can be achieved with their combination into carbon supports. Nonetheless, the presence of both FePc and CoPc does not significantly improve the OER electroactivity compared to the CoPc-doped material [147]. However, the balance between their ORR and OER performances is essential to achieve a BOC. Table 1.1 presents some examples of BOCs using Fe and/or Co and/or N on carbon supports by displaying their reported ORR's $E_{1/2}$, the OER's E_{10} and the overpotential gap between both oxygen reactions (ΔE).

Table 1.1 - E_{10}, $E_{1/2}$ and ΔE of some state-of-the-art electrocatalysts (adapted from [115]).

Sample	E_{10} (V)	$E_{1/2}$ (V)	ΔE (V)	Ref.
Co/$CoFe_2O_4$@N-graphene	1.62	0.63	0.99	[150]
$FeCo_2O_4$/C	1.72	0.76	0.96	[151]
Co3O4/N-rGO	1.72	0.79	0.93	[152]
Co@N-CNT-1000	1.74	0.82	0.91	[139]
Co_xO_y/NC	1.66	0.76	0.90	[153]
Co@N-CNT-800	1.72	0.84	0.88	[139]
Fe@N-C-700	1.71	0.83	0.88	[154]
Co@N-CNT-900	1.71	0.84	0.87	[139]
Fe/Fe_2O_3@Fe-N-C-1000	1.66	0.79	0.87	[155]
Co-N/PC@CNT-700	1.63	0.77	0.86	[156]
Co@Co_3O4/NC-1	1.65	0.80	0.85	[157]
Co$(OH)_x$-NCNT	1.58	0.74	0.84	[158]
$CoFe_2O_4$ NP/rod-like OMC	1.56	0.72	0.84	[159]
Co_3O_4/NHPC	1.65	0.83	0.82	[160]
CoNPC-71	1.63	0.81	0.82	[161]
FeCo-NPC-1100	1.60	0.79	0.81	[162]
Co/CoO@Co-N-C-800	1.60	0.79	0.81	[163]
3D Co-N-C NN-800	1.70	0.90	0.80	[164]
Fe-N-CNT/OMC	1.65	0.85	0.80	[138]
Co@Co_3O_4@NC-900	1.60	0.80	0.80	[165]
Co/N-CNT	1.62	0.84	0.78	[140]
Co_3O_4/NcsCNT-GNR	1.59	0.81	0.78	[166]
Fe_3C@NG800-0.2	1.58	0.80	0.78	[167]
N-Co_3O_4@NC-2	1.55	0.77	0.78	[168]
Co@N-CNTF	1.58	0.81	0.77	[169]
Fe/C/N	1.59	0.83	0.76	[170]
N-CG-CoO	1.57	0.81	0.76	[171]

Table 1.1 - E_{10}, $E_{1/2}$ and ΔE of some state-of-the-art electrocatalysts (adapted from [115]) - continuation.

Sample	E_{10} (V)	$E_{1/2}$ (V)	ΔE (V)	Ref.
Co/N-CNSNs	1.57	0.84	0.73	[172]
CoO/NGHSs	1.56	0.83	0.73	[171]
Co/Co-N-C	1.51	0.78	0.73	[173]
1 nm-CoO_x/N-RGO	1.60	0.89	0.71	[174]
Co_3O_4/Hollow N-Doped Carbon	1.54	0.83	0.71	[175]
Co-CoO/N-rGO	1.47	0.77	0.70	[176]
Co@NCNT	1.55	0.87	0.68	[177]

1.3. Motivation and objectives

The urgent necessity for nations to create energetic independency from fossil fuels and reduce their reliance on other nations to suppress their energy needs is one of the hottest research topics for the future. The use of hydrogen is one of the proposed strategies to produce green energy and achieve a climate-neutral planet in the next decades. The unitized regenerative fuel cell (URFC) is one of the rising electrochemical devices that can use hydrogen as fuel, alongside oxygen, and may be commercially attractive to fight the climate crisis. Nonetheless, this technology still has not reached a mature phase and requires further investigation and optimization, especially its sluggish oxygen reduction and evolution reactions. Therefore, the main goal of this PhD thesis is to prepare highly electroactive and stable bifunctional oxygen electrocatalysts using carbon supports using environmentally friendly methods for their synthesis and emphasizing the importance of their textural, physical, and chemical properties to achieve such electroactivity. The accomplishment of this goal involves the attainment of several specific objectives (Figure 1.7) associated with the preparation of carbon materials with different properties, their physico-chemical characterization, and the assessment of their electroactivity towards oxygen reduction and evolution reactions.

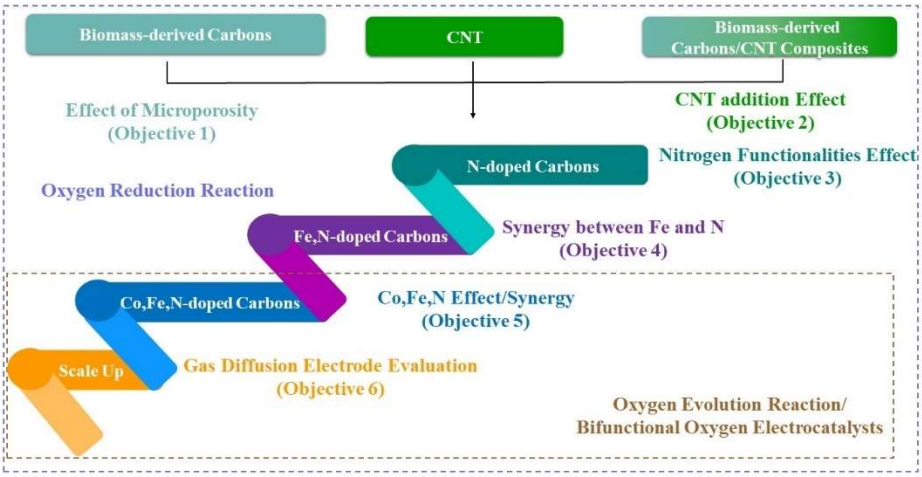


Figure 1.7 – Materials synthesized and their respective target oxygen reaction(s) to accomplish the objectives proposed.

To achieve the optimal energy scenario, all materials used in energy conversion devices should be provided by renewable energy sources using simple, low cost and environmentally friendly methods, such as biomass-derived carbon materials and the hydrothermal carbonization (HTC) method. Nonetheless, these materials can not be directly used as highly efficient electrocatalysts for the URFC's reactions and need further modifications to generate porosity and increase their intrinsic activity. Moreover, it should be highlighted that most studies based on carbon materials are related to the effect of heteroatoms and metals and the synergies between them, leaving the effect of porosity often aside. Although the importance of microporosity towards the ORR has been suggested [45, 46], there is still a lack of scientific research and knowledge about its effect on the performance of carbon electrocatalysts. Taking this into account, the first objective of this PhD thesis is to modify the properties of biomass-derived carbon materials prepared by HTC and establish relationships between these properties and their electroactivity towards the ORR, paying special attention to the effect of microporosity (Figure 1.7).

Besides porosity, using carbon materials with high electrical conductivity is crucial to achieving enhanced electrocatalytic activities. Moreover, interesting synergies can be observed between graphitic structures with π-π systems and some metallic complexes. In this context, CNT presenting these characteristics are postulated as excellent carbon

support for the ORR and OER. Besides, porous carbons and CNT display complementary properties; hence their combination to form a carbon composite may result in a material with porosity and high electrical conductivity, which can enhance the electroactivity of the catalysts and reduce the electrocatalysts' production cost. Therefore, the synthesis of highly electroactive composite materials using biomass-derived carbons and CNT as carbon support has been defined as the second of the specific objectives of this PhD thesis.

Incorporating nitrogen functionalities is crucial to achieving outstanding ORR/OER electrocatalytic performances. Nonetheless, there is still some controversy related to the importance and role of each nitrogen functionality towards each oxygen reaction. The functionalization conditions such as temperature, atmosphere and carbon support employed have an essential role in the formation of surface nitrogen groups. Therefore, a comprehensive study on nitrogen functionalization and its consequent effect on the ORR/OER needs to be addressed. Accordingly, the third objective of this PhD thesis focuses on the incorporation of nitrogen functionalities in different carbon supports and their effect on the material's electroactivity.

Similarly, transition metals are also crucial to obtain bifunctional oxygen electrocatalysts due to their intrinsic catalytic activity towards the oxygen reactions. Although existing literature around this topic is already extensive, there is a gap regarding the optimization of transition metals supported on carbon materials, namely: i) the oxidation states more favorable to achieve the highest electroactivities, ii) the optimal synthesis route to incorporate the transition metal, iii) the effect of the carbon's properties and, iv) the evaluation of the synergy between transition metals and nitrogen functionalities, which can be crucial to enhance the electrocatalyst's performance. Therefore, the fourth specific objective of this PhD thesis involves the incorporation of the most influent transition metal towards the ORR, i.e. iron, on the surface of different undoped and N-doped carbon materials to study their effect on the electroactivity. To address this objective, Fe and N were introduced onto the carbon structures using iron oxide and melamine, respectively, or iron(II) phthalocyanine (FePc), which contains the heteroatom and transition metal in a single molecule. On the other hand, the fifth specific objective focuses on the addition of Co species onto the N-Fe carbon materials using cobalt(II) phthalocyanine or cobalt

nitrate. The sixth and final objective of this PhD thesis is the scale up electrochemical assessments of the most promising synthesized materials. The carbon materials functionalized with a combination of different nitrogen functionalities and transition metals, using a single precursor with the required elements or multiple precursors with one element each, were also studied as bifunctional electrocatalysts in gas diffusion electrodes to evaluate their performance and their possible industrialization.

1.4. Thesis outline

This thesis is organized into 10 main chapters whose content is detailed below.

The first chapter, *State-of-the-art, Motivation, Objectives and Thesis Outline*, explains the necessity to optimize the unitized regenerative fuel cell system (URFC) and the main concerns around the device, especially those related to the main challenges of the involved electrochemical reactions and the state-of-the-art focused on the carbon materials employed as electrocatalysts.

The second chapter, *Materials and Methods*, describes in detail all the reagents, synthesis procedures, and characterization techniques used to develop all the work that encompasses this PhD thesis.

The following chapters (*Chapters 3-8*) constitute the bulk of the thesis and are based on published or submitted peer-reviewed articles, as shown in Table 1.2.

Table 1.2 – Published or submitted peer-reviewed articles.

Chapter	Publication
3	R. G. Morais, N. Rey-Raap, J. L. Figueiredo, M. F.R. Pereira, *Glucose-derived carbon materials with tailored properties as electrocatalysts for the oxygen reduction reaction,* Beilstein J. Nanotechnol., 10 (2019) 1089-1102.
4	R. G. Morais, N. Rey-Raap, R. Costa, C. Pereira, A. Guedes, J. L. Figueiredo, M. F. R. Pereira, *Hydrothermal Carbon/Carbon Nanotube Composites as Electrocatalysts for the Oxygen Reduction Reaction,* J. Compos. Sci., 4 (2020) 1-14.
5	R.G. Morais, N. Rey-Raap, J.L. Figueiredo, M.F.R. Pereira, *Improving the electrocatalytic activity of glucose/carbon nanotube composites for the oxygen reduction reaction by doping with nitrogen and iron*.
6	R.G. Morais, N. Rey-Raap, J.L. Figueiredo, M.F.R. Pereira, *Highly electroactive N–Fe hydrothermal carbons and carbon nanotubes for the oxygen reduction reaction*, J. Energy Chem., 50 (2020) 260-270.
7	R.G. Morais, N. Rey-Raap, J.L. Figueiredo, M.F.R. Pereira, *Fe, Co, N-doped carbon nanotubes as bifunctional oxygen electrocatalysts*, Appl. Surf. Sci., 572 (2022) 151459.
8	R.G. Morais, N. Rey-Raap, J.L. Figueiredo, M.F.R. Pereira, *Optimization of cobalt on CNT towards the oxygen evolution reaction and its synergy with iron (II) phthalocyanine as bifunctional oxygen electrocatalyst*, Catalysis Today, (2023) 114057.

In the third chapter, *Glucose-derived carbon materials with tailored properties as electrocatalysts for the oxygen reduction reaction*, the importance of the textural properties of biomass-derived carbons and the influence of nitrogen functionalities towards the oxygen reduction reaction (ORR) is assessed.

The fourth chapter, *Hydrothermal Carbon/Carbon Nanotube Composites as Electrocatalysts for the Oxygen Reduction Reaction*, focuses on the influence of the presence of carbon nanotubes (CNT) during the hydrothermal carbonization of glucose. Moreover, the importance of the carbons' electrical conductivity and nitrogen functionalities towards the ORR is discussed.

The main objective of the work detail in the fifth chapter, *Improving the electrocatalytic activity of glucose/carbon nanotube composites for the oxygen reduction reaction by doping with nitrogen and iron*, was to understand the influence of the thermal treatments employed during the incorporation of nitrogen and iron on the carbon support and the consequent electrocatalytic activity in the ORR.

In the sixth chapter, *Highly electroactive N–Fe hydrothermal carbons and carbon nanotubes for the oxygen reduction reaction*, the influence of the porosity of the carbon support on the incorporation of FePc and synergy between the CNT's π-π systems and the structure of the phthalocyanines, and hence, on the chemical and electrochemical properties as well as on the ORR performance were studied.

The main goal of the study presented in the seventh chapter, *Fe, Co, N-Doped Carbon Nanotubes as Bifunctional Oxygen Electrocatalysts*, was to prepare carbon electrocatalysts with high electrocatalytic activity in the ORR and OER. Moreover, iron(II) phthalocyanine (FePc) and cobalt(II) phthalocyanine (CoPc) were added separately or simultaneously to the CNT to study the effect of each macrocycle and their synergy towards the ORR and OER.

In the eighth chapter, *Optimization of cobalt on CNT towards the oxygen evolution reaction and its synergy with iron (II) phthalocyanine as bifunctional oxygen electrocatalyst*, the influence of cobalt species supported on CNT on the OER was investigated. Moreover, the combination of the most electroactive OER cobalt species and FePc was studied as bifunctional oxygen electrocatalysts.

The most promising bifunctional oxygen electrocatalysts from chapter eight were electrochemically evaluated using a gas diffusion electrode in the ninth chapter, *Gas diffusion electrode evaluation*.

The main conclusions of this PhD thesis are presented alongside suggestions for future work in the tenth chapter, *Conclusions and Future Work*.

1.5. References

[1] I.E. Agency, Global electricity demand growth is slowing, weighed down by economic weakness and high prices, 2022.
[2] B. Pretoleum, Statistical Review of World Energy, 2019.
[3] J. Zhao, K. Dong, X. Dong, M. Shahbaz, How renewable energy alleviate energy poverty? A global analysis, Renew. Energy, 186 (2022) 299-311.
[4] S. Kanwal, M.T. Mehran, M. Hassan, M. Anwar, S.R. Naqvi, A.H. Khoja, An integrated future approach for the energy security of Pakistan: Replacement of fossil fuels with syngas for better environment and socio-economic development, Renew. Sust. Energ. Rev., 156 (2022) 111978.
[5] J. Stacy, Y.N. Regmi, B. Leonard, M. Fan, The recent progress and future of oxygen reduction reaction catalysis: A review, Renew. Sust. Energ. Rev., 69 (2017) 401-414.
[6] A. Kirubakaran, S. Jain, R.K. Nema, A review on fuel cell technologies and power electronic interface, Renew. Sust. Energ. Rev., 13 (2009) 2430-2440.
[7] T.M. Gulotta, R. Salomone, F. Lanuzza, G. Saija, G. Mondello, G. Ioppolo, Life Cycle Assessment and Life Cycle Costing of unitized regenerative fuel cell: A systematic review, Environ. Impact Assess. Rev., 92 (2022) 106698.
[8] M. Company, Global Energy Perspective 2022, 2022.
[9] B. Paul, J. Andrews, PEM unitised reversible/regenerative hydrogen fuel cell systems: State of the art and technical challenges, Renew. Sust. Energ. Rev., 79 (2017) 585-599.
[10] Q. Guo, H. Guo, F. Ye, L. Xing, C.F. Ma, A numerical study of dynamic behaviors of a unitized regenerative fuel cell during gas purging, Int. J. Hydrog. Energy, 47 (2022) 22203-22214.
[11] H. Guo, J. Song, F. Ye, M.A. Chong Fang, Dynamic response during mode switching of unitized regenerative fuel cells with orientational flow channels, Renew. Energy, 188 (2022) 698-710.
[12] N. ul Hassan, P. Ganesan, A.A. Lando, W.E. Mustain, H.R. Colón-Mercado, Stable, high-performing bifunctional electrodes for anion exchange membrane-based unitized regenerative fuel cells, J. Power Sources, 541 (2022) 231599.
[13] P. Gayen, S. Saha, X. Liu, K. Sharma, V.K. Ramani, High-performance AEM unitized regenerative fuel cell using Pt-pyrochlore as bifunctional oxygen electrocatalyst, Proc. Natl. Acad. Sci., 118 (2021) e2107205118.
[14] Y. Wang, D.Y.C. Leung, J. Xuan, H. Wang, A review on unitized regenerative fuel cell technologies, part-A: Unitized regenerative proton exchange membrane fuel cells, Renew. Sust. Energ. Rev., 65 (2016) 961-977.
[15] T. Sadhasivam, K. Dhanabalan, S.-H. Roh, T.-H. Kim, K.-W. Park, S. Jung, M. Kurkuri, H.-Y. Jung, A comprehensive review on unitized regenerative fuel cells: Crucial challenges and developments, 2016.
[16] K. Dutta, D. Rana, H.S. Han, P.P. Kundu, Unitized Regenerative Fuel Cells: A Review on Developed Catalyst Systems and Bipolar Plates, Fuel Cells, 17 (2017) 736-751.
[17] Y. Wang, D.Y.C. Leung, J. Xuan, H. Wang, A review on unitized regenerative fuel cell technologies, part B: Unitized regenerative alkaline fuel cell, solid oxide fuel cell, and microfluidic fuel cell, Renew. Sust. Energ. Rev., 75 (2017) 775-795.
[18] M.M. Mohideen, Y. Liu, S. Ramakrishna, Recent progress of carbon dots and carbon nanotubes applied in oxygen reduction reaction of fuel cell for transportation, Appl. Energy, 257 (2020) 114027.
[19] T. Wang, X. Cao, L. Jiao, PEM water electrolysis for hydrogen production: fundamentals, advances, and prospects, Carb. Neutrality, 1 (2022) 21.
[20] Z. Wang, C. Cao, Y. Zheng, S. Chen, F. Zhao, Abiotic Oxygen Reduction Reaction Catalysts Used in Microbial Fuel Cells, ChemElectroChem, 1 (2014) 1813-1821.
[21] J.L. Figueiredo, Nanostructured porous carbons for electrochemical energy conversion and storage, Surf. Coat. Technol., 350 (2018) 307-312.

[22] Z. Wu, M. Song, J. Wang, X. Liu, Recent Progress in Nitrogen-Doped Metal-Free Electrocatalysts for Oxygen Reduction Reaction, Catalysts, 8 (2018) 196.
[23] R. Ma, G. Lin, Y. Zhou, Q. Liu, T. Zhang, G. Shan, M. Yang, J. Wang, A review of oxygen reduction mechanisms for metal-free carbon-based electrocatalysts, Npj Comput. Mater., 5 (2019) 78.
[24] Y. Li, Q. Li, H. Wang, L. Zhang, D.P. Wilkinson, J. Zhang, Recent Progresses in Oxygen Reduction Reaction Electrocatalysts for Electrochemical Energy Applications, Electrochemical Energy Reviews, 2 (2019) 518-538.
[25] X. Ge, A. Sumboja, D. Wuu, T. An, B. Li, F.W.T. Goh, T.S.A. Hor, Y. Zong, Z. Liu, Oxygen Reduction in Alkaline Media: From Mechanisms to Recent Advances of Catalysts, ACS Catal., 5 (2015) 4643-4667.
[26] C. Ho Lee, S. Uck Lee, Theoretical Basis of Electrocatalysis, 2018.
[27] Q. Liang, G. Brocks, A. Bieberle-Hütter, Oxygen evolution reaction (OER) mechanism under alkaline and acidic conditions, JPhys. Energy, 3 (2021) 026001.
[28] J. Song, C. Wei, Z.-F. Huang, C. Liu, L. Zeng, X. Wang, Z.J. Xu, A review on fundamentals for designing oxygen evolution electrocatalysts, Chem. Soc. Rev., 49 (2020) 2196-2214.
[29] N.-T. Suen, S.-F. Hung, Q. Quan, N. Zhang, Y.-J. Xu, H.M. Chen, Electrocatalysis for the oxygen evolution reaction: recent development and future perspectives, Chem. Soc. Rev., 46 (2017) 337-365.
[30] A. Vazhayil, L. Vazhayal, J. Thomas, S. Ashok C, N. Thomas, A comprehensive review on the recent developments in transition metal-based electrocatalysts for oxygen evolution reaction, Appl. Surf. Sci. Adv., 6 (2021) 100184.
[31] J. Li, Oxygen Evolution Reaction in Energy Conversion and Storage: Design Strategies Under and Beyond the Energy Scaling Relationship, Nano-Micro Lett., 14 (2022) 112.
[32] T. Sadhasivam, K. Dhanabalan, S.-H. Roh, T.-H. Kim, K.-W. Park, S. Jung, M. Kurkuri, H.-Y. Jung, A comprehensive review on unitized regenerative fuel cells: Crucial challenges and developments, Int. J. Hydrog. Energy, 42 (2016) 1-19.
[33] W.E. Mustain, M. Chatenet, M. Page, Y.S. Kim, Durability challenges of anion exchange membrane fuel cells, Energy Environ. Sci., 13 (2020) 2805-2838.
[34] S. Gottesfeld, D.R. Dekel, M. Page, C. Bae, Y. Yan, P. Zelenay, Y.S. Kim, Anion exchange membrane fuel cells: Current status and remaining challenges, J. Power Sources, 375 (2018) 170-184.
[35] A. Sarapuu, E. Kibena-Põldsepp, M. Borghei, K. Tammeveski, Electrocatalysis of oxygen reduction on heteroatom-doped nanocarbons and transition metal–nitrogen–carbon catalysts for alkaline membrane fuel cells, J. Mater. Chem. A, 6 (2018) 776-804.
[36] Z.F. Pan, L. An, T.S. Zhao, Z.K. Tang, Advances and challenges in alkaline anion exchange membrane fuel cells, Progress in Energy and Combustion Science, 66 (2018) 141-175.
[37] R. Doyle, M. Lyons, The Oxygen Evolution Reaction: Mechanistic Concepts and Catalyst Design, 2016, pp. 41-104.
[38] F. Song, L. Bai, A. Moysiadou, S. Lee, C. Hu, L. Liardet, X. Hu, Transition Metal Oxides as Electrocatalysts for the Oxygen Evolution Reaction in Alkaline Solutions: An Application-Inspired Renaissance, J. Am. Chem. Soc., 140 (2018) 7748-7759.
[39] K.G.C. Senarathna, H.M.S.P. Randiligama, R.M.G. Rajapakse, Preparation, characterization and oxygen reduction catalytic activities of nanocomposites of Co(ii)/montmorillonite containing polypyrrole, polyaniline or poly(ethylenedioxythiophene), RSC Adv., 6 (2016) 112853-112863.
[40] C. Hu, R. Paul, Q. Dai, L. Dai, Carbon-based metal-free electrocatalysts: from oxygen reduction to multifunctional electrocatalysis, Chem. Soc. Rev., 50 (2021) 11785-11843.
[41] D. Liu, Y. Tong, X. Yan, J. Liang, S.X. Dou, Recent Advances in Carbon-Based Bifunctional Oxygen Catalysts for Zinc-Air Batteries, Batter. Supercaps, 2 (2019) 743-765.
[42] Z. Gao, Y. Zhang, N. Song, X. Li, Biomass-derived renewable carbon materials for electrochemical energy storage, Materials Research Letters, 5 (2017) 69-88.

[43] S. Iqbal, H. Khatoon, A. Hussain Pandit, S. Ahmad, Recent development of carbon based materials for energy storage devices, Mater. Sci. Energ.Technol., 2 (2019) 417-428.
[44] M. Titirici, A. Funke, A. Kruse, Hydrothermal Carbonization of Biomass, 2015, pp. 325-352.
[45] M. Lefevre, F. Jaouen, J.-P. Dodelet, X.H. Li, K. Chen, A. Hay, Fe-Based Catalyst for Oxygen Reduction: Functionalization of Carbon Black and Importance of the Microporosity, ECS Trans., 3 (2006) 201-210.
[46] X. Bo, L. Guo, Ordered mesoporous boron-doped carbons as metal-free electrocatalysts for the oxygen reduction reaction in alkaline solution, Phys. Chem. Chem. Phys., 15 (2013) 2459-2465.
[47] D. Barrera, M. Florent, K. Sapag, T.J. Bandosz, Insight into the Mechanism of Oxygen Reduction Reaction on Micro/Mesoporous Carbons: Ultramicropores versus Nitrogen-Containing Catalytic Centers in Ordered Pore Structure, ACS Appl. Energy Mater., 2 (2019) 7412-7424.
[48] S.S. Sekhon, J. Lee, J.-S. Park, Biomass-derived bifunctional electrocatalysts for oxygen reduction and evolution reaction: A review, J. Energy Chem., 65 (2022) 149-172.
[49] W. Wijayanti, K.-i. Tanoue, Char Formation and Gas Products of Woody Biomass Pyrolysis, Energy Procedia, 32 (2013) 145-152.
[50] M. McGuire, G. Neighbour, Pyrolysis of Carbon-based Waste Materials – A Review, Carbon 2010USA, 2010.
[51] B. Viswanathan, I. Pulidindi, T. K. Varadarajan, Methods of Activation and Specific Applications of Carbon Materials, 2009.
[52] A. Mestre, A. Carvalho, Nanoporous Carbon Synthesis: An Old Story with Exciting New Chapters, 2018, pp. 34.
[53] A. Stein, Z. Wang, M.A. Fierke, Functionalization of Porous Carbon Materials with Designed Pore Architecture, Adv. Mater., 21 (2009) 265-293.
[54] H. Marsh, F. Rodríguez-Reinoso, Chapter 5 - Activation Processes (Thermal or Physical), in: H. Marsh, F. Rodríguez-Reinoso (Eds.) Activated Carbon, Elsevier Science Ltd, Oxford, 2006, pp. 243-321.
[55] D. Bergna, T. Hu, H. Prokkola, H. Romar, U. Lassi, Effect of Some Process Parameters on the Main Properties of Activated Carbon Produced from Peat in a Lab-Scale Process, Waste and Biomass Valorization, (2019).
[56] M. Shoaib, H. M. Al-Swaidan, Ramp Rate Influence on Synthesis of Sliced Porous Activated Carbon from Date Palm Tree by Physical Activation Method, Asian Journal of Chemistry, 26 (2014) 5295-5297.
[57] H. Marsh, F. Rodríguez-Reinoso, CHAPTER 6 - Activation Processes (Chemical), in: H. Marsh, F. Rodríguez-Reinoso (Eds.) Activated Carbon, Elsevier Science Ltd, Oxford, 2006, pp. 322-365.
[58] R.P. Rocha, O.S.G.P. Soares, J.L. Figueiredo, M.F.R. Pereira, Tuning CNT Properties for Metal-Free Environmental Catalytic Applications, C, 2016.
[59] C. Domínguez, F.J. Pérez-Alonso, M. Abdel Salam, S.A. Al-Thabaiti, A.Y. Obaid, A.A. Alshehri, J.L. Gómez de la Fuente, J.L.G. Fierro, S. Rojas, On the relationship between N content, textural properties and catalytic performance for the oxygen reduction reaction of N/CNT, Appl. Catal. B-Environ., 162 (2015) 420-429.
[60] X.-L. Ye, J. Cai, X.-D. Yang, X.-Y. Tang, Z.-Y. Zhou, Y.-Z. Tan, S.-Y. Xie, L.-S. Zheng, Quantifying defect-enhanced chemical functionalization of single-layer graphene and its application in supramolecular assembly, J. Mater. Chem. A, 5 (2017) 24257-24262.
[61] M. Enterría, J.L. Figueiredo, Nanostructured mesoporous carbons: Tuning texture and surface chemistry, Carbon, 108 (2016) 79-102.
[62] M.L. Toebes, J. M.P van Heeswijk, J.H. Bitter, A. Jos van Dillen, K. De Jong, The influence of oxidation on the texture and the number of oxygen-containing surface groups of carbon nanofibers, 2004.
[63] J.L. Figueiredo, M.F.R. Pereira, M.M.A. Freitas, J.J.M. Órfão, Modification of the surface chemistry of activated carbons, Carbon, 37 (1999) 1379-1389.

[64] J.R.A. Sietsma, A. Jos van Dillen, P.E. de Jongh, K.P. de Jong, Application of ordered mesoporous materials as model supports to study catalyst preparation by impregnation and drying, in: E.M. Gaigneaux, M. Devillers, D.E. De Vos, S. Hermans, P.A. Jacobs, J.A. Martens, P. Ruiz (Eds.) Studies in Surface Science and Catalysis, Elsevier2006, pp. 95-102.
[65] P. Munnik, P.E. de Jongh, K.P. de Jong, Recent Developments in the Synthesis of Supported Catalysts, Chemical Reviews, 115 (2015) 6687-6718.
[66] M. Schwickardi, T. Johann, W. Schmidt, O. Busch, F. Schüth, High surface area metal oxides from matrix assisted preparation in activated carbons, in: E. Gaigneaux, D.E. De Vos, P. Grange, P.A. Jacobs, J.A. Martens, P. Ruiz, G. Poncelet (Eds.) Studies in Surface Science and Catalysis, Elsevier2000, pp. 93-100.
[67] X. Fan, C. Yu, Z. Ling, J. Yang, J. Qiu, Hydrothermal Synthesis of Phosphate-Functionalized Carbon Nanotube-Containing Carbon Composites for Supercapacitors with Highly Stable Performance, ACS Appl. Mater. Interfaces, 5 (2013) 2104-2110.
[68] L. Roldán, L. Truong-Phuoc, A. Ansón-Casaos, C. Pham-Huu, E. García-Bordejé, Mesoporous carbon doped with N,S heteroatoms prepared by one-pot auto-assembly of molecular precursor for electrocatalytic hydrogen peroxide synthesis, Catalysis Today, 301 (2018) 2-10.
[69] R. Yadav, C.K. Dixit, Synthesis, characterization and prospective applications of nitrogen-doped graphene: A short review, Journal of Science: Advanced Materials and Devices, 2 (2017) 141-149.
[70] G. Wu, A. Santandreu, W. Kellogg, S. Gupta, O. Ogoke, H. Zhang, H.-L. Wang, L. Dai, Carbon nanocomposite catalysts for oxygen reduction and evolution reactions: From nitrogen doping to transition-metal addition, Nano Energy, 29 (2016) 83-110.
[71] H. Hosseini, M. Ghaffarzadeh, Surface functionalization of carbon nanotubes via plasma discharge: A review, Inorg. Chem. Commun., 138 (2022) 109276.
[72] F.V. Ferreira, W. Franceschi, B.R.C. Menezes, A.F. Biagioni, A.R. Coutinho, L.S. Cividanes, Chapter One - Synthesis, Characterization, and Applications of Carbon Nanotubes, in: S. Yaragalla, R. Mishra, S. Thomas, N. Kalarikkal, H.J. Maria (Eds.) Carbon-Based Nanofillers and Their Rubber Nanocomposites, Elsevier2019, pp. 1-45.
[73] Y. Cheng, Y. Tian, X. Fan, J. Liu, C. Yan, Boron doped multi-walled carbon nanotubes as catalysts for oxygen reduction reaction and oxygen evolution reactionin in alkaline media, Electrochim. Acta, 143 (2014) 291-296.
[74] S. Morales-Torres, T.L.S. Silva, L.M. Pastrana-Martínez, A.T.S.C. Brandão, J.L. Figueiredo, A.M.T. Silva, Modification of the surface chemistry of single- and multi-walled carbon nanotubes by HNO3 and H2SO4 hydrothermal oxidation for application in direct contact membrane distillation, Phys. Chem. Chem. Phys., 16 (2014) 12237-12250.
[75] I.M. Rocha, O.S.G.P. Soares, J.L. Figueiredo, C. Freire, M.F.R. Pereira, Bifunctionality of the pyrone functional group in oxidized carbon nanotubes towards oxygen reduction reaction, Catal. Sci. Technol., 7 (2017) 1868-1879.
[76] Y.-C. Chiang, W.-H. Lin, Y.-C. Chang, The influence of treatment duration on multi-walled carbon nanotubes functionalized by H2SO4/HNO3 oxidation, Appl. Surf. Sci., 257 (2011) 2401-2410.
[77] H.-L. Chiang, P.C. Chiang, C.P. Huang, Ozonation of activated carbon and its effects on the adsorption of VOCs exemplified by methylethylketone and benzene, Chemosphere, 47 (2002) 267-275.
[78] D. Iglesias, E. Senokos, B. Alemán, L. Cabana, C. Navío, R. Marcilla, M. Prato, J.J. Vilatela, S. Marchesan, Gas-Phase Functionalization of Macroscopic Carbon Nanotube Fiber Assemblies: Reaction Control, Electrochemical Properties, and Use for Flexible Supercapacitors, ACS Appl. Mater. Interfaces, 10 (2018) 5760-5770.
[79] F.G. Mendonça, J.D. Ardisson, R.M. Lago, J.C. Tristão, Selective Oxidation of Amorphous Carbon by CO2 to Produce Fe@C Nanoparticles from Bulky Fe/C Matrices, J. Braz. Chem. Soc., 26 (2015) 2379-2383.

[80] X. Wang, C. Ouyang, S. Dou, D. Liu, S. Wang, Oxidized carbon nanotubes as an efficient metal-free electrocatalyst for the oxygen reduction reaction, RSC Adv., 5 (2015) 41901-41904.
[81] K.-H. Wu, D.-W. Wang, X. Zong, B. Zhang, Y. Liu, I.R. Gentle, D.-S. Su, Functions in cooperation for enhanced oxygen reduction reaction: the independent roles of oxygen and nitrogen sites in metal-free nanocarbon and their functional synergy, J. Mater. Chem. A, 5 (2017) 3239-3248.
[82] N. Cheng, Q. Liu, J. Tian, Y. Xue, A.M. Asiri, H. Jiang, Y. He, X. Sun, Acidically oxidized carbon cloth: a novel metal-free oxygen evolution electrode with high catalytic activity, Chem. Commun., 51 (2015) 1616-1619.
[83] X. Lu, W.-L. Yim, B.H.R. Suryanto, C. Zhao, Electrocatalytic Oxygen Evolution at Surface-Oxidized Multiwall Carbon Nanotubes, J. Am. Chem. Soc., 137 (2015) 2901-2907.
[84] Y. Deng, Y. Xie, K. Zou, X. Ji, Review on recent advances in nitrogen-doped carbons: preparations and applications in supercapacitors, J. Mater. Chem. A, 4 (2016) 1144-1173.
[85] O.S.G.P. Soares, R.P. Rocha, A.G. Gonçalves, J.L. Figueiredo, J.J.M. Órfão, M.F.R. Pereira, Easy method to prepare N-doped carbon nanotubes by ball milling, Carbon, 91 (2015) 114-121.
[86] R. Sibul, E. Kibena-Põldsepp, S. Ratso, M. Kook, M. Käärik, M. Merisalu, P. Paiste, J. Leis, V. Sammelselg, K. Tammeveski, Nitrogen-doped carbon-based electrocatalysts synthesised by ball-milling, Electrochem. Commun., 93 (2018) 39-43.
[87] L.T. Soo, K.S. Loh, A.B. Mohamad, W.R.W. Daud, The effect of varying N/C ratios of nitrogen precursors during non-metal graphene catalyst synthesis, Int. J. Hydrog. Energy, 42 (2017) 9069-9076.
[88] L. Lai, J.R. Potts, D. Zhan, L. Wang, C.K. Poh, C. Tang, H. Gong, Z. Shen, J. Lin, R.S. Ruoff, Exploration of the active center structure of nitrogen-doped graphene-based catalysts for oxygen reduction reaction, Energy Environ. Sci., 5 (2012) 7936-7942.
[89] W. Wei, H. Liang, K. Parvez, X. Zhuang, X. Feng, K. Müllen, Nitrogen-Doped Carbon Nanosheets with Size-Defined Mesopores as Highly Efficient Metal-Free Catalyst for the Oxygen Reduction Reaction, Angew. Chem., 126 (2014) 1596-1600.
[90] Q. Wei, X. Tong, G. Zhang, J. Qiao, Q. Gong, S. Sun, Nitrogen-Doped Carbon Nanotube and Graphene Materials for Oxygen Reduction Reactions, Catalysts, 5 (2015).
[91] I.M. Rocha, O.S.G.P. Soares, D.M. Fernandes, C. Freire, J.L. Figueiredo, M.F.R. Pereira, N-doped Carbon Nanotubes for the Oxygen Reduction Reaction in Alkaline Medium: Synergistic Relationship between Pyridinic and Quaternary Nitrogen, ChemistrySelect, 1 (2016) 2522-2530.
[92] Z. Guo, G. Ren, C. Jiang, X. Lu, Y. Zhu, L. Jiang, L. Dai, High Performance Heteroatoms Quaternary-doped Carbon Catalysts Derived from Shewanella Bacteria for Oxygen Reduction, Sci. Rep., 5 (2015) 17064.
[93] J. Zheng, C. Guo, C. Chen, M. Fan, J. Gong, Y. Zhang, T. Zhao, Y. Sun, X. Xu, M. Li, R. Wang, Z. Luo, C. Chen, High content of pyridinic- and pyrrolic-nitrogen-modified carbon nanotubes derived from blood biomass for the electrocatalysis of oxygen reduction reaction in alkaline medium, Electrochim. Acta, 168 (2015) 386-393.
[94] K. Mamtani, D. Jain, D. Dogu, V. Gustin, S. Gunduz, A. Co, U. Ozkan, Insights into Oxygen Reduction Reaction (ORR) and Oxygen Evolution Reaction (OER) Active Sites for Nitrogen-doped Carbon Nanostructures (CN x) in Acidic Media, Appl. Catal. B-Environ., 220 (2017).
[95] H. Niwa, K. Horiba, Y. Harada, M. Oshima, T. Ikeda, K. Terakura, J.-i. Ozaki, S. Miyata, X-ray absorption analysis of nitrogen contribution to oxygen reduction reaction in carbon alloy cathode catalysts for polymer electrolyte fuel cells, J. Power Sources, 187 (2009) 93-97.
[96] D. Geng, Y. Chen, Y. Chen, Y. Li, R. Li, X. Sun, S. Ye, S. Knights, High oxygen-reduction activity and durability of nitrogen-doped graphene, Energy Environ. Sci., 4 (2011) 760-764.
[97] H.B. Yang, J. Miao, S.-F. Hung, J. Chen, H.B. Tao, X. Wang, L. Zhang, R. Chen, J. Gao, H.M. Chen, L. Dai, B. Liu, Identification of catalytic sites for oxygen reduction and oxygen evolution in N-doped graphene materials: Development of highly efficient metal-free bifunctional electrocatalyst, Science Advances, 2 (2016) e1501122.

[98] L. Yan, J. Yu, J. Houston, N. Flores, H. Luo, Biomass derived porous nitrogen doped carbon for electrochemical devices, Green Energy Environ., 2 (2017) 84-99.
[99] Z. Wang, S. Xiao, Z. Zhu, X. Long, X. Zheng, X. Lu, S. Yang, Cobalt-Embedded Nitrogen Doped Carbon Nanotubes: A Bifunctional Catalyst for Oxygen Electrode Reactions in a Wide pH Range, ACS Appl. Mater. Interfaces, 7 (2015) 4048-4055.
[100] M. Li, Z. Liu, F. Wang, J. Xuan, The influence of the type of N dopping on the performance of bifunctional N-doped ordered mesoporous carbon electrocatalysts in oxygen reduction and evolution reaction, J. Energy Chem., 26 (2017) 422-427.
[101] G. Murdachaew, K. Laasonen, Oxygen Evolution Reaction on Nitrogen-Doped Defective Carbon Nanotubes and Graphene, J. Phys. Chem. C, 122 (2018) 25882-25892.
[102] X. Xie, L. Du, L. Yan, S. Park, Y. Qiu, J. Sokolowski, W. Wang, Y. Shao, Oxygen Evolution Reaction in Alkaline Environment: Material Challenges and Solutions, Advanced Functional Materials, 32 (2022) 2110036.
[103] F. Davodi, M. Tavakkoli, J. Lahtinen, T. Kallio, Straightforward synthesis of nitrogen-doped carbon nanotubes as highly active bifunctional electrocatalysts for full water splitting, Journal of Catalysis, 353 (2017) 19-27.
[104] S. Chen, J. Duan, M. Jaroniec, S.-Z. Qiao, Nitrogen and Oxygen Dual-Doped Carbon Hydrogel Film as a Substrate-Free Electrode for Highly Efficient Oxygen Evolution Reaction, Adv. Mater., 26 (2014) 2925-2930.
[105] L. Li, H. Yang, J. Miao, L. Zhang, H.-Y. Wang, Z. Zeng, W. Huang, X. Dong, B. Liu, Unraveling Oxygen Evolution Reaction on Carbon-Based Electrocatalysts: Effect of Oxygen Doping on Adsorption of Oxygenated Intermediates, ACS Energy Letters, 2 (2017) 294-300.
[106] V. Vij, S. Sultan, A.M. Harzandi, A. Meena, J.N. Tiwari, W.-G. Lee, T. Yoon, K.S. Kim, Nickel-Based Electrocatalysts for Energy-Related Applications: Oxygen Reduction, Oxygen Evolution, and Hydrogen Evolution Reactions, ACS Catal., 7 (2017) 7196-7225.
[107] Y. Liu, Y.-S. Fan, Z.-M. Liu, Pyrolysis of iron phthalocyanine on activated carbon as highly efficient non-noble metal oxygen reduction catalyst in microbial fuel cells, Chem. Eng. J., 361 (2019) 416-427.
[108] W. Kiciński, B. Dembinska, M. Norek, B. Budner, M. Polański, P.J. Kulesza, S. Dyjak, Heterogeneous iron-containing carbon gels as catalysts for oxygen electroreduction: Multifunctional role of sulfur in the formation of efficient systems, Carbon, 116 (2017) 655-669.
[109] G. Wu, K.L. More, C.M. Johnston, P. Zelenay, High-Performance Electrocatalysts for Oxygen Reduction Derived from Polyaniline, Iron, and Cobalt, Science, 332 (2011) 443.
[110] P. Xu, W. Chen, Q. Wang, T. Zhu, M. Wu, J. Qiao, Z. Chen, J. Zhang, Effects of transition metal precursors (Co, Fe, Cu, Mn, or Ni) on pyrolyzed carbon supported metal-aminopyrine electrocatalysts for oxygen reduction reaction, RSC Adv., 5 (2015) 6195-6206.
[111] F. Li, G.-F. Han, H.-J. Noh, S.-J. Kim, Y. Lu, H.Y. Jeong, Z. Fu, J.-B. Baek, Boosting oxygen reduction catalysis with abundant copper single atom active sites, Energy Environ. Sci., 11 (2018) 2263-2269.
[112] M.A. Thorseth, C.E. Tornow, E.C.M. Tse, A.A. Gewirth, Cu complexes that catalyze the oxygen reduction reaction, Coordination Chemistry Reviews, 257 (2013) 130-139.
[113] Y. Gorlin, C.-J. Chung, D. Nordlund, B.M. Clemens, T.F. Jaramillo, Mn3O4 Supported on Glassy Carbon: An Active Non-Precious Metal Catalyst for the Oxygen Reduction Reaction, ACS Catal., 2 (2012) 2687-2694.
[114] Y. Wang, J. Li, Z. Wei, Transition-metal-oxide-based catalysts for the oxygen reduction reaction, J. Mater. Chem. A, 6 (2018) 8194-8209.
[115] X. Wu, C. Tang, Y. Cheng, X. Min, S.P. Jiang, S. Wang, Bifunctional Catalysts for Reversible Oxygen Evolution Reaction and Oxygen Reduction Reaction, Chem. Eur. J., 26 (2020) 3906-3929.
[116] K.B. Ibrahim, M.-C. Tsai, S.A. Chala, M.K. Berihun, A.W. Kahsay, T.A. Berhe, W.-N. Su, B.-J. Hwang, A review of transition metal-based bifunctional oxygen electrocatalysts, J. Chin. Chem. Soc., 66 (2019) 829-865.

[117] Z. Liu, Z. Zhao, B. Peng, X. Duan, Y. Huang, Beyond Extended Surfaces: Understanding the Oxygen Reduction Reaction on Nanocatalysts, J. Am. Chem. Soc., 142 (2020) 17812-17827.
[118] I. Alves, J. Santos, D. Viégas, E. Marques, C. Lacerda, L. Zhang, J. Zhang, A. Marques, Nanoparticles of Fe2O3 and Co3O4 as Efficient Electrocatalysts for Oxygen Reduction Reaction in Acid Medium, J. Braz. Chem. Soc., 30 (2019).
[119] E. Laouini, M. Hamdani, M.I. Pereira, J. Douch, M. Mendonça, Y. Berghoute, R. Singh, Preparation and electrochemical characterization of spinel type Fe–Co3O4 thin film electrodes in alkaline medium, Int. J. Hydrog. Energy, 33 (2008) 4936-4944.
[120] T. Grewe, X. Deng, H. Tüysüz, Influence of Fe Doping on Structure and Water Oxidation Activity of Nanocast Co3O4, Chem. Mater., 26 (2014) 3162–3168.
[121] C. Xiao, X. Lu, C. Zhao, Unusual synergistic effects upon incorporation of Fe and/or Ni into mesoporous Co3O4 for enhanced oxygen evolution, Chem. Commun., 50 (2014) 10122-10125.
[122] Q. Zhao, Z. Yan, C. Chen, J. Chen, Spinels: Controlled Preparation, Oxygen Reduction/Evolution Reaction Application, and Beyond, Chemical Reviews, 117 (2017) 10121-10211.
[123] Y. Sheng, M.L. Botero, M.Y. Manuputty, M. Kraft, R. Xu, Co3O4 and FexCo3–xO4 Nanoparticles/Films Synthesized in a Vapor-Fed Flame Aerosol Reactor for Oxygen Evolution, ACS Appl. Energy Mater., 1 (2018) 655-665.
[124] R.D.L. Smith, M.S. Prévot, R.D. Fagan, Z. Zhang, P.A. Sedach, M.K.J. Siu, S. Trudel, C.P. Berlinguette, Photochemical Route for Accessing Amorphous Metal Oxide Materials for Water Oxidation Catalysis, Science, 340 (2013) 60-63.
[125] R. Gao, J. Zhu, X. Xiao, Z. Hu, J. Liu, X. Liu, Facet-Dependent Electrocatalytic Performance of Co3O4 for Rechargeable Li–O2 Battery, J. Phys. Chem. C, 119 (2015) 4516-4523.
[126] S.-F. Hung, Y.-Y. Hsu, C.-J. Chang, C.-S. Hsu, N.-T. Suen, T.-S. Chan, H.M. Chen, Unraveling Geometrical Site Confinement in Highly Efficient Iron-Doped Electrocatalysts toward Oxygen Evolution Reaction, Adv. Energy Mater., 8 (2018) 1701686.
[127] H.-Y. Wang, S.-F. Hung, H.-Y. Chen, T.-S. Chan, H.M. Chen, B. Liu, In Operando Identification of Geometrical-Site-Dependent Water Oxidation Activity of Spinel Co3O4, J. Am. Chem. Soc., 138 (2016) 36-39.
[128] V. Tripkovic, H.A. Hansen, T. Vegge, From 3D to 2D Co and Ni Oxyhydroxide Catalysts: Elucidation of the Active Site and Influence of Doping on the Oxygen Evolution Activity, ACS Catal., 7 (2017) 8558-8571.
[129] K. Song, E. Cho, Y.-M. Kang, Morphology and Active-Site Engineering for Stable Round-Trip Efficiency Li–O2 Batteries: A Search for the Most Active Catalytic Site in Co3O4, ACS Catal., 5 (2015) 5116-5122.
[130] C.N. Brodsky, R.G. Hadt, D. Hayes, B.J. Reinhart, N. Li, L.X. Chen, D.G. Nocera, In situ characterization of cofacial Co(IV) centers in Co4O4 cubane: Modeling the high-valent active site in oxygen-evolving catalysts, Proc. Natl. Acad. Sci., 114 (2017) 3855-3860.
[131] P. Stelmachowski, J. Duch, D. Sebastián, M.J. Lázaro, A. Kotarba, Carbon-Based Composites as Electrocatalysts for Oxygen Evolution Reaction in Alkaline Media, Materials, 2021.
[132] Q. Wang, K. Cui, D. Liu, Y. Wu, S. Ren, Co–N Active Sites between Co Nanoparticles and N-Doped Carbon toward Remarkably Enhanced Electrocatalytic Oxygen Evolution and Hydrogen Evolution Reactions, Energy Fuels, 36 (2022) 1688-1696.
[133] G.L. Li, G.C. Cheng, W.W. Chen, C.D. Liu, L.F. Yuan, B.B. Yang, C. Hao, N/S/B-doped graphitized carbon encased Fe species as a highly active and durable catalyst towards oxygen reduction reaction, J. Colloid Interface Sci., 514 (2018) 108-116.
[134] Z. Yan, C. Dai, M. Zhang, X. Lv, X. Zhao, J. Xie, Nitrogen doped porous carbon with iron promotion for oxygen reduction reaction in alkaline and acidic media, International Journal of Hydrogen Energy, 44 (2019) 4090-4101.

[135] Y. Liu, B. Huang, X. Zhang, X. Huang, Z. Xie, In-situ fabrication of nitrogen-doped carbon nanosheets containing highly dispersed single iron atoms for oxygen reduction reaction, J. Power Sources, (2019) 125-133.
[136] Y. Li, B. Chen, X. Duan, S. Chen, D. Liu, K. Zang, R. Si, F. Lou, X. Wang, M. Rønning, L. Song, J. Luo, D. Chen, Atomically dispersed Fe-N-P-C complex electrocatalysts for superior oxygen reduction, Appl. Catal. B-Environ., 249 (2019) 306-315.
[137] Y. Liu, H. Jiang, Y. Zhu, X. Yang, C. Li, Transitional Metal (Fe, Co, Ni) Encapsulated in Nitrogen-Doped Carbon Nanotubes as Bi-functional Catalysts for Oxygen Electrode Reactions, 2016.
[138] L. Zhao, Q. Wang, X. Zhang, C. Deng, Z. Li, Y. Lei, M. Zhu, Combined Electron and Structure Manipulation on Fe-Containing N-Doped Carbon Nanotubes To Boost Bifunctional Oxygen Electrocatalysis, ACS Appl. Mater. Interfaces, 10 (2018) 35888-35895.
[139] L. Song, H. Fan, T. Wang, T. Xiang, M. Zhang, C. Hu, W. Zhou, J. He, Facile synthesis of Co, N enriched carbon nanotube and active site identifications for bifunctional oxygen reduction and evolution catalysis, Energy Storage Mater., 43 (2021) 365-374.
[140] Y. Liu, H. Jiang, Y. Zhu, X. Yang, C. Li, Transition metals (Fe, Co, and Ni) encapsulated in nitrogen-doped carbon nanotubes as bi-functional catalysts for oxygen electrode reactions, J. Mater. Chem. A, 4 (2016) 1694-1701.
[141] J. Jia, Z. Liu, F. Han, G.-J. Kang, L. Liu, J. Liu, Q.-D. Wang, The identification of active N species in N-doped carbon carriers that improve the activity of Fe electrocatalysts towards the oxygen evolution reaction, RSC Adv., 9 (2019) 4806-4811.
[142] D.-S. Yang, M.Y. Song, K.P. Singh, J.-S. Yu, The role of iron in the preparation and oxygen reduction reaction activity of nitrogen-doped carbon, Chem. Commun., 51 (2015) 2450-2453.
[143] Y. Zhan, F. Xie, H. Zhang, Z. Lin, J. Huang, W. Zhang, X. Sun, Y. Zhang, J. Chen, H. Meng, Non Noble Metal Catalyst for Oxygen Reduction Reaction and Its Characterization by Simulated Fuel Cell Test, 2018.
[144] S. Kattel, P. Atanassov, B. Kiefer, A density functional theory study of oxygen reduction reaction on non-PGM Fe–Nx–C electrocatalysts, Phys. Chem. Chem. Phys., 16 (2014) 13800-13806.
[145] Y. Yan, H. Cheng, Z. Qu, R. Yu, F. Liu, Q. Ma, S. Zhao, H. Hu, Y. Cheng, C. Yang, Z. Li, X. Wang, S. Hao, Y. Chen, M. Liu, Recent progress on the synthesis and oxygen reduction applications of Fe-based single-atom and double-atom catalysts, J. Mater. Chem. A, 9 (2021) 19489-19507.
[146] S. Kattel, P. Atanassov, B. Kiefer, Catalytic activity of Co–Nx/C electrocatalysts for oxygen reduction reaction: a density functional theory study, Phys. Chem. Chem. Phys., 15 (2013) 148-153.
[147] Y. Kumar, E. Kibena-Põldsepp, J. Kozlova, M. Rähn, A. Treshchalov, A. Kikas, V. Kisand, J. Aruväli, A. Tamm, J.C. Douglin, S.J. Folkman, I. Gelmetti, F.A. Garcés-Pineda, J.R. Galán-Mascarós, D.R. Dekel, K. Tammeveski, Bifunctional Oxygen Electrocatalysis on Mixed Metal Phthalocyanine-Modified Carbon Nanotubes Prepared via Pyrolysis, ACS Appl. Mater. Interfaces, 13 (2021) 41507-41516.
[148] Q. Zhang, Z. Duan, M. Li, J. Guan, Atomic cobalt catalysts for the oxygen evolution reaction, Chem. Commun., 56 (2020) 794-797.
[149] T. Tang, Z. Duan, D. Baimanov, X. Bai, X. Liu, L. Wang, Z. Wang, J. Guan, Synergy between isolated Fe and Co sites accelerates oxygen evolution, Nano Res., 16 (2023) 2218-2223.
[150] Y. Niu, X. Huang, L. Zhao, W. Hu, C.M. Li, One-Pot Synthesis of Co/CoFe2O4 Nanoparticles Supported on N-Doped Graphene for Efficient Bifunctional Oxygen Electrocatalysis, ACS Sustain. Chem. Eng., 6 (2018) 3556-3564.
[151] W. Yan, Z. Yang, W. Bian, R. Yang, FeCo2O4/hollow graphene spheres hybrid with enhanced electrocatalytic activities for oxygen reduction and oxygen evolution reaction, Carbon, 92 (2015) 74-83.

[152] Y. Li, C. Zhong, J. Liu, X. Zeng, S. Qu, X. Han, Y. Deng, W. Hu, J. Lu, Atomically Thin Mesoporous Co3O4 Layers Strongly Coupled with N-rGO Nanosheets as High-Performance Bifunctional Catalysts for 1D Knittable Zinc–Air Batteries, Adv. Mater., 30 (2018) 1703657.
[153] J. Masa, W. Xia, I. Sinev, A. Zhao, Z. Sun, S. Grützke, P. Weide, M. Muhler, W. Schuhmann, MnxOy/NC and CoxOy/NC Nanoparticles Embedded in a Nitrogen-Doped Carbon Matrix for High-Performance Bifunctional Oxygen Electrodes, Angew. Chem., Int. Ed. Engl., 53 (2014) 8508-8512.
[154] J. Wang, H. Wu, D. Gao, S. Miao, G. Wang, X. Bao, High-density iron nanoparticles encapsulated within nitrogen-doped carbon nanoshell as efficient oxygen electrocatalyst for zinc–air battery, Nano Energy, 13 (2015) 387-396.
[155] Y. Zang, H. Zhang, X. Zhang, R. Liu, S. Liu, G. Wang, Y. Zhang, H. Zhao, Fe/Fe2O3 nanoparticles anchored on Fe-N-doped carbon nanosheets as bifunctional oxygen electrocatalysts for rechargeable zinc-air batteries, Nano Res., 9 (2016) 2123-2137.
[156] J. Ban, G. Xu, L. Zhang, G. Xu, L. Yang, Z. Sun, D. Jia, Efficient Co–N/PC@CNT bifunctional electrocatalytic materials for oxygen reduction and oxygen evolution reactions based on metal–organic frameworks, Nanoscale, 10 (2018) 9077-9086.
[157] A. Aijaz, J. Masa, C. Rösler, W. Xia, P. Weide, A.J.R. Botz, R.A. Fischer, W. Schuhmann, M. Muhler, Co@Co3O4 Encapsulated in Carbon Nanotube-Grafted Nitrogen-Doped Carbon Polyhedra as an Advanced Bifunctional Oxygen Electrode, Angew. Chem., Int. Ed. Engl., 55 (2016) 4087-4091.
[158] J.E. Kim, J. Lim, G.Y. Lee, S.H. Choi, U.N. Maiti, W.J. Lee, H.J. Lee, S.O. Kim, Subnanometer Cobalt-Hydroxide-Anchored N-Doped Carbon Nanotube Forest for Bifunctional Oxygen Catalyst, ACS Appl. Mater. Interfaces, 8 (2016) 1571-1577.
[159] P. Li, R. Ma, Y. Zhou, Y. Chen, Z. Zhou, G. Liu, Q. Liu, G. Peng, Z. Liang, J. Wang, In situ growth of spinel CoFe2O4 nanoparticles on rod-like ordered mesoporous carbon for bifunctional electrocatalysis of both oxygen reduction and oxygen evolution, J. Mater. Chem. A, 3 (2015) 15598-15606.
[160] J. Guan, Z. Zhang, J. Ji, M. Dou, F. Wang, Hydrothermal Synthesis of Highly Dispersed Co3O4 Nanoparticles on Biomass-Derived Nitrogen-Doped Hierarchically Porous Carbon Networks as an Efficient Bifunctional Electrocatalyst for Oxygen Reduction and Evolution Reactions, ACS Appl. Mater. Interfaces, 9 (2017) 30662-30669.
[161] J. Sanetuntikul, S. Hyun, P. Ganesan, S. Shanmugam, Cobalt and nitrogen co-doped hierarchically porous carbon nanostructure: a bifunctional electrocatalyst for oxygen reduction and evolution reactions, J. Mater. Chem. A, 6 (2018) 24078-24085.
[162] B. Guo, Q. Ju, R. Ma, Z. Li, Q. Liu, F. Ai, M. Yang, S. Kaskel, J. Luo, T. Zhang, J. Wang, Mechanochemical synthesis of multi-site electrocatalysts as bifunctional zinc–air battery electrodes, J. Mater. Chem. A, 7 (2019) 19355-19363.
[163] X. Zhang, R. Liu, Y. Zang, G. Liu, G. Wang, Y. Zhang, H. Zhang, H. Zhao, Co/CoO nanoparticles immobilized on Co–N-doped carbon as trifunctional electrocatalysts for oxygen reduction, oxygen evolution and hydrogen evolution reactions, Chem. Commun., 52 (2016) 5946-5949.
[164] R. Wang, J. Cao, S. Cai, X. Yan, J. Li, W.M. Yourey, W. Tong, H. Tang, MOF@Cellulose Derived Co–N–C Nanowire Network as an Advanced Reversible Oxygen Electrocatalyst for Rechargeable Zinc–Air Batteries, ACS Appl. Energy Mater., 1 (2018) 1060-1068.
[165] Z. Guo, F. Wang, Y. Xia, J. Li, A.G. Tamirat, Y. Liu, L. Wang, Y. Wang, Y. Xia, In situ encapsulation of core–shell-structured Co@Co3O4 into nitrogen-doped carbon polyhedra as a bifunctional catalyst for rechargeable Zn–air batteries, J. Mater. Chem. A, 6 (2018) 1443-1453.
[166] X. Lu, H.M. Chan, C.-L. Sun, C.-M. Tseng, C. Zhao, Interconnected core–shell carbon nanotube–graphene nanoribbon scaffolds for anchoring cobalt oxides as bifunctional electrocatalysts for oxygen evolution and reduction, J. Mater. Chem. A, 3 (2015) 13371-13376.

[167] H. Jiang, Y. Yao, Y. Zhu, Y. Liu, Y. Su, X. Yang, C. Li, Iron Carbide Nanoparticles Encapsulated in Mesoporous Fe–N-Doped Graphene-Like Carbon Hybrids as Efficient Bifunctional Oxygen Electrocatalysts, ACS Appl. Mater. Interfaces, 7 (2015) 21511-21520.
[168] Z. Wang, W. Xu, X. Chen, Y. Peng, Y. Song, C. Lv, H. Liu, J. Sun, D. Yuan, X. Li, X. Guo, D. Yang, L. Zhang, Defect-Rich Nitrogen Doped Co3O4/C Porous Nanocubes Enable High-Efficiency Bifunctional Oxygen Electrocatalysis, Advanced Functional Materials, 29 (2019) 1902875.
[169] H. Guo, Q. Feng, J. Zhu, J. Xu, Q. Li, S. Liu, K. Xu, C. Zhang, T. Liu, Cobalt nanoparticle-embedded nitrogen-doped carbon/carbon nanotube frameworks derived from a metal–organic framework for tri-functional ORR, OER and HER electrocatalysis, J. Mater. Chem. A, 7 (2019) 3664-3672.
[170] Y. Zhao, K. Kamiya, K. Hashimoto, S. Nakanishi, Efficient Bifunctional Fe/C/N Electrocatalysts for Oxygen Reduction and Evolution Reaction, J. Phys. Chem. C, 119 (2015) 2583-2588.
[171] S. Mao, Z. Wen, T. Huang, Y. Hou, J. Chen, High-performance bi-functional electrocatalysts of 3D crumpled graphene–cobalt oxide nanohybrids for oxygen reduction and evolution reactions, Energy Environ. Sci., 7 (2014) 609-616.
[172] X. Huang, Y. Zhang, H. Shen, W. Li, T. Shen, Z. Ali, T. Tang, S. Guo, Q. Sun, Y. Hou, N-Doped Carbon Nanosheet Networks with Favorable Active Sites Triggered by Metal Nanoparticles as Bifunctional Oxygen Electrocatalysts, ACS Energy Letters, 3 (2018) 2914-2920.
[173] P. Yu, L. Wang, F. Sun, Y. Xie, X. Liu, J. Ma, X. Wang, C. Tian, J. Li, H. Fu, Co Nanoislands Rooted on Co–N–C Nanosheets as Efficient Oxygen Electrocatalyst for Zn–Air Batteries, Adv. Mater., 31 (2019) 1901666.
[174] T. Zhou, W. Xu, N. Zhang, Z. Du, C. Zhong, W. Yan, H. Ju, W. Chu, H. Jiang, C. Wu, Y. Xie, Ultrathin Cobalt Oxide Layers as Electrocatalysts for High-Performance Flexible Zn–Air Batteries, Adv. Mater., 31 (2019) 1807468.
[175] D. Ji, L. Fan, L. Tao, Y. Sun, M. Li, G. Yang, T.Q. Tran, S. Ramakrishna, S. Guo, The Kirkendall Effect for Engineering Oxygen Vacancy of Hollow Co3O4 Nanoparticles toward High-Performance Portable Zinc–Air Batteries, Angew. Chem., Int. Ed. Engl., 58 (2019) 13840-13844.
[176] X. Liu, W. Liu, M. Ko, M. Park, M.G. Kim, P. Oh, S. Chae, S. Park, A. Casimir, G. Wu, J. Cho, Metal (Ni, Co)-Metal Oxides/Graphene Nanocomposites as Multifunctional Electrocatalysts, Advanced Functional Materials, 25 (2015) 5799-5808.
[177] Y. Li, J. Gao, F. Zhang, Q. Qian, Y. Liu, G. Zhang, Hierarchical 3D macrosheets composed of interconnected in situ cobalt catalyzed nitrogen doped carbon nanotubes as superior bifunctional oxygen electrocatalysts for rechargeable Zn–air batteries, J. Mater. Chem. A, 6 (2018) 15523-15529.

Chapter 2

Materials and Methods

The second chapter focuses on the presentation of the materials used to synthesize the electrocatalysts. A description of each synthesis procedure employed and a thorough description of all the characterization techniques are detailed. Besides, the different experimental setups used for the electrocatalysts' performance analysis are presented, in which the different components and functions are explained. The experimental procedures, their outputs, and key electrochemical parameters calculated through them are thoroughly described.

2.1. Reagents

The use of chemical reagents is crucial for the preparation of carbon electrocatalysts and their characterization. A list of the reagents and their application is presented in this section.

Ultrapure water and distilled water were used to prepare electrocatalysts' dispersions and during synthesis procedures, respectively. The ultrapure water was produced by filtration through inverse osmose by a Panice device with a conductivity of 18 μs cm^{-1} and the high-quality distilled water in a distillation unit on-site with a conductivity of 4 μs cm^{-1}. For the preparation of carbon supports, D(+)Glucose and multiwalled carbon nanotubes were used. D(+)Glucose anhydrous (> 99%) was purchased from HiMedia, whereas commercial multiwalled carbon nanotubes (CNT) from NC3100 series with an average diameter of 9.5 nm, an average length of 1.5 μm, and carbon purity higher than 95% were purchased from Nanocyl. Potassium hydroxide (KOH) pellets with a purity higher than 85% were purchased from José Manuel Gomes dos Santos, Lda. and were used to prepare the electrolyte solutions. The reagents employed to functionalize the carbon supports were melamine ($C_3H_6N_6$, 99%), iron(III) oxide (Fe_2O_3, ≥ 99%), iron(II) phthalocyanine (FePc, 90%), cobalt(II) phthalocyanine (CoPc, 97%), cobalt(II) nitrate hexahydrate ($Co(NO_3)_2.6H_2O$, 99%), all purchased from Sigma-Aldrich. Nitric acid (HNO_3, ≥ 65%) was supplied by Honeywell and used in the oxidation processes, and sulfuric acid (H_2SO_4, 95%) supplied by VWR chemicals was employed for purification processes. Nafion and absolute ethanol were used for the preparation of the electrocatalysts' dispersions, whereas methanol (CH_3OH) was employed to modify the electrolyte's properties. Nafion (5 wt% in a mixture of water (15-20%) and aliphatic alcohols) was purchased from

Sigma-Aldrich, and absolute ethanol and CH_3OH (≥ 99.9%) were obtained from VWR chemicals. Ruthenium(IV) oxide (RuO_2, 99.9% trace metals basis) provided by Sigma-Aldrich and platinum on carbon black (Pt/C, platinum nominal 20% on carbon black) supplied by Alfa-Aesar were used as benchmark catalysts. A solution containing 10 ppm of 33 different metals, including iron and cobalt, was purchased from Sigma-Aldrich and used to prepare diluted standards for characterization techniques. Polytetrafluoroethylene (PTFE, 50 wt% in H_2O) supplied by Sigma-Aldrich was used to prepare sample films to be used in some characterization techniques. The gases nitrogen (N_2, 99.999%), helium (He, 99.999%), argon (Ar, 99.999%), carbon dioxide (CO_2, 99.9%), oxygen (O_2, 99.995%), and hydrogen (H_2, 99.999%) were supplied by Air Liquid. All the chemicals were purchased from commercial sources and used as received unless otherwise stated.

2.2. Electrocatalysts preparation

Three different carbon materials were used to prepare the electrocatalysts: glucose-derived carbons, commercial CNT, and glucose-derived carbon/CNT composites. The surface chemistry of these carbon supports was then modified by the incorporation of nitrogen and/or transition metals to achieve highly electroactive catalysts.

2.2.1. Carbon supports

Glucose-derived carbon materials

Glucose-derived carbon materials were prepared by hydrothermal carbonization (HTC) of a solution containing glucose (85 wt%, 51 g) and deionized water (15 wt%, 9 g). The solution was enclosed in a Teflon-lined stainless-steel autoclave with a maximum capacity of 95 mL and ultra-sonicated for at least 30 min followed by HTC at 180 °C for 12 h. The resulting material was then washed with deionized water and dried overnight at 100 °C. The brown opaque solid material was then carbonized or activated. The carbonization of the polymerized glucose was performed inside a quartz reactor in a tubular vertical furnace under an N_2 atmosphere for 2 h, at 700 °C or 800 °C (CG samples), whereas the activation was performed at 900 °C for 1, 3, 4 or 6 h under a CO_2 flow rate of 80 $cm^3\ min^{-1}\ g^{-1}$ (AG samples). Both carbonization and activation were performed using a heating rate of 10 °C min^{-1}. To reduce the particle size of the carbonized and activated samples, samples CG and AG_{6h} were modified by ball milling

in a Retsch MM200 apparatus. In this technique, the carbons were enclosed in a flask with two zirconia balls for 4 h at a frequency of 15 Hz. A schematic representation of the synthesis of glucose-derived carbon is presented in Figure 2.1.

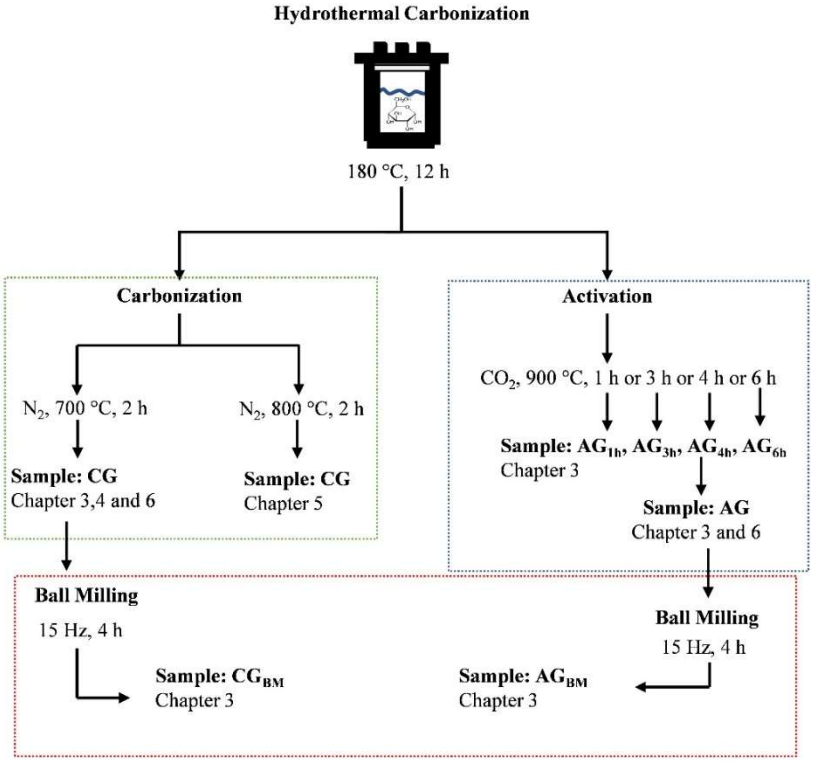


Figure 2.1 - Scheme of the synthesis methodologies employed to prepare carbonized and activated glucose-derived carbons.

Carbon nanotubes

The commercial multiwalled CNT employed in the present work were modified by two different techniques: purification and liquid-phase oxidation. The purification of the CNT was performed to remove any impurities that could affect the electrochemical performance of the prepared electrocatalysts and ensure that the synthesis processes could be performed on a material with a fully known composition. The purification was performed by adding 6 g of commercial multiwalled CNT into a 500 mL round-bottom boiling flask, followed by the addition of 300 mL of a 1:1 volume ratio solution of distilled water and sulfuric acid (H_2SO_4). This flask was selected because it allows

uniform heating of the solution. Moreover, a stir bar was added to dissipate the heat, achieve even heat and avoid a tumultuous ebullition of the solution. The round-bottom boiling flask was immersed in a paraffin bath which was heated by a hot plate with stirring. Moreover, a thermometer was placed inside the bath to control its temperature. The opening of the flask was connected to a condenser in which water entered nearer the flask and exited from the top of the condenser to ensure the reflux of the purification solution. The purification was then achieved by refluxing the solution at 140 °C for 4 h with constant stirring. After cooling, the CNTs were removed from the solution and filtrated under vacuum using a sintered frit filtration funnel and an Erlenmayer. The first washing step was performed with hot distilled water to facilitate the removal of any alumina catalyst that could still be present on the material. Afterwards, the CNT were then washed with abundantly distilled water until the filtrated solution's pH was the same as that of the distilled water. Finally, the CNT were dried at 100 °C for 24 h.

Commercial multiwalled CNT were also oxidized by liquid-phase oxidation to incorporate oxygen functionalities on the CNT to elucidate the role of these functional groups in the polymerization of glucose. The oxidation was performed by adding 1 g of commercial multiwalled CNT and 75 mL of a 7 mol L^{-1} solution of nitric acid (HNO_3) into a round-bottom boiling flask along with a stir bar to avoid an uncontrolled boiling of the solution. The flask was immersed in a paraffin bath which was heated by a hot plate with stirring and a thermometer was placed inside the paraffin to control the bath's temperature. The flask was connected to a condenser to allow the reflux of the boiling acid solution. The bath was then heated until the oxidation solution started to boil and was maintained at that temperature for 3 h. After cooling, the oxidized CNT were filtrated under vacuum using a sintered frit filtration funnel and an Erlenmayer. The CNT were then washed with abundantly distilled water until the filtrated solution's pH was the same as that of the distilled water. Finally, the CNT were dried at 100 °C for 24 h.

Glucose-derived carbon composites

Hydrothermal glucose/carbon nanotube composites were prepared by adding as received commercial CNT or the oxidized CNT to the precursor solution before the HTC of glucose. In this synthesis, a solution containing glucose (14.7 wt%, 9.00 g), CNT or oxidized CNT (0.3 wt%, 0.18 g), and distilled water (85 wt%, 52.02 g) was ultra-

sonicated inside a Teflon-lined stainless-steel autoclave with a maximum capacity of 95 mL for at least 30 min. Afterwards, hydrothermal carbonization at 180 °C for 12 h was performed and the resulting material was washed with distilled water and dried at 100 °C overnight. The brown opaque material was then carbonized inside a quartz reactor inside a tubular vertical furnace under an N_2 atmosphere for 2 h, at 700 °C or 800 °C, using a heating rate of 10 °C min^{-1}. The synthesis procedure of these composites is represented in Figure 2.2.

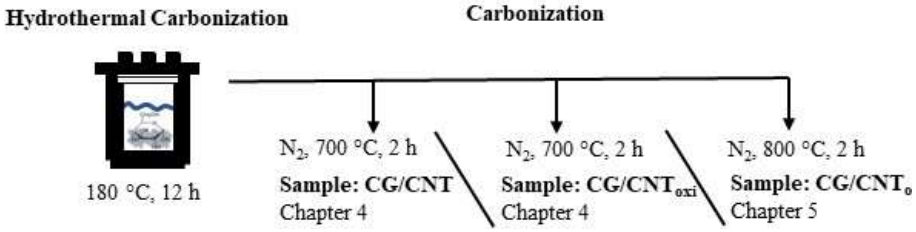


Figure 2.2 - Scheme of the synthesis methodologies employed to prepare glucose-derived carbon/CNT composites.

2.2.2. Nitrogen functionalization

The incorporation of nitrogen-containing surface groups into the carbon materials was performed by following two different methodologies. In the first methodology, the nitrogen precursor (melamine) and the carbon support were mechanically mixed by ball milling using a 2:3 melamine:carbon support mass ratio. The mixture was enclosed inside a flask with two zirconia balls for 4 h at a frequency of 15 Hz. Afterwards, the milled material was thermally treated in a quartz reactor inside a tubular vertical furnace under a N_2 atmosphere at 700 °C using a fixed heating rate of 10 °C min^{-1}. In the second methodology, the carbon support and the melamine were mixed in a 2:3 melamine:carbon support mass ratio using a spatula until a homogeneous material was observed. This mixture was then placed in a quartz reactor placed inside a tubular vertical furnace and treated under a N_2 atmosphere at 700 °C or 600 °C using a fixed heating rate of 10 °C min^{-1}. These two methodologies employed to incorporate nitrogen functionalities into the carbon supports are represented in Figure 2.3.

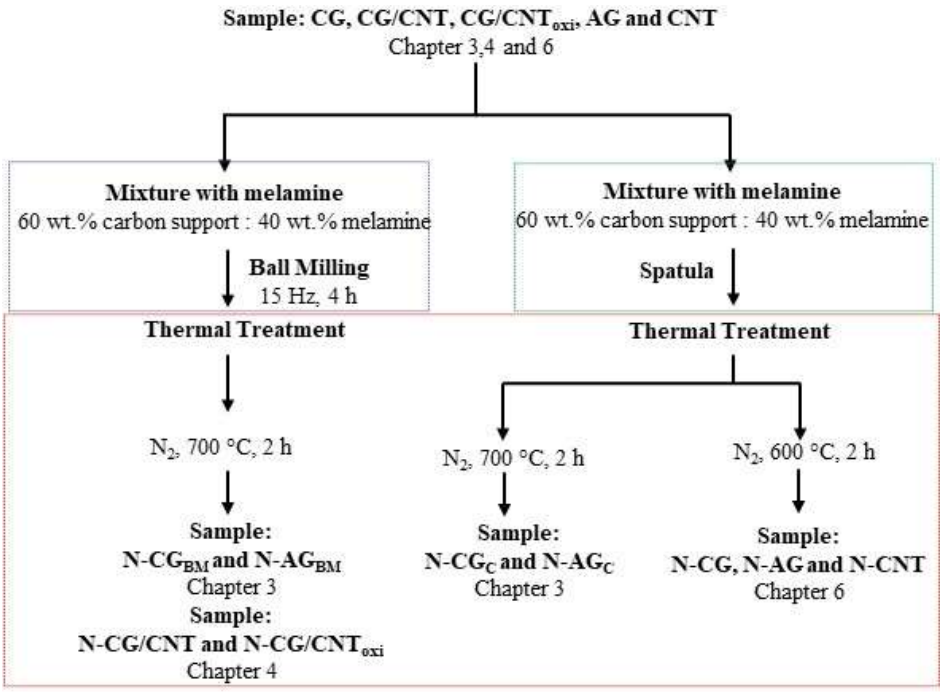


Figure 2.3 - Scheme of the synthesis methodologies employed to prepare N-doped carbons.

2.2.3. Incorporation of transition metals

The surface chemistry of the carbon supports was modified by the incorporation of different transition metals. In this PhD thesis, two different transition metals were used: iron and cobalt.

The incorporation of iron was performed on the carbonized glucose and glucose/carbon nanotube composites (*Chapter 5*). In these cases, different amounts of Fe_2O_3 were dissolved in ethanol and added dropwise by incipient wetness impregnation (IWI) to the carbon support under sonication for 30 min and then dried at 100 °C overnight (Figure 2.4). Afterwards, the dried material was thermally treated in a quartz reactor inside a tubular vertical furnace under N_2 atmosphere for 2 h, followed by H_2 atmosphere for an additional 2 h at 650 ºC using a fixed heating rate of 10 °C min^{-1}. The treatment under the inert atmosphere was performed to favor the annealing between the carbon structure and the metal, whereas the H_2 atmosphere was employed to perform the reduction of the iron oxide. Moreover, the different amounts of metal precursor used during IWI were

selected to achieve three different wt% of iron on the final carbon sample: 0.5 wt%, 1 wt% or 5 wt%, samples $CG_{0.5Fe}$, $CG_{1Fe,}$ and CG_{5Fe}, respectively. Additionally, Fe_2O_3 was also incorporated into the previously synthesized CG/CNT_O composite by IWI. In this case, only a material with a final iron content of 5 wt% was prepared. After ultra-sonication and drying processes, the resulting material was placed in a quartz reactor inside a tubular vertical furnace and thermally treated for 2 h under N_2 atmosphere (annealing), followed by an additional 2 h in H_2 atmosphere at 650 ºC (reduction) using a fixed heating rate of 10 °C min^{-1} ($CG/CNT_{O,5Fe}$).

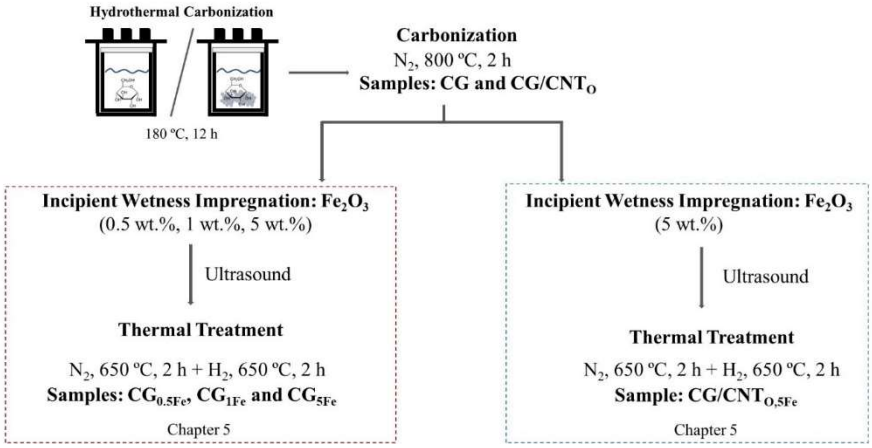


Figure 2.4 - Scheme of the synthesis methodologies employed to prepare Fe-doped carbon composites.

The incorporation of cobalt was exclusively performed on purified CNT. In this case, 1.25 g of cobalt (II) nitrate hexahydrate per gram of purified CNT were dissolved in ethanol. Afterwards, the solution was added dropwise by IWI to the carbon support in an ultra-sonication bath for 30 min and dried overnight at 100 °C (Figure 2.5). The amount of cobalt precursor was chosen to achieve a final cobalt content, after thermal treatments, of around 20 wt%. After drying, the impregnated sample was thermally treated under different conditions of temperature and/or atmosphere to achieve different states of oxidation of the cobalt species. The thermal treatments were performed under N_2 atmosphere or N_2 atmosphere followed by H_2 atmosphere (Figure 2.5). Four portions of the impregnated sample were separately placed in a quartz reactor inside a tubular vertical furnace and thermally treated under N_2 atmosphere for 2 h at 150 °C, 185 °C, 350 °C, or

900 °C (CNT_{Co_150N2}, CNT_{Co_185N2}, CNT_{Co_350N2}, and CNT_{Co_900N2}, respectively). Additionally, two portions of the impregnated sample were also placed in a quartz reactor inside a tubular vertical furnace and thermally treated under N_2 atmosphere for 2 h. Then, the gas atmosphere was changed to H_2 and maintained for another 2 h at the same temperature. These 2 samples were treated at 185 °C or 350 °C (CNT_{Co_185H2} and CNT_{Co_350H2}, respectively). All six samples were prepared using a fixed heating rate of 10 °C min^{-1}.

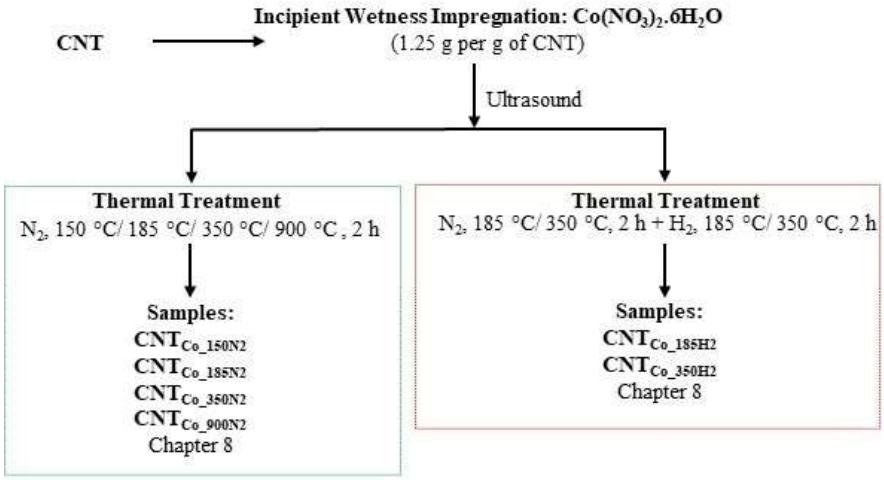


Figure 2.5 - Scheme of the synthesis methodologies employed to prepare Fe-doped carbon composites.

2.2.4. Incorporation of nitrogen and transition metals

The crucial synergy between heteroatoms and transition metals was also studied at different points of this PhD thesis using two different approaches: i) the incorporation of the nitrogen and metal precursors (iron or cobalt) separately, and ii) the incorporation of a single precursor, in this case, phthalocyanines (Pcs), containing nitrogen and the transition metal (iron or cobalt).

Incorporation of Nitrogen and Iron

Nitrogen and iron were incorporated into the carbonized glucose (CG) and the carbonized glucose/oxidized CNT composite (CG/CNT_O), by using melamine and Fe_2O_3 as precursors. Two different methodologies were followed to achieve Fe,N-doped carbons

(Figure 2.6). One of the approaches was focused on the incorporation of nitrogen into the Fe-doped samples (CG_{5Fe} and $CG/CNT_{O,5Fe}$). In this case, melamine was mixed with the carbon supports containing iron in a 2:3 melamine:carbon support ratio using a spatula until a homogeneous material was obtained.

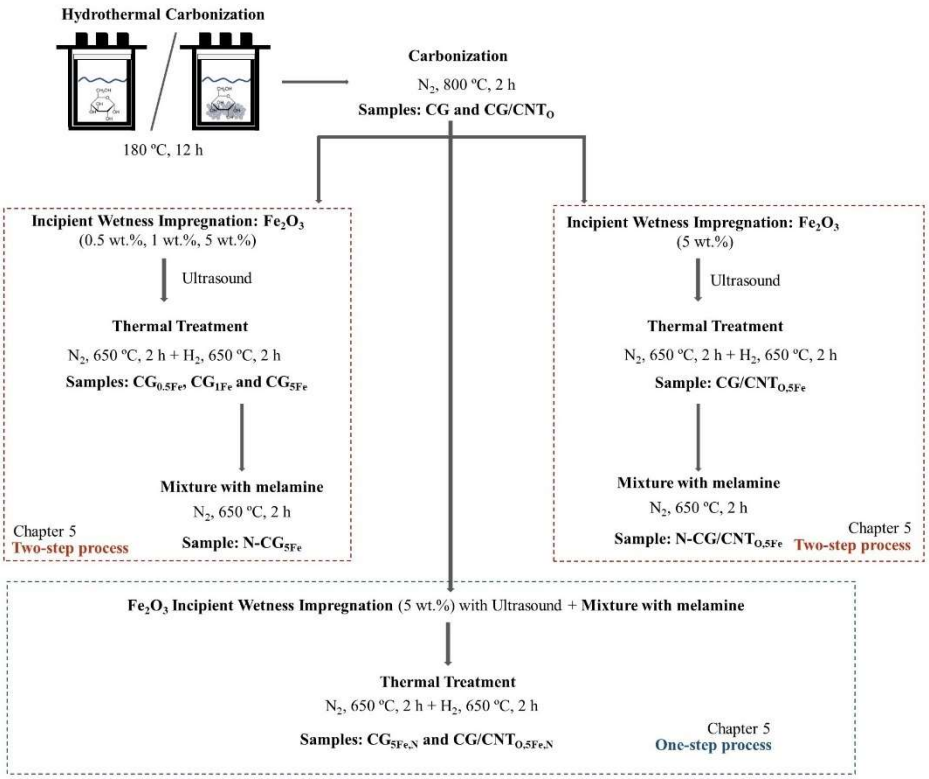


Figure 2.6 - Scheme of the synthesis methodologies employed to prepare Fe,N-doped carbon composites.

This material was then placed in a quartz reactor that was heated inside a tubular vertical furnace at 650 °C in a N_2 atmosphere for 2 h using a fixed heat rate of 10 °C min^{-1}. This procedure has been defined as the two-step method as it involved the incorporation of iron on the carbon support followed by the incorporation of nitrogen. Fe,N-functionalization was also achieved by simultaneously incorporating the heteroatom and the transition metal in a single thermal treatment. To achieve this, Fe_2O_3 was dissolved in ethanol and added dropwise to CG or CG/CNT_O by IWI under-ultrasonication for 30 min and dried overnight at 100 °C. Afterwards, the dried material was mixed using a spatula with a 2:3 melamine:carbon support ratio until a homogeneous material was

obtained. The mixed material was then placed in a quartz reactor inside a tubular vertical furnace and heated at 650 °C, using a fixed heating rate of 10 °C min^{-1}, for 2 h. After that time, the N_2 gas flow was changed to H_2, which was then maintained for an additional 2 h. This procedure has been defined as the one-step method as it involved the incorporation of iron and nitrogen on the carbon support using a single thermal treatment.

Moreover, nitrogen and iron were incorporated into the carbon supports (CG, AG and CNT) by using melamine and/or iron (II) phthalocyanine (FePc) as precursors. The modification of the surface chemistry of the carbon materials was achieved using two different methods (Figure 2.7). The first technique involved the use of FePc, which contains both nitrogen and iron in a single molecule. To prepare the Fe,N-doped carbons, 50 mg of FePc per gram of carbon support were dissolved in ethanol and added dropwise by IWI to the carbon material under ultra-sonication for 30 min. Afterwards, the sample was dried overnight at 100 °C and then placed in a quartz reactor inside a tubular vertical furnace at 500 °C with a heating rate of 10 °C min^{-1} in a N_2 atmosphere for 2 h. The second methodology involved the incorporation of the FePc on the N-doped carbon supports (N-CG, N-AG, and N-CNT). In this procedure, 50 mg of FePc per gram of carbon support were dissolved in ethanol and added dropwise by IWI to the carbon material in an ultra-sonication bath for 30 min and dried overnight at 100 °C. The dried material was then placed in a quartz reactor inside a tubular vertical furnace at 500 °C with a heating rate of 10 °C min^{-1} in a N_2 atmosphere for 2 h.

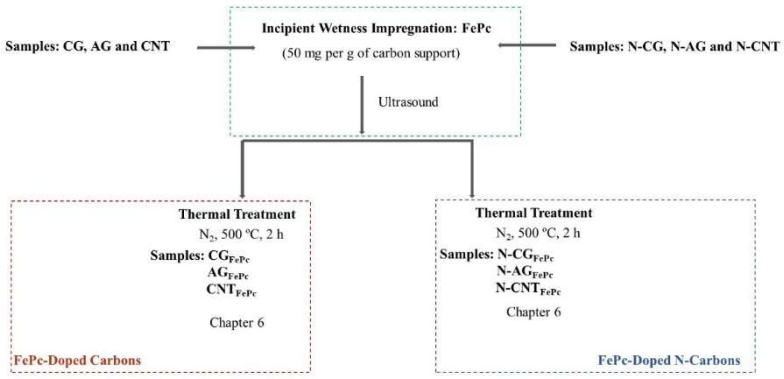


Figure 2.7 - Scheme of the synthesis methodologies employed to prepare Fe,N-doped carbon electrocatalysts.

Incorporation of Nitrogen, Iron and Cobalt

The incorporation of Co/N was performed on purified carbon nanotubes by using cobalt(II) phthalocyanine (CoPc). Moreover, the synergy between Fe and Co was studied by incorporating both iron and cobalt phthalocyanines (Pcs) on the CNT. The functionalization was performed by dissolving 50 mg of FePc or CoPc in ethanol and then adding it dropwise by IWI to the CNT (1 g) in an ultra-sonication bath for 30 min and dried overnight at 100 °C (Figure 2.8). The dried material was then placed in a quartz reactor inside a vertical tubular furnace at 500 °C with a heating rate of 10 °C min^{-1} in a N_2 atmosphere for 2 h. The thermal treatment employed led to Fe,N-doped CNT (CNT_{Fe}) and Co,N-doped CNT (CNT_{Co}) materials. Afterwards, four different methodologies were studied to prepare Co,Fe,N-doped samples (Figure 2.8).

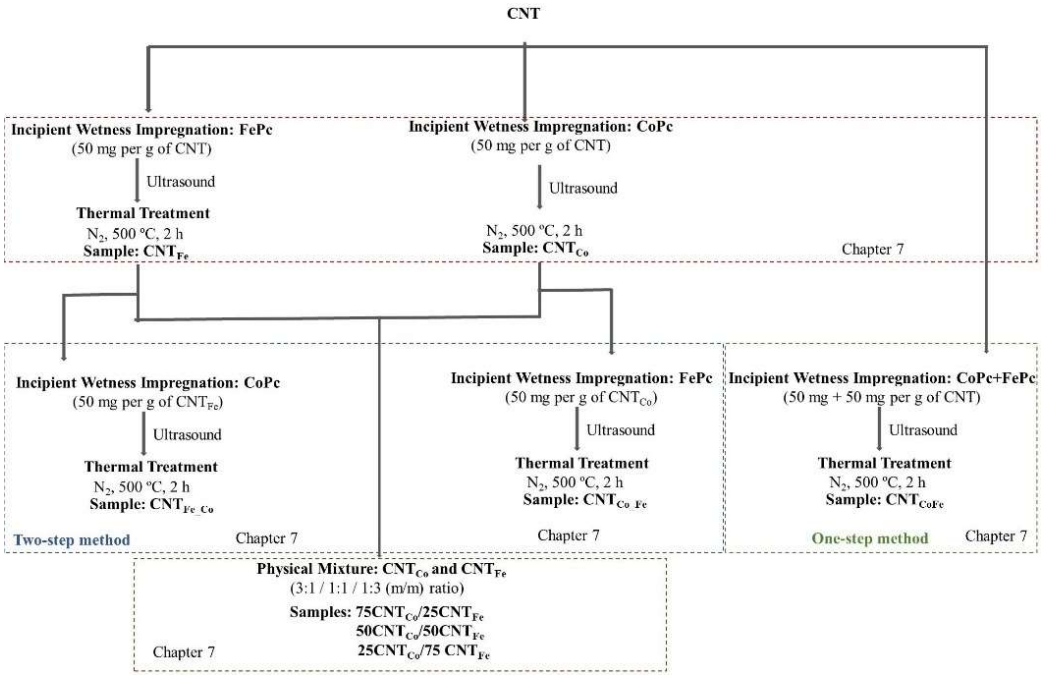


Figure 2.8 - Scheme of the synthesis methodologies employed to prepare CoPc,FePc-doped carbons.

Three of those procedures relied on the impregnation of both FePc and CoPc on the CNT using a one-step or two-step method. The one-step method was performed by dissolving 50 mg per gram of CNT of both FePc and CoPc and adding them dropwise by IWI to the CNT in an ultra-sonication bath for 30 min and dried overnight at 100 °C. Afterwards,

the dried material was then placed in a quartz reactor inside a vertical tubular furnace at 500 °C with a heating rate of 10 °C min^{-1} in a N_2 atmosphere for 2 h (CNT_{CoFe}). The two-step method involved the impregnation of 50 mg CoPc per gram of CNT on the CNT_{Fe} sample or 50 mg of FePc per gram of CNT on the CNT_{Co} sample. The impregnation was achieved dropwise by IWI in an ultra-sonication bath for 30 min and dried overnight at 100 °C. Afterwards, the dried material was then placed in a quartz reactor inside a vertical tubular furnace at 500 °C with a heating rate of 10 °C min^{-1} in a N_2 atmosphere for 2 h (CNT_{Fe_Co} and CNT_{Co_Fe}, respectively). The fourth procedure to prepare Fe,Co,N-doped CNT was achieved by mixing in a 1:1 mass ratio of the samples CNT_{Co} and CNT_{Fe} using a spatula until a homogeneous mixture was obtained ($50CNT_{Co}/50CNT_{Fe}$) without performing any other thermal treatment. In addition, samples CNT_{Co} and CNT_{Fe} were also physically mixed using two additional CNT_{Co}:CNT_{Fe} ratios, 3:1 (m/m) (sample $75CNT_{Co}/25CNT_{Fe}$) and 1:3 (m/m) (sample $25CNT_{Co}/75CNT_{Fe}$). A schematic resume of the synthesis procedures and the resulting materials is presented in Figure 2.8.

The incorporation of nitrogen, iron, and cobalt was also achieved by using FePc and cobalt (II) nitrate hexahydrate as Fe,N and cobalt precursors. In this case, three methodologies (Figure 2.9) were used to prepare Fe,Co,N-doped. FePc was dissolved in ethanol (50 mg per gram of Co-doped CNT) and added dropwise by IWI to the CNT_{Co_185H2} or the cobalt precursor was dissolved in ethanol and added dropwise by IWI to CNT_{Fe} in an ultra-sonication bath for 30 min and dried overnight at 100 °C. Afterwards, the dried material was then placed in a quartz reactor inside a vertical tubular furnace at 500 °C with a heating rate of 10 °C min^{-1} in a N_2 atmosphere for 2 h ($CNT_{Co_185H2_Fe}$ and $CNT_{Fe_Co_185H2}$, respectively). The third approach was the physical mixture with a spatula of CNT_{Co_185H2} and CNT_{Fe} using a 1:1 mass ratio until a homogeneous mixture was obtained (CNT_{Fe}/CNT_{Co_185H2}). This sample did not undergo any further thermal treatment.

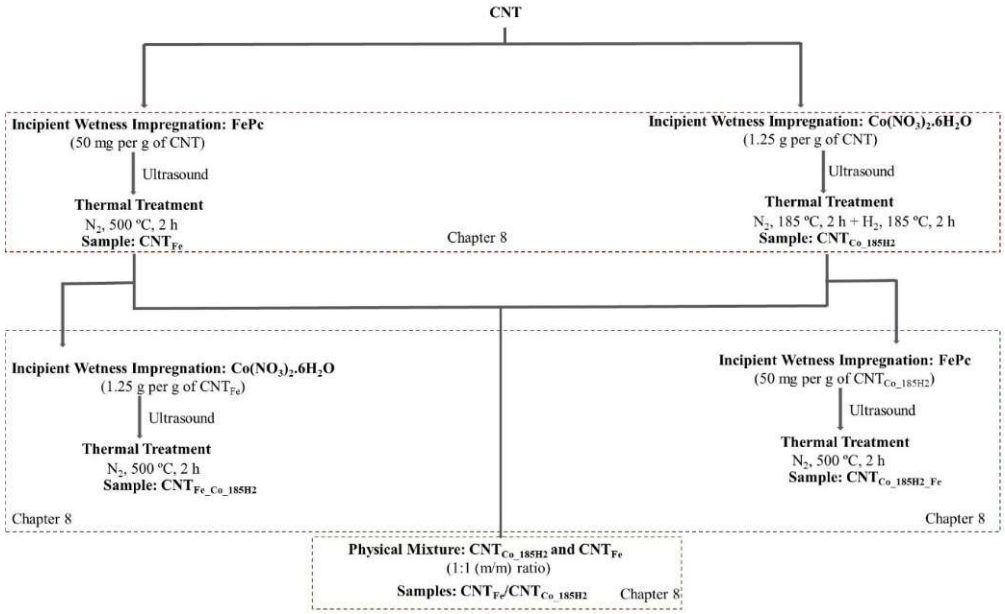


Figure 2.9 - Scheme of the synthesis methodologies employed to prepare Co,Fe,N-doped carbons.

2.3. Physicochemical characterization

The textural, physical, morphological and chemical properties of the synthesized materials were determined by a wide variety of characterization techniques. Unless otherwise stated, all characterization techniques were performed by the author at LSRE-LCM.

2.3.1. Textural properties

N_2 adsorption-desorption isotherms

In this technique, the physisorption of the N_2 molecules (adsorbate) on the surface of the sample (adsorbent) takes place at -196 °C, which is the boiling temperature of liquid nitrogen. Therefore, nitrogen molecules are adsorbed on the sample's surface resulting in an adsorption isotherm. After adsorption, the desorption of the adsorbed molecules is performed, and the resulting desorption isotherm can provide crucial information regarding the type of pores present in the sample. Before the analysis, nitrogen is dosed into the sample's analysis tube to determine the saturation pressure (P_0). During analysis,

at each of the different relative pressures analyzed, the complete adsorption of nitrogen at a steady state is determined (equilibration). Moreover, at low pressures, most of the nitrogen atoms are involved in the filling of the micropores, whereas, in large pores, their adsorption occurs on the pores' walls. The presence of micropores is observable at very low relative pressures (< 0.03 P/P_0) of the adsorption isotherm that is recorded. Afterwards, a single layer of nitrogen atoms (monolayer) is formed on the surface of the larger pores which normally occurs between 0.05 and 0.30 relative pressures (P/P_0). Nonetheless, each sample's isotherm needs to be very carefully analyzed as this range does not always apply. For example, in very microporous samples the monolayer formation tends to take place at pressures closer to 0.05 and sometimes even lower. After adsorption of the monolayer, nitrogen atoms start adsorbing on the already adsorbed atoms forming more layers, which is called multilayer adsorption. Close to saturation pressure (P/P_0 = 1), the mesopores and macropores continue to be filled with the adsorbate, and the last point measured is usually considered to calculate the total pore volume as it is as close as the experiment can get to the full filling of the pores. After adsorption, the relative pressure is decreased to achieve desorption, which leads to a desorption branch. The adsorption-desorption isotherm is then used to calculate different parameters of interest and understand what type of porous structures are present in the analyzed materials.

The textural properties of the materials prepared in this PhD thesis were characterized by N_2 adsorption-desorption isotherms carried out at -196 ºC in a Quantachrome Autosorb iQ automated gas sorption analyzer. This equipment allows the determination of adsorption points at very low relative pressures (10^{-6}), which is very important for microporous structures that are filled with the adsorbate at those pressures. Prior to the analysis, ca. 100 mg of each sample was weighed and outgassed under high vacuum at different temperature levels. The cell containing the sample was heated to 50 °C and maintained at that temperature for 2 h. Afterwards, it was heated to 80 °C and then 120 °C and kept at those temperatures for 1 h each. All three temperatures were achieved using a heating rate of 5 °C min^{-1}. To complete the last outgassing step, the cell temperature was risen to 150 °C using a heating rate of 10 °C min^{-1} and maintained for 12 h to ensure a full degasification of the sample. The slow increase in temperature allows

the sample to desorb species from the surface without compromising the material's structure. After this process, the cells with the degasified samples were immersed in liquid nitrogen and the analysis was started as explained above. After the analysis, the surface area of each material was calculated using the Brunauer-Emmett-Teller (BET) equation (Eq. A1.1, shown in Appendix A) within the 0.05-0.30 range of relative pressure [1]. The total pore volume (V_p) was calculated as the volume of nitrogen adsorbed at the saturation point ($P/P_0 = 0.99$), and the volume of micropores was calculated either using the Dubinin-Radushkevich (DR) method (V_{DR}) or by the t-plot method (V_{micro}). The DR method is ascribed by Eq. A1.2. The t-plot method was also used to calculate the external surface areas of the samples (S_{ext}). This method correlates the statistical film thickness of a standard adsorption isotherm with the pressure, using the same temperature and adsorbate during sample analysis [2]. In this work, the reference material chosen to be used for the t-plot calculations was carbon black. The *Novawin* software provides the amount of gas adsorbed (n^a) on the samples and the average thickness of the film adsorbed of the reference isotherm (t) values. The resulting n^a vs t plot can be conveniently analyzed to provide a slope and an interception at the y-axis that are used to determine the S_{ext} and V_{micro}, respectively [2]. The Quenched Solid Density Functional Theory (QSDFT) was used to obtain the pore size distribution of selected samples, by assuming the presence of cylindric pores and using the adsorption branch for calculations.

2.3.2. Physical properties

Electrical conductivity

The determination of the electrical conductivity of the electrocatalysts is crucial as it plays a very important role in electrochemical reactions. The electrical conductivity was measured by the four-point probe method applied to a disc-shaped piece of 1 cm in diameter made of each carbon sample. The disks were prepared by mixing the carbon material in powder form and a liquid binder (PTFE, 50 wt% in H_2O) using a 1:9 mass ratio which was stretched to form a thin film. Afterwards, the film was cut into disc-shaped pellets. These pieces were then pressed at 8 t in a mold for 60 s to ensure that the disc's thickness was uniform. In this characterization technique, four metal tips are disposed linearly and in contact with the disc surface. Usually, the two outer electrodes

measure the current that passes through them, whereas the two inner electrodes indicate the potential across them. In this work, a potential between 0 V and 2 V was applied to the electrodes and the current response was measured using a SourceMeter® unit instrument (Keithley 2400) and recorded with LabView software. A linear relationship between the potential applied and the current response measured was obtained. Ohm's law, in which the resistivity is equal to the multiplication of the current intensity and potential applied, was used to calculate the resistivity of each sample, and in turn, the electrical conductivity.

2.3.3. Morphological properties

Raman spectroscopy

Raman spectroscopy was performed on carbon materials in powder form. In this analysis, the microscope uses a laser beam with a wavelength of 532 nm to excite the sample. The light is then absorbed by the sample and some of it is transmitted through the sample, and a portion of what is transmitted is scattered in all directions. Most of the scattered light displays the same frequency as the incident light frequency, which results in a Rayleigh scattering. Nonetheless, a very small portion of the scattered light has the particularity of presenting a different frequency than the incident light's frequency, which leads to Raman scattering [3]. This variation of frequency occurs when the electrons are excited by the monochromatic laser and absorb energy, rising to a virtual state of energy and then losing a different level of energy than that absorbed. Therefore, two different levels of Raman scattering may occur: i) the scattered light's frequency is lower than the incident light's frequency which results in the appearance of Stokes lines on the Raman spectrum or ii) the scattered light's frequency is higher than the incident light's frequency and anti-Stokes lines are obtained. The scattered light is then collected by an objective lens, according to the material which is being analyzed (in this work, 50x ampliation), and passes through a pinhole that functions as a spatial filter and only allows light that is in focus to pass, which enhances the spatial resolution. The collected light is then redirected onto a spectrometer that disperses the light into its component wavelengths and detects the signal consistent with Raman scattering. This signal can then provide crucial information about the structure of the sample. The Raman spectra obtained in this work

were a result of 60 accumulations using an integration time of 1 s and a laser power of 5 mW in an Alpha 300 apparatus (WiTec).

Transmission electron microscopy (TEM)

The atomic arrangements of selected electrocatalysts were investigated by transmission electron microscopy (TEM). This system is composed of a light source and a filament (electron source), a condenser lens (electromagnetic lens system), a sample holder, and an objective and projector lens (imaging system) [4]. In a TEM apparatus, the light source is an electron gun that emits electrons which are accelerated by a high voltage to produce an electron beam with high energy. These electrons are then deflected or focused using electromagnetic lenses as glass can not deflect or focus electrons [5]. Afterwards, condenser lenses are used to adjust the illumination intensity and part of the sample is illuminated by adjusting the current in the electromagnetic lenses of the condensers. The electron beam then reaches the sample and some electrons are scattered or go through the sample (unscattered electrons). The heavier elements will absorb more electrons than the lighter elements, which results in more unscattered electrons through lighter elements. The TEM images obtained are in black and white, hence the heavier elements will be observed closer to black due to their lack of transmitted electrons, whereas lighter elements will be closer to white as most of the incident light passes through them. After passing the sample, the electron beam goes through the electromagnetic objective lens, which ensures that the single electron beam is maintained, and through a projector lens that amplifies the signal. The signal then reaches an imaging device that provides an image of the sample's structure. TEM analyzes are performed inside a vacuum chamber to avoid the destruction of the electron beam by air interferences. In this work, the characterizations were performed at *Serviço de Microscopia da Universidade de Aveiro*, using a JEOL 2200 FS apparatus with an electro-optical system with Schottky emission electron gun and an acceleration voltage of 200 kV. Prior to the analysis, a very small amount of the samples was diluted in ethanol and a drop was added to the sample's grid, which was then carefully dried and placed under vacuum.

Scanning electron microscopy (SEM)

The morphology of the samples was studied by scanning electron microscopy (SEM). In this technique, the sample is bombarded with electrons from an electron source. The electrons are accelerated at an anode and pass a condenser that reduces the crossover diameter of the electron beam and an objective lens that focuses the electron beam on the sample. The beam is then deflected by scan coils to ensure that the scanning of the sample takes place over a rectangular area of the sample's surface. The electrons can then pass through the sample (unscattered electrons) or be reflected by the sample. The electrons reflected by the sample can then be backscattered electrons (BSEs), which are produced when elastic scattering occurs, or they can be secondary electrons (SEs), which are generated from inelastic scattering phenomena resulting from electron ejection from the sample's atoms [6]. BSEs usually have low deflection angles and retain most of the energy of the incident electrons, whereas SEs have large deflection angles and display very low energy compared to those electrons. The inelastic scattering electrons in atoms receive kinetic energy from the incident electrons and, when sufficient kinetic energy is transferred, the electron leaves its orbital and becomes a SE. The low energy of SEs makes them prime candidates to achieve a topographic contrast of the sample, whereas BSEs can be used to obtain an elemental composition contrast. Moreover, due to their low energy, SEs only escape to a depth up to 50 nm, which provides a much better spatial resolution than the BSEs that can distance themselves from the surface up to 300 nm. During SEM analysis an Everhart-Thornley detector (ETD) is normally used with a Faraday cage in front of it. This cage can then be charged according to the signal desired. A positively charged cage (up to 250 V) is normally used to attract secondary electrons, whereas a negative charge will repel SE with low energies (< 50 eV). Afterwards, a scintillator converts those electrons into photons using an accelerating voltage (> 12 kV) which is then conducted through a light guide to a photomultiplier tube to amplify the signal. SEM measurements are performed side by side, which allows the detector to generate a corresponding point-to-point image according to the electron signals collected from each pixel analyzed. Additionally, BSEs can be used to determine the compositional contrast to complement the topographic contrast obtained from SEs. The detection of BSEs can be performed using the same ETD as the SEs analysis but negatively charging

the Faraday cage, which will repel SEs, or the SEM apparatus can be equipped with another detector dedicated to collecting BSEs. In the compositional contrast analysis, the black and white image formed will present differences in its gray levels which are caused by the different capability of BSEs to escape from the sample according to the specimen's atomic number. The backscattered coefficient is given by the ratio of escaping BSEs to incident electrons and increases with the atomic number. Therefore, elements with higher atomic numbers such as transition metals will display higher brightness levels than elements with lower atomic numbers such as carbon. The BSE analysis is also performed side by side and generates a similar 3D image to the SEs image but according to the chemical composition of the sample. The elemental composition of the sample can be determined by energy dispersive spectroscopy (EDS), which is detailed in section 2.3.4. In this PhD thesis, SEM was performed using two different devices, according to the availability of the equipment. Some SEM analyzes were performed at *Centro de Materiais da Universidade do Porto* (CEMUP) in a Quanta FEG 400 (FEI Company), using an ETD and an accelerating voltage of 15 kV. Additionally, samples were morphologically characterized at Serviços de Caracterização de Materiais (SEMAT) da Universidade do Minho using a Nova NanoSEM 200 (FEI Company) and an ETD at an accelerating voltage of 10 kV (*Chapter 6*). Prior to analysis, the samples in powder form were pressed at 5-8 t for about 1 min and attached to an aluminum pin using conductive carbon double-sided adhesive tape.

2.3.4. Chemical properties

Energy-dispersive spectroscopy (EDS)

To understand the chemical composition variation within samples observed by backscattered electrons analysis, an X-ray fluorescence spectrometry (XRF) analysis of a sample's X-ray emission after being radiated with high-energy X-rays can be useful to comprehend its elemental composition. The most commonly used XRF is the EDS. The EDS system mainly consists of an X-ray source, a detector, and a system that will collect data and process it. Commonly, an X-ray tube operated with high voltage, which ensures that the critical potential of exciting characteristic X-rays from the elements in the samples is exceeded, is used to generate primary X-rays that excite the atoms of the

sample [7]. The emitted X-rays are then collected by a photon detector, usually a Si(Li) diode, that collects the characteristic X-ray photons according to their energies, which are attributed to specific elements. The photons collected generate electron-hole pairs, which usually require 3.8 eV for each pair to be generated. Therefore, more pairs can be produced with increasing photon energy, which is then correlated to the characteristic energy of the X-ray photons of each element. The EDS spectrometer is commonly included in SEM apparatus due to its compactness and utility. The main difference between the stand-alone EDS and the one included in a SEM system is that, in a SEM, the X-ray source is a high-energy electron beam instead of an X-ray beam. The synergy between SEM and EDS allows the analysis of chemical elements in microscopic volume due to the very small area analyzed. In this work, EDS was performed in stationary mode rather than scanning as it allows to analyze a specific location until the chemical composition of that area is completed. Moreover, EDS allows the detection of elements present in low concentrations (< 1 wt%) by increasing the dwell time of analysis. The results of EDS can then be presented in the form of a spectrum of X-ray energy versus intensity, which allows the identification of different elements, or in the form of a 2D image in which each element is represented by a separate or combined image according to their presence in the area of analysis. These images are the elemental mapping distribution of the samples. In this PhD thesis, this analysis was performed at CEMUP in a Quanta FEG 400 (FEI Company) or at SEMAT using a Nova NanoSEM 200 (FEI Company). Analyzes were performed using a Si(Li) detector with a super ultra-thin window (SUTW) to assess the mapping of the elements of interest. The resulting images were produced by 200 scans of each region of interest using a dwell time of 200 μs.

Elemental analysis

The chemical bulk composition of the carbon samples was determined by elemental analysis (EA) in two different pieces of equipment. Carbon, hydrogen, nitrogen and sulfur (CHNS mode) contents were determined in a Vario Micro Cube Analyzer from Elemental GmbH in CHNS mode. Prior to the analysis, each sample was weighed (1.5-2.0 mg) in a tin boat-shaped crucible in triplicate. Each sample was introduced one by one in the system in which they were combusted at 1050 °C inside a combustion tube with an O_2-enriched atmosphere forming CO_2, H_2O, N_2, nitrogen oxides (NO_x), SO_2 and

SO_3. The CHNS mode requires that the combustion tube is filled with WO_3 granulate to provide additional oxygen as catalyst, prevent the formation of non-volatile sulfates and bind undesired alkali and earth alkali elements to ensure proper analysis of the four elements of interest. The gases resulting from the combustion are then transferred to the reduction tube (850 °C) by the carrier gas (He) flow in which nitrogen oxides are reduced to N_2, SO_3 is reduced to SO_2, and the volatile halogen compounds are retained by silver wool. The reaction mixture is then transferred to an adsorption column in which the components are adsorbed and posteriorly measured. In the operation mode used, N_2 is not adsorbed in the adsorption column and is the first component to enter the thermal conductivity detector (TCD) and to be quantified, whereas the other components are adsorbed in the adsorption column. Afterwards, the column is heated to H_2O desorption temperature. The water is desorbed and goes into the detector with the He gas. This is followed by further heating of the adsorption column to the SO_2 desorption temperature, which will then be desorbed and entered into the detector to be quantified. Any traces of H_2O will be bonded by an additional absorption tube between the column and the TCD. The adsorption column is then cooled down by fans to the defined cooling temperature and the cycle is repeated for another sample until all samples are analyzed. Before the analysis, the equipment is calibrated by performing three separate assessments on the standard compound for the CHNS method: sulfanilamide (16.25 wt% of N, 41.81 wt% of C, 4.65 wt% of H and 18.62 wt% of S).

Oxygen contents were determined in a Rapid OXY Cube analyzer from Elemental GmbH in O mode. Prior to analysis, each sample was weighed (1.5-2.0 mg) in a silver boat-shaped crucible in triplicate. Each sample was introduced one by one in the apparatus in which they were pyrolyzed at 1450 °C. In this equipment, the reaction gas mixture after pyrolysis is composed of H_2, CO, CH_4 and various radicals such as N, C and S. The carrier gas flow (He) transfers the gaseous products into the absorption tube in which chemical absorption of alkaline and acidic pyrolysis products takes place, whereas the abovementioned gas mixture enters the adsorption column. N_2 is not adsorbed in the adsorption column and is the first component to enter the TCD whereas CO is adsorbed in the adsorption column. Afterwards, the adsorption column is heated to CO desorption temperature. The CO desorbs from the column and enters the TCD for quantification.

Subsequently, the adsorption column is cooled down and the next measurement starts. Prior to the analysis, the equipment is calibrated in triplicate using a standard compound: benzoic acid (26.2 wt% of O).

In both equipment, all samples were analyzed in triplicate to ensure the homogeneity of the material's composition. These samples were pre-dried in the oven to remove any water adsorbed that could modify the real values of the chemical composition. Between different samples, a blank measurement was performed and subtracted from the results obtained for the series of samples that are analyzed after the blank.

X-ray photoelectron spectroscopy (XPS)

The elemental chemical surface composition of the prepared carbon materials was analyzed by X-Ray Photoelectron Spectroscopy (XPS). In this analysis, the sample is irradiated with X-rays that penetrate the solid around 1 to 10 nm [8]. This radiation interacts with surface atoms resulting in the ejection of electrons on the inner shells (photoelectric effect). The kinetic energies (KEs) of the emitted electrons can then be calculated by subtracting the binding energy (BE) of the atomic orbital in which the electron resided from the photon energy. The energy of the ejected electrons is unique to each element; hence it is possible to determine the surface chemical composition. Due to the electron ejection, the ion analyzed will reach an excited state which requires an outer electron to fall and fill the inner orbital vacancy while simultaneously emitting a second electron possessing the excess energy. These types of emitted electrons are called Auger electrons. The photo-emitted electrons pass by an electron collection lens and an electron detector that counts the electrons and measures their kinetic energies. The KE can then be transformed into BE using the known variables abovementioned resulting in a spectrum with BE as the x-axis, which is the most commonly used. XPS analyzes were performed at CEMUP or at *Instituto de Ciencia y Tecnología del Carbono* (INCAR, *Chapter 5*). Regardless of the institution, all the analyzes presented in this PhD thesis were carried out in a Kratos AXIS Ultra HSA spectrometer using a monochromatic Al Kα radiation (1486.7 eV) at 15 kV (90 W) or 14 kV (175 W, *Chapter 5*), in fixed analyzer transmission (FAT) mode, with a pass energy of 80 eV for the survey and 40 eV for regions of interest (ROI). The data acquisition was performed at pressures lower than 10^{-6} Pa using VISION and the spectra modeling was performed using CASAXPS software.

Before the deconvolution of the obtained spectra, all peak positions for the elements of interest were corrected by considering the BE of the carbon sp^2 (C=C) as 284.6 eV. The deconvolution of the spectra into different peaks was performed by applying least-squares using the Gaussian-Lorentzian fitting, except for the C=C asymmetric peaks, which required a Lorentzian finite (LF) approach. A Shirley-type background was used for subtraction. Before analysis, the samples in powder form were pressed at 5-8 t for about 1 min and attached to a conductive carbon double-sided adhesive tape. The pressing is important to achieve a maximum reduction of the space between the particles, avoiding interferences from the carbon tape. Furthermore, all samples were placed under an ultra-high vacuum before entering the XPS apparatus to ensure that no powder would detach from the adhesive tape and damage the equipment.

Temperature-programmed desorption (TPD)

The identification and quantification of oxygen surface functionalities were determined by temperature-programmed desorption (TPD) analysis. The measurements were carried out in an AMI-300 Catalyst Characterization equipment (Altamira Instruments) connected to a Dycor Dymaxion quadrupole Mass Spectrometer (Ametek). In a typical analysis, around 100 mg of the sample was placed inside a U-shaped quartz tube situated inside an electrical furnace. The sample was then heated up to 1050 ºC at 10 ºC min^{-1} under a He flow rate of 25 cm^3 min^{-1}. During heating, several gases are released according to the samples' composition. In this PhD thesis, the analyzed materials were mainly composed of carbon (> 90 wt%) and some oxygen and hydrogen. Therefore, the main gases released during TPD analyzes were CO, CO_2 and H_2O. The gases of interest (CO and CO_2) were monitored throughout the analysis to plot their TPD profiles. The calibration was performed at the end of each day by feeding 10 pulses of calibrated loop volume of 64 µL of CO and CO_2 pure gases. The resulting CO and CO_2 profiles were then integrated to calculate the proportionality constant to be applied to the analyzes of the samples. The range of temperatures for the decomposition of each functional group is different and widely reported (Table 2.1) [9-11]. The decomposition temperature and the species released by each oxygen functional group allow their identification and, posteriorly, their quantification by deconvolution and integration of the CO and CO_2 TPD profiles.

Table 2.1 - Decomposition temperature ranges of different oxygen functional groups [9].

Functional Groups	Species Released	Temperature Range (°C)
Carboxylic acid	CO_2	200-450
Lactone		600-700
Carboxylic Anhydride	CO_2 + CO	350-650
Phenol	CO	600-750
Ether		700
Carbonyl/Quinone		700-950

The obtained TPD profiles were then deconvoluted into the different oxygen functional groups following the methodology described by Figueiredo et al. [9, 12]. Firstly, the CO_2 peak was deconvoluted into carboxylic acids, lactones and carboxylic anhydrides using a Gauss distribution fitting. Afterwards, considering that the carboxylic anhydride's contribution is the same in both CO and CO_2 profiles, the deconvoluted peak was replicated in the CO profile before the deconvolution of the other species. The remaining species present on the CO profile (phenol, carbonyl/quinone and ether) were then fitted using the Gauss distribution fitting. Both profiles were also integrated to calculate the CO and CO_2 amounts released during the TPD measurements and, consequently, the content of oxygenated groups on the material's surface.

Fourier transform infrared spectroscopy (FTIR)

Fourier transform infrared spectroscopy (FTIR) was used to evaluate the surface chemistry of prepared materials in powder form. This procedure is non-destructive, fast, accurate, and has high sensitivity [13]. This technology uses the atomic vibrations of different molecules, which absorb specific energies of infrared (IR) radiation [13]. In the most recent equipment, an IR light enters an interferometer and is directed at a beam splitter which redirects the light to a fixed mirror and movable mirror that reflects it to the beam splitter. The movement of the mirror causes the beams to go in and out of phase with each other, which originates an interference pattern. The two beams are then recombined at the beam splitter, and this newly formed modulated beam is then focused on the material and will either be reflected or absorbed by the material. The absorbed energy can then trigger three different types of molecule vibration: deformation vibration,

symmetric stretching vibration, or anti-symmetric stretching vibration. This absorbed energy is consumed by the sample, hence the remaining light presents different energy levels according to the sample's chemical composition. This light is then transmitted by the sample and collected by a detector which produces an electronic signal. The detector produces a raw signal of light intensity versus mirror position. Prior to the sample analysis, a blank measurement is performed to obtain a raw signal (interferogram), which is transformed into an IR plot of intensity versus wavenumber by Fourier transform and is used as the reference spectrum. After sample analysis, the spectrum obtained is divided by the reference spectrum, which results in the transmission spectrum of the analyzed material. This spectrum is then used to identify and understand variations of the chemical composition between different materials. In this work, FTIR measurements were performed using the attenuated total reflection (ATR) method. In this method, the IR light is transmitted at a critical angle through a crystal and bounces through the crystal as long as the incidence angle is equal to or lower than the critical angle. The IR light interacts with the sample on top of that crystal during bouncing, which produces evanescent waves that carry the sample's chemical information to the detector. In this PhD thesis, a JASCO FT/IR 6800 spectrometer was used to characterize the carbons by recording FTIR spectra at a maximum resolution of 4 cm^{-1} over a range between 4000 and 400 cm^{-1}. Each sample was analyzed using 256 scans.

Inductively coupled plasma optical emission spectrometry (ICP-OES)

The quantification of the metal loading of the prepared materials was performed by inductively coupled plasma optical emission spectrometry (ICP-OES). Before analysis, different solutions were prepared by diluting a commercial standard containing the metals of interest (10 ppm of either iron or cobalt) into different concentrations to be used as standards to create a calibration curve for each batch of samples tested. Moreover, the organic component of the prepared carbon materials had to be digested using an acid digestion procedure to prepare a solution only containing the inorganic component (metals) of the samples. In this work, 20-25 mg of sample were added in 10 mL of nitric acid (HNO_3) in a commercial modified polytetrafluoroethylene (mPTFE) 100 mL vessel that was then enclosed. The mPTFE cup was then placed inside a Start D microwave digestion system (Milestone) to control the temperature and pressure inside the vessel.

The enclosed mixture was heated to 200 °C for 15 min using a maximum power of 1000 W. The digested material was then transferred to a volumetric flask and diluted until the theoretical metal content was within the calibration curve that would be used during ICP measurements. After dilution, the solution was filtered using syringe filters (diameter of 0.2 μm, Whatman) to ensure that no solid particles were present in the solution that would be analyzed. The ICP-OES analysis is then performed by introducing the liquid sample into the system at a constant flow using a peristaltic bomb. Afterwards, argon at very high speed is used to break small liquid particles and obtain an aerosol, which is then introduced in a pulverization chamber that removes the bigger particles allowing only the fine aerosol particles to enter the plasma. The heat of the hot plasma (ca. 10000 °C) vaporizes the sample and excites the ions and atoms, resulting in the emission of light at the characteristic wavelengths of the elements present. This light is separated into spectral lines in the optical system and the intensity observed is correlated to the concentration of the element being analyzed. In this PhD thesis, the analyzes were carried out in a Perkin Elmer Optima 4300 using an optic with Echelle polychromator. The prepared materials were analyzed in duplicate to ensure the homogeneity of the samples and the reproducibility of the results.

X-ray diffraction (XRD)

The composition of the crystal structure of selected materials was analyzed by X-ray diffraction (XRD) at *Unidade de Microscopia Eletrónica da Universidade de Trás-os-Montes e Alto Douro* (UTAD). In this technique, an X-ray tube and a detector move in synchrony. The tube illuminates the sample with X-rays and the detector records the signal originated from the sample. The wavelength of the X-rays is similar to the distance between atoms inside a crystal, and the interaction between X-rays may result in different types of interferences. The alignment of X-ray waves leads to an amplification of the signal (constructive interference), whereas waves out of alignment nullify the signal (destructive interference). The energy of an X-ray is not enough to release an electron when it absorbs the radiation, hence it has to re-emit the absorbed energy in the form of a new X-ray. This phenom is called elastic scattering. At a crystal scale, this process occurs at multiple atoms simultaneously and, at certain angles, will result in scattered waves with constructive interference that will generate an amplified signal (diffraction).

The angle formed between the incident and scattered rays is called 2θ. During diffraction, the wavelength movement occurs half as incident and half as scattered. The diffraction phenom occurs at an angle (θ) that is half the angle between the incident and scattered beams, which is also the angle between the incident beam and the crystallographic plane. Considering an atomic plane between two atoms separated by a certain distance (d), half of the wavelength ($\lambda/2$) and the 90° formed between the diffraction and wavelength, θ can be calculated by a sine function (Eq. A1.6), which rearranged results in the Bragg's Law equation (Eq. A1.7) used to calculate θ. After diffraction, the X-ray beam passes through a monochromator which suppresses wavelengths different than Kα radiation and then generates a profile with the intensities observed at each 2θ. Each angle is correlated to a specific crystal phase which allows the identification of the crystalline phases present in the samples. In this PhD thesis, a X'Pert Pro diffractometer (PANalytical, Malvern, UK) composed of a PIXcel detector and employing a Cu Kα radiation with a wavelength of 1.541874 Å at 45 kV and 40 mA was used. The XRD assessments were performed using a scan speed of 0.01° s^{-1} between 20-80° (2θ) through a Bragg-Brentano configuration. In this specific configuration, the incident X-ray beam is fixed, whereas the sample stage rotates to create different incident angles. Furthermore, the sizes of the crystalline domains were calculated using the Scherrer equation (Eq. A1.8) [14].

2.4. Electrochemical characterization

2.4.1. Electrochemical setup

The electrochemical characterization was performed in a three-electrode system (Figure 2.10a), involving a reference electrode (RE), a counter electrode (CE), and a working electrode (WE), connected to a PGSTAT 302N potentiostat/galvanostat controlled by a Nova 2.1 software. In this PhD thesis, a beaker-type cell was used to avoid the possible formation of a vortex due to the rotation that sometimes is applied to the working electrode. For each experiment, the cell was filled with 100 mL of 0.1 mol L^{-1} KOH electrolyte solution in which the three electrodes were immersed. Regardless of the reaction studied, an Ag/AgCl (KCL 3 mol L^{-1}) and a carbon rod were used as reference and counter electrodes, respectively. Two different working electrodes were used during

the electrochemical characterization: a rotating disk electrode (RDE, Figure 2.10b) and a rotating-ring disk electrode (RRDE, Figure 2.10c).

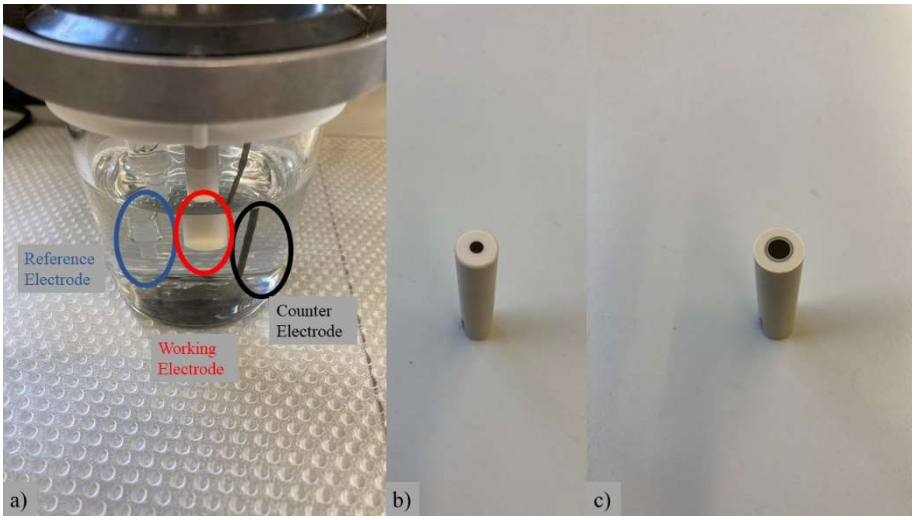


Figure 2.10 - Three-electrode cell used for oxygen reduction and evolution reactions electrochemical characterization (a), rotating disc electrode (b) and rotating ring-disc electrode (c).

The selection of the working electrodes was based on the data collection desired for each experiment, which is thoroughly explained in the following section (section 2.4.2).

2.4.2. Working electrodes

2.4.2.1. Rotating disk electrode (RDE)

One of the most important steps to assess an electrocatalyst is to study its electrochemical performance towards the reactions of interest, which in this PhD thesis were the oxygen reduction reaction (ORR) and the oxygen evolution reaction (OER). This information is commonly achieved by using a RDE as the working electrode [15]. The RDE employed is composed of a central disc made of glassy carbon, which is not electroactive towards either ORR or OER, and a larger insulating sheath made of polyether ether ketone (PEEK). The electrocatalysts are drop-casted on top of the glassy carbon disk. The electrochemical measurements were performed under rotation, so a speed controller is connected to the RDE, which is crucial for fundamental studies such as convection and diffusion kinetics as well as the determination of the number of electrons exchanged (n_e)

during the reaction [16, 17]. The WE's rotation limits the diffusion layer thickness (δ) and rapidly reaches a high rate of steady-state mass transport and reproducibly controlled convection [16]. In measurements performed using an RDE, the convection and diffusion of reactants to the electrodes are reproducible as the electrode is uniformly accessible by applying a rotation between 400 and a theoretical maximum of 10000 rpm [15, 18]. It should be noted that low rotations (100 rpm) are insufficient to eliminate the effect of natural convection, whereas too high rotations may produce a turbulent flow that will cause measurement errors, and may reduce the service life of the electrode and rotation motor [18]. According to the Nernst diffusion layer model, two different zones are observed using rotation: i) a stagnant layer between the electrode surface and a certain distance (δ), in which mass transportation occurs due to diffusion, and ii) an outside layer after δ distance controlled by strong convection maintaining a concentration at the bulk value [19]. Furthermore, δ is dependent on the rotation speed as the diffusion-layer thickness decreases with increasing rotation speed. One of the main uses of the RDE is to perform analysis under hydrodynamic conditions due to the rotation applied to the WE that creates an electrolyte flow relative to the WE. These analyzes can then be used to determine several characteristics of the materials and crucial electrochemical parameters to understand the electrocatalyst's performance.

2.4.2.2. Rotating ring-disk electrode (RRDE)

The rotating ring-disk electrode (RRDE) is one of the most important improvements of the RDE for hydrodynamic analyzes. In addition to the central disk composed of glassy carbon surrounded by the PEEK insulating material, the RRDE also has a concentric ring used as a secondary working electrode [16, 18, 19]. The configuration of the RRDE is essential to perform generation-collection experiments and was initially designed to detect unstable intermediates formed during the electrochemical reactions [19]. The rotation applied to the RRDE pulls the solution towards the center of the disk, which is posteriorly dispersed out radially across the electrode surface [19]. The design of the RRDE ensures that the electrochemical reaction products are detected at the ring after the mass transport across the insulating gap between the disc and the ring by forced convection. Nonetheless, a high enough potential must be applied to the ring to ensure that all by-products are immediately oxidized or reduced [18]. The current generated at

the ring can then be used to determine the number of electrons exchanged during an electrochemical reaction with a higher level of precision than the RDE and understand the reaction mechanisms that are taking place. Therefore, the RRDE can be employed to determine the same materials' characteristics/electrochemical parameters as the RDE in addition to the determination of the by-production formation.

2.4.3. Electrode preparation

The preparation of the electrodes involves the dispersion of each sample in a solution containing ultrapure water, absolute ethanol and Nafion. The dispersion was ultrasonicated for at least 30 min until achieving homogeneity. Afterwards, the solution was drop-cast onto the glassy carbon surface of the RDE or RRDE to achieve a certain electrocatalyst mass loading. Due to the different nature of the carbon supports employed in this PhD thesis, two different dispersions were prepared to ensure the homogeneity of the electrodes: i) 1 mg of sample was dispersed in 460 μL of a solution containing ultrapure water, ethanol and Nafion with a 2.3:1.5:1 volume ratio, and ii) 1 mg of sample was dispersed in 160 μL of a solution containing ultrapure water, ethanol and Nafion with a 6:1:1 volume ratio. On the other hand, the nature of the carbon support along with the electrocatalyst mass loading may modify the electrochemical performances, so three different electrocatalyst mass loadings were defined: 0.09 mg cm^{-2}, 0.27 mg cm^{-2}, and 0.81 mg cm^{-2}. For very electroactive catalysts like Pt/C, small loadings are enough to achieve high electrochemical performances, whereas higher loadings are needed for electrocatalysts with lower performances. This is due to the fact that using insufficient electrocatalyst mass loading results in an insufficient number of active sites to properly reduce the oxygen molecule, while an excessive amount of electrocatalyst will not enhance the electroactivity due to the limited oxygen dissolved in the electrolyte [20]. Moreover, increasing the catalyst loading decreases the accessibility of the electrocatalyst towards the electrolyte, which is a consequence of the greater distance of electron transportation over the electrode and hinders the reaction [21]. Therefore, it is essential to optimize the mass loading for each electrocatalyst.

2.4.4. Oxygen Reduction Reaction (ORR) and Oxygen Evolution Reaction (OER)

The electrochemical performance of the electrocatalysts towards the oxygen reactions was evaluated using an RDE or an RRDE by cyclic voltammetry (CV), linear sweep voltammetry (LSV), and chronoamperometry techniques using the electrochemical set-up detail in section 2.4.1.

Cyclic voltammetry

The evolution of the current intensity as a function of the applied voltage was studied by CV to evaluate the reactivity of the electrocatalysts towards the ORR and determine their electrochemical active surface area (ECSA). For the ORR assessment, CV measurements were carried out at a scan rate of 5, 20, 60 and 100 mV s^{-1} between 1.15 V and -0.05 V (vs RHE), without rotation of the working electrode, in a N_2- and O_2-saturated electrolyte. CVs performed in a N_2-saturated electrolyte were crucial to understanding the redox processes occurring on the surface of the electrocatalyst, while in the O_2-saturated electrolyte, the CVs presented additional peaks corresponding to the reduction of oxygen molecules. Prior to the determination of the ECSA, CVs were performed in N_2-saturated electrolyte at 5 mV s^{-1} between 1.15 V and -0.05 V (vs RHE), without rotation of the working electrode, to assess the potentials at which the electrocatalysts remain unreactive and with no Faradaic current [22]. Then, CVs at different scan rates ranging from 5 to 220 mV s^{-1} were performed, within the determined potential window at which no Faradaic reactions were observed, to determine the double-layer capacitance (C_{dl}). The C_{dl} is a crucial parameter to calculate the ECSA, which is essential to understand the accessibility of the electrocatalyst's metal active centers [23]. The ECSA can be calculated by using Eq. (A1.9).

Linear sweep voltammetry

The variation of the current density produced as a function of the applied voltage was studied under hydrodynamic conditions using linear cathodic sweeps to evaluate the electroactivity of the prepared materials towards the ORR. LSV measurements were performed at a scan rate of 5 mV s^{-1} with a rotation speed ranging from 400 to 3000 rpm (applied to the WE by a rotation speed controller) in both N_2- and O_2-saturated

electrolyte. These assessments were performed between 1.10 V and -0.05 V (vs RHE). The LSVs obtained in N_2-saturated electrolyte were used to understand which current density was generated by non-oxygen reduction processes, while in O_2-saturated electrolyte the current produced would mainly be attributed to oxygen reduction mechanisms. Nonetheless, the current density attributed only to the ORR was determined by subtraction of the LSV obtained in N_2-saturated medium to the one measured in the O_2-saturated electrolyte. During the ORR LSVs measurements at different rotation speeds, the current density measured on the RDE reaches a maximum if the reaction is fast enough. Nonetheless, three different regions are observed during an ORR LSV measurement (Figure 2.11) [24]: i) a kinetic-controlled region in which the overpotential applied is insufficient to overcome the reaction barrier and properly reduce oxygen, ii) a diffusion-controlled region as explained above in which a plateau is reached and iii) a mixed region between the kinetic and diffusion controlled regions. In each of these regions, different ORR electrochemical parameters can be determined (Figure 2.11).

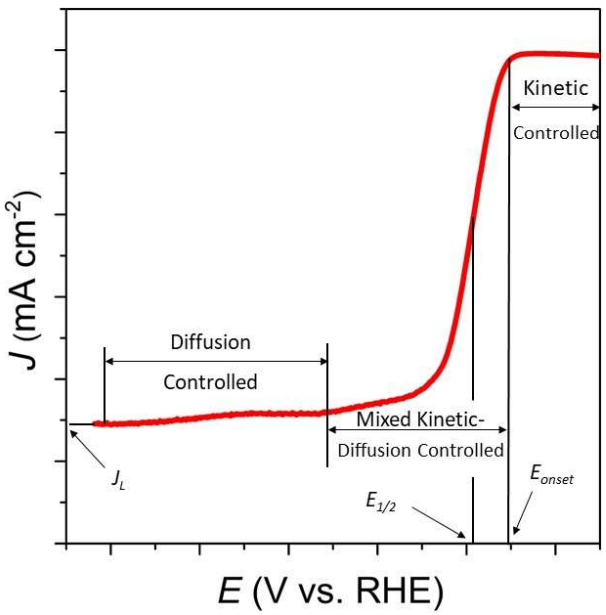


Figure 2.11 - A typical ORR linear sweep voltammetry curve with different reaction regions and main ORR parameters.

In the kinetic-controlled region, the onset potential (E_{onset}) can be determined and is considered the potential at which the kinetic barrier is overcome, and the oxygen

reduction starts taking place. This value is usually considered the potential at which a current density of 0.1 mA cm^{-2} is reached. In the diffusion-controlled region, the diffusion limiting current density (J_L) occurs and is considered the maximum diffusion current produced. This value is usually observed at the reaction's plateau at lower potentials. The theoretical maximum limiting current density can be expressed by the Levich equation (Eq. A1.10) [19, 20, 24], due to the reaction conditions limiting the oxygen reduction. Considering that all LSVs were performed in 0.1 mol L^{-1} KOH using a scan rate of 5 mV s^{-1} and a working electrode rotation of 1600 rpm and assuming an ideal four-electron mechanism, all variables to determine the theoretical maximum J_L are known. By replacing the Levich equation's variables with the values reported for the electrolyte used and the abovementioned operation conditions/reaction mechanism, a theoretical maximum current density of ca. 6 mA cm^{-2} is calculated. In the mixed region, a critical ORR parameter used to evaluate the electrocatalyst activity is calculated – the half-wave potential ($E_{1/2}$). The $E_{1/2}$ is generally considered as the potential required to produce half of the limiting current density observed for each material. Furthermore, it can be considered to be half of the maximum theoretical current density (3 mA cm^{-2}), which can be called E_3. Moreover, considering that the ORR is affected by both mass transfer and surface reaction, which is described by the Koutecký-Levich (KL) equation (Eq. A.12) [24], the number of electrons exchanged and the kinetic current density can also be determined using Eq. A.13 and A.14. Although the number of electrons can be calculated by the widely used KL equation, this equation does not represent the most accurate method to determine n_e as the ORR is neither a single-step nor a one-way reaction and does not fulfill the KL assumptions, from a theoretical viewpoint [25]. Experimentally, it has also been reported that n_e varies with the rotation speed, contradicting the constant number of exchanged electrons of the KL method [25]. Therefore, the determination of this parameter with the current densities of both disk and ring, i.e., using the RRDE, taking into account the respective collection efficiency, is a more proper methodology to assess the reaction mechanism. Figure 2.12 displays the ORR reaction mechanism considering an ideal scenario in which the by-products do not disproportionate and do not adsorb on the disc electrode and the oxygen reaction is irreversible.

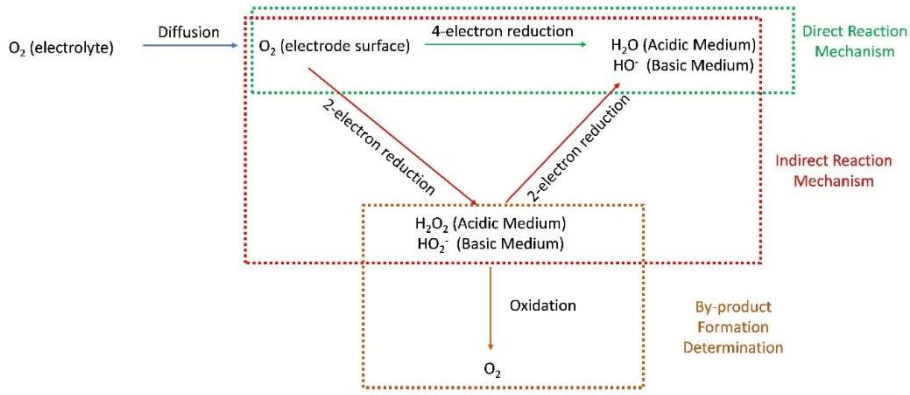


Figure 2.12 - Mechanisms of the oxygen reduction reaction.

As displayed in Figure 2.12, to determine the by-product formation, the oxidation of the by-products needs to take place, which is only possible using the RRDE. In the measurements performed with the RRDE, the reduction of oxygen occurs in the disk, while the formation of hydrogen peroxide (H_2O_2, acidic medium) or hydroperoxide ion (HO_2^-, basic medium) is detected in the ring. Therefore, the currents detected in the disk and the ring can be expressed as Eq. A1.15 and A1.16, respectively. The n_e can be calculated using the total number of electrons transferred and the total number of oxygen molecules participating in the ORR (Eq. A1.19). This equation can then be rearranged using the disk and ring current densities to determine n_e (Eq. A1.24). Similarly, the production of by-products can be calculated using the total number of by-product molecules formed and the total number of oxygen molecules participating in the reaction (Eq. A1.25). Further transforming this equation, a simpler equation using the disk and ring current densities can be used to determine the by-product formation (Eq. A1.29).

In a typical OER experiment, an anodic LSV is performed to evaluate the electroactivity of the synthesized materials by observing the variation of current density produced with increasing potentials. The electrocatalysts were tested under N_2-saturated medium by LSV using a scan rate of 5 mV s^{-1} at 1600 rpm (applied to the working electrode by a rotation speed controller) within a 1.00 V to 1.85 V potential range (vs RHE). Additionally, tests were performed in O_2-saturated KOH to ensure that no significant differences would occur due to the selected saturation gas. All OER measurements were performed using an RDE as WE. The RDE plays a very important role to understand the

electrocatalysis of the OER by the synthesized materials and to determine crucial electrochemical parameters. Although in this reaction there is no significant importance of the electrode rotation speed towards a limiting current density as there are no diffusional limitations, the rotation applied during the OER LSVs also plays a very important role during this reaction due to the removal of products from the electrocatalyst's surface that block its active sites [26]. Before the determination of the OER electrochemical parameters, the obtained LSVs must be corrected to determine the influence of the uncompensated electrolyte ohmic resistance (R_u). This resistance was obtained by the *i*-interrupt method [27] and was used to correct the raw LSV by using the E-iR$_u$ relationship, where i is the obtained current and R_u is the uncompensated electrolyte ohmic resistance. The OER electrochemical parameters obtained from these LSVs curves were: i) the potential at which a current density of 10 mA cm^{-2} was achieved (E_{10}), ii) the Tafel slopes, calculated by plotting E vs log(J), and iii) the turnover frequency (TOF), obtained from Eq. A1.30 [28, 29]. The E_{10} is the potential necessary to replicate a 10% efficient conversion device that uses a solar-to-fuels technique under 1 sun illumination (10 mA cm^{-2}) [30]. The Tafel slope values can be obtained by using the slope of the linear regression of the E vs log(J) plot after the OER has started. The determination of this slope provides the Tafel slope value, which correlates with the increase of potential necessary to increase the current density by a 10 factor. Moreover, LSVs were used to understand the long-term performance of the prepared electrocatalysts towards the OER. In this case, 1000 LSVs were performed between 1.00 V and 1.85 V vs RHE using a scan rate of 100 mV s^{-1} at 1600 rpm. Nonetheless, the first and last LSVs were performed using a scan rate of 5 mV s^{-1} to ensure their comparability with the literature and the other OER LSVs carried out during this work. The first LSV represents the original OER performance of each electrocatalyst whereas the 1000th LSV displays the electroactivity of the material after its long-term use. After the stability testing, these two LSVs were compared and the difference between their E_{10} was calculated. To maximize the electrocatalysts performance towards the OER, the overpotential should be as minimum as possible. Therefore, the loss of performance will increase with increasing E_{10}.

Chronoamperometry

Chronoamperometry measurements were performed using the RDE as WE to understand the long-term performance of the prepared electrocatalysts towards the ORR. In this electrochemical characterization, the 0.1 mol L^{-1} KOH electrolyte was saturated with oxygen and then a potential of 0.4 V vs RHE was applied for 10000 s. The long-term performance of each electrocatalyst was determined by the relation between the initial current density produced and that obtained at the last current density measured. The current density retention after the chronoamperometry is crucial for a potential scale-up of the electrocatalysts. Moreover, the methanol poisoning of the most promising materials was assessed by adding 1.5 mL of methanol during the chronoamperometry measurement at ca. 1000 s. Methanol present in the reaction medium may be oxidized and newly formed CO molecules can be adsorbed to the electrocatalysts' surface. The adsorbed molecules are blocking the active centers, which leads to a decrease in the electrocatalysts' performance and hinders the reaction. This is observed by a decrease in the current density produced during the chronoamperometry assessments.

2.4.5 Oxygen bifunctionality

The use of an electrocatalyst in a unitized regenerative fuel cell requires that it can efficiently catalyze both the ORR and the OER. The oxygen bifunctionality was determined by the potential gap (ΔE), which is the difference between the OER's E_{10} value and the ORR's $E_{1/2}$ or E_3 values. A low value of ΔE indicates a high bifunctional oxygen electroactivity as the combination of both reactions' overpotential will be at its minimum.

2.4.6. Additional electrochemical characterizations

To further characterize the electrocatalysts, electrochemical impedance spectroscopy (EIS) was applied to some materials. The EIS can provide critical information regarding Ohmic resistance, charge transfer resistance, and diffusion processes. An EIS assessment consists of the application of an alternate current (AC, input voltage signal), which results in a different output current signal that represents the flow of electrons. This analysis is performed with an AC as it allows reaching the steady-state conditions more slowly than using direct current (DC), and hence, granting a more detailed characterization. An AC

impedance presents two different components: a real part that impedes current by dissipating energy (resistance) and an imaginary component that impedes current by storing energy (reactant). These components are determined by the magnitude of impedance and the phase difference between the input voltage and the output current. The output signal can then be modulated using different types of electrical devices. A Nyquist plot is obtained by plotting the negative reactance against the resistance. The Nyquist plot (Figure 2.13) displays three different regions: i) at high frequencies, the Ohmic resistance related to the electrolyte resistance is measured, ii) at medium frequencies, the charge transfer resistance is determined and iii) at low frequencies, the diffusion resistance processes are observed. In this PhD thesis, the EIS measurements were performed in N_2-saturated electrolyte (0.1 mol L^{-1} KOH) without rotation of the WE. The EIS was performed using a frequency range from 10000 Hz to 10 Hz and 10 mV of amplitude. Afterwards, the Nyquist plot was prepared and an equivalent circuit model was created to describe the electrochemical system. To properly determine the circuit model, a resistor, a capacitor and the Warburg impedance were employed. The equations used to determine the resistances of these elements and any conjugation of a system used are ascribed by Eq. A27-A32.

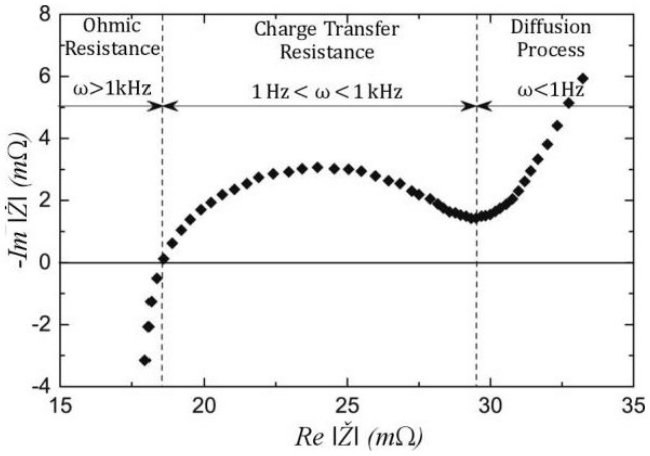


Figure 2.13 - Electrochemical impedance spectroscopy Nyquist plot regions (Reprinted with permission from [31]).

2.5. Electrochemical application

The electrochemical application of the most promising bifunctional oxygen electrocatalysts (BOCs) was assessed during a three-month stay abroad funded by the Erasmus mobility program at the Technische Universität Darmstadt (TU Darmstadt) supervised by Professor Bastian Etzold.

Experimental Setup

The electrochemical application of the synthesized materials was assessed in a three-electrode system (Figure 2.14a) composed of a RE, a CE, and a WE using an Ivium Octostat 5000 multichannel potentiostat controlled by IviumSoft software.

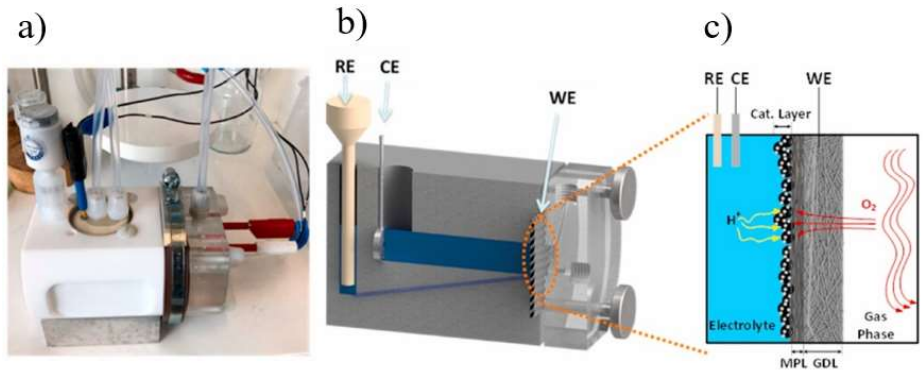


Figure 2.14 - a) Photograph of the assembled half-cell gas diffusion electrode setup. b) Cross-section of the cell showing the position of working (WE), counter (CE), and reference electrode (RE) and the connection of the reference electrode via a lugging capillary. c) Function principle of the characterization technique (Reprinted with permission from [32]).

A commercially available gas diffusion electrode (GDE) half-cell was used as the reaction cell for the ORR and OER. A Hg/HgO electrode filled with the electrolyte solution (2 mol L^{-1} KOH) was used as RE, whereas a commercial gas diffusion layer (GDL) bearing the electrocatalyst layer (CL) on its surface (gas diffusion electrode, GDE) was employed as WE. Due to the different requirements of the ORR and OER, two different CE were used. A titanium mesh coated with an Ir/Ta mixed oxide was employed as CE in the ORR testing, whereas the OER was performed using a Pt wire as CE. In this setup, gas flow is provided from the backside of the GDL, while the catalyst-coated

microporous layer (MPL) side is in contact with the electrolyte, providing protons/anions for the ongoing reaction. A representation of the experimental setup, its cross-section, and the function principle is displayed in Figure 2.14.

Gas diffusion electrode

The use of GDEs on half-cell setups provides an analysis of the electrocatalyst's performance closer to the reality of a commercial fuel cell. Figure 2.15 displays the three main levels of electrochemical catalyst evaluation and the advantages/disadvantages of each technique. The most basic level of evaluation is the fundamental studies that are performed using an RDE or an RRDE as the working electrode. This electrochemical characterization is mainly focused on the catalyst material performance and is the most well-established of the three levels of evaluation. These fundamental studies allow studying the reaction mechanism and reaction kinetics using a chosen electrocatalyst while using fast procedures. The following level involves the use of a GDE as WE and is used to understand the performance of a CL. The GDE provides reproducible results using fast procedures like the RDE/RRDE but at reaction conditions more similar to a large-scale application. During GDE studies, high current densities are produced using realistic mass transport phenomena. The GDE is the closest that an electrocatalyst's performance towards a reaction can be studied before its application in a membrane exchange assembly (MEA). The MEA (highest level of electrochemical evaluation) is used to study the system performance of a large-scale apparatus. The MEA requires high catalyst quantities to provide real performance data and is a very expensive electrocatalyst evaluation technique. Moreover, varying operation conditions occur at the MEA level, which can lead to disparities between assessments which is far from ideal.

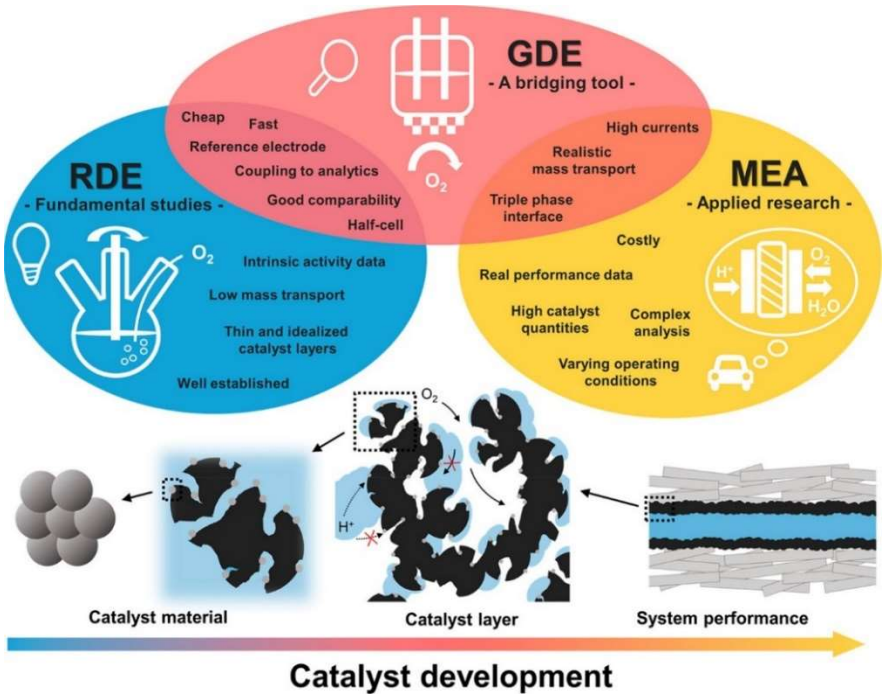


Figure 2.15 - Comparison of different levels of electrochemical catalyst (layer) evaluation. Reprinted with permission from [17]. Copyright 2022 American Chemical Society.

As displayed in Figure 2.15, the GDE works as a bridging tool between the fundamental studies performed using an RDE/RRDE and the use of MEA setups. Although the GDE can not be used to determine reaction kinetics and formation of by-products as the RDE/RRDE, it still provides a good reproducibility of the results between replicates, which is very important to assert confidence in the results obtained. Moreover, the GDE can provide the much-needed high current densities compared to the maximum ORR's 6 mA cm^{-2} using an RDE/RRDE, which is much closer to the values of the real application. Furthermore, the use of a catalyst layer instead of a thin catalyst film (RDE/RRDE) allows the evaluation of the electrocatalysts' performance without mass transport limitation, hence the stability and selectivity under more realistic mass transport conditions can be analyzed [17].

Electrode preparation

As mentioned, the GDE is a GDL in which the surface has been covered with a catalyst layer. The GDL is usually composed of an MPL and a gas diffusion substrate [33]. These components play two crucial roles in the application of the GDL. The MPL reduces the interface impedance and increases the water removal capacity, whereas the gas diffusion substrate promotes the distribution of the reaction gas [33]. Therefore, a GDL facilitates the gas transport towards the CL and its hydrophobic nature prevents the electrolyte solution from blocking its pores [34]. The catalyst ink deposited on the GDE was prepared using a procedure priorly optimized by the TU Darmstadt colleagues. The ink was prepared by mixing in an Eppendorf tube 4 mg of the electrocatalyst's material with 4.85 mL of a solution containing purified water (produced by reverse osmose and capacitive deionization, VWR Chemicals), ultrapure ethanol (> 99.8%, Fischer Scientific) and Nafion (5 wt% in mixture of lower aliphatic alcohols and water, 45% water, Sigma-Aldrich) in a 178:146:1 volume ratio, respectively. The ink inside the Eppendorf was dispersed in an ultrasonic processor before being loaded into the spray coating apparatus. A PTFE cover was used to fixate the GDL and restrict the geometric surface area that was coated with the electrocatalysts. The dispersion was then loaded onto the microporous layer side of the PTFE-coated GDL (Sigracet 25 BC) by ultrasound spray coating at 125 °C, and a final mass loading of ca. 0.5 ± 0.1 mg cm^{-2} was achieved. The water and ethanol volume ratio on the dispersion used was 55% and 45%, respectively. Higher water:ethanol ratios may hinder the full wetting of the GDL, whereas a penetration into the porous layer can occur for low water:ethanol ratios. The later ratios dramatically reduce the ECSA and, consequently, the performance of the electrocatalysts [32].

Experimental assessments

All experiments were performed using a 2 mol L^{-1} KOH electrolyte (prepared by dilution of a 45% solution supplied by Carl Roth) with the respective RE, CE and WE previously described. Prior to the ORR measurements, all electrocatalyst layers underwent 200 activation cycles between 1.20 and 0.05 V (vs RHE) at 500 mV s^{-1}, whereas for OER measurements the catalyst layers underwent 50 activation cycles ranging from 1.65 V to 0.15 V (vs RHE) at 500 mV s^{-1}, both in N_2-saturated electrolyte. Both ORR and OER

were then assessed by applying different galvanostatic steps and measuring the resulting potential for each step. These results obtained for each step were then used to plot polarization curves of each material. Nonetheless, due to the varying uncompensated resistance (*iR* drop) at each step, several EIS were performed to determine such resistance and to properly perform a post-correction of all the measured potentials. The ORR galvanostatic procedure was performed in O_2-saturated electrolyte by applying negative current densities. The ORR procedure was composed of initial steps at low current densities (-7.5 μA cm^{-2}, -25 μA cm^{-2}, -100 μA cm^{-2}, -250 μA cm^{-2}, -500 μA cm^{-2}, -1 mA cm^{-2}, -2.5 mA cm^{-2}, -5 mA cm^{-2}, -10 mA cm^{-2}, -25 mA cm^{-2} and -50 mA cm^{-2}). The first step (-7.5 μA cm^{-2}) was applied for 600 s, whereas -25 μA cm^{-2} and -100 μA cm^{-2} were applied for 90 s, -250 μA cm^{-2} and -500 μA cm^{-2} were measured for 60 s, -1 mA cm^{-2}, -2.5 mA cm^{-2}, -5 mA cm^{-2} and -10 mA cm^{-2} were applied for 30 s and -25 mA cm^{-2} and -50 mA cm^{-2} were measured for 5 s. High current densities can lead to an increase in the electrolyte temperature which influences the reaction taking place [32]. Therefore, to minimize the electrolyte heating, the holding times of each galvanostatic step decrease with increasing current density until a minimum time of 5 s is reached to ensure that a steady-state is achieved and enough points are available to determine an average potential read. Up to -50 mA cm^{-2}, the *iR* drop was very similar and, consequently, EIS was only measured prior to the last current density applied (-50 mA cm^{-2}). The EIS was performed by applying the step's current density using a frequency range from 10000 Hz to 10 Hz with a 2.5 mA of amplitude. Afterwards, due to the variation of the *iR* drop with the variation of current density, an EIS measurement was performed before each galvanostatic step. The following steps were achieved by applying -100 mA cm^{-2}, -250 mA cm^{-2}, -500 mA cm^{-2}, -1000 mA cm^{-2} and -2000 mA cm^{-2} for 5 s each. Prior to each step, an EIS was performed at the current density that was being applied using a frequency range from 10000 Hz to 10 Hz and an amplitude of 5% of the absolute value of the current density applied (e.g. for -100 mA cm^{-2} an amplitude of 5 mA was used, whereas an amplitude of 100mA was employed for -2000 mA cm^{-2}). This ORR procedure was considered as the forward scan. Afterwards, a backward procedure was applied using the same galvanostatic steps and EIS measurements as explained for the forward scan. In this case, different steps were applied from -1000 mA cm^{-2} to -7.5 μA cm^{-2}. The -2000

mA cm^{-2} was the maximum current density applied, hence its measurement was considered for both forward and backward scans.

The OER galvanostatic procedure was very similar to the ORR measurements but applying positive current densities. Initially, a forward scan was obtained by applying steps at low current densities (7.5 µA cm^{-2}, 25 µA cm^{-2}, 100 µA cm^{-2}, 250 µA cm^{-2}, 500 µA cm^{-2}, 1 mA cm^{-2}, 2.5 mA cm^{-2}, 5 mA cm^{-2}, 10 mA cm^{-2}, 25 mA cm^{-2} and 50 mA cm^{-2}) using the same holding times as their ORR counterparts. An EIS was performed before the galvanostatic step at 50 mA cm^{-2} using a frequency range from 10000 Hz to 10 Hz and with an amplitude of 2.5 mA. Afterwards, due to the variation of the *iR* drop with the variation of current density, an EIS measurement was performed before each galvanostatic step. The following steps were achieved by applying 100 mA cm^{-2}, 250 mA cm^{-2}, 500 mA cm^{-2}, 1000 mA cm^{-2} and 2000 mA cm^{-2} for 5 s each. Prior to each step, an EIS was performed at the current density that was being applied using a frequency range from 10000 Hz to 10 Hz and an amplitude of 5% of the absolute value of the current density applied. It should be noted that the polarization curves were constructed using only the average potential read for the last 3 s of each step for both reactions. Additionally, the *iR* drop was determined for each EIS measurement by creating an equivalent system and determining the uncompensated resistance. Moreover, the stability of the electrocatalysts was assessed towards both reactions.

The long-term performance towards the ORR of the materials was assessed by performing the full ORR procedure followed by an accelerated stability testing (AST) of 5000 CVs using a scan rate of 100 mV s^{-1} from 1.0 to 0.6 V (vs RHE) in O_2-saturated electrolyte followed by another full ORR procedure. The difference between the polarization curves from both procedures was the performance loss of each electrocatalyst.

On the other hand, the stability of the materials towards the OER was measured by chronoamperometry by applying 10 mA cm^{-2} for 1 h after performing the catalyst layer activation procedure abovementioned (50 CVs ranging from 1.65 V to 0.15 V (vs RHE) at 500 mV s^{-1} in N_2-saturated electrolyte). EIS measurements were performed prior and after the chronopotentiometry to ensure that no significant alteration of the *iR* drop value occurred. The increase of potential between the starting and final potential measured

represented the increase of overpotential during the chronoamperometry measurements. One of the main performance parameters towards the oxygen reactions is the overpotential required to catalyze these reactions. Therefore, any increase in overpotential represents a decrease in the electrocatalysts' performance. Furthermore, the materials should present the minimum possible overpotential to be considered high bifunctional oxygen electrocatalysts.

2.6. References

[1] J.L. Figueiredo, F.R. Ribeiro, Catálise heterogénea, Calouste Gulbenkian2007.
[2] A. Galarneau, F. Villemot, J. Rodriguez, F. Fajula, B. Coasne, Validity of the t-plot method to assess microporosity in hierarchical micro/mesoporous materials, Langmuir, 30 (2014) 13266-13274.
[3] G.S. Bumbrah, R.M. Sharma, Raman spectroscopy – Basic principle, instrumentation and selected applications for the characterization of drugs of abuse, Egyptian Journal of Forensic Sciences, 6 (2016) 209-215.
[4] Y. Leng, Transmission Electron Microscopy, Materials Characterization2013, pp. 83-126.
[5] S.J. Pennycook, Transmission Electron Microscopy, in: F. Bassani, G.L. Liedl, P. Wyder (Eds.) Encyclopedia of Condensed Matter Physics, Elsevier, Oxford, 2005, pp. 240-247.
[6] W. Zhou, R. Apkarian, Z.L. Wang, D. Joy, Fundamentals of Scanning Electron Microscopy (SEM), in: W. Zhou, Z.L. Wang (Eds.) Scanning Microscopy for Nanotechnology: Techniques and Applications, Springer New York, New York, NY, 2007, pp. 1-40.
[7] J. Bergström, 2 - Experimental Characterization Techniques, in: J. Bergström (Ed.) Mechanics of Solid Polymers, William Andrew Publishing2015, pp. 19-114.
[8] D.N.G. Krishna, J. Philip, Review on surface-characterization applications of X-ray photoelectron spectroscopy (XPS): Recent developments and challenges, Appl. Surf. Sci. Adv., 12 (2022) 100332.
[9] J.L. Figueiredo, M.F.R. Pereira, M.M.A. Freitas, J.J.M. Órfão, Modification of the surface chemistry of activated carbons, Carbon, 37 (1999) 1379-1389.
[10] J.-H. Zhou, Z.-J. Sui, J. Zhu, P. Li, D. Chen, Y.-C. Dai, W.-K. Yuan, Characterization of surface oxygen complexes on carbon nanofibers by TPD, XPS and FT-IR, Carbon, 45 (2007) 785-796.
[11] A. Kalijadis, M. Vukcevic, Z. Jovanovic, Z. Laušević, M. Laušević, Characterization of surface oxygen groups on different carbon materials by the Boehm method and temperature programmed desorption, J. Serb. Chem. Soc., 76 (2011) 757-768.
[12] J.L. Figueiredo, M.F.R. Pereira, M.M.A. Freitas, J.J.M. Órfão, Characterization of Active Sites on Carbon Catalysts, Ind. Eng. Chem. Res., 46 (2007) 4110-4115.
[13] V.K. Undavalli, C. Ling, B. Khandelwal, Chapter 6 - Impact of alternative fuels and properties on elastomer compatibility, in: B. Khandelwal (Ed.) Aviation Fuels, Academic Press2021, pp. 113-132.
[14] V.S. Vinila, J. Isac, Chapter 14 - Synthesis and structural studies of superconducting perovskite GdBa2Ca3Cu4O10.5+δ nanosystems, in: S. Thomas, N. Kalarikkal, A.R. Abraham (Eds.) Design, Fabrication, and Characterization of Multifunctional Nanomaterials, Elsevier2022, pp. 319-341.
[15] G. Denuault, M. Sosna, K.-J. Williams, 11 - Classical Experiments, in: C.G. Zoski (Ed.) Handbook of Electrochemistry, Elsevier, Amsterdam, 2007, pp. 431-469.
[16] C. Du, Q. Tan, G. Yin, J. Zhang, 5 - Rotating Disk Electrode Method, in: W. Xing, G. Yin, J. Zhang (Eds.) Rotating Electrode Methods and Oxygen Reduction Electrocatalysts, Elsevier, Amsterdam, 2014, pp. 171-198.
[17] K. Ehelebe, N. Schmitt, G. Sievers, A.W. Jensen, A. Hrnjić, P. Collantes Jiménez, P. Kaiser, M. Geuß, Y.-P. Ku, P. Jovanovič, K.J.J. Mayrhofer, B. Etzold, N. Hodnik, M. Escudero-Escribano, M. Arenz, S. Cherevko, Benchmarking Fuel Cell Electrocatalysts Using Gas Diffusion Electrodes: Inter-lab Comparison and Best Practices, ACS Energy Letters, 7 (2022) 816-826.
[18] Z. Jia, G. Yin, J. Zhang, 6 - Rotating Ring-Disk Electrode Method, in: W. Xing, G. Yin, J. Zhang (Eds.) Rotating Electrode Methods and Oxygen Reduction Electrocatalysts, Elsevier, Amsterdam, 2014, pp. 199-229.
[19] J.H. Moore, N.D. Spencer, Encyclopedia of Chemical Physics and Physical Chemistry: Fundamentals. Vol. 1, Inst. of Physics Publ.2001.

[20] G. Zhong, S. Xu, L. Liu, C.Z. Zheng, J. Dou, F. Wang, X. Fu, W. Liao, H. Wang, Effect of Experimental Operations on the Limiting Current Density of Oxygen Reduction Reaction Evaluated by Rotating-Disk Electrode, ChemElectroChem, 7 (2020) 1107-1114.
[21] L. Yu, S. Sun, H. Li, Z.J. Xu, Effects of catalyst mass loading on electrocatalytic activity: An example of oxygen evolution reaction, Fundam. res., 1 (2021) 448-452.
[22] Y.P. Zhu, Y. Jing, A. Vasileff, T. Heine, S.-Z. Qiao, 3D Synergistically Active Carbon Nanofibers for Improved Oxygen Evolution, Adv. Energy Mater., 7 (2017) 1602928.
[23] Y. Peng, J.-Y. Choi, T. Fürstenhaupt, K. Bai, Y. Zhang, D. Banham, New approach for rapidly determining Pt accessibility of Pt/C fuel cell catalysts, J. Mater. Chem. A, 9 (2021) 13471-13476.
[24] J. Wang, C.-X. Zhao, J.-N. Liu, D. Ren, B.-Q. Li, J.-Q. Huang, Q. Zhang, Quantitative kinetic analysis on oxygen reduction reaction: A perspective, Nano Materials Science, 3 (2021) 313-318.
[25] R. Zhou, Y. Zheng, M. Jaroniec, S.-Z. Qiao, Determination of the Electron Transfer Number for the Oxygen Reduction Reaction: From Theory to Experiment, ACS Catal., 6 (2016) 4720-4728.
[26] P. Jovanovič, K. Stojanovski, M. Bele, G. Dražić, G. Koderman Podboršek, L. Suhadolnik, M. Gaberščček, N. Hodnik, Methodology for Investigating Electrochemical Gas Evolution Reactions: Floating Electrode as a Means for Effective Gas Bubble Removal, Analytical Chemistry, 91 (2019) 10353-10356.
[27] R.P. Forslund, W.G. Hardin, X. Rong, A.M. Abakumov, D. Filimonov, C.T. Alexander, J.T. Mefford, H. Iyer, A.M. Kolpak, K.P. Johnston, K.J. Stevenson, Exceptional electrocatalytic oxygen evolution via tunable charge transfer interactions in La0.5Sr1.5Ni1−xFexO4±δ Ruddlesden-Popper oxides, Nat. Commun., 9 (2018) 3150.
[28] M. Tahir, L. Pan, F. Idrees, X. Zhang, L. Wang, J.-J. Zou, Z.L. Wang, Electrocatalytic oxygen evolution reaction for energy conversion and storage: A comprehensive review, Nano Energy, 37 (2017) 136-157.
[29] Z.-F. Huang, J. Wang, Y. Peng, C.-Y. Jung, A. Fisher, X. Wang, Design of Efficient Bifunctional Oxygen Reduction/Evolution Electrocatalyst: Recent Advances and Perspectives, Adv. Energy Mater., 7 (2017) 1700544.
[30] C.C.L. McCrory, S. Jung, I.M. Ferrer, S.M. Chatman, J.C. Peters, T.F. Jaramillo, Benchmarking Hydrogen Evolving Reaction and Oxygen Evolving Reaction Electrocatalysts for Solar Water Splitting Devices, J. Am. Chem. Soc., 137 (2015) 4347-4357.
[31] M.S. Hosen, R. Gopalakrishnan, T. Kalogiannis, J. Jaguemont, J. Van Mierlo, M. Berecibar, Impact of Relaxation Time on Electrochemical Impedance Spectroscopy Characterization of the Most Common Lithium Battery Technologies—Experimental Study and Chemistry-Neutral Modeling, World Electr. Veh. J., 2021.
[32] N. Schmitt, M. Schmidt, G. Hübner, B.J.M. Etzold, Oxygen reduction reaction measurements on platinum electrocatalysts in gas diffusion electrode half-cells: Influence of electrode preparation, measurement protocols and common pitfalls, J. Power Sources, 539 (2022) 231530.
[33] Y. Yang, X. Zhou, B. Li, C. Zhang, Recent progress of the gas diffusion layer in proton exchange membrane fuel cells: Material and structure designs of microporous layer, Int. J. Hydrog. Energy, 46 (2021) 4259-4282.
[34] S. Hernandez-Aldave, E. Andreoli, Fundamentals of Gas Diffusion Electrodes and Electrolysers for Carbon Dioxide Utilisation: Challenges and Opportunities, Catalysts, 2020.

Chapter 3

Glucose-derived carbons with tailored properties as electrocatalysts for the oxygen reduction reaction

R. G. Morais, N. Rey-Raap, J. L. Figueiredo, M. F.R. Pereira, Glucose-derived carbon materials with tailored properties as electrocatalysts for the oxygen reduction reaction, Beilstein J. Nanotechnol., 10 (2019) 1089-1102.

Abstract

Nitrogen-doped biomass-derived carbons were prepared by hydrothermal carbonization of glucose, and their textural and chemical properties were subsequently tailored to achieve materials with enhanced electrochemical performance towards the oxygen reduction reaction. Carbonization and physical activation were applied to modify the textural properties, while nitrogen functionalities were incorporated via different N-doping methodologies (ball milling and conventional methods) using melamine. A direct relationship between the microporosity of the activated carbons and the limiting current density was found, with the increase of microporosity leading to interesting improvements of the limiting current density. Regardless of the doping method used, similar amounts of nitrogen were incorporated into the carbon structures. However, significant differences were observed in the nitrogen functionalities according to the doping method applied: ball milling appeared to originate preferentially quaternary and oxidized nitrogen groups, while the formation of pyridinic and pyrrolic groups was favored by conventional doping. The onset potential was improved and the two-electron mechanism of the original activated sample was shifted closer to a four-electron pathway due to the presence of nitrogen. Interestingly, the high pyridinic content allied to a high ratio of pyridinic/quaternary nitrogen results in an increase of the onset potential, while a decrease in the quaternary/pyrrolic nitrogen ratio favors an increase in the number of electrons. Accordingly, the electrocatalyst with the highest performance was obtained from the activated sample doped with nitrogen by the conventional method, which combined the most appropriate textural and chemical properties: high microporosity and adequate proportion of the nitrogen functionalities.

3.1. Introduction

Due to the recent increase of interest for more sustainable, renewable and cheaper energy, multiple conversion devices are being developed using new and innovating materials. Fuel cells are outstanding conversion devices, as they convert chemical energy directly into electrical energy with high efficiency and low emission of pollutants (the by-products are water and heat) [1,2]. Fuel cells offer the best advantages of engines, as they are able to function as long as there is fuel, and of batteries, as they have similar characteristics to them under load condition [1]. The performance of a fuel cell is mainly controlled by the oxygen reduction reaction (ORR) that takes place at the cathode [2], specifically by the electrocatalyst used for the reaction. The most commonly used electrocatalysts to supply faster kinetics and a four-electron pathway are platinum-based materials [3,4], which are costly and may assume up to 50% of the total cost of a fuel cell [5].

Transition metals [6,7], metal oxides [8,9] and carbon materials [3,4] have been widely studied as electrocatalysts in ORR due to their attractive physical and electrochemical properties. Among these materials, metal-free carbons have received tremendous attention due to their versatility and lower price in comparison with metal-based materials [2]. The main advantage of carbon materials is the possibility of modifying their physical and chemical properties resulting in a more electroactive material [2,3, 10], an especially important feature for the ORR. The incorporation of heteroatoms like nitrogen [11,12], oxygen [13], sulfur [14,15], phosphorous [16,17] and boron [18,19] has been proven to enhance the electroactivity of carbon materials. Nitrogen has been the most studied heteroatom in the context of the reaction mechanism, inasmuch as nitrogen-doped materials can achieve a four-electron pathway towards ORR [20-22]. However, there is some controversy related to the effect of the different nitrogen functionalities in the process. Some investigations suggest that the reduction of oxygen is promoted by pyridinic groups [23], other researchers reported that quaternary nitrogen groups are the most active sites [24,25], and some studies assume that both functionalities contribute to enhance the performance of the materials towards ORR [20]. In addition, a recent study with carbon nanotubes (CNTs) reported that an increase of the pyridinic-N/quaternary-N and pyridinic-N/pyrrolic-N ratios increases the electroactivity, and that decreasing the

quaternary-N/pyrrolic-N ratio increases the number of electrons involved in the ORR [12]. The differences reported on the influence of the nitrogen functionalities may be related to the nature and type of the carbon material employed, which in turn, depends on the precursors used and the method of synthesis applied.

Nitrogen-doped carbons have been synthesized by applying different doping methods to different types of materials, such as CNTs [12, 23, 26], graphene [20, 25, 27], carbon aerogels [15, 28], carbon nanofibers [29], carbon nitrides [30], activated carbons [31] or mesoporous carbons [32,33]. Some of these materials are obtained from chemical compounds, fossil-fuels or by complex and expensive synthesis procedures. In order to keep fuel cells as greener as possible, the use of biomass as a carbon source appears to be an attractive alternative. In this context, hydrothermal carbonization (HTC) has appeared in recent years as an interesting strategy to obtain biomass-derived carbons due to its low cost and mild synthesis conditions, making the process environmentally friendly [34]. However, the main drawback of HTC is that the as-prepared hydrothermal carbons usually exhibit limited porosity and inadequate chemical properties for the ORR. To solve this problem, different strategies can be addressed: i) carbonization and activation methods to tailor the porosity and ii) the incorporation of heteroatoms to modify the surface chemistry, specifically by adding nitrogen functionalities. Biomass-derived carbons have been functionalized by applying thermal treatments in the presence of a gaseous or solid nitrogen precursor [35,36] or without any precursor in the case biomass already containing nitrogen in its constitution [11, 37], and by in-situ methods in which nitrogen precursors are introduced during the hydrothermal carbonization [38]. An additional strategy that can be applied to biomass is ball milling, which has been proposed as a green, cheap and easy method to incorporate nitrogen atoms and to modify the surface chemistry of carbon materials [39,40]. Some of these doping techniques have shown to provide materials with similar ORR performances as the commercial Pt/C electrocatalysts [39]. However, most of these studies have been focused only on the effect of nitrogen functionalities on the ORR, leaving aside the effect of porosity. In fact, although some studies suggest the importance of microporosity on the ORR [41], there is a lack of knowledge about its real effect on the ORR performance of nitrogen-doped porous carbon materials, and more specifically, of biomass-derived carbons.

Therefore, the aim of this study is to prepare glucose-derived carbons with different textural and chemical properties and to correlate these properties with the performance towards ORR. Activated carbons with different microporosity were prepared by activating the samples at different times to determine the relationship between the textural properties and the ORR performance. Moreover, different doping strategies were applied to assess the effect of such methods on the incorporation of nitrogen functionalities, and to evaluate the influence of the different functional groups on the response of the electrocatalyst towards the oxygen reduction reaction.

3.2. Experimental

3.2.1. Preparation of carbon materials

Carbon materials were prepared from an initial solution of glucose (HiMedia, > 99%) and deionized water (produced by filtration through inverse osmose by a Panice equipment) in a 1:6 ratio. The solutions were mixed and then closed in a Teflon-lined stainless steel autoclave and hydrothermally carbonized during 12 h at 180 ºC. The obtained material was washed with deionized water and dried at 100 ºC overnight. The dried material was then activated under a CO_2 flow of 80 cm^3 min^{-1} g^{-1} at 900 ºC for 1, 3, 4 and 6 h. Samples were labeled AG_X, where X are the hours used for activation.

The sample activated for 6 h was also doped with nitrogen by using melamine (≥ 99%, Sigma-Aldrich) as a precursor. Two different approaches were studied: i) the activated carbon material was mixed with melamine by using ball milling and ii) the activated carbon material was manually mixed with melamine, henceforth referred as conventional method. Ball milling process was performed in an enclosed flask with two zirconia balls at 15 Hz of frequency during 4 h using a Retsch MM200 equipment. Regardless of the doping method used, all samples underwent a subsequent thermal treatment under N_2 atmosphere for 2 h at 700 ºC to force the decomposition of melamine and to incorporate nitrogen atoms into the carbon structure. Additionally, a carbonized sample was prepared under a N_2 flow of 150 cm^3 min^{-1} at 700 ºC for 2 h, to isolate the effect of functionalization in respect to the surface area. This sample also underwent the same two doping methods as the activated sample. All treatments were carried out in a vertical furnace in which a heating rate of 10 ºC min^{-1} was fixed. Samples were labeled XG_Y and N-XG_Y for undoped

and N-doped samples, respectively; where X can assume the form of A for activated samples and C for carbonized samples and Y is represented by BM for ball milled samples and C for conventionally doped samples. Activated and carbonized samples were also ball milled in the absence of any precursor for comparison, employing the same conditions as in doped samples.

3.2.2. Materials characterization

The textural characterization was carried out by N_2 adsorption at -196 °C performed in a Quantachrome Autosorb iQ automated gas sorption analyzer. All samples were degassed under vacuum at 150 ºC for 12 h prior to the analysis. The specific surface area (S_{BET}) was determined according to the Brunauer-Emmett-Teller (BET) equation, the total pore volume (V_p) was calculated as the volume of nitrogen adsorbed at the saturation point (relative pressure of 0.99) and the micropore volume (V_{DR}) was evaluated by the Dubinin-Radushkevich method.

The chemical composition of the samples was determined by elemental analysis. Carbon, hydrogen and nitrogen (C, H and N) were determined in a Vario Micro Cube Analyzer (Elementar GmbH), by combustion of the sample at 1050 ºC. The oxygen content was determined using a Rapid Oxy Cube Analyzer (Elementar GmbH) in which the sample underwent pyrolysis at 1450 ºC. Each sample was analyzed in triplicate. X-ray photoelectron spectroscopy (XPS) was employed to study the surface chemical composition of the samples. The analyzes were carried out in a Kratos AXIS Ultra HAS spectrometer using a monochromatic Al Kα radiation (1486.7 eV) at 15 kV (90 W), in fixed analyzer transmission mode, performing a pass energy of 80 eV for the general spectra and 40 eV for regions of interest. Temperature-programmed desorption (TPD) was performed to determine and quantify the surface oxygenated groups of the samples by using an Altamira Instruments AMI-300 equipment. The samples were heated with a 10 ºC min^{-1} ramp until 1050 ºC. At the end of each analysis, a calibration of the CO and CO_2 evolved was carried out, allowing the quantification of the TPD profiles.

3.2.3. Electrochemical characterization

The electrochemical measurements were performed on a PGSTAT 302N potentiostat/galvanostat by using a three-electrode cell configuration. Ag/AgCl (KCl 3 M) and a glassy carbon rod were used as reference and counter electrode, respectively. Working electrodes were prepared by depositing a suspension of the carbon samples on a glassy carbon rotating disk electrode (3 mm of diameter, Metrohm). These suspensions were prepared by dispersing 1 mg of the prepared samples in a solution containing 220 µL of ultrapure water (Millipore), 142 µL of ethanol (≥ 99%,Valente e Ribeiro) and 96 µL of Nafion (5 wt%, Sigma-Aldrich). The suspension was sonicated for 30 min until a homogeneous dispersion was obtained. The mass loading of all samples was ca. 0.1 mg cm^{-2}. A rotation speed controller allowed adjusting the rotations of the working electrode according to the assessments being done.

The experiments were carried out at room temperature in a 0.1 mol L^{-1} KOH solution saturated with N_2 or O_2 for 30 min before the cyclic voltammetry (CV) and linear sweep voltammetry (LSV) were performed. The CVs measurements were accomplished at a scan rate of 5, 20, 60 and 100 mV s^{-1} and the LSVs at a scan rate of 5 mV s^{-1} with a rotation speed range from 400 to 3000 rpm, both within a 1.2 V to –0.1 V potential range (vs RHE). The measured current was determined by subtracting the current obtained from the electrolyte saturated with N_2 from the current measured in the O_2-saturated electrolyte, Electrochemical impedance spectroscopy (EIS) was also applied at 0 V in the frequency region of 10 kHz to 10 mHz with AC amplitude of 10 mV. EIS was performed in the same type of cell, with N_2-saturated electrolyte (KOH 0.1 mol L^{-1}) and with no rotation.

The current density at the disk can be expressed by the Koutecký-Levich equation:

$$\frac{1}{J} = \frac{1}{J_L} + \frac{1}{J_K} = \frac{1}{B\omega^{\frac{1}{2}}} + \frac{1}{J_K} \tag{3.1}$$

where J is the measured current density (mA cm^{-2}), J_L is the O_2 diffusion-limited current density (mA cm^{-2}), J_K is the kinetic current density (mA cm^{-2}), ω is the electrode rotation rate (rpm) and B represents the Levich Constant related to the diffusion limiting current density given by equation 3.2.

$$B = 0.2 n_e F D^{\frac{2}{3}} v^{-\frac{1}{6}} C \quad (3.2)$$

where F is the Faraday constant (96 486 C mol^{-1}), D is the diffusion coefficient of O_2 (1.95 x 10^{-5} cm^2 s^{-1}), v is the kinematic viscosity of the electrolyte (0.008977 cm^2 s^{-1}) and C is the bulk concentration of O_2 (1.15 x 10^{-3} mol L^{-1}).

The number of electrons (n_e) was calculated at different potentials for each LSV recorded by applying equations 3.1 and 3.2.

The percentage of hydrogen peroxide (H_2O_2) produced during the ORR was also measured by using a rotating ring-disk electrode (5 mm of diameter, 24.9% collection efficiency, Methrom) as working electrode, which was prepared by depositing a solution of the carbon samples on the disk area. The dispersions were prepared as detailed above and the mass loading was fixed at ca. 0.1 mg cm^{-2}. The H_2O_2 percentage was calculated by equation 3.3.

$$H_2O_2(\%) = 200 \times \frac{I_R/N}{I_D + I_R/N} \quad (3.3)$$

where I_R is the ring current density (mA cm^{-2}), I_D is the disk current density of the disk (mA cm^{-2}) and N is the collection efficiency (0.249).

3.3. Results and discussion

3.3.1. Effect of microporosity

The nitrogen adsorption-desorption isotherms and the pore size distributions obtained by applying the Quenched Solid Density Functional Theory (QSDFT) are presented in Figure 3.1a and 3.1b, respectively.

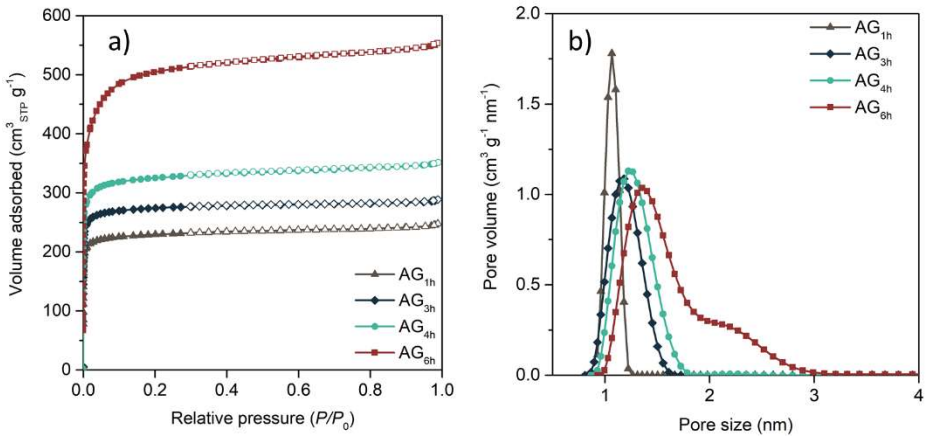


Figure 3.1 - N_2 adsorption/desorption isotherms (a) and pore size distributions (b) of the activated carbons.

Activated carbons display isotherms type I according to the International Union of Pure and Applied Chemistry (IUPAC) classification, attributed to microporous materials. As expected, the volume of nitrogen adsorbed at low relative pressures increases with the time of activation, resulting in materials with larger volume of micropores (Table 3S.1). This effect is due to the reverse Boudouard reaction, which extracts carbon atoms from the carbon structure developing porosity [42]. Accordingly, a prolonged contact time between the carbon material and the activating agent results in materials with a more developed microporosity. In addition, the pore size of the samples is also broadened by increasing the contact time (Figure 3.1b). The reaction occurring during the physical activation of the samples removes carbon atoms, giving rise to larger voids inside the particles, and hence, to larger pore sizes.

Regarding the chemical composition, activated samples are mainly composed of carbon, with a percentage of oxygen in the range of 2-4 wt% (Table 3S.2). Although these values are not too high, oxygen functionalities can modify the electroactivity of carbon materials [13], so the nature of these functional group has been analyzed by temperature-programmed desorption experiments to evaluate possible differences in the oxygen functionalities. The total amounts of CO (anhydrides, phenols, carbonyls) and CO_2 (carboxylic acids, anhydrides, lactones) released were calculated from the corresponding TPD profiles and the values obtained are compiled in Table 3S.3. The CO_2 and CO

desorption profiles, obtained for AG_{1h} and AG_{6h} samples are also shown in Figure 3S.1. The TPD profiles show that the sample with the highest degree of activation (AG_{6h}) has lower amount of phenols due to the higher time used for the activation. However, in general terms, the released CO and CO_2 and their ratio are quite similar, so it can be assumed that there are no significant differences between the chemical composition of the samples and therefore, any difference in the ORR performance can be exclusively related to the microporosity and/or the degree of activation.

Linear sweep voltammograms (LSV) recorded in an O_2-saturated basic electrolyte at 1600 rpm and the Nyquist plot obtained from electrochemical impedance spectroscopy measurements are shown in Figure 3.2a and 3.2b, respectively.

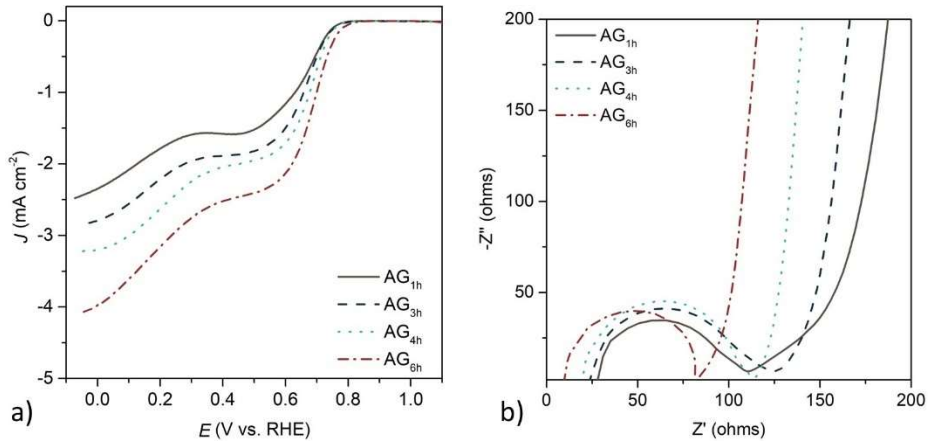


Figure 3.2 - Linear sweep voltammetry recorded in an O_2-saturated 0.1 mol L^{-1} KOH electrolyte at 1600 rpm (a) and Nyquist plot obtained from electrochemical impedance spectroscopy (b).

To evaluate the performance of the prepared electrocatalysts, cyclic voltammetries (CV) and linear sweep voltammetries (LSV) were performed. LSV curves of the activated samples show two main differences: i) the onset potential shifts to more positive values by increasing the time of activation, which can be related to the more graphitic structure that is generated during activation; and ii) the value of the limiting current density increases with microporosity, which can be related to the more developed porous structure. These two effects can be confirmed by the electrochemical impedance spectroscopy measurements (Figure 3.2b). The Nyquist plot shows that higher degree of

activation results in smaller semicircle at high frequencies, indicating a lower charge transfer resistance, which allows to speed up the kinetics of the ORR, and, consequently, a higher onset potential is observed for sample AG_{6h} (the values of the onset potential are shown in Table 3S.4). A direct relationship was observed for microporosity and limiting current density for these carbon materials (Figure 3.3).

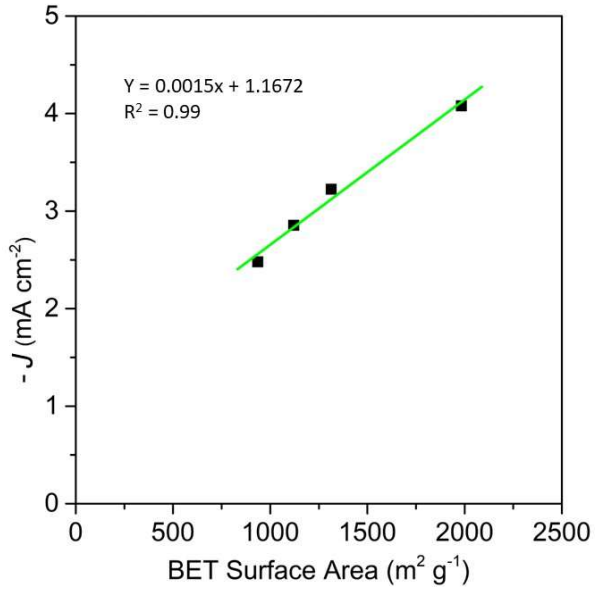


Figure 3.3 - Relation between BET surface area and the limiting current density of the activated samples.

In addition, the electrolyte resistance (R_s) decreases by increasing the BET surface area of the samples, which suggests that a more developed microporous structure favors the electrolyte transfer to the most electrochemically active pores, which also contributed to the ORR kinetics. Moreover, clear differences regarding ionic transportation are also observed at medium frequencies. Sample AG_{1h} shows a more defined Warburg impedance, indicating a higher resistance of the electrolyte ions diffusion into the porous structure, and hence, a lower value of limiting current density. These diffusion limitations are less evident for those samples with wider pore size, as pores act as diffusion channels favoring the kinetics of the ORR. However, regardless of the time used for the activation, all samples originate a LSV curve with similar shape. The reduction reaction occurs at two different potentials (0.75-0.78 V and 0.30-0.33 V), indicating that the ORR

mechanism proceeds via the two-electron pathway producing hydrogen peroxide. More than 18% of hydrogen peroxide was produced with AG_{6h} (Figure 3S.2), which is not desirable for the ORR. These results indicate that further modifications of this sample are needed to enhance the performance of the biomass-derived carbons towards ORR.

3.3.2. Effect of the surface chemistry

In order to improve the performance of glucose-derived activated carbons, the surface chemistry of the sample AG_{6h} (from now on simply named AG) was modified by applying different doping methods: ball milling and conventional mixing. In addition, such methods were also applied to a carbonized sample to evaluate the effect of the doping method according to the microporosity generated from the initial thermal treatment. Both activated and carbonized samples also underwent the ball milling method without nitrogen precursor to discriminate among the modifications resulting from ball milling and those due to the conjugation of ball milling and the nitrogen precursor. The results obtained from the elemental analysis are presented in Table 3.1.

Table 3.1 - Chemical composition determined by elemental analysis.

Sample	C (wt%)	N (wt%)	O (wt%)	H (wt%)
AG	97.3	-	2.4	0.3
AG_{BM}	89.4	-	9.5	1.1
N-AG_{BM}	87.3	4.3	7.0	1.4
N-AG_{C}	90.1	4.1	4.9	0.9
CG	93.6	-	4.7	1.6
CG_{BM}	85.5	-	12.3	2.2
N-CG_{BM}	82.9	6.9	8.8	1.4
N-CG_{C}	83.1	6.2	9.2	1.5

As expected, all samples are mainly composed of carbon, being the percentage slightly higher for activated samples than for carbonized materials, due to the higher temperature used for activation (900 ºC). The application of ball milling in both activated and carbonized samples results in a noticeable increase in the oxygen content. This phenomenon may be due to the defects created in the carbon structure during the milling

process that react with air and incorporate oxygen. This effect is also observed for N-doped samples by ball milling. However, doped samples undergo a second thermal treatment that partially removes the oxygen incorporated during the ball milling process, resulting in a lower oxygen content. Nevertheless, although the amount of oxygen in samples doped by ball milling is lower than in undoped samples, the percentage detected is still significant. As for conventionally doped samples, the oxygen content is twice the oxygen found in the original samples. Regardless of the degree of activation of the samples, the amount of nitrogen incorporated by the ball milling method is similar to that obtained by the conventional method. However, the incorporation of oxygen and nitrogen in the activated structures is lower than in carbonized samples. Activation at high temperature results in a structure with higher chemical stability and lower amount of defects in which heteroatoms can be incorporated, and so materials with lower degree of functionalization are obtained.

Further understanding of the functionalities of the carbon materials was achieved by analyzing their surface composition by X-ray photoelectron spectroscopy. The XPS spectra in the C 1s, O 1s and N 1s regions were deconvoluted to identify the types of functionalities present in the surface of the carbon materials. The deconvolution of the C 1s spectra for undoped samples presents five main peaks (Figure 3S.3), representing the following by increasing binding energy: i) carbon sp^2 (C=C, Peak I) at 284.6 ± 0.1 eV; ii) carbon in phenol, alcohol, ether bonds (C–O, Peak II) at 285.8 ± 0.2 eV; iii) carbonyl or quinone groups (C=O, Peak III) at 287.2 ± 0.2 eV; iv) carboxyl groups (COOH, Peak IV) at 288.9 eV ± 0.3; and v) the shake-up satellite due to π-π* transitions in aromatic rings (Peak V) at 290.6 ± 0.5 eV [43]. Carbon sp^2 (Peak I) is an asymmetric peak consisting of a tail towards higher binding energies that represents ca. 80% of surface carbon, not revealing significant differences for activated and carbonized samples. However, noticeable differences in the peaks attributed to carbon-oxygen bonds are observed due to the ball milling process and the doping methods applied. The peak attributed to carboxylic acids (Peak IV) is significantly more pronounced for ball milled samples (AG_{BM} and CG_{BM}), suggesting that the increase of oxygen detected by elemental analysis (Table 3.1) was due to the formation of a large amount of carboxylic acids, which further reinforces the possible reaction between the defects generated on the sample

during the ball milling process and air moisture. The XPS spectra for C 1s region of the doped samples exhibit the same five peaks as those observed for the undoped samples. However, peak II and peak III also have contributions of C-N and of C=N interactions, respectively [15]. These phenomena result in a significantly higher contribution of these two peaks than those observed for the undoped samples. Additionally, peak IV in conventionally doped materials (N-AG_C and N-CG_C) is more pronounced than that of their doped ball milled counterparts. This peak can be assigned to sp^2-hybridized carbons in a triazine aromatic ring (N-C=N) [30], which may result from the polymerization of melamine during the subsequent thermal treatment. This effect is less notorious in the spectra of the activated sample, as its higher chemical stability results in a lower degree of functionalization and, therefore, lower formation of the triazine aromatic ring.

The high-resolution N 1s spectra of doped samples was deconvoluted into three different peaks (Figure 3.4) representing the three major nitrogen groups, which are, by increasing binding energy: pyridinic at 398.4 ± 0.1 eV (N-6), pyrrolic at 400.0 ± 0.1 eV (N-5) and quaternary nitrogen at 401.4 ± 0.3 eV (N-Q) [12, 26]. Additionally, another peak was observed at 403.2 ± 0.1 eV in samples N-AG_{BM} and N-CG_{BM}, attributed to oxidized nitrogen groups (N-X) [26], suggesting that the ball milling process is favoring the appearance of oxidized groups, as this peak is not observed for samples conventionally doped (sample N-AG_C and N-CG_C). The ball milling method seems to modify the carbon structure promoting the contact between nitrogen and oxygen, which will react during the subsequent thermal treatment, oxidizing the nitrogen groups. In addition, differences in the contribution of each nitrogen group due to the doping method were also observed.

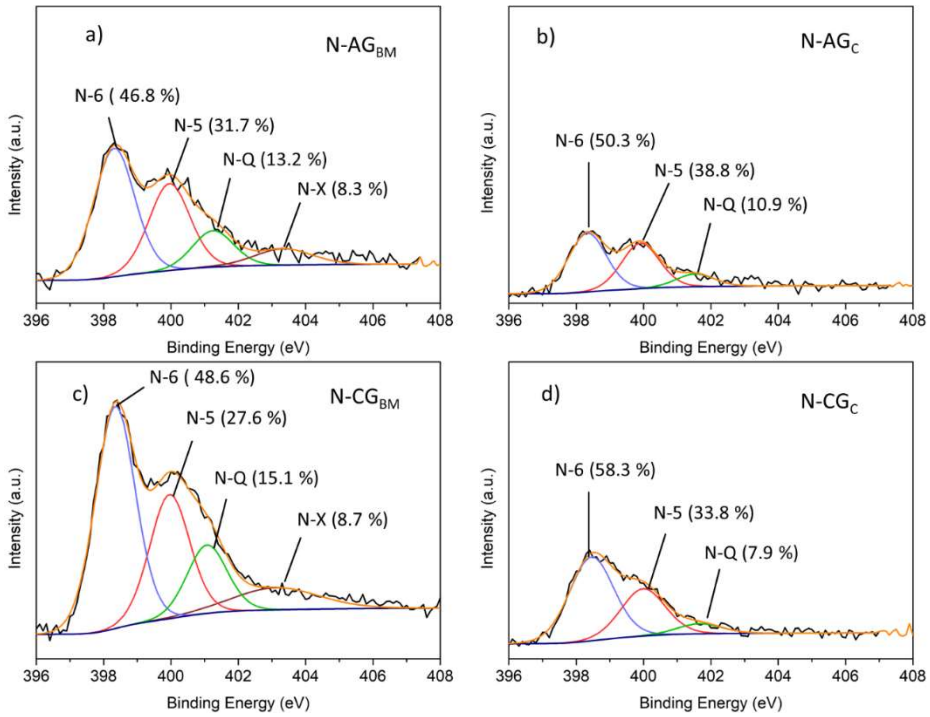


Figure 3.4 - Deconvolution of the XPS N 1s spectra for N-AG$_{BM}$ (a) N-AG$_C$ (b), N-CG$_{BM}$ (c) and N-CG$_C$ (d).

Samples doped via ball milling (Figure 3.4a and 3.4c) exhibit slightly lower percentages of pyridinic and pyrrolic groups than their conventionally doped counterparts (Figure 3.4b and 3.4d). Regarding quaternary nitrogen, significant differences were observed for both the doping method and the structure of the carbon. Activated samples exhibit similar contributions (13% and 11% for samples N-AG$_{BM}$ and N-AG$_C$, respectively), although ball milling seems to favor the incorporation of a slightly larger amount of N-Q. This effect is much more pronounced in carbonized samples that present larger differences as a function of the doping method: N-CG$_{BM}$ incorporated almost twice N-Q groups as N-CG$_C$. These results suggest that the ball milling process is more prone to incorporate quaternary groups as it creates defects in the activated and carbonized glucose structure creating more sites to form quaternary structures inside the carbon matrix.

The XPS spectra in the O 1s region are shown in Figure 3S.4. Three main oxygen peaks were identified, attributed to C=O bonds at 530.7 ± 0.3 eV (Peak I), C–O groups at 532.0 ± 0.2 eV (Peak II) and carboxylic acids at 533.3 ± 0.2 eV (Peak III) [27]. Interesting

differences are detected for N-doped carbons prepared by the ball milling method, as an additional peak is detected at higher binding energies corresponding to N–O–C bonds (Peak IV), which is in agreement with the oxidized nitrogen peak also shown in the N 1s spectra. In addition, different contributions of the oxygen functionalities related to carbon bonds are presented, which is in agreement with those results obtained by the deconvolution of the C 1s spectra, especially for undoped ball milled samples that exhibited a pronounced peak attributed to carboxylic acids. The O 1s spectra deconvolution does not clearly distinguish the contribution of the various surface groups due to overlaps in their binding energies, therefore, the oxygen-containing surface groups contribution in undoped samples was further analyzed by TPD. The CO and CO_2 measurements obtained for undoped activated and carbonized samples are presented in Figure 3.5, while the deconvolution of the profiles is shown in Figure 3S.5, 3S.6, 3S.7 and 3S.8.

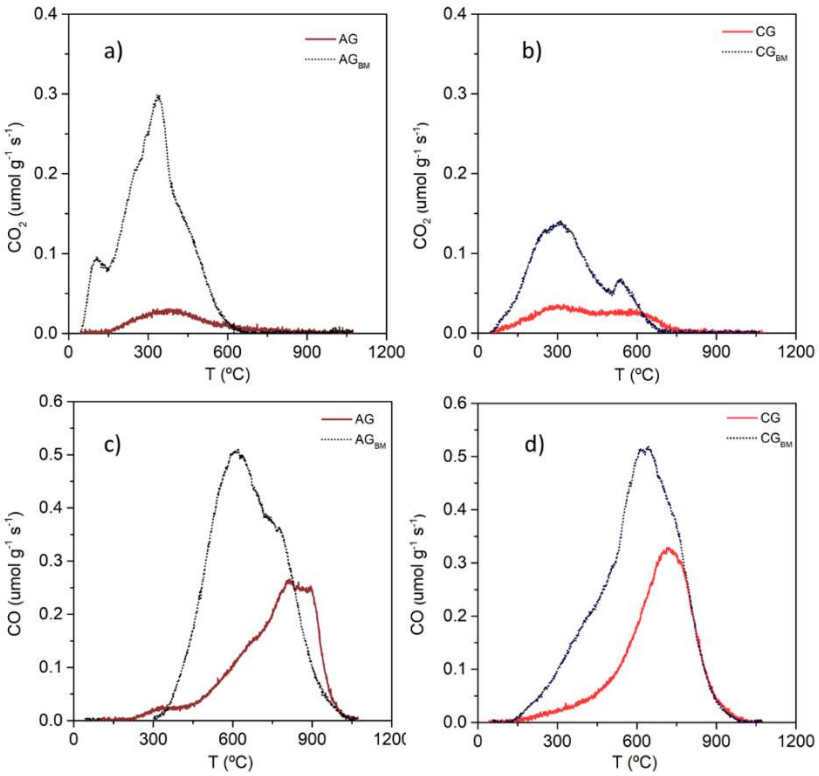


Figure 3.5 - TPD profiles of CO_2 for activated samples (a) and carbonized samples (b) and CO profiles of activated samples (c) and carbonized samples (d).

The amounts of CO_2 and CO released from ball milled samples are significantly higher than those of their original counterparts. Analyzing the CO_2 profiles of activated samples three peaks can be observed (Figure 3.S5a and 3.S6a), which could be attributed to carboxylic acids, anhydride and lactone groups, respectively [26, 44]. The peaks presented for the ball milled activated sample are much more intense, especially the carboxylic acids peak, which is in agreement with the results obtained from XPS. Deconvolution of CO profiles (Figure 3S.5b, 3S.6b, 3S.7b and 3S.8b) of all samples showed the presence of three main peaks corresponding to anhydrides, phenols and carbonyl/quinone groups [26, 44]. Ball milled samples present a much more significant contribution of phenols, corroborating the hypothesis of ball milling generating oxygen functional groups with weaker bonds due to reactions with air moisture. It should be also noted that the temperature at which oxygen groups are released as CO_2 and CO is higher for sample AG than for sample CG, confirming that the activated sample is more chemically stable.

The doping methods employed may also have an effect on the textural properties, which, as explained above, may modify the electroactive character of the biomass-derived carbons. Therefore, to evaluate the modifications caused to the textural properties due to the surface chemistry changes, nitrogen adsorption-desorption isotherms were obtained (Figure 3.6). The pore size distributions determined by applying the QSDFT are shown in Figure 3S.9.

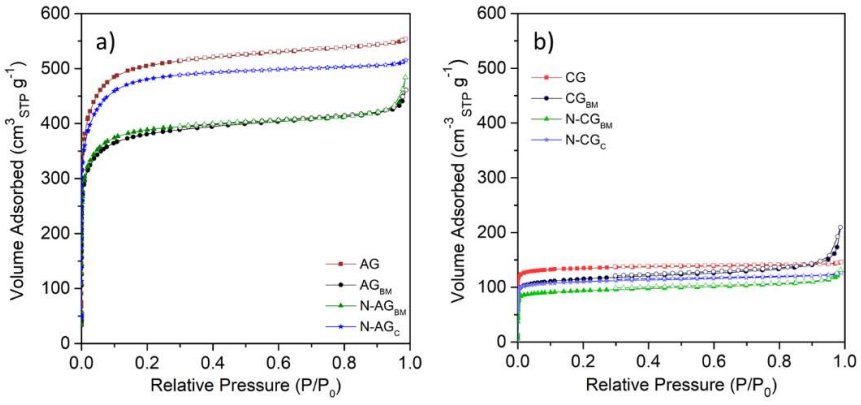


Figure 3.6 - N_2 adsorption/desorption isotherms at -196 ºC for activated carbons (a) and carbonized carbons (b).

Like activated samples shown in Figure 3.1, modified activated and carbonized carbons display type I isotherms, characteristic of microporous materials. The application of ball milling and the different doping methods to both activated and carbonized samples led to a decrease in the volume of nitrogen adsorbed at low relative pressures, resulting in materials with smaller volume of micropores (Table 3S.5) and lower surface area (a decrease of ca. 500 and 100 m^2 g^{-1} is observed after ball-milling, in the activated and carbonized samples, respectively). This decrease in microporosity suggests that the carbon material suffered changes in its structure due to the ball milling process, especially for the activated sample. This effect may be due to the loss of mass during the activation that results in materials with lower mechanical resistance than that of carbonized samples [45-46]. Moreover, ball milled samples exhibit an increase of nitrogen adsorbed at high relative pressures ($P/P_0 > 0.9$), suggesting the formation of macropores. The addition of nitrogen by conventional mixing the carbon materials with melamine also results in a decrease in the surface area. In this case, the decrease is analogous for both activated and carbonized sample, suggesting that the N-groups introduced into the structure are blocking some pores, preventing the access of N_2 to the innermost pores of the carbon material during the isotherm measurements. The incorporation of nitrogen functionalities by using the ball milling process also modified the microporosity of the samples. However, differences are observed for the activated and carbonized sample. In the case of the activated sample, the incorporation of nitrogen does not seem to produce a noticeable blockage of the pores as previously observed for sample N-AG_C, resulting in a material with a BET surface area similar to that obtained for sample AG_{BM}, with ball milling being the predominant effect. In the case of sample N-CG_{BM}, the ball milling process and the incorporation of nitrogen seem to have a synergistic effect, resulting in a decrease of the S_{BET} almost equivalent to the sum of that observed for sample CG_{BM} and N-CG_C.

3.3.3. Electrochemical measurements

Cyclic voltammograms recorded for activated samples and carbonized samples in a N_2- and O_2-saturated basic electrolyte at 5 mV s^{-1} are shown in Figure 3S.10, while LSV of activated and carbonized samples recorded in an O_2-saturated basic electrolyte at 1600 rpm are shown in Figure 3.7a and 3.7b, respectively.

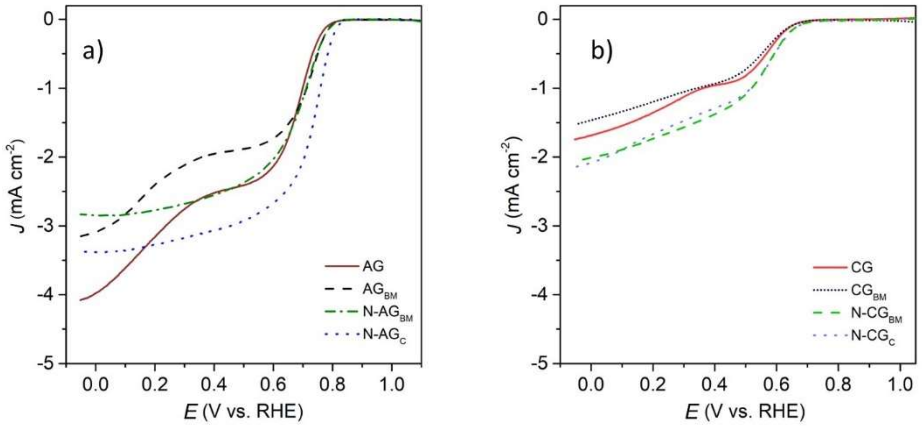


Figure 3.7 - Linear sweep voltammetry recorded in an O_2-saturated 0.1 mol L^{-1} KOH electrolyte at 1600 rpm for activated (a) and carbonized (b) samples.

Cyclic voltammograms measured in O_2-saturated electrolyte (Figure 3S.10a) and LSV of activated samples show a reduction reaction peak starting at 0.78-0.82 V. This peak does not appear for N_2-saturared cyclic voltammograms (Figure 3S.10c), thus confirming that catalytic activity of the prepared electrocatalysts exists at the mentioned potentials. A resume table of electrochemical results of the samples is presented by Table 3.2.

Table 3.2 - Electrochemical results of the synthesized samples.

Sample	E_{onset} (V vs RHE)	J_L (mA cm^{-2})	n_e [a]	H_2O_2 (%)
AG	0.78	4.08	2.3	18
AG_{BM}	0.79	3.15	2.0	21
N-AG_{BM}	0.79	2.83	2.9	9
N-AG_C	0.82	3.37	3.2	7
CG	0.64	1.74	1.8	-
CG_{BM}	0.64	1.53	2.3	-
N-CG_{BM}	0.67	2.05	2.1	-
N-CG_C	0.67	2.15	2.1	-

[a] – Calculated at 0.4 V vs RHE.

The onset potential of sample AG slightly shifts to more positive values from 0.78 V to 0.79 V by ball milling the sample (AG_{BM}) as shown in Figure 3.7a and Table 3.2. This increase may be due to the smaller particle size obtained after ball milling, which could result in a material with higher electrical conductivity; or by the higher amount of oxygen [13]. The LSV of carbonized samples reveals that, although sample CG_{BM} presents a much higher oxygen content, CG and CG_{BM} samples display the same onset potential (0.64 V), which suggests that the more positive onset potential of sample AG_{BM} is due to its higher conductivity. Moreover, samples AG and AG_{BM} exhibit a second shoulder at more negative potentials, indicating that the ORR mechanism proceeds via the two-electron pathway producing hydrogen peroxide. This second reduction shoulder does not appear for the doped activated samples, suggesting that the mechanism of the reaction has shifted to the four-electron pathway. However, the incorporation of nitrogen atoms by ball milling the activated sample (N-AG_{BM}) does not modify the onset potential when compared to the undoped counterpart (AG_{BM}). This indicates that the simple incorporation of nitrogen atoms is not enough to increase the onset potential to more positive values for this type of carbon material. Contrary to activated samples, the incorporation of nitrogen atoms using the ball milling method in the carbonized sample (N-CG_{BM}) slightly increases the onset potential regarding the undoped sample (CG_{BM}) from 0.64 V to 0.67 V. Like in activated samples, this is probably due to the smaller

particle size obtained after ball milling, which could result in a material with higher electrical conductivity.

The onset potential of sample N-AG_C is shifted to more positive values in relation to AG (from 0.78 V to 0.82 V). AG and N-AG_C do not present significant differences in the nature and amount of oxygen groups at their surface (Figure 3S.4), which suggests that the increase in the onset potential is due to the incorporation of nitrogen. However, sample N-AG_{BM} and N-AG_C present similar content of nitrogen (Table 3.1), but different values of onset potential are obtained, suggesting that the percentage of incorporated nitrogen is not the key factor, but the type of nitrogen functionalities. Likewise, the addition of nitrogen using the conventional method (N-CG_C) also results in the same slight shift of the onset potential to more positive values in relation to CG and CG_{BM}.

In order to further understand the effect of nitrogen functionalities in the ORR, doped samples must be deeply compared. A difference in the content of pyridinic nitrogen is observed for doped-activated samples (50% vs 47% for N-AG_C and N-AG_{BM}, respectively, Table 3S.6). Accordingly, the increase of the onset potential may be due to the presence of pyridinic nitrogen groups in the N-AG_C sample, which is in agreement with some studies in literature [23]. The pyridinic-N/quaternary-N ratio for N-AG_C and N-AG_{BM} (4.6 vs 3.6, respectively) allied to a slightly higher pyridinic-N/pyrrolic-N ratio for N-AG_C corroborates the theory that the increase of these two ratios is beneficial for the electrochemical activity of the prepared electrocatalysts [12]. This is not observed for carbonized samples as they do not present superior textural properties, compromising some of the effects that nitrogen could have on the carbon as a catalyst.

Information about the limiting kinetic current density can also be obtained from the LSV curves. As previously observed for activated samples at different times, there is a direct relationship between microporosity and the limiting kinetic current density (Figure 3.3). This trend is also observed for sample group AG, AG_{BM}, CG and CG_{BM} and for samples N-AG_C, N-AG_{BM}, CG_C and N-CG_{BM} (Figure 3.8).

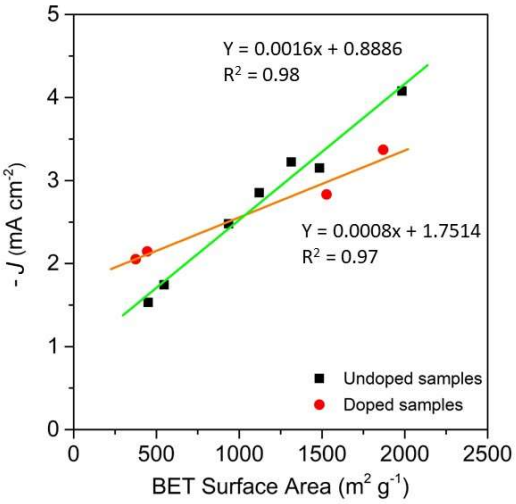


Figure 3.8 - Relation between BET surface area and limiting current density of undoped samples and doped samples.

These results indicate that the effect of microporosity cannot be compared between doped and undoped samples, suggesting that the limiting kinetic current density does not only depend on microporosity, but also on the surface chemistry of the samples.

Significant differences in the shape of the LSVs shown in Figure 3.6 are also observed due to the incorporation of nitrogen, which is related to the reaction mechanism. All activated samples present, at lower potentials, more than 3 electrons exchanged during the reduction reaction (Figure 3S.11a). Regarding carbonized samples (Figure 3S.11b), the number of electrons of CG and CG_{BM} represents a two-pathway mechanism at all potentials applied, unlike AG electrocatalysts. The AG sample's electrons exchanged is reduced to 2 as the potential increases. The same effect was registered for the AG_{BM} sample that, even with a slightly inferior number of electrons exchanged at the lowest potential, the number of electrons also decreases to 2 as the potential applied increases. The incorporation of nitrogen atoms with the ball milling method (N-AG_{BM}) mitigated this effect, as the number of electrons exchanged during the oxygen reduction reaction stays at approximately three electrons, demonstrating that nitrogen incorporation helps to stabilize the number of electrons for a larger potential range. The conventionally doped

sample (N-AG_C) shows the same pattern as the ball milled doped sample, but its electrons exchanged stabilize slightly closer to the four-electron mechanism, probably due to the higher catalytic performance of pyridinic nitrogen groups, which maintains the reaction mechanism closer to a four-electron pathway. On the other hand, the decrease of the quaternary-N/pyrrolic-N ratio (from 0.42 to 0.28 for N-AG_{BM} and N-AG_C, respectively) resulted in an increase of the number of electrons involved, which is in agreement with recent studies [12]. Unlike in activated samples, the addition of nitrogen atoms through ball milling (N-CG_{BM}) does not result in an increase of electrons exchanged neither in a stabilization of that number throughout the different applied potentials. This sample has a high quaternary-N/pyrrolic-N ratio (0.54), which does not favor the four-electron pathway.

Carbonized samples present a mechanism close to two-electrons throughout all potentials. Without a considerable number of electrons exchanged during the ORR, the nitrogen atoms do not seem to improve their stability to stay closer to a four-electron pathway. However, the conventionally doped sample (N-CG_C) displays a slight increase of electrons exchanged at low potentials, but still shifts to a two-electron pathway with the increasing potential applied. The slight increase of the electrons may be related to the very low quaternary-N/pyrrolic-N ratio (0.23), which is reported to influence the number of electrons. The fact that the addition of nitrogen functionalities on carbonized samples does not seem to enhance the electroactivity as for activated samples indicates that it is fundamental to design both the surface chemistry and the textural proprieties of the carbon materials, as the modification of a single parameter is not enough to obtain acceptable electrocatalysts for ORR.

The approximation to a four-electron pathway with the modification of the surface chemistry is important to reduce the amount of hydrogen peroxide produced. The production of H_2O_2 was only determined for activated samples, since they have a mechanism closer to four-electrons, whereas carbonized samples have a two-electron mechanism that would result in high amounts of this intermediate product. The improvement of reaction mechanism of the modified activated carbon materials led to a decrease in the production of H_2O_2 from 18% with sample AG to 7% with N-AG_C (Figure 3S.12). These results show that the proper combination of high microporosity associated

with high pyridinic-N/quaternary-N ratio and low quaternary-N/pyrrolic-N ratio is essential to enhance the electrochemical performance of the developed electrocatalysts.

3.4. Conclusions

In this study, the effect of microporosity of glucose-derived carbon materials on the catalytic activity towards ORR was demonstrated. The increase of microporosity led to an increase of the limiting current density and a slight increase of the onset potential, thus playing a key role in the ORR. The incorporation of nitrogen functionalities by employing different doping methods was also investigated. The amount of nitrogen incorporated was similar for all methods. However, the ball milling doping method led to higher contents of quaternary nitrogen and to the formation of oxidized nitrogen, while conventional doping favored the incorporation of pyridinic and pyrrolic functionalities. The results obtained reveal that the content of nitrogen is not as important as the type of functional groups incorporated, for improving the performance of carbon materials towards ORR. In fact, a relationship between the nitrogen functionalities and the electroactivity of the biomass-derived carbons has been determined. Is has been observed that a higher pyridinic-N/quaternary-N ratio favors the onset potential, while a lower quaternary-N/pyrrolic-N ratio favors the number of electrons exchanged during ORR. However, these results are only significant for highly microporous materials, demonstrating that the adequate combination of textural and chemical properties is essential for improving the electroactivity of biomass-derived carbons. In fact, the combination between high surface area, high pyridinic-N/quaternary-N ratio and low quaternary-N/pyrrolic-N ratio resulted in a material with an onset potential value of 0.82 V, a stable number of electrons involved in the reaction mechanism close to four throughout the studied potential range and a production of H_2O_2 lower than 7%.

3.5. Supporting Information

3.5.1. Effect of microporosity

Table 3S.1 - Textural characterization of samples activated during different times.

Sample	S_{BET} (m^2 g^{-1})	V_p (cm^3 g^{-1})	V_{DR} (cm^3 g^{-1})
AG_{1h}	936	0.38	0.35
AG_{3h}	1121	0.44	0.43
AG_{4h}	1314	0.54	0.52
AG_{6h}	1984	0.85	0.82

Table 3S.2 - Elemental analysis of samples activated during different times.

Sample	C (wt%)	O (wt%)	H (wt%)
AG_{1h}	96.3	3.3	0.4
AG_{3h}	96.6	3.0	0.4
AG_{4h}	96.8	2.8	0.4
AG_{6h}	97.3	2.4	0.3

Table 3S.3 - CO and CO_2 amounts obtained from TPD measurements of AG_{1h} and AG_{6h}

Sample	CO (µmol g^{-1})	CO_2 (µmol g^{-1})	CO/CO_2	Oxygen (%)
AG_{1h}	1111	172	6.5	2.33
AG_{6h}	971	136	7.2	1.99

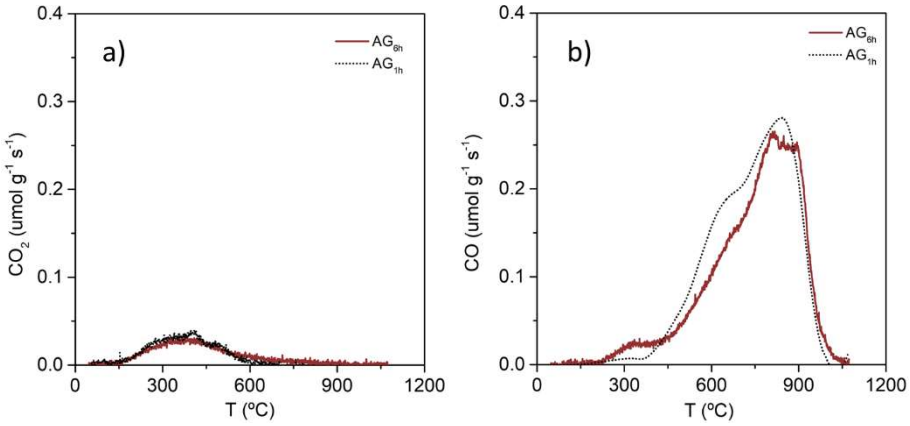


Figure 3S.1 - TPD profiles of CO_2 (a) and CO (b) for AG_{6h} and AG_{1h}.

Table 3S.4 - Onset potential of samples activated during different times.

Sample	Onset Potential (V)
AG_{1h}	0.75
AG_{3h}	0.75
AG_{4h}	0.76
AG_{6h}	0.78

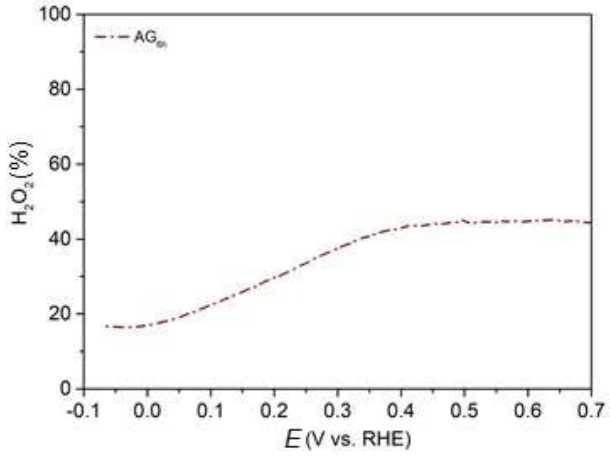


Figure 3S.2 - Hydrogen peroxide production for sample AG_{6h}.

3.5.2. Effect of the surface chemistry

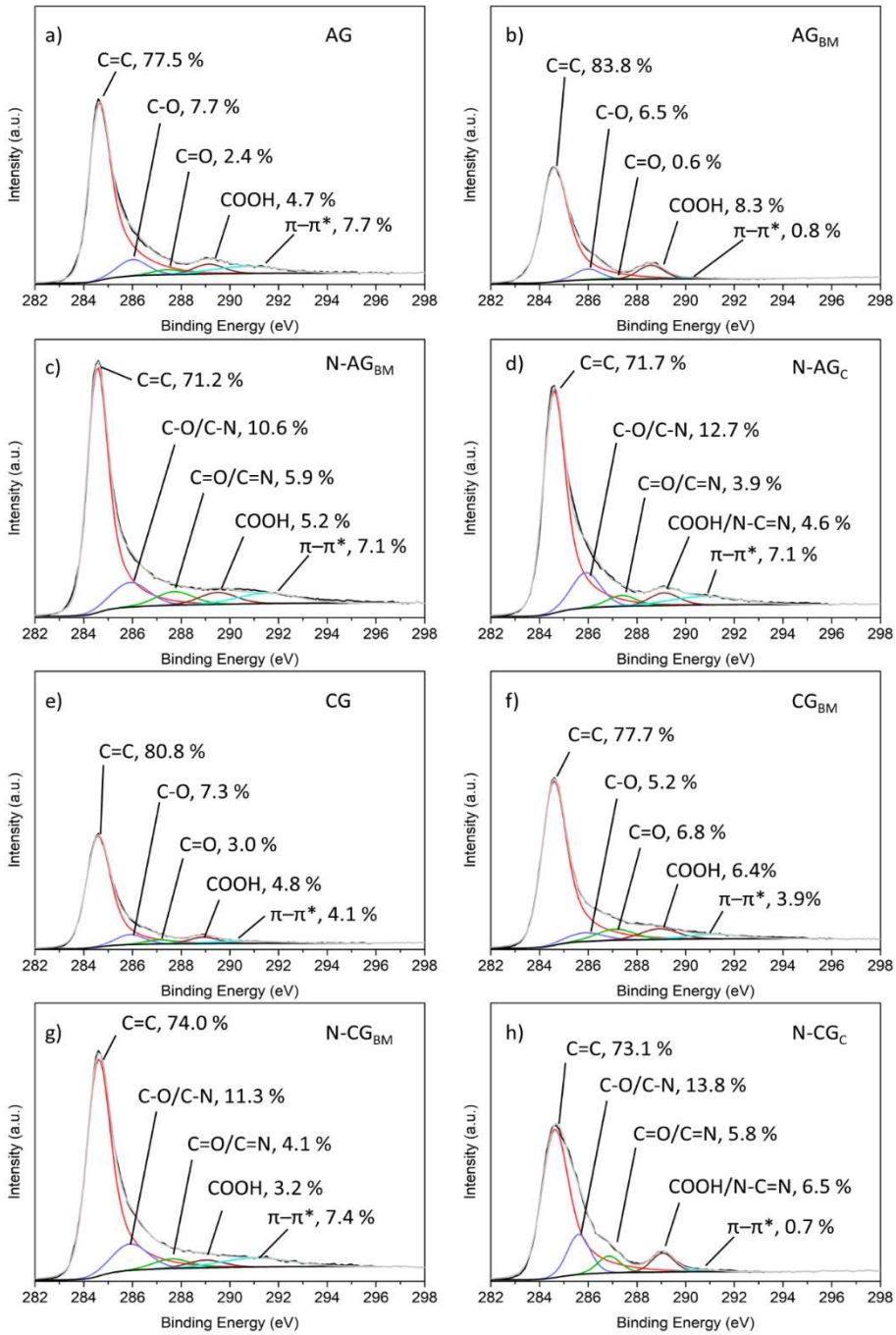


Figure 3S.3 - C 1s spectra deconvolution of AG (a), AG_{BM} (b), N-AG_{BM} (c), N-AG_{C} (d), CG (e), CG_{BM} (f), N-CG_{BM} (g), N-CG_{C} (h).

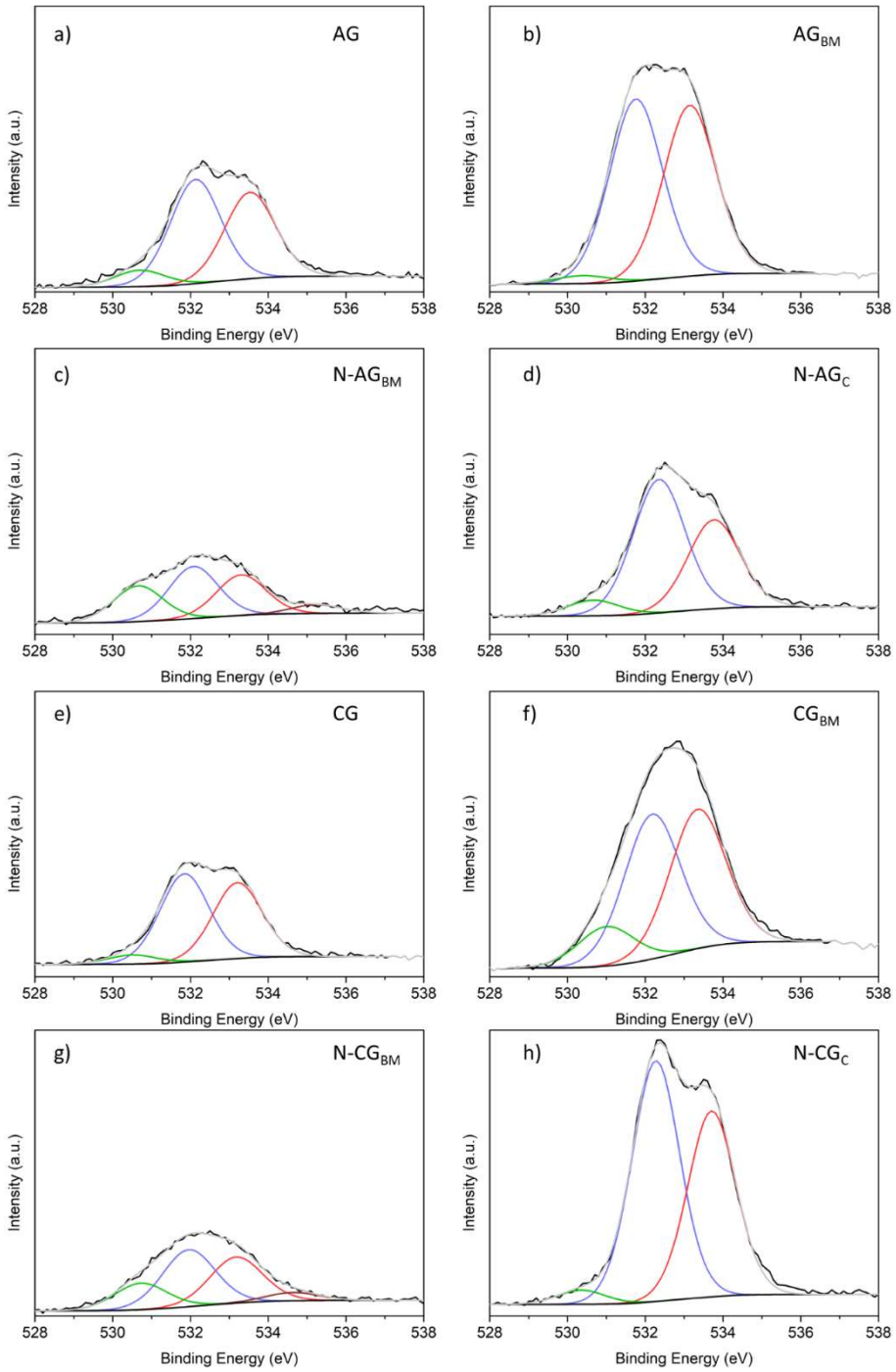


Figure 3S.4 - O 1s spectra deconvolution of AG (a), AG_{BM} (b), N-AG_{BM} (c), N-AG_{C} (d), CG (e), CG_{BM} (f), N-CG_{BM} (g), N-CG_{C} (h).

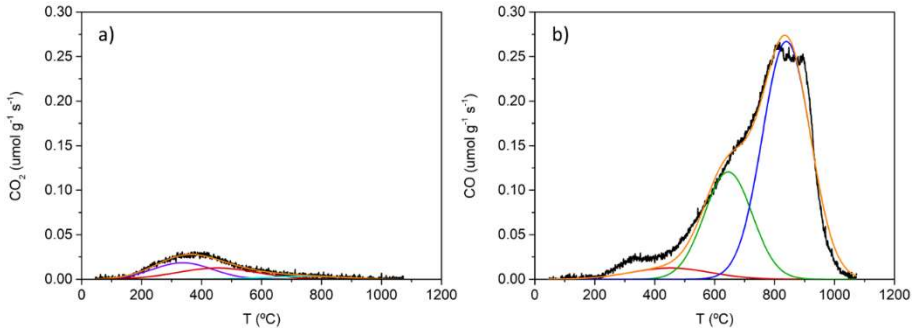


Figure 3S.5 - TPD profile deconvolution of AG for CO_2 (a) and CO (b).

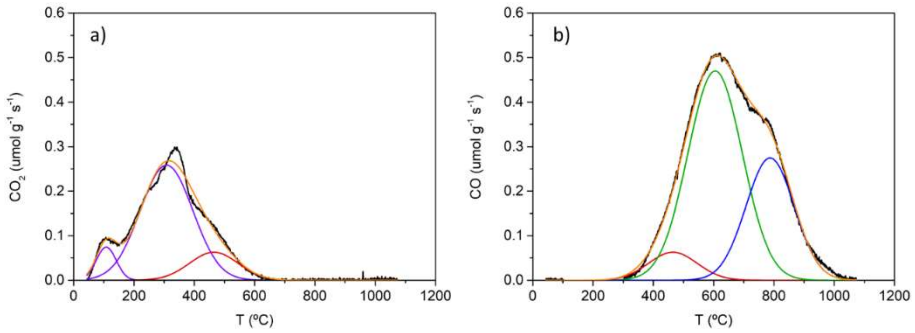


Figure 3S.6 - TPD profile deconvolution of AG_{BM} for CO_2 (a) and CO (b).

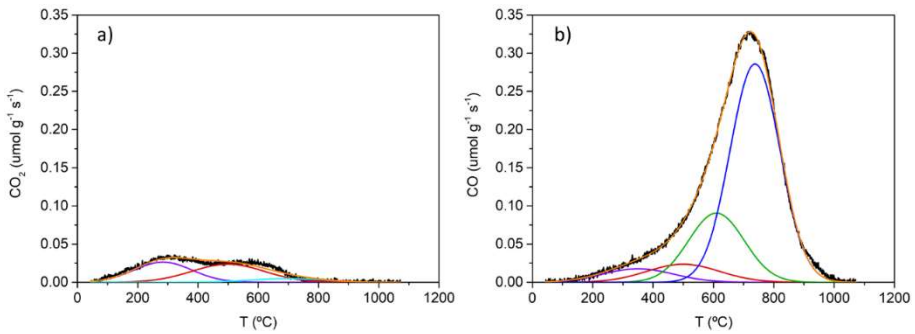


Figure 3S.7 - TPD profile deconvolution of CG for CO_2 (a) and CO (b).

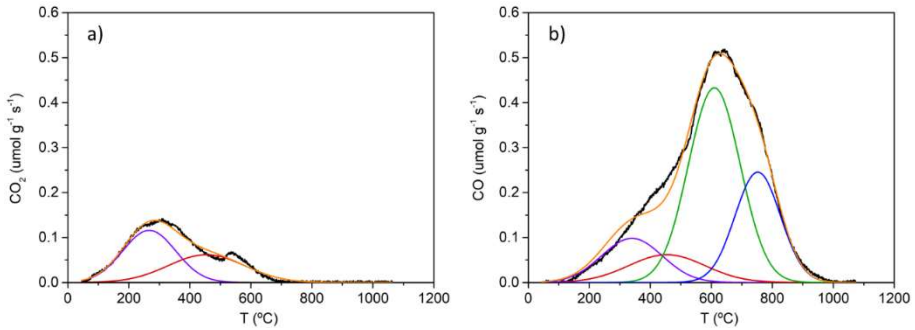


Figure 3S.8 - TPD profile deconvolution of CG_{BM} for CO_2 (a) and CO (b).

The CO_2 profile of sample AG presents all three peaks observed for a CO_2 deconvolution. However, its CO_2 profile of AG_{BM} closes at lower temperatures than the CO_2 profile of AG, thus almost not presenting the peak attributed of lactones. The CO_2 profile of sample CG (Figure 3S.7a) also presents the same three peaks as the activated sample. Similar to activated samples, the modification of the structure by the ball milling method (Figure 3S.8a) results in an almost depletion of the lactone group and in a significant increase of the carboxylic acids, once again corroborating the XPS results. Since lactones are cyclic esters of carboxylic acids, the defects created by ball milling may be opening the cycle creating the opportunity for the chain to react with air moisture and thus originating carboxylic functional groups. As a result of the decrease of lactones detected from CO_2 release, an increase of carboxylic acids occurs.

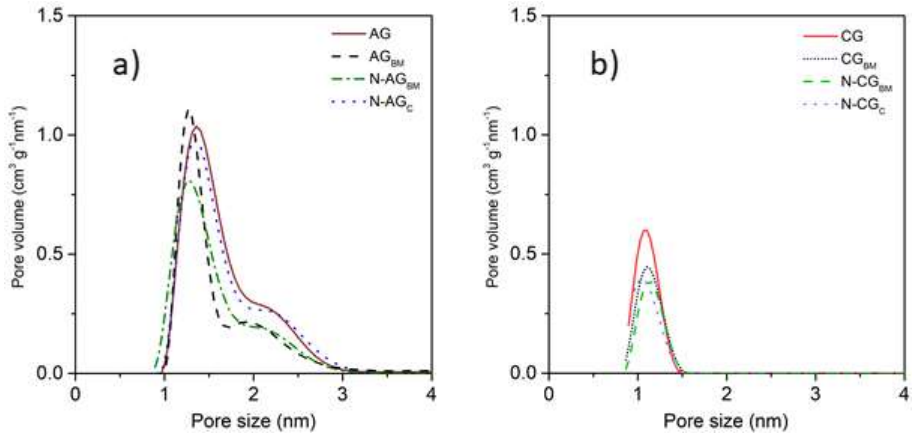


Figure 3S.9 - Pore size distributions for activated samples (a) and carbonized samples (b).

Table 3S.5 - Textural characterization of activated and carbonized samples.

Sample	S_{BET} ($m^2\ g^{-1}$)	V_p ($cm^3\ g^{-1}$)	V_{DR} ($cm^3\ g^{-1}$)
AG	1984	0.85	0.82
AG_{BM}	1486	0.71	0.54
N-AG_C	1870	0.79	0.68
N-AG_{BM}	1528	0.75	0.55
CG	547	0.23	0.20
CG_{BM}	451	0.32	0.17
N-CG_C	445	0.20	0.17
N-CG_{BM}	375	0.20	0.15

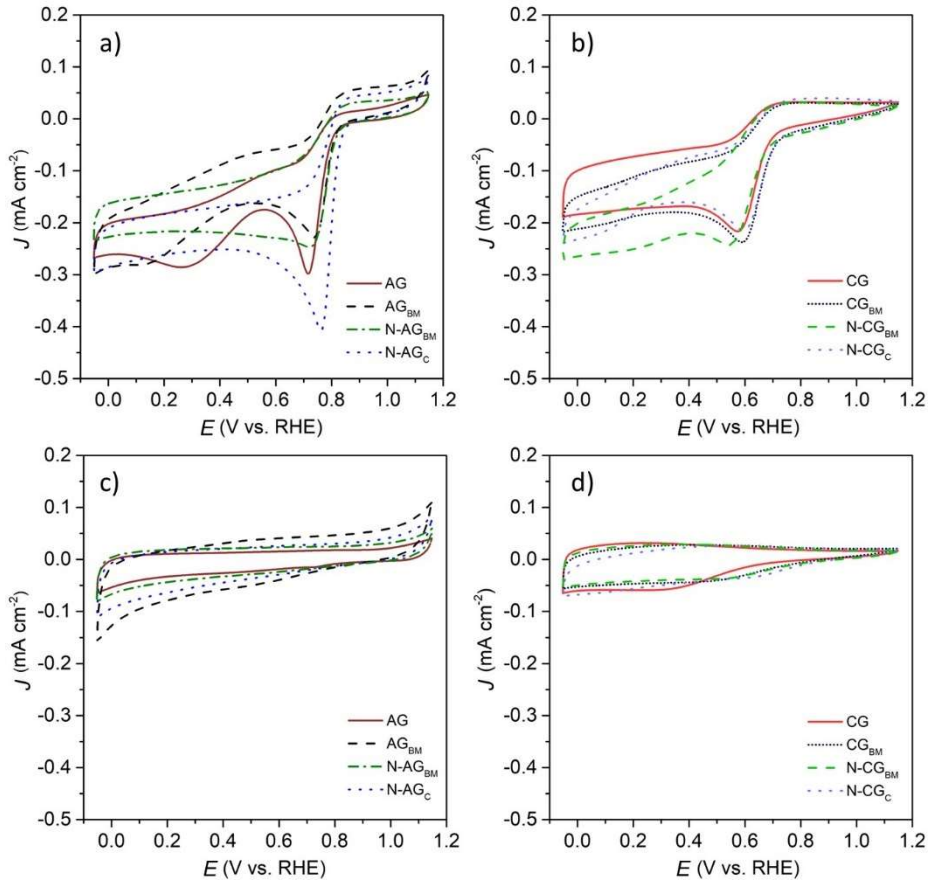


Figure 3S.10 - O_2-saturated cyclic voltammograms for activated samples (a) and carbonized samples (b) and N_2-saturated cyclic voltammograms for activated samples (c) and carbonized samples (d).

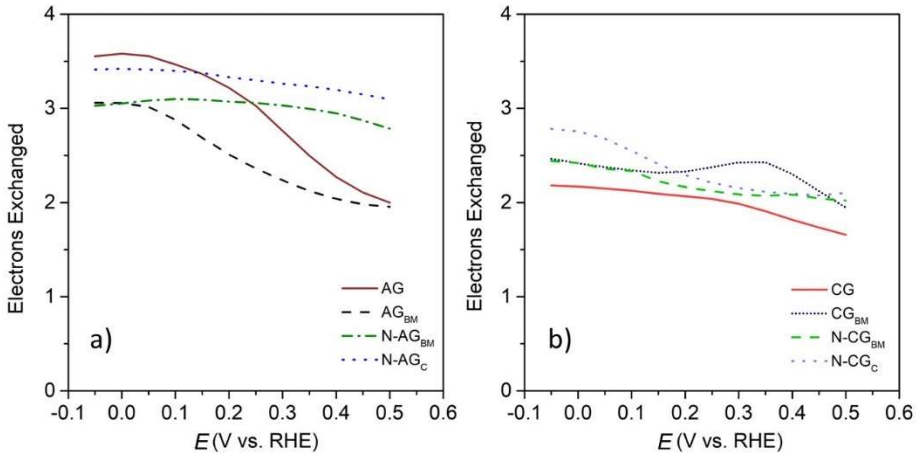


Figure 3S.11 - Number of electrons exchanged for activated samples (a) and carbonized samples (b) at different potentials.

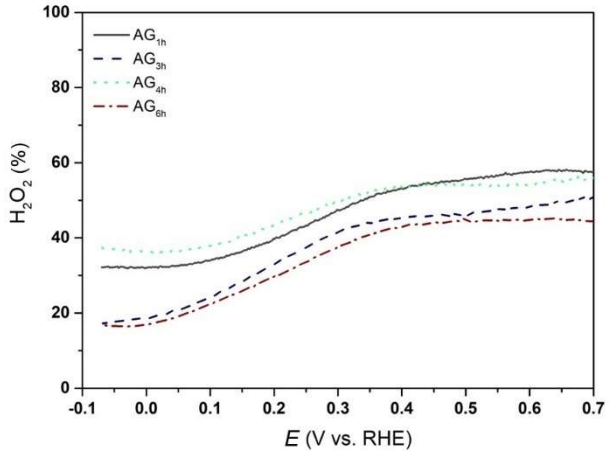


Figure 3S.12 - Hydrogen peroxide production for activated samples.

3.6. References

[1] A. Kirubakaran, S. Jain, R.K. Nema, A review on fuel cell technologies and power electronic interface, Renew. Sust. Energ. Rev., 13 (2009) 2430-2440.
[2] J. Stacy, Y.N. Regmi, B. Leonard, M. Fan, The recent progress and future of oxygen reduction reaction catalysis: A review, Renew. Sust. Energ. Rev., 69 (2017) 401-414.
[3] J.L. Figueiredo, Nanostructured porous carbons for electrochemical energy conversion and storage, Surf. Coat. Technol., 350 (2018) 307-312.
[4] Z. Wu, M. Song, J. Wang, X. Liu, Recent Progress in Nitrogen-Doped Metal-Free Electrocatalysts for Oxygen Reduction Reaction, Catalysts, 8 (2018) 196.
[5] K. Lee, L. Zhang, H. Lui, R. Hui, Z. Shi, J. Zhang, Oxygen reduction reaction (ORR) catalyzed by carbon-supported cobalt polypyrrole (Co-PPy/C) electrocatalysts, Electrochim. Acta, 54 (2009) 4704-4711.
[6] M. Kobayashi, H. Niwa, M. Saito, Y. Harada, M. Oshima, H. Ofuchi, K. Terakura, T. Ikeda, Y. Koshigoe, J.I. Ozaki, S. Miyata, Indirect contribution of transition metal towards oxygen reduction reaction activity in iron phthalocyanine-based carbon catalysts for polymer electrolyte fuel cells, Electrochim. Acta, 74 (2012) 254-259.
[7] J. Luo, X. Tian, J. Zeng, Y. Li, H. Song, S. Liao, Limitations and Improvement Strategies for Early-Transition-Metal Nitrides as Competitive Catalysts toward the Oxygen Reduction Reaction, ACS Catal., 6 (2016) 6165-6174.
[8] B. Rezaei, A.R. Taghipour Jahromi, A.A. Ensafi, Porous magnetic iron- manganese oxide nanocubes derived from metal organic framework deposited on reduced graphene oxide nanoflake as a bi-functional electrocatalyst for hydrogen evolution and oxygen reduction reaction, Electrochim. Acta, 283 (2018) 1359-1365.
[9] Y. Xue, S. Sun, Q. Wang, Z. Dong, Z. Liu, Transition metal oxide-based oxygen reduction reaction electrocatalysts for energy conversion systems with aqueous electrolytes, J. Mater. Chem. A, 6 (2018) 10596-10626.
[10] M. Borghei, J. Lehtonen, L. Liu, O.J. Rojas, Advanced Biomass-Derived Electrocatalysts for the Oxygen Reduction Reaction, Adv. Mater., 30 (2017) 1703691.
[11] H. Huang, X. Wei, S. Gao, Nitrogen-Doped Porous Carbon Derived from Malachium Aquaticum Biomass as a Highly Efficient Electrocatalyst for Oxygen Reduction Reaction, Electrochim. Acta, 220 (2016) 427-435.
[12] I.M. Rocha, O.S.G.P. Soares, D.M. Fernandes, C. Freire, J.L. Figueiredo, M.F.R. Pereira, N-doped Carbon Nanotubes for the Oxygen Reduction Reaction in Alkaline Medium: Synergistic Relationship between Pyridinic and Quaternary Nitrogen, ChemistrySelect, 1 (2016) 2522-2530.
[13] I.M. Rocha, O.S.G.P. Soares, J.L. Figueiredo, C. Freire, M.F.R. Pereira, Bifunctionality of the pyrone functional group in oxidized carbon nanotubes towards oxygen reduction reaction, Catal. Sci. Technol., 7 (2017) 1868-1879.
[14] C. Wang, F. Yang, C. Xu, Y. Cao, H. Zhong, Y. Li, Sulfur-doped porous graphene frameworks as an efficient metal-free electrocatalyst for oxygen reduction reaction, Mater. Lett., 214 (2018) 209-212.
[15] S.-A. Wohlgemuth, R.J. White, M.-G. Willinger, M.-M. Titirici, M. Antonietti, A one-pot hydrothermal synthesis of sulfur and nitrogen doped carbon aerogels with enhanced electrocatalytic activity in the oxygen reduction reaction, Green Chem., 14 (2012) 1515-1523.
[16] J. Wu, Z. Yang, Q. Sun, X. Li, P. Strasser, R. Yang, Synthesis and electrocatalytic activity of phosphorus-doped carbon xerogel for oxygen reduction, Electrochim. Acta, 127 (2014) 53-60.
[17] D.S. Yang, D. Bhattacharjya, S. Inamdar, J. Park, J.S. Yu, Phosphorus-doped ordered mesoporous carbons with different lengths as efficient metal-free electrocatalysts for oxygen reduction reaction in alkaline media, J. Am. Chem. Soc., 134 (2012) 16127-16130.
[18] Y. Cheng, Y. Tian, X. Fan, J. Liu, C. Yan, Boron doped multi-walled carbon nanotubes as catalysts for oxygen reduction reaction and oxygen evolution reactionin in alkaline media, Electrochim. Acta, 143 (2014) 291-296.

[19] L. Yang, S. Jiang, Y. Zhao, L. Zhu, S. Chen, X. Wang, Q. Wu, J. Ma, Y. Ma, Z. Hu, Boron-doped carbon nanotubes as metal-free electrocatalysts for the oxygen reduction reaction, Angew. Chem., Int. Ed. Engl., 50 (2011) 7132-7135.
[20] L. Lai, J.R. Potts, D. Zhan, L. Wang, C.K. Poh, C. Tang, H. Gong, Z. Shen, J. Lin, R.S. Ruoff, Exploration of the active center structure of nitrogen-doped graphene-based catalysts for oxygen reduction reaction, Energy Environ. Sci., 5 (2012) 7936-7942.
[21] W. Wei, H. Liang, K. Parvez, X. Zhuang, X. Feng, K. Müllen, Nitrogen-Doped Carbon Nanosheets with Size-Defined Mesopores as Highly Efficient Metal-Free Catalyst for the Oxygen Reduction Reaction, Angew. Chem., 126 (2014) 1596-1600.
[22] Q. Wei, X. Tong, G. Zhang, J. Qiao, Q. Gong, S. Sun, Nitrogen-Doped Carbon Nanotube and Graphene Materials for Oxygen Reduction Reactions, Catalysts, 5 (2015).
[23] J. Zheng, C. Guo, C. Chen, M. Fan, J. Gong, Y. Zhang, T. Zhao, Y. Sun, X. Xu, M. Li, R. Wang, Z. Luo, C. Chen, High content of pyridinic- and pyrrolic-nitrogen-modified carbon nanotubes derived from blood biomass for the electrocatalysis of oxygen reduction reaction in alkaline medium, Electrochim. Acta, 168 (2015) 386-393.
[24] H. Niwa, K. Horiba, Y. Harada, M. Oshima, T. Ikeda, K. Terakura, J.-i. Ozaki, S. Miyata, X-ray absorption analysis of nitrogen contribution to oxygen reduction reaction in carbon alloy cathode catalysts for polymer electrolyte fuel cells, J. Power Sources, 187 (2009) 93-97.
[25] D. Geng, Y. Chen, Y. Chen, Y. Li, R. Li, X. Sun, S. Ye, S. Knights, High oxygen-reduction activity and durability of nitrogen-doped graphene, Energy Environ. Sci., 4 (2011) 760-764.
[26] P.R. Rocha, S.O. Soares, L.J. Figueiredo, F.M. Pereira, Tuning CNT Properties for Metal-Free Environmental Catalytic Applications, C, 2 (2016).
[27] L. Zhang, l. Zhang, D.-W. Li, D. Karpuzov, Y.-T. Long, Electrocatalytic Oxidation of NADH on Graphene Oxide and Reduced Graphene Oxide Modified Screen-Printed Electrode, Int. J. Electrochem., 6 (2011) 819-829.
[28] X. Tian, M. Zhou, C. Tan, M. Li, L. Liang, K. Li, P. Su, KOH activated N-doped novel carbon aerogel as efficient metal-free oxygen reduction catalyst for microbial fuel cells, Chem. Eng. J., 348 (2018) 775-785.
[29] R. Li, X. Shao, S. Li, P. Cheng, Z. Hu, D. Yuan, Metal-free N-doped carbon nanofibers as an efficient catalyst for oxygen reduction reactions in alkaline and acid media, Nanotechnology, 27 (2016).
[30] J. Fang, H. Fan, M. Li, C. Long, Nitrogen self-doped graphitic carbon nitride as efficient visible light photocatalyst for hydrogen evolution, J. Mater. Chem. A, 3 (2015) 13819-13826.
[31] B. Zhang, Z. Wen, S. Ci, S. Mao, J. Chen, Z. He, Synthesizing nitrogen-doped activated carbon and probing its active sites for oxygen reduction reaction in microbial fuel cells, ACS Appl. Mater. Interfaces, 6 (2014) 7464-7470.
[32] X. Li, Y. Fang, S. Zhao, J. Wu, F. Li, M. Tian, X. Long, J. Jin, J. Ma, Nitrogen-doped mesoporous carbon nanosheet/carbon nanotube hybrids as metal-free bi-functional electrocatalysts for water oxidation and oxygen reduction, J. Mater. Chem. A, 4 (2016) 13133-13141.
[33] G.A. Ferrero, A.B. Fuertes, M. Sevilla, M.-M. Titirici, Efficient metal-free N-doped mesoporous carbon catalysts for ORR by a template-free approach, Carbon, 106 (2016) 179-187.
[34] A. Jain, R. Balasubramanian, M.P. Srinivasan, Hydrothermal conversion of biomass waste to activated carbon with high porosity: A review, Chem. Eng. J., 283 (2016) 789-805.
[35] D. Gu, R. Ma, Y. Zhou, F. Wang, K. Yan, Q. Liu, J. Wang, Synthesis of Nitrogen-Doped Porous Carbon Spheres with Improved Porosity toward the Electrocatalytic Oxygen Reduction, ACS Sustain. Chem. Eng., 5 (2017) 11105-11116.
[36] S. Baskar, C. Murugesan, P. Barpanda, Highly Porous N-Doped Graphitic Carbon from Bio-Waste as Bifunctional Electrocatalyst for Hybrid Na-Air Battery, ECS Trans., 80 (2017) 425-430.
[37] D. Gu, Y. Zhou, R. Ma, F. Wang, Q. Liu, J. Wang, Facile Synthesis of N-Doped Graphene-Like Carbon Nanoflakes as Efficient and Stable Electrocatalysts for the Oxygen Reduction Reaction, Nano-Micro Lett., 10 (2017) 29.

[38] F. Liu, H. Peng, C. You, Z. Fu, P. Huang, H. Song, S. Liao, High-performance doped carbon catalyst derived from nori biomass with melamine promoter, Electrochim. Acta, 138 (2014) 353-359.
[39] M. Borghei, J. Lehtonen, L. Liu, O.J. Rojas, Advanced Biomass-Derived Electrocatalysts for the Oxygen Reduction Reaction, Adv. Mater., 30 (2018) 1703691.
[40] R. Sibul, E. Kibena-Põldsepp, S. Ratso, M. Kook, M. Käärik, M. Merisalu, P. Paiste, J. Leis, V. Sammelselg, K. Tammeveski, Nitrogen-doped carbon-based electrocatalysts synthesised by ball-milling, Electrochem. Commun., 93 (2018) 39-43.
[41] M. Lefevre, F. Jaouen, J.-P. Dodelet, X.H. Li, K. Chen, A. Hay, Fe-Based Catalyst for Oxygen Reduction: Functionalization of Carbon Black and Importance of the Microporosity, ECS Trans., 3 (2006) 201-210.
[42] H. Marsh, F. Rodríguez-Reinoso, Chapter 5 - Activation Processes (Thermal or Physical), in: H. Marsh, F. Rodríguez-Reinoso (Eds.) Activated Carbon, Elsevier Science Ltd, Oxford, 2006, pp. 243-321.
[43] J.-H. Zhou, Z.-J. Sui, J. Zhu, P. Li, D. Chen, Y.-C. Dai, W.-K. Yuan, Characterization of surface oxygen complexes on carbon nanofibers by TPD, XPS and FT-IR, Carbon, 45 (2007) 785-796.
[44] J.L. Figueiredo, M.F.R. Pereira, M.M.A. Freitas, J.J.M. Órfão, Modification of the surface chemistry of activated carbons, Carbon, 37 (1999) 1379-1389.
[45] M.J. Prauchner, F. Rodríguez-Reinoso, Chemical versus physical activation of coconut shell: A comparative study, Microporous Mesoporous Mater., 152 (2012) 163-171.
[46] A. Amorós-Pérez, L. Cano-Casanova, M. Ouzzine, M. Rufete-Beneite, A.J. Romero-Anaya, M.Á. Lillo-Ródenas, Á. Linares-Solano, Spherical activated carbons with high mechanical strength directly prepared from selected spherical seeds, Materials, 11 (2018).

Chapter 4

Hydrothermal carbon/carbon nanotube composites as electrocatalysts for the oxygen reduction reaction

R. G. Morais, N. Rey-Raap, R. Costa, C. Pereira, A. Guedes, J. L. Figueiredo, M. F. R. Pereira, Hydrothermal Carbon/Carbon Nanotube Composites as Electrocatalysts for the Oxygen Reduction Reaction, J. Compos. Sci., 4 (2020) 1-14.

Abstract

The oxygen reduction reaction is an essential reaction in several energy conversion devices such as fuel cells and batteries. So far, the best performance is obtained by using platinum-based electrocatalysts which make the devices really expensive, and thus, new and more affordable materials should be designed. Biomass-derived carbons were prepared by hydrothermal carbonization in the presence of carbon nanotubes with different oxygen surface functionalities to evaluate their effect on the final properties. Additionally, nitrogen functional groups were also introduced by ball milling the carbon composite together with melamine. The oxygen groups on the surface of the carbon nanotubes favor their dispersion into the precursor mixture and the formation of a more homogenous carbon structure with higher mechanical strength. This type of structure partially avoids the crushing of the nanotubes and the carbon spheres during the ball milling, resulting in a carbon composite with enhanced electrical conductivity. Undoped and N-doped composites were used as electrocatalysts for the oxygen reduction reaction. The onset potential increases by 16% due to the incorporation of CNT and nitrogen, which increases the number of active sites and improves the chemical reactivity, while the limiting current density increases by 33% due to the higher electrical conductivity.

4.1. Introduction

In the last decades, researchers have focused on developing new innovative materials to enhance the performance of environmentally friendly energy conversion devices. In this context, fuel cells are considered an interesting alternative towards greener electrical energy conversion due to their high efficiency and low emission of pollutants [1,2]. However, the overall performance of these devices is limited by the sluggish kinetics of the oxygen reduction reaction (ORR) that takes place at the cathode [1,3]. Nowadays, the most efficient electrocatalyst towards the ORR is based on platinum [3,4], which is a scarce and expensive noble metal that extremely pushes up the cost of the fuel cell [5]. Consequently, extensive research efforts have been made to develop non-noble metal catalysts, or metal-free catalysts, exhibiting good catalytic activity towards ORR and excellent durability [1,3,4,6-8].

Carbon materials are a promising alternative to Pt-based electrocatalysts. Carbon nanotubes, carbon nanofibers, activated carbons, carbon xerogels, and graphene-based materials have been widely studied as electrocatalysts [6,9-15]. Among them, activated carbons are interesting materials, as they can be obtained by low-cost and environmentally friendly routes [16]. In fact, the use of hydrothermal processes to prepare carbon materials from biomass has emerged recently as an interesting strategy [12,17-20]. Biomass is an abundant, low-cost, and environmental-friendly source [21], which makes hydrothermal carbons (HTCs) good candidates to replace Pt-based electrocatalysts [2,8,22]. HTCs are commonly made up of spherical particles, which size can be controlled by modifying the synthesis conditions: concentration and type of saccharide precursor and temperature and time of the hydrothermal treatment [20]. Nevertheless, the chemical properties of HTCs need to be modified in order to approach the outstanding electrochemical performance of Pt-electrocatalyst reference materials [23,24]. These modifications can be achieved by the incorporation of heteroatoms like nitrogen, sulfur, phosphorus, or boron and/or advanced carbon materials like graphene oxide or carbon nanotubes (CNT) [9,12,13,17,25-28]. Nitrogen is the most promising heteroatom for ORR, as pyridinic nitrogen favors the bonding of oxygen to the adjacent carbon, while the presence of quaternary nitrogen favors oxygen dissociation [7,29]. Therefore, the appropriate nitrogen functionalities seem to be essential to improve the electroactivity of

the carbon materials towards the ORR. On the other hand, the use of CNT to prepare carbon composites is an interesting solution to stabilize the surface chemistry, to increase the graphitic domains and to accelerate electron transfer [30-32]. A recent publication has shown the benefits of adding CNT during the polymerization of glucose, ascertaining the optimum dose of CNT to maximize the performance of the composites in supercapacitor applications [31]. In the same line, carbide-derived carbons, graphene, chitosan, carbonized MOF and activated carbons have been combined with CNT to obtained composites with improved performance towards the ORR [5,10,11,30,33-35]. Nonetheless, most of these carbon composites contain also metals to enhance the electroactivity of the carbons, which may somewhat hinder the real effects of the CNT on the properties of the composites.

Most of these published works are mainly focused on the preparation and application of carbon composites bearing CNT. However, little attention has been paid to the surface chemistry of the CNT, which can modify the final textural and chemical properties of the hydrothermal carbons, and hence, the effectiveness of the subsequent stages used to incorporate heteroatoms or metals. Accordingly, this work aims to study the isolated role of CNT during the hydrothermal carbonization of glucose by evaluating the modifications caused by the incorporation of CNT into the structure and electrochemical performance of the hydrothermal carbon/carbon nanotube composites. The composites were prepared by hydrothermal carbonization of glucose in the presence of multiwalled CNT and oxidized CNT. An attempt has been made to evaluate the effect of the surface chemistry of CNT in the polymerization of glucose and in the final properties of the composites. Besides, nitrogen functionalities were incorporated into the as-prepared composites. The effect of the structure of the composites, due to the presence of the CNT, on the functionalization process and on the nature of the nitrogen functionalities, has also been assessed. Electrochemical measurements were performed to fully characterize the electrocatalytic activity of the composites towards the oxygen reduction reaction. Interesting results regarding the electrochemical performance of the composites are detailed, showing the advantage of adding CNT during the hydrothermal polymerization of glucose to convert biomass into a high-value carbon composite.

4.2. Materials and methods

4.2.1. Chemicals and materials

The reagents used for the synthesis of the carbon materials were: D-glucose (Merck), multiwalled carbon nanotubes (Nanocyl NC3100 series, with average diameter of 9.5 nm, average length of 1.5 μm, carbon purity higher than 95%), distilled water (from a Panice reverse osmosis water system), nitric acid (Fluka ≥ 65%) and melamine (Sigma-Aldrich, ≥ 99%). The reagents used for the preparation of the electrode were: ultrapure water (Milipore), absolute ethanol (VWR Chemicals, ≥ 99.5%) and Nafion (Sigma Aldrich, solution of 5 wt% in a mixture of water (15-20%) and aliphatic alcohols).

4.2.2. Materials preparation

The glucose-derived carbon/CNT composite (CG/CNT) was synthesized by hydrothermal polymerization of glucose in the presence of CNT. Briefly, glucose (15.0 wt%) and CNT (0.3 wt%) were dispersed in distilled water (84.7 wt%) in an unsealed Teflon lined reactor chamber under sonication for 30 min at room temperature. After sonication, the Teflon lined reactor chamber was introduced into a stainless steel autoclave, sealed and heated at 180 °C for 12 h. The autoclave was then cooled down naturally to room temperature, and the organic polymer obtained was filtered and washed with abundant distilled water. Finally, the sample was dried at 80 °C for 24 h and carbonized at 700 °C under a nitrogen flow of 150 cm^3 min^{-1}. The carbonization process was performed in a vertical furnace using a heating rate of 10 ºC min^{-1} and 2 h as the residence time. In order to evaluate the effect of the surface chemistry of CNT on the polymerization of glucose, oxidized CNT were also employed to prepare the composite CG/CNT_{oxi}, following the methodology described above for sample CG/CNT. The oxidation of CNT was performed by the typical liquid-phase oxidation method. Briefly, 1 g of CNT were boiled with 75 ml of a 7 mol L^{-1} solution of nitric acid for 3 h. The oxidized material was then washed with abundant distilled water until neutral pH was reached and then dried at 80 °C for 24 h. The prepared materials (CG/CNT and CG/CNT_{oxi}) were functionalized with nitrogen by ball milling the carbon composite (60 wt%) with melamine (40 wt%). The ball milling process was performed in an enclosed flask with two zirconia balls at 15 Hz frequency during 4 h using a Retsch MM200 mixer

mill. Then, the samples were treated in a vertical furnace at 700 °C for 2 h under a nitrogen flow of 150 cm^3 min^{-1} to force the decomposition of melamine. The heating rate was fixed at 10 °C min^{-1}. Functionalized samples were labeled N-CG/CNT and N-CG/CNT_{oxi}. Additionally, a sample composed only by glucose (CG) was also prepared following the methodology described above for sample CG/CNT without the addition of CNT.

4.2.3. Physicochemical characterization

The textural properties of all samples were determined by nitrogen adsorption-desorption isotherms performed at -196 ºC. Before the analysis, the samples were degassed under vacuum at 150 °C overnight. The isotherms were obtained in a Quantachrome Autosorb iQ automated gas sorption analyzer. The specific surface area (S_{BET}) was estimated by applying the Brunauer-Emmett-Teller (BET) equation to the nitrogen adsorption branch of the isotherm. The micropore volume (V_{micro}) and the external surface area (S_{ext}) were determined by applying the t-plot method. The morphology of the composites was studied using a scanning electron microscope (Quanta FEG 400, FEI Company). The composites were previously attached to an aluminum pin using conductive double-sided adhesive tape. A secondary electron detector Everhart-Thornley and an accelerating voltage of 15 kV were used in all the analyzes. In addition, the surface chemistry of the HTC composites was evaluated by Fourier transform infrared spectroscopy (FTIR). FTIR spectra were recorded using a JASCO FT/IR 6800 spectrometer at a maximum resolution of 4 cm^{-1} over a range between 4000 and 400 cm^{-1}. The spectra were collected in attenuated total reflectance (ATR) mode over 256 scans. Raman spectra were measured directly on the carbon materials using a Jobin-Yvon XPLORA apparatus (Horiba Scientific) with a monochromatic wavelength laser of 532 nm. The chemical composition was determined by Elemental Analysis performed in a Vario Micro Cube analyzer from Elementar. This technique involves the combustion of the sample at a temperature close to 1000 °C in an oxygen-rich atmosphere. Analysis of the combustion products allows determining the contents of C, H, N, and S, while oxygen content is determined by difference. The nitrogen surface functionalities of the N-doped composites were analyzed in a Kratos AXIS Ultra HSA X-ray photoelectron spectrometer (XPS). VISION and CASAXPS software were used for data acquisition and data analysis, respectively. The

XPS measurements were performed with a monochromatic Al Ka X-ray source (1486.7 eV), operating at 15 kV in hybrid mode, with a pass energy of 40 eV for regions of interest and 80 eV for the survey. The C 1s peak position was fixed at 284.6 eV and used as a reference to locate the other peaks. The fitting of the XPS in the N 1s region was performed by least squares using Shirley line as background and Gaussian-Lorentzian peak shape. The electrical conductivity was measured by the four-point probe method applied to a disc-shaped piece of 1 cm diameter made of each carbon sample. The disc-shaped pieces were prepared by pressing at 8 t in a mold for 60 s. The four points were placed in contact with the carbon surface, and a potential between 0 and 2 V was applied. The current response was measured using a SourceMeter® unit instrument (Keithley 2400) and recorded with LabView software. A linear relationship between the potential applied and the current measured was obtained, following the Ohm Law, from which the resistivity of the samples, and in turn, the electrical conductivity, can be calculated.

4.2.4. Electrode preparation

Each sample (1 mg) was first dispersed in 450 µL of a solution containing 20% of Nafion and 80% of a liquid solution composed of ultrapure water and ethanol (1:1.5, v:v). The suspension was sonicated for 30 min until a homogeneous dispersion was obtained. Finally, the dispersion was deposited on a glassy carbon rotating ring-disk electrode (electrode from Metrohm that consists of a 5 mm disc of glassy carbon with a concentric platinum ring at a distance of 375 µm) to have a mass loading of 0.1 mg cm^{-2}.

4.2.5. Electrochemical measurements

The electrochemical measurements were performed on a PGSTAT 302N potentiostat/galvanostat (Metrohm) by using a three-electrode cell configuration, which involves a beaker-type cell with three electrodes (working, counter, and reference) immersed in 0.1 mol L^{-1} KOH electrolyte solution. The rotating ring-disk electrode with the sample deposited on it was used as working electrode, while an Ag/AgCl (KCl 3 mol L^{-1}) and a glassy carbon rod were used as reference and counter electrode, respectively. Initially, nitrogen gas was bubbled through the electrolyte for 30 min to remove all oxygen in the electrolyte solution. Cyclic voltammetry (CV) experiments were performed by changing the scan rates from 5 to 100 mV s^{-1} using a voltage window of 1.2 V (from

0.2 to -1.0 V vs the reference electrode). Linear sweep voltammetry (LSV) measurements were also performed in the same potential range at a scan rate of 5 mV s^{-1} with a disk rotation speed range from 400 to 3000 rpm. After the measurements with the electrolyte saturated in nitrogen, the electrolyte was saturated with oxygen for 30 min. Then, the CV and LSV experiments described above were performed to evaluate the performance of the materials towards the ORR. The current density measured at the ring and disk was calculated by subtracting the current obtained from the electrolyte saturated with N_2 from the current measured in the O_2-saturated electrolyte. The onset potential (E_{onset}) was determined from the LSV curve recorded at 1600 rpm for a current density of -0.1 mA cm^{-2} and converted to the reversible hydrogen electrode (RHE) scale according to the Nernst equation (equation 4S.12 in the supporting information). The percentage of hydrogen peroxide (H_2O_2) produced during the ORR, and the number of electrons transferred were calculated from the current measured at the ring and disk following the equations 4S.11 and 4S.7 shown in the supporting information. The chronoamperometric response was measured by applying 0.4 V vs RHE for 10000 s to compare the stability of the different electrocatalysts.

4.3. Results and discussion

4.3.1. Textural, morphological and chemical properties

The changes in the textural properties due to the presence of CNT during the polymerization of glucose were evaluated by nitrogen adsorption at -196 ºC. The shape of the isotherms is displayed in Figure 4.1, while the textural parameters are shown in Table 4.1. Sample CG exhibits a type I isotherm characteristic of exclusively microporous materials. The incorporation of CNT and oxidized CNT (CNT_{oxi}) during the polymerization of glucose results in composites with different porous structures (CG/CNT and CG/CNT_{oxi}). The specific surface area of the composite CG/CNT is quite similar to that of the sample CG (Table 4.1), but interesting differences in the isotherm shape at medium and high relative pressure are observed (Figure 4.1b). The volume of nitrogen adsorbed remains constant at low-medium relative pressures (from 0.1 to 0.5), and then, abruptly increases at high relative pressure, which is characteristic of macroporous adsorbents. Besides, the isotherm of this composite exhibits a hysteresis

loop at medium-high pressures produced by capillary condensation, which can be attributed to materials with mesopores corresponding to interparticle spaces, like carbon nanotubes (Figure 4S.1).

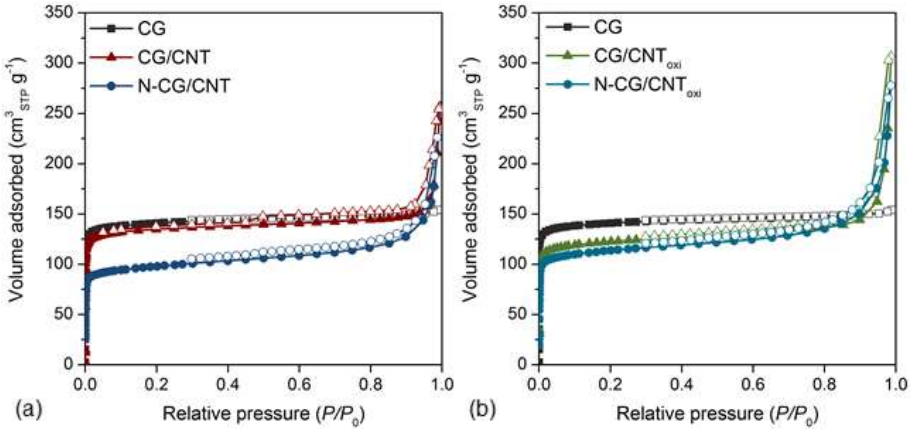


Figure 4.1 - N_2 adsorption-desorption isotherms of carbonized glucose and undoped and N-doped carbon composites prepared by introducing CNT (a) and oxidized CNT (b). Filled symbols: adsorption; open symbols: desorption.

On the other hand, the specific surface area of the composite CG/CNT_{oxi} is 15% and 10% lower than that of the sample CG and composite CG/CNT (Table 4.1), respectively. This result suggests that the presence of CNT_{oxi} has an effect on the polymerization of glucose or the carbonization process, resulting in a material with lower microporosity. The shape of the isotherm at medium-high relative pressure, assigned to the presence of CNT, is similar to that of the composite CG/CNT, indicating that the oxidation of the CNT does not alter the volume of pores of the composites. In fact, it has been observed that CNT_{oxi} exhibit similar pore volume as the non-oxidized CNT (Table 4S.1). On the other hand, the external surface areas are also modified due to the presence of CNT and CNT_{oxi} during the polymerization of glucose. The external surface area of CNT and CNT_{oxi} is much higher than that of sample CG (Table 4S.1), and hence, the composite exhibits a larger external surface area than sample CG, demonstrating the presence of CNT inside the structure. However, although the same amount of CNT and CNT_{oxi} was introduced for the preparation of the composites, differences in the external surface area are observed. This result indicates that the presence of CNT_{oxi} during the hydrothermal process modifies the polymerization reaction, resulting in a material with a higher external

surface area. So, to better understand the morphological changes resulting from the incorporation of CNT and CNT_{oxi} during the polymerization of glucose, the samples were examined by scanning electron microscopy (SEM). Sample CG is composed of spheres of 0.69 ± 0.09 μm diameter (Figure 4.2a), which is a typical morphology of hydrothermal carbons [20,23]. The presence of CNT gives rise to an inhomogeneous material with two different carbon sphere size distributions (0.24 ± 0.03 μm and 0.40 ± 0.05 μm), while the incorporation of CNT_{oxi} results in a homogenous material with carbon spheres of 0.25 ± 0.04 μm.

Table 4.1 - Textural properties of carbonized glucose and undoped and N-doped carbon composites.

Sample	S_{BET} ($m^2\ g^{-1}$)	V_{micro} ($cm^3\ g^{-1}$)	S_{ext} ($m^2\ g^{-1}$)
CG	574	0.22	15
CG/CNT	545	0.21	21
CG/CNT_{oxi}	489	0.20	37
N-CG/CNT	387	0.16	44
$N\text{-}CG/CNT_{oxi}$	451	0.19	57

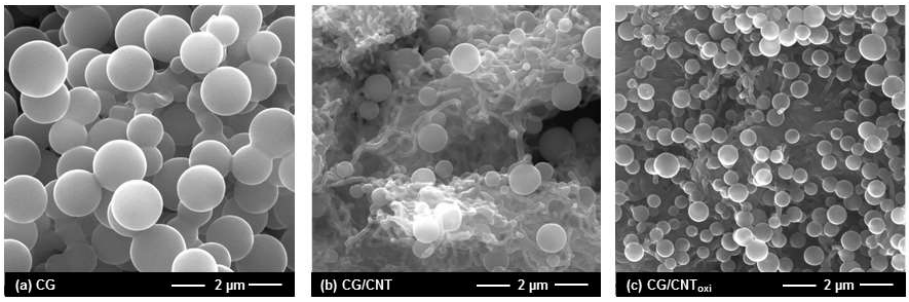


Figure 4.2 - SEM micrographs of carbonized glucose (a) and carbon composites prepared by introducing CNT (b) and oxidized CNT (c).

It can be deduced from the SEM images that the chemical surface properties of the CNT have a noticeable effect on the formation of the carbon spheres. The growth mechanism of the spheres involves a complex set of simultaneous chemical reactions (isomerization, dehydration, condensation or addition) that take place during the polymerization of glucose [19,20]. Initially, the dehydration of glucose is promoted, giving rise to anions

that react with each other via polymerization reactions [16]. Then, the aromatization of these molecules occurs, resulting in condensed furan rings bridged by aliphatic regions. These reactions proceed until the polymerized intermediates achieve a critical concentration, which produces the nucleation and growth of the particles forming a spherical-shaped structure [19,23]. The presence of CNT during the polymerization of glucose results in materials with smaller spheres, which suggests that CNT may promote the formation of nucleation points leading to a large number of small spherical particles, and hence, to a larger external surface area (Table 4.1) [31]. Besides, the oxygen groups on the surface of CNT_{oxi} also favor the dispersion of the CNT into the precursor mixture, and hence, the appearance of the nucleation points is more homogeneous. The assistance of CNT during the polymerization of glucose can be confirmed by FTIR spectroscopy (Figure 4.3a). The polymerized glucose obtained prior to carbonization (sample G) presents four main bands of interest: i) an intense peak at 3400 cm^{-1}, which is attributed to O-H stretching vibration, ii) a double-peak at 1700-1600 cm^{-1}, which is assigned to carbonyl groups, iii) some peaks in the absorption region of 1200 cm^{-1} ascribed to C-O-C stretching groups and iv) some peaks in the absorption band ca. 800 cm^{-1} attributed to C-O-H bonds. These results demonstrate that the organic spheres obtained from the hydrothermal process exhibit a large amount of oxygen functional groups. The intensity of these peaks decreases by introducing CNT, being almost negligible for the composite prepared with CNT_{oxi}, especially the band assigned to -OH groups. These results suggest that the incorporation of CNT_{oxi} gives rise to materials with a lower concentration of oxygen functional groups (sample G/CNT_{oxi}), indicating a higher degree of polymerization compared to the sample that bears the pristine CNT (sample G/CNT) and the polymerized glucose (sample G).

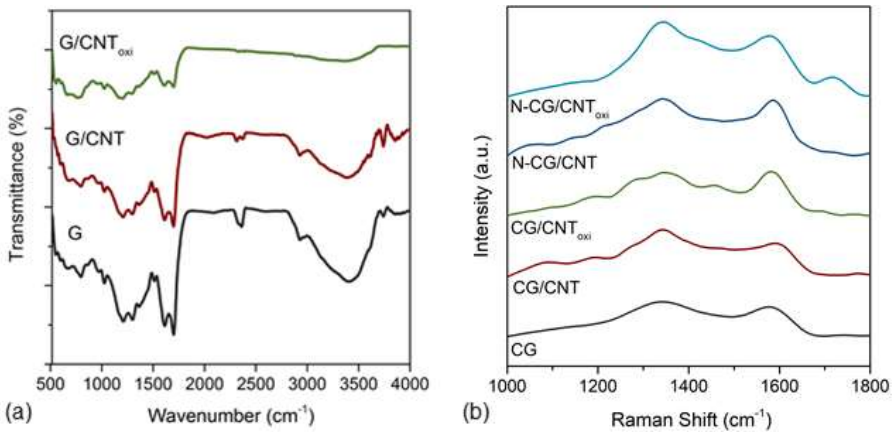


Figure 4.3 - (a) FTIR spectra of hydrothermal glucose prepared without CNT (G) and in the presence of CNT (G/CNT) and CNT_{oxi} (G/CNT_{oxi}) and (b) Raman spectra of carbonized glucose and undoped and N-doped carbon composites prepared by introducing CNT and oxidized CNT.

These changes in the morphology due to the presence of CNT and CNT_{oxi} may also modify the effect of the ball milling process employed to incorporate nitrogen functionalities, as observed from the textural properties. The functionalization of CG/CNT with melamine gives rise to a material (N-CG/CNT) with a lower volume adsorbed at high relative pressure (Figure 4.1), which loses 29% of its BET surface area due to the functionalization process (Table 4.1). However, sample N-CG/CNT_{oxi} remains almost identical to CG/CNT_{oxi}, as only a decrease of 8% is observed in the BET surface area. This difference could be due to the final morphology of the composites that could give rise to a different behavior during the ball milling process. Some of the CNT and carbon spheres are crushed due to the ball milling (Figure 4S.2), especially in the composite N-CG/CNT, which explains the significant loss in microporosity mentioned above. Besides, the thermal treatment applied to decompose melamine after ball milling seems to rearrange (or merge) the particles. These effects are less evident in the case of N-CG/CNT_{oxi}, although some loss of sphericity and some merged particles are also observed (Figure 4S.2b). These differences between the N-doped composites may be due to the more heterogeneous structure obtained by the incorporation of CNT_{oxi} that probably results in a carbon structure with higher mechanical strength, and hence, the

textural and morphological properties suffer fewer modifications during the functionalization process.

As stated above, the surface chemistry of the CNT affects the polymerization of glucose, as the incorporation of CNT_{oxi} results in a material with a higher degree of polymerization. This modification in the polymerization reaction also results in differences in the ordering of the final carbon structure, which has been evaluated by Raman spectroscopy. Figure 4.3b shows the Raman spectra for all undoped and doped carbons. The samples show a band at 1580 cm^{-1} ascribed to the graphitic domains (G band) and a second broad band centered at 1350 cm^{-1} (D band), which indicates disordered structures of turbostratic carbon layers. The intensity of both bands increases due to the addition of CNT and after the incorporation of nitrogen functionalities, especially for those samples prepared with oxidized CNT, suggesting a higher degree of ordering. The Raman spectra were further analyzed considering the splitting of the Raman features commonly employed for disordered carbonaceous materials [36]. The integrated areas of the main D and G bands were obtained from the deconvolution as a measure of relative disorder in carbon materials. The A_D/A_G ratio calculated from the integration of the peaks of the different spectra decreases by introducing CNT during the polymerization of glucose, especially by using CNT_{oxi} (Table 4S.2). In addition, the relative decrease in the A_D/A_G ratio indicates the existence of a more ordered structure after the doping process. It should be highlighted that the A_D/A_G ratio usually increases after nitrogen functionalization due to the nitrogen replacing the carbon atoms, which increases the number of defects [15]. However, the degree of disorder of these samples is quite high, and hence, the Raman spectrum of N-CG/CNT_{oxi} is still attributed to a disordered carbonaceous material with a large number of defects.

Regarding the chemical composition, all samples are mainly composed of carbon (Table 4.2), with some contribution of hydrogen and oxygen. The differences in the amount of oxygen between CNT and CNT_{oxi} demonstrate that the CNT have been successfully oxidized. On the other hand, carbonized glucose (sample CG) exhibits a percentage of oxygen around 4.1%, which is within the range typically observed in HTC carbon materials [23,31]. The amount of oxygen decreases due to the presence of CNT and CNT_{oxi}, which is in agreement with the hypothesis mentioned above about the higher

degree of polymerization of these samples after the hydrothermal synthesis, as observed by FTIR. On the other hand, the amount of oxygen in the N-doped composites has been doubled due to the ball milling process. This phenomenon may be due to the defects created, which then react with air, incorporating oxygen into the carbon structure [24]. Besides, the ball milling process allows the successful introduction of nitrogen, the incorporation of this heteroatom in the composite N-CG/CNT being higher. This effect is due to the lower degree of polymerization of the composite CG/CNT that allows a higher degree of functionalization.

Table 4.2 - Chemical composition and electrical conductivity of carbonized glucose, undoped and N-doped carbon composites, carbon nanotubes, and oxidized carbon nanotubes.

Sample	**C (wt%)**	**H (wt%)**	**O (wt%)**	**N (wt%)**	***K*** **(S m^{-1})**
CG	93.9	2.0	4.1	0.0	11
CG/CNT	94.3	2.1	3.6	0.0	150
CG/CNT$_{oxi}$	94.6	2.1	3.3	0.0	400
N-CG/CNT	85.1	1.7	6.4	6.8	280
N-CG/CNT$_{oxi}$	86.5	1.7	6.2	5.6	714
CNT	99.5	0.1	0.4	0.0	2500
CNT$_{oxi}$	95.3	0.9	3.8	0.0	1900

All these differences in the textural, morphological and chemical properties result in materials with different electrical conductivities, as shown in Table 4.2. Carbon nanotubes exhibit a high electrical conductivity, which decreases up to 24% due to the presence of oxygen functionalities (CNT$_{oxi}$). On the other hand, the electrical conductivity of carbonized glucose is significantly low, but it can be increased up to 150 and 400 S m^{-1} due to the incorporation of CNT and CNT$_{oxi}$, respectively. It should be highlighted that the composite CG/CNT$_{oxi}$ exhibits a higher electrical conductivity than CG/CNT, despite CNT$_{oxi}$ having lower conductivity than the pristine CNT. It is well-known that oxygen functional groups decrease the electrical conductivity but increase the wettability of carbon materials [37]. In this case, CNT$_{oxi}$ has been used to assist the polymerization of glucose, so after the hydrothermal process and subsequent

carbonization, the oxygen functional groups are no longer on the surface of the CNT_{oxi}. Consequently, both composites (CG/CNT and CG/CNT_{oxi}) exhibit similar chemical composition, as shown in Table 4.2. However, the use of CNT_{oxi} favors the formation of a more homogeneous structure with a larger degree of ordering and higher mechanical strength that partially prevents the crushing of the CNT and the carbon spheres, and hence, leads to a carbon structure with enhanced electrical conductivity. Besides, the addition of nitrogen functionalities also improves the electrical conductivity of the composites up to 87 and 78% for N-CG/CNT and N-CG/CNT_{oxi}, respectively. In this case, the increase is very similar for both composites, despite sample N-CG/CNT bearing a higher amount of nitrogen. This difference could be due to the type of nitrogen functional groups that have been identified by XPS (Figure 4.4). The high-resolution XPS spectra in the N 1s region were deconvoluted into the three main nitrogen contributions: pyridinic nitrogen (398.4 ± 0.1 eV), pyrrolic nitrogen (400.1 ± 0.1 eV) and quaternary nitrogen (401.3 ± 0.1 eV). The proportion of pyridinic nitrogen in the composite N-CG/CNT_{oxi} is slightly lower, while the contribution of the peak attributed to quaternary nitrogen is 30% higher in comparison with N-CG/CNT. These quaternary groups may create donor electronic states near the Fermi level, enhancing the electrical conductivity [37]. Therefore, both the amount and type of nitrogen functional group are essential to increase the electrical conductivity of carbon materials.

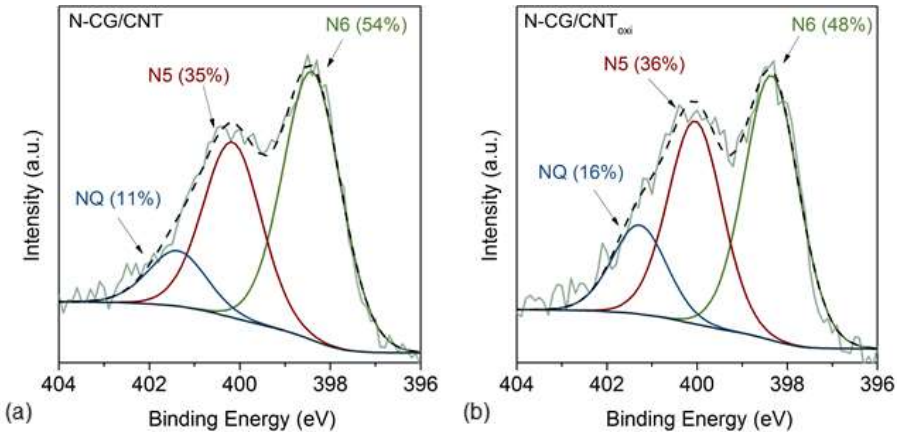


Figure 4.4 - XPS spectra of N 1s for N-doped composites N-CG/CNT (a) and N-CG/CNT_{oxi} (b).

4.3.2. Electrochemical measurements

The electrochemical activity of the carbon composites towards the oxygen reduction reaction (ORR) was determined by cyclic voltammetry (CV) in a rotating ring-disk electrode (RRDE). Featureless cyclic voltammograms are obtained from the measurement performed with the electrolyte saturated with N_2, demonstrating that the samples do not present any electrocatalytic activity under these conditions (Figure 4S.3). Nonetheless, well-defined cathodic peaks are detected from the measurement performed with the electrolyte saturated with O_2, which indicates that all materials are electrochemically active towards the ORR (Figure 4S.3). Similar results are observed for the N-doped composites (Figure 4S.4). However, significant differences in the electroactivity can be found due to their distinct physico-chemical properties. Therefore, the performance of the carbon composites as electrocatalysts for the ORR was evaluated by linear sweep voltammetry (LSV) to elucidate the relationship between the electroactivity and the physico-chemical properties. The LSV recorded at 1600 rpm and the number of electrons transferred are plotted in Figure 4.5. Two crucial parameters can be obtained from the LSV: the onset potential (V) and the limiting current density (mA cm^{-2}), their values being shown in Table 4.3. The onset potential increases by the formation of the composite (3%) and the incorporation of nitrogen (6%), probably due to the higher amount of active sites provided by the CNT and the nitrogen functionalities. Similar results are obtained for the composites prepared with CNT_{oxi} (Figure 4.5b), increasing 7% the onset potential due to the introduction of CNT_{oxi} and 11% more due to the nitrogen functionalities. So, the most remarkable enhancement is observed for the N-doped composite N-CG/CNT_{oxi}, shifting the onset potential from 0.66 V (sample CG) to 0.79 V. This value is similar to those previously reported for biomass-derived carbons [24,38].

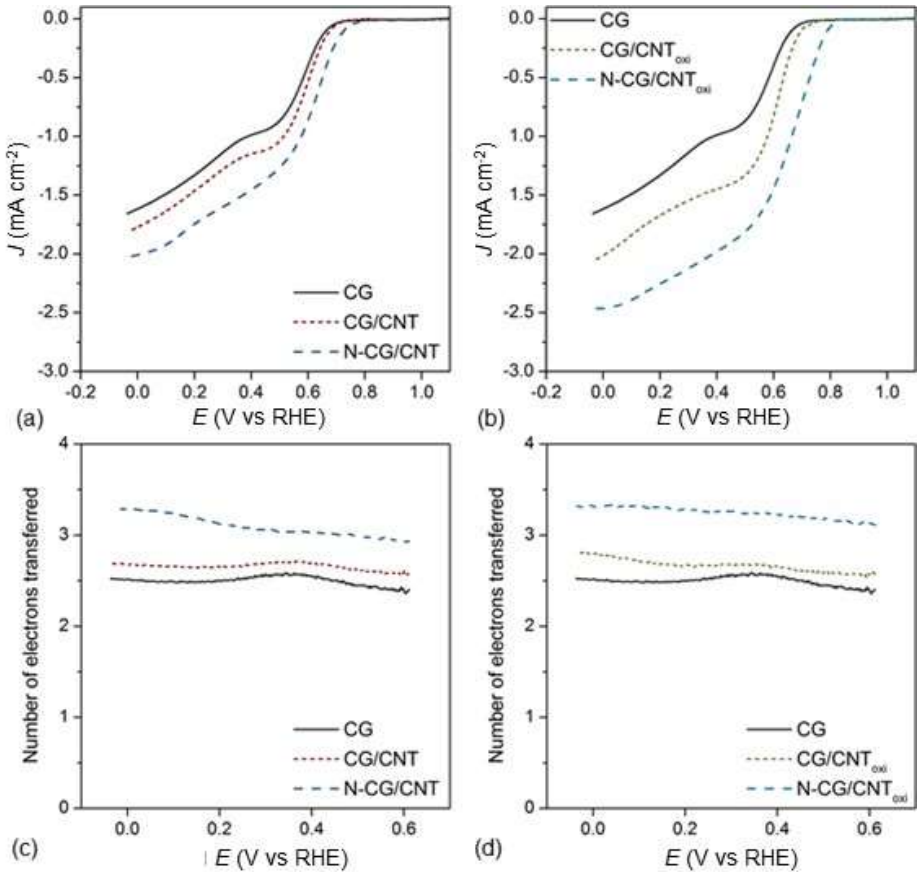


Figure 4.5 - Linear sweep voltammograms (LSV) and the number of electrons transferred measured at 1600 rpm for the carbonized glucose and the undoped and N-doped carbon composites prepared by introducing CNT (a and c) and oxidized CNT (b and d).

The limiting current density also follows the same trend. However, in this case, the increase can be attributed to the higher electrical conductivity of the samples, as a direct relationship has been found between the limiting current density and the electrical conductivity (Figure 4S.5). These results demonstrate the importance of incorporating CNT into the hydrothermal carbon structures, especially CNT_{oxi}, and introducing nitrogen functionalities. Besides, the measurements performed using an RRDE allow evaluating the efficiency of the oxygen reduction process by calculating the production of sub-products during the reaction (Table 4.3), which is related to the mechanism of the reaction. Sample CG produces a considerable amount of sub-products that decreases due to the presence of CNT, and the drop is even more significant upon the incorporation of

nitrogen functional groups. These results are correlated with the number of electrons transferred, a number of electrons transferred close to 4 indicating that the oxygen reduction is accomplished in a single step, while a number close to 2 corresponds to the production of sub-products. So, from the values shown in Figure 4.5c and 4.5d, it can be concluded that the incorporation of CNT and CNT_{oxi} does not seem to produce any significant effect on the reaction mechanism, as the values obtained are quite similar to those of the carbonized glucose (CG). However, the introduction of nitrogen functionalities results in a noticeable improvement in the efficiency of the oxygen reduction, as the N-doped composites shift the mechanism of the reaction towards the four-electron pathway (number of electrons transferred = 3.3, measured at -0.2 V). This value is higher than those previously shown for HTC [24,38]. This effect is due to the presence of nitrogen into the carbon structure that improves its electronic structure and chemical reactivity [15].

Table 4.3 - Electrochemical parameters obtained from linear sweep voltammetry measurements.

Sample	E_{onset} (V)[1]	J_L (mA cm^{-2})	H_2O_2 (%)[2]	J_K (mA cm^{-2})[3]
CG	0.66	1.7	75	1.3
CG/CNT	0.68	1.8	67	2.0
CG/CNT_{oxi}	0.70	2.1	67	3.1
N-CG/CNT	0.73	2.0	43	2.3
$N\text{-}CG/CNT_{oxi}$	0.79	2.5	36	5.7

[1] Onset potential measured at -0.1 mA cm^{-2}.

[2] Production of hydrogen peroxide at 0.2 V vs RHE.

[3] Kinetic current density measured at 0.4 V vs RHE.

Another important parameter which is commonly used to evaluate the activity of the electrocatalysts towards the ORR is the kinetic current density (J_K), which is calculated from the Koutecký-Levich equation (equation 12 shown in the supporting information). The J_K value calculated for $N\text{-}CG/CNT_{oxi}$ is higher than that of composite N-CG/CNT (Table 4.3) despite both having a similar nitrogen content, which suggests that the presence of nitrogen is not enough to enhance the reaction. This difference in the J_K

values of the N-doped samples could be due to the type of nitrogen functionalities or to the modification produced by the incorporation of oxidized CNT. The comparison between composite N-CG/CNT and CG/CNT_{oxi} (composites with similar onset potential and J_L) reveals that, in these samples, the improvement in the J_K value is due to the modification of the physico-chemical properties produced by the introduction of CNT_{oxi} during the polymerization of the glucose, as CG/CNT_{oxi} exhibits a higher J_K value than N-CG/CNT. The long-term stability is another critical parameter to assess the performance of carbon materials as electrocatalysts towards the ORR. Therefore, the durability of all the samples was tested by chronoamperometry performed at 0.4 V vs RHE for 10000 seconds (Figure 4.6). It can be observed that the carbonized glucose sample loses 53% of its initial current density, which was already the lowest current density registered (Table 4.3). Nonetheless, the stability is highly increased by introducing CNT and CNT_{oxi} (13% and 27% more retention than CG, respectively) and is even further increased by the introduction of nitrogen. In fact, the N-doped composites exhibit current density retention of more than 80%, especially composite N-CG/CNT_{oxi}. Therefore, taking into account all the important electrochemical parameters, composite N-CG/CNT_{oxi} exhibits the highest electrocatalytic performance which can be attributed to its high external surface area, its higher electrical conductivity and the larger number of active sites offered by the quaternary and pyridinic nitrogen functional groups.

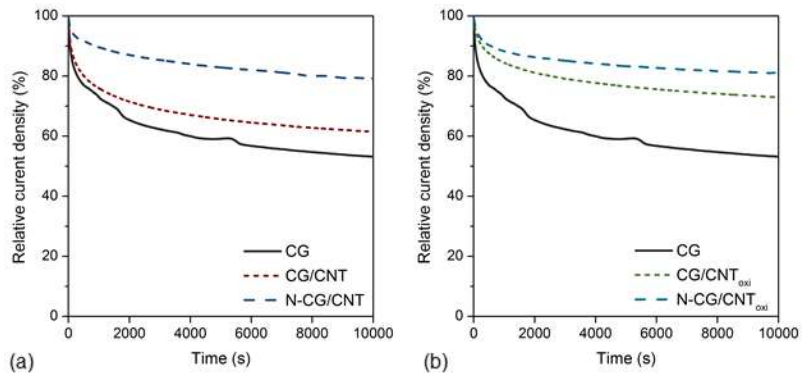


Figure 4.6 - Chronoamperometry experiments measured at 0.4 V vs RHE for 10000 seconds for the carbonized glucose and the undoped and N-doped carbon composites prepared by introducing CNT (a) and oxidized CNT (b).

4.4. Conclusions

Biomass-derived carbon composites were prepared by hydrothermal carbonization in the presence of CNT and oxidized CNT (CNT_{oxi}) to evaluate the effect of the different oxygen functional groups on the hydrothermal polymerization of glucose and on the final physico-chemical properties. The presence of CNT during the polymerization of glucose promotes the formation of nucleation points that leads to a large number of small spherical particles. The incorporation of CNT_{oxi} also favors the dispersion of the CNT into the precursor mixture, giving rise to a more homogenous carbon structure with a large number of small spheres (64% smaller than those of sample CG). Besides, the presence of CNT_{oxi} results in materials with a lower concentration of oxygen functional groups, suggesting a higher degree of polymerization compared to the sample that bears the pristine CNT. The efficiency of the ball milling employed to functionalize the composites is also modified due to these features provided by the CNT_{oxi}. The composite with the more homogeneous structure (CG/CNT_{oxi}) exhibits higher mechanical strength, and henceforth, the textural and morphological properties suffer fewer modifications during the functionalization process. In fact, a decrease of only 8% is observed in the BET surface area of sample $N\text{-}CG/CNT_{oxi}$, while this value rises to 29% for the composite N- CG/CNT. On the other hand, the ball milling process doubles the amount of oxygen and allows the successful introduction of nitrogen. However, differences between the incorporation of these heteroatoms are observed due to the final degree of polymerization of the samples. Lower incorporation of oxygen and nitrogen is detected for the composite with a higher degree of polymerization ($N\text{-}CG/CNT_{oxi}$). Besides, the textural, morphological and chemical properties obtained for the composite $N\text{-}CG/CNT_{oxi}$ result in a material with enhanced electrical conductivity (from 11 to 714 S m^{-1}). Regarding the electrochemical performance, the onset potential increases by 16% due to the presence of CNT and nitrogen functional groups that act as active sites; the limiting current density increases linearly with the electrical conductivity, being improved by 33%; the production of sub-products decreases from 75% to 36% due to the incorporation of nitrogen, which shifts the mechanism of the reaction to the four-electron pathway; the kinetic current density increases from 1.3 to 3.1 mA cm^{-2} due to the addition of CNT_{oxi} during the polymerization of glucose and up to 5.7 mA cm^{-2} due to the presence of

nitrogen functionalities; and the stability improves due to the nitrogen content, retaining almost 90% of the initial current density after 10000 s. Therefore, considering all the important electrochemical parameters, sample N-CG/CNT_{oxi} exhibits the highest electrocatalytic performance which can be attributed to its high external surface area, its higher electrical conductivity and the large number of active sites offered by the CNT and the nitrogen functional groups.

4.5. Supplementary Information

4.5.1. Electrocatalyst's properties

Textural and morphological properties of carbon nanotubes and oxidized carbon nanotubes.

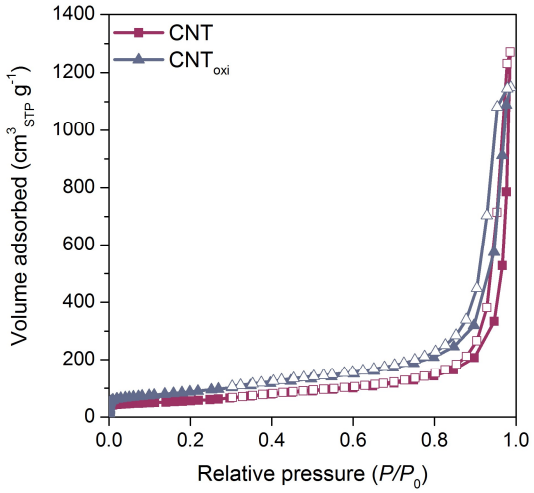


Figure 4S.1 - N_2 adsorption-desorption isotherms of carbon nanotubes and oxidized carbon nanotubes.

Table 4S.1 - Textural properties of carbon nanotubes and oxidized carbon nanotubes.

Sample	S_{BET} (m^2/g)	V_{micro} (cm^3/g)	S_{ext} (m^2/g)
CNT	224	0.08	234
CNT_{oxi}	319	0.12	488

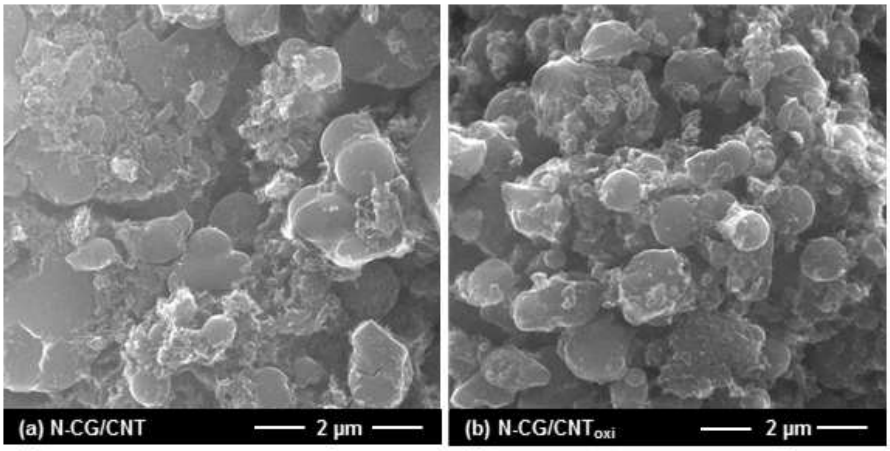


Figure 4S.2 - SEM micrographs of N-doped composites with carbon nanotubes and with oxidized carbon nanotubes.

Table 4S.2 - Integrated areas of the peaks D and G obtained by Raman spectroscopy.

Sample	A_D	A_G	A_D/A_G
CG	1418	511	2.8
CG/CNT	1291	580	2.2
CG/CNT_{oxi}	1190	715	1.7
N-CG/CNT	1115	808	1.4
$N\text{-}CG/CNT_{oxi}$	1055	1039	1.0

4.5.2. Electrochemical measurements

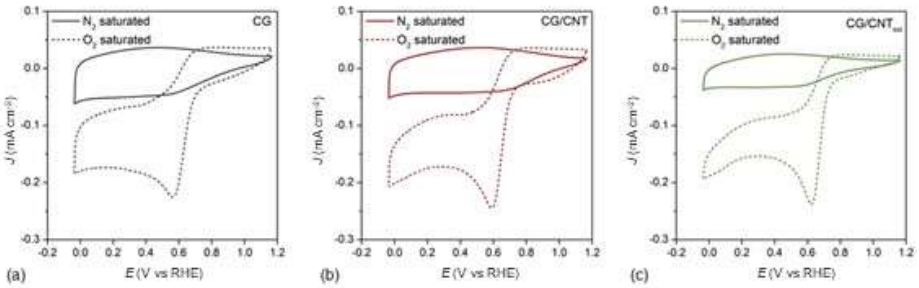


Figure 4S.3 - Cyclic Voltammograms measured at a scan rate of 5 mV s^{-1} in an electrolyte saturated with N_2 and O_2 for carbonized glucose (a), composite CG/CNT (b) and composite CG/CNT_{oxi} (c).

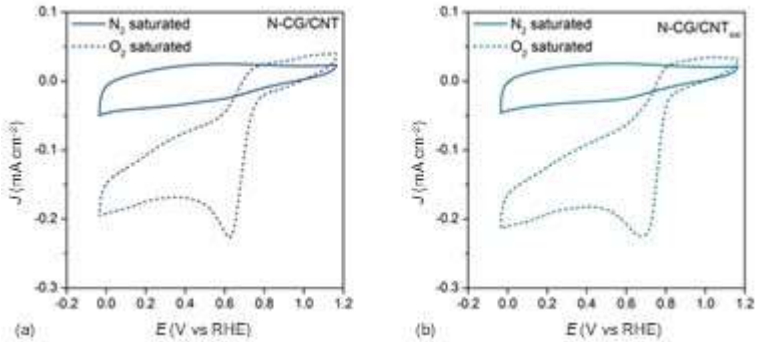


Figure 4S.4 - Cyclic Voltammograms measured at a scan rate of 5 mV s^{-1} in an electrolyte saturated with N_2 and O_2 for N-doped composites prepared with CNT (a) and CNT_{oxi} (b).

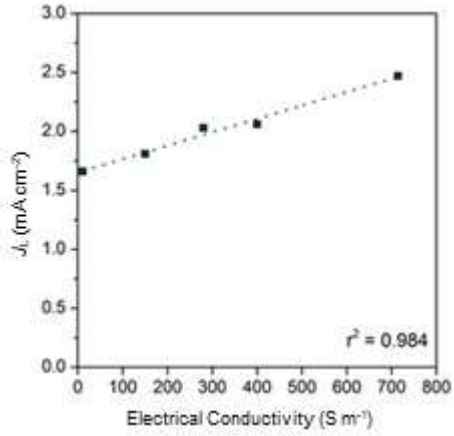


Figure 4S.5 - Relationship between the limiting current density and electrical conductivity.

4.5.3. Equations

The oxygen reduction reaction (ORR) in basic media can be explained by two different mechanisms. The first one is a dissociative mechanism of four-electrons known as direct mechanism (reaction 1), while the second is related to an associative mechanism of two-electrons known as indirect mechanism (reaction 2 and 3) in which the formation of by-products occurs.

$$O_2 + 2H_2O + 4e^- \rightarrow 4OH^- \quad \text{(reaction 1)}$$

$$O_2 + H_2O + 2e^- \rightarrow HO_2^- + OH^- \quad \text{(reaction 2)}$$

$$HO_2^- + H_2O + 2e^- \rightarrow 3OH^- \quad \text{(reaction 3)}$$

In the measurements performed with the ring-disk electrode (RRDE), the reduction of oxygen occurs in the disk, while the formation of hydrogen peroxide is detected in the ring. Therefore, the currents detected in the disk and the ring can be expressed as equation 4S.1 and 4S.2, respectively.

$$I_D = I_{4e} + I_{2e} + I_{2e'} \quad \text{(4S.1)}$$

$$I_{R=N(I_{2e}-I_{2e'})} \quad \text{(4S.2)}$$

Where I_D is the Faradaic current at the disk; I_{4e} is the Faradaic current related to the direct mechanism (reaction 1); I_{2e} and $I_{2e'}$ are the Faradaic currents related to the indirect

pathway shown in reactions 2 and 3, respectively; I_R is the Faradaic current at the ring and N is the collection coefficient at the ring (N = 0.249).

The total number of electrons (n_e) detected by each oxygen molecule can be determined by:

$$n_e = \frac{N_e}{N_{O_2}} \quad (4S.3)$$

Where N_e and N_{O2} are the total number of electrons transferred and the total number of oxygen molecules participating in the ORR, respectively. These two parameters can be expressed as:

$$N_e = \frac{N_A \Delta t}{F} (I_{4e} + I_{2e} + I_{2e'}) \quad (4S.4)$$

$$N_{O_2} = \frac{N_A \Delta t}{F} \left(\frac{I_{4e}}{4} + \frac{I_{2e}}{2}\right) \quad (4S.5)$$

Where N_A is the constant of Avogadro and F is Faraday's constant.

Therefore, equation 4S.3 can be expressed as:

$$n_e = \frac{N_e}{N_{O_2}} = \frac{\frac{N_A \Delta t}{F}(I_{4e} + I_{2e} + I_{2e'})}{\frac{N_A \Delta t}{F}\left(\frac{I_{4e}}{4} + \frac{I_{2e}}{2}\right)}$$

$$n_e = \frac{(I_{4e} + I_{2e} + I_{2e'})}{\left(\frac{I_{4e}}{4} + \frac{I_{2e}}{2}\right)} \quad (4S.6)$$

The combination of equation 4S.1, 4S.2 and 4S.6, results in:

$$n_e = \frac{4I_D}{I_D + \left(\frac{I_R}{N}\right)} \quad (4S.7)$$

Similarly, the production of hydrogen peroxide can be expressed as the fraction between the number of hydrogen peroxide molecules formed and the total number of oxygen molecules participating in the ORR:

$$H_2O_2 = \frac{N_{H2O2}}{N_{O2}} \quad (4S.8)$$

Where N_{H2O2} is the total number of hydrogen peroxide molecules that can be expressed as:

$$N_{H2O2} = \frac{N_A \Delta t}{F} \left(\frac{I_{2e}}{2} - \frac{I_{2e'}}{2}\right) \quad (4S.9)$$

The combination of equation 4S.8, 4S.9 and 4S.5, results in:

$$H_2O_2 = \frac{N_{H2O2}}{N_{O2}} = \frac{\frac{N_A \Delta t}{F}\left(\frac{I_{2e}}{2} - \frac{I_{2e\prime}}{2}\right)}{\frac{N_A \Delta t}{F}\left(\frac{I_{4e}}{4} + \frac{I_{2e}}{2}\right)}$$

$$H_2O_2 = \frac{2(I_{2e} - I_{2e\prime})}{I_{4e} + 2I_{2e}} \quad (4S.10)$$

Finally, the combination of equation 4S.1, 4S.2 and 4S.10, results in:

$$H_2O_2 = \frac{2\left(\frac{I_R}{N}\right)}{I_D + \left(\frac{I_R}{N}\right)} \quad (4S.11)$$

The experimental potential was set according to the reference electrode employed: Ag/AgCl (KCl 3 mol L^{-1}). Then, the final potential was converted to the reversible hydrogen electrode (RHE) scale according to the Nernst equation:

$$E_{RHE} = 0.059\, pH + E^0_{Ag/AgCl} + E_{Ag/AgCl} \quad (4S.12)$$

Where pH referes to the pH of the electrolyte, $E_{Ag/AgCl}$ is the measured potential vs Ag/AgCl (KCl 3 mol L^{-1}) and $E^0_{Ag/AgCl}$ = 0.21 V (measured at 20 ºC).

The kinetic current density (J_K) is calculated from the Koutecký-Levich equation:

$$\frac{1}{J} = \frac{1}{J_L} + \frac{1}{J_K} = \frac{1}{B\omega^{1/2}} + \frac{1}{J_K} \quad (4S.13)$$

Where J is the measured current density, J_K is the kinetic current density, J_L is the diffusion-limited current density, ω is the electrode rotation rate (rpm), and B is:

$$B = 0.2 n_e F C_0 (D_0)^{\frac{2}{3}} v^{-\frac{1}{6}} \quad (4S.14)$$

where n_e is the number of electrons transferred, F is the Faraday constant (96485 C/mol), C_0 is the bulk concentration of O_2 (1.15×10^{-3} mol cm^{-3}), D_0 is the diffusion coefficient of O_2 (1.95×10^{-5} cm^2 s^{-1}) and v is the kinematic viscosity of the electrolyte (0.009 cm^2 s^{-1}).

4.6. References

[1] M.M. Mohideen, Y. Liu, S. Ramakrishna, Recent progress of carbon dots and carbon nanotubes applied in oxygen reduction reaction of fuel cell for transportation, Appl. Energy, 257 (2020) 114027.
[2] P. Kaur, G. Verma, S.S. Sekhon, Biomass derived hierarchical porous carbon materials as oxygen reduction reaction electrocatalysts in fuel cells, Prog. Mater. Sci., 102 (2019) 1-71.
[3] Z. Wu, M. Song, J. Wang, X. Liu, Recent Progress in Nitrogen-Doped Metal-Free Electrocatalysts for Oxygen Reduction Reaction, Catalysts, 8 (2018) 196.
[4] J. Stacy, Y.N. Regmi, B. Leonard, M. Fan, The recent progress and future of oxygen reduction reaction catalysis: A review, Renew. Sust. Energ. Rev., 69 (2017) 401-414.
[5] Y. Zhang, W.-J. Jiang, X. Zhang, L. Guo, J.-S. Hu, Z. Wei, L.-J. Wan, Engineering self-assembled N-doped graphene–carbon nanotube composites towards efficient oxygen reduction electrocatalysts, Phys. Chem. Chem. Phys., 16 (2014) 13605-13609.
[6] A. Sarapuu, E. Kibena-Põldsepp, M. Borghei, K. Tammeveski, Electrocatalysis of oxygen reduction on heteroatom-doped nanocarbons and transition metal–nitrogen–carbon catalysts for alkaline membrane fuel cells, J. Mater. Chem. A, 6 (2018) 776-804.
[7] R. Paul, Q. Dai, C. Hu, L. Dai, Ten years of carbon-based metal-free electrocatalysts, Carbon Energy, 1 (2019) 19-31.
[8] R. Paul, F. Du, L. Dai, Y. Ding, Z.L. Wang, F. Wei, A. Roy, 3D Heteroatom-Doped Carbon Nanomaterials as Multifunctional Metal-Free Catalysts for Integrated Energy Devices, Adv. Mater., 31 (2019) 1805598.
[9] D. Wu, C. Zhu, Y. Shi, H. Jing, J. Hu, X. Song, D. Si, S. Liang, C. Hao, Biomass-Derived Multilayer-Graphene-Encapsulated Cobalt Nanoparticles as Efficient Electrocatalyst for Versatile Renewable Energy Applications, ACS Sustain. Chem. Eng., 7 (2019) 1137-1145.
[10] Y. Zheng, F. He, J. Wu, D. Ma, H. Fan, S. Zhu, X. Li, Y. Lu, Q. Liu, X. Hu, Nitrogen-Doped Carbon Nanotube-Graphene Frameworks with Encapsulated Fe/Fe3N Nanoparticles as Catalysts for Oxygen Reduction, ACS Appl. Nano Mater., 2 (2019) 3538-3547.
[11] Y. Zhang, L. Lu, S. Zhang, Z. Lv, D. Yang, J. Liu, Y. Chen, X. Tian, H. Jin, W. Song, Biomass chitosan derived cobalt/nitrogen doped carbon nanotubes for the electrocatalytic oxygen reduction reaction, J. Mater. Chem. A, 6 (2018) 5740-5745.
[12] A. Wütscher, T. Eckhard, D. Hiltrop, K. Lotz, W. Schuhmann, C. Andronescu, M. Muhler, Nitrogen-Doped Metal-Free Carbon Materials Derived from Cellulose as Electrocatalysts for the Oxygen Reduction Reaction, ChemElectroChem, 6 (2019) 514-521.
[13] B. Huang, M. Xia, J. Qiu, Z. Xie, Biomass Derived Graphene-Like Carbons for Electrocatalytic Oxygen Reduction Reaction, ChemNanoMat, 5 (2019) 682-689.
[14] D. Gu, Y. Zhou, R. Ma, F. Wang, Q. Liu, J. Wang, Facile Synthesis of N-Doped Graphene-Like Carbon Nanoflakes as Efficient and Stable Electrocatalysts for the Oxygen Reduction Reaction, Nano-Micro Lett., 10 (2018).
[15] R. Kumar, E.T.S.G. da Silva, R.K. Singh, R. Savu, A.V. Alaferdov, L.C. Fonseca, L.C. Carossi, A. Singh, S. Khandka, K.K. Kar, O.L. Alves, L.T. Kubota, S.A. Moshkalev, Microwave-assisted synthesis of palladium nanoparticles intercalated nitrogen doped reduced graphene oxide and their electrocatalytic activity for direct-ethanol fuel cells, J. Colloid Interface Sci., 515 (2018) 160-171.
[16] Z. Fang, R.L. Smith Jr, J.A. Kozinski, T. Minowa, K. Arai, Reaction of d-glucose in water at high temperatures (410 °C) and pressures (180 MPa) for the production of dyes and nano-particles, J. Supercrit. Fluids, 56 (2011) 41-47.
[17] Y. Sun, R. Zhong, H. Zhang, T. Huang, J. Yu, H. Fang, D. Liang, Z. Guo, Soybean milk derived carbon intercalated with reduced graphene oxide as high efficient electrocatalysts for oxygen reduction reaction, Int. J. Hydrog. Energy, 44 (2019) 21790-21802.

[18] M. Shi, J. Ma, Z. Yao, Z. Li, H. Mi, Y. Xie, Iron and nitrogen co-doped porous carbon derived from soybean dregs with enhanced catalytic performance for oxygen reduction, J. Electroanal. Chem., 839 (2019) 141-148.
[19] M.M. Titirici, Hydrothermal Carbons: Synthesis, Characterization, and Applications, Novel Carbon Adsorbents, Elsevier Ltd2012, pp. 351-399.
[20] M. Sevilla, A.B. Fuertes, Chemical and Structural Properties of Carbonaceous Products Obtained by Hydrothermal Carbonization of Saccharides, Chem. Eur. J., 15 (2009) 4195-4203.
[21] R. Kumar, R.K. Singh, D.P. Singh, Natural and waste hydrocarbon precursors for the synthesis of carbon based nanomaterials: Graphene and CNTs, Renew. Sust. Energ. Rev., 58 (2016) 976-1006.
[22] L. Liu, G. Zeng, J. Chen, L. Bi, L. Dai, Z. Wen, N-doped porous carbon nanosheets as pH-universal ORR electrocatalyst in various fuel cell devices, Nano Energy, 49 (2018) 393-402.
[23] C. Falco, J.P. Marco-Lozar, D. Salinas-Torres, E. Morallón, D. Cazorla-Amorós, M.M. Titirici, D. Lozano-Castelló, Tailoring the porosity of chemically activated hydrothermal carbons: Influence of the precursor and hydrothermal carbonization temperature, Carbon, 62 (2013) 346-355.
[24] R.G. Morais, N. Rey-Raap, J.L. Figueiredo, M.F.R. Pereira, Glucose-derived carbon materials with tailored properties as electrocatalysts for the oxygen reduction reaction, Beilstein J. Nanotechnol., 10 (2019) 1089-1102.
[25] S.S. Xu, S.W. Qiu, Z.Y. Yuan, T.Z. Ren, T.J. Bandosz, Nitrogen-containing activated carbon of improved electrochemical performance derived from cotton stalks using indirect chemical activation, J. Colloid Interface Sci., 540 (2019) 285-294.
[26] T.N. Tran, M.Y. Song, T.H. Kang, J. Samdani, H.Y. Park, H. Kim, S.H. Jhung, J.S. Yu, Iron Phosphide Incorporated into Iron-Treated Heteroatoms-Doped Porous Bio-Carbon as Efficient Electrocatalyst for the Oxygen Reduction Reaction, ChemElectroChem, 5 (2018) 1944-1953.
[27] M.J. Kim, J.E. Park, S. Kim, M.S. Lim, A. Jin, O.H. Kim, M.J. Kim, K.S. Lee, J. Kim, S.S. Kim, Y.H. Cho, Y.E. Sung, Biomass-Derived Air Cathode Materials: Pore-Controlled S,N-Co-doped Carbon for Fuel Cells and Metal-Air Batteries, ACS Catal., 9 (2019) 3389-3398.
[28] X. Li, B.Y. Guan, S. Gao, X.W. Lou, A general dual-templating approach to biomass-derived hierarchically porous heteroatom-doped carbon materials for enhanced electrocatalytic oxygen reduction, Energy Environ. Sci., 12 (2019) 648-655.
[29] J. Quílez Bermejo, m. melle franco, E. San Fabián, E. Morallon, D. Cazorla-Amorós, Towards understanding of the active sites for ORR in N-doped carbon materials through a fine-tuning of nitrogen functionalities: An experimental and computational approach, J. Mater. Chem. A, (2019).
[30] S. Ratso, M. Käärik, M. Kook, P. Paiste, J. Aruväli, S. Vlassov, V. Kisand, J. Leis, A.M. Kannan, K. Tammeveski, High performance catalysts based on Fe/N co-doped carbide-derived carbon and carbon nanotube composites for oxygen reduction reaction in acid media, Int. J. Hydrog. Energy, 44 (2019) 12636-12648.
[31] N. Rey-Raap, M. Enterría, J.I. Martins, M.F.R. Pereira, J.L. Figueiredo, Influence of Multiwalled Carbon Nanotubes as Additives in Biomass-Derived Carbons for Supercapacitor Applications, ACS Appl. Mater. Interfaces, 11 (2019) 6066-6077.
[32] M. Borghei, J. Lehtonen, L. Liu, O.J. Rojas, Advanced Biomass-Derived Electrocatalysts for the Oxygen Reduction Reaction, Adv. Mater., 30 (2018).
[33] X. Wang, Z. Ma, L. Chai, L. Xu, Z. Zhu, Y. Hu, J. Qian, S. Huang, MOF derived N-doped carbon coated CoP particle/carbon nanotube composite for efficient oxygen evolution reaction, Carbon, 141 (2019) 643-651.
[34] M. Li, Y. Xiong, X. Liu, C. Han, Y. Zhang, X. Bo, L. Guo, Iron and nitrogen co-doped carbon nanotube@hollow carbon fibers derived from plant biomass as efficient catalysts for the oxygen reduction reaction, J. Mater. Chem. A, 3 (2015) 9658-9667.
[35] H.T. Chung, J.H. Won, P. Zelenay, Active and stable carbon nanotube/nanoparticle composite electrocatalyst for oxygen reduction, Nat. Commun., 4 (2013) 1922.

[36] S.L.H. Rebelo, A. Guedes, M.E. Szefczyk, A.M. Pereira, J.P. Araújo, C. Freire, Progress in the Raman spectra analysis of covalently functionalized multiwalled carbon nanotubes: unraveling disorder in graphitic materials, Phys. Chem. Chem. Phys., 18 (2016) 12784-12796.
[37] A. Barroso Bogeat, Understanding and Tuning the Electrical Conductivity of Activated Carbon: A State-of-the-Art Review, Crit. Rev. Solid State Mater. Sci., (2019) 1-37.
[38] M. Nunes, I.M. Rocha, D.M. Fernandes, A.S. Mestre, C.N. Moura, A.P. Carvalho, M.F.R. Pereira, C. Freire, Sucrose-derived activated carbons: Electron transfer properties and application as oxygen reduction electrocatalysts, RSC Adv., 5 (2015) 102919-102931.

Chapter 5

Improving the electrocatalytic activity of glucose/carbon nanotube composites for the oxygen reduction reaction by doping with nitrogen and iron

Abstract

Glucose-derived carbon composites were synthesized by hydrothermal treatment in the presence of oxidized carbon nanotubes. Additionally, iron and nitrogen functionalities were incorporated into the carbon structure using different methodologies. The introduction of iron and nitrogen in a single step under H_2 atmosphere favored the formation of quaternary nitrogen and oxidized nitrogen, whereas the incorporation of nitrogen under N_2 atmosphere after doping the composite with iron mainly produced pyridinic nitrogen. The presence of iron and nitrogen on the composites increases the onset potential towards oxygen reduction in KOH 0.1 mol L^{-1} by 130 mV, in comparison to carbonized glucose, whereas the incorporation of quaternary nitrogen appears to improve the reaction mechanism by decreasing the formation of by-products to 25%. Furthermore, the incorporation of iron and nitrogen in a single step enhanced the long-term performance of the prepared electrocatalysts, which may be also due to the higher relative amount of quaternary nitrogen.

5.1. Introduction

The optimization of environmentally friendly energy devices, and more particularly the development of new innovative and low-cost materials, has been one of the main goals of scientific research [1, 2]. In this regard, fuel cells represent one of the most promising alternatives to fossil fuels for sustainable green electrical energy conversion due to the low emission of pollutants, high efficiency, and non-polluting reaction products [3, 4]. However, the oxygen reduction reaction (ORR) that takes place at the cathode presents highly sluggish kinetics and hinders the overall device operation [4-11]. Platinum-based electrocatalysts are the most commonly used to supply faster kinetics [5, 7, 8, 10, 12-15]. However, Pt is a scarce and expensive noble metal, contributing to the high costs associated with fuel cell production [16]. Consequently, the growing need to optimize green energy conversion devices led to an ever-increasing number of efforts to design non-noble metal electrocatalysts, displaying high electroactivity towards ORR and long-term durability.

The high versatility and lower price of carbon materials in comparison with metal-based materials make them one of the most interesting supports for electrocatalysts [4, 17, 18]. The modification of the physical and chemical properties of carbons can result in materials with higher electroactivity, which is essential for the ORR. In order to preserve the ecological friendliness of carbon materials, the combination of a green carbon source and an adequate synthesis method is essential. The use of biomass and hydrothermal carbonization (HTC) are presented as two interesting strategies for the abovementioned objective. Biomass is one of the most abundant carbon sources in the world and presents a relatively low cost. Furthermore, HTC is an emerging low-cost methodology to obtain biomass-derived carbons using mild operating conditions via an environmentally friendly process [19-23]. This combination results in spherical particles that usually display low porosity and low electroactivity towards the ORR [20-23]. To overcome this drawback, tailoring the properties of carbons obtained by HTC is necessary. Carbonization and activation methods are usually employed to develop porosity, while the chemical properties can be modified by the incorporation of heteroatoms and/or transition metals. Nitrogen is considered the most effective heteroatom to enhance the carbon electrocatalyst's activity towards the ORR [20, 22-27]. The presence of pyridinic

nitrogen is important for O_2 bonding, whereas the incorporation of quaternary nitrogen favors oxygen dissociation [21]. Additionally, carbon nanotubes (CNTs) can also be added during the polymerization of glucose to increase the stability of the surface chemistry and the graphitization level of the HTC carbons, in order to enhance the electron transfer kinetics during the ORR [20, 23]. Nonetheless, the obtained electroactivities are still inferior to those of benchmark catalysts, and the incorporation of transition metals is essential to enhance the electroactivity of these composites. Among the studied transition metals, iron is largely reported to give rise to high electroactivities toward the ORR [28, 29]. Besides, the synergy between nitrogen and iron is one of the most important features in the reduction of oxygen and has been reported to achieve outstanding performances [30-34]. However, the effect of nitrogen and iron on carbon materials and their synergy largely depends on the structure and morphology of the supports [35] and the methodology employed for their incorporation [28]. Therefore, this work aims to shed light on the synergistic effect between nitrogen and iron incorporated by different methodologies and to evaluate which are the most promising to obtain electrocatalysts with high efficiency and electroactivity towards the ORR. Accordingly, this work studies the effect of a wide range of iron concentrations added to carbonized glucose (CG). Additionally, the effect of the incorporation of a selected amount of iron on both CG and CG/CNT composites was studied, determining the influence of CNTs on the single incorporation of the transition metal. The effect of the methodology employed to introduce nitrogen on the CG and composites has also been assessed by following two different pathways to achieve Fe,N-doped carbon samples: i) a two-step method, by incorporation of iron oxide followed by its reduction and subsequent incorporation of melamine employing a thermal treatment under inert atmosphere or ii) a one-step method, by incorporation of iron oxide and melamine followed by thermal treatment under H_2 atmosphere. These methodologies allow to understand how nitrogen functionalities are affected by the process and by the base carbon employed (CG or composite), and hence, the electroactivity towards the ORR.

5.2. Experimental

5.2.1. Preparation of electrocatalysts

Glucose-derived carbon materials were prepared by hydrothermal treatment of glucose. Briefly, glucose (15.0 wt%, HiMedia, > 99%) was dispersed under sonication in distilled water (85.0 wt%, Panice) for 30 min in a Teflon-lined reactor chamber. Afterward, the solution was closed in a Teflon-lined stainless steel autoclave and underwent hydrothermal processing at 180 °C for 12 h. The resulting organic polymer was then abundantly washed with distilled water, filtered at room temperature, and dried at 100 °C for 16 h. The material was then carbonized under N_2 atmosphere for 2 h at 800 °C.

The surface chemistry of the carbonized glucose sample was then modified by incorporating iron or iron/nitrogen according to three different methodologies, as detailed in Figure 5.1 : i) different amounts of Fe_2O_3 (Sigma-Aldrich, ≥ 99%) were impregnated onto the carbonized material by incipient wetness impregnation and treated under N_2 atmosphere for 2 h, followed by H_2 atmosphere for an additional 2 h at 650 ºC to achieve a certain final wt% of iron on the carbon sample (0.5 wt%, 1 wt% or 5 wt%, samples $CG_{0.5Fe}$, CG_{1Fe} and CG_{5Fe}, respectively); ii) the prepared CG_{5Fe} sample was mixed with melamine in a 2:3 melamine:CG ratio, followed by thermal treatment at 650 ºC in N_2 atmosphere for 2 h (two-step method, sample N-CG_{5Fe}) and, iii) simultaneous incorporation of 5 wt% of iron oxide and melamine in a 2:3 melamine:CG ratio followed by a single thermal treatment, first in N_2 (2 h) and then under H_2 atmosphere (2 h) at 650 ºC (one-step method, sample $CG_{5Fe,N}$). All treatments were performed with a gas flow rate of 150 cm^3 min^{-1} and a heating rate of 10 ºC min^{-1}.

Additionally, a series of composites was prepared by adding oxidized carbon nanotubes (CNT_O) during the hydrothermal treatment of glucose, as described elsewhere [20]. A typical liquid-phase oxidation method was employed to obtain CNT_O. Briefly, a 7 mol L^{-1} solution of HNO_3 was used to oxidize CNTs for 3 h at the boiling temperature using a ratio of 75 mL of nitric acid per g of CNTs. The resulting oxidized material was then abundantly washed with distilled water until the water pH was attained and subsequently dried for 24 h at 80 °C. The hydrothermal composite was prepared following the same hydrothermal treatment procedure as that employed for the CG sample but using 14.7

wt% of glucose, 0.3 wt% of CNT_O and 85.0 wt% of distilled water as the initial dispersion. The resulting hydrothermal composite was carbonized under an inert atmosphere for 2 h at 800 °C and labeled CG/CNT_O. Afterwards, the surface chemistry of the composite was also modified, as detailed in Figure 5.1. Fe_2O_3 was incorporated on CG/CNT_O by incipient wetness impregnation, followed by thermal treatment in N_2 (2 h) and then in H_2 atmosphere (2 h) at 650 ºC to achieve a final iron content of 5 wt% ($CG/CNT_{O,5Fe}$). Moreover, $CG/CNT_{O,5Fe}$ was mixed with melamine in a 2:3 melamine:CG/CNT_O ratio followed by the same thermal treatment as sample $N\text{-}CG_{5Fe}$ (two-step method, $N\text{-}CG/CNT_{O,5Fe}$). Lastly, iron and nitrogen were simultaneously incorporated onto CG/CNT_O following the same methodology as that used to prepare $CG_{5Fe,N}$ (one-step method, $CG/CNT_{O,5Fe,N}$).

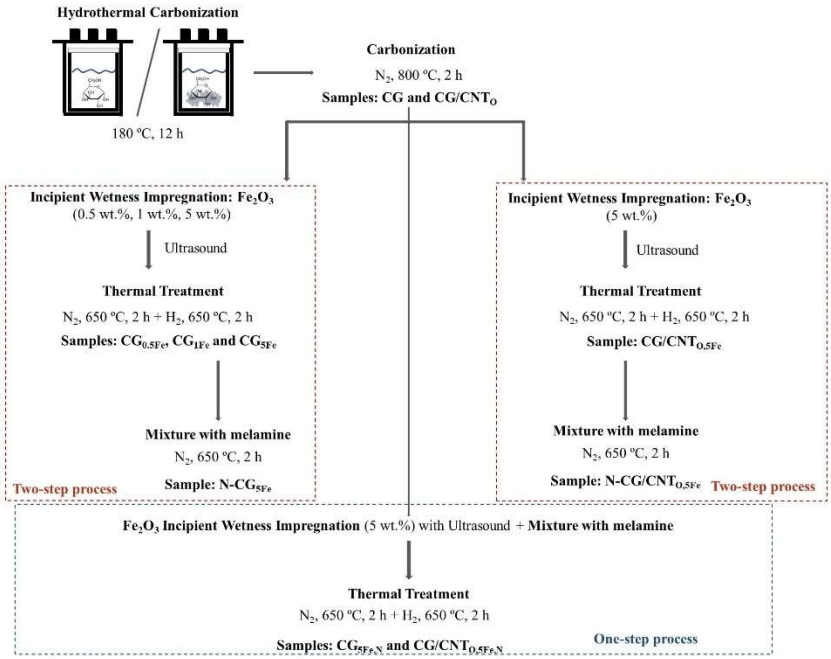


Figure 5.1 - Scheme of the synthesis methodologies employed to prepare Fe,N-doped carbon electrocatalysts.

5.2.2. Chemical and textural characterization

The contents of carbon, hydrogen and nitrogen (C, H, and N) in the electrocatalysts were assessed by combusting the sample at 1050 °C using a Vario Micro Cube analyzer, whereas the oxygen content was measured by pyrolyzing the sample at 1450 °C in a

Rapid Oxy Cube analyzer. Equipment is from Elementar GmbH. To ensure the homogeneity and reproducibility of all results, triplicate analyzes were performed for each material. To further understand the full composition of the prepared carbons, a Perkin Elmer Optima 4300 spectrometer was used to perform inductively coupled plasma (ICP) analysis to quantify the iron loading of Fe-doped samples. This spectrometer was composed of an Echelle polychromator optic. To further understand the composition of each sample, a Kratos AXIS Ultra HAS spectrometer was used to perform X-ray photoelectron spectroscopy (XPS) to determine their chemical surface composition. The analyzes were carried out in fixed analyzer transmission mode at 14 kV (175 W) using monochromatic radiation (Al Kα, 1486.7 eV). Regarding the textural properties, N_2 adsorption-desorption isotherms at −196 °C were obtained for each carbon material using an automated gas sorption analyzer (Autosorb iQ, Quantachrome). Before the analysis, all samples underwent degasification for 12 h at 150 °C. The specific surface area (S_{BET}) was calculated using the Brunauer-Emmett-Teller (BET) equation, whereas the volume of nitrogen adsorbed at a relative pressure of 0.99 (saturation point) was used to calculate the total pore volume (V_p). The microporous volume (V_{micro}) was determined by the t-plot method. All samples were analyzed by scanning electron microscopy (SEM) to observe their morphology, and the Fe,N-doped composites were also analyzed by elemental map distribution. These analyzes were performed in a Nova NanoSEM 200 (FEI Company). A conductive carbon double-sided adhesive tape was used to attach the powders of each sample onto an aluminum pin. During SEM analysis, an Everhart-Thornley detector (ETD) was used. Regarding elemental mapping, a Si(Li) detector was employed. Raman spectroscopy was performed using a monochromatic wavelength laser of 532 nm in an Alpha 300 apparatus (WiTec, Germany), by directly measuring the spectra on the carbons.

5.2.3. Electrochemical characterization

The synthesized electrocatalysts were electrochemically characterized using a PGSTAT 302N potentiostat/galvanostat and a 3-electrode beaker-type cell. The reference and counter electrodes used in this system were Ag/AgCl (KCl 3 mol L^{-1}) and a glassy carbon rod, respectively. A rotating ring-disk electrode (RRDE, Metrohm, 24.9% collection efficiency, 5 mm in diameter) composed of a glassy carbon disk and a Pt ring was used

as the working electrode for linear sweep voltammetry (LSV) and cyclic voltammetry (CV) assessments. Additionally, a rotating disk electrode (RDE, Metrohm, 3 mm in diameter) also consisting of a glassy carbon disk was used as working electrode to perform chronoamperometric measurements. These electrodes were prepared by drop casting of a suspension containing the carbon electrocatalysts to achieve a final mass loading of ca. 0.27 mg cm^{-2}. The suspension was prepared by mixing 4 mg of the electrocatalyst, 470 µL of ultrapure water (Millipore), 80 µL of Nafion (5 wt% in lower aliphatic alcohols and water, Sigma-Aldrich) and 80 µL of ethanol (≥ 99.5%, VWR Chemicals). Before drop casting, the suspension underwent sonication for at least 30 min until homogeneity was achieved.

The ORR activity was initially analyzed by LSV and CV measurements, which were performed in N_2-saturated 0.1 mol L^{-1} KOH followed by experiments in O_2-saturated electrolyte. An initial screening of redox reactions that could take place under the inert medium was accomplished by CV using a scan rate that ranged from 5 to 100 mV s^{-1} with no rotation. Afterward, LSVs were performed by rotating the working electrode from 400 to 3000 rpm and using a scan rate of 5 mV s^{-1}. Both measurements were performed from 1.15 V to -0.05 V (vs RHE). The O_2-saturated assessments were performed using the same procedure after completion of the experiments in the N_2-saturated electrolyte. The experimental current densities were obtained by subtracting the results obtained in N_2-saturated KOH from those measured in O_2-saturated electrolyte to guarantee that only the current densities of phenomena related to the reduction of oxygen were represented. From this corrected LSV it is possible to obtain different crucial ORR parameters: i) the onset potential (E_{onset}) at a current density of 0.1 mA cm^{-2}; and ii) the current density produced at 0.4 V vs RHE ($J_{0.4}$). The reaction mechanism was evaluated by using the current produced by the disk and ring of the RRDE. These values can be used to calculate the formation of by-products from a two-electron mechanism (H_2O_2) and the number of electrons exchanged (n_e) at each step of the reaction. Both were calculated with the currents obtained at 1600 rpm using Eqs. (5.1) and (5.2), respectively:

$$H_2O_2(\%) = 200 \times \frac{\frac{I_R}{N}}{I_D + \frac{I_R}{N}} \quad (5.1)$$

$$n_e = \frac{4I_D}{I_D + \frac{I_R}{N}} \quad (5.2)$$

where I_R is the ring current (mA), I_D is the disk current (mA), and N is the collection efficiency (0.249).

Moreover, the long-term performance (10000 s) of each material towards ORR was determined by applying 0.4 V vs RHE. Besides, samples CG and CG/CNT_O were also analyzed by electrochemical impedance spectroscopy (EIS) with an AC amplitude of 10 mV and a frequency range from 1 MHz to 10 mHz using at 0 V.

5.3. Results and discussion

5.3.1. Chemical properties

Elemental and ICP analyzes were performed to determine the bulk composition of the electrocatalyst. The results obtained are detailed in Table 5.1.

Table 5.1 - Chemical composition determined by elemental analysis and ICP.

Sample	C (wt%)	H (wt%)	O (wt%)	N (wt%)	Fe (wt%)
CG	90.8	1.7	7.5	n.d	-
CG/CNT_O	92.7	0.8	6.5	n.d	-
$CG_{0.5Fe}$	93.4	1.3	5.0	n.d	0.3
CG_{1Fe}	92.2	1.0	5.4	n.d	1.4
CG_{5Fe}	87.4	1.3	6.2	n.d	5.1
CG/$CNT_{O,5Fe}$	90.6	0.8	3.7	n.d	4.9
N-CG_{5Fe}	81.9	1.3	8.1	3.3	5.4
N-CG/$CNT_{O,5Fe}$	83.4	1.1	6.4	5.1	4.0
$CG_{5Fe,N}$	82.2	1.4	8.6	2.0	5.8
CG/$CNT_{O,5Fe,N}$	85.4	1.0	7.2	2.2	4.2

n.d.- not detected

The carbonized hydrothermal samples (CG and CG/CNT_O) were primarily composed of carbon (Table 5.1), with some hydrogen and oxygen. The oxygen content decreases in the presence of oxidized CNTs, indicating that the hydrothermal treatment increased the degree of polymerization [20]. On the other hand, the incorporation of iron onto CG and CG/CNT_O leads to a decrease in the relative oxygen content due to thermal treatment applied after the wetness impregnation with iron oxide. Nonetheless, increasing the amount of iron precursor during the impregnation process leads to an increase in the oxygen content due to the oxygen contribution of the Fe_2O_3 added that is not totally reduced in the final material, especially when employing CG as support. Furthermore, interesting differences are observed regarding the oxygen content due to the methodology employed to incorporate iron and nitrogen. The addition of melamine to CG_{5Fe} and $CG/CNT_{O,5Fe}$ (samples N-CG_{5Fe} and N-$CG/CNT_{O,5Fe}$, respectively) leads to a lower content of oxygen than the simultaneous addition of Fe and N (samples $CG_{5Fe,N}$ and $CG/CNT_{O,5Fe,N}$, respectively), which may be due to the different types of bond formed during the thermal treatments employed. The use of H_2 not only reduces Fe_2O_3 but also favors the formation of new oxygen bonds in the carbon structure.

Regarding nitrogen content, the opposite trend is observed, which indicates that there are more possibilities for nitrogen bonding after the incorporation of iron due to the previous formation of stable species on the carbon matrix that will not compete with nitrogen upon the second thermal treatment. Lastly, the iron content follows the same trends as oxygen, in which the simultaneous incorporation of both precursors (one-step method) leads to a higher content of iron than using a two-step method. Besides, interesting differences in the chemical composition were also detected due to the synthesis process. Regardless of the doping method employed, the addition of CNTs to the hydrothermal polymerization results in composites that present lower oxygen and iron contents but higher nitrogen percentages than their non-composite counterparts (Table 5.1), which suggests that the presence of CNTs favors the preferential incorporation of nitrogen functionalities instead of iron oxide.

To fully understand the differences due to the methodologies employed for the Fe,N doping process, the surface composition of these four samples was determined by XPS. The survey spectra are presented in Figure 5S.1 and their chemical compositions are

detailed in Table 5S.1. The XPS surveys indicate the presence of carbon, oxygen and nitrogen, but do not indicate the presence of iron on the materials' surface analyzed, which suggests that iron is probably incorporated inside the porous structure of the carbons instead of on the surface [36], which is confirmed by the ICP analysis (Table 5.1). The surface chemical composition obtained by XPS follows the same trend as that obtained by elemental analysis. The presence of CNTs or the use of the two-step method for doping results in a higher nitrogen content (Table 5S.1). To further understand the nitrogen bonds formed during the thermal treatments, the high-resolution XPS N 1s spectra of those samples prepared by the two-step method (N-CG_{5Fe} and N-$CG/CNT_{O,5Fe}$) and one-step method ($CG_{5Fe,N}$ and $CG/CNT_{O,5Fe,N}$) were deconvoluted into the main four nitrogen functionalities (Figure 5.2): pyridinic nitrogen (N-6) at 398.4 ± 0.1 eV, pyrrolic nitrogen (N-5) at 400.1 ± 0.2 eV, quaternary nitrogen (N-Q) at 401.7 ± 0.3 eV, and oxidized nitrogen (N-X) at 403.9 ± 0.1 eV [37]. Interesting differences are observed for the most common nitrogen functionalities. The relative composition of N-6 is higher in those materials in which the nitrogen precursor was treated under an inert atmosphere (N-CG_{5Fe} and N-$CG/CNT_{O,5Fe}$), while similar percentages of N-5 are observed in comparison with those samples treated under H_2 ($CG_{5Fe,N}$ and $CG/CNT_{O,5Fe,N}$). Besides, the percentage of N-Q and N-X increase after the treatment under H_2 (Figure 5.2b and 5.2d). The increase of N-Q may be an effect of the time used during the one-step method (4 h) in comparison to the two-step method (2 h), which favors the transformation of N-6 into N-5 and N-5 into N-Q. On the other hand, the oxygen removed during the reduction of iron oxide may react with nitrogen forming a large number of N-X bonds.

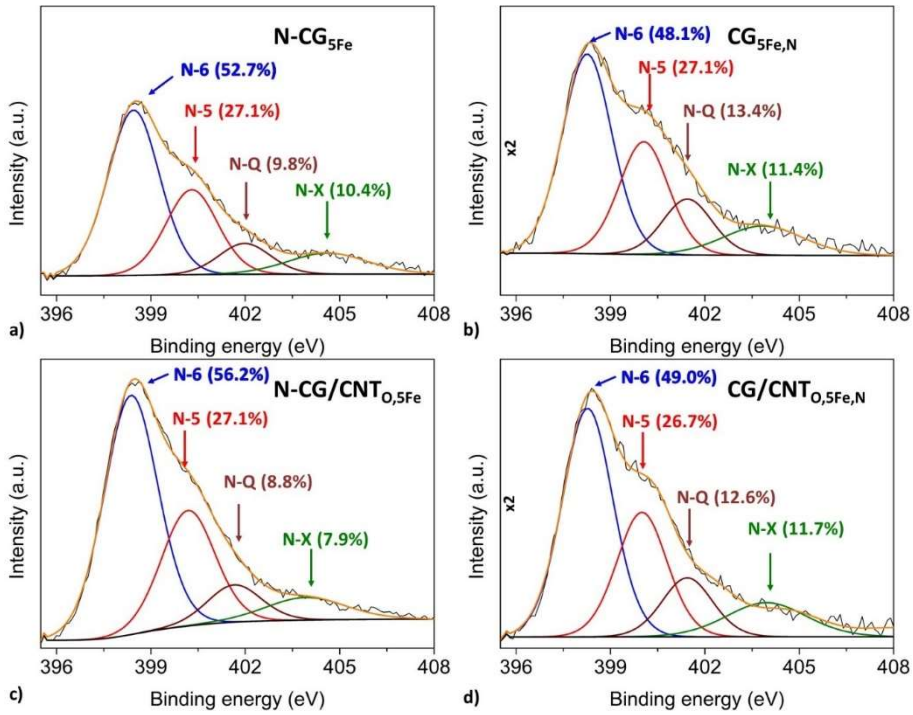


Figure 5.2 - Deconvolution of the N 1s X-ray photoelectron spectra of N-CG_{5Fe} (a), $CG_{5Fe,N}$ (b) N-$CG/CNT_{O,5Fe}$ (c) and $CG/CNT_{O,5Fe,N}$ (d) electrocatalysts.

Nitrogen adsorption-desorption isotherms performed at -196 °C were used to evaluate the textural properties of the prepared carbons and are displayed in Figure 5S.2. The main textural parameters calculated from the isotherms are shown in Table 5.2. Sample CG exhibits a type I isotherm characteristic of microporous materials [38]. Nonetheless, the presence of the oxidized CNTs modifies the isotherm to a type IV [38, 39], with a type H3 hysteresis loop characteristic of slit-shaped pores [39, 40]. Besides, the composite obtained (CG/CNT_O) presents a slight decrease in microporosity, which may have been caused by the low microporosity from the CNTs.

Table 5.2 - Textural properties determined by N_2 adsorption/desorption isotherms at -196 ºC.

Sample	S_{BET} (m^2 g^{-1})	V_p (cm^3 g^{-1})	V_{micro} (cm^3 g^{-1})
CG	468	0.20	0.18
CG/CNT_O	418	0.27	0.15
$CG_{0.5Fe}$	549	0.22	0.21
CG_{1Fe}	517	0.21	0.19
CG_{5Fe}	530	0.22	0.20
$CG/CNT_{O,5Fe}$	441	0.31	0.16
$N\text{-}CG_{5Fe}$	396	0.18	0.14
$N\text{-}CG/CNT_{O,5Fe}$	59	0.12	0.01
$CG_{5Fe,N}$	440	0.19	0.16
$CG/CNT_{O,5Fe,N}$	316	0.26	0.11

The incorporation of a 5 wt% of iron led to an increase of the S_{BET} for both CG (from 468 to 530 m^2 g^{-1}) and CG/CNT_O (from 418 to 441 m^2 g^{-1}), as well as in the pore volume (from 0.20 to 0.22 cm^3 g^{-1} and 0.27 to 0.31 cm^3 g^{-1}, respectively), which suggest that iron may be acting as an activating agent [41]. Regardless of the methodology employed to dope the carbons, Fe,N-doping decreases the microporosity, especially in those samples prepared by the two-step method. This effect may be due to the time and atmosphere employed for the thermal treatments. In the two-step process, the melamine was only treated for 2 h under N_2 atmosphere, while in the one-step process, the treatment took place for 2 h under N_2 and 2 h under H_2. Therefore, not only the time for the nitrogen precursor to decompose was increased but the decomposition of melamine may be also favored by reaction with the H_2 carrier. The N-containing surface groups may have blocked some of the pores, hence hindering the access of N_2 to the innermost pores during the isotherm measurements [21, 36].

The morphological changes that occur during both the hydrothermal processes and the subsequent incorporation of iron (5 wt%) and nitrogen were observed by scanning electron microscopy (SEM). The corresponding micrographs are displayed in Figure 5.3.

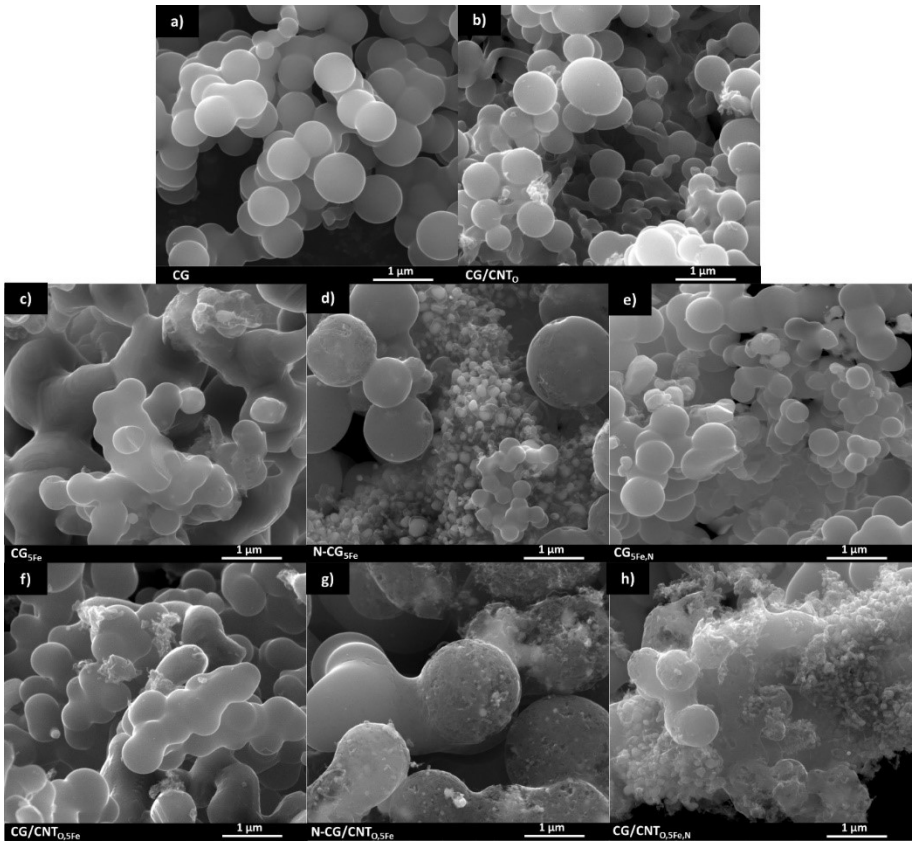


Figure 5.3 - SEM micrographs of CG (a), CG/CNT$_O$ (b), CG$_{5Fe}$ (c), N-CG$_{5Fe}$ (d), CG$_{5Fe,N}$ (e), CG/CNT$_{O,5Fe}$ (f), N-CG/CNT$_{O,5Fe}$ (g) and CG/CNT$_{O,5Fe,N}$ (h) electrocatalysts

Sample CG is composed of spheres without defects (Figure 5.3a), which is a typical morphology of hydrothermal carbons [42, 43]. The incorporation of CNT$_O$ during the hydrothermal polymerization results in a combination of the carbon spheres and the CNTs, with bonds connecting both types of carbon structures (Figure 5.3b). The addition of iron to the pristine samples (CG and CG/CNT$_O$) results in materials with interesting differences in their morphology. The micrographs of CG$_{5Fe}$ (Figure 5.3c) and CG/CNT$_{O,5Fe}$ (Figure 5.3f) exhibit some of the spheres observed in the non-doped samples but also a large number of carbon spheres that have agglomerated into a single large cluster. The incorporation of nitrogen results in materials with different morphologies (Figure 5.3d, 5.3e, 5.3g and 5.3h) compared to those of the Fe-doped samples (Figure 5.3c, and 5.3f) with the appearance of several defects on the surface of the spheres (Figure 5.3d, 5.3e, 5.3g and 5.3h), probably due to the formation of C-N

bonds during the decomposition of the melamine. Besides, the iron dispersion on the carbon materials, specifically in Fe,N-doped composites (N-CG/$CNT_{O,5Fe}$ and CG/$CNT_{O,5Fe,N}$), was analyzed by elemental mapping (Figure 5S.3). The resulting micrographs indicate that iron is well dispersed in the area investigated, which indicates the successful incorporation of the metallic element across the carbon support.

To further address the changes attributed to the presence of CNT_O and/or the incorporation of iron and/or nitrogen, Raman spectroscopy was performed. The resulting spectra are exhibited in Figure 5S.4. All carbons exhibit two main peaks: one associated with the carbon structure's basal plane defects (D band) at ca. 1350 cm^{-1} and another peak attributed to the material's graphitic domains (G band) at ca. 1580 cm^{-1}. These two main bands were further deconvoluted to gain some insight into the number of defects of each material. The integration of the peak areas resulting from the deconvolution (A_D and A_G) was then used to calculate the A_D/A_G ratio (Table 5.S2). As expected, the presence of CNT_O decreases the value of the A_D/A_G ratio in comparison to CG, due to the highly graphitic nature of the CNTs. The incorporation of iron does not significantly modify the structure of CG. However, the incorporation of 5 wt% of iron on the CG/CNT_O composite results in a higher A_D/A_G ratio, which may be attributed to the anchoring of the precursor nanoparticles on the carbon structure, which leads to a more disordered matrix [44]. The incorporation of nitrogen by the two-step method (N-CG_{5Fe} and N-CG/$CNT_{O,5Fe}$) produces different variations depending on the pristine carbon (CG or CG/CNT_O). N-CG_{5Fe} presents a slightly lower A_D/A_G ratio (2.36) than CG (2.44) and CG_{5Fe} (2.41), which indicates that each step of the electrocatalyst preparation contributes to increase the degree of order. Contrarily, N-CG/$CNT_{O,5Fe}$ presents a higher A_D/A_G ratio (2.93) than both CG/CNT_O (2.22) and CG/$CNT_{O,5Fe}$ (2.57), which indicates that the precursor added is generating defects on the structure [20]. On the other hand, the simultaneous incorporation of iron and nitrogen ($CG_{5Fe,N}$ and CG/$CNT_{O,5Fe,N}$) results in a slight increase of the A_D/A_G ratio in comparison to their undoped counterparts (CG and CG/CNT_O, respectively) which indicates that the number of defects of the catalysts' is increased during the doping process. These results indicate that the carbon support, precursors and thermal treatments applied to synthesize these electrocatalysts are important parameters in the formation of defects.

5.3.2. Electrochemical assessments

Oxygen Reduction Reaction

The synthesized electrocatalysts were initially screened towards the ORR by CV in a rotating ring-disk electrode (RRDE), using a scan rate range between 5 and 100 mV s^{-1} in inert and O_2-saturated electrolyte without rotation. Measurements under N_2-saturated medium (Figure 5S.5) displayed featureless cyclic voltammograms, which indicate that no electrocatalytic activity took place under these conditions. However, CVs performed in O_2-saturated KOH (Figure 5S.5) show well-defined cathodic peaks, which confirms the electroactivity of all electrocatalysts towards ORR. Nonetheless, electrochemical differences are observed between samples due to their physico-chemical properties, hence the performance of all catalysts was assessed by LSV to correlate the electrochemical results and the properties of the materials. The LSVs of the electrocatalysts recorded in O_2-saturated 0.1 mol L^{-1} KOH electrolyte at 1600 rpm and the respective number of electrons exchanged are plotted in Figure 5.4a-b and Figure 5.4c-d, respectively. The corresponding LSV and number of electrons exchanged by Pt/C are displayed in Figure 5S.6. The main electrochemical parameters obtained from the LSVs are exhibited in Table 5.3.

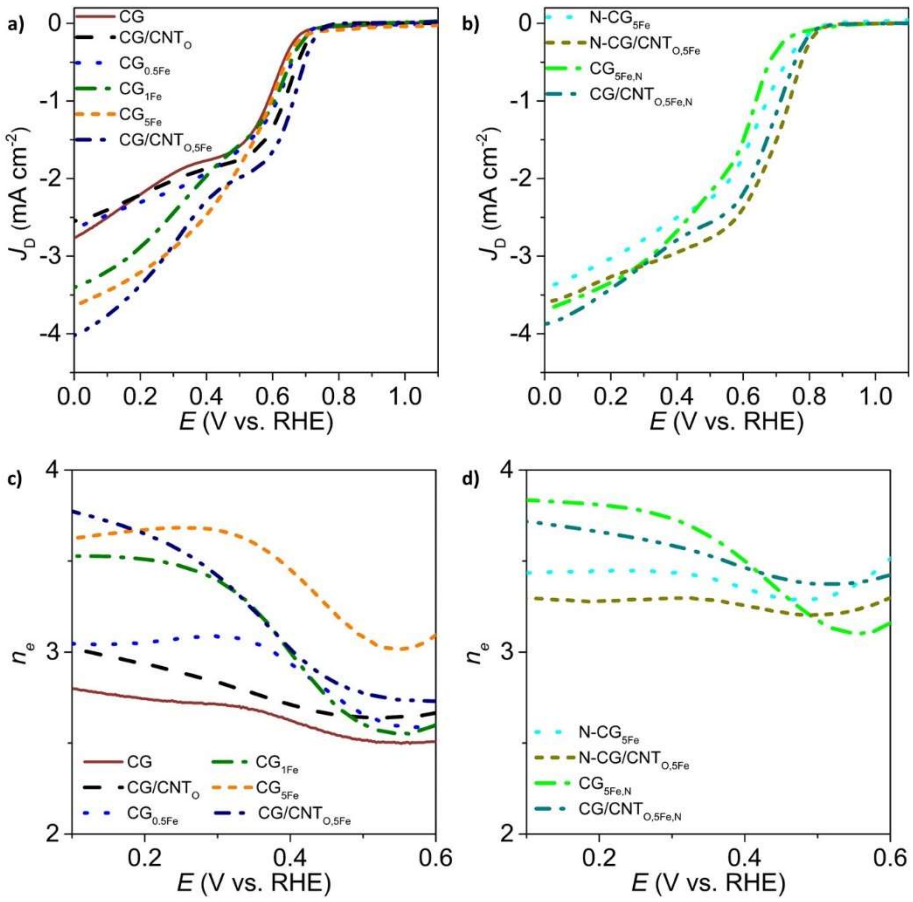


Figure 5.4 - Disk current density produced by undoped and Fe-doped (a) and Fe,N-doped (b) electrocatalysts at 1600 rpm in O_2-saturated electrolyte (0.1 mol L^{-1} KOH) and number of electrons exchanged during the oxygen reduction reaction for undoped and Fe-doped (c) and Fe,N-doped (d) electrocatalysts.

Table 5.3 - Main electrochemical parameters: onset potential (E_{onset}), current density ($J_{0.4}$), hydrogen peroxide (H_2O_2) formation, and the number of electrons exchanged (n_e) for the synthesized materials and commercial Pt/C.

Sample	E_{onset} (V)	$J_{0.4}$ (mA cm^{-2}) [a]	H_2O_2 (%)[a]	n_e[a]
CG	0.70	1.77	69	2.6
CG/CNT$_O$	0.73	1.87	64	2.7
CG$_{0.5Fe}$	0.71	1.92	53	2.9
CG$_{1Fe}$	0.72	1.97	50	3.0
CG$_{5Fe}$	0.75	2.47	27	3.5
CG/CNT$_{O,5Fe}$	0.74	2.29	49	3.0
N-CG$_{5Fe}$	0.81	2.50	33	3.3
N-CG/CNT$_{O,\ 5Fe}$	0.83	2.95	37	3.3
CG$_{5Fe,\ N}$	0.79	2.67	25	3.5
CG/CNT$_{O,\ 5Fe,\ N}$	0.81	2.79	27	3.5
Pt/C	0.98	5.41	3	3.9

[a] - Calculated at 0.4 V vs RHE

The base CG and the composite CG/CNT$_O$ were tested to evaluate their performance toward the ORR. The presence of CNT$_O$ in the carbon structure shifts the E_{onset} by 30 mV from 0.70 V to 0.73 V, probably due to the higher number of active sites that were formed during the synthesis process. Furthermore, this composite exhibits an increase in $J_{0.4}$ of 6% and a small shift of the reaction mechanism from the two to the four-electron pathway. These improvements are probably due to an increase in the electrical conductivity of the electrocatalyst [20]. To further investigate this hypothesis, electrochemical impedance spectroscopy (EIS) was performed on samples CG and CG/CNT$_O$. The resultant Nyquist plots are displayed in Figure 5S.7. These plots demonstrate that the presence of CNT$_O$ led to a smaller semicircle in the higher frequency range, which is equivalent to a decrease of the charge transfer resistance. This analysis suggests that the glucose/CNT composite has a higher electrical conductivity than the CG sample, which corroborates the previous statement.

The incorporation of different amounts of iron on the CG sample leads to an increase in E_{onset} and $J_{0.4}$. In fact, a direct relationship between these parameters and the amount of iron present in the electrocatalysts has been found (Figure 5S.8). Besides, a decrease in the formation of by-products and an increase in the number of electrons exchanged is also observed by increasing the percentage of iron. Similarly, the addition of 5 wt% of iron to the composite ($CG/CNT_{O,5Fe}$) increases the onset potential, current density, and number of electrons exchanged and decreases the formation of by-products. Regarding the incorporation of nitrogen, several interesting differences are observed in the ORR, which are probably correlated to the amount and type of functionalities present in each material. Overall, the incorporation of nitrogen increases the onset potential from 0.75 V (CG_{5Fe}) to 0.81 V ($N\text{-}CG_{5Fe}$) and 0.79 V ($CG_{5Fe,N}$) and from 0.74 V ($CG/CNT_{O,5Fe}$) to 0.83 V ($N\text{-}CG/CNT_{O,5Fe}$) and 0.81 V ($CG/CNT_{O,5Fe,N}$). The incorporation of nitrogen after iron (two-step method) results in a higher increase of the onset potential than the single-step method. This difference may be explained by the presence of larger amounts of N-6 in samples $N\text{-}CG_{5Fe}$ and $N\text{-}CG/CNT_{O,5Fe}$ than $CG_{5Fe,N}$ and $CG/CNT_{O,5Fe,N}$, respectively, which is believed to govern the E_{onset} [45]. Regarding the current density of these four samples, a different trend is observed. CG presents a higher increase of $J_{0.4}$ after a single-step functionalization ($CG_{5Fe,N}$), whereas the composite sample presents a higher increase for the sample prepared by the two-step methodology ($N\text{-}CG/CNT_{O,5Fe}$), which may be related to a larger number of defects on the carbon structure of the composite, as observed by the Raman spectra (Table 5S.2). The use of a single-step functionalization leads to less side products and a larger number of electrons transferred due to the presence of a large number of N-Q functionalities, which is reported to favor oxygen adsorption and dissociation and to accomplish oxygen reduction through the four-electron mechanism [36, 46]. Once again, the incorporation of CNT_O improves the E_{onset} and the $J_{0.4}$ but does not produce any significant effect on the reaction mechanism, as $N\text{-}CG/CNT_{O,5Fe}$ and $CG/CNT_{O,5Fe,N}$ present the same values of by-products and number of electrons transferred as their counterparts. Overall, N-6 functionalities increase the E_{onset}, whereas the number of defects and disorder of the carbon matrix increase the $J_{0.4}$ and the N-Q groups favor a more direct reaction mechanism (4-electrons) and decrease the formation of by-products.

To further evaluate the performance of the electrocatalysts towards the ORR, another critical parameter was analyzed, namely the long-term stability. Therefore, chronoamperometry measurements were performed on all electrocatalysts by applying 0.4 V (vs RHE) during 10000 s. The results obtained are exhibited in Figure 5.5.

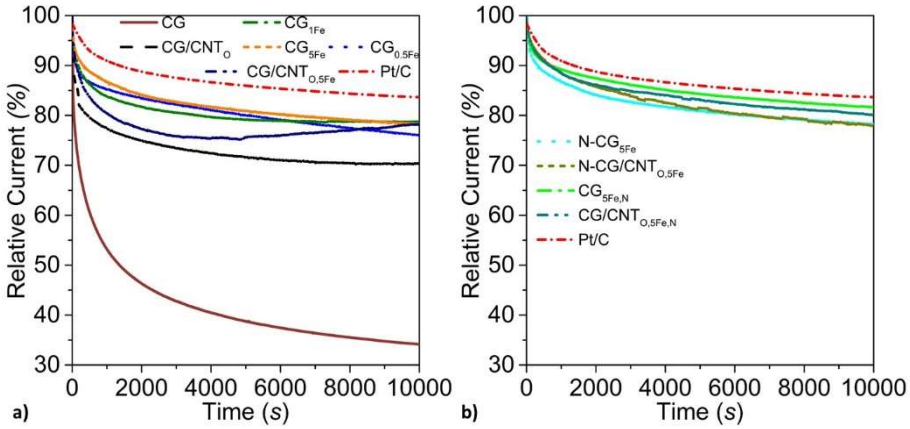


Figure 5.5 - Chronoamperometry measurements (0.4 V for 10000 s) for undoped and Fe-doped electrocatalysts (a), and Fe,N-doped electrocatalysts (b) in an O_2-saturated 0.1 mol L^{-1} KOH electrolyte at 1600 rpm.

CG exhibits very low long-term stability, losing 66% of its current density after 10000 s, which is not ideal for upscale applications. The presence of CNT_O increases the current density retention of the electrocatalysts by 36%, which can be attributed to the higher performance stability of the CNTs [20] and the modification of the carbon properties during synthesis. Nonetheless, this value is still not ideal for long-term applications. It should be noted that there is a large amount of by-products formed with both electrocatalysts (Table 5.3), which may lead to the oxidation of the carbon surface [47-49], hindering their ability for O_2-adsorption and, consequently, their performance towards the ORR. The incorporation of iron leads to an increase in the catalysts' stability, as iron species act as the main active centers towards the ORR, and highlights a lower degradation level in comparison to the undoped carbons. Furthermore, interesting differences are observed due to the methodology followed to incorporate iron and nitrogen. Samples prepared by incorporating iron and then nitrogen (two-step method) display the same stability as their Fe-doped counterparts. This indicates that even though different active centers are present on the carbon (nitrogen and iron), the overall

degradation of these sites maintains the same level as the samples without nitrogen. On the other hand, samples prepared by the simultaneous incorporation of iron and nitrogen functionalities have higher stability, which may be due to the higher relative content of N-Q. These functional groups present strong bonds that may favor the retention of the current density, hence the better long-term application of these catalysts. Overall, the Fe,N-doped samples using the single-step methodology ($CG_{5Fe,N}$ and $CG/CNT_{O,5Fe,N}$) display very similar current density retentions (82% and 80%, respectively) in comparison to that of Pt/C (84%). Although the current density produced by these carbon electrocatalysts is still not to par with the commercial catalyst, the long-term stability indicates that some positive aspects have already been developed and that further tailoring of the surface chemistry may lead to ORR performances similar to Pt/C. Due to the importance of CNTs on the performance of the composites, slightly increasing their amount during the hydrothermal process may lead to even higher electroactivities towards ORR. Moreover, the incorporation of single atoms instead of using two different precursors may also improve the performance of the electrocatalysts and reduce their overall synthesis time and production costs. Therefore, the composites prepared in this work provide a good starting point towards the development of green, sustainable and cheap ORR electrocatalysts.

5.4. Conclusions

Carbon composites prepared by hydrothermal treatment of glucose in the presence of oxidized CNTs were tailored by incorporating iron and/or nitrogen on their surface using two different methodologies: i) incorporation of iron followed by nitrogen doping or ii) simultaneous incorporation of the transition metal and the heteroatom in a single thermal treatment. The presence of CNT_O favored the polymerization of glucose during the hydrothermal treatment resulting in materials with a lower concentration of functional groups than their glucose-derived carbon counterparts. Nitrogen doping of the Fe-doped samples results in materials with a much higher concentration of nitrogen than the Fe,N-doped samples prepared using a single thermal treatment. The use of H_2 atmosphere during the thermal decomposition of melamine leads to lower contents of N-6, and higher amounts of N-Q and N-X. Regarding the electrochemical performance, E_{onset} increases by 130 mV in comparison to the carbonized glucose sample due to the presence of active

centers such as CNT_O, iron and nitrogen functional groups, whereas the current density increases linearly with the iron content. The reaction mechanism is improved by the addition of nitrogen functionalities, in particular N-Q groups, which decrease the formation of by-products to 25% and shift the mechanism to the four-electron pathway. The long-term durability of the carbon composites is higher than that of the glucose-derived carbon and increases due to the incorporation of iron and N-Q moieties. Therefore, considering the overall ORR performance parameters, the Fe,N-doped carbon composite prepared using the one-step method presents the highest long-term stability and lowest formation of by-products, whereas the composite prepared by the two-step method exhibits the highest onset potential and current density. Overall, Fe,N-doped carbon composites present different advantages that may prove useful as a starting point to develop new electrocatalysts to replace the Pt/C benchmark.

5.5. Supplementary Information

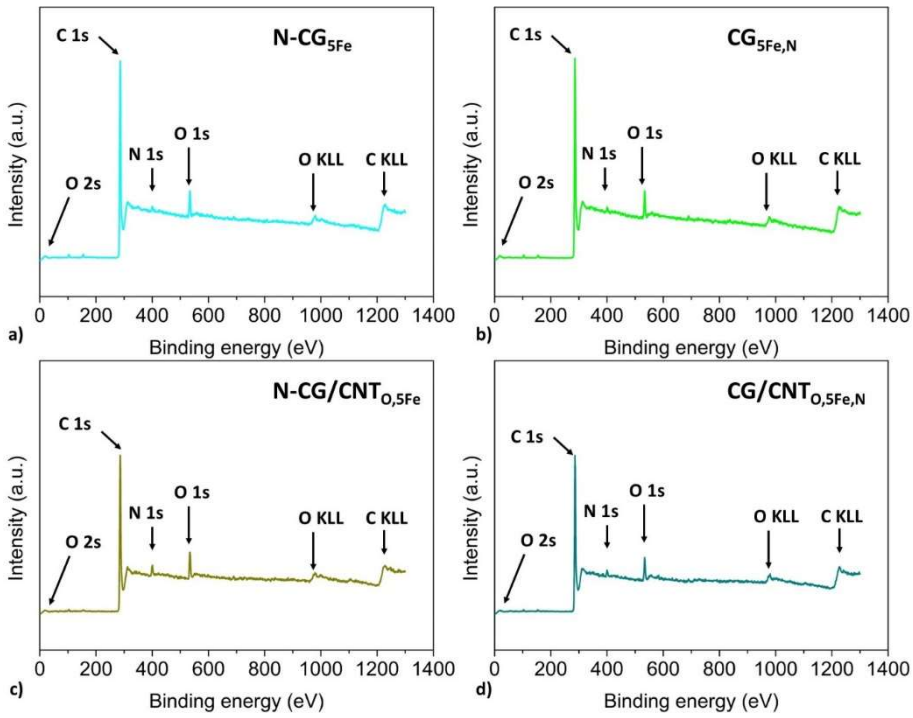


Figure 5S.1 - XPS survey spectra of the prepared Fe,N-doped CG (a,b) and CG/CNT composites (c,d) electrocatalysts, in which N-CG_{5Fe} and N-$CG/CNT_{O,5Fe}$ were prepared using a two-step method and $CG_{5Fe,N}$ and CG/CNT_O were prepared using a one-step method.

Table 5S.1 - Surface chemical composition determined by XPS.

Sample	C (wt%)	O (wt%)	N (wt%)
N-CG_{5Fe}	91.0	6.2	2.8
N-$CG/CNT_{O,5Fe}$	87.5	7.8	4.7
$CG_{5Fe,N}$	91.4	6.6	2.0
$CG/CNT_{O,5Fe,N}$	89.8	7.5	2.7

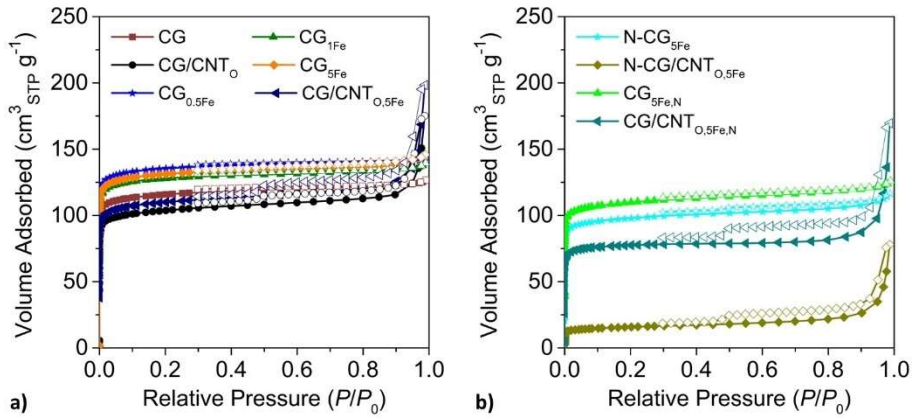


Figure 5S.2 - N_2 adsorption-desorption isotherms at -196 ºC of undoped, CG_{XFe} and $CG/CNT_{O,5Fe}$ (a), and $N\text{-}CG_{5Fe}$, $N\text{-}CG/CNT_{O,5Fe}$, $CG_{5Fe,N}$ and $CG/CNT_{O,5Fe,N}$ (b) electrocatalysts.

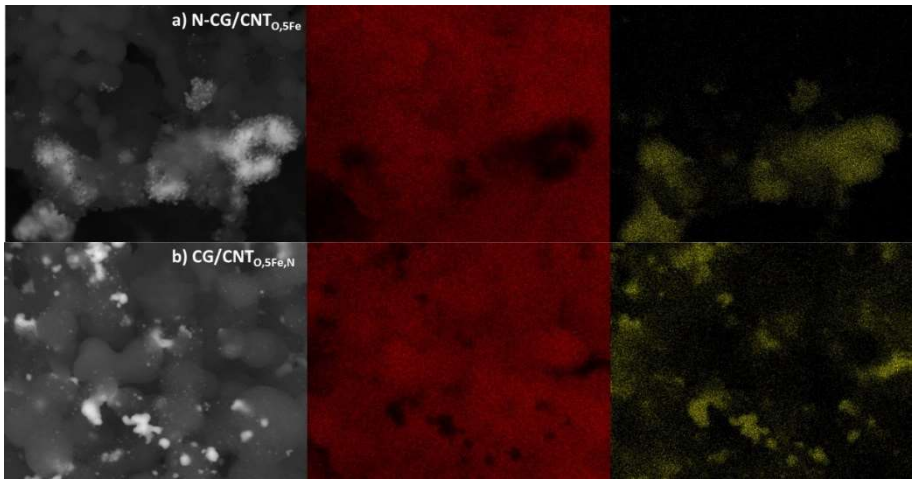


Figure 5S.3 - Elemental mapping of $N\text{-}CG/CNT_{O,5Fe}$ (a) and $CG/CNT_{O,5Fe,N}$ (b). Red – Carbon, Yellow – Iron.

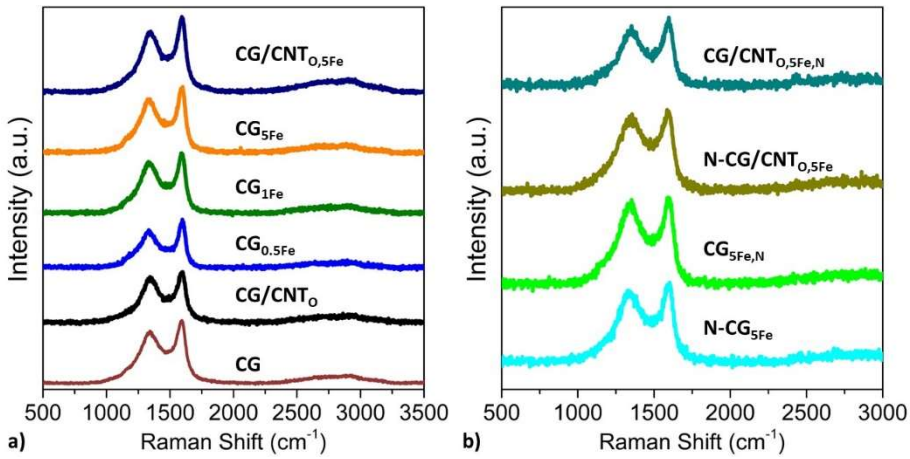


Figure 5S.4 - Raman spectra of undoped and Fe-doped electrocatalysts (a), and Fe,N-doped electrocatalysts (b).

Table 5S.2 - Ratio of the integrated D and G peaks obtained by Raman spectroscopy.

Sample	A_D/A_G
CG	2.44
CG/CNT$_O$	2.22
CG$_{0.5Fe}$	2.48
CG$_{1Fe}$	2.44
CG$_{5Fe}$	2.41
CG/CNT$_{O,5Fe}$	2.57
N-CG$_{5Fe}$	2.36
N-CG/CNT$_{O,5Fe}$	2.66
CG$_{5Fe,N}$	2.93
CG/CNT$_{O,5Fe,N}$	2.35

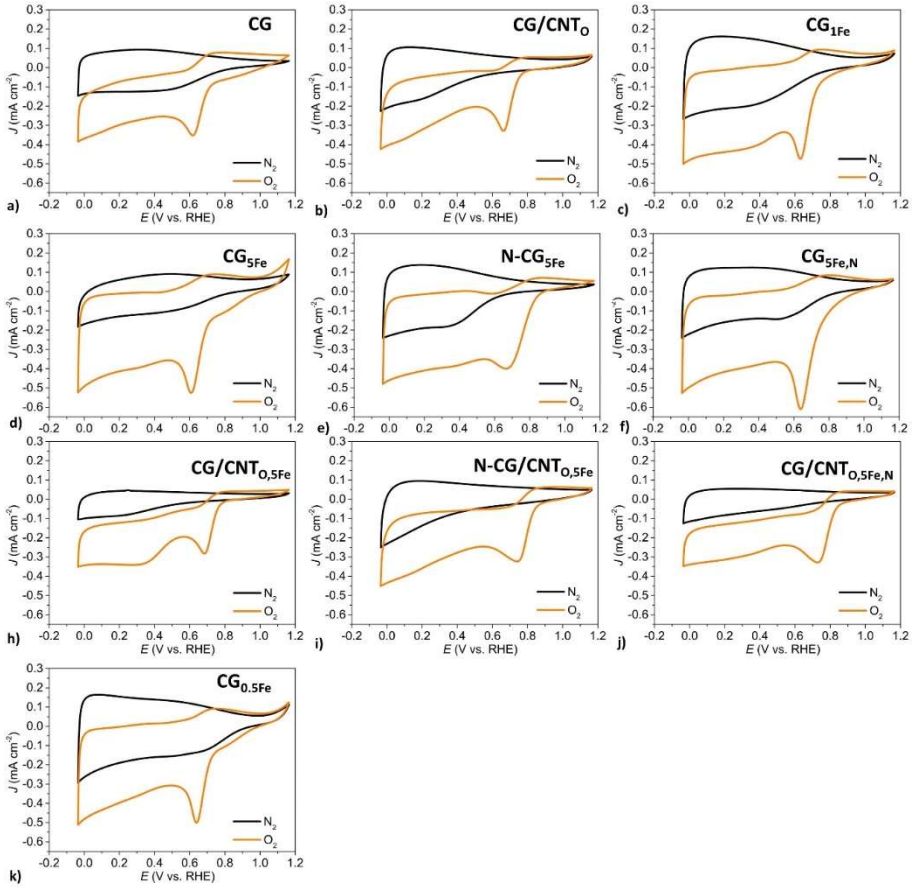


Figure 5S.5 - Cyclic voltammograms recorded at 5 mV s^{-1} in N_2- and O_2-saturated 0.1 mol L^{-1} KOH electrolyte from 1.15 V to -0.05 V.

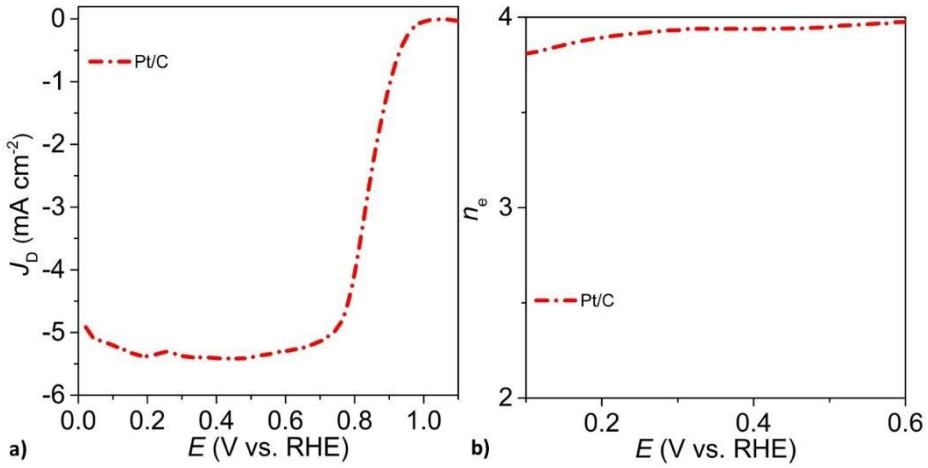


Figure 5S.6 - Disk current density produced (a) at 1600 rpm in O_2-saturated electrolyte (0.1 mol L^{-1} KOH) and number of electrons exchanged during the oxygen reduction reaction for Pt/C.

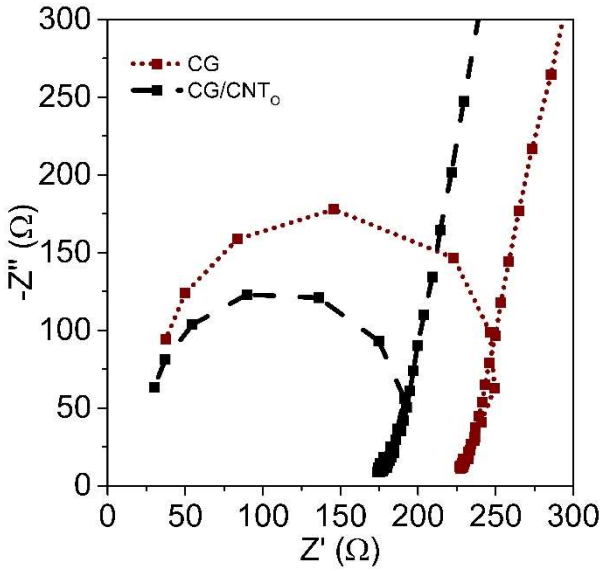


Figure 5S.7 - Nyquist plots for CG and CG/CNT_O obtained by electrochemical impedance spectroscopy.

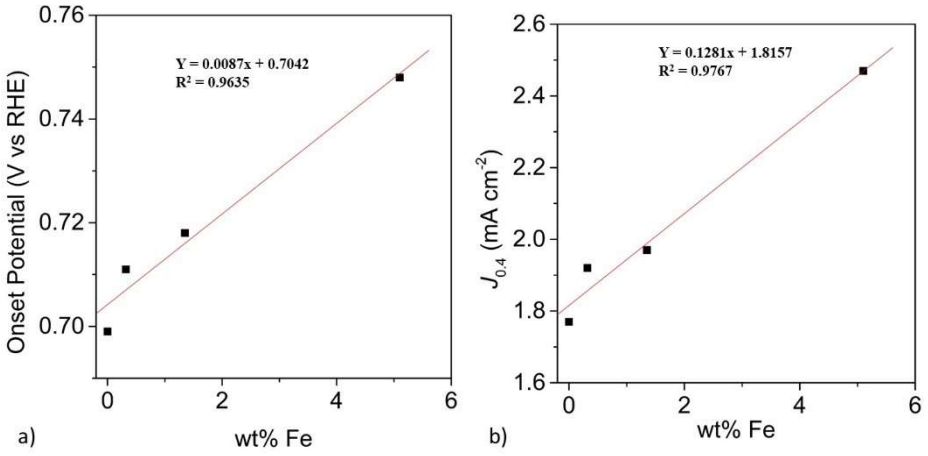


Figure 5S.8 - Onset potential (a) and current density at a potential of 0.4 V (b) obtained from the linear sweep voltammetry curves of Figure 5a (a) for the CG_{XFe} samples versus the percentage of Fe calculated by ICP.

5.6. References

[1] Y. Wang, D.Y.C. Leung, J. Xuan, H. Wang, A review on unitized regenerative fuel cell technologies, part-A: Unitized regenerative proton exchange membrane fuel cells, Renew. Sust. Energ. Rev., 65 (2016) 961-977.
[2] Y. Lv, C. Han, Y. Zhu, T. Zhang, S. Yao, Z. He, L. Dai, L. Wang, Recent advances in metals and metal oxides as catalysts for vanadium redox flow battery: Properties, structures, and perspectives, J. Mater. Sci. Technol., 75 (2021) 96-109.
[3] A. Kirubakaran, S. Jain, R.K. Nema, A review on fuel cell technologies and power electronic interface, Renew. Sust. Energ. Rev., 13 (2009) 2430-2440.
[4] J. Stacy, Y.N. Regmi, B. Leonard, M. Fan, The recent progress and future of oxygen reduction reaction catalysis: A review, Renew. Sust. Energ. Rev., 69 (2017) 401-414.
[5] C. Goswami, K.K. Hazarika, P. Bharali, Transition metal oxide nanocatalysts for oxygen reduction reaction, Mater. Sci. Energ.Technol., 1 (2018) 117-128.
[6] J. Yang, F. Toshimitsu, Z. Yang, T. Fujigaya, N. Nakashima, Pristine carbon nanotube/iron phthalocyanine hybrids with a well-defined nanostructure show excellent efficiency and durability for the oxygen reduction reaction, J. Mater. Chem. A, 5 (2017) 1184-1191.
[7] N. Komba, G. Zhang, Q. Wei, X. Yang, J. Prakash, R. Chenitz, F. Rosei, S. Sun, Iron (II) phthalocyanine/N-doped graphene: A highly efficient non-precious metal catalyst for oxygen reduction, Int. J. Hydrog. Energy, 44 (2019) 18103-18114.
[8] K. Hyun, T. Ueno, G. Panomsuwan, O.L. Li, N. Saito, Heterocarbon nanosheets incorporating iron phthalocyanine for oxygen reduction reaction in both alkaline and acidic media, Phys. Chem. Chem. Phys., 18 (2016) 10856-10863.
[9] S. Han, X. Hu, X. Fang, Y. Zhu, Novel Route to Fe-Based Cathode as an Efficient Bifunctional Catalysts for Rechargeable Zn-Air Battery, Adv. Energy Mater., (2018) 1800955.
[10] H.T. Chung, D.A. Cullen, D. Higgins, B.T. Sneed, E.F. Holby, K.L. More, P. Zelenay, Direct atomic-level insight into the active sites of a high-performance PGM-free ORR catalyst, Science, 357 (2017) 479.
[11] S. Zhao, D.-W. Wang, R. Amal, L. Dai, Carbon-Based Metal-Free Catalysts for Key Reactions Involved in Energy Conversion and Storage, Adv. Mater., 31 (2019) 1801526.
[12] J.L. Figueiredo, Nanostructured porous carbons for electrochemical energy conversion and storage, Surf. Coat. Technol., 350 (2018) 307-312.
[13] Z. Wu, M. Song, J. Wang, X. Liu, Recent Progress in Nitrogen-Doped Metal-Free Electrocatalysts for Oxygen Reduction Reaction, Catalysts, 8 (2018) 196.
[14] J. Wang, H. Wang, Y. Fan, Techno-Economic Challenges of Fuel Cell Commercialization, Engineering, 4 (2018) 352-360.
[15] C. He, S. Sankarasubramanian, I. Matanovic, P. Atanassov, V. Ramani, Understanding the Oxygen Reduction Reaction Activity and Oxidative Stability of Pt Supported on Nb-Doped TiO2, ChemSusChem, 12 (2019) 3468-3480.
[16] K. Lee, L. Zhang, H. Lui, R. Hui, Z. Shi, J. Zhang, Oxygen reduction reaction (ORR) catalyzed by carbon-supported cobalt polypyrrole (Co-PPy/C) electrocatalysts, Electrochim. Acta, 54 (2009) 4704-4711.
[17] R. Paul, Q. Dai, C. Hu, L. Dai, Ten years of carbon-based metal-free electrocatalysts, Carbon Energy, 1 (2019) 19-31.
[18] L. Yan, J. Yu, J. Houston, N. Flores, H. Luo, Biomass derived porous nitrogen doped carbon for electrochemical devices, Green Energy Environ., 2 (2017) 84-99.
[19] A. Jain, R. Balasubramanian, M.P. Srinivasan, Hydrothermal conversion of biomass waste to activated carbon with high porosity: A review, Chemical Engineering Journal, 283 (2016) 789-805.
[20] R. G. Morais, N. Rey-Raap, R. Costa, C. Pereira, A. Guedes, J. L. Figueiredo, M. F. R. Pereira, Hydrothermal Carbon/Carbon Nanotube Composites as Electrocatalysts for the Oxygen Reduction Reaction, J. Compos. Sci., 4 (2020) 1-14.

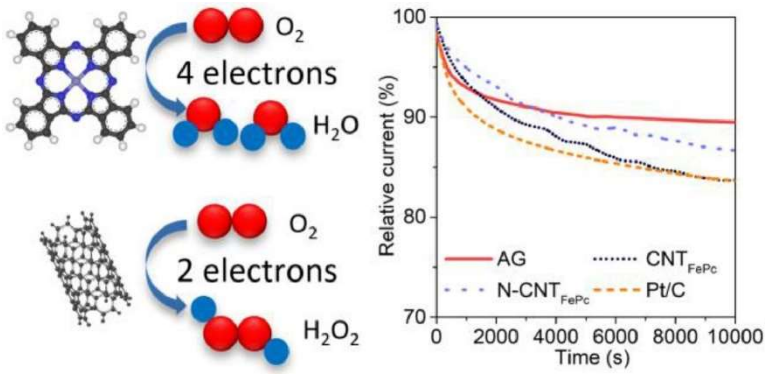
[21] R. G. Morais, N. Rey-Raap, J. L. Figueiredo, M. F.R. Pereira, Glucose-derived carbon materials with tailored properties as electrocatalysts for the oxygen reduction reaction, Beilstein J. Nanotechnol., 10 (2019) 1089-1102.
[22] K.I. John, M.O. Omorogie, Biomass-based hydrothermal carbons for catalysis and environmental cleanup: a review, Green Chem. Lett. Rev., 15 (2022) 162-186.
[23] M. Skorupska, A. Ilnicka, J.P. Lukaszewicz, Successful Manufacturing Protocols of N-Rich Carbon Electrodes Ensuring High ORR Activity: A Review, Processes, 2022.
[24] C. Sathiskumar, S. Ramakrishnan, M. Vinothkannan, A. Rhan Kim, S. Karthikeyan, D.J. Yoo, Nitrogen-Doped Porous Carbon Derived from Biomass Used as Trifunctional Electrocatalyst toward Oxygen Reduction, Oxygen Evolution and Hydrogen Evolution Reactions, Nanomaterials, 10 (2020) 1-17.
[25] E.Y. Choi, D.E. Kim, S.Y. Lee, C.K. Kim, Electrocatalytic activity of nitrogen-doped holey carbon nanotubes in oxygen reduction and evolution reactions and their application in rechargeable zinc–air batteries, Carbon, 166 (2020) 245-255.
[26] A. Liu, M. Ma, X. Zhang, J. Ming, L. Jiang, Y. Li, Y. Zhang, S. Liu, A biomass derived nitrogen doped carbon fibers as efficient catalysts for the oxygen reduction reaction, J. Electroanal. Chem., 824 (2018) 60-66.
[27] D. Barrera, M. Florent, M. Kulko, T. Bandosz, Ultramicropore-influenced mechanism of oxygen electroreduction on metal-free carbon catalysts, J. Mater. Chem. A, 7 (2019).
[28] W. Wang, Q. Jia, S. Mukerjee, S. Chen, Recent Insights into the Oxygen-Reduction Electrocatalysis of Fe/N/C Materials, ACS Catal., 9 (2019) 10126-10141.
[29] Q. Ma, H. Jin, J. Zhu, Z. Li, H. Xu, B. Liu, Z. Zhang, J. Ma, S. Mu, Stabilizing Fe–N–C Catalysts as Model for Oxygen Reduction Reaction, Adv. Sci., 8 (2021) 2102209.
[30] K. Mamtani, D. Jain, A.C. Co, U.S. Ozkan, Nitrogen-Coordinated Iron−Carbon as Efficient Bifunctional Electrocatalysts for the Oxygen Reduction and Oxygen Evolution Reactions in Acidic Media, Energy Fuels, 31 (2017) 6541-6547.
[31] Z. Yan, C. Dai, M. Zhang, X. Lv, X. Zhao, J. Xie, Nitrogen doped porous carbon with iron promotion for oxygen reduction reaction in alkaline and acidic media, Int. J. Hydrog. Energy, 44 (2019) 4090-4101.
[32] Y. Liu, B. Huang, X. Zhang, X. Huang, Z. Xie, In-situ fabrication of nitrogen-doped carbon nanosheets containing highly dispersed single iron atoms for oxygen reduction reaction, J. Power Sources, (2019) 125-133.
[33] A. Abdelwahab, A.A. Farghali, A. Enaiet Allah, Synergy between iron oxide sites and nitrogen-doped carbon xerogel/diamond matrix for boosting the oxygen reduction reaction, Nanoscale Adv., 4 (2022) 837-848.
[34] J. Xia, K. Li, G.-L. Zhao, Electric Field Polarization To Increase Bifunctional Oxygen Electrocatalyst Performance of Nitrogen–Iron Functionalized Carbon Nanomaterials, ACS Appl. Energy Mater., 3 (2020) 1484-1495.
[35] M. Canal-Rodríguez, N. Rey-Raap, J.Á. Menéndez, M.A. Montes-Morán, J.L. Figueiredo, M.F.R. Pereira, A. Arenillas, Effect of porous structure on doping and the catalytic performance of carbon xerogels towards the oxygen reduction reaction, Microporous Mesoporous Mater., 293 (2020) 109811.
[36] R.G. Morais, N. Rey-Raap, J.L. Figueiredo, M.F.R. Pereira, Highly electroactive N–Fe hydrothermal carbons and carbon nanotubes for the oxygen reduction reaction, J. Energy Chem., 50 (2020) 260-270.
[37] H. Ba, C. Duong-Viet, Y. Liu, J.-M. Nhut, P. Granger, M.J. Ledoux, C. Pham-Huu, Nitrogen-doped carbon nanotube spheres as metal-free catalysts for the partial oxidation of H2S, C. R. Chim., 19 (2016) 1303-1309.
[38] R. Kecili, C.M. Hussain, Chapter 4 - Mechanism of Adsorption on Nanomaterials, in: C.M. Hussain (Ed.) Nanomaterials in Chromatography, Elsevier2018, pp. 89-115.

[39] S.-S. Chang, B. Clair, J. Ruelle, J. Beauchene, F. Di Renzo, F. Quignard, G.-J. Zhao, H. Yamamoto, J. Gril, Mesoporosity as a new parameter for understanding tension stress generation in trees, Journal of Experimental Botany, (2009).
[40] S. Yurdakal, C. Garlisi, L. Özcan, M. Bellardita, (Photo)catalyst Characterization Techniques, 2019, pp. 87-152.
[41] J. Bedia, V.M. Monsalvo, J.J. Rodriguez, A.F. Mohedano, Iron catalysts by chemical activation of sewage sludge with FeCl3 for CWPO, Chem. Eng. J., 318 (2017) 224-230.
[42] C. Falco, J.P. Marco-Lozar, D. Salinas-Torres, E. Morallón, D. Cazorla-Amorós, M.M. Titirici, D. Lozano-Castelló, Tailoring the porosity of chemically activated hydrothermal carbons: Influence of the precursor and hydrothermal carbonization temperature, Carbon, 62 (2013) 346-355.
[43] M. Sevilla, A.B. Fuertes, Chemical and Structural Properties of Carbonaceous Products Obtained by Hydrothermal Carbonization of Saccharides, Chem. Eur. J., 15 (2009) 4195-4203.
[44] L. Xiao, M. Schroeder, S. Kluge, A. Balducci, U. Hagemann, C. Schulz, H. Wiggers, Direct self-assembly of Fe2O3/reduced graphene oxide nanocomposite for high-performance lithium-ion batteries, J. Mater. Chem. A, 3 (2015) 11566-11574.
[45] R. Ma, G. Lin, Y. Zhou, Q. Liu, T. Zhang, G. Shan, M. Yang, J. Wang, A review of oxygen reduction mechanisms for metal-free carbon-based electrocatalysts, Npj Comput. Mater., 5 (2019) 78.
[46] E. Haque, A. Zavabeti, N. Uddin, Y. Wang, M.A. Rahim, N. Syed, K. Xu, A. Jannat, F. Haque, B.Y. Zhang, M.A. Shoaib, S. Shamsuddin, M. Nurunnabi, A.I. Minett, J.Z. Ou, A.T. Harris, Deciphering the Role of Quaternary N in O2 Reduction over Controlled N-Doped Carbon Catalysts, Chem. Mater., 32 (2020) 1384-1392.
[47] Y. Peng, H. Liu, Effects of Oxidation by Hydrogen Peroxide on the Structures of Multiwalled Carbon Nanotubes, Ind. Eng. Chem. Res., 45 (2006) 6483-6488.
[48] H. Singh, S. Zhuang, B. Ingis, B.B. Nunna, E.S. Lee, Carbon-based catalysts for oxygen reduction reaction: A review on degradation mechanisms, Carbon, 151 (2019) 160-174.
[49] R.G. Morais, N. Rey-Raap, J.L. Figueiredo, M.F.R. Pereira, Fe, Co, N-doped carbon nanotubes as bifunctional oxygen electrocatalysts, Appl. Surf. Sci., 572 (2022) 151459.

Chapter 6

Highly electroactive N–Fe hydrothermal carbons and carbon nanotubes for the oxygen reduction reaction

R.G. Morais, N. Rey-Raap, J.L. Figueiredo, M.F.R. Pereira, Highly electroactive N–Fe hydrothermal carbons and carbon nanotubes for the oxygen reduction reaction, J. Energy Chem., 50 (2020) 260-270.



Abstract

Glucose-derived carbons were prepared by hydrothermal carbonization of glucose followed by carbonization or activation to obtain carbon materials with different microporosities. These microporous carbons and carbon nanotubes (CNTs) were functionalized with melamine and/or iron(II) phthalocyanine (FePc) following three different methodologies: i) functionalization with melamine via thermal treatment, ii) incorporation of the lowest amount of FePc reported in the literature via incipient wetness impregnation followed by thermal treatment and iii) functionalization with melamine followed by FePc incorporation. The chemical and textural characterization of the prepared materials and their electrochemical assessment allowed to understand the role of microporosity in the incorporation of FePc and its effect on the oxygen reduction reaction (ORR). It was observed that FePc was preferentially incorporated inside the porous structure, especially in samples with more developed microporosity. However, functionalization with melamine modified the textural properties and the surface chemistry, favoring the incorporation of FePc on the surface. Regarding the electrochemical performance, the presence of FePc greatly enhanced the electroactivity of the microporous catalysts. An onset potential of 0.88 V and a four-electron pathway were obtained for glucose-derived carbons, whereas the limiting current densities and kinetic current densities rose by 126% and 222%, respectively, in comparison to the base sample. Notwithstanding, the highest electrochemical activity was observed for the sample prepared with CNTs, due to the synergy between the active metal centers and their highly graphitic carbon structure. The electrochemical parameters of CNT_{FePc} surpass the commercial Pt/C. The half-wave potential is 40 mV higher, the limiting current density increases by 17%, and a negligible production of by-products (< 1%) was observed.

6.1. Introduction

The oxygen reduction reaction (ORR) takes places in several electrochemical systems such as fuel cells and metal-air batteries [1-7]. The main problem of this reaction is its slow kinetics, that hinders the overall performance of these electrochemical devices [2-5, 7-10]. Platinum-derived electrocatalysts are commonly used to overcome these limitations and obtain faster reaction kinetics. However, platinum is a scarce material which represents very high costs towards the overall price of the electrochemical cell [2, 6, 8-10]. Therefore, it is urgent to develop new green and economical materials that optimize the ORR, paving the way towards a sustainable future. Carbon materials exhibit a high versatility and competitive price, which make them a serious contender to replace Pt. In fact, one of the major advantages of carbon materials is the possibility to tune their chemical and textural properties, enhancing their electroactivity towards the ORR [1, 11-14].

One of the most frequently employed methods to tune the chemical properties of carbon materials is the incorporation of heteroatoms, which changes their surface chemistry and forms new active sites. Among all the heteroatoms, nitrogen is the most studied as it promotes the mechanism of the reaction to the four-electron pathway, reducing oxygen directly without the generation of sub-products [12, 15, 16]. However, depending on the nature of the carbon material, the incorporation of nitrogen functionalities does not always result in a competitive material against Pt-based electrocatalysts. Therefore, further modifications such as the incorporation of transition metals (cobalt, manganese, nickel or iron) are crucial for the development of new electrocatalysts [8, 10, 16-19]. Iron offers interesting advantages due to its abundance, economic competitiveness and selectivity towards ORR compared to the other transition metals [8, 10]. Although iron promotes the formation of more active sites and increases the electrical conductivity of electrocatalysts towards ORR [20], the single incorporation of iron in a carbon matrix may result in materials with lower electrochemical performance than Pt/C. Therefore, the combination of heteroatoms and transition metals seems to be essential to improve the electrocatalytic activity of carbon materials. The combination of nitrogen and iron has been applied to different carbons supports such as activated carbons [21, 22], porous carbons [23, 24], carbon nanosheets [8, 25], carbon black [24, 26, 27], graphene [2, 28],

carbon nanotubes [24, 29-31] and black pearls [29, 30]. The most commonly used methodologies to incorporate both nitrogen and iron use either two precursors, one that contains nitrogen and another that encloses iron [23, 25], or one precursor that contains both elements [28, 32-35]. Recently, the incorporation of Fe-N_4 complexes, such as porphyrins and metal-centered phthalocyanines (Pc), has emerged as an interesting strategy to achieve high electrochemical activities in ORR [3, 17, 21, 36]. Among these complexes, iron Pcs are preferred due to their higher availability and lower costs in comparison to porphyrins [37]. Although several studies have already been published focused on the incorporation of iron(II) phthalocyanine (FePc) into carbon structures and its effect on the electrochemical performance towards ORR, there are still some aspects that should be addressed, as most of the published studies either use a large quantity of FePc for the preparation of the catalyst [21, 22, 28, 29, 32] or apply a high number of steps to reach the final catalyst [26, 29, 30]. These two factors lead to high fabrication costs, which should be minimized in case of a scaled-up production. Furthermore, the effect of porosity regarding the incorporation of FePc in porous carbons and, consequently, its effect towards the ORR, has not been reported in the literature.

Herein, the main objective of this study is to prepare electrocatalysts from glucose-derived carbons and carbon nanotubes (CNTs) with high electrocatalytic activity towards ORR. Glucose-derived carbons were prepared by hydrothermal carbonization followed by carbonization or activation to obtain materials with different degrees of microporosity. Nitrogen functionalities and FePc were incorporated into the glucose-derived carbons and CNTs. A very low ratio of FePc:carbon material was used to minimize the electrocatalyst's production cost. The influence of microporosity on the incorporation of FePc and the effect of the chemical properties on the ORR were studied. The incorporation of a small amount of FePc on the glucose-derived carbons and CNTs resulted in a remarkable improvement, showing the effectiveness of the functionalization method in converting green biomass-derived carbons into high-value electrocatalysts with outstanding electrochemical activities towards ORR.

6.2. Experimental

6.2.1. Preparation of electrocatalysts

Different carbon supports were used for the preparation of the electrocatalysts: carbonized and activated glucose-derived carbon materials and purified carbon nanotubes. The carbonized and activated glucose-derived carbons were prepared from an initial mixture of glucose (HiMedia, > 99%) and deionized water (produced by filtration through inverse osmose in a Panice equipment) in a 1:6 mass ratio. The mixture was sonicated for 30 min, closed in a Teflon-lined stainless steel autoclave and underwent hydrothermal carbonization at 180 °C for 12 h. The prepared material was then washed with deionized water and dried at 80 °C overnight. The dried material was carbonized at 800 °C under N_2 atmosphere for 2 h or activated under a CO_2 flow of 80 cm^3 min^{-1} g^{-1} at 900 °C for 4 h. CNTs were purified following the methodology described elsewhere [38]. Briefly, CNTs were refluxed in a 1:1 ratio solution of sulfuric acid and distilled water at 140 °C for 4 h to remove impurities, washed with hot distilled water until neutral pH was achieved, and dried at 100 °C for 1 day.

The carbonized (CG) and activated (AG) hydrothermal carbons and the purified carbon nanotubes (CNT) were then modified by introducing nitrogen and/or iron in the carbon structure following three different methodologies: i) nitrogen functionalization using melamine (Sigma-Aldrich, ≥ 99%) as nitrogen precursor, ii) incorporation of iron(II) phthalocyanine (FePc, Sigma-Aldrich, 90%) into the carbon structure by the incipient wetness impregnation method, and iii) nitrogen functionalization followed by the incorporation of FePc. The nitrogen functionalization was performed by mixing the carbon material with melamine (400 mg melamine per 600 mg carbon material), followed by a subsequent thermal treatment under N_2 atmosphere at 600 °C for 2 h to decompose the nitrogen precursor and to incorporate the nitrogen atoms into the carbon structure. For the incipient wetness impregnation, a certain amount of FePc complex was dissolved in ethanol and added dropwise to the carbon material under sonication. The impregnated sample was kept under sonication for 30 min and dried at 80 °C overnight. The dried material underwent a subsequent thermal treatment in an N_2 atmosphere at a selected temperature for 2 h. In order to assess the optimal amount of the FePc precursor and the

temperature to be employed, different carbonized samples were prepared using two different quantities of FePc (incorporation of 50 mg and 100 mg of FePc into 1 g of carbon) and two different temperatures (500 ºC and 800 ºC). The optimum amount of FePc (50 mg) and temperature (500 ºC) were selected according to the electrochemical results shown in the supporting information (Figure 6S.1). Samples doped with nitrogen were designated N-X, the samples with FePc were represented by X_{FePc} and samples prepared with both precursors were labeled N-X_{FePc}, where X can assume the form of CG for carbonized samples, AG for activated samples and CNT for carbon nanotubes.

6.2.2. Textural and chemical characterization

The textural characterization of the prepared materials was carried out by N_2 adsorption at -196 °C performed in a Quantachrome Autosorb iQ automated gas sorption analyzer. Prior to the analysis, all samples were degassed under vacuum for 12 h at 150 °C. The Brunauer-Emmett-Teller (BET) equation was used to calculate the specific surface area (S_{BET}), the total pore volume (V_p) was calculated as the volume of nitrogen adsorbed at the saturation point (relative pressure of 0.99), the micropore volume (V_{micro}) was determined by the t-plot method and the pore size distribution was obtained by applying the Quenched Solid Density Functional Theory (QSDFT). The chemical composition of the carbon materials was determined by elemental analysis. Carbon, hydrogen and nitrogen (C, H and N) contents were determined using a Vario Micro Cube Analyzer (Elementar GmbH), in which the sample underwent combustion at 1050 °C, whereas the oxygen content was obtained in a Rapid Oxy Cube Analyzer (Elementar GmbH), by pyrolysis at 1450 °C. The quantification of the metal loading was performed by inductively coupled plasma (ICP) emission spectrometry. The analyzes were carried out in a Perkin Elmer Optima 4300 using an optic with Echelle polychromator. The surface chemical composition of the samples was studied by X-ray photoelectron spectroscopy (XPS). The analyzes were performed in a Kratos AXIS Ultra HAS spectrometer using a monochromatic Al Kα radiation (1486.7 eV) at 15 kV (90 W) in fixed analyzer transmission mode. The morphology of the samples and the elemental mapping distribution were evaluated by scanning electron microscopy (SEM) and energy-dispersive spectroscopy (EDS) using a Nova NanoSEM 200 (FEI Company). The samples powders were previously attached to an aluminum pin using conductive carbon

double-sided adhesive tape. An Everhart-Thornley detector was used as a secondary detector during SEM analysis and a Si(Li) detector was used for EDS and mapping analysis.

6.2.3. Electrochemical characterization

The electrochemical characterization was performed in a PGSTAT 302N potentiostat/galvanostat by using a three-electrode cell configuration. A glassy carbon rod and an Ag/AgCl (KCl 3 mol L^{-1}) electrode were used as counter and reference electrode, respectively. Working electrodes were prepared by deposition of a prepared solution of the carbon samples on a glassy carbon rotating disk electrode (3 mm of diameter, Metrohm). These solutions were obtained by dispersing 1 mg of the carbon sample in a solution containing 96 µL of Nafion (5 wt% in lower aliphatic alcohols and water, Sigma-Aldrich), 142 µL of ethanol (≥ 99.5%, VWR Chemicals) and 220 µL of ultrapure water (Milipore). The solution was sonicated for at least 30 min until a homogeneous dispersion was obtained prior to deposition. The mass loading of all samples was ca. 0.1 mg cm^{-2}. The rotations of the working electrode were adjusted by a rotation speed controller, according to the assessment performed. All the electrochemical experiments were carried out at room temperature in a 0.1 mol L^{-1} KOH solution saturated with N_2 or O_2 for 30 min before performing cyclic voltammetry (CV) and linear sweep voltammetry (LSV) tests. The CV measurements were accomplished at a scan rate of 5, 20, 60 and 100 mV s^{-1} and the LSV at a scan rate of 5 mV s^{-1} with a rotation speed range from 400 to 3000 rpm, both within a -0.05 V to 1.1 V potential range (vs RHE). The experimental current was determined by subtracting the current obtained from the electrolyte saturated with N_2 from the current measured in the O_2-saturated electrolyte. Different electrochemical parameters were evaluated from the LSV data: onset potential (E_{onset}), half-wave potential ($E_{1/2}$), limiting current density (J_L) and kinetic current density (J_K). E_{onset} was determined at a current density of 0.1 mA cm^{-2}. $E_{1/2}$ was calculated from the derivative of the current-potential curve. The derivative curve, assuming an ideal sigmoid, exhibits a maximum value corresponding to half the diffusion-limited current, which is attributed to the $E_{1/2}$ [39]. J_L was considered as the current density measured in the linear sweep voltammograms at 0.15 V. J_K was calculated from the Koutecký-Levich equation:

$$\frac{1}{J} = \frac{1}{J_L} + \frac{1}{J_k} = \frac{1}{B\omega^{\frac{1}{2}}} + \frac{1}{J_k} \quad (6.1)$$

where J is the measured current density (mA cm^{-2}), J_L is the O_2 diffusion-limited current density (mA cm^{-2}), J_K is the kinetic current density (mA cm^{-2}), ω is the electrode rotation rate (rpm) and B represents the Levich constant related to the diffusion limiting current density given by equation 6.2.

$$B = 0.2 n_e F D^{\frac{2}{3}} v^{-\frac{1}{6}} C \quad (6.2)$$

where n_e is the number of electrons exchanged, F is the Faraday constant (96 486 C mol^{-1}), D is the diffusion coefficient of O_2 (1.95 x 10^{-5} cm^2 s^{-1}), v is the kinematic viscosity of the electrolyte (0.008977 cm^2 s^{-1}) and C is the bulk concentration of O_2 (1.15 x 10^{-3} mol L^{-1}).

The percentage of hydrogen peroxide (H_2O_2) produced and the number of electrons transferred during the ORR were measured by using a rotating ring-disk electrode (5 mm of diameter, 24.9% collection efficiency, Methrom) as the working electrode, which was prepared by depositing the solution of the carbon samples on the disk area. The dispersion was prepared as detailed above and the mass loading was fixed at ca. 0.1 mg cm^{-2}. The H_2O_2 percentage and the number of electrons were calculated from the LSV recorded at 1600 rpm by Eq. 6.3 and 6.4, respectively.

$$H_2O_2(\%) = 200 \times \frac{I_R/N}{I_D + I_R/N} \quad (6.3)$$

$$n_e = \frac{4I_D}{I_D + I_R/N} \quad (6.4)$$

where, I_R is the ring current density (mA cm^{-2}), I_D is the disk current density (mA cm^{-2}) and N is the collection efficiency (0.249).

Additionally, the stability of the prepared electrocatalyst was assessed by chronoamperometry, applying a potential of 0.4 V vs RHE for 10000 s.

6.3. Results and discussion

6.3.1. Textural and morphological properties

The nitrogen adsorption-desorption isotherms obtained for the carbonized, activated and CNT samples are presented in Figure 6.1a, 6.1b and 6.1c, respectively. Table 6S.1 shows a summary of the textural parameters obtained by the N_2 adsorption-desorption characterization of the carbon samples.

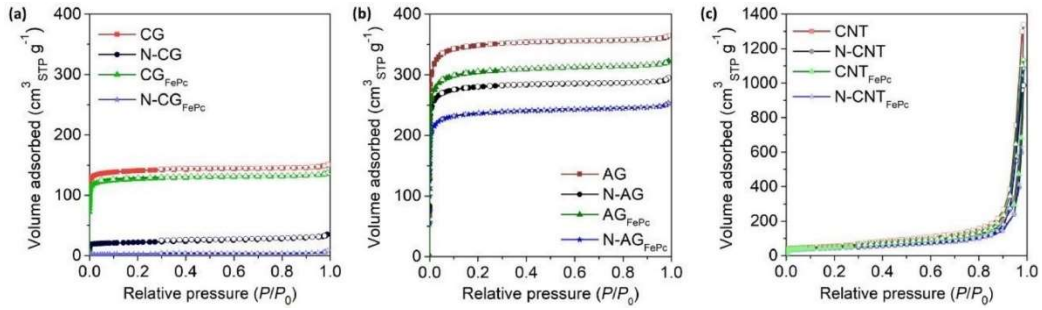


Figure 6.1 - N_2 adsorption-desorption isotherms of carbonized samples (a), activated samples (b) and carbon nanotubes (c).

Carbonized and activated glucose-derived carbons display type I isotherms according to the International Union of Pure and Applied Chemistry (IUPAC) classification, characteristic of microporous materials, whereas carbon nanotube samples display type II isotherms, attributed to multi-layered materials [40]. Regardless of the nature of the carbon support, the functionalization process employed to introduce nitrogen functionalities in the porous materials led to a decrease of the nitrogen adsorbed at low pressures, and hence, to a reduction of the surface area (S_{BET}, Table 6S.1). However, noticeable differences in the loss of surface area are observed between the different carbon supports. In carbonized samples, a reduction of 85% was detected, whereas in activated samples, the surface area decreases 20% due to the incorporation of nitrogen functionalities. These results suggest that the functionalization process blocks some of the pores preventing the access of N_2 to the innermost part of the carbon structure. This effect may be due to the temperature employed to decompose melamine, that may lead to the formation of some carbon nitride clusters [41], which are located close to the pores. The pore size of the carbonized glucose is much lower than that of the activated glucose,

as shown in Figure 6S.2 (0.55 nm and 1.18 nm, respectively), and hence, the clusters formed are probably large enough to block some of the pores, inhibiting the passage of N_2 during the isotherm measurements and highly decreasing the S_{BET}. A schematic description of this hypothesis is presented in Figure 6.2.

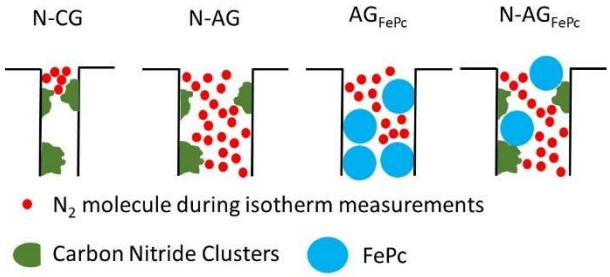


Figure 6.2 - Schematic illustration of the pore blockage and the effect on the incorporation of FePc.

Similar to N-AG, N-CNT loses 28% of its S_{BET} due to the functionalization process. In this case, the decrease is probably due to the incorporation of nitrogen functional groups, which increases the electrostatic affinity between the CNT. This effect is confirmed by the decrease of the volume of N_2 adsorbed at high pressures ($P/P_0 > 0.9$), which suggests that the space within the CNT bundles decreases and corroborates the increase of affinity between the tubes. Similar but less marked trends are observed by the incorporation of FePc (X_{FePc} series). In the carbonized sample (CG_{FePc}), the S_{BET} decreases 10%, which is a much lower value than that observed for N-CG (85%). Although some pore blockage occurs due to the incorporation of FePc, the quantity of iron precursor used was much lower than that of melamine (50 and 667 mg of FePc and melamine for 1 g of carbon material, respectively), which explains the lower impact in the pore blockage. Analogously, the S_{BET} of the activated sample (AG_{FePc}) also suffers a smaller decrease (13%) than that observed for N-AG (20%), due to the incorporation of the iron precursor (Table 6S.1). Similarly, the S_{BET} of CNT_{FePc} decreases by 19%, which is also a lower value compared to the surface area of N-CNT (28%). This difference is, once again, due to the low amount of iron precursor used. The incorporation of FePc in N-X samples resulted in a synergetic effect, involving the effects observed for the N-X and X_{FePc} series. I.e. the surface area of N-X_{FePc} is much lower than that of samples N-X and X_{FePc}, which

demonstrates that both precursors are responsible for the blockage of some pores, and hence, for the decrease of the microporosity.

To better understand the modifications caused by the incorporation of FePc, samples X_{FePc} and N-X_{FePc} were examined by scanning electron microscopy (SEM). The obtained images are displayed in Figure 6.3.

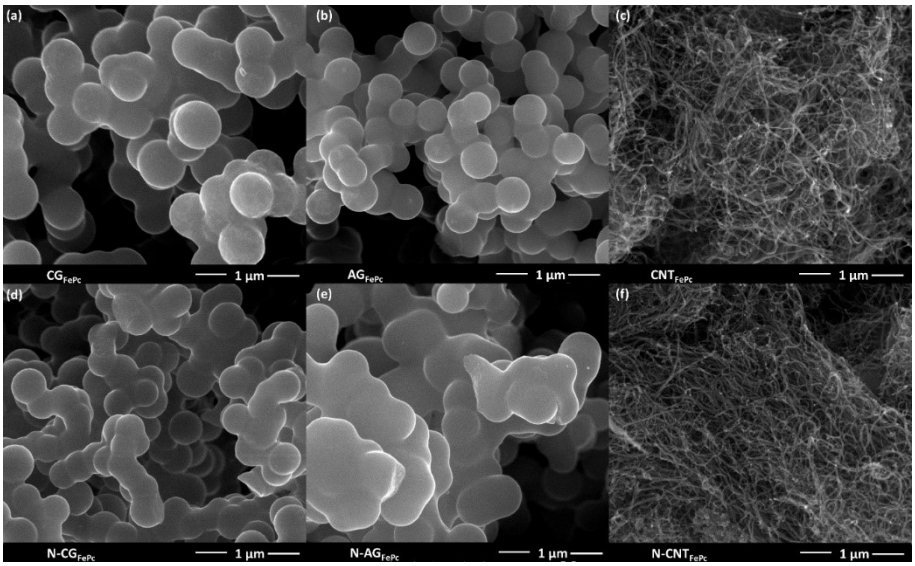


Figure 6.3 - SEM micrographs of CG_{FePc} (a), AG_{FePc} (b), CNT_{FePc} (c), N-CG_{FePc} (d), N-AG_{FePc} (e) and N-CNT_{FePc} (f).

Commonly, the hydrothermal polymerization of glucose and subsequent thermal treatment led to the formation of carbon spheres [14, 42]. The incorporation of FePc in CG and AG does not seem to modify the morphology of the samples, keeping the spherical shape of the particles (Figure 6.3a and 6.3b). Similarly, the SEM image of CNT_{FePc} (Figure 6.3c) exhibits defined carbon nanotubes with no visible differences in the CNT structure. Therefore, the introduction of FePc does not affect the morphology of the samples. The mixing of melamine with the hydrothermal carbons and the subsequent thermal treatment resulted in the agglomeration of the carbon spheres, especially in the activated sample (Figure 6.3e). SEM image of N-AG_{FePc} highly remarks the junction between carbon spheres, which resulted in a material with almost undistinguishable spheres. Conversely, the functionalization with melamine and the

subsequent incorporation of the FePc does not modify the morphology of the CNT (Figure 6.3f).

6.3.2. Chemical properties

The surface chemistry of each carbon support (carbonized and activated glucose-derived carbon and carbon nanotubes) was modified by applying different methodologies: i) nitrogen functionalization, ii) incorporation of iron(II) phthalocyanine (FePc) and iii) nitrogen functionalization followed by FePc incorporation. The bulk chemical composition obtained from the elemental analysis and inductively coupled plasma (ICP), and the surface composition determined by X-ray spectroscopy (XPS) are presented in Table 6.1. Samples CG and AG present very similar chemical compositions with a percentage of oxygen ca. 4 wt%, whereas the CNT exhibits a carbon content higher than 99 wt% with a very low amount of oxygen and hydrogen. As expected, the samples functionalized with nitrogen (N-CG, N-AG and N-CNT) show a noticeable content of nitrogen (6.3 wt%, 6.8 wt% and 9.4 wt%, respectively), demonstrating the successful functionalization of the samples. The amount of nitrogen incorporated is quite high in comparison to the values already reported in the literature for carbon materials functionalized by similar procedures [43, 44]. This effect can be due to the decomposition of melamine into carbon nitrides that results in a high content of nitrogen. The incorporation of FePc in the initial samples results in materials with a low percentage of nitrogen and iron (CG_{FePc}, AG_{FePc} and CNT_{FePc}). These values are in agreement with the theoretical values (0.84 wt% and 0.42 wt% for nitrogen and iron, respectively), demonstrating the successful incorporation of the iron precursor into the different carbon materials. Lastly, the incorporation of FePc in N-X samples results in materials with similar nitrogen contents as those obtained by the functionalization only with melamine, as the amount of nitrogen incorporated due to FePc is really low in comparison with the amount of nitrogen introduced due to melamine.

Table 6.1 - Chemical composition determined by Elemental Analysis, ICP and XPS.

	Bulk Composition (wt%)					**Surface Composition (wt%)**			
	Elemental Analysis				ICP	XPS			
Samples	C	O	N	H	Fe	C	O	N	Fe
CG	94.4	4.0	-	1.6	-	89.4	10.6	-	-
N-CG	85.7	6.6	6.3	1.4	-	86.3	9.4	4.3	-
CG_{FePc}	93.0	4.6	0.8	1.2	0.4	81.8	13.7	2.9	1.6
$N\text{-}CG_{FePc}$	84.7	7.4	6.2	1.4	0.3	72.3	15.2	5.7	1.8
AG	95.0	3.9	-	1.1	-	84.7	15.3	-	-
N-AG	82.9	7.7	6.8	2.6	-	84.7	11.6	3.7	-
AG_{FePc}	94.0	3.5	1.1	0.9	0.5	88.1	11.9	-	-
$N\text{-}AG_{FePc}$	80.5	10.2	6.9	2.1	0.3	87.0	8.0	4.9	0.1
CNT	99.3	0.6	-	0.1	-	98.3	1.7	-	-
N-CNT	89.1	1.1	9.4	0.4	-	91.4	1.3	7.3	-
CNT_{FePc}	98.1	0.5	0.8	0.2	0.4	96.7	6.8	1.8	0.7
$N\text{-}CNT_{FePc}$	89.2	1.3	8.6	0.5	0.4	90.3	1.5	7.7	0.5

However, interesting differences in the percentage of iron are observed. The iron content in the microporous samples N-CG_{FePc} and N-AG_{FePc} is lower than that registered for CG_{FePc} and AG_{FePc}, which could be explained by the previous functionalization process performed to incorporate nitrogen. Samples N-CG and N-AG exhibited lower microporosity (Figure 6.1 and Table 6S.1), and hence, a reduced number of pores. Therefore, the probability of incorporating FePc inside the porous structure is reduced and, consequently, FePc is preferentially located on the surface. However, the surface chemistry was also modified by the functionalization with nitrogen, which could have resulted in a lower affinity between FePc and the carbon structure, and therefore, a lower amount of precursor is incorporated. These differences are not observed between N-CNT_{FePc} and CNT_{FePc} due to the lack of microporosity, resulting in the incorporation of the same iron content (0.4 wt%). The surface chemistry of the prepared material was determined by X-ray spectroscopy (XPS) to evaluate this hypothesis. The results obtained from the surface composition of N-X samples suggest that the microporosity of glucose-derived carbons and the bundles of CNT favor the incorporation of the nitrogen functionalities in the bulk (HTC carbons) or in the free space of CNT bundles, as a decrease of 2 wt% of the nitrogen content (Table 6.1) is observed between the values obtained from elemental analysis and those obtained by XPS. In the case of the samples impregnated with FePc, notorious differences have been observed due to the nature of the carbon support. The percentages of nitrogen and iron of samples CG_{FePc} (2.9 wt% and 1.6 wt%, respectively) and CNT_{FePc} (1.8 wt% and 0.7 wt%, respectively) suggest that the incorporation of FePc occurred mainly at the surface due to a higher content of both elements than the total theoretical content (0.84 wt% and 0.42 wt%, respectively). Conversely, AG_{FePc} presents neither nitrogen nor iron functionalities on the surface, despite ICP analysis confirming the presence of iron in the structure. These results suggest that the FePc precursor is incorporated inside the porous structure, which is corroborated by the decrease of S_{BET} (13%), and hence, is not detected by XPS. On the other hand, N-X_{FePc} samples exhibit an increase of the nitrogen content in comparison to their N-X counterparts, which confirms the incorporation of FePc in the carbon's surface, even for sample N-AG_{FePc}. This effect could be due to the initial functionalization process

that blocks some of the pores of the activated sample, favoring the incorporation of FePc on the surface of the N-AG_{FePc} sample.

The high-resolution XPS spectra in the C 1s, N 1s and Fe 2p regions were deconvoluted to identify the different types of functionalities existing in the surface of the prepared electrocatalysts (Figure 6S.3, 6S.4 and 6S.5, respectively). The deconvolution of the C 1s spectrum of the base samples (CG, AG and CNT) led to the following five main peaks: i) carbon sp^2 (C=C, first peak) at 284.6 ± 0.1 eV, ii) carbon present in ether, alcohol or phenol bonds (C–O) at 285.6 ± 0.2 eV (Peak II), iii) quinone or carbonyl (C=O) 286.8 ± 0.2 eV (Peak III), iv) carboxyl groups (COOH) at 289.0 ± 0.3 eV (Peak IV) and v) the shake-up satellite due to π-π* transitions in aromatic rings (Peak V) at binding energies higher than 290 eV. The appearance of Peaks II, III and IV in CG and AG demonstrates the presence of oxygen, which is in agreement with the results from elemental analysis. However, both samples presented a low contribution of Peak V, which suggests a low contribution of the π-π* transitions. The C 1s spectrum of the CNT corroborates the low content of oxygen obtained by elemental analysis due to the lack of Peak IV and the small contribution of Peaks II and III. Besides, the large contribution of peak V suggests the presence of a high amount of π-π bonds in CNT. The deconvolution of the C 1s spectrum of the N-X samples shows that the intensities of Peaks II and III increase due to the functionalization with nitrogen. These binding energies are also attributed to C-N and C=N bonds. Therefore, the higher intensity of these two peaks suggests the formation of C-N and C=N groups in the N-X samples. Furthermore, the formation of carbon nitrides during the decomposition of melamine may have led to the formation of N=C-(N_2) bonds detected at a binding energy of 288.7 eV, which is overlapped with the peak attributed to COOH (Peak IV). The low oxygen content of N-CNT suggests that the appearance of this peak is not due to formation of COOH, but due to the decomposition of melamine into carbon nitride, which corroborates the assumption made in the elemental analysis about the carbon nanotubes presenting a high percentage of nitrogen due to the formation of carbon nitrides. In the case of the microporous samples, the contribution of this peak is hindered by the high contribution of oxygen functionalities. However, as the functionalization method applied was the same as in N-CNT, and high quantities of

nitrogen were detected (Table 6.1), the contribution of the Peak IV is probably due to both COOH and N=C-(N_2).

The deconvolution of the N 1s region is crucial to further understand the functionalities of the prepared samples and their effect on the ORR mechanism (Figure 6S.4). Generally, the deconvolution of N-doped carbons presents three main peaks representing the following nitrogen functionalities: i) pyridinic nitrogen (N-6) at 398.5 ± 0.2 eV, ii) pyrrolic nitrogen (N-5) at 399.9 ± 0.2 eV and iii) quaternary nitrogen (N-Q) at 401.0 ± 0.2 eV. The incorporation of nitrogen using melamine allows the formation of these three main functionalities. Furthermore, a fourth peak was observed at 405.0 ± 0.2 eV in samples N-CNT and N-CNT_{FePc}, corresponding to C=N-C in carbon nitrides, corroborating the previous hypothesis. Additionally, the peak corresponding to Fe-N_x bonds is ascribed to similar binding energy as that of the N-5 peak, which results in an overlap of both peaks [3, 31]. Therefore, in the X_{FePc} and N-X_{FePc} series, the pyrrolic peak will also include the contribution of Fe-N_x bonds. The relative content of each nitrogen functionality is presented in Figure 6.4.

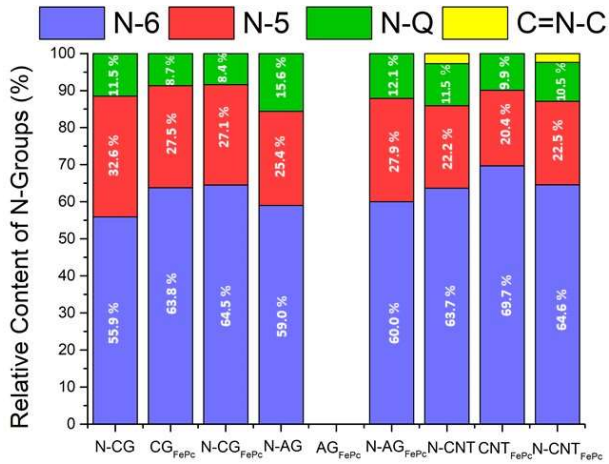


Figure 6.4 - Relative content of each nitrogen functionality in each carbon sample functionalized with melamine and/or that incorporated FePc.

The relative content of N-6 in N-X samples increases with the degree of graphitization of the initial sample (CG < AG < CNT). Besides, a low relative content of N-Q is observed, due to the low temperature employed for the functionalization [45, 46]. The

incorporation of FePc results in materials with different nitrogen functionalities. In CG_{FePc} and CNT_{FePc}, the peaks attributed to N-6 and N-5 groups appear due to the presence of the FePc (the iron complex is mainly composed of 90.5% of N-6 and 9.5% of N-5, as shown in the deconvolution of the N 1s spectra presented in Figure 6S.6). Besides, the iron precursor reacts with the carbon structure generating N-Q groups due to dehydrogenation of pyridinic nitrogen followed by an atomic rearrangement [47]. On the other hand, the nitrogen functionalities were not detected in sample AG_{FePc}. As explained before, FePc is probably located in the interior of the porous structure (Figure 6.2) and, therefore, is not detected by XPS. Similar to the samples functionalized with nitrogen (N-X series), the incorporation of FePc in N-X samples results in materials with the three nitrogen functionalities (N-6, N-5 and N-Q). Besides, the amount of the N-6 group is higher than that present in the N-X samples due to the presence of the nitrogen functionalities attributed to FePc.

The deconvolution of the Fe 2p spectrum of samples CG_{FePc} and N-CG_{FePc} resulted in two different peaks and their respective spin-orbit splitting at + 13.1 eV: i) Fe^{2+} at 710.4 eV and ii) Fe^{3+} at 712.3 ± 0.1 eV (Figure 6S.5) [48]. These results demonstrate the coexistence of both Fe^{2+} and Fe^{3+} species on the carbon structure. Samples CNT_{FePc} and N-CNT_{FePc} exhibited the same two peaks but at lower binding energies, 709.1 eV and 711.0 eV, respectively, due to the different carbon structure of CNT. To further assess the successful incorporation of FePc in the carbon structures, EDS and elemental mapping measurements were performed. All the samples containing FePc presented an iron content between 1.4 wt% and 1.9 wt%. Besides, the mapping images of N-CG_{FePc} and N-CNT_{FePc} (Figure 6S.7), demonstrate that iron is homogeneously dispersed across the mapping region.

6.3.3. Electrochemical assessments

The cyclic voltammograms (CV) of carbonized, activated and CNT samples recorded in an N_2-saturated 0.1 mol L^{-1} KOH electrolyte at 5 mV s^{-1} scan rate are displayed in Figure 6.5a, 6.5b and 6.5c.

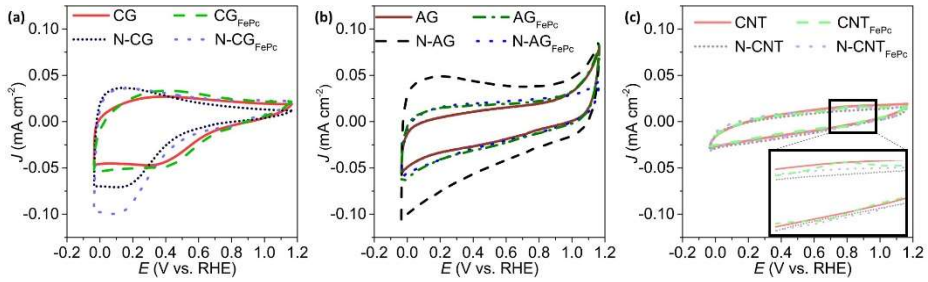


Figure 6.5 - N_2-saturated cyclic voltammograms for carbonized samples (a), activated samples (b) and CNTs (c) in 0.1 mol L^{-1} KOH electrolyte at 5 mV s^{-1}.

The voltammograms of the carbonized (CG) and activated (AG) samples display similar intensities. However, interesting differences in the shape of the CV are observed, which could be due to the different textural properties between CG and AG. Sample CG has lower microporosity than AG, which results in a slower diffusion of the electrolyte, and consequently, in the appearance of a plateau at potentials lower than 0.35 V. Conversely, the voltammograms of the CNT series exhibit remarkably low current densities (Figure 6.5c), indicating that the electrocatalytic activity is almost inexistent under these conditions. However, it should be noted in the voltammogram of sample CNT_{FePc} (Figure 6.5c) the appearance of two very small peaks, one reduction peak and one oxidation peak at 0.78 V and 0.83 V, respectively. In order to further evaluate these peaks, cyclic voltammetry tests at a higher scan rate (100 mV s^{-1}) have been performed (Figure 6S.8). In this case, two reduction and two oxidation peaks are identified. The reduction peak at lower potentials (0.23 V) can be associated with the reduction processes within the Pc ring, whereas the reduction peak at higher potentials (0.78 V) may be caused by the redox pair Fe(III)/Fe(II) [4, 34]. The appearance of these peaks only in the sample CNT_{FePc} (the CV of CG_{FePc} and AG_{FePc} does not exhibit any similar peak as shown in Figure 6S.8) can be explained by the different behavior of the electron transport mechanism between glucose-derived carbons and CNT. Although FePc presents low electrical conductivity [24, 49], the neighboring of the material in which the iron is incorporated is crucial to determine the electroactivity of the metal complex. FePc achieves high current densities in the presence of π-electron systems in carbon materials, which are responsible for increasing the coupling of electrons around FePc [34]. Therefore, the low content of π-π* transitions in glucose-derived samples detected by XPS does not favor the electron

coupling of FePc, and hence, the peaks attributed to the redox pair Fe(III)/Fe(II) are not detected. Conversely, in CNT_{FePc}, the highly graphitic carbon structure with a significant π-π system favors the appearance of the redox reactions, and hence, the peaks attributed to the iron are observed. Notwithstanding, despite CNT showing these peaks attributed to the redox pair of iron, it can be concluded that, when the electrolyte was saturated with N_2, all the electrocatalysts prepared exhibited featureless profiles (Figure 6.5). Therefore, in the case in which the electrolyte was saturated with O_2, the appearance of any significant peaks would be related to the oxygen reduction reaction (Figure 6S.9). In this case, all samples displayed one reduction peak that is not observed in N_2-saturated media, thus confirming the electrocatalytic activity of the electrocatalysts towards the ORR. To further assess the performance of the prepared carbon materials, linear sweep voltammetry was performed and the formation of H_2O_2 was calculated. Linear sweep voltammograms of carbonized, activated and CNT samples recorded in an O_2-saturated 0.1 mol L^{-1} KOH electrolyte at 1600 rpm are represented in Figure 6a, 6b and 6c, respectively, whereas the formation of H_2O_2 is represented in Figure 6d, 6e and 6f, respectively. The onset potential, half-wave potential, limiting current density, kinetic current density, by-products formation and number of electrons exchanged for each electrocatalyst are presented in Table 6.2.

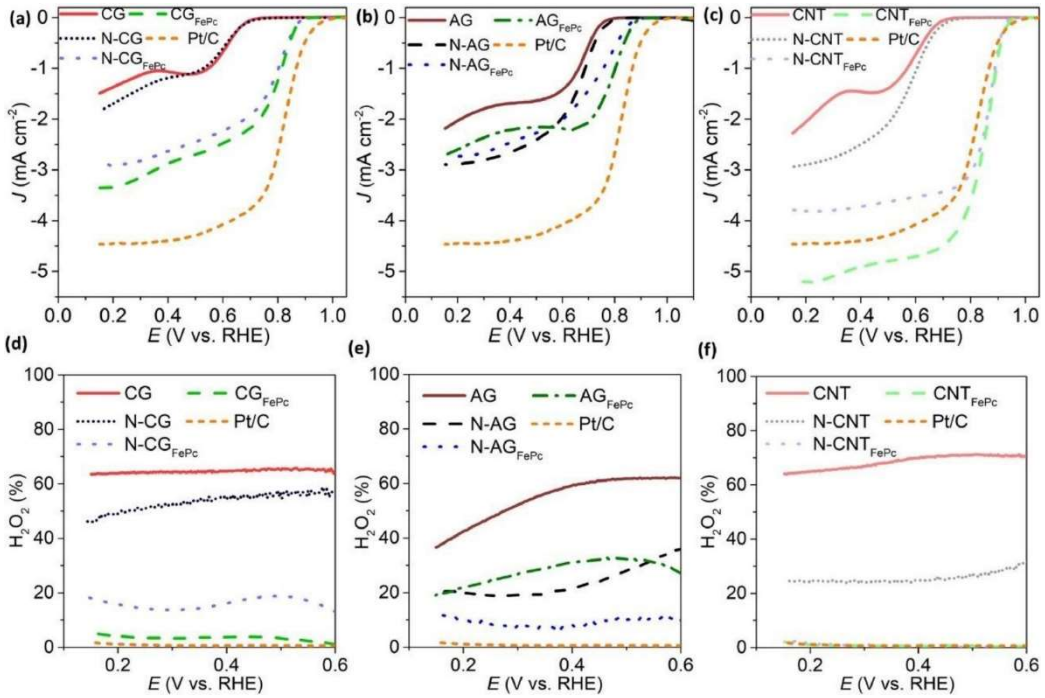


Figure 6.6 - Linear sweep voltammetry recorded in an O_2-saturated 0.1 mol L^{-1} KOH electrolyte at 1600 rpm for carbonized samples (a), activated samples (b) and CNTs (c) and the production of hydrogen peroxide for carbonized samples (d), activated samples (e) and CNTs (f).

Table 6.2 - Onset potential (E_{onset}), half-wave potential ($E_{1/2}$), limiting current density (J_L), kinetic current density (J_K), hydrogen peroxide (H_2O_2) formation and the number of electrons exchanged (n_e) for the prepared electrocatalysts and the commercial Pt/C catalyst.

Samples	E_{onset} (V)	$E_{1/2}$ (V)	J_L (mA cm^{-2})	J_K (mA cm^{-2})[a]	H_2O_2 (%)[a]	Electrons exchanged (n_e)[a]
CG	0.68	0.61	1.49	1.84	65	2.7
N-CG	0.69	0.61	1.84	1.80	54	3.1
CG_{FePc}	0.88	0.82	3.36	5.92	4	3.9
N-CG_{FePc}	0.87	0.82	2.90	6.19	16	3.7
AG	0.80	0.73	2.62	9.07	59	2.8
N-AG	0.78	0.69	2.89	6.78	22	3.6
AG_{FePc}	0.88	0.81	2.71	5.46	31	3.4
N-AG_{FePc}	0.86	0.79	2.70	5.20	8	3.8
CNT	0.69	0.60	2.27	3.15	70	2.6
N-CNT	0.71	0.61	2.94	5.52	25	3.5
CNT_{FePc}	0.94	0.87	5.20	30.55	< 1	4.0
N-CNT_{FePc}	0.93	0.88	3.77	15.85	< 1	4.0
Pt/C	0.96	0.83	4.46	17.43	< 1	4.0

[a] calculated at 0.4 V vs RHE

Activated glucose (AG) exhibited the highest electrocatalytic activity towards ORR (higher $E_{onset,}$ $E_{1/2}$, J_L, and J_K (Table 6.2)) among the three base samples (CG, AG and CNT) due to the higher developed porous structure [15]. The electroactivity of base samples solely depends on the carbon structure and its properties. In undoped metal-free porous carbon materials, microporosity plays a crucial role in improving the kinetics of ORR [13, 15]. Microporosity functions as actives centers during ORR due to the strong adsorption potential of O_2 molecules by the small pores, promoting the electrochemical reaction [13, 15]. Therefore, AG exhibits higher electrochemical activity than CG. On the other hand, although CG and CNT present very similar E_{onset} and $E_{1/2}$, CNT provides a much higher J_L and J_K, which can be related to the more graphitic structure of CNT that favors the transportation of electrons, hence rising the current densities observed. The number of electrons exchanged in CG, AG and CNT is closer to 2 electrons than to 4 electrons. These results reveal that O_2 is first reduced to H_2O_2, and then, further reduced to H_2O, which is a two-step reaction (indirect mechanism). As a result, all the base samples exhibit a large formation of H_2O_2 as shown in Figure 6.6d, 6.6e and 6.6f. However, although AG produces a lower amount of H_2O_2 than CG and CNT, the production is not stable in all the potential range applied, whereas the by-product formation in CG and CNT is linear (Figure 6.6d and 6.6f, respectively). Although the results obtained for these three base samples are quite interesting, their electrochemical performance is still far from the performances achieved with the commercial Pt/C catalyst (Table 6.2). Therefore, their properties have been further tailored by the incorporation of nitrogen functionalities and iron.

The incorporation of nitrogen groups in carbon materials by decomposing melamine enhances their electrochemical performance. However, the nature of the carbon material plays a crucial role in the influence of the nitrogen functional groups. The onset potential of N-CG and N-CNT samples increased slightly and the half-wave potential remained almost invariable, whereas in N-AG both E_{onset} and $E_{1/2}$ decrease. These results suggest that not only nitrogen has a little influence over these parameters, but that the microporosity loss in N-AG results in a decrease of these electrochemical variables. Regarding the limiting current density, an increase was observed (23%, 10% and 30% in N-CG, N-AG and N-CNT, respectively), due to the presence of the nitrogen functional

groups that act as active centers towards O_2 reduction. Although the kinetic current density of N-CG remains unchanged in comparison to CG, a remarkable decrease of J_K is observed for N-AG (25%) compared to AG, which demonstrates the effect of microporosity on the reaction kinetics. The kinetic current density increased by 75% in N-CNT, which highlights the importance of nitrogen towards this electrochemical parameter. The number of electrons exchanged in N-X samples is higher than in CG, AG and CNT, due to the presence of the nitrogen functionalities. The presence of quaternary nitrogen results in an electron density movement that enhances O_2 dissociation, whereas N-6 intensifies the bonding of oxygen in nearby carbon atoms [15]. The increase of electrons exchanged to values closer to 4 electrons means that the reaction mechanism is produced via the direct reduction of O_2 to H_2O (a direct mechanism). Therefore, a decrease in the formation of H_2O_2 was observed in N-X samples (Figure 6.6d, 6.6e and 6.6f). However, interesting differences were found in the magnitude of this decrease. The by-product formation of N-CG only decreased by 9% in comparison to CG, whereas the production of H_2O_2 decreased by 30% and 45% in N-AG and N-CNT, respectively, in comparison to their respective base samples. The lower decrease in N-CG can be explained by the lower electroactivity of CG and the lower incorporation of N-6 functionalities (55.9%), which has been reported to play a crucial role in ORR [50, 51]. The higher amount of N-6 groups in N-AG and N-CNT (59.0% and 63.7%, respectively), gives rise to a lower amount of by-products. In addition, it should be highlighted that the reaction mechanism for N-AG and N-CNT is very close to the four-electron pathway and the formation of by-products is lower than 25%, which is quite close to the value obtained for the Pt/C electrocatalyst.

The incorporation of FePc in the base carbon materials greatly enhanced their electrochemical performance. However, although FePc complexes may act as active centers towards ORR [30, 33], the nature of the carbon supports played a crucial role in the overall effects that FePc may have during the electrochemical assessment. The incorporation of FePc in CG (CG_{FePc}) increased the onset potential and half-wave potential by 200 mV and 210 mV, respectively, in comparison to CG, and the limiting current density and kinetic current density by 126% and 222%, respectively. Additionally, the number of electrons exchanged is close to 4 (3.9 electrons) and the by-

product formation is almost negligible (4%). Therefore, CG_{FePc} presents remarkable results with very impressive values of E_{onset} and $E_{1/2}$ and a reaction mechanism close to that of Pt/C. The incorporation of FePc in AG (AG_{FePc}) increased the onset potential and half-wave potential from 0.80 V and 0.73 V to 0.88 V and 0.81 V, respectively. Furthermore, the limiting current density increased by 3% and the kinetic current density decreased by 21% in comparison to AG. Additionally, the number of electrons exchanged is closer to 4 electrons (3.4 electrons) and the production of by-product is much lower (31%) than AG, demonstrating the beneficial effect of FePc to achieve a direct reaction mechanism. Although the incorporation of FePc into the glucose-derived carbons results in a high enhancement of their electrochemical performance, some interesting differences are observed. Regardless of microporosity, sample CG_{FePc} and AG_{FePc} present very similar E_{onset} and $E_{1/2}$, which suggests that the increase of these parameters is due to the presence of FePc. However, J_L and J_K are higher in CG_{FePc}, and the reaction mechanism is also closer to the direct pathway. These results indicate that the incorporation of FePc inside the porous structure (AG_{FePc}) or on the surface (CG_{FePc}) of the carbon materials modifies their electrochemical activities. FePc located on the surface adsorbs O_2 and reduces oxygen in a direct pathway (4 electrons, as observed in CG_{FePc}), whereas FePc located in the bulk requires O_2 to diffuse into the pores to be adsorbed by FePc. This diffusion hinders the overall reduction of oxygen at the FePc active centers, which results in a reaction mechanism with contributions from the reduction of oxygen in the activated carbon surface (two-electron pathway) and from FePc (four-electron pathway), decreasing the values of J_L and J_K. This hypothesis is also corroborated by the number of electrons exchanged, which shows a value of 3.4 for sample AG_{FePc}, average between the value obtained for AG (2.8 electrons) and the ideal 4-electron mechanism. The incorporation of FePc in CNT (CNT_{FePc}) displayed similar but more marked trends than CG_{FePc}. The onset potential and half-wave potentials increased to 0.94 V and 0.87 V, respectively, and J_L and J_K increased by 129% and 870%, respectively, in comparison to CNT. Similarly to the microporous samples, the onset potential of CNT_{FePc} increases due to the presence of FePc. Besides, the J_K increases due to the FePc, as microporosity is not a determining factor in CNTs. The reaction mechanism in CNT_{FePc} shifted to the direct pathway with negligible formation of by-products (< 1%). The lack of porosity favored the incorporation of FePc on the carbon's surface leading to a higher number of available

active sites. Therefore, the impressive electrocatalytic activity of CNT_{FePc} can be explained by the FePc active sites and the higher electrical conductivity of CNT in comparison to glucose-derived carbon materials [14]. Besides, CNT_{FePc} presents a $E_{1/2}$ 40 mV higher than Pt/C, and a higher limiting current density and kinetic current density of 17% and 75%, respectively.

The incorporation of FePc within N-X samples also resulted in highly electrochemically active electrocatalysts. The incorporation of FePc in N-CG (N-CG_{FePc}) increased the E_{onset} and $E_{1/2}$ from 0.69 V to 0.87 V and from 0.61 V to 0.82 V, respectively, whereas J_L and J_K increased by 58% and 244%, respectively, in comparison to N-CG. Furthermore, the number of electrons exchanged is close to 4 (3.7 electrons) and the amount of H_2O_2 determined is 16%, indicating an almost completely direct mechanism. The E_{onset}, $E_{1/2}$ and number of electrons exchanged increased to values closer to those obtained for the Pt/C electrocatalyst, demonstrating that N-CG_{FePc} is a promising electrocatalyst for the ORR. The incorporation of FePc in N-AG (N-AG_{FePc}) increased the onset potential by 80 mV and the half-wave potential by 100 mV, in comparison to N-AG. The limiting current density and kinetic current density slightly decreased, due to a decrease of microporosity (Table 6S.1), demonstrating the importance of keeping the microporosity to achieve high current densities in highly microporous materials. Besides, the reaction mechanism shifted to an almost entirely direct mechanism (3.8 electrons and 8% production of H_2O_2), due to the presence of FePc on the surface of the activated carbon, in comparison to AG_{FePc}. However, it should be highlighted that, in general terms, the electrochemical activities of N-X_{FePc} are lower than those of X_{FePc}. This can be explained by the fact that the functionalization with melamine in glucose-derived samples led to smaller incorporation of FePc, and hence, to a lower electroactivity. The incorporation of FePc in N-CNT led to an increase of E_{onset} and $E_{1/2}$ from 0.71 V to 0.93 V and from 0.61 V to 0.88 V, respectively, and an increase of the J_L and J_K of 28% and 187%, respectively, in comparison to N-CNT. The reaction pathway shifted to a direct mechanism with negligible formation of by-products (< 1%). These results suggest that the incorporation of FePc active sites on the surface of highly graphitic structures further enhances the electroactivity. However, it should be noted that the electroactivity of this sample (N-CNT_{FePc}) is lower than that of CNT_{FePc}. Although both samples exhibit similar iron

content, two very different active sites are present in N-CNT_{FePc}, those from N-groups and those from FePc. Among these two active centers, FePc is much more active, and hence, the less efficient O_2 adsorption, dissociation and desorption over N active centers hindered the overall current densities, resulting in a material with lower J_L and J_K (N-CNT_{FePc}).

To further evaluate the electrochemical performance of the prepared carbon materials, chronoamperometry measurements were performed by applying a potential of 0.4 V (vs RHE) during 10000 s. The results obtained are shown in Figure 6.7. These experiments allow to determine the retention of the current density of each material over time at the selected potential, to assess the electrocatalysts' stability. The stability tests performed for the base samples (CG, AG and CNT) demonstrated that CG and CNT have low stabilities (34.1% and 59.0%, respectively), whereas AG presents very high stability throughout all the experiment (89.5%). These results can be related to the activation process that gave rise to a chemically stable material, which chemically resists the possible attack produced by the basic medium [52]. In addition, AG showed higher stability in its current density than Pt/C (83.6%) at 0.4 V vs RHE, which reflects the electrocatalyst potential for high performances during long-term use.

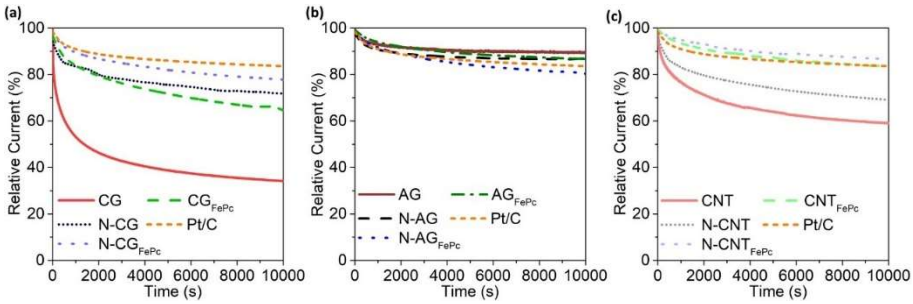


Figure 6.7 - Chronoamperometry measurements for carbonized samples (a), activated samples (b) and CNTs (c) applying 0.4 V during 10000 s at 1600 rpm in 0.1 mol L^{-1} KOH electrolyte.

The incorporation of nitrogen functional groups increases the stability of CG and CNT, with higher impact over the carbonized sample (increase by 37.6% and 11.9% for N-CG and N-CNT, respectively), whereas a slight decrease is observed for sample N-AG (2.6%). Nitrogen functionalities act as active sites in ORR, and therefore, are also pivotal

to the stability of the electrocatalysts. In fact, the deterioration of these functional groups could result in a decrease in the measured current density over time. However, the use of an alkaline medium avoids the protonation of the N-6 functional groups [36], which results in the retention of N-6's activity. Furthermore, the existence of strong bonds in N-Q functional groups also favors the retention of the current density [23, 36]. Therefore, the stability of samples N-CG and N-CNT is higher than that of CG and CNT. However, this effect is not observed for the activated sample. The decrease in the stability of the N-doped activated sample may be due to the high stability of the initial sample (AG), which could be caused by its high microporosity. Although nitrogen functionalities are important to achieve higher current densities and retention of current density over time, as observed in N-CG and N-CNT, the decrease of retention due to the loss of microporosity in N-AG overlaps the enhancements due to the presence of nitrogen functional groups. Nonetheless, N-AG presents higher retention of current density over time (86.9%) than the commercial catalyst (83.6%), demonstrating its potential for applications that require long operation times. The introduction of the FePc complex led to the same trend as that observed for the samples N-X. However, the use of different carbon supports resulted in stability modifications with different magnitudes. Although the stability of both CG and CNT increased with the incorporation of FePc (30.6% and 24.8%, respectively), an interesting difference is observed. The stability of CG grasps the 65% current density retention, whereas CNT_{FePc} is able to retain 83.6% of the initial current density. This difference of almost 20% may be explained by the higher affinity of FePc to the CNT structure (π electron system) than to the CG structure, resulting in stronger bonds. Additionally, the presence of strong N-Q bonds in CNT_{FePc} (Figure 6.4) may play a crucial role in the stability enhancement. The incorporation of FePc in the activated sample (AG_{FePc}) led to a similar decrease of the current density retention (3.1%) such as N-AG (2.6%), further corroborating that the highly stable activated structure due to microporosity plays a major role to achieve a high retention of the current density. Similarly to N-AG, AG_{FePc} also exhibits higher stability (86.4%) than Pt/C (83.6%), confirming the potential of this sample for long-term applications. The incorporation of FePc in the N-X series also led to an increase of the stability of $N\text{-}CG_{FePc}$ and $N\text{-}CNT_{FePc}$, to 77.8% and 86.7%, respectively. The retention of current density displayed by $N\text{-}CNT_{FePc}$ (Figure 6.7) is much higher than that of Pt/C, which demonstrates the importance

of combining nitrogen functionalities and iron particles to achieve higher stabilities (the stability of N-CNT_{FePc} is 2.9% higher than that of CNT_{FePc}). N-AG_{FePc} also showed a conjugation of the decreases observed in N-AG and AG_{FePc}, achieving stability of 80.5% after 10000 seconds. This result further indicates the relevance of microporosity to achieve higher retention of current densities, as the gradual decrease of the surface area in the activated samples led to a decrease of the electrocatalysts' stabilities. Therefore, these results suggest that the development of microporosity leads to higher retention of the current density over time and that the nitrogen functionalities act as actives sites, enhancing the stability of electrocatalysts with low performances.

6.4. Conclusions

Glucose-derived carbons were prepared by hydrothermal carbonization of glucose followed by carbonization or activation to prepare carbons with different porosities. In addition, commercial CNTs were also used as a carbon electrocatalyst without microporosity. The carbon materials were then doped with nitrogen, FePc and both nitrogen and FePc. Regardless of the microporosity, functionalization with melamine resulted in the incorporation of nitrogen functionalities on the surface of the carbons and the formation of carbon nitrides. Conversely, the incorporation of FePc was greatly influenced by the microporosity. In the highly microporous activated sample, FePc was located inside the porous structure, whereas in the carbonized sample FePc is deposited on the surface. However, functionalization with melamine before the incorporation of FePc modified the preferential location of the metal complex inside the activated sample, leading to the deposition of iron on the surface. Regarding the electrochemical characterization, the incorporation of FePc inside the porous carbon structure gave rise to slower reaction kinetics that hinders the reaction mechanism to achieve the four-electron pathway, while the previous functionalization with melamine shifted the mechanism of the reaction to the four-electron pathway. Regardless of the microporosity of the hydrothermal carbons, the incorporation of FePc resulted in similar onset (0.88 V) and half-wave potentials (0.82 V), demonstrating the crucial role of FePc. Besides, the incorporation of FePc in CNT resulted in an electrocatalyst with a high onset potential (0.94 V) and half-wave potential (0.87 V) with negligible formation of by-products (< 1%). These results are significantly better than those obtained for the commercial

catalyst, which makes this sample a promising material to replace Pt/C. Moreover, the preparation of these electrocatalysts with outstanding performance was performed using the lowest FePc:carbon ratio reported to date, which is an interesting starting point for future work towards optimization/industrialization of carbon materials to produce green energy.

6.5. Supplementary Information

6.5.1. Experimental

In order to assess the optimal amount of FePc and temperature to be employed, three different carbonized samples were prepared: i) 50 mg of FePc was incorporated into 1 g of carbon and treated at 500 ºC for 2 h (CG_{FePc}), ii) 100 mg of FePc was incorporated into 1 g of carbon and treated at 500 ºC for 2 h ($CG_{2x\text{-}FePc}$) and iii) 50 mg of FePc was incorporated into 1 g of carbon and treated at 800 ºC for 2 h (800-CG_{FePc}). To assess the electrochemical performance of these three samples, linear sweep voltammetry was performed at 1600 rpm in an O_2-saturated 0.1 mol L^{-1} KOH electrolyte. The obtained voltammograms are presented in Figure 6S.1.

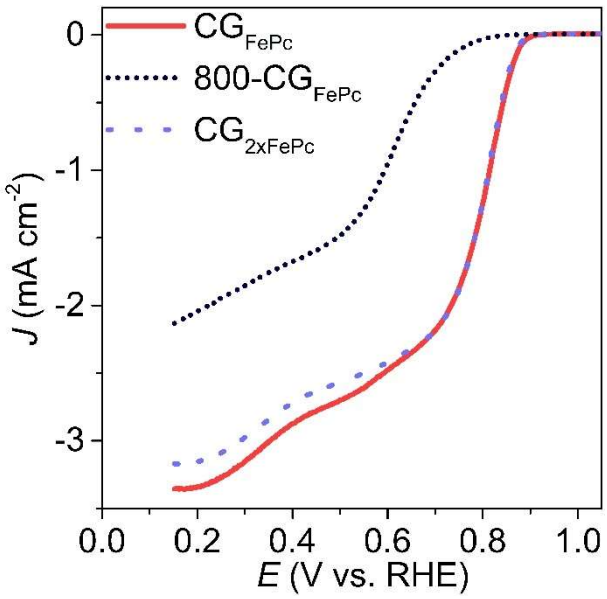


Figure 6S.1 - Linear sweep voltammogram of samples CG_{FePc}, $CG_{2x\text{-}FePc}$ and 800-CG_{FePc} at 5 mV s^{-1} and 1600 rpm in 0.1 mol L^{-1} KOH.

At 800 ºC the Fe-N_4 structure can partially decompose to small iron particles [16] and the phthalocyanine ring can be destroyed [32] resulting in a considerable loss of electroactivity. Additionally, increasing the amount of FePc ($CG_{2x\text{-}FePc}$) did not result in an improvement in comparison to the sample prepared using 50 mg of FePc. Therefore, the sample prepared using 50 mg of FePc and treated at 500 ºC was selected for the study.

6.5.2. Results and discussion

6.5.2.1. Textural properties

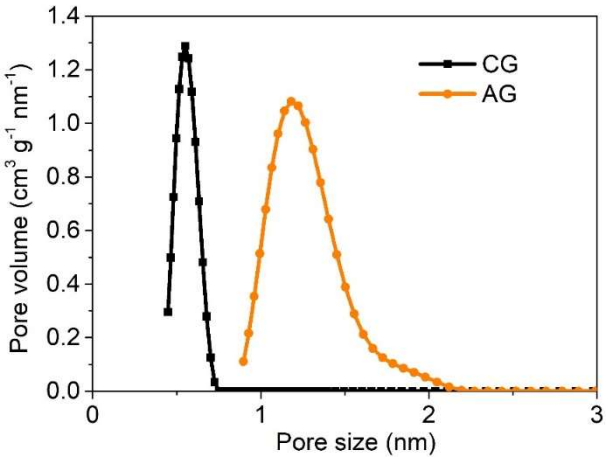


Figure 6S.2 - Pore size distribution of CG and AG.

Table 6S.1 - Textural properties of the prepared carbon materials determined by N_2 adsorption/desorption isotherms at -196 ºC.

Samples	S_{BET} (m^2 g^{-1})	V_p (cm^3 g^{-1})	V_{micro} (cm^3 g^{-1})
CG	573	0.23	0.22
N-CG	84	0.05	0.03
CG_{FePc}	518	0.21	0.19
N-CG_{FePc}	11	0.01	0.00
AG	1412	0.56	0.54
N-AG	1135	0.45	0.43
AG_{FePc}	1229	0.50	0.47
N-AG_{FePc}	954	0.39	0.36
CNT	223	2.06	0.02
N-CNT	161	1.52	0.00
CNT_{FePc}	181	1.75	0.01
N-CNT_{FePc}	155	1.67	0.00

6.5.2.2. Chemical Properties

The deconvolution of the C 1s spectrum of the base samples (CG, AG and CNT) led to the following five main peaks: i) carbon sp^2 (C=C, first peak) at 284.6 ± 0.1 eV; ii) carbon present in ether, alcohol or phenol bonds (C–O) at 285.6 ± 0.2 eV (Peak II); iii) quinone or carbonyl (C=O) 286.8 ± 0.2 eV (Peak III); iv) carboxyl groups (COOH) at 289.0 ± 0.3 eV (Peak IV); and v) the shake-up satellite due to π-π* transitions in aromatic rings (Peak V) at energy binding values higher than 290 eV. The intensity of Peaks II and III increases due to the functionalization with nitrogen. These binding energies are also attributed to C-N and C=N bonds. Furthermore, the formation of carbon nitrides during the decomposition of melamine may have led to the formation of N=C-(N_2) bonds detected at a binding energy of 288.7 eV, which is overlapped with the peak attributed to COOH (Peak IV).

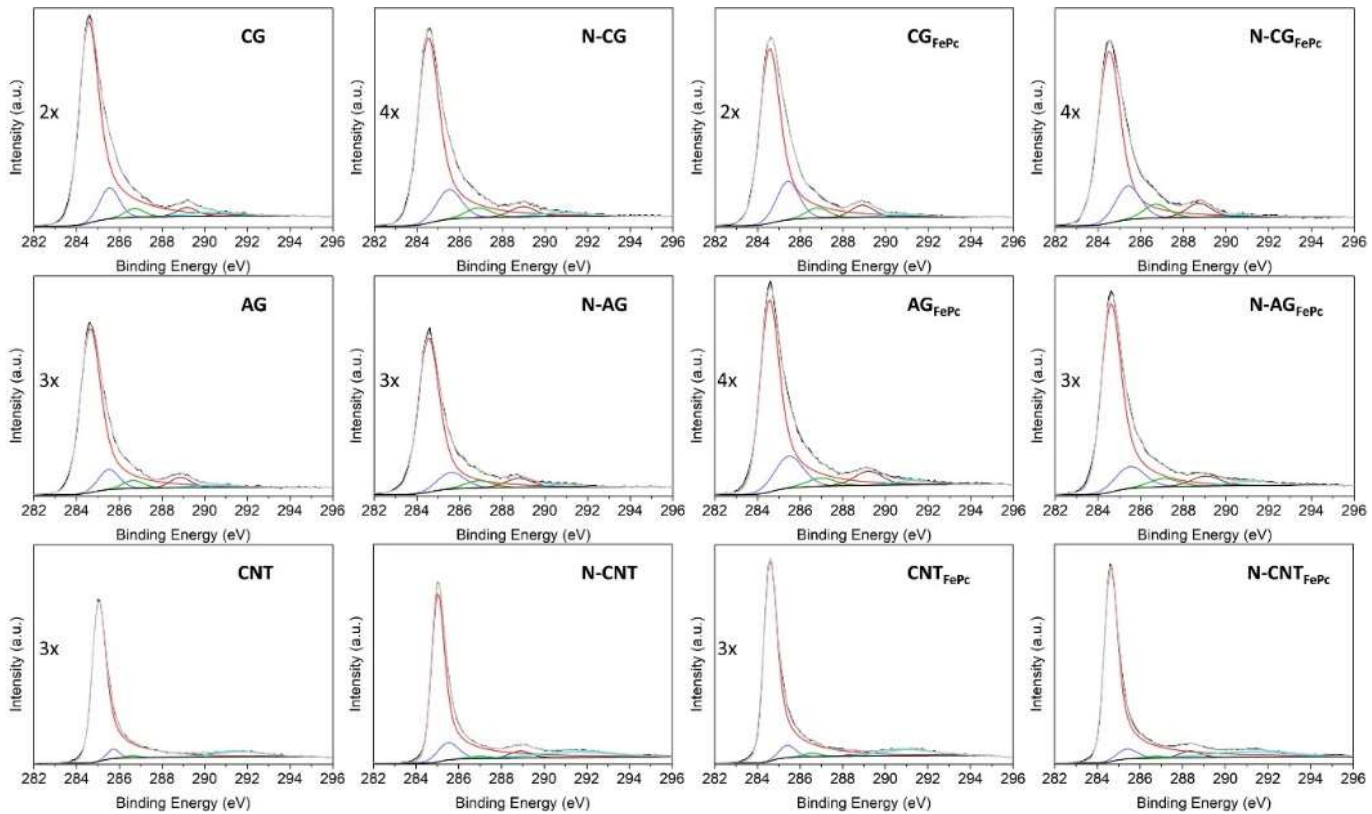


Figure 6S.3 - Deconvolution of the C 1s spectrum for all the prepared samples.

The deconvolution of the N 1s region in N-doped carbons presents three main peaks representing the following nitrogen functionalities: i) pyridinic nitrogen (N-6) at 398.5 ± 0.2 eV; ii) pyrrolic nitrogen (N-5) at 399.9 ± 0.2 eV; and iii) quaternary nitrogen (N-Q) at 401.0 ± 0.2 eV. The incorporation of nitrogen using melamine allows the formation of these three main functionalities. Furthermore, a fourth peak was observed in samples N-CNT and N-CNT_{FePc} at 405.0 ± 0.2 eV, corresponding to C=N-C in carbon nitrides. Additionally, the peak corresponding to Fe-N_x bonds is ascribed to a similar binding energy than that of the N-5 peak, which results in an overlap of both peaks.

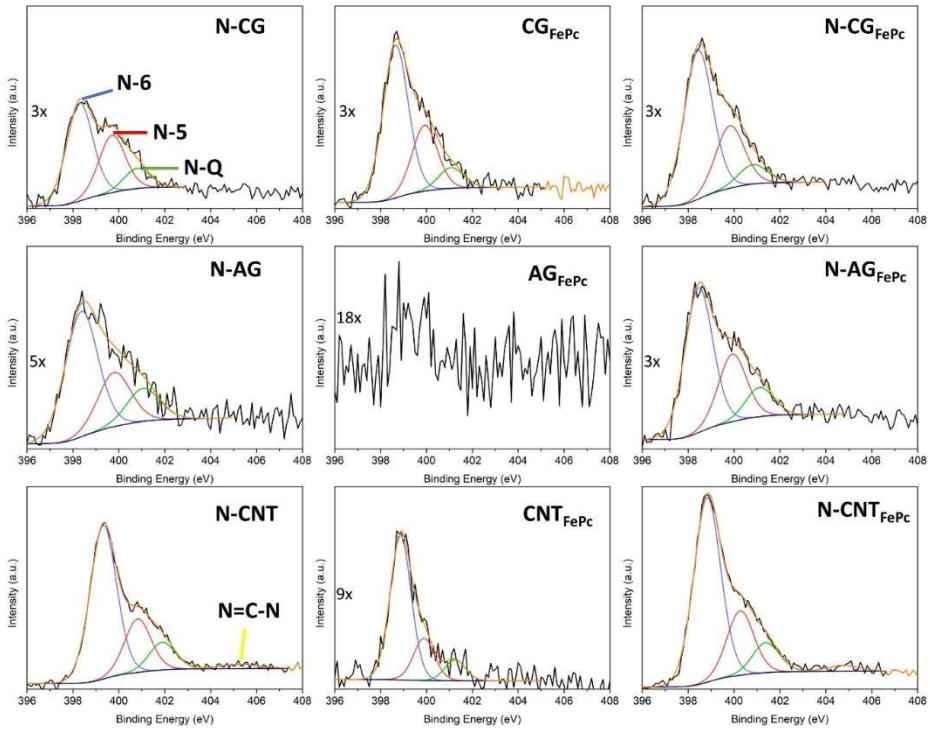


Figure 6S.4 - Deconvolution of the N 1s spectrum for the functionalized carbon materials.

The deconvolution of the Fe 2p spectrum of samples CG_{FePc} and N-CG_{FePc} resulted in two different peaks and their respective spin-orbit splitting at + 13.1 eV: i) Fe^{2+} at 710.4 eV and ii) Fe^{3+} at 712.3 ± 0.1 eV (Figure 6S.5) [46]. These results demonstrate the coexistence of both Fe^{2+} and Fe^{3+} species on the carbon structure. Samples CNT_{FePc} and N-CNT_{FePc} presented the same two peaks but at lower binding energies, 709.1 eV and 711.0 eV, respectively, due to the different carbon structure of CNT.

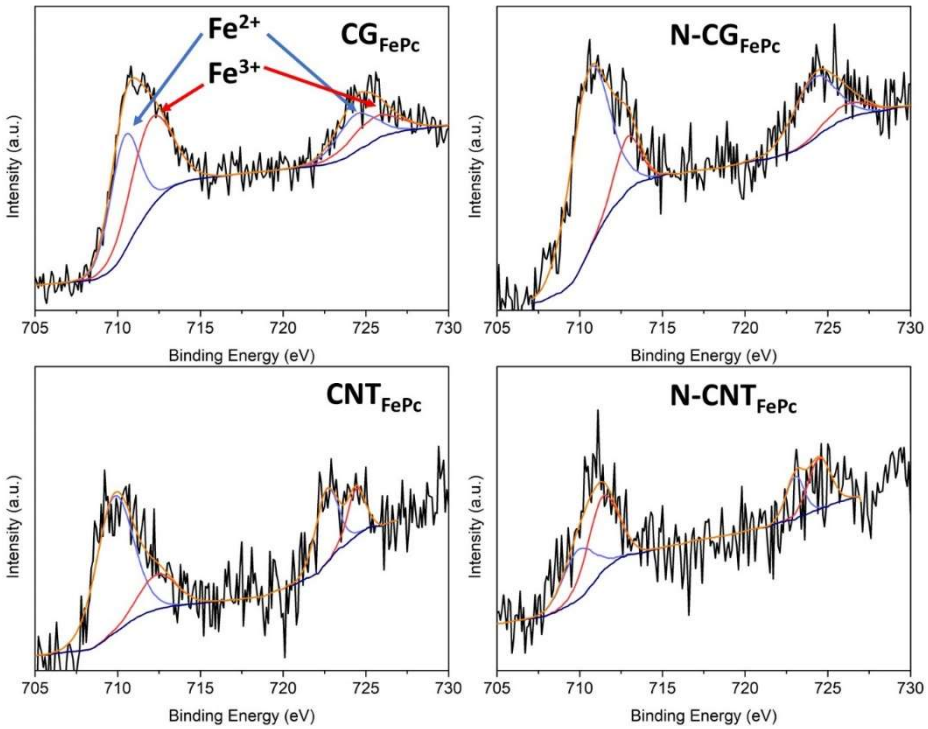


Figure 6S.5 - Deconvolution of the Fe 2p spectrum for samples CG_{FePc}, $N\text{-}CG_{FePc}$, CNT_{FePc} and $N\text{-}CNT_{FePc}$.

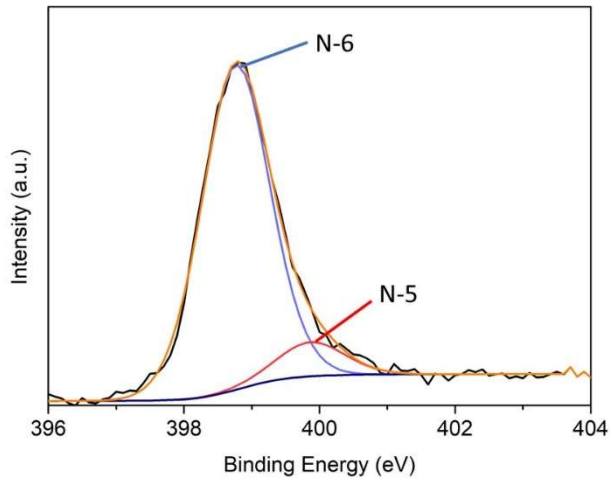


Figure 6S.6 - Deconvolution of the N 1s spectrum of FePc.

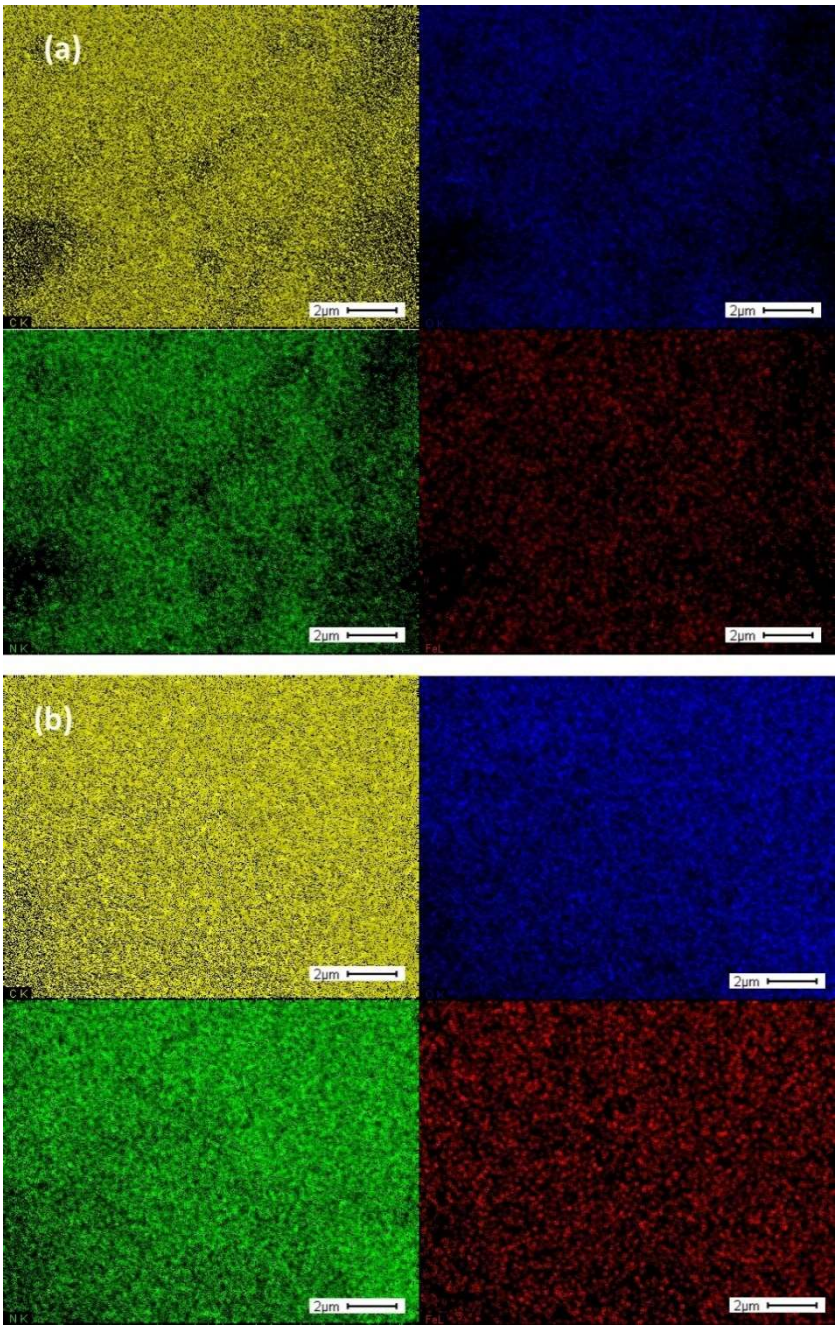


Figure 6S.7 - Elemental mapping analysis of N-CG_{FePc} (a) and N-CNT_{FePc} (b). Yellow – Carbon, Blue – Oxygen, Green – Nitrogen, Red – Iron.

6.5.2.3. Electrochemical assessment

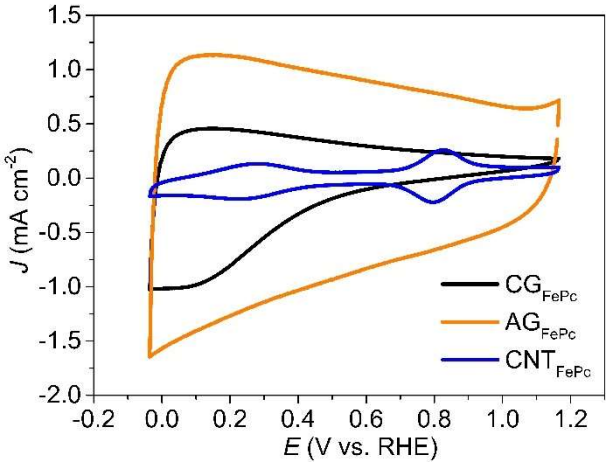


Figure 6S.8 - Cyclic voltammogram of CG_{FePc}, AG_{FePc} and CNT_{FePc} at 100 mV s^{-1} in N_2-saturated 0.1 mol L^{-1} KOH.

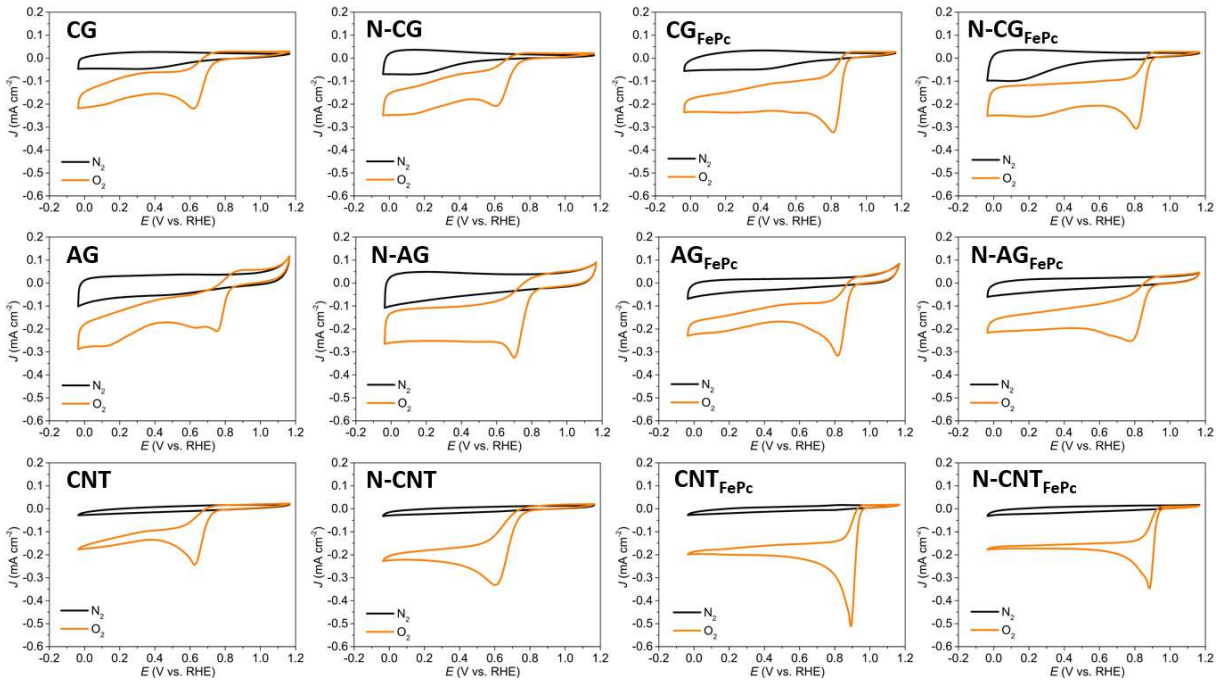


Figure 6S.9 - Cyclic voltammogram of the prepared electrocatalysts at 100 mV s^{-1} in 0.1 mol L^{-1} KOH.

6.6. References

[1] R. Paul, Q. Dai, C. Hu, L. Dai, Ten years of carbon-based metal-free electrocatalysts, Carbon Energy, 1 (2019) 19-31.
[2] N. Komba, G. Zhang, Q. Wei, X. Yang, J. Prakash, R. Chenitz, F. Rosei, S. Sun, Iron (II) phthalocyanine/N-doped graphene: A highly efficient non-precious metal catalyst for oxygen reduction, Int. J. Hydrog. Energy, 44 (2019) 18103-18114.
[3] S. Han, X. Hu, X. Fang, Y. Zhu, Novel Route to Fe-Based Cathode as an Efficient Bifunctional Catalysts for Rechargeable Zn-Air Battery, Adv. Energy Mater., (2018) 1800955.
[4] J. Yang, F. Toshimitsu, Z. Yang, T. Fujigaya, N. Nakashima, Pristine carbon nanotube/iron phthalocyanine hybrids with a well-defined nanostructure show excellent efficiency and durability for the oxygen reduction reaction, J. Mater. Chem. A, 5 (2017) 1184-1191.
[5] S. Zhao, D.-W. Wang, R. Amal, L. Dai, Carbon-Based Metal-Free Catalysts for Key Reactions Involved in Energy Conversion and Storage, Adv. Mater., 31 (2019) 1801526.
[6] K.-H. Wu, M. Allen-Ankins, Q. Zeng, B. Zhang, J. Pan, J. Zhang, D.-S. Su, I.R. Gentle, D.-W. Wang, Benchmarking the Oxygen Reduction Electroactivity of First-Row Transition-Metal Oxide Clusters on Carbon Nanotubes, ChemElectroChem, 5 (2018) 1862-1867.
[7] J. Song, T. Liu, S. Ali, B. Li, D. Su, The synergy effect and reaction pathway in the oxygen reduction reaction on the sulfur and nitrogen dual doped graphene catalyst, Chemical Physics Letters, 677 (2017) 65-69.
[8] K. Hyun, T. Ueno, G. Panomsuwan, O.L. Li, N. Saito, Heterocarbon nanosheets incorporating iron phthalocyanine for oxygen reduction reaction in both alkaline and acidic media, Phys. Chem. Chem. Phys., 18 (2016) 10856-10863.
[9] H.T. Chung, D.A. Cullen, D. Higgins, B.T. Sneed, E.F. Holby, K.L. More, P. Zelenay, Direct atomic-level insight into the active sites of a high-performance PGM-free ORR catalyst, Science, 357 (2017) 479.
[10] C. Goswami, K.K. Hazarika, P. Bharali, Transition metal oxide nanocatalysts for oxygen reduction reaction, Mater. Sci. Energ.Technol., 1 (2018) 117-128.
[11] P. Yan, B. Zhang, K.-H. Wu, D. Su, W. Qi, Surface chemistry of nanocarbon: Characterization strategies from the viewpoint of catalysis and energy conversion, Carbon, 143 (2019) 915-936.
[12] L. Yan, J. Yu, J. Houston, N. Flores, H. Luo, Biomass derived porous nitrogen doped carbon for electrochemical devices, Green Energy Environ., 2 (2017) 84-99.
[13] D. Barrera, M. Florent, M. Kulko, T. Bandosz, Ultramicropore-influenced mechanism of oxygen electroreduction on metal-free carbon catalysts, J. Mater. Chem. A, 7 (2019).
[14] R. G. Morais, N. Rey-Raap, R. Costa, C. Pereira, A. Guedes, J. L. Figueiredo, M. F. R. Pereira, Hydrothermal Carbon/Carbon Nanotube Composites as Electrocatalysts for the Oxygen Reduction Reaction, J. Compos. Sci., 4 (2020) 1-14.
[15] R. G. Morais, N. Rey-Raap, J. L. Figueiredo, M. F.R. Pereira, Glucose-derived carbon materials with tailored properties as electrocatalysts for the oxygen reduction reaction, Beilstein J. Nanotechnol., 10 (2019) 1089-1102.
[16] Y. Li, Q. Li, H. Wang, L. Zhang, D.P. Wilkinson, J. Zhang, Recent Progresses in Oxygen Reduction Reaction Electrocatalysts for Electrochemical Energy Applications, Electrochemical Energy Reviews, 2 (2019) 518-538.
[17] H.A. Miller, M. Bellini, W. Oberhauser, X. Deng, H. Chen, Q. He, M. Passaponti, M. Innocenti, R. Yang, F. Sun, Z. Jiang, F. Vizza, Heat treated carbon supported iron(ii)phthalocyanine oxygen reduction catalysts: elucidation of the structure–activity relationship using X-ray absorption spectroscopy, Phys. Chem. Chem. Phys., 18 (2016) 33142-33151.

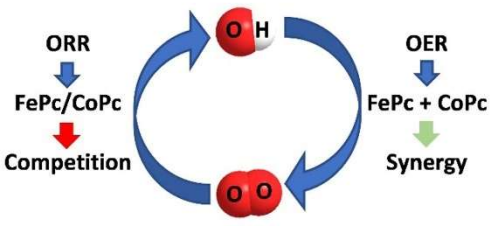
[18] B. Jeong, D. Shin, M. Choun, S. Maurya, J. Baik, B.S. Mun, S.-H. Moon, D. Su, J. Lee, Nitrogen-Deficient ORR Active Sites Formation by Iron-Assisted Water Vapor Activation of Electrospun Carbon Nanofibers, J. Phys. Chem. C, 120 (2016) 7705-7714.
[19] K.H. Wu, W. Shi, D. Wang, J. Xu, Y. Ding, Y. Lin, W. Qi, B. Zhang, D. Su, In Situ Electrostatic Modulation of Path Selectivity for the Oxygen Reduction Reaction on Fe-N Doped Carbon Catalyst, Chem. Mater., 29 (2017) 4649-4653.
[20] D.-S. Yang, M.Y. Song, K.P. Singh, J.-S. Yu, The role of iron in the preparation and oxygen reduction reaction activity of nitrogen-doped carbon, Chem. Commun., 51 (2015) 2450-2453.
[21] Y. Liu, Y.-S. Fan, Z.-M. Liu, Pyrolysis of iron phthalocyanine on activated carbon as highly efficient non-noble metal oxygen reduction catalyst in microbial fuel cells, Chem. Eng. J., 361 (2018).
[22] B. Liang, S. Guo, Y. Zhao, I.U. Khan, X. Zhang, K. Li, C. Lv, Single iron atoms anchored on activated carbon as active centres for highly efficient oxygen reduction reaction in air-cathode microbial fuel cell, J. Power Sources, 450 (2020) 227683.
[23] Z. Yan, C. Dai, M. Zhang, X. Lv, X. Zhao, J. Xie, Nitrogen doped porous carbon with iron promotion for oxygen reduction reaction in alkaline and acidic media, International Journal of Hydrogen Energy, 44 (2019) 4090-4101.
[24] J. Yang, J. Tao, T. Isomura, H. Yanagi, I. Moriguchi, N. Nakashima, A comparative study of iron phthalocyanine electrocatalysts supported on different nanocarbons for oxygen reduction reaction, Carbon, 145 (2019) 565-571.
[25] Y. Liu, B. Huang, X. Zhang, X. Huang, Z. Xie, In-situ fabrication of nitrogen-doped carbon nanosheets containing highly dispersed single iron atoms for oxygen reduction reaction, J. Power Sources, (2019) 125-133.
[26] Z. Zhang, M. Dou, J. Ji, F. Wang, Phthalocyanine tethered iron phthalocyanine on graphitized carbon black as superior electrocatalyst for oxygen reduction reaction, Nano Energy, 34 (2017) 338-343.
[27] Y. Zhu, B. Zhang, Z. Feng, D.S. Su, Synthesis-structure-performance correlation for poly(phenylenediamine)s/iron/carbon non-precious metal catalysts for oxygen reduction reaction, Catalysis Today, 260 (2016) 112-118.
[28] C. Zhang, R. Hao, H. Yin, F. Liu, Y. Hou, Iron phthalocyanine and nitrogen-doped graphene composite as a novel non-precious catalyst for the oxygen reduction reaction, Nanoscale, 4 (2012) 7326-7329.
[29] A. Iannaci, B. Mecheri, A. D'Epifanio, M.J. Lázaro Elorri, S. Licoccia, Iron–nitrogen-functionalized carbon as efficient oxygen reduction reaction electrocatalyst in microbial fuel cells, Int. J. Hydrog. Energy, 41 (2016) 19637-19644.
[30] C. Santoro, R. Gokhale, B. Mecheri, A. D'Epifanio, S. Licoccia, A. Serov, K. Artyushkova, P. Atanassov, Design of Iron(II) Phthalocyanine-Derived Oxygen Reduction Electrocatalysts for High-Power-Density Microbial Fuel Cells, ChemSusChem, 10 (2017) 3243-3251.
[31] G. Dakai, S. Han, Y. Zhu, MIL-100-Fe Derived N-doped Fe/Fe 3 C@C Electrocatalysts for Efficient Oxygen Reduction Reaction, Appl. Surf. Sci., 434 (2017).
[32] Y. Liu, Y.S. Fan, Z.M. Liu, Pyrolysis of iron phthalocyanine on activated carbon as highly efficient non-noble metal oxygen reduction catalyst in microbial fuel cells, Chem. Eng. J., (2019) 416-427.
[33] A. Alsudairi, J. Li, N. Ramaswamy, S. Mukerjee, K.M. Abraham, Q. Jia, Resolving the Iron Phthalocyanine Redox Transitions for ORR Catalysis in Aqueous Media, J. Phys. Chem. Lett., 8 (2017) 2881-2886.
[34] T. Koczorowski, W. Szczolko, T. Goslinski, Physicochemical Properties and Catalytic Applications of Iron Porphyrazines and Phthalocyanines, in: M.M. Rahman, A.M. Asiri (Eds.) Recent Progress in Organometallic Chemistry, IntechOpen2017, pp. 101-121.
[35] M. Canal-Rodríguez, N. Rey-Raap, J.Á. Menéndez, M.A. Montes-Morán, J.L. Figueiredo, M.F.R. Pereira, A. Arenillas, Effect of porous structure on doping and the catalytic performance

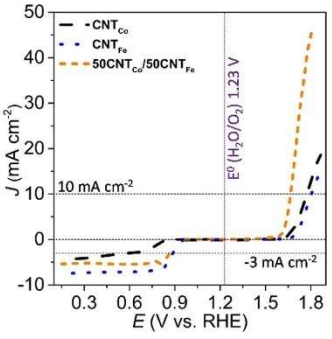
of carbon xerogels towards the oxygen reduction reaction, Microporous Mesoporous Mater., 293 (2020) 109811.
[36] G. Liu, X. Li, B. Popov, Stability Study of Nitrogen-Modified Carbon Composite Catalysts for Oxygen Reduction Reaction in Polymer Electrolyte Membrane Fuel Cells, ECS Trans., 25 (2009).
[37] R.-M. Ion, The Use of Phthalocyanines and Related Complexes in Photodynamic Therapy, in: T. Nyokong, V. Ahsen (Eds.) Photosensitizers in Medicine, Environment, and Security, Springer Netherlands2012, pp. 315-349.
[38] A. Solhy, B.F. Machado, J. Beausoleil, Y. Kihn, F. Gonçalves, M.F.R. Pereira, J.J.M. Órfão, J.L. Figueiredo, J.L. Faria, P. Serp, MWCNT activation and its influence on the catalytic performance of Pt/MWCNT catalysts for selective hydrogenation, Carbon, 46 (2008) 1194-1207.
[39] A. Bonakdarpour, T. Dahn, R. Atanasoski, M. Debe, J. Dahn, H2O2 Release during Oxygen Reduction Reaction on Pt Nanoparticles, Electrochem. Solid-State Lett., 11 (2008) B208-B211.
[40] R. Kecili, C.M. Hussain, Chapter 4 - Mechanism of Adsorption on Nanomaterials, in: C.M. Hussain (Ed.) Nanomaterials in Chromatography, Elsevier2018, pp. 89-115.
[41] H.-S. Zhai, L. Cao, X.-H. Xia, Synthesis of graphitic carbon nitride through pyrolysis of melamine and its electrocatalysis for oxygen reduction reaction, Chinese Chemical Letters, 24 (2013) 103-106.
[42] N. Rey-Raap, M. Enterría, J.I. Martins, M.F.R. Pereira, J.L. Figueiredo, Influence of Multiwalled Carbon Nanotubes as Additives in Biomass-Derived Carbons for Supercapacitor Applications, ACS Appl. Mater. Interfaces, 11 (2019) 6066-6077.
[43] E.N. Gribov, A.N. Kuznetsov, V.A. Golovin, D.V. Krasnikov, V.L. Kuznetsov, Effect of modification of multi-walled carbon nanotubes with nitrogen-containing polymers on the electrochemical performance of Pt/CNT catalysts in PEMFC, Materials for Renewable and Sustainable Energy, 8 (2019) 7.
[44] Z.-H. Sheng, L. Shao, J.-J. Chen, W.-J. Bao, F.-B. Wang, X.-H. Xia, Catalyst-Free Synthesis of Nitrogen-Doped Graphene via Thermal Annealing Graphite Oxide with Melamine and Its Excellent Electrocatalysis, ACS Nano, 5 (2011) 4350-4358.
[45] K. Stańczyk, R. Dziembaj, Z. Piwowarska, S. Witkowski, Transformation of nitrogen structures in carbonization of model compounds determined by XPS, Carbon, 33 (1995) 1383-1392.
[46] M. Xiao, J. Zhu, L. Ma, Z. Jin, J. Ge, X. Deng, Y. Hou, Q. He, J. Li, Q. Jia, S. Mukerjee, R. Yang, Z. Jiang, D. Su, C. Liu, W. Xing, Microporous Framework Induced Synthesis of Single-Atom Dispersed Fe-N-C Acidic ORR Catalyst and Its in Situ Reduced Fe-N4 Active Site Identification Revealed by X-ray Absorption Spectroscopy, ACS Catal., 8 (2018) 2824-2832.
[47] X.-F. Li, K.-Y. Lian, L. Liu, Y. Wu, Q. Qiu, J. Jiang, M. Deng, Y. Luo, Unraveling the formation mechanism of graphitic nitrogen-doping in thermally treated graphene with ammonia, Sci. Rep., 6 (2016) 23495.
[48] K. Moura, R. Lima, A. Coelho, E. Souza-Junior, J. Duque, C. Meneses, Tuning the surface anisotropy in Fe-doped NiO nanoparticles, Nanoscale, 6 (2013).
[49] T.A. Jones, B. Bott, Gas-induced electrical conductivity changes in metal phthalocyanines, Sensors and Actuators, 9 (1986) 27-37.
[50] D. Guo, R. Shibuya, C. Akiba, S. Saji, T. Kondo, J. Nakamura, Active sites of nitrogen-doped carbon materials for oxygen reduction reaction clarified using model catalysts, Science, 351 (2016) 361.
[51] N. Zhou, N. Wang, Z. Wu, L. Li, Probing Active Sites on Metal-Free, Nitrogen-Doped Carbons for Oxygen Electroreduction: A Review, Catalysts, 8 (2018) 509.
[52] W.M.T.M. Reimerink, The use of activated carbon as catalyst and catalyst carrier in industrial applications, in: A. Dąbrowski (Ed.) Studies in Surface Science and Catalysis, Elsevier1999, pp. 751-769.

Chapter 7

Fe, Co, N-doped carbon nanotubes as bifunctional oxygen electrocatalysts

R.G. Morais, N. Rey-Raap, J.L. Figueiredo, M.F.R. Pereira, Fe, Co, N-doped carbon nanotubes as bifunctional oxygen electrocatalysts, Appl. Surf. Sci., 572 (2022) 151459.





Abstract

Carbon nanotubes were modified towards oxygen reduction and evolution reactions by incorporation of cobalt and/or iron phthalocyanines (CoPc and FePc, respectively). The obtained monometallic samples were physically mixed in different ratios to assess the importance of each phthalocyanine. The increase of FePc content enhanced the electroactivity towards the oxygen reduction reaction, especially the limiting current density and reaction mechanism, for which two relationships were found by varying the CoPc:FePc mass ratio. Samples with a mass ratio (FePc:CoPc) $\geq$ 1 surpassed the electroactivity of the current commercial electrocatalyst (Pt/C) and presented similarly high long-term durability (82-85%). Interestingly, a synergetic effect between both types of metallic active centers was observed for the oxygen evolution reaction. A 1:1 CoPc:FePc mass ratio provided the highest oxygen evolution reaction electroactivity, displaying a potential of 1.67 V at 10 mA cm^{-2}, higher than that of the commercial RuO_2 catalyst (1.58 V). This sample also presented the lowest potential gap (0.81 V), which is much lower than that of Pt/C (1.20 V) and RuO_2 (1.41 V), demonstrating the high potential of these materials as substitutes of noble metal electrocatalysts.

7.1. Introduction

The escalating world industrialization, population, and increasing use of portable electronic devices are leading to a significant increase in the global energy demand. Moreover, a transition from fossil fuels to renewable green energies is crucial for the planet's sustainability [1, 2]. Nonetheless, due to the intermittency of renewable energies, there is a need to store energy when its production is higher than the demand and reconvert stored power into electrical energy when the demand is higher than its production. Therefore, the combination of conversion and storage devices is of utmost importance to achieve maximum energy efficiency. Regarding conversion devices, fuel cells are known to be environmentally friendly energy conversion systems with high efficiencies and non-polluting products [3, 4]. Additionally, a coupled electrolyzer can use the low power inputs of the renewable energies to split water and generate the necessary fuels for the conversion device [5]. A compact system consisting of a fuel cell and an electrolyzer in a single electrochemical cell (the unitized regenerative fuel cell (URFC)) is one of the most promising devices regarding the future of green energy [1, 5-8]. This device involves four different electrochemical reactions: the oxygen reduction reaction (ORR) and the hydrogen oxidation reaction (HOR) that take place in the fuel cell mode, and the oxygen evolution reaction (OER) and the hydrogen evolution reaction (HER) that take place in the electrolyzer mode. The most mature URFC technology is the proton-exchange membrane fuel cell (PEMFC) [1, 5, 9, 10], which operates under acidic conditions, but the corresponding benchmark catalysts are based on noble metals which are scarce and increase the overall cost of the device [11]. To compete with PEMFC, a technology that has gained increased scientific interest as an alternative towards future energy sustainability is the use of anion-exchange membrane fuel cells (AEMFC), which operate under basic conditions [11-13]. Non-precious metal catalysts are reported to achieve high catalytic efficiencies and long-term stability in alkaline media [12]. Consequently, a basic medium opens the possibility to use a wider range of materials as electrocatalysts in comparison to acidic media that mostly favor noble metals and their oxides [1, 5-7, 9]. Nonetheless, the sluggish kinetics of the URFC's oxygen reactions (ORR and OER) hinders the round-trip efficiency of the device and requires further investigation to optimize the overall performance of the URFC without the use of

noble-metals [1]. Carbon materials are an interesting alternative to the benchmark catalysts, due to their lower costs and wider availability [14]. Moreover, the possibility to tune the properties of carbon materials is essential for the optimization of their electroactivity [15, 16]. A wide variety of carbon materials such as porous carbons [17-19], carbon nanotubes [19-22], and graphene [21-24] have been studied as bifunctional electrocatalysts for ORR and OER, achieving interesting results. The introduction of different heteroatoms (nitrogen [17-21, 23-27], phosphorus [18, 24], and sulfur [21, 22, 28]) into the carbon structures is a common strategy used to modulate the catalyst's chemical properties. The incorporation of transition metals is also a much-studied subject to achieve bifunctional oxygen electrocatalysts [29-31]. Furthermore, the synergy between transition metals and heteroatoms, in particular nitrogen and sulfur, has been reported to highly increase the electroactivity of carbon materials [32-41]. Transition metals and heteroatoms can be found in a single precursor, especially by using macrocycles with both elements. The use of macrocycles can lead to a decrease in production costs, as it allows incorporating the metal and heteroatom in a single-step thermal treatment [42]. The most commonly used macrocycles are the metal-centered phthalocyanines (Pcs), particularly cobalt(II) phthalocyanine (CoPc) and iron(II) phthalocyanine (FePc). FePc has been widely studied towards the ORR [42-48]. These studies suggest that FePc is highly electroactive towards the ORR and favors the direct reduction of oxygen through the 4-electron mechanism [41, 49]. Although CoPc is electroactive in ORR, this macrocycle presents lower current density than FePc and high formation of by-products, requiring further tailoring [44, 50]. On the other hand, there is a lack of knowledge about the electrochemical behavior of these two Pcs (CoPc and FePc) when they are incorporated together on the same carbon surface, i.e., the synergy between them towards the ORR and OER. Moreover, despite the enhanced electrochemical performance of Pcs, major gaps still exist in the literature regarding the bifunctionality of these macrocycles. In fact, the combination of these phthalocyanines in a single carbon support as bifunctional oxygen electrocatalyst has not yet been reported.

This work aims to prepare carbon electrocatalysts with high electrocatalytic activity towards ORR and OER. Carbon nanotubes (CNTs) were used as carbon support due to the synergy of their π-π systems with phthalocyanines, which is important to enhance

their electroactivity towards ORR and OER [42, 51, 52]. A very small amount of CoPc and/or FePc was incorporated on the CNTs to maintain a low production cost of the electrocatalysts. Furthermore, CoPc and FePc were added separately into the CNTs, to study the effect of each individual macrocycle on both reactions. Additionally, CoPc and FePc were incorporated simultaneously on the CNTs following different methodologies, achieving remarkable improvements compared to the incorporation of a single Pc.

7.2. Experimental

7.2.1. Preparation of electrocatalysts

Purified multi-walled carbon nanotubes (sample CNT) were used for the development of highly electroactive bifunctional ORR/OER electrocatalysts. Briefly, commercial CNTs (Nanocyl, > 95% C) underwent reflux at 140 ºC for 4 h in a 1:1 (v/v) ratio solution of sulfuric acid (95%, VWR Chemicals) and distilled water (produced by filtration through inverse osmosis in a Panice equipment) to remove impurities. Afterwards, CNTs were washed with hot distilled water until a neutral pH was achieved and dried at 120 ºC for 1 day. The purified CNTs were then tailored by incorporating two different Pcs: cobalt(II) phthalocyanine (CoPc, Sigma-Aldrich, 97%) and iron(II) phthalocyanine (FePc, Sigma-Aldrich, 90%). Pcs were incorporated by the incipient wetness impregnation method. Briefly, 50 mg of the selected macrocycle per g of CNT was dissolved in ethanol and added dropwise to CNT under sonication, maintained in the ultra-sonication bath for 30 min and dried overnight at 100 ºC, followed by a thermal treatment in N_2 atmosphere at 500 ºC for 2 h. This temperature was selected based on previously published research works, in which it was demonstrated that FePc suffers degradation at temperatures of 600 ºC and higher [42, 53]. Furthermore, these works demonstrate high electroactivity of FePc between 500 ºC and 700 ºC; therefore, 500 ºC was the selected temperature. The introduction of cobalt and iron macrocycles led to samples CNT_{Co} and CNT_{Fe}, respectively.

Four different methodologies were studied to assess the optimal procedure to incorporate both molecules: i) incorporation of CoPc on the CNT_{Fe} sample (CNT_{Fe_Co}); ii) incorporation of FePc on the CNT_{Co} sample (CNT_{Co_Fe}), iii) incorporation of CoPc and FePc on the CNTs by a single-step impregnation process (CNT_{CoFe}), following the

methodology described above for a single metal; and iv) sample CNT_{Co} and CNT_{Fe} were weighted using a 1:1 (m/m) ratio and physically mixed for a few minutes until a visually homogeneous mixture was obtained ($50CNT_{Co}/50CNT_{Fe}$). The sample obtained after mixing was used directly as catalyst without any further modification, hence avoiding the formation of a cobalt-iron alloy as no thermal treatment took place after mixing. It should be noted that the $50CNT_{Co}/50CNT_{Fe}$ sample presents only half of the total metal loading in comparison to CNT_{Fe_Co}, CNT_{Co_Fe}, and CNT_{CoFe}. These four materials were electrochemically characterized and the results obtained are shown in Figure 7S.1. The electrochemical measurements (Figure 7S.1) showed that the best procedure to achieve a bifunctional material was the physical mixture of CNT_{Fe} and CNT_{Co}, i.e. sample $50CNT_{Co}/50CNT_{Fe}$. To further optimize the electrocatalysts' preparation process, a sample following the same methodology as $50CNT_{Co}/50CNT_{Fe}$ was prepared by adding twice the amount of CoPc and FePc. This synthesized electrocatalyst ($50CNT_{2Co}/50CNT_{2Fe}$) was used to determine the best metal loading on the CNTs. The incorporation of twice the amount of macrocycle molecules did not result in a higher performance towards ORR/OER (Figure 7S.2). Therefore, the physical mixture using 50 mg of CoPc/FePc molecules per g of CNT ($50CNT_{Co}/50CNT_{Fe}$) was selected as the best procedure according to the electrochemical results displayed in the supporting information (Figure 7S.1 and Figure 7S.2). In addition, samples CNT_{Co} and CNT_{Fe} were physically mixed using two additional CNT_{Co}:CNT_{Fe} ratios, 3:1 (m/m) (sample $75CNT_{Co}/25CNT_{Fe}$) and 1:3 (m/m) (sample $25CNT_{Co}/75CNT_{Fe}$).

7.2.2. Textural and chemical characterization

The chemical composition of the prepared carbon materials was obtained by elemental analysis. A Vario Micro Cube analyzer (Elementar GmbH) was used to determine the carbon, hydrogen, and nitrogen (C, H, and N) contents by sample combustion at 1050 ºC. A Rapid Oxy Cube analyzer (Elementar GmbH) was used to determine each sample's oxygen content by pyrolysis at 1450 ºC. Each sample was analyzed in triplicate. The quantification of cobalt and/or iron loading on each sample was performed by inductively coupled plasma (ICP) emission spectrometry. The analyzes were carried out in a Perkin Elmer Optima 4300 spectrometer using an optic with Echelle polychromator. Furthermore, the samples' surface chemical composition was determined by X-ray

photoelectron spectroscopy (XPS). The analyzes were performed in a Kratos AXIS Ultra HAS spectrometer using a monochromatic Al *K*α radiation (1486.7 eV) at 15 kV (90 W) in fixed analyzer transmission mode. To observe the morphology of the CNT samples and the elemental map distribution, a Nova NanoSEM 200 (FEI Company) was used to perform scanning electron microscopy (SEM) and energy dispersive spectroscopy (EDS). The samples, in powder form, were previously attached to an aluminum pin using conductive carbon double-sided adhesive tape. An Everhart-Thornley detector (ETD) and a backscattered electron detector (BSTD) were used as secondary detectors during SEM analysis, and a Si(Li) detector was used for EDS and mapping analyzes. A JEOL 2200 FS apparatus was used to perform transmission electron microscopy (TEM). Raman spectra were measured directly on the carbon materials using an Alpha 300 apparatus (WiTec, Germany) with a monochromatic wavelength laser of 532 nm. The textural properties of the synthesized carbon materials were obtained by N_2 adsorption at -196 ºC performed in a Quantachrome Autosorb iQ automated gas sorption analyzer. All samples were degassed under vacuum at 150 ºC for 12 h before the analyzes. The Brunauer-Emmett-Teller (BET) equation was used to determine the specific surface area (S_{BET}), and the volume of nitrogen adsorbed at the saturation point (relative pressure of 0.99) was considered as the total pore volume (V_p).

7.2.3. Electrochemical characterization

The electrochemical characterization of the prepared carbon electrocatalysts was performed in a PGSTAT 302N potentiostat/galvanostat using a three-electrode cell configuration. A glassy carbon rod and an Ag/AgCl (KCL 3 mol L^{-1}) electrode were used as counter and reference electrodes, respectively, for the ORR measurements, whereas a Pt foil was used as a counter electrode for the OER assessments. Working electrodes were prepared by deposition of a prepared suspension of the synthesized materials on a glassy carbon disk-platinum ring electrode (RRDE 5 mm in diameter, 24.9% collection efficiency, Methrom) for cyclic voltammetry (CV) and linear sweep voltammetry (LSV) during ORR measurements. A glassy carbon rotating disk electrode (RDE 3 mm in diameter, Metrohm) was used as the working electrode for ORR chronoamperometric tests, OER assessments, and for the CV performed to calculate the double-layer capacitance (C_{dl}).

The suspensions were obtained by dispersing 4 mg of the carbon sample in a solution containing 80 µL of Nafion (5 wt% in lower aliphatic alcohols and water, Sigma-Aldrich), 80 µL of ethanol (≥ 99.5%, VWR Chemicals), and 470 µL of ultrapure water (Millipore). The suspension was sonicated for at least 30 min until a homogeneous dispersion was obtained prior to deposition. The mass loading of all samples was ca. 0.8 mg cm^{-2}. The electrochemical measurements were carried out at room temperature in a 0.1 mol L^{-1} KOH solution saturated with N_2 or O_2 for 30 min before performing the specific electrochemical experiments. The ORR assessments consisted of CV and LSV experiments in both N_2 and O_2-saturated media. The CV measurements were accomplished at scan rates of 5, 20, 60, and 100 mV s^{-1}, and the LSV at a scan rate of 5 mV s^{-1} with a rotation speed ranging from 400 to 3000 rpm (applied to the working electrode by a rotation speed controller). The potential range employed for the CV and LSV was between 1.10 V and -0.05 V (vs RHE). The experimental current from LSV and CV was determined by subtracting the current obtained from the electrolyte saturated with N_2 from the current measured in the O_2-saturated medium. Different electrochemical parameters were obtained from the LSV data: i) onset potential (E_{onset}), which value was considered at a current density of 0.1 mA cm^{-2}; ii) half-wave potential ($E_{1/2}$), determined from the derivative of the current-potential curve, in which a maximum value, corresponding to half the diffusion-limited current, is ascribed to $E_{1/2}$ [54]; iii) the potential at which a current density of 3 mA cm^{-2} was achieved (E_3); and iv) the limiting current density measured at 0.4 V vs RHE (J_L). Furthermore, the disk and ring currents obtained from the RRDE LSV were used to calculate the percentage of hydrogen peroxide (H_2O_2) produced and the number of electrons transferred (n_e) during the ORR. The H_2O_2 percentage and the number of electrons were calculated from the LSV recorded at 1600 rpm by Eqs. (7.1) and (7.2), respectively:

$$H_2O_2(\%) = 200 \times \frac{\frac{I_R}{N}}{I_D + \frac{I_R}{N}} \tag{7.1}$$

$$n_e = \frac{4I_D}{I_D + \frac{I_R}{N}} \tag{7.2}$$

where I_R is the ring current (mA), I_D is the disk current (mA) and N is the collection efficiency (0.249).

Additionally, the stability of the prepared electrocatalyst during ORR was assessed by chronoamperometry, in which a potential of 0.4 V vs RHE was applied for 10000 s. Furthermore, the methanol tolerance was studied by adding 1.5 mL of methanol to the O_2-saturated electrolyte at 1000 s of the chronoamperometry measurement. Moreover, all the procedures performed for the prepared carbon materials were replicated for the ORR benchmark catalyst, Pt/C (20 wt%, Alfa Aesar), to be used as reference during the discussion of the results.

Regarding the OER, sample $25CNT_{Co}/75CNT_{Fe}$ was initially tested in both N_2- and O_2-saturated media to ensure that no significant differences would occur due to the selected saturation gas (Figure 7S.3). The obtained LSVs were identical and, consequently, it was concluded that, for these specific samples, the saturation gas does not affect the electrochemical OER measurements. Accordingly, the electrochemical assessments to evaluate the performance towards the OER consisted of LSV experiments in a N_2-saturated electrolyte.

The LSV measurements were obtained at a scan rate of 5 mV s^{-1} with a rotation speed of 1600 rpm within a 1.00 V to 1.85 V potential range (vs RHE). The obtained LSV was corrected using the E-*i*R relationship, where i is the obtained current and R is the uncompensated electrolyte ohmic resistance, which was obtained by the *i*-interrupt method [55]. The electrochemical parameters obtained from the abovementioned experiments were: i) the potential at which a current density of 10 mA cm^{-2} was achieved (E_{10}), ii) the Tafel slopes, calculated by plotting E vs log(J), and iii) the turnover frequency (TOF), obtained from Eq. 7.3 [56, 57]:

$$\mathrm{TOF} = \frac{J \times A}{4 \times F \times n} \tag{7.3}$$

where J (mA cm^{-2}) is the current density at a selected overpotential, A is the area of the working electrode (cm^2), F is the Faraday constant (96 486 C mol^{-1}) and n is the number of moles of the active material. The TOF was calculated at a potential of 1.73 V, in which all metallic samples present a significant current density, and by using the number of

moles of the metallic active centers calculated from the ICP results instead of the nominal values or the XPS results, due to the low amount of metal employed which is more accurately assessed by ICP. Additionally, the catalyst's stability towards OER was measured by performing 1000 LSV between 1.00 and 1.85 V and calculating the increase of the evolution overpotential between the first and last LSV.

Finally, the bifunctionality of the carbon samples was assessed by the potential gap (ΔE), which is considered as the difference between the OER threshold (E_{10}) and one of the potential parameters calculated for ORR (both $E_{1/2}$ or E_3 are commonly used in literature).

To further electrochemically characterize the prepared carbon materials, the double-layer capacitance (C_{dl}) was determined by cycling the loaded working electrodes at different scan rates. The CV measurements were performed under N_2-saturated media at a scan rate ranging from 5 mV s^{-1} to 220 mV s^{-1} within a potential range of 1.08 V and 1.18 V to ensure that no Faradic current is taking place [58]. The current intensity (I) recorded at a potential of 1.13 V for each CV was plotted *vs.* the employed scan rate. The C_{dl} value is the slope of the linear fit between I and the scan rate. The C_{dl} is a crucial parameter to calculate the electrochemical active surface area (ECSA), which is essential to understand the accessibility of the electrocatalyst's metal active centers [59]. The ECSA can be calculated by using Eq. 7.4:

$$\mathrm{ECSA} = \frac{C_{\mathrm{dl}}}{C_{\mathrm{S}}} \tag{7.4}$$

where C_S is the specific capacitance of the catalyst's ideal flat surface. Nonetheless, due to the very similar chemical nature of the prepared carbon materials, it can be considered that they present the same C_S value. Therefore, the C_{dl} value is expected to be proportional to the ECSA. Moreover, a recent study has reported a relationship between the C_{dl} and the accessibility of metallic active centers on carbon supports [59]. Hence, the C_{dl} can be helpful to compare how easily the main promoters of ORR and OER (active sites) can be reached by the O_2 and H_2O molecules, respectively.

7.3. Results and discussion

7.3.1. Chemical properties

The surface chemistry of the CNTs was chemically modified by the incorporation of CoPc or FePc molecules. The bulk chemical composition of each material, obtained from elemental analysis and ICP, is presented in Table 7.1.

Table 7.1 - Chemical composition determined by elemental analyzes and ICP.

Sample	C (wt%)	H (wt%)	N (wt%)	O (wt%)	Co (wt%)	Fe (wt%)
CNT	99.32	0.12	-	0.56	-	-
CNT_{Co}	98.37	0.14	0.95	0.14	0.40	-
CNT_{Fe}	97.99	0.15	1.04	0.47	-	0.35
$75CNT_{Co}/25CNT_{Fe}$	97.99	0.16	1.10	0.28	0.36	0.11
$50CNT_{Co}/50CNT_{Fe}$	98.22	0.16	0.92	0.33	0.23	0.14
$25CNT_{Co}/75CNT_{Fe}$	98.01	0.17	1.03	0.40	0.11	0.28

The initial CNT sample displays a very high content of carbon (99.32 wt%) and very small amounts of oxygen and hydrogen. The incorporation of CoPc in the carbon nanotubes (CNT_{Co}) results in a material with low contents of nitrogen and cobalt, 0.95 wt% and 0.40 wt%, respectively. These values are in agreement with the theoretical values corresponding to the amount of CoPc added (0.90 wt% and 0.48 wt% for nitrogen and cobalt, respectively). Likewise, the incorporation of FePc into the base sample (CNT_{Fe}) also leads to low contents of nitrogen and iron (1.04 wt% and 0.35 wt%, respectively), which are also similar to the theoretical ones (0.84 wt% and 0.42 wt%, respectively). These results demonstrate that the Pcs were successfully introduced onto CNT. All the samples prepared by physical mixture of CNT_{Co} and CNT_{Fe} follow the expected pattern for their chemical composition based on the mixture ratio. CoPc and FePc present the same chemical structure, only differing in the central metallic atom. Therefore, the percentage of nitrogen revolves around the same values previously described for CNT_{Co} and CNT_{Fe}. On the other hand, the metal content observed represents each metal initially incorporated onto CNT, according to the mass ratio used. It should be noted that the small deviations observed for the ICP results may be due to the

experimental error associated with the analysis, which is within 0.10 wt% of the theoretical value. Overall, these results suggest that all samples were successfully prepared.

The surface composition determined by X-ray photoelectron spectroscopy (XPS) and the survey spectra are presented in Table 7S.1 and Figure 7S.4, respectively. The survey spectra confirm that only the elements discussed during the elemental/ICP analyzes were detected on the catalysts' surface. The small amounts of Pcs employed in each sample lead to small amounts of the metallic elements on the surface of the CNTs (≤ 0.60 wt%), but the remarks made about the ICP results also apply at the surface chemical level. However, interesting differences between the bulk and the surface compositions were detected. Samples CNT_{Co} and $75CNT_{Co}/25CNT_{Fe}$ exhibit the same surface cobalt amount (0.60 wt%), which is slightly higher than that shown in Table 7.1. These results indicate that the CoPc molecules are preferentially located on the surface rather than in the bulk of the CNT bundles. Iron was not detected by XPS in $75CNT_{Co}/25CNT_{Fe}$ due to the low load of iron that did not reach the equipment detection threshold. Sample CNT_{Fe} exhibits a similar surface iron percentage as that observed by ICP, while sample $50CNT_{Co}/50CNT_{Fe}$ presents a slightly higher surface concentration of cobalt and a similar composition for iron (0.33 wt% and 0.17 wt%, respectively). These results suggest that FePc is homogeneously distributed on the CNT structure. The different behavior between CoPc and FePc may be attributed to the smaller particle size of the FePc molecule in comparison to the CoPc, which favors the incorporation of the iron species beyond the surface of the CNT bundles. Sample $25CNT_{Co}/75CNT_{Fe}$ presents similar amounts of both metallic elements on its surface, which differs from the percentage of each metal incorporated. Once again, this result demonstrates the cobalt's preference for attaching to the surface. The high-resolution XPS spectra of N 1s and of Co 2p and Fe 2p regions are presented in Figure 7S.5 and 7S.6, respectively. The N 1s region was deconvoluted in three main peaks representing: i) pyridinic nitrogen (N-6) at 398.9 ± 0.1 eV, ii) pyrrolic nitrogen (N-5) at 399.9 ± 0.2 eV and iii) quaternary nitrogen (N-Q) at 401.0 ± 0.2 eV [60]. Interesting differences are observed for the monometallic samples. CNT_{Co} presents three very well-defined peaks corresponding to the abovementioned nitrogen species, while CNT_{Fe} only presents the contribution of N-6 and N-5 functional groups.

Phthalocyanines only present two types of nitrogen groups (N-6 and N-5) as corroborated by the XPS data (Figure 7S.5) and already reported in the literature [61]. Further comparison of the nitrogen spectra and nitrogen deconvolution of FePc and CNT_{Fe} leads to interesting findings. The incorporation of FePc on the CNT results in a decrease of N-6 contribution towards the total nitrogen content from 90.50% to 83.49% and an increase of the N-5 from 9.50% to 16.51% (Table 7S.1). These results suggest that a slight decomposition of FePc takes place, and a FePc/CNT interaction occurs leading to the formation of N-5 functionalities. Nonetheless, the small nitrogen concentrations detected by XPS may be insufficient to assess the formation of N-Q on CNT_{Fe}, which has been detected in our previous publication [62]. Contrarily, the higher nitrogen surface content of CNT_{Co} allows a proper N 1s deconvolution from which it can be observed that some nitrogen atoms separate from the macrocycle in sample CNT_{Co} and forms N-Q on the CNT surface as observed in the N 1s deconvolution (Figure 7S.5). The nitrogen decomposition of CoPc may have occurred due to the temperature of the thermal treatment (500 ºC) [62]. The N-Q contribution in the mixed samples decreases with the amount of CoPc. The Co 2p region was deconvoluted in two different peaks and their respective spin-orbit splitting at 15.2 eV: i) Co^{3+} at 780.8 ± 0.1 eV and ii) Co^{2+} at 782.8 ± 0.2 eV (Figure 7S.6). These peaks were deconvoluted for all samples containing Co, except for sample $25CNT_{Co}/75CNT_{Fe}$, in which the percentage of Co is too low to allow deconvolution of the spin-orbit splits. Similarly, the low percentage of iron detected on the surface of the samples makes it difficult to deconvolute the high-resolution XPS spectrum of the Fe 2p region and its respective peaks (Figure 7S.6). However, the Fe 2p deconvolution of a sample similar to CNT_{Fe} was reported in our previous publication, from which the presence of two iron species (Fe^{2+} and Fe^{3+}) was confirmed [42].

7.3.2. Morphological and textural properties

To analyze the presence of cobalt and iron, and possible modifications in the CNTs due to the impregnation method, samples CNT_{Co}, $CNT_{Fe,}$ and $50CNT_{Co}/50CNT_{Fe}$ were examined by scanning electron microscopy (SEM). The corresponding micrographs using an Everhart-Thornley detector (ETD) are displayed in Figure 7S.7. The typical CNT morphology is observed for all samples, indicating that the incorporation of the Pcs does not modify the sample's morphology. The CNT morphology was also confirmed by

transmission electron microscopy (TEM) performed on samples CNT_{Co} and $50CNT_{Co}/50CNT_{Fe}$ (Figure 7S.8). The presence of transition metals was not detected by TEM due to the small quantity of Pc incorporated. However, a Backscattered Electron Detector (BSED) was employed to observe different levels of brightness between the CNTs and the metals. This technique was only effective to detect iron due to its high brightness during the analyzes, whereas cobalt was not distinguishable from the CNTs. The absence of cobalt during analyzes may be due to the high thermal stability of the cobalt atom within the CoPc molecule that did not transform into metallic cobalt, avoiding Co agglomerations. The BSED micrographs of sample CNT_{Fe} and $50CNT_{Co}/50CNT_{Fe}$ are displayed in Figure 7.1a and 7.1b, respectively. The nanoscale of the iron macrocycle and the small amount supported onto the CNTs prevent the detection of isolated FePc molecules. However, some iron particles were detected in the SEM micrographs, which probably result from the agglomeration of iron during the thermal treatments.

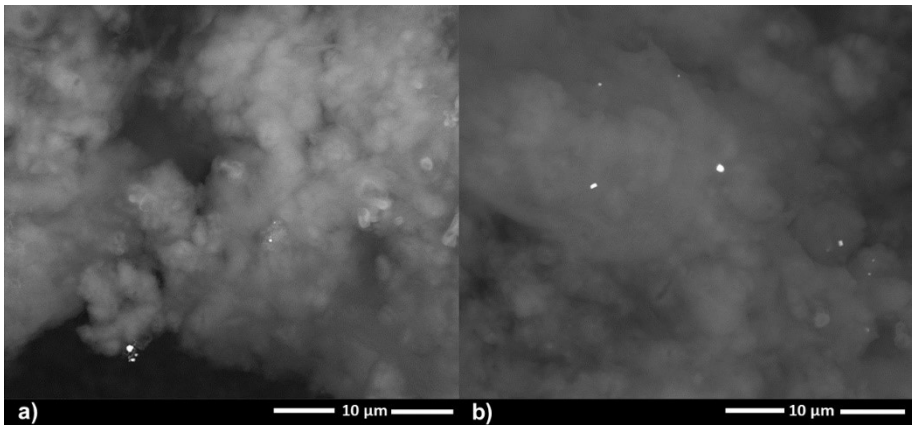


Figure 7.1 - SEM micrographs of CNT_{Fe} (a) and $50CNT_{Co}/50CNT_{Fe}$ (b).

Energy-dispersive spectroscopy (EDS) was performed to identify the metallic elements dispersion across CNT_{Co}, $CNT_{Fe,}$ and $50CNT_{Co}/50CNT_{Fe}$ (Figure 7S.9). The elemental mapping of CNT_{Co} (Figure 7S.9b) and CNT_{Fe} (Figure 7S.9d) confirms the presence, and a large-scale dispersion, of cobalt and iron on the CNTs, which is favored by the low content of Co/Fe elements in these samples. The physical mixture of these two samples ($50CNT_{Co}/50CNT_{Fe}$) exhibits a slightly less intense color of the mapping images (Figure

7S.9f and 7S.9g) in comparison to CNT_{Co} and CNT_{Fe}, since it only contains half of their metal contributions.

To further address the modifications attributed to the incorporation of the phthalocyanines, all samples were analyzed by Raman spectroscopy. The obtained spectra are presented in Figure 7.2.

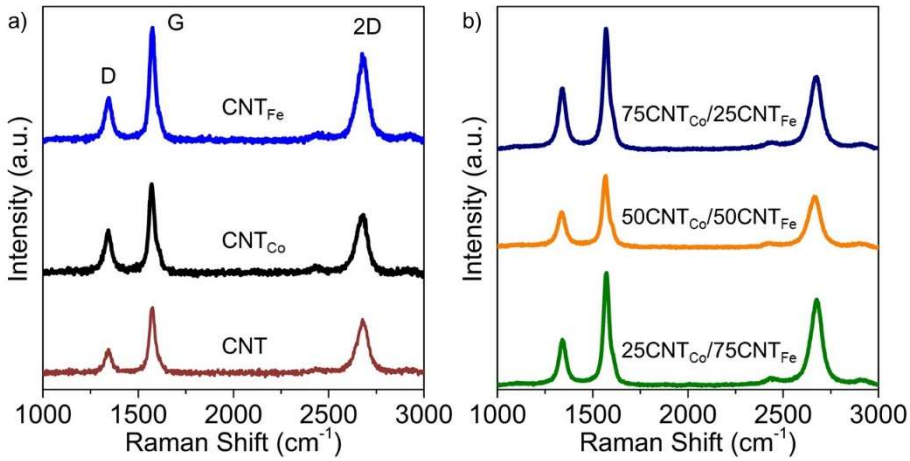


Figure 7.2 - Raman spectra of CNT and the monometallic electrocatalysts (a) and bimetallic electrocatalysts (b).

The samples exhibit a peak at ca. 1350 cm^{-1} (D band) ascribed to the basal plane defects of the carbon structure and a second peak at ca. 1580 cm^{-1} (G band), which is associated with the graphitic domains of the samples [15, 60, 63, 64]. A third peak at higher shifts (ca. 2700 cm^{-1}) related to the π band in the electronic structure is also observed, which is characteristic of CNTs. The spectra were split into the Raman features commonly observed for carbon nanotube materials. The main D and G bands were deconvoluted, and the respective peak areas were integrated to provide additional information on the relative defects of the samples. The relative A_D/A_G ratio (Table 7S.2) of CNT (0.39) increases with the incorporation of either CoPc (0.54) or FePc (0.42), which indicates an increase in the number of defects due to the presence of the metal phthalocyanines [65]. Regarding the bimetallic samples (Figure 7.2b), the maximum number of defects is observed for the sample $50CNT_{Co}/50CNT_{Fe}$ (0.67), which could have been achieved by the coexistence of two different types of effects brought by each monometallic sample.

The textural properties of the synthesized carbon materials were studied by nitrogen adsorption-desorption isotherms, displayed in Figure 7.3. The main textural parameters calculated from the isotherms are shown in Table 7S.3.

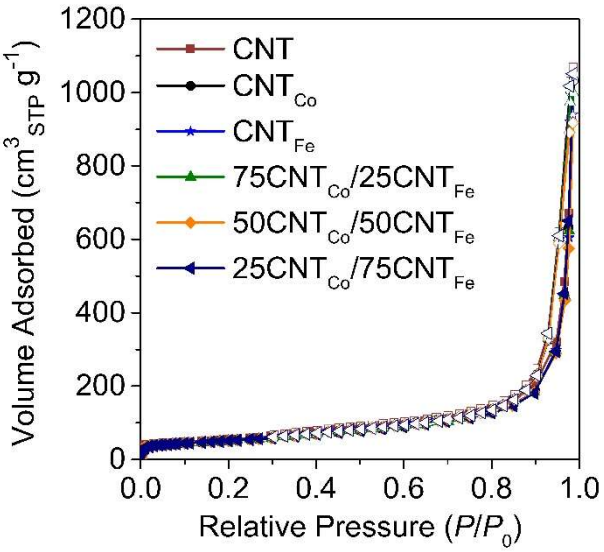


Figure 7.3 - N_2 adsorption-desorption isotherms at -196 ºC of CNT, and the monometallic and bimetallic electrocatalysts.

All samples display type II isotherms, consistent with multi-layered materials such as carbon nanotubes [66]. The base CNT sample presents a S_{BET} of 218 $m^2\ g^{-1}$. The incorporation of CoPc and FePc on the CNT sample decreases the S_{BET} by 16% and 14%, respectively. The loss of S_{BET} is higher in CNT_{Co} than in CNT_{Fe}, probably due to the larger amount of CoPc detected on the CNT surface in comparison to the amount of FePc (Table 7S.1). A decrease of V_p ($P/P_0 > 0.9$) upon the addition of CoPc or FePc is also observed, which may be caused by variations of the electrostatic charges between the CNTs upon the incorporation of the metallic complexes. Regardless of the ratio between the metals, the physical mixture of CNT_{Co} and CNT_{Fe} leads to very similar values of S_{BET} (S_{BET} ranging from 181 to 184 $m^2\ g^{-1}$). These results indicate that the physical mixture of the samples does not modify their textural properties, as expected.

7.3.3. Electrochemical assessments

The ORR electroactivity of the prepared carbon samples was preliminarily assessed by CV measurements in both inert (N_2-saturated) and O_2-saturated media. Initially, N_2-

saturated media voltammograms were recorded at 100 mV s^{-1} to identify the possible redox peaks. The obtained CVs are presented in Figure 7.4.

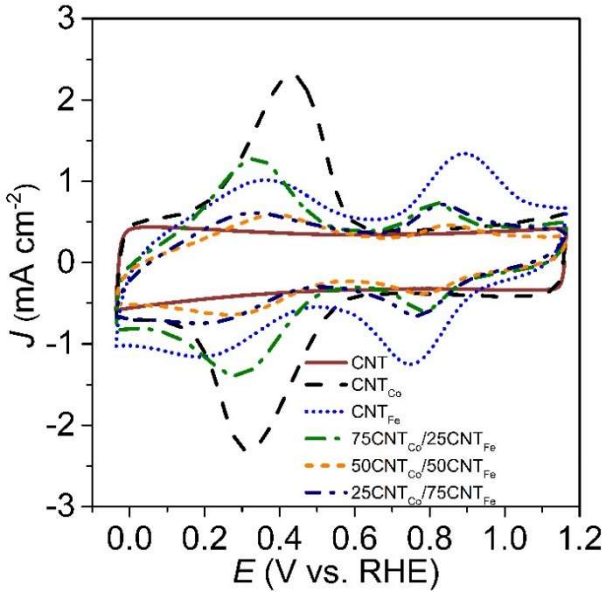


Figure 7.4 - Cyclic voltammograms recorded at 100 mV s^{-1} in N_2-saturated 0.1 mol L^{-1} KOH electrolyte from 1.10 to -0.05 V using a rotating ring-disk glassy carbon electrode with a Pt ring.

CNT displays a featureless voltammogram in the N_2-saturated medium. The addition of CoPc (CNT_{Co}) results in the appearance of a reduction peak and its respective oxidation counterpart at low potentials (0.31 V and 0.40 V, respectively). These peaks are attributed to the redox reactions that occur on the Pc ring [42, 52]. Similarly, the incorporation of FePc on CNT (CNT_{Fe}) also leads to the same two reduction and oxidation peaks but at slightly lower potentials (0.19 V and 0.36 V, respectively), which are attributed to the Pc ring around the iron atom [67]. The CV of CNT_{Fe} also presents the appearance of peaks at ca. 0.75 V and 0.89 V attributed to the oxidation and reduction reaction of the redox couple Fe(III)/Fe(II), respectively [42, 52]. Like in CNT_{Fe}, all mixed samples present the Pc-ring redox pair and the Fe(III)/Fe(II) redox pair. However, two interesting differences are observed for both pairs in the mixed samples: i) the Pc redox peaks appear in the potential range between the CNT_{Co} and CNT_{Fe} reduction and oxidation peaks; and ii) the reduction and oxidation peaks for the Fe(III)/Fe(II) species appear at higher and lower

potentials than in CNT_{Fe}, respectively. This shift is probably due to the presence of CoPc that modifies the surface chemistry of the CNTs and to the charge transference between Co and Fe atoms that, consequently, modify the potentials needed for the redox reactions.

CVs were also measured in a N_2- and O_2-saturated electrolyte at 5 mV s^{-1} (Figure 7.5), which is the common scan rate employed for LSV. The redox peaks attributed to the Pc-ring and Fe(III)/Fe(II) redox pair are also observed despite the lower scan rate employed. The reduction and oxidation peaks observed at 5 mV s^{-1} appear at higher and lower potentials, respectively, compared to the CVs recorded at 100 mv s^{-1}. At low scan rates, the active species of the Pc and the electrolyte ions have enough residence time to interact, favoring the reduction and oxidation of the species, and hence, shifting the reduction and oxidation potentials to higher and lower values, respectively. The cyclic voltammograms recorded in the O_2-saturated electrolyte display the respective O_2 reduction peaks of the prepared samples. The voltammogram recorded in O_2-saturated medium in Figure 7.5a shows that CNT displays a single reduction peak at 0.71 V, which is attributed to the ORR, since the N_2-saturated electrolyte voltammogram is featureless. CNT_{Co} displays the redox pair of the Pc ring previously observed in Figure 7.4, and a peak at 0.80 V corresponding to the ORR. Regarding CNT_{Fe}, the peaks of the two redox pairs previously described still occur. Besides, the oxygen reduction peak is also observed, but at a higher onset potential (0.89 V) and with a much more significant current density. The simultaneous presence of the Fe(III)/Fe(II) reduction peak and the oxygen reduction peak may cause an overlap during the LSV assessments, which causes a modification in the shape of the curve after the ORR peak (Figure 7.5c, 7.5d and 7.5f). The different combinations of CNT_{Co} and CNT_{Fe} present the redox peaks and the oxygen reduction peak (0.89 V) at the same potentials as CNT_{Fe}. Moreover, the current density observed for the O_2-saturated voltammogram also increases with the amount of FePc, due to its high electroactivity.

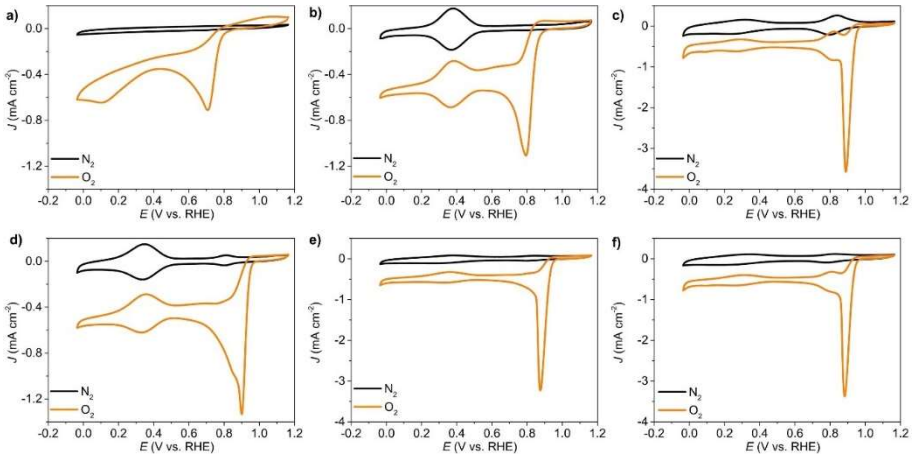


Figure 7.5 - Cyclic voltammograms recorded at 5 mV s^{-1} in N_2 (black) and O_2-saturated (orange) 0.1 mol L^{-1} KOH electrolytes from 1.10 to -0.05 V of CNT (a), CNT_{Co} (b), CNT_{Fe} (c), $75CNT_{Co}/25CNT_{Fe}$ (d), $50CNT_{Co}/50CNT_{Fe}$ (e) and $25CNT_{Co}/75CNT_{Fe}$ (f) using a rotating ring-disk glassy carbon electrode with a Pt ring.

The disk current density, ring current density, H_2O_2 formation, and number of electrons exchanged obtained from the LSV tests are displayed in Figure 7.6a, 7.6b, 7.6c, and 7.6d, respectively. The main electrochemical parameters obtained for the electrocatalysts prepared and the reference material (Pt/C) are presented in Table 7.2. The base carbon sample (CNT) displays low E_{onset} and $E_{1/2}$ values (0.76 V and 0.65 V, respectively). Furthermore, CNT does not reach the 3 mA cm^{-2} threshold, usually considered for oxygen bifunctionality, and displays a current density of 1.91 mA cm^{-2} at 0.4 V. Additionally, the reaction follows a 2-electron ORR pathway and generates a high percentage of the undesired H_2O_2 (79%). Hence, the need to incorporate CoPc and FePc active centers to enhance the ORR electroactivity of the CNTs. The incorporation of CoPc (CNT_{Co}) results in a significant increase in the determined ORR parameters in comparison to CNT. The E_{onset} and $E_{1/2}$ increase by 90 mV and 110 mV, respectively, and a current density of 3 mA cm^{-2} is achieved at 0.6 V. At 0.4 V, the current density increases 96% in comparison to CNT and the formation of H_2O_2 is reduced by 21%. However, the number of electrons exchanged is 2.8, which means that the reaction mechanism of CNT_{Co} is still far from the desired 4-electron pathway. Conversely, the introduction of the FePc complex in the CNT sample leads to a much higher increase of electroactivity than that observed for CNT_{Co}, and the electrochemical parameters are comparable with the ORR benchmark catalyst,

Pt/C. The E_{onset} increases from 0.76 V (CNT) to 0.96 V (CNT_{Fe}), whereas the $E_{1/2}$ rises from 0.65 V to 0.88 V, which is even higher than the Pt/C half-wave potential (0.81 V). Besides, the observed E_3 is 0.89 V, which is also higher than that observed for Pt/C (0.82 V). Regarding the current density at 0.4 V, J_L increases 279% compared to CNT. This value is also 35% higher than the current density measured for Pt/C at the same applied potential. The formation of H_2O_2 at 0.4 V is almost negligible (2%), and the number of electrons exchanged achieves a value of 4.0. Therefore, CNT_{Fe} exhibits a very similar ORR electroactivity as Pt/C, surpassing the benchmark electrocatalyst in almost all the electrochemical parameters. These results also suggest that the incorporation of FePc rather than CoPc greatly increases the ORR performance of the CNT. It should be noted that CNT_{Fe} presents a reduction current density higher than the theoretical diffusion-limited current density for ORR (ca. 6 mA cm^{-2}) [68], suggesting that a secondary reaction is also taking place during the ORR assessments. This secondary reaction is attributed to the presence of Fe(III) on the catalyst, generating a small peak at ca. 0.8 V in those samples with the highest concentration of FePc. This peak appears near the ORR, producing an overlap between the ORR current density and the Fe(III)/Fe(II) reduction peak [42, 52]. Afterwards, both reduction reactions reach equilibrium, in which a current density is maintained throughout the plateau, giving rise to a current density higher than 6 mA cm^{-2}.

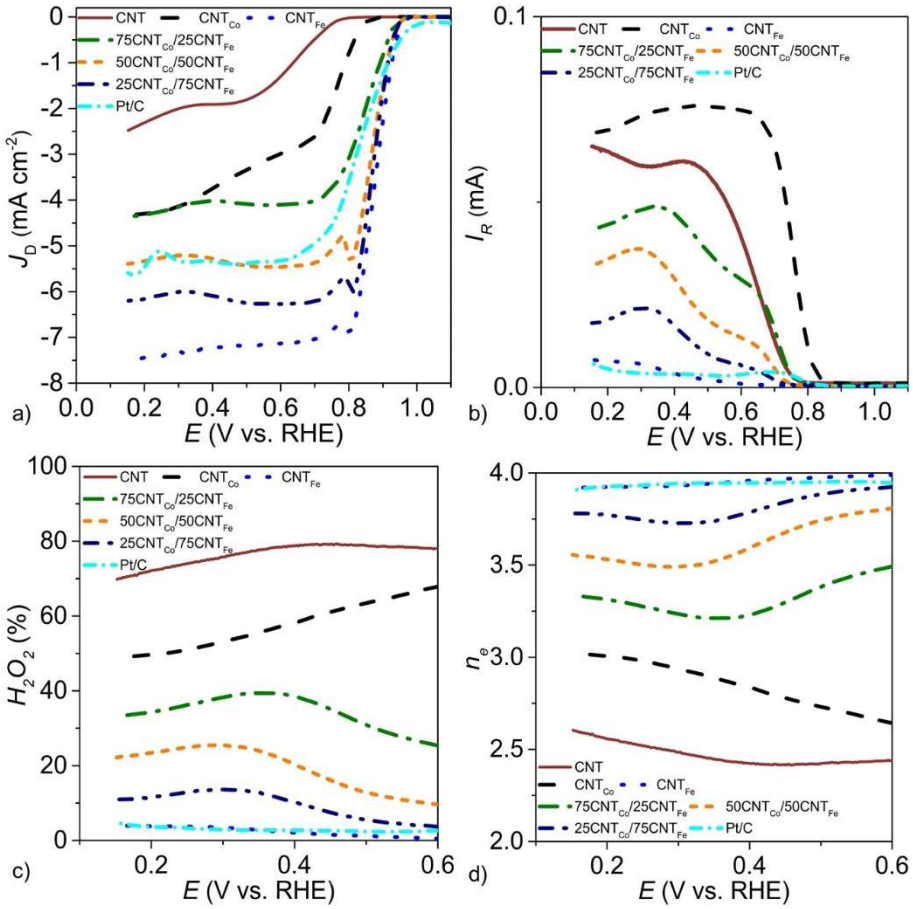


Figure 7.6 - Disk current density (a) and ring current (b) of the linear sweep voltammetry curves recorded at 5 mV s^{-1} in O_2-saturated 0.1 mol L^{-1} KOH electrolyte at 1600 rpm from 1.10 V to 0.15 V using a rotating ring-disk glassy carbon electrode with a Pt ring, production of hydrogen peroxide (c) and number of electrons exchanged (d) for the prepared samples.

Table 7.2 - Onset potential (E_{onset}), half-wave potential ($E_{1/2}$), the potential at which a current density of 3 mA cm^{-2} is achieved (E_3), limiting current density (J_L), hydrogen peroxide (H_2O_2) formation, and the number of electrons exchanged (n_e) for the prepared electrocatalysts and the commercial Pt/C catalyst.

Sample	E_{onset} (V)	$E_{1/2}$ (V)	E_3 (V)	J_L (mA cm^{-2})[a]	H_2O_2 (%)[a]	n_e[a]
CNT	0.76	0.65	-	1.91	79	2.4
CNT_{Co}	0.85	0.76	0.60	3.75	58	2.8
CNT_{Fe}	0.96	0.88	0.89	7.23	2	4.0
$75CNT_{Co}/25CNT_{Fe}$	0.94	0.86	0.80	4.02	39	3.2
$50CNT_{Co}/50CNT_{Fe}$	0.95	0.86	0.87	5.28	20	3.6
$25CNT_{Co}/75CNT_{Fe}$	0.95	0.86	0.88	6.09	10	3.8
Pt/C	1.01	0.81	0.82	5.35	3	3.9

[a] – Calculated at 0.4 V vs RHE.

The differences in the onset potential and reaction mechanism between CoPc and FePc can be explained by the oxygen and H_2O_2 adsorption steps, respectively. The O_2 adsorption in Pcs occurs mainly on the central metal atom, and it is reported to have lower adsorption energy for FePc than for CoPc [50]. The lower value of binding energy for O_2 at the active site results in stronger adsorption of O_2 to the catalyst, which correlates with the higher E_{onset} of CNT_{Fe} shown in Table 7.2. On the other hand, the direct reduction pathway observed in CNT_{Fe} results from the adsorption of H_2O_2, in which both O atoms bind to the Fe atom, increasing the length of the O-O bond beyond the theoretical value (from 1.487 Å to 2.368 Å) [50], as shown in Figure 7.7. This increase causes bond breakage between oxygen atoms, favoring the reaction through the 4-electron pathway. Conversely, the adsorption of H_2O_2 in CoPc assumes a different configuration, as shown in Figure 7.7. The distance between oxygen atoms is similar to the equilibrium bond length, preventing bond breaking and leading to the indirect reaction mechanism [50].

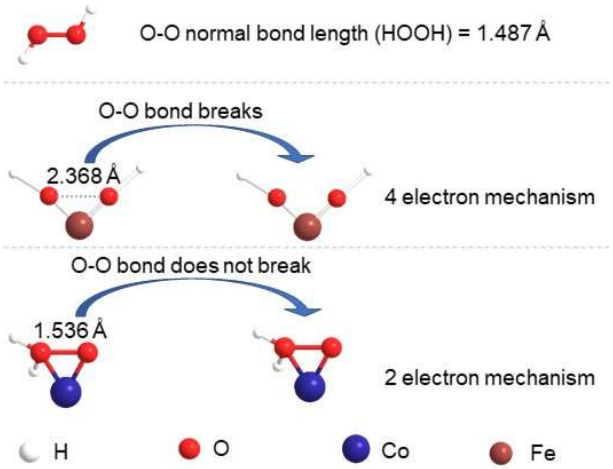


Figure 7.7 - Schematic illustration of H_2O_2 adsorption on iron and cobalt phthalocyanines and their respective reaction mechanisms.

The mixture of CNT_{Co} and CNT_{Fe} in a 3:1 ratio ($75CNT_{Co}/25CNT_{Fe}$) displays an increase in performance compared to the CNT_{Co} sample. The E_{onset} increases 90 mV in comparison to CNT_{Co}, whereas the $E_{1/2}$ increases by 110 mV. At 3 mA cm^{-2} a potential of 0.80 V is recorded, and a current density of 4.32 mA cm^{-2} is achieved at 0.4 V. The by-product formation decreases to 33%, corresponding to 3.3 electrons exchanged at 0.4 V. Moreover, sample $75CNT_{Co}/25CNT_{Fe}$ presents a higher half-wave potential than the commercial Pt/C. These results demonstrate that the incorporation of a small amount of FePc significantly improves the electroactivity of CNT_{Co} towards the ORR. Further tailoring was performed by increasing the percentage of CNT_{Fe} in the mixture. A CNT_{Co}:CNT_{Fe} ratio of 1:1 (sample $50CNT_{Co}/50CNT_{Fe}$) results in improved ORR electrochemical parameters (Table 7.2). The onset slightly increases (10 mV) in comparison to $75CNT_{Co}/25CNT_{Fe}$, whereas a small decrease of $E_{1/2}$ (10 mV) occurs. Nonetheless, a significant increase is observed for E_3 (70 mV), which is a key parameter towards oxygen bifunctionality. The current densities after reaching a plateau (potentials lower than 0.6 V) and at 0.4 V (5.28 mA cm^{-2}) overlap almost perfectly with the current densities obtained for Pt/C. The formation of by-products further decreases to 20% in comparison to $75CNT_{Co}/25CNT_{Fe}$, whereas the number of electrons exchanged increases to 3.6. These results suggest that the overall performance of CNT_{Co} can be improved by increasing the percentage of FePc. However, the E_{onset}, $E_{1/2}$, and E_3 recorded for sample

$25CNT_{Co}/75CNT_{Fe}$ are very similar to those of $50CNT_{Co}/50CNT_{Fe}$, which suggests that after a 1:1 CNT_{Co}:CNT_{Fe} ratio, further addition of FePc does not significantly increase these electrochemical parameters. Nonetheless, an increase of 22% of current density upon reaching a plateau is observed in comparison to $50CNT_{Co}/50CNT_{Fe}$. The formation of by-products further decreases to 10% compared to the other mixtures, and the number of electrons transferred shifts to a value close to the direct mechanism (3.8 electrons). These results indicate that the ratio of CoPc:FePc active sites on the carbon structure plays a crucial role in the current density and the reaction mechanism. In fact, two interesting relationships were found between the FePc contribution calculated using the ICP values and the current densities at potentials where a plateau has been reached (Figure 7.8a) and the number of electrons exchanged (Figure 7.8b).

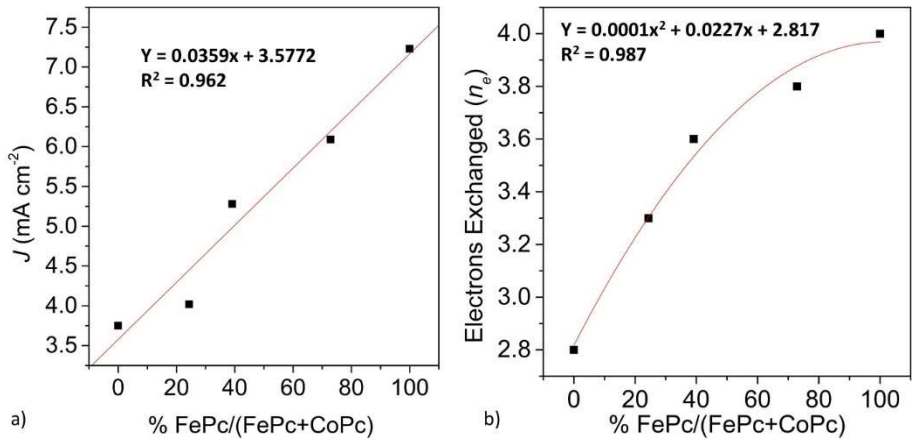


Figure 7.8 - Current density obtained from the linear sweep voltammetry curves of Figure 7.6a (a) and the number of electrons exchanged obtained from Figure 7.6d (b) at a potential of 0.4 V for the prepared samples versus the percentage of FePc against the total Pcs content calculated by ICP.

The current densities of the electrocatalysts increase with the percentage of FePc (Figure 7.8a), due to the higher electroactivity of FePc centers towards oxygen reduction. FePc contributes more to the total current density than CoPc, indicating that more O_2 molecules are reduced at FePc actives centers than at CoPc sites. Therefore, increasing the percentage of FePc also shifts the reaction mechanism closer to the four-electron pathway, as experimentally confirmed (Figure 7.8b). It should be noted that the sample with 25% FePc presents a lower current density (Figure 7.8a), possibly due to the smaller

number of defects in comparison to the sample without FePc and the other bimetallic samples, as observed in the Raman measurements.

Another key parameter to assess the performance of an electrocatalyst towards the ORR is its stability, which affects the lifetime of the final device. Therefore, the stabilities of the prepared carbon materials and the reference electrocatalyst were measured by RDE chronoamperometry, in which a potential of 0.4 V was applied over 10000 s. The methanol tolerance of sample $50CNT_{Co}/50CNT_{Fe}$ was also assessed by the addition of 1.5 mL of methanol at 1000 s during a chronoamperometry measurement. The stability and methanol tolerance results are presented in Figure 7.9.

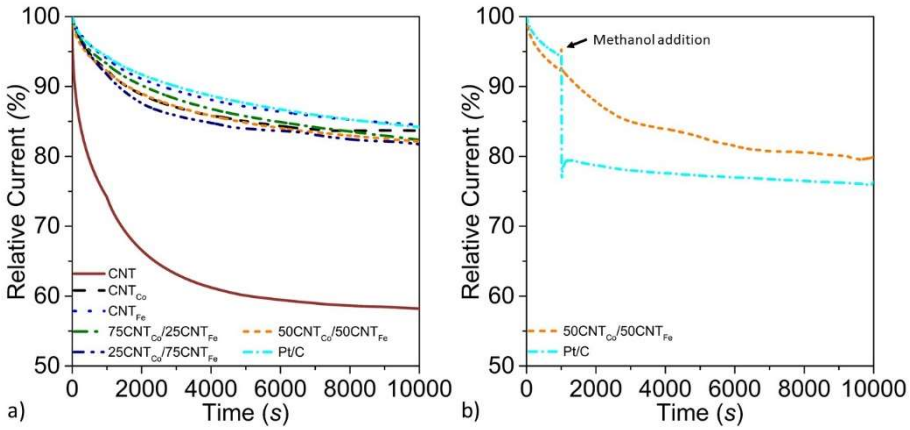


Figure 7.9 - Chronoamperometry measurements for the prepared samples (a) and methanol resistance of sample $50CNT_{Co}/50CNT_{Fe}$ (b) applying 0.4 V during 10000 s at 5 mV s^{-1} and 1600 rpm in an O_2-saturated 0.1 mol L^{-1} KOH electrolyte using a rotating disk glassy carbon electrode.

CNT exhibits stability of 58% during the chronoamperometric test, which is not ideal for long-term applications. The high formation of H_2O_2 during the electrochemical assessments may result in the oxidation of carbon through the byproduct's decomposition, which can lead to a weaker O_2-adsorption that hinders the ORR electrocatalysis [69]. The addition of CoPc and FePc active centers leads to a significant increase in current density retention (84% and 85% retention after 10000s, respectively). It should be noted that CoPc and FePc molecules act as active sites towards the ORR, contributing to a large fraction of the measured current density and, consequently, to the

overall catalyst's stability. However, it should be highlighted that FePc contributes more to keep a high current density than CoPc, as shown in Figure 7.9a. Besides, CNT_{Fe} exhibits similar chronoamperometric results during the 10000 s test as Pt/C, while CNT_{Co} retains less relative current density than Pt/C during most of the analysis. Nonetheless, after reaching a relative current density of 84%, CNT_{Co} does not present further significant density losses. Overall, despite some differences between CNT_{Co} and the other two samples (CNT_{Fe} and Pt/C) during the early stages of the assessment, they all retain the same relative current density at the end of the stability test. Hence these electrocatalysts present the potential to achieve high performances during long-term use and to be promising candidates to replace Pt/C. Regarding the samples obtained by mixing CNT_{Co} and CNT_{Fe}, they all present the same level of retention (82% of their respective current densities after 10000 s). This high stability is a result of the very stable CoPc and FePc active centers that do not suffer significant degradation after the physical mixture of both base samples. Therefore, all the studied samples could be selected to replace the Pt/C commercial electrocatalyst. Additionally, it is shown in Figure 7.9b that the addition of methanol to sample $50CNT_{Co}/50CNT_{Fe}$ during the chronoamperometric assessments increases momentarily the produced current density upon its addition. Moreover, the ORR current of $50CNT_{Co}/50CNT_{Fe}$ remains almost unaffected after the addition of methanol, demonstrating its high methanol tolerance. This result is in agreement with existing literature that remarks the exceptional tolerance of metal-nitrogen-carbon electrocatalysts, in particular Fe-N_4 sites [70]. More importantly, the prepared catalyst does not suffer the significant performance loss that is recorded for the benchmark catalyst, which is another crucial advantage of these materials in comparison to Pt/C.

The prepared carbon electrocatalysts were also evaluated towards the OER to assess their potential bifunctionality. LSV performed in N_2-saturated medium at 5 mV $s^{-1,}$ and the Tafel slopes derived from the LSV are presented in Figure 7.10a and 7.10b, respectively.

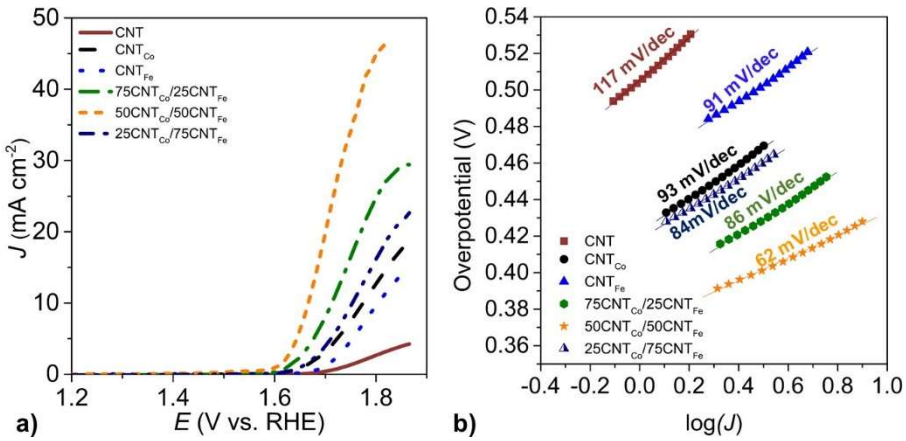


Figure 7.10 - Linear sweep voltammetry curves recorded at 5 mV s^{-1} in an N_2-saturated 0.1 mol L^{-1} KOH electrolyte at 1600 rpm from 1.00 to 1.85 V (a) and their corresponding Tafel plots (b) using a rotating disk glassy carbon electrode.

The CNT sample only starts catalyzing the OER near 1.70 V and does not reach the minimum 10 mA cm^{-2} threshold that is one of the most important parameters towards the OER [29]. The incorporation of CoPc (CNT_{Co}) increases the electroactivity of the carbon material, lowering the potential at which the reaction starts and achieving a E_{10} of 1.77 V. The introduction of the FePc molecules (CNT_{Fe}) enhances the performance of CNT towards OER due to the presence of FePc macrocycles resulting in a potential of 1.80 V at 10 mA cm^{-2}. Contrary to the electrochemical behavior towards the ORR, CNT_{Co} presents a slightly higher OER electroactivity than CNT_{Fe}. The physical mixture with a 3:1 CNT_{Co}:CNT_{Fe} ratio ($75CNT_{Co}/25CNT_{Fe}$) further increases the electroactivity of the material in comparison to CNT_{Co} and CNT_{Fe}, and an E_{10} of 1.73 V is achieved. It should be noted that, contrarily to the competition between both active sites observed towards the ORR, the coexistence of both species seems to provide a synergetic effect towards the electrocatalysis of the OER. The results obtained from the sample with the 1:1 ratio ($50CNT_{Co}/50CNT_{Fe}$) further corroborate this theory, as an additional increase of electroactivity is observed. The LSV of $50CNT_{Co}/50CNT_{Fe}$ displays an increase of current density at even lower potentials and provides the threshold current density at 1.67 V. This value is only 90 mV higher than the value reported for the benchmark RuO_2 electrocatalyst (1.58 V) [71]. Further increasing the percentage of CNT_{Fe} in the sample (sample $25CNT_{Co}/75CNT_{Fe}$) results in an increase of electroactivity in comparison to

CNT_{Fe}, decreasing the E_{10} to 1.75 V. However, the electroactivity of $25CNT_{Co}/75CNT_{Fe}$ is lower than that of $50CNT_{Co}/50CNT_{Fe}$, which suggests that there is an optimal ratio of metallic macrocycles to achieve the best OER performance. Interestingly, comparison between $75CNT_{Co}/25CNT_{Fe}$ and $25CNT_{Co}/75CNT_{Fe}$ highlights the same trends observed for CNT_{Co} and CNT_{Fe}, in which an amount of CoPc larger than FePc seems to contribute slightly more to achieve high performances towards the OER. Although $75CNT_{Co}/25CNT_{Fe}$ presents a lower number of defects than $25CNT_{Co}/75CNT_{Fe}$ (Table 7S.2), a higher content of CoPc results in higher OER performance, further corroborating the importance of the cobalt active centers. Sample $50CNT_{Co}/50CNT_{Fe}$ exhibits the best OER performance of all samples while displaying a similar degree of disorder/graphitization as $25CNT_{Co}/75CNT_{Fe}$. This demonstrates that an optimal ratio of CoPc and FePc is essential to enhance the CNT's OER activity. The presence of both molecules and their synergy is crucial to enhance the electroactivity of CNT as the performance of any mixture is higher than that of CNT_{Co} and CNT_{Fe}.

Another crucial parameter determined was the Tafel slope (Figure 7.10b). CNT presents a Tafel slope of 117 mV/dec. The incorporation of CoPc leads to a decrease to 93 mV/dec, which indicates a faster initial step towards the OER. Similarly, the incorporation of FePc presents a decrease in the Tafel slope value (91 mV/dec), which can be explained by the presence of FePc active centers that may have led to faster kinetics due to the lower adsorption energy of H_2O compared to CoPc [50]. The use of a 3:1 CNT_{Co}:CNT_{Fe} ratio results in a sample with a slightly lower Tafel slope value (86 mV/dec) than that of CNT_{Fe}, which indicates that even though CoPc is the primary molecule of this sample, the synergetic effect of both macrocycles results in enhanced kinetics. Sample $50CNT_{Fe}/50CNT_{Co}$ further highlights this synergetic effect between the phthalocyanines by presenting the fastest kinetics with a Tafel slope value of 62 mV/dec. This value is lower than that reported for the benchmark catalyst RuO_2 (88 mV/dec) [72], which attests to the prepared electrocatalyst's fast kinetics. The calculated kinetics of $50CNT_{Fe}/50CNT_{Co}$ is also similar to some state-of-the-art CNT catalysts that support Co/N (53.7 and 62.0 mV/dec) [73]. Regarding sample $75CNT_{Fe}/25CNT_{Co}$, a similar value (84 mV/dec) as that observed in $25CNT_{Fe}/75CNT_{Co}$ is obtained. To further understand the kinetic differences and the improved OER electroactivity, the double-layer

capacitance (C_{dl}) was calculated for each carbon material (Figure 7S.10). CNT presents a low value of C_{dl} (3.74 x 10^{-8} F). The incorporation of CoPc and FePc leads to a decrease of C_{dl} by 34% and 26%, respectively. It should be noted that the calculations used for the double-layer capacitance determination have been recently reported as part of a novel methodology to compare the metallic centers accessibility between catalysts where a metal species is supported on a carbon material [59]. This methodology suggests that a higher value of C_{dl} is correlated with a higher accessibility to the metallic active species present on the electrocatalyst tested. Therefore, the C_{dl} measurements of CNT_{Co} and CNT_{Fe} indicate that the incorporation of a single metal macrocycle presents a low accessibility to the metallic centers. Nonetheless, sample CNT must not be compared to the other samples prepared as it does not present metal active centers that are important to achieve faster kinetics and to apply this methodology. Furthermore, the comparison of the kinetics and C_{dl} of CNT_{Co} and CNT_{Fe} corroborates this methodology's hypothesis. The incorporation of FePc led to a higher value of C_{dl} than the incorporation of the CoPc molecules, which followed the same trend as the calculated kinetics, in which CNT_{Fe} presented the fastest one of the monometallic samples. A 3:1 CNT_{Co}:CNT_{Fe} mixture ratio leads to an increase of the C_{dl} to 23% more than the base CNT, and 87% and 67% higher than CNT_{Co} and CNT_{Fe}, respectively. This result indicates that the presence of two different types of active centers plays a crucial role to boost the capacity of the CNTs. Increasing the FePc contribution using a 1:1 CNT_{Co}:CNT_{Fe} ratio results in a very high increase of the calculated C_{dl} to 2.84 x 10^{-7} F. This value represents an increase of 401%, 660% and 578% in comparison to CNT, $CNT_{Co,}$ and CNT_{Fe}, respectively. Moreover, the high C_{dl} of $50CNT_{Co}/50CNT_{Fe}$ is also coincident with the highest number of defects displayed in the Raman spectra, which could indicate that both the macrocycle molecules and the number of defects generated are important to increase the number of active sites. Further increasing the FePc contribution by preparing a sample with a 1:3 CNT_{Co}:CNT_{Fe} ratio leads to a decrease of the C_{dl} to values similar to those observed on $75CNT_{Co}/25CNT_{Fe}$. Therefore, the increasing order of C_{dl} is $CNT_{Co} < CNT_{Fe} < CNT < 75CNT_{Co}/25CNT_{Fe} < 25CNT_{Co}/75CNT_{Fe} < 50CNT_{Co}/50CNT_{Fe}$. These results suggest that the synergy between both metallic species increases the C_{dl}, and in turn, the metal sites accessibility of the electrocatalysts, which is crucial towards the adsorption of H_2O. The CNT_{Co} sample presents the lowest metal species accessibility, which results in a

higher Tafel slope value than CNT_{Fe}. $75CNT_{Co}/25CNT_{Fe}$ presents lower C_{dl} than $25CNT_{Co}/75CNT_{Fe}$, which is also in agreement with the slower kinetics calculated. Furthermore, $50CNT_{Co}/50CNT_{Fe}$ has the highest metallic center accessibility, and hence, the fastest kinetics. This higher accessibility, in comparison to the other samples, indicates that the active centers are more easily reached by the H_2O molecules in the electrolyte and, consequently, facilitates their adsorption and subsequent evolution at the active centers. Therefore, the conjugation of higher accessibility of the catalyst's metal species and the metal active center's synergy towards the OER appears to explain the low Tafel slope value of $50CNT_{Co}/50CNT_{Fe}$.

The turnover frequency (TOF) was also calculated from the LSV, which is another important parameter to assess the OER performance of an electrocatalyst, as it represents its intrinsic activity [57]. Samples CNT_{Co} and CNT_{Fe} present TOFs of 0.268 s^{-1} and 0.157 s^{-1}, respectively. Therefore, these initial results suggest that the cobalt macrocycle is more active towards the OER than the iron macrocycle. The mixture of both these samples in a 3:1 CNT_{Co}:CNT_{Fe} ratio increases the TOF to 0.519 s^{-1}, which represents increases of 94% and 231% in comparison to CNT_{Co} and CNT_{Fe}, respectively. Sample $50CNT_{Co}/50CNT_{Fe}$ achieved an even higher TOF reaching 1.480 s^{-1}, corresponding to increases of 353% and 843% compared to CNT_{Co} and CNT_{Fe}, respectively. Regarding the last mixture prepared ($25CNT_{Co}/75CNT_{Fe}$), the TOF value obtained is 0.336 s^{-1}, which is higher than that of the initial samples but lower than the values obtained for the 3:1 and 1:1 ratios. These results demonstrate that CoPc is more important towards OER than FePc, as the samples present improved performances when CoPc is the predominant active center. Nonetheless, a perfect balance between cobalt and iron molecules is necessary to achieve the highest electroactivity towards the OER, giving rise to the highest intrinsic activity for the sample with a mass ratio of 1:1. Stability tests for $50CNT_{Co}/50CNT_{Fe}$ were also carried out to investigate its durability towards OER. The results obtained are presented in Figure 7.11.

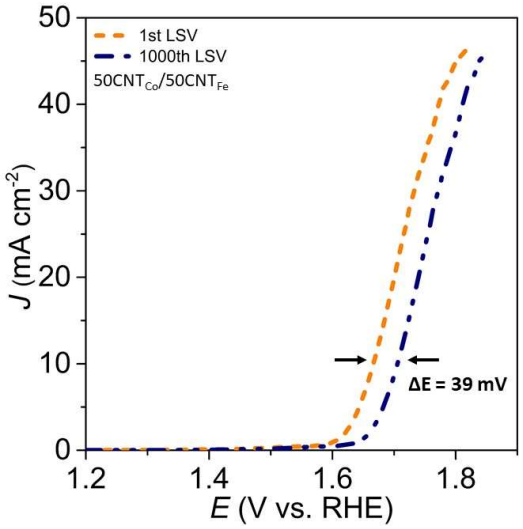


Figure 7.11 - Linear sweep voltammetry curves of $50CNT_{Co}/50CNT_{Fe}$ before and after the stability test.

As shown in Figure 11, after 1000 LSVs, the overpotential of the electrocatalyst increased by 39 mV at a current density of 10 mA cm^{-2}, indicating that the bimetallic sample remains highly electroactive after long-term use. Overall, this catalyst presents high durability towards both oxygen reduction and evolution and an almost unchanged behavior towards methanol poisoning, which is important for scale-up applications.

The bifunctional activity, evaluated by the potential gap (ΔE) between E_{10} for the OER and $E_{1/2}$ or E_3 for the ORR, for the prepared carbon and the benchmark electrocatalysts, is presented in Table 7.3. This parameter is crucial to assess the overall oxygen activity.

Table 7.3 - $E_{1/2}$, E_3, E_{10} and ΔE for the prepared samples and benchmark catalysts.

Sample	$E_{1/2}$ (V)	E_3 (V)	E_{10} (V)	ΔE (V)[a]	ΔE (V)[b]
CNT_{Co}	0.76	0.60	1.78	1.02	1.18
CNT_{Fe}	0.88	0.89	1.80	0.92	0.91
$75CNT_{Co}/25CNT_{Fe}$	0.86	0.80	1.73	0.87	0.93
$50CNT_{Co}/50CNT_{Fe}$	0.86	0.87	1.67	0.81	0.80
$25CNT_{Co}/75CNT_{Fe}$	0.86	0.88	1.75	0.89	0.87
Pt/C	0.81	0.83 [71]	2.01 [71]	1.20	1.18
RuO_2	–	0.10 [71]	1.58 [71]	–	1.48

[a] – $\Delta E = E_{10} - E_{1/2}$

[b] – $\Delta E = E_{10} - E_3$

The potentials observed towards the ORR ($E_{1/2}$) for the carbon samples containing iron reveal very slight differences, as shown in Table 7.3. Consequently, the major factor to achieve a low ΔE is to obtain the lowest possible E_{10} value for the OER. Therefore, the high OER electroactivity of $50CNT_{Co}/50CNT_{Fe}$ makes it the best-suited bifunctional electrocatalyst. Besides, all samples containing FePc are more suitable bifunctional electrocatalysts than the benchmark catalysts used nowadays, exhibiting much lower potential gaps. Furthermore, the results obtained are similar or better than some of the state-of-the-art metal/heteroatom-doped carbon materials already reported [57, 72, 74-78]. For instance, the incorporation of cobalt on carbon nanofibers has achieved a ΔE of 0.82 V [78], the use of cobalt and nitrogen on CNTs has been reported to achieve a potential gap of 0.78 V [75], whereas the incorporation of iron and nitrogen on CNTs accomplished a ΔE of 0.80 V [76], both very similar to $50CNT_{Co}/50CNT_{Fe}$. Moreover, $50CNT_{Co}/50CNT_{Fe}$ presents a slightly lower or identical ΔE (0.81 V) compared to reported state-of-the-art carbon materials with both metallic species such as $CoFe_2O_4$/CNTs (1.02 V) [77], $FeCo_2O_4$/hollow reduced graphene oxide spheres (0.96 V) [77], $CoFe_2O_4$ nanoparticles/rod-like ordered mesoporous carbon (0.84 V) [77], and FeCo-NPC-1100 (0.81 V) [72]. Notwithstanding, the electrocatalysts of the present study offer several advantages in comparison to most of those reported in the literature, such as: i) a reduced number of synthesis steps, ii) the incorporation of a very small amount

of macrocycle molecules (environmentally and cost-wise), and iii) an easily scalable procedure.

7.4. Conclusions

Commercial CNTs were used as bifunctional oxygen electrocatalysts by incorporating two different metal macrocycles onto the carbon structure: CoPc (CNT_{Co}) and FePc (CNT_{Fe}). These two samples were then physically mixed using different CNT_{Co}:CNT_{Fe} mass ratios (3:1, 1:1, and 1:3). ICP analyzes indicated the successful incorporation of the metal complexes, with percentages similar to the theoretical values. Regarding the ORR assessments, CNTs supporting FePc presented higher onsets (0.96 V) than those of CNTs with CoPc (0.85 V), and a reaction mechanism closer to the four-electron pathway due to the lower O_2 adsorption energy and longer O-O bonds formed in FePc active sites. This effect was also shown for the mixed samples, in which the electroactivity increased with the content of FePc, achieving electrochemical performances that surpassed that of Pt/C. Additionally, all CNT samples containing Pcs presented high capabilities to perform efficiently during long-term use with durabilities similar to the benchmark catalyst (Pt/C). Regarding the OER measurements, a totally different behavior was observed. Although CNT_{Co} and CNT_{Fe} presented low OER performances, the physical mixture of these samples led to a synergetic effect that significantly improved the electrochemical performance of CNTs towards the OER. The best OER electroactivity was observed when the mixture was prepared using the same amount of CNT_{Co} and CNT_{Fe} ($50CNT_{Co}/50CNT_{Fe}$), achieving a potential of 1.67 V at the 10 mA cm^{-2} threshold. This sample also exhibited the lowest potential gap (0.81 V), demonstrating its great potential as a bifunctional oxygen electrocatalyst. Besides, sample $50CNT_{Co}/50CNT_{Fe}$ was prepared using a minimal amount of macrocycle molecules, which may lead to low production costs and high up-scaling potential towards producing carbon material for green energy applications.

7.5. Supplementary Information

7.5.1. Electrocatalysts preparation

The samples prepared following the methodology described in the experimental section of the manuscript (CNT_{Fe_Co}, CNT_{Co_Fe}, CNT_{CoFe}, and $50CNT_{Co}/50CNT_{Fe}$) were electrochemically characterized to determine their performances towards the oxygen reduction reaction (ORR) and the oxygen evolution reaction (OER). Linear sweep voltammetry (LSV) at 1600 rpm in O_2- or N_2- saturated 0.1 mol L^{-1} KOH electrolytes was performed for ORR and OER, respectively. The obtained voltammograms are presented in Figure 7S.1.

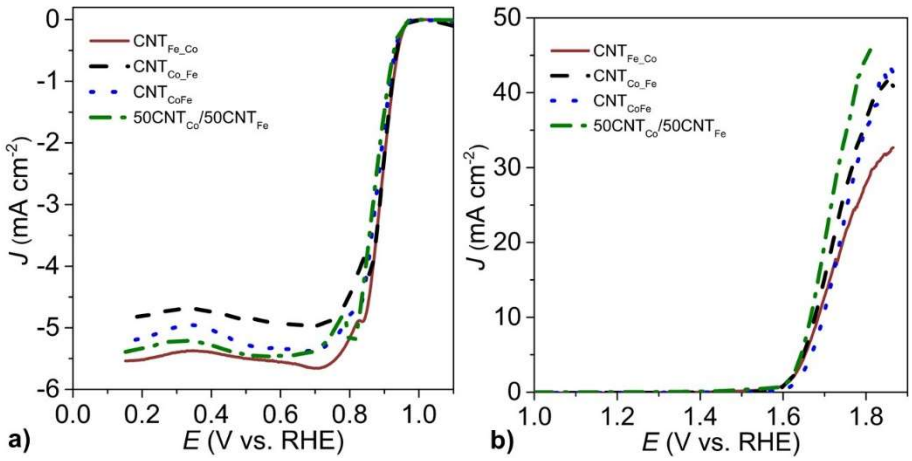


Figure 7S.1 - Linear sweep voltammograms of the prepared samples recorded at 5 mv s^{-1} and 1600 rpm in (a) O_2-saturated 0.1 mol L^{-1} KOH electrolyte from 1.10 to 0.15 V to evaluate the performance towards the ORR using a rotating ring-disk glassy carbon electrode with a Pt ring and (b) N_2-saturated 0.1 mol L^{-1} KOH electrolyte from 1.00 to 1.85 V to evaluate the performance towards the OER using a rotating disk glassy carbon electrode.

All samples present very similar onset potentials towards the ORR, in which CNT_{Fe_Co} and $50CNT_{Fe}/50CNT_{Co}$ present slightly higher current densities. Regarding OER, sample $50CNT_{Fe}/50CNT_{Co}$ displays the highest current density and lowest overpotential of the four samples. Therefore, considering the higher bifunctional electroactivity of $50CNT_{Fe}/50CNT_{Co}$ and the reduced use of metal precursors, the physical mixture was

considered the best procedure to prepare further electrocatalysts. In addition, to further optimize the electrocatalysts' preparation process, a sample following the same methodology as $50CNT_{Co}/50CNT_{Fe}$ was prepared by adding twice the amount of CoPc and FePc. This synthesized catalyst ($50CNT_{2Co}/50CNT_{2Fe}$) was used to determine the optimal loading of metal on the CNTs. This sample was electrochemically characterized towards ORR and OER by LSV. Linear sweep voltammetry was performed at 1600 rpm in an O_2-saturated 0.1 mol L^{-1} KOH electrolyte for ORR and at 1600 rpm in a N_2-saturated 0.1 mol L^{-1} KOH electrolyte for the OER. The obtained voltammograms for samples $50CNT_{2Co}/50CNT_{2Fe}$ and $50CNT_{Co}/50CNT_{Fe}$ are presented in Figure 7S.2.

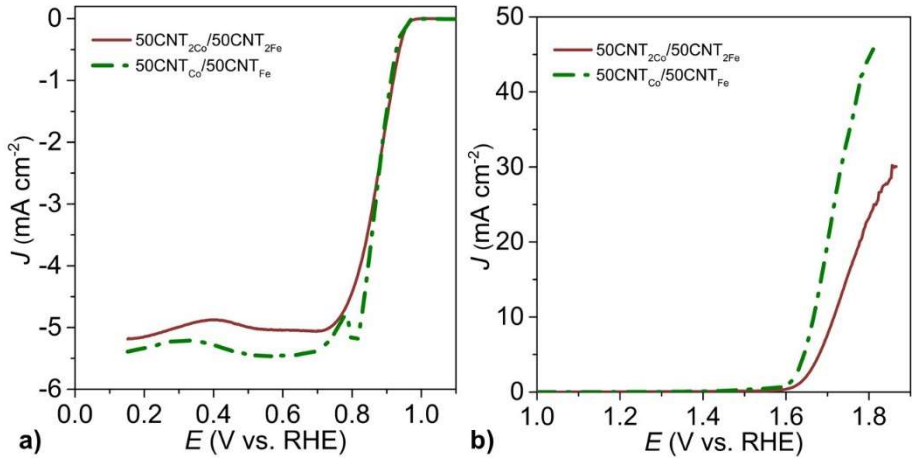


Figure 7S.2 - Linear sweep voltammograms of the physically mixed samples recorded at 5 mv s^{-1} and 1600 rpm in (a) O_2-saturated 0.1 mol L^{-1} KOH electrolyte from 1.10 to 0.15 V to evaluate the performance towards the ORR using a rotating ring-disk glassy carbon electrode with a Pt ring and (b) N_2-saturated 0.1 mol L^{-1} KOH electrolyte from 1.00 to 1.85 V to evaluate the performance towards the OER using a rotating disk glassy carbon electrode.

The results obtained exhibit higher electroactivity towards both reactions for the $50CNT_{Co}/50CNT_{Fe}$ sample. Therefore, a physical mixture using the samples CNT_{Co} and CNT_{Fe} was the procedure chosen to prepare the remaining samples of this study.

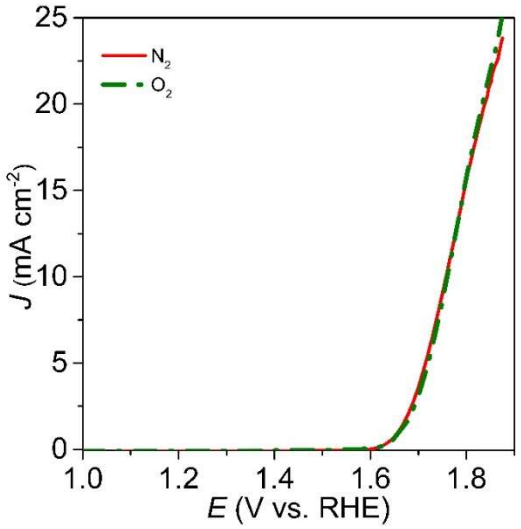


Figure 7S.3 - Linear sweep voltammogram of sample $25CNT_{Co}/75CNT_{Fe}$ recorded at 5 mv s^{-1} and 1600 rpm in N_2-saturated (red) and O_2-saturated (green) 0.1 mol L^{-1} KOH electrolyte from 1.00 to 1.85 V to evaluate the performance towards the OER using a rotating disk glassy carbon electrode.

The results obtained display the same electrocatalytic activity towards OER in KOH saturated with either N_2 or O_2 gases. Hence, using N_2 rather than O_2 does not seem to hinder the OER performance of the prepared samples and the use of N_2 was implemented throughout all assessments.

7.5.2. Electrocatalysts characterization

Table 7S.1 - Surface chemical composition determined by XPS.

Sample	C (wt%)	N (wt%)	O (wt%)	Co (wt%)	Fe (wt%)	N-6 (%)	N-5 (%)	N-Q (%)
CNT	97.41	n.d.	2.59	n.d.	n.d.	n.d.	n.d.	n.d.
CNT_{Co}	98.05	1.03	0.32	0.60	n.d.	70.87	20.63	8.50
CNT_{Fe}	98.41	0.81	0.51	n.d.	0.27	83.49	16.51	n.d.
$75CNT_{Co}/25CNT_{Fe}$	97.71	1.39	0.30	0.60	n.d.	74.68	17.41	7.91
$50CNT_{Co}/50CNT_{Fe}$	98.07	0.99	0.44	0.33	0.17	79.52	15.49	4.99
$25CNT_{Co}/75CNT_{Fe}$	98.12	0.73	0.76	0.19	0.20	82.85	17.15	n.d.
FePc	74.81	16.54	2.73	n.d.	5.99	90.50	9.50	-

n.d. – not detected

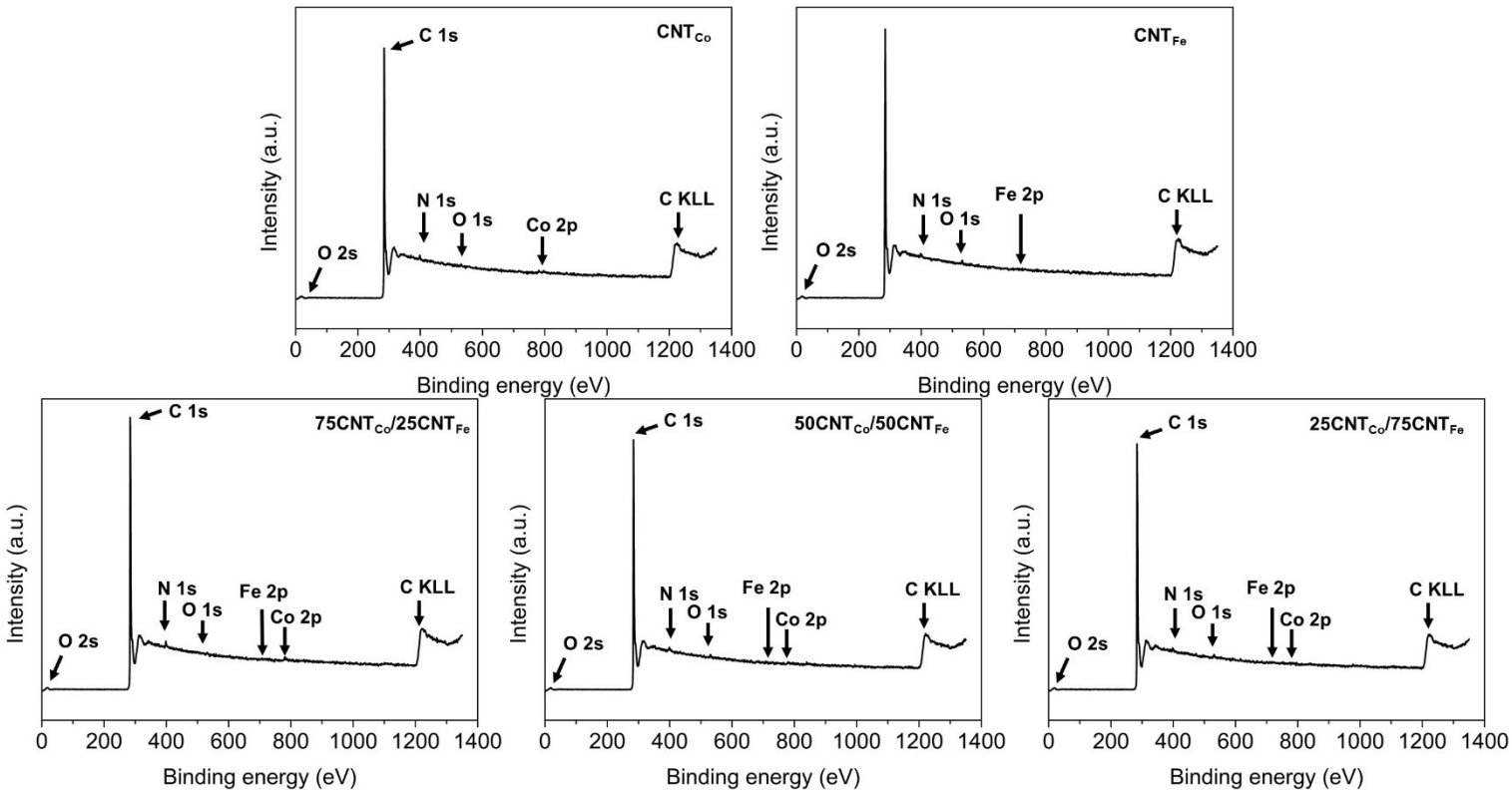


Figure 7S.4 - Survey spectra of the prepared monometallic and bimetallic electrocatalysts.

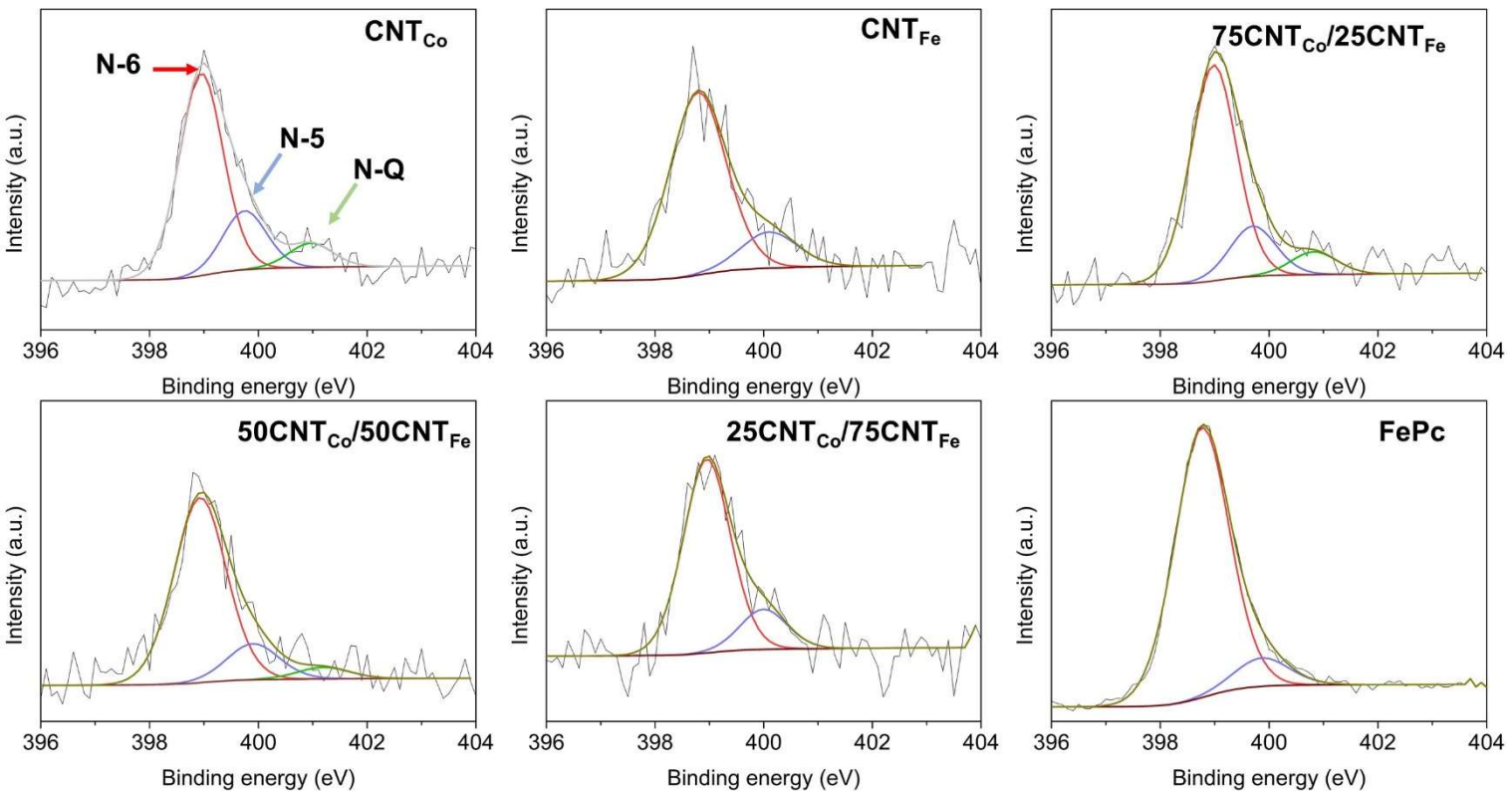


Figure 7S.5 - Deconvolution of the N 1s X-ray photoelectron spectra of the prepared monometallic and bimetallic electrocatalysts and FePc.

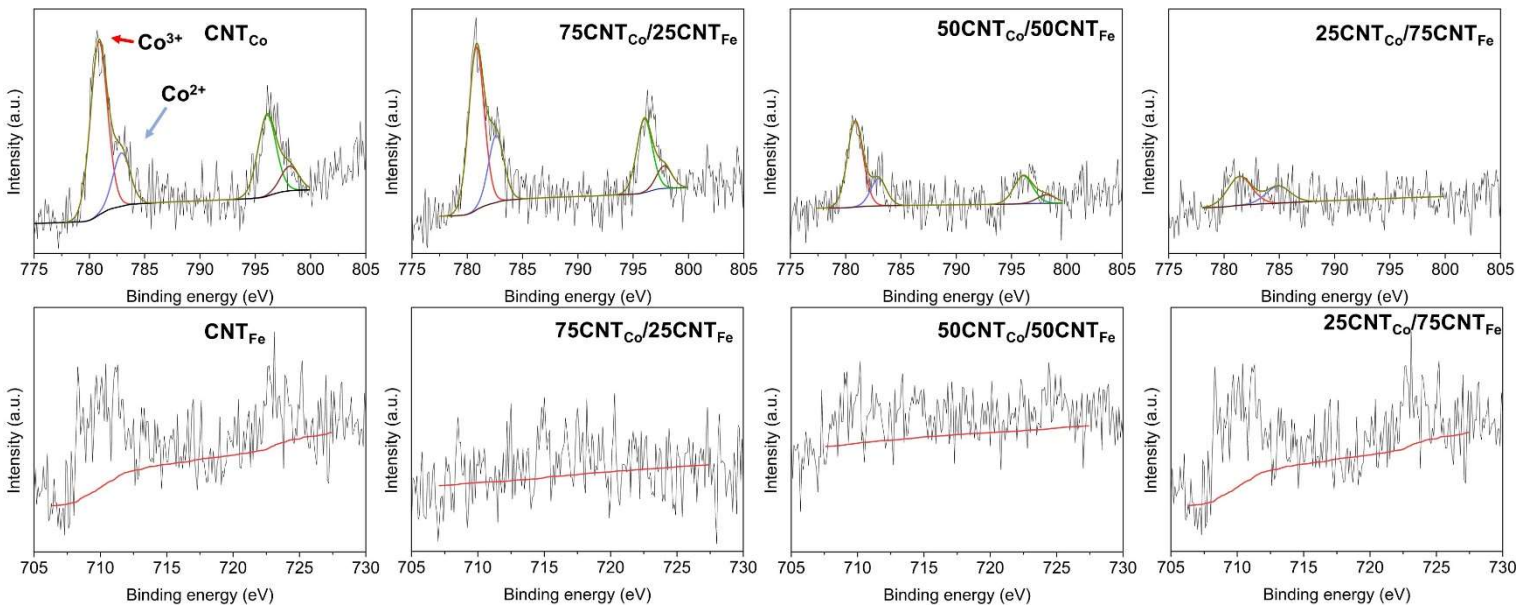


Figure 7S.6 - Deconvolution of the Co 2p (top row) and the Fe 2p (bottom row) X-ray photoelectron spectra of the prepared monometallic and bimetallic electrocatalysts.

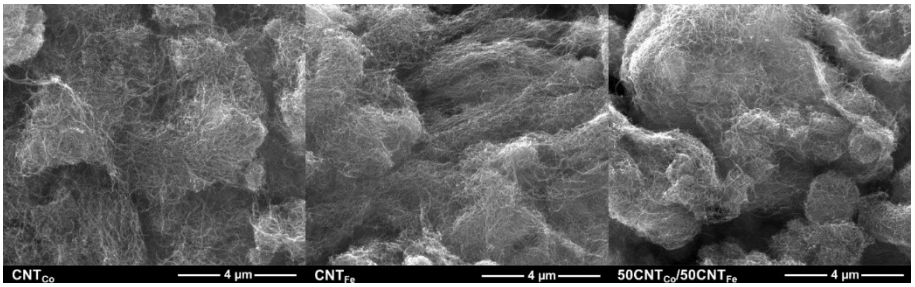


Figure 7S.7 - SEM micrographs of CNT_{Co}, CNT_{Fe} and $50CNT_{Co}/50CNT_{Fe}$.

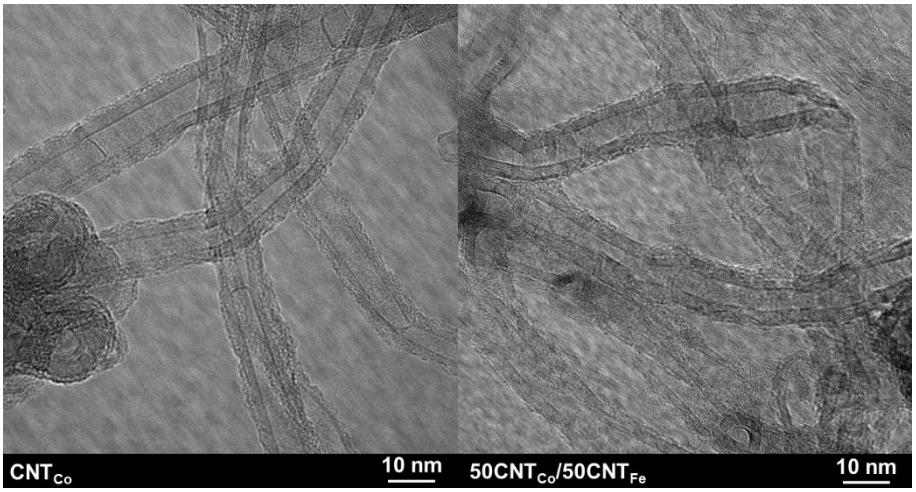


Figure 7S.8 - TEM micrograph of CNT_{Co} and $50CNT_{Co}/50CNT_{Fe}$.

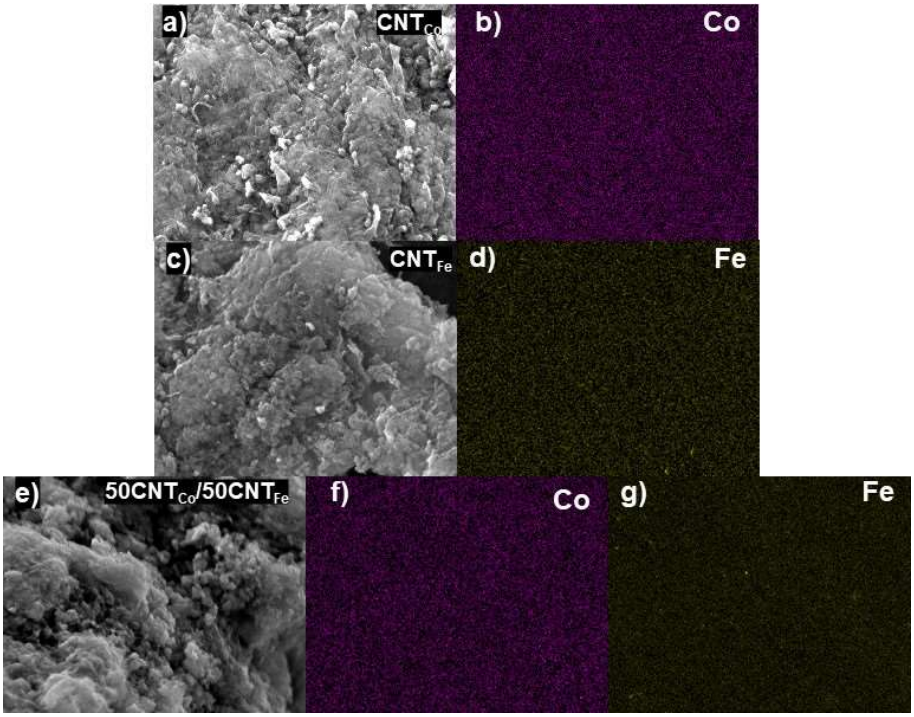


Figure 7S.9 - SEM micrographs and respective elemental mapping analysis of CNT_{Co} (a and b), CNT_{Fe} (c and d) and $50CNT_{Co}/50CNT_{Fe}$ (e, f and g). Purple – Cobalt (b and f), Yellow – Iron (d and g).

Table 7S.2 - Ratio of the integrated D and G peaks obtained by Raman spectroscopy.

Sample	A_D/A_G
CNT	0.39
CNT_{Co}	0.54
CNT_{Fe}	0.42
$75CNT_{Co}/25CNT_{Fe}$	0.50
$50CNT_{Co}/50CNT_{Fe}$	0.67
$25CNT_{Co}/75CNT_{Fe}$	0.64

Table 7S.3 - Textural properties determined by N_2 adsorption/desorption isotherms at -196 ºC.

Sample	S_{BET} ($m^2\ g^{-1}$)	V_p ($cm^3\ g^{-1}$)
CNT	217	1.65
CNT_{Co}	183	1.59
CNT_{Fe}	187	1.45
$75CNT_{Co}/25CNT_{Fe}$	183	1.54
$50CNT_{Co}/50CNT_{Fe}$	181	1.41
$25CNT_{Co}/75CNT_{Fe}$	184	1.62

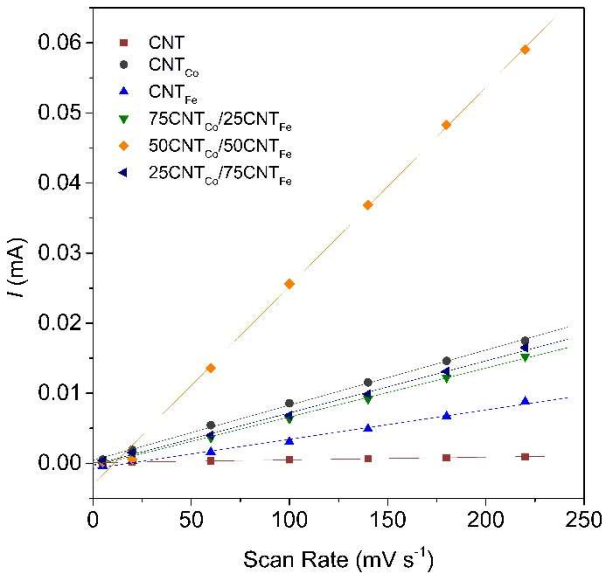


Figure 7S.10 - Linear fitting of capacitive currents at 1.13 V vs RHE plotted against the scan rate obtained from cyclic voltammograms recorded at a scan rate range between 5 mV s^{-1} and 220 mV s^{-1} in N_2-saturated 0.1 mol L^{-1} KOH electrolyte.

7.6. References

[1] Y. Wang, D.Y.C. Leung, J. Xuan, H. Wang, A review on unitized regenerative fuel cell technologies, part-A: Unitized regenerative proton exchange membrane fuel cells, Renew. Sust. Energ. Rev., 65 (2016) 961-977.
[2] Y. Lv, C. Han, Y. Zhu, T. Zhang, S. Yao, Z. He, L. Dai, L. Wang, Recent advances in metals and metal oxides as catalysts for vanadium redox flow battery: Properties, structures, and perspectives, J. Mater. Sci. Technol., 75 (2021) 96-109.
[3] J. Stacy, Y.N. Regmi, B. Leonard, M. Fan, The recent progress and future of oxygen reduction reaction catalysis: A review, Renew. Sust. Energ. Rev., 69 (2017) 401-414.
[4] A. Kirubakaran, S. Jain, R.K. Nema, A review on fuel cell technologies and power electronic interface, Renew. Sust. Energ. Rev., 13 (2009) 2430-2440.
[5] B. Paul, J. Andrews, PEM unitised reversible/regenerative hydrogen fuel cell systems: State of the art and technical challenges, Renew. Sust. Energ. Rev., 79 (2017) 585-599.
[6] T. Sadhasivam, K. Dhanabalan, S.-H. Roh, T.-H. Kim, K.-W. Park, S. Jung, M. Kurkuri, H.-Y. Jung, A comprehensive review on unitized regenerative fuel cells: Crucial challenges and developments, Int. J. Hydrog. Energy, 42 (2016) 1-19.
[7] K. Dutta, D. Rana, H.S. Han, P.P. Kundu, Unitized Regenerative Fuel Cells: A Review on Developed Catalyst Systems and Bipolar Plates, Fuel Cells, 17 (2017) 736-751.
[8] Z. Pu, G. Zhang, A. Hassanpour, D. Zheng, S. Wang, S. Liao, Z. Chen, S. Sun, Regenerative fuel cells: Recent progress, challenges, perspectives and their applications for space energy system, Appl. Energy, 283 (2021) 116376.
[9] Y. Wang, D.Y.C. Leung, J. Xuan, H. Wang, A review on unitized regenerative fuel cell technologies, part B: Unitized regenerative alkaline fuel cell, solid oxide fuel cell, and microfluidic fuel cell, Renew. Sust. Energ. Rev., 75 (2017) 775-795.
[10] M.M. Mohideen, Y. Liu, S. Ramakrishna, Recent progress of carbon dots and carbon nanotubes applied in oxygen reduction reaction of fuel cell for transportation, Appl. Energy, 257 (2020) 114027.
[11] S. Gottesfeld, D.R. Dekel, M. Page, C. Bae, Y. Yan, P. Zelenay, Y.S. Kim, Anion exchange membrane fuel cells: Current status and remaining challenges, J. Power Sources, 375 (2018) 170-184.
[12] W.E. Mustain, M. Chatenet, M. Page, Y.S. Kim, Durability challenges of anion exchange membrane fuel cells, Energy Environ. Sci., 13 (2020) 2805-2838.
[13] A. Sarapuu, E. Kibena-Põldsepp, M. Borghei, K. Tammeveski, Electrocatalysis of oxygen reduction on heteroatom-doped nanocarbons and transition metal–nitrogen–carbon catalysts for alkaline membrane fuel cells, J. Mater. Chem. A, 6 (2018) 776-804.
[14] Y. Qian, Z. Hu, X. Ge, S. Yang, Y. Peng, Z. Kang, Z. Liu, J.Y. Lee, D. Zhao, A metal-free ORR/OER bifunctional electrocatalyst derived from metal-organic frameworks for rechargeable Zn-Air batteries, Carbon, 111 (2017) 641-650.
[15] R. G. Morais, N. Rey-Raap, R. Costa, C. Pereira, A. Guedes, J. L. Figueiredo, M. F. R. Pereira, Hydrothermal Carbon/Carbon Nanotube Composites as Electrocatalysts for the Oxygen Reduction Reaction, J. Compos. Sci., 4 (2020) 1-14.
[16] R. G. Morais, N. Rey-Raap, J. L. Figueiredo, M. F.R. Pereira, Glucose-derived carbon materials with tailored properties as electrocatalysts for the oxygen reduction reaction, Beilstein J. Nanotechnol., 10 (2019) 1089-1102.
[17] C. Sathiskumar, S. Ramakrishnan, M. Vinothkannan, A. Rhan Kim, S. Karthikeyan, D.J. Yoo, Nitrogen-Doped Porous Carbon Derived from Biomass Used as Trifunctional Electrocatalyst toward Oxygen Reduction, Oxygen Evolution and Hydrogen Evolution Reactions, Nanomaterials, 10 (2020) 1-17.
[18] Y. Xiao, S. Deng, M. Li, Q. Zhou, L. Xu, H. Zhang, D. Sun, Y. Tang, Immobilization of Fe-Doped Ni2P Particles Within Biomass Agarose-Derived Porous N,P-Carbon Nanosheets for Efficient Bifunctional Oxygen Electrocatalysis, Front. Chem., 7 (2019) 1-13.

[19] T. Pan, H. Liu, G. Ren, Y. Li, X. Lu, Y. Zhu, Metal-free porous nitrogen-doped carbon nanotubes for enhanced oxygen reduction and evolution reactions, Sci. Bull., 61 (2016) 889-896.
[20] E.Y. Choi, D.E. Kim, S.Y. Lee, C.K. Kim, Electrocatalytic activity of nitrogen-doped holey carbon nanotubes in oxygen reduction and evolution reactions and their application in rechargeable zinc–air batteries, Carbon, 166 (2020) 245-255.
[21] J. Zhang, X. Song, P. Li, Z. Wu, Y. Wu, S. Wang, X. Liu, Sulfur, nitrogen co-doped nanocomposite of graphene and carbon nanotube as an efficient bifunctional electrocatalyst for oxygen reduction and evolution reactions, J. Taiwan Inst. Chem. Eng., 93 (2018) 336-341.
[22] A.M. El-Sawy, I.M. Mosa, D. Su, C.J. Guild, S. Khalid, R. Joesten, J.F. Rusling, S.L. Suib, Controlling the Active Sites of Sulfur-Doped Carbon Nanotube–Graphene Nanolobes for Highly Efficient Oxygen Evolution and Reduction Catalysis, Adv. Energy Mater., 6 (2016) 1501966.
[23] J. Zhang, Y. Sun, J. Zhu, Z. Gao, S. Li, S. Mu, Y. Huang, Ultranarrow Graphene Nanoribbons toward Oxygen Reduction and Evolution Reactions, Adv. Sci., 5 (2018) 1801375.
[24] R. Li, Z. Wei, X. Gou, Nitrogen and Phosphorus Dual-Doped Graphene/Carbon Nanosheets as Bifunctional Electrocatalysts for Oxygen Reduction and Evolution, ACS Catal., 5 (2015) 4133-4142.
[25] H. Shen, H. Peng, R. Cao, L. Yang, Y. Gao, A. Turak, T. Thomas, X. Guo, Y. Zhu, J. Wang, M. Yang, Oxygen Coordination on Fe–N–C to Boost Oxygen Reduction Catalysis, J. Phys. Chem. Lett., 12 (2021) 517-524.
[26] D. Barrera, M. Florent, K. Sapag, T.J. Bandosz, Insight into the Mechanism of Oxygen Reduction Reaction on Micro/Mesoporous Carbons: Ultramicropores versus Nitrogen-Containing Catalytic Centers in Ordered Pore Structure, ACS Appl. Energy Mater., 2 (2019) 7412-7424.
[27] S.S. Sekhon, J. Lee, J.-S. Park, Biomass-derived bifunctional electrocatalysts for oxygen reduction and evolution reaction: A review, J. Energy Chem., 65 (2022) 149-172.
[28] M. Seredych, K. László, E. Rodríguez-Castellón, T.J. Bandosz, S-doped carbon aerogels/GO composites as oxygen reduction catalysts, J. Energy Chem., 25 (2016) 236-245.
[29] H. Zhong, C.A. Campos-Roldán, Y. Zhao, S. Zhang, Y. Feng, N. Alonso-Vante, Recent Advances of Cobalt-Based Electrocatalysts for Oxygen Electrode Reactions and Hydrogen Evolution Reaction, Catalysts, 8 (2018) 1-43.
[30] K.B. Ibrahim, M.-C. Tsai, S.A. Chala, M.K. Berihun, A.W. Kahsay, T.A. Berhe, W.-N. Su, B.-J. Hwang, A review of transition metal-based bifunctional oxygen electrocatalysts, J. Chin. Chem. Soc., 66 (2019) 829-865.
[31] H. Osgood, S.V. Devaguptapu, H. Xu, J. Cho, G. Wu, Transition metal (Fe, Co, Ni, and Mn) oxides for oxygen reduction and evolution bifunctional catalysts in alkaline media, Nano Today, 11 (2016) 601-625.
[32] P. Ganesan, M. Prabu, J. Sanetuntikul, S. Shanmugam, Cobalt Sulfide Nanoparticles Grown on Nitrogen and Sulfur Codoped Graphene Oxide: An Efficient Electrocatalyst for Oxygen Reduction and Evolution Reactions, ACS Catal., 5 (2015) 3625-3637.
[33] T. Oh, K. Kim, J. Kim, Controllable active sites and facile synthesis of cobalt nanoparticle embedded in nitrogen and sulfur co-doped carbon nanotubes as efficient bifunctional electrocatalysts for oxygen reduction and evolution reactions, J. Energy Chem., 38 (2019) 60-67.
[34] N. Li, Y. Nam, J. Yong Lee, Catalytic nature of iron-nitrogen-graphene heterogeneous catalysts for oxygen evolution reaction and oxygen reduction reaction, Appl. Surf. Sci., 514 (2020) 146073.
[35] K. Mamtani, D. Jain, A.C. Co, U.S. Ozkan, Nitrogen-Coordinated Iron−Carbon as Efficient Bifunctional Electrocatalysts for the Oxygen Reduction and Oxygen Evolution Reactions in Acidic Media, Energy Fuels, 31 (2017) 6541-6547.
[36] C. Li, T. Huang, Z. Huang, J. Sun, C. Zong, J. Yang, W. Deng, F. Dai, A sulfonated cobalt phthalocyanine/carbon nanotube hybrid as a bifunctional oxygen electrocatalyst, Dalton Trans., 48 (2019) 17258-17265.

[37] L. Osmieri, R. Escudero-Cid, A.H.A. Monteverde Videla, P. Ocón, S. Specchia, Performance of a Fe-N-C catalyst for the oxygen reduction reaction in direct methanol fuel cell: Cathode formulation optimization and short-term durability, Appl. Catal. B-Environ., 201 (2017) 253-265.
[38] A. Arul, H. Pak, K.U. Moon, M. Christy, M.Y. Oh, K.S. Nahm, Metallomacrocyclic–carbon complex: A study of bifunctional electrocatalytic activity for oxygen reduction and oxygen evolution reactions and their lithium-oxygen battery applications, Appl. Catal. B-Environ., 220 (2018) 488-496.
[39] X. Ge, A. Sumboja, D. Wuu, T. An, B. Li, F.W.T. Goh, T.S.A. Hor, Y. Zong, Z. Liu, Oxygen Reduction in Alkaline Media: From Mechanisms to Recent Advances of Catalysts, ACS Catal., 5 (2015) 4643-4667.
[40] Y. Kumar, E. Kibena-Põldsepp, J. Kozlova, A. Kikas, M. Käärik, J. Aruväli, V. Kisand, J. Leis, A. Tamm, K. Tammeveski, Bimetal Phthalocyanine-Modified Carbon Nanotube-Based Bifunctional Catalysts for Zinc-Air Batteries, ChemElectroChem, 8 (2021) 2662-2670.
[41] G. Abarca, M. Viera, C. Aliaga, J.F. Marco, W. Orellana, J.H. Zagal, F. Tasca, In search of the most active MN4 catalyst for the oxygen reduction reaction. The case of perfluorinated Fe phthalocyanine, J. Mater. Chem. A, 7 (2019) 24776-24783.
[42] R.G. Morais, N. Rey-Raap, J.L. Figueiredo, M.F.R. Pereira, Highly electroactive N–Fe hydrothermal carbons and carbon nanotubes for the oxygen reduction reaction, J. Energy Chem., 50 (2020) 260-270.
[43] J. Yang, J. Tao, T. Isomura, H. Yanagi, I. Moriguchi, N. Nakashima, A comparative study of iron phthalocyanine electrocatalysts supported on different nanocarbons for oxygen reduction reaction, Carbon, 145 (2019) 565-571.
[44] A. Morozan, S. Campidelli, A. Filoramo, B. Jousselme, S. Palacin, Catalytic activity of cobalt and iron phthalocyanines or porphyrins supported on different carbon nanotubes towards oxygen reduction reaction, Carbon, 49 (2011) 4839-4847.
[45] M. Canal-Rodríguez, N. Rey-Raap, J.Á. Menéndez, M.A. Montes-Morán, J.L. Figueiredo, M.F.R. Pereira, A. Arenillas, Effect of porous structure on doping and the catalytic performance of carbon xerogels towards the oxygen reduction reaction, Microporous Mesoporous Mater., 293 (2020) 109811.
[46] B. Mecheri, V.C.A. Ficca, M.A. Costa de Oliveira, A. D'Epifanio, E. Placidi, F. Arciprete, S. Licoccia, Facile synthesis of graphene-phthalocyanine composites as oxygen reduction electrocatalysts in microbial fuel cells, Appl. Catal. B-Environ., 237 (2018) 699-707.
[47] Y. Jiang, Y. Lu, X. Lv, D. Han, Q. Zhang, L. Niu, W. Chen, Enhanced Catalytic Performance of Pt-Free Iron Phthalocyanine by Graphene Support for Efficient Oxygen Reduction Reaction, ACS Catal., 3 (2013) 1263-1271.
[48] R. Jasinski, A New Fuel Cell Cathode Catalyst, Nature, 201 (1964) 1212-1213.
[49] R. Venegas, F.J. Recio, J. Riquelme, K. Neira, J.F. Marco, I. Ponce, J.H. Zagal, F. Tasca, Biomimetic reduction of O2 in an acid medium on iron phthalocyanines axially coordinated to pyridine anchored on carbon nanotubes, J. Mater. Chem. A, 5 (2017) 12054-12059.
[50] R. Chen, H. Li, D. Chu, G. Wang, Unraveling Oxygen Reduction Reaction Mechanisms on Carbon-Supported Fe-Phthalocyanine and Co-Phthalocyanine Catalysts in Alkaline Solutions, J. Phys. Chem. C, 113 (2009) 20689-20697.
[51] R.-M. Ion, The Use of Phthalocyanines and Related Complexes in Photodynamic Therapy, in: T. Nyokong, V. Ahsen (Eds.) Photosensitizers in Medicine, Environment, and Security, Springer Netherlands2012, pp. 315-349.
[52] T. Koczorowski, W. Szczolko, T. Goslinski, Physicochemical Properties and Catalytic Applications of Iron Porphyrazines and Phthalocyanines, in: M.M. Rahman, A.M. Asiri (Eds.) Recent Progress in Organometallic Chemistry, IntechOpen2017, pp. 101-121.
[53] H.A. Miller, M. Bellini, W. Oberhauser, X. Deng, H. Chen, Q. He, M. Passaponti, M. Innocenti, R. Yang, F. Sun, Z. Jiang, F. Vizza, Heat treated carbon supported iron(ii)phthalocyanine oxygen reduction catalysts: elucidation of the structure–activity

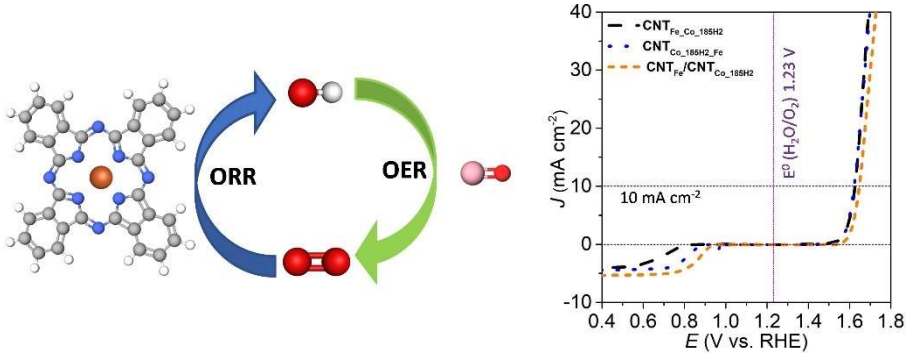
relationship using X-ray absorption spectroscopy, Phys. Chem. Chem. Phys., 18 (2016) 33142-33151.
[54] A. Bonakdarpour, T. Dahn, R. Atanasoski, M. Debe, J. Dahn, H2O2 Release during Oxygen Reduction Reaction on Pt Nanoparticles, Electrochem. Solid-State Lett., 11 (2008) B208-B211.
[55] R.P. Forslund, W.G. Hardin, X. Rong, A.M. Abakumov, D. Filimonov, C.T. Alexander, J.T. Mefford, H. Iyer, A.M. Kolpak, K.P. Johnston, K.J. Stevenson, Exceptional electrocatalytic oxygen evolution via tunable charge transfer interactions in La0.5Sr1.5Ni1−xFexO4±δ Ruddlesden-Popper oxides, Nat. Commun., 9 (2018) 3150.
[56] M. Tahir, L. Pan, F. Idrees, X. Zhang, L. Wang, J.-J. Zou, Z.L. Wang, Electrocatalytic oxygen evolution reaction for energy conversion and storage: A comprehensive review, Nano Energy, 37 (2017) 136-157.
[57] Z.-F. Huang, J. Wang, Y. Peng, C.-Y. Jung, A. Fisher, X. Wang, Design of Efficient Bifunctional Oxygen Reduction/Evolution Electrocatalyst: Recent Advances and Perspectives, Adv. Energy Mater., 7 (2017) 1700544.
[58] Y.P. Zhu, Y. Jing, A. Vasileff, T. Heine, S.-Z. Qiao, 3D Synergistically Active Carbon Nanofibers for Improved Oxygen Evolution, Adv. Energy Mater., 7 (2017) 1602928.
[59] Y. Peng, J.-Y. Choi, T. Fürstenhaupt, K. Bai, Y. Zhang, D. Banham, New approach for rapidly determining Pt accessibility of Pt/C fuel cell catalysts, J. Mater. Chem. A, 9 (2021) 13471-13476.
[60] Y. Jiang, M. Du, G. Cheng, P. Gao, T. Dong, J. Zhou, X. Feng, Z. He, Y. Li, L. Dai, W. Meng, L. Wang, Nanostructured N-doped carbon materials derived from expandable biomass with superior electrocatalytic performance towards V2+/V3+ redox reaction for vanadium redox flow battery, J. Energy Chem., 59 (2021) 706-714.
[61] P. Subramanian, A. Schechter, Electrochemical Oxygen Reduction Activity of Cobalt-Nitrogen-Carbon Composite Catalyst Prepared by Single Precursor Pyrolysis under Autogenic Pressure, J. Electrochem. Soc., 163 (2016) F428-F436.
[62] L.N. Ramavathu, K.K. Maniam, K. Gopalram, R. Chetty, Effect of pyrolysis temperature on cobalt phthalocyanine supported on carbon nanotubes for oxygen reduction reaction, J. Appl. Electrochem., 42 (2012) 945-951.
[63] A. Jorio, R. Saito, Raman spectroscopy for carbon nanotube applications, J. Appl. Phys., 129 (2021) 021102.
[64] K. Zhang, C. Yan, A. Tang, Oxygen-induced electrode activation and modulation essence towards enhanced anode redox chemistry for vanadium flow batteries, Energy Storage Mater., 34 (2021) 301-310.
[65] E.N. Kaya, T. Basova, M. Polyakov, M. Durmuş, B. Kadem, A. Hassan, Hybrid materials of pyrene substituted phthalocyanines with single-walled carbon nanotubes: structure and sensing properties, RSC Adv., 5 (2015) 91855-91862.
[66] R. Kecili, C.M. Hussain, Chapter 4 - Mechanism of Adsorption on Nanomaterials, in: C.M. Hussain (Ed.) Nanomaterials in Chromatography, Elsevier2018, pp. 89-115.
[67] J. Zagal, M. Páez, A.A. Tanaka, J.R. dos Santos, C.A. Linkous, Electrocatalytic activity of metal phthalocyanines for oxygen reduction, J. Electroanal. Chem., 339 (1992) 13-30.
[68] G. Zhong, S. Xu, L. Liu, C.Z. Zheng, J. Dou, F. Wang, X. Fu, W. Liao, H. Wang, Effect of Experimental Operations on the Limiting Current Density of Oxygen Reduction Reaction Evaluated by Rotating-Disk Electrode, ChemElectroChem, 7 (2020) 1107-1114.
[69] H. Singh, S. Zhuang, B. Ingis, B.B. Nunna, E.S. Lee, Carbon-based catalysts for oxygen reduction reaction: A review on degradation mechanisms, Carbon, 151 (2019) 160-174.
[70] Q. Shi, Y. He, X. Bai, M. Wang, D.A. Cullen, M. Lucero, X. Zhao, K.L. More, H. Zhou, Z. Feng, Y. Liu, G. Wu, Methanol tolerance of atomically dispersed single metal site catalysts: mechanistic understanding and high-performance direct methanol fuel cells, Energy Environ. Sci., 13 (2020) 3544-3555.

[71] J. Xia, K. Li, G.-L. Zhao, Electric Field Polarization To Increase Bifunctional Oxygen Electrocatalyst Performance of Nitrogen–Iron Functionalized Carbon Nanomaterials, ACS Appl. Energy Mater., 3 (2020) 1484-1495.
[72] B. Guo, Q. Ju, R. Ma, Z. Li, Q. Liu, F. Ai, M. Yang, S. Kaskel, J. Luo, T. Zhang, J. Wang, Mechanochemical synthesis of multi-site electrocatalysts as bifunctional zinc–air battery electrodes, J. Mater. Chem. A, 7 (2019) 19355-19363.
[73] C. Huang, D. Wu, P. Qin, K. Ding, C. Pi, Q. Ruan, H. Song, B. Gao, H. Chen, P.K. Chu, Ultrafine Co nanodots embedded in N-doped carbon nanotubes grafted on hexagonal VN for highly efficient overall water splitting, Nano Energy, 73 (2020) 104788.
[74] D.U. Lee, P. Xu, Z.P. Cano, A.G. Kashkooli, M.G. Park, Z. Chen, Recent progress and perspectives on bi-functional oxygen electrocatalysts for advanced rechargeable metal–air batteries, J. Mater. Chem. A, 4 (2016) 7107-7134.
[75] Y. Liu, H. Jiang, Y. Zhu, X. Yang, C. Li, Transition metals (Fe, Co, and Ni) encapsulated in nitrogen-doped carbon nanotubes as bi-functional catalysts for oxygen electrode reactions, J. Mater. Chem. A, 4 (2016) 1694-1701.
[76] L. Zhao, Q. Wang, X. Zhang, C. Deng, Z. Li, Y. Lei, M. Zhu, Combined Electron and Structure Manipulation on Fe-Containing N-Doped Carbon Nanotubes To Boost Bifunctional Oxygen Electrocatalysis, ACS Appl. Mater. Interfaces, 10 (2018) 35888-35895.
[77] X. Wu, C. Tang, Y. Cheng, X. Min, S.P. Jiang, S. Wang, Bifunctional Catalysts for Reversible Oxygen Evolution Reaction and Oxygen Reduction Reaction, Chem. Eur. J., 26 (2020) 3906-3929.
[78] J. Yan, Y. Wang, Y. Zhang, S. Xia, J. Yu, B. Ding, Direct Magnetic Reinforcement of Electrocatalytic ORR/OER with Electromagnetic Induction of Magnetic Catalysts, Adv. Mater., 33 (2021) 2007525.

Chapter 8

Optimization of cobalt on CNT towards the oxygen evolution reaction and its synergy with iron (II) phthalocyanine as bifunctional oxygen electrocatalyst

R.G. Morais, N. Rey-Raap, J.L. Figueiredo, M.F.R. Pereira, Optimization of cobalt on CNT towards the oxygen evolution reaction and its synergy with iron (II) phthalocyanine as bifunctional oxygen electrocatalyst, Catalysis Today, (2023) 114057.



Abstract

Monometallic cobalt catalysts supported on carbon nanotubes (Co/CNT) were optimized for the oxygen evolution reaction (OER). The optimized Co/CNT catalyst was physically mixed with another catalyst composed of carbon nanotubes and iron phthalocyanine to achieve an electrocatalyst able to catalyse both the OER and the oxygen reduction reaction (ORR). A 1:1 mass ratio provided a similar OER electroactivity in comparison to the monometallic catalyst (1.64 V) and a high half-wave potential (0.88 V), which is much higher than that of the commercial Pt/C (0.83 V). This sample also produced the lowest potential gap (0.76 V), which is much lower than the commercial electrocatalysts and most state-of-the-art carbon-supported electrocatalysts.

8.1. Introduction

Nowadays, nations need to be energetically independent of fossil fuels and less reliant on other nations for their required energy supply. Furthermore, an energy transition from fossil fuels towards cleaner alternatives is of the greatest importance. The European Commission has proposed hydrogen as a strategy for a climate-neutral Europe [1]. One of the electrochemical devices that is quickly gaining attention from the scientific community is the unitized regenerative fuel cell (URFC). The URFC aims to achieve maximum energy efficiency by combining an electrolyzer and a fuel cell in a single device, producing non-polluting by-products and presenting several advantages in comparison to other systems, namely its portability and high durability [1-6]. The URFC is environmentally friendly, as the electrolyzer mode results in water splitting (H_2O) to generate the necessary fuels for the fuel cell (H_2 and O_2), whereas the generation of energy in the fuel cell mode does not generate polluting products, only H_2O and heat [4, 7, 8]. This device not only complies with the European strategy on adaptation to climate change but is also one of the most promising devices for the short and long-term future of green energy. The URFC involves four different electrochemical reactions: two reactions that take place while operating in the electrolyzer mode – the oxygen evolution reaction (OER) and the hydrogen evolution reaction (HER) - and another pair of reactions that take place in the fuel cell mode – the oxygen reduction reaction (ORR) and the hydrogen oxidation reaction (HOR) [2]. One of the main challenges in the development of this technology is the design of efficient bifunctional electrocatalysts, as they need to catalyze either ORR/OER or HOR/HER, due to the compartmentalization of the URFC device. Regarding both pairs of reactions, the oxygen pair presents much more sluggish kinetics and overall performance, hence needing further improvements to avoid hindering the overall URFC performance. Furthermore, the most developed URFC technology is based on the proton-exchange membrane fuel cell (PEMFC) [1, 6, 9-12], which operates under acidic conditions and requires the use of noble metals. In fact, the current benchmark catalysts for the oxygen reactions are Pt, Ir and Ru, which are scarce and very expensive, increasing the overall cost of the device and limiting its commercialization [6]. One of the main targets of the scientific community is to reduce these costs [2, 6, 13-15]. This can be achieved by changing the operating conditions to basic media, using an

anion-exchange membrane fuel cell (AEMFC) while maintaining high performance. This technology enables the use of a wider range of materials than PEMFC, especially the use of widely available and low-cost carbon materials [6]. These materials have been successfully tailored as bifunctional electrocatalysts towards ORR and OER [16-21], but still require further improvements before achieving large-scale production. The incorporation of different heteroatoms and transition metals, in particular cobalt and iron, is a commonly used methodology to modulate the electrocatalyst properties [16, 18, 22]. Regarding the ORR, iron(II) phthalocyanine (FePc) macrocycles containing both nitrogen and iron provide an interesting synergy between both elements and a constant 4-electron reaction pathway with high electroactivity [16, 23-29]. Similarly, the use of the cobalt(II) phthalocyanine (CoPc) has also displayed interesting performances towards OER [16, 25]. So, the combination of FePc and CoPc results in highly electroactive bifunctional materials [16, 25]. Nonetheless, there is still room for improvement regarding both the electrochemical performances and the production costs. Cobalt has been widely reported as an interesting OER electrocatalyst [30, 31] and can be incorporated into carbon supports using a large variety of methodologies and precursors. Moreover, carbon-based materials doped with cobalt species can also provide high bifunctional catalytic activity towards both ORR and OER [17, 22, 32-35]. Nonetheless, i) a comprehensive study of the evolution of cobalt species and their effect on the OER, ii) their synergy with FePc towards the ORR, and iii) their performance as bifunctional oxygen electrocatalysts are yet to be reported. Therefore, the focus of this work is to investigate the influence of cobalt species supported on carbon nanotubes (CNT) on the OER by incorporating a low-cost cobalt precursor. Furthermore, this study aims to synthesize carbon electrocatalysts with high electrocatalytic performance with regard to both oxygen reactions (OER and ORR) by mixing the optimized Co-doped CNT with a Fe-doped CNT with very high electroactivity towards the ORR. The use of cobalt nitrate as precursor resulted in low production costs due to its low price and the lower thermal treatment temperature needed to achieve the materials with the most promising OER performance. The synergy between both monometallic CNT-based electrocatalyst resulted in remarkable improvements towards bifunctionality, in comparison to the addition of only one metal species.

8.2. Experimental

8.2.1. Preparation of electrocatalysts

Highly electroactive bifunctional ORR/OER electrocatalysts were prepared using purified multi-walled carbon nanotubes. The purification process is explained elsewhere [16]. The CNT were then modified for the OER by addition of cobalt using cobalt (II) nitrate as a precursor. The cobalt precursor was added by the incipient wetness impregnation method. Briefly, 1.25 g of cobalt (II) nitrate hexahydrate (99%, Sigma Aldrich) per gram of purified CNT (Nanocyl, > 95%) was dissolved in ethanol and added dropwise to the CNT under sonication, maintained in the ultra-sonication bath for 30 min and dried overnight at 100 °C. After cobalt impregnation, 6 different samples were prepared using different thermal treatment temperatures and/or atmospheres. Four samples were prepared in a N_2 atmosphere at 150 °C, 185 °C, 350 °C, and 900 °C for 2 h (CNT_{Co_150N2}, CNT_{Co_185N2}, $CNT_{Co_350N2,}$ and CNT_{Co_900N2}, respectively), and two additional samples were prepared by further treating CNT_{Co_185N2} and CNT_{Co_350N2} for 2 h in a H_2 atmosphere (CNT_{Co_185H2} and CNT_{Co_350H2}, respectively). Furthermore, three bifunctional samples were prepared by incorporating iron(II) phthalocyanine (FePc) into the electrocatalysts. Several methodologies were used to incorporate FePc: i) incorporation of FePc using a 1:20 mass ratio (FePc:Co-doped CNT) by incipient wetness impregnation and consequent thermal treatment in a N_2 atmosphere at 500 ºC ($CNT_{Co_185H2_Fe}$); ii) incorporation of FePc using a 1:20 mass ratio (FePc:CNT) and consequent thermal treatment in inert atmosphere at 500 ºC (CNT_{Fe}) and subsequent incorporation of the cobalt nitrate as mentioned in the initial procedure for the sample CNT_{Co_185H2} ($CNT_{Fe_Co_185H2}$) and iii) physical mixture of sample CNT_{Co_185H2} and CNT_{Fe} using a 1:1 mass ratio until a homogeneous mixture was obtained (CNT_{Fe}/CNT_{Co_185H2}). Besides, sample CNT_{Fe}/CNT_{Co_185H2} presents only half of each metal compared to monometallic samples and other Fe,Co-doped materials prepared.

8.2.2. Chemical and textural characterization

Sample combustion at 1050 °C was performed to assess the content of carbon, hydrogen and nitrogen (C, H and N), whereas pyrolysis at 1450 °C was conducted to determine the oxygen content of each prepared material. C, H and N determination was done in a Vario

Micro Cube equipment, whereas oxygen determination was performed using a Rapid Oxy Cube analyzer, both from Elementar GmbH. Moreover, transition metal quantification (cobalt and iron) was determined using a polychromator Echelle in a Perkin Elmer Optima 4300 spectrometer by inductively coupled plasma (ICP) optical emission spectrometry. Additionally, the samples were analyzed in a Kratos AXIS Ultra HAS spectrometer to determine their surface chemical composition by X-ray photoelectron spectroscopy (XPS). This was achieved using a fixed analyzer transmission mode at 15 kV (90 W) and a monochromatic Al Kα radiation (1486.7 eV). Furthermore, N_2 adsorption-desorption isotherms were performed at -196 °C for each material to determine their textural properties. The analyzes took place in an automated gas sorption analyzer (Quantachrome Autosorb iQ). Prior to analyzes, degasification at 150 °C under vacuum conditions took place for 12 h. The specific surface area (S_{BET}) was determined by applying the Brunauer-Emmett-Teller equation. All materials were also analyzed by Raman spectroscopy at a 532 nm monochromatic wavelength in an Alpha 300 equipment (WiTec, Germany). Lastly, selected materials were analyzed by X-ray diffraction (XRD) to determine the composition of their crystalline phases. All XRD experiments took place at 45 kV and 40 mA on a X'Pert Pro diffractometer (PANalytical, Malvern, UK) composed by a PIXcel detector and employing a Cu Kα radiation with a wavelength of 1.541874 Å. The analyzes were performed using a scan speed of 0.01° s^{-1} between 20-80° (2θ) through a Bragg-Brentano configuration.

8.2.3. Electrochemical characterization

All samples were electrochemically characterized using a three-electrode system with a reference (Ag/AgCl, KCL 3 mol L^{-1}) and a counter electrode (carbon rod). The working electrode was composed of a glassy carbon (GC) disk. Two different types of working electrodes were employed according to the data collection desired: i) a rotating disk electrode with a radius of 1.5 mm (RDE, Metrohm) for OER measurements and cyclic voltammetry (CV) that are crucial to determine the double-layer capacitance (C_{dl}), as well as stability tests towards the ORR and ii) a rotating ring-disk electrode (RRDE) with a 2.5 mm radius and a Pt ring (Methrom) that was used for linear sweep voltammetry (LSV) towards ORR assessments. The working electrode with each electrocatalyst was prepared by deposition of ca. 0.27 mg cm^{-2}, of a suspension containing the active material. Each

suspension was prepared by sonication until homogeneity was achieved. The dispersion was prepared with 4 mg of each carbon material and a 1:1:6 solution ratio of Nafion (5 wt% in lower aliphatic alcohols and water, Sigma-Aldrich), ethanol (≥ 99.5%, VWR Chemicals) and ultrapure water (Milipore). All assessments were performed using a PGSTAT 302N potentiostat/galvanostat and a 0.1 mol L^{-1} KOH medium at ambient temperature.

Regarding OER characterization, all samples were tested by performing LSV measurements at 1600 rpm and employing a scan rate of 5 mV s^{-1} up to a potential of 1.85 V (vs RHE). Prior to each LSV, the ohmic resistance (*R*) of each electrocatalyst in the electrolyte was determined using the i-interrupt method [36], which was then used to correct the LSVs obtained during the OER by using the *E-iR* equation, in which *i* corresponds to each current obtained during the electrochemical characterization. After the LSVs, several important parameters used to compare samples worldwide were determined: i) the E_{10}, which is the potential necessary to replicate a 10% efficient conversion device that uses a solar-to-fuels technique (10 mA cm^{-2}) and ii) the Tafel slopes obtained from the LSVs through the *E* vs log (*J*) plots. Furthermore, the long-term performance of the materials was determined by performing 1000 LSVs between the initial potential applied (1.00 V) and the last point measured (1.85 V).

On the other hand, ORR testing (LSV) was achieved in an inert and O_2-saturated medium. Similarly to OER measurements, the scan rate employed for the LSVs was fixed at 5 mv s^{-1}, whereas different rotation speeds were recorded (400-3000 rpm). The rotation speeds were controlled by a rotation speed controller that applied each rotation selected to the working electrode. All ORR experiments took place by applying a potential between 1.10 V and 0.15 V (vs RHE). The final LSV current for each electrocatalyst was obtained by subtracting the current produced during the inert saturation assessments from that obtained in the KOH saturated with O_2. Furthermore, from the subtracted LSV, several ORR parameters were determined: i) the onset potential (E_{onset}) at 0.1 mA cm^{-2}; ii) the half-wave potential ($E_{1/2}$), corresponding to the maximum value obtained by deriving the current-potential curve, which is equivalent to the potential at which the highest increase of *J* between two potentials occurs [37]; and iii) the limiting current density measured at 0.4 V vs RHE (J_L). Additionally, the by-product formation (H_2O_2) of each electrocatalyst

and the respective reaction mechanism (electrons transferred, n_e), were determined by the disk and ring currents obtained from the LSVs measured using a RRDE. These last two parameters were obtained by applying Eqs. (8.1) and (8.2), respectively, to the LSVs measured at 1600 rpm:

$$H_2O_2(\%) = 200 \times \frac{\frac{I_R}{N}}{I_D + \frac{I_R}{N}} \tag{8.1}$$

$$n_e = \frac{4I_D}{I_D + \frac{I_R}{N}} \tag{8.2}$$

where I_R is the ring current (mA), I_D is the disk current (mA), and N is the collection efficiency (0.249).

The long-term durability of each carbon material towards the ORR was measured using a chronoamperometry procedure. The test was performed for 10000 s by employing a potential of 0.4 V vs RHE in O_2-saturated electrolyte. Additionally, to understand the poisoning tolerance of the electrocatalysts with the most interesting performances, methanol (1.5 mL) was added to the reaction medium during the chronoamperometry assessment at ca. 1000 s. Furthermore, each procedure was then replicated for Pt/C (20.2 wt%, 2.5 nm Pt particle size, Alfa Aesar), as a comparison standard for result discussion. Finally, the oxygen bifunctionality performance of the synthesized materials was determined by subtracting the main potential parameter of OER (E_{10}) from the value of $E_{1/2}$ obtained from the ORR assessments. This parameter is known as the potential gap (ΔE) between both reactions and is usually accepted as a good method to determine the bifunctionality of electrocatalysts.

The prepared carbon materials were also electrochemically characterized to determine the double-layer capacitance (C_{dl}) by performing CVs at several scan rates (5-220 mV s^{-1}). These assessments were performed in an inert saturated medium within a potential range in which no Faradic current is produced. Afterwards, the intensity is plotted vs the scan rate and fitted to a straight line. The value of the slope is considered the C_{dl} value. Furthermore, the electrochemical active surface area (ECSA) of each

material, which is essential to gain some insight regarding the accessibility of the active centers [38], is calculated by dividing the C_{dl} by the specific capacitance (C_S) (Eq. 8.3):

$$\mathrm{ECSA} = \frac{C_{\mathrm{dl}}}{C_{\mathrm{S}}} \tag{8.3}$$

Nonetheless, all samples prepared were synthesized using the same materials and very similar procedures, hence very few differences are expected in their chemical nature. Consequently, the ECSA can be considered to be proportional to the double-layer capacitance and can be directly correlated to the main active centers in both reactions.

8.3. Results and discussion

8.3.1. Chemical properties

The surface chemistry of the carbon support was tailored by the incorporation of cobalt nitrate and FePc molecules. The bulk chemical composition of each electrocatalyst obtained from elemental analysis and ICP is presented in Table 8.1. The CNT_{Co_150N2} sample treated at the lowest temperature (150 °C) in the N_2 atmosphere displays the highest oxygen content (11.3 wt%) and the lowest cobalt content (19.6 wt%) of all monometallic cobalt-doped samples, and is the only one of those samples that present nitrogen due to the presence of some cobalt precursor that is not removed at 150 °C [39]. The oxygen content of the samples decreases by increasing the thermal treatment temperature (11.3 wt% > 9.4 wt% > 7.5 wt% > 2.7 wt%) and, consequently, the contribution of cobalt in the global composition increases (19.6 wt% < 20.6 wt% < 21.2 wt% < 22.4 wt%) as the absolute cobalt content remains the same whereas the sum of contributions of all elements decreases. The percentage of oxygen was further reduced after the thermal treatment under the H_2 atmosphere. This reduction is more significant at higher temperatures (350 °C), in which half of the initial oxygen content was lost (from 7.5 wt% to 3.7 wt%). Once again, an increase in the relative cobalt content is observed due to the decrease in oxygen. These results demonstrate that the cobalt precursor was successfully incorporated into the carbon support, although the different thermal treatment conditions resulted in materials with significantly different compositions.

Table 8.1 - Chemical composition determined by elemental analyzes and ICP, and values of S_{BET} obtained from the N_2 adsorption-desorption isotherms.

Sample	C (wt%)	H (wt%)	N (wt%)	O (wt%)	Co (wt%)	Fe (wt%)	S_{BET} ($m^2\ g^{-1}$)
CNT_{Co_150N2}	68.0	0.3	0.8	11.3	19.6	0.0	148
CNT_{Co_185N2}	69.9	0.1	0.0	9.4	20.6	0.0	142
CNT_{Co_185H2}	70.7	0.2	0.0	8.0	21.1	0.0	158
CNT_{Co_350N2}	71.2	0.1	0.0	7.5	21.2	0.0	154
CNT_{Co_350H2}	73.2	0.1	0.0	3.7	23.0	0.0	156
CNT_{Co_900N2}	74.8	0.1	0.0	2.7	22.4	0.0	164
$CNT_{Co_185H2_Fe}$	72.5	0.1	0.0	6.9	20.1	0.4	157
$CNT_{Fe_Co_185H2}$	67.9	0.3	0.0	10.8	20.6	0.4	152
CNT_{Fe}/CNT_{Co_185H2}	82.7	0.1	0.5	4.7	11.8	0.2	149

Regarding the bimetallic samples, interesting differences are observed. Sample $CNT_{Co_185H2_Fe}$ presents a lower oxygen content than sample CNT_{Co_185H2} (6.9 wt% vs 8.0 wt%, respectively) due to the higher temperature applied during the incorporation of FePc (500 °C) compared to that used in the sample with only cobalt nitrate (185 °C). This result is in agreement with the conclusion drawn from the monometallic samples. Moreover, the cobalt content remains similar to that in CNT_{Co_185H2}. Sample $CNT_{Fe_Co_185H2}$ presents very similar oxygen and cobalt contents in comparison to CNT_{Co_185H2} due to the addition of the cobalt nitrate on the CNT_{Fe} sample, which resulted in a single thermal treatment applied to the cobalt nitrate equal to that applied in sample CNT_{Co_185H2}. In both samples ($CNT_{Co_185H2_Fe}$ and $CNT_{Fe_Co_185H2}$) the iron content is in agreement with the theoretical value (0.4 wt%). The content of FePc employed in these two bimetallic samples is too low, so nitrogen was not detected by elemental analysis, while ICP is a more suitable technique to determine low contents of target elements, allowing the detection of low iron amounts in the samples. The bimetallic sample CNT_{Fe}/CNT_{Co_185H2} presents around half of the oxygen, cobalt and iron contents of the monometallic samples, and nitrogen is detected derived from the FePc precursor, indicating that the mixture between samples was successful.

The surface composition determined by X-ray photoelectron spectroscopy (XPS) and the survey spectra are presented in Table 8S.1 and Figure 8S.1, respectively. The survey spectra confirm the presence of all elements discussed during the elemental/ICP analysis except for iron. This absence is related to the much higher Co content than Fe, which results in the overlap of the Fe 2p region and the Co LMM region, from which only the Co peaks are perceptible. Regarding the overall composition of the samples, interesting differences are observed between XPS and elemental/ICP analyzes. The surface oxygen and cobalt contents of all samples are lower than the overall values, indicating that the precursors incorporated are preferentially located in the CNT bundles rather than on their external surfaces. Furthermore, the effect of the temperature and gas composition employed in the thermal treatments is the same as that discussed for the elemental analysis and ICP, with two exceptions. The first exception is a slightly higher oxygen content on the surface of sample CNT_{Co_185N2}. Even though it has a lower overall oxygen content than its counterpart treated at 150 ºC, the higher temperature employed may have

dislocated some of the oxygen to the catalyst's surface. The second exception is the slightly lower surface cobalt content of CNT_{Co_350H2} in comparison to CNT_{Co_350N2}. This difference is not observed for the pair of samples treated at a lower temperature (185 °C), which indicates that the gas composition employed during the treatment does not have a significant effect. However, the temperature may have favored the precursor transition into the bulk of the CNT bundles, hence the lower Co surface content. These results demonstrate that temperature plays a key role in the location of the functional groups.

The high-resolution XPS spectra of the Co 2p regions are presented in Figure 8S.2. The Co 2p region displays two distinct sharp peaks at 780.0 ± 0.4 eV and at 795.2 ± 0.5 eV corresponding to Co $2p_{3/2}$ and Co $2p_{1/2}$, respectively [40], with a spin-orbit splitting of 15.2 eV [41]. The deconvolution of the Co $2p_{3/2}$ region demonstrates the presence and coexistence of Co^{2+} and Co^{3+}, which peaks appear at 779.9 ± 0.1 eV and 781.6 ± 0.3 eV, respectively. Furthermore, two shake-up satellite peaks are also detected at higher binding energies (784.7 ± 0.3 eV and 789.4 ± 1.2 eV), attributed to the presence of Co^{2+} and Co^{3+} species [42]. These four peaks present their corresponding spin-orbit splitting of 15.2 eV. Regardless of the atmosphere employed, the results of the deconvolution indicate an increase in Co^{2+} content and a decrease in Co^{3+} as the temperature increases (Table 8S.1). These results are in agreement with the reaction mechanism ascribed to the thermal decomposition of the cobalt nitrate hexahydrate [43]. Briefly, after the dehydration of the cobalt precursor (150 ºC), Co_2O_3 species are formed, in which the cobalt is in a Co^{3+} oxidation state. Afterwards, an increase in temperature from 150 ºC up to 185 ºC and 350 ºC favors the conversion of Co_2O_3 into Co_3O_4, which presents a mix of Co^{2+} and Co^{3+} species instead of just Co^{3+}, hence increasing the relative content of Co^{2+}, as observed by XPS. Moreover, at temperatures above 700 °C, the formation of CoO also occurs [44], and, consequently, an increase of Co^{2+} is observed for the sample treated at 900 °C. Moreover, the subsequent thermal treatment under H_2 after the one in N_2 further reduces Co_3O_4 to CoO [39], further increasing the relative content of Co^{2+}, as observed by XPS. Regarding bimetallic samples, the deconvolution of the Co 2p region of the sample $CNT_{Fe_Co_185H2}$ presents a lower contribution of Co^{2+} in comparison to CNT_{Co_185H2}, which indicates that the previous incorporation of FePc hinders the effect of the H_2 atmosphere and, consequently, the formation of Co^{2+} species. On the other hand,

$CNT_{Co_185H2_Fe}$ shows an increase of Co^{2+} and a decrease of Co^{3+} species in comparison to CNT_{Co_185H2}, which follows the same trend as the monometallic samples due to the higher temperature applied during the second thermal treatment (500 °C). Lastly, the sample obtained by mixing both monometallic samples (CNT_{Fe}/CNT_{Co_185H2}) displays the same Co^{2+}/Co^{3+} ratio as CNT_{Co_185H2} as no further thermal treatment nor significant mechanical modifications were performed on the bimetallic sample in comparison to the monometallic ones.

The nitrogen adsorption-desorption isotherms of the prepared carbon materials are displayed in Figure 8S.3 and the values of the BET surface area (S_{BET}) are presented in Table 8.1. All samples exhibit a type II isotherm, attributed to multi-layered adsorption commonly observed for carbon nanotubes [45]. Although different temperatures and atmospheres were employed during the thermal treatments, all samples display very similar textural properties. The S_{BET} of all prepared Co-doped materials varies from 142 to 164 $m^2\ g^{-1}$, which is lower than that of the purified CNT (217 $m^2\ g^{-1}$). This is due to the presence of cobalt in the carbon structure. Regarding bimetallic samples, all samples are within the same range as monometallic samples, ranging from 149 to 157 $m^2\ g^{-1}$, which is similar to the base Co-CNT sample prepared using similar conditions (CNT_{Co_185H2}). These results indicate that the methodology employed to incorporate the transition metals does not modify the textural properties.

To further study the changes assigned to the addition of the metallic precursors and/or the thermal treatments applied, all synthesized carbons were analyzed by Raman spectroscopy. The obtained spectra are presented in Figure 8.1.

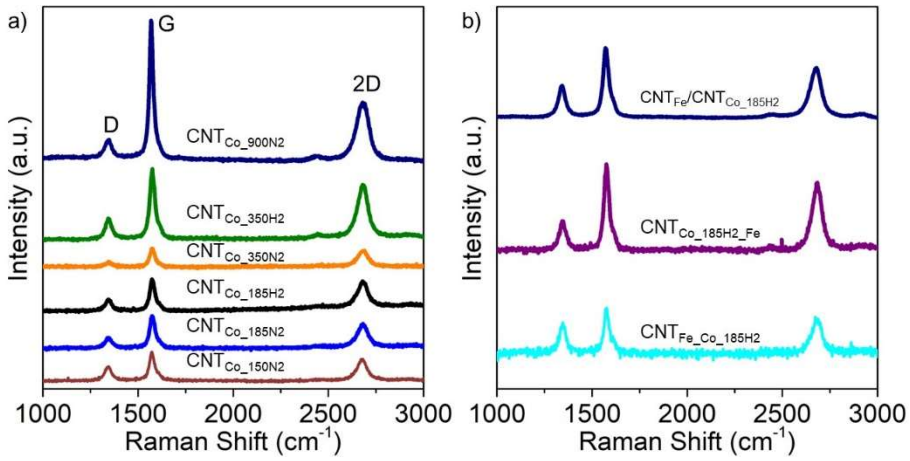


Figure 8.1 - Raman spectra of the Co-doped (a) and Co,Fe-doped electrocatalysts (b).

All samples display two main peaks at ca. 1350 cm^{-1} (D band) associated with the basal plane defects of the carbon structure and a second peak at ca. 1580 cm^{-1} (G band), ascribed to graphitic domains, which are prevalent on CNT. Moreover, at higher shifts (ca. 2700 cm^{-1}), a third peak attributed to the π band in the electronic structure is also observed. To obtain additional information on the relative amount of defects, the peak areas of the respective D and G bands were integrated. The A_D/A_G ratio of all samples is presented in Table 8S.2. The Co-doped CNT treated at the lowest temperature (CNT_{Co_150N2}) presents an A_D/A_G ratio of 0.58. The ratio decreases from 0.58 to 0.20 by increasing the temperature from 150 ºC to 900 ºC, suggesting the formation of a more graphitic structure with a smaller number of defects. Further treatment under H_2 atmosphere slightly increases the A_D/A_G ratio in comparison to their N_2 counterparts (0.40 vs 0.42 and 0.32 vs 0.36, at 185 °C and 350 °C, respectively). These differences suggest that the reduction of cobalt oxides due to the use of H_2 generates defects in the carbon structure.

Regarding the bimetallic samples, interesting differences are observed in comparison to Co-doped samples. Sample $CNT_{Co_185H2_Fe}$ presents an A_D/A_G ratio of 0.39, which is slightly lower than the base sample CNT_{Co_185H2} (0.42), probably due to the high temperature employed (500 °C). Nonetheless, both Co-doped samples treated at 350 ºC present lower values than 0.39, indicating that the incorporation of FePc is probably generating defects in the carbon structure. This effect, due to the presence of FePc, has

been previously reported in the literature [16, 46]. Sample $CNT_{Fe_Co_185H2}$ exhibits an A_D/A_G ratio of 0.77, which is higher than either those of CNT_{Fe} (0.52) or CNT_{Co_185H2} (0.42), which indicates that the incorporation of Co on the CNT_{Fe} sample is leading to the formation of additional defects on the carbon structure. Lastly, sample $CNT_{Fe}/CNT_{20Co_185H2}$ presents an A_D/A_G ratio of 0.51, which is in between the values of the monometallic samples employed in the mixture. This value was expected as this electrocatalyst was not subjected to any further thermal treatment.

To further understand the differences between the synthesized materials, the composition of the crystalline phases of the Co-doped CNTs was studied by X-ray diffraction (XRD). The obtained patterns are displayed in Figure 8S.4 and a detailed discussion is presented in the supplementary material. Briefly, from XRD patterns it can be inferred that using H_2 atmosphere and increasing the temperature of the thermal treatments favors the formation of CoO. In addition, the crystallite size increases from 58 nm to 130 nm by increasing the reduction temperature from 185 °C to 350 °C.

8.3.2. Electrochemical assessments

8.3.2.1. Oxygen Evolution Reaction

The OER electroactivity of the synthesized monometallic Co-doped carbon samples was measured by LSV in a N_2-saturated medium at a scan rate of 5 mV s^{-1} and 1600 rpm (Figure 8.2a).

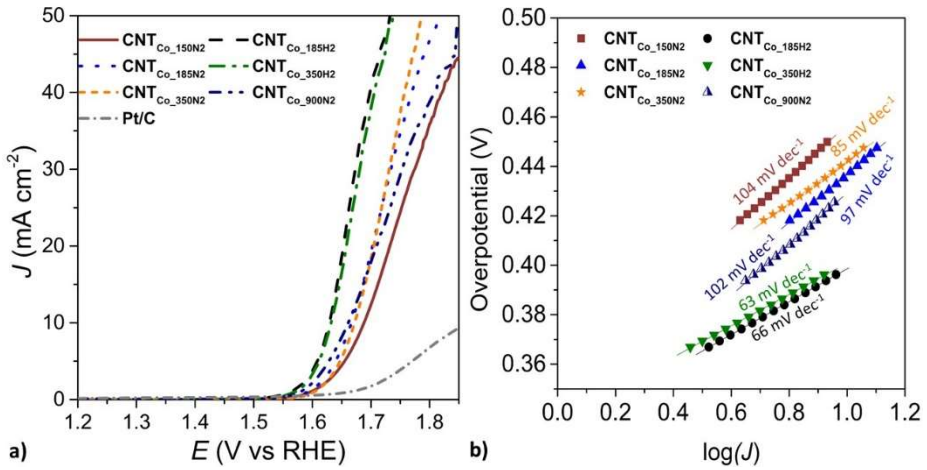


Figure 8.2 - Co-doped samples' (a) OER LSV curves recorded at 1600 rpm using a scan rate of 5 mV s^{-1} in a N_2-saturated 0.1 mol L^{-1} KOH electrolyte, and respective Tafel plots (b).

The E_{10} decreases with temperature from 1.69 V to 1.66 V (from 150 °C to 900 °C) which is likely due to the increase in the relative content of Co^{2+} and the Co^{2+}/Co^{3+} ratio on the surface (Table 8S.1 – XPS). The formation of CoO species results in a very significant decrease of the unit cell length to almost half in comparison to Co_3O_4 [47], which may favor the adsorption and, consequently, the evolution of oxygen. Samples further treated under H_2 atmosphere display even lower values of E_{10} (1.63 V) due to the higher content of Co^{2+} in these samples. Nonetheless, CNT_{Co_900N2} presents a higher Co^{2+} content than the other samples but not the highest electroactivity. This may be explained by the presence of metallic Co that hinders its performance. Accordingly, it is important to select the appropriate temperature and atmosphere to perform the reduction of cobalt species in order to obtain the highest percentage of Co^{2+} and not further reduced species. The reaction kinetics follow the same trend. The Tafel slope decreases (faster kinetics) with increasing temperature from 150 °C (104 mV dec^{-1}) to 350 °C (85 mV dec^{-1}), which is in agreement with the importance of Co^{2+} species towards the electrocatalyst performance. Nonetheless, at 900 °C, the reaction kinetics is slower (102 mV dec^{-1}) than that measured at 350 °C, which seems to be related to the presence of non-oxidized Co species. Regarding samples further treated in H_2, they present very similar Tafel slope values (Figure 8.2b), with a slightly lower value for CNT_{Co_350H2}. This further corroborates the

importance of Co species, as a higher relative Co^{2+} content leads to slightly faster reaction kinetics.

The bimetallic carbon materials were also tested as electrocatalysts in the OER. The LSV curves performed in a N_2-saturated medium at 5 mV s^{-1} are presented in Figure 8.3a.

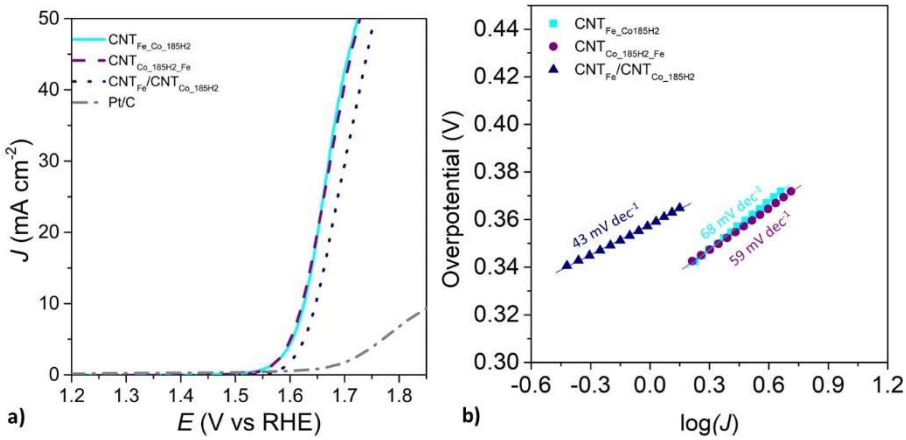


Figure 8.3 - Co,Fe-doped samples' (a) OER LSV curves recorded at 1600 rpm using a scan rate of 5 mV s^{-1} in a N_2-saturated 0.1 mol L^{-1} KOH electrolyte, and respective Tafel plots (b).

The sample $CNT_{Fe_Co_185H2}$ gives rise to a J of 10 mA cm^{-2} at 1.63 V (E_{10}), which is the same value as that obtained with sample CNT_{Co_185H2}. This result indicates that the incorporation of FePc on the carbon support does not provide a significant improvement in the OER activity. This effect may be due to the sample's preparation method and to the small amount of iron incorporated, which is 50 times smaller than that of cobalt. Consequently, the addition of a large amount of cobalt precursor on top of CNT_{Fe} and its very small amount of FePc may have led to the inhibition of iron active centers due to blocking by the cobalt species. Sample $CNT_{Co_185H2_Fe}$ results in an E_{10} of 1.62 V, which is 10 mV lower than that of CNT_{Co_185H2}, suggesting that, despite cobalt species being the main active centers, the presence of FePc contributes to some extent to improve the electrocatalytic performance. This improvement is probably due to the preparation method that led to the presence of the iron active centers on the catalyst's surface avoiding the inhibition observed during the screening of $CNT_{Fe_Co_185H2}$. Therefore, the order in which each metal is incorporated seems to play an important role in the material's

electrochemical performance. The sample prepared from the physical mixture of two monometallic samples (CNT_{Fe}/CNT_{Co_185H2}) resulted in a slight increase in the E_{10} value in comparison to the abovementioned bimetallic electrocatalysts (1.64 V). This effect is probably due to the total content of cobalt. Although the cobalt content is reduced to half, the E_{10} only increases by 10 mV, which is a very low difference in comparison to sample CNT_{Co_185H2}. To further understand the interaction of both monometallic samples, CNT_{Fe} was tested towards the OER (Figure 8S.5) as well as a sample prepared using the same methodology as CNT_{Co_185H2} but using only half of the cobalt precursor content ($CNT_{0.5Co_185H2}$, Figure 8S.6). It is possible to observe that CNT_{Fe} presents a low electroactivity towards OER (1.79 V), whereas $CNT_{0.5Co_185H2}$ presents a slight increase of E_{10} (1.65 V) in comparison to CNT_{Co_185H2} (1.63 V). The physical mixture of Fe-doped CNT and CNT_{Co_185H2} (CNT_{Fe}/CNT_{Co_185H2}) displays an E_{10} of 1.64 V, which, similarly to $CNT_{Co_185H2_Fe}$, exhibits a decrease of 10 mV in comparison to the Co-doped CNT with similar cobalt content ($CNT_{0.5Co_185H2}$). This result further infers that FePc contributes to improving the electrocatalyst's performance towards the OER. From these results, it should be highlighted that bimetallic samples present very close E_{10} values to those of the benchmark RuO_2 catalyst (1.58 V [18]).

The reaction kinetics of the bimetallic samples provide interesting insights into the OER performance. Firstly, sample $CNT_{Fe_Co_185H2}$ presents a very similar Tafel slope value (68 mV dec^{-1}) in comparison to the monometallic cobalt sample CNT_{Co_185H2}, which indicates that the cobalt active centers control the electrocatalyst performance. Nonetheless, the addition of FePc on the surface of CNT_{Co_185H2} (sample $CNT_{Co_185H2_Fe}$) results in a Tafel slope of 59 mV dec^{-1}, which suggests that the presence of iron on the electrocatalyst surface has a positive outcome on the performance of the electrocatalyst. This effect is even more evident in the sample CNT_{Fe}/CNT_{Co_185H2}, in which both metals are incorporated into the CNT separately, favoring the synergy between the FePc and the CNT through their π-π systems [16, 23, 48], which enhances the electroactivity of the material and drops the Tafel slope to 43 mV dec^{-1}. Therefore, even though a slight performance loss is observed for CNT_{Fe}/CNT_{Co_185H2} due to the lower cobalt content, an impressive improvement in the reaction kinetics is achieved. The drop in the Tafel slope value of the mixed sample may be related to its ECSA. The analysis of the double-layer

capacitance (C_{dl}) of the electrocatalysts (Figure 8S.7) suggests that CNT_{Fe}/CNT_{Co_185H2} has a much higher active area than the other samples, which may explain the enhanced reaction kinetics due to the larger amount of available active sites.

Stability tests for the bimetallic samples were also performed to understand their long-term use towards the OER. The LSVs obtained are displayed in Figure 8.4.

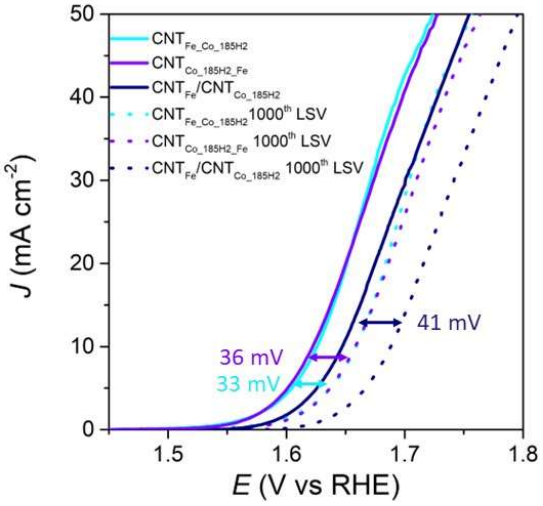


Figure 8.4 - 1st and 1000th OER LSV curves of bimetallic samples obtained in the stability test.

As shown in Figure 8.4, after 1000 LSVs, all samples remain highly electroactive towards the OER. Sample $CNT_{Fe_Co_185H2}$ presents the lowest loss of electroactivity by increasing its overpotential by 33 mV, which is most likely caused by the deactivation of cobalt active sites since, in this sample, iron does not appear to be catalyzing the OER, as previously discussed. Regarding $CNT_{Co_185H2_Fe}$, the overpotential increases by 36 mV, which means that its stability is lower than that of $CNT_{Fe_Co_185H2}$. This effect can be attributed to the degradation of FePc active sites that, in this sample, are crucial in the OER electroactivity. Lastly, CNT_{Fe}/CNT_{Co_185H2} presents an increase of overpotential of 41 mV, which may be attributed to the lower amount of cobalt. Although this sample only presents half of the cobalt content in comparison to the other bimetallic samples, its reaction kinetics are faster, resulting in a higher turnover frequency of the active centers and, consequently, in their deactivation.

8.3.2.2. Oxygen Reduction Reaction

The prepared bimetallic electrocatalysts were tested in the ORR by LSV, using a scan rate of 5 mV s^{-1} in a O_2-saturated 0.1 mol L^{-1} KOH electrolyte at 1600 rpm. Besides these electrocatalysts, samples CNT_{Co_185H2} and CNT_{Fe} were also assessed to further evaluate the modifications of each synthesis. Moreover, the ORR performance of Pt/C was also studied as a benchmark for comparisons with the prepared carbons. The disk current density and number of electrons exchanged are represented in Figure 8.5a and 8.5b, respectively. ORR values determined for materials assessed and Pt/C are exhibited in Table 8.2.

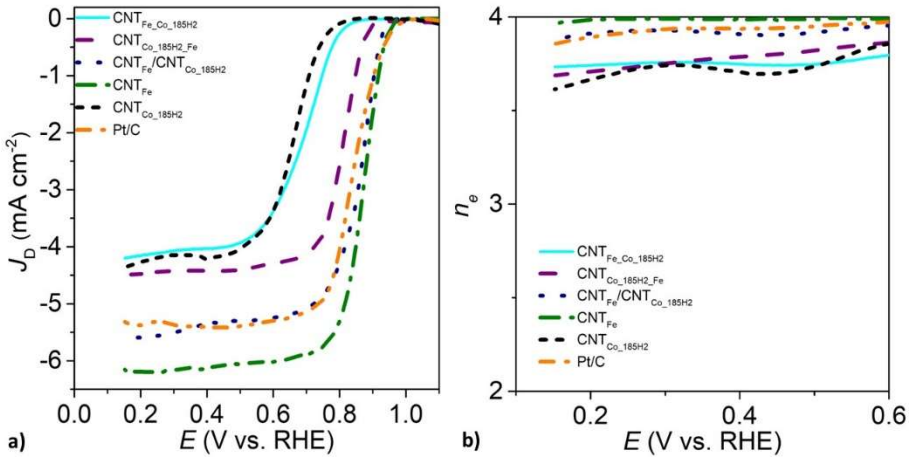


Figure 8.5 - Disk current density of the oxygen reduction reaction curves recorded at 1600 rpm and 5 mV s^{-1} in O_2-saturated 0.1 mol L^{-1} KOH electrolyte (a) and number of electrons exchanged (b).

Table 8.2 - Main electrochemical ORR parameters: Onset potential (E_{onset}), half-wave potential ($E_{1/2}$), limiting current density (J_L), by-product (H_2O_2) production, and the number of electrons exchanged (n_e) for the synthesized electrocatalysts and Pt/C catalyst.

Sample	E_{onset} (V)	$E_{1/2}$ (V)	J_L (mA cm^{-2})[a]	H_2O_2 (%)[a]	n_e[a]
CNT_{Co_185H2}	0.80	0.68	4.21	15	3.7
CNT_{Fe}	0.96	0.88	6.10	< 1	4.0
$CNT_{Fe_Co_185H2}$	0.83	0.73	4.03	13	3.7
$CNT_{Co_185H2_Fe}$	0.90	0.81	4.43	11	3.8
CNT_{Fe}/CNT_{Co_185H2}	0.94	0.88	5.36	5	3.9
Pt/C	0.98	0.83	5.41	3	3.9

[a] – Calculated at 0.4 V vs RHE.

Initially, samples CNT_{Co_185H2} and CNT_{Fe} were analyzed to evaluate their performance towards the ORR. CNT_{Co_185H2} displays a low E_{onset} (0.80 V) and $E_{1/2}$ (0.68 V), and a limiting current density of 4.21 mA cm^{-2}. The electroactivity of this material is lower than state-of-the-art Co-doped carbons prepared specifically to catalyze the ORR [15, 49]. However, this sample presents an interesting reaction mechanism, almost achieving a 4-electron pathway (3.7 electrons) and a low by-product formation of 15%. Therefore, it is essential to further tailor its active centers to properly electrocatalyze both the OER and the ORR. The incorporation of FePc on the CNT results in a much higher electroactivity towards ORR in comparison to CNT_{Co_185H2}, a high current density, and an $E_{1/2}$ value higher than Pt/C (0.88 V vs 0.83 V, respectively). Moreover, this sample displays a 4-electron reaction mechanism with a negligible formation of H_2O_2. Furthermore, this sample presents higher current density and overall higher electrochemical performance than similar state-of-the-art CNT_{FePc}, in which much higher contents of FePc were employed [50-53] and additional steps were needed to functionalize the material [50, 52]. Moreover, the onset potentials obtained for CNT_{Fe} and CNT_{Fe}/CNT_{Co_185H2} (0.96 V and 0.94 V vs RHE, respectively) were higher than the values previously reported in the state-of-the-art with similar materials such as CNT dopped with FePc prepared by also using low amounts of precursor and a similar number of steps (0.90 V vs RHE) [54] and (0.91 V vs RHE) [55]. In comparison to carbon materials doped with iron porphyrins, which

are very similar to FePc, the onset potential obtained is also slightly higher than those reported in literature (0.93 V and 0.83 V vs RHE) [56].Therefore, the methodology presented in this work is more suitable to produce an electrocatalyst for the ORR by cutting on raw material amount/costs and overall production costs.

This work aims to develop efficient bifunctional oxygen electrocatalysts, so, taking into consideration the results from the OER assessment using Co-doped CNT and the performance of CNT_{Co_185H2} and CNT_{Fe} towards the ORR, different combinations of these two materials (bimetallic samples) were tested. Regarding the incorporation of cobalt on CNT_{Fe} ($CNT_{Fe_Co_185H2}$), a decrease of 130 mV and 150 mV is observed for E_{onset} and $E_{1/2}$, respectively, in comparison to CNT_{Fe}. Regarding the reaction mechanism, the blockage of FePc sites hinders the number of electrons exchanged, leading to the increase of by-products formed in comparison to CNT_{Fe}. Moreover, this mechanism is very similar to CNT_{Co_185H2}, which is probably due to the outer structure being very similar in both cases (cobalt treated at 185 °C in N_2 atmosphere followed by H_2 atmosphere), hence the same amount/type of active sites reducing O_2. Although $CNT_{Fe_Co_185H2}$ has a lower electrochemical performance than the monometallic iron sample, it is still more electroactive towards the ORR than CNT_{Co_185H2} and is very electroactive towards the OER, which is not the case for CNT_{Fe} (Figure 8S.5). The incorporation of FePc on CNT_{Co_185H2} ($CNT_{Co_185H2_Fe}$) results in a much higher electroactivity than the monometallic CNT_{Co_185H2} due to the presence of FePc on the outer layer of the electrocatalyst. The sample exhibits E_{onset} and $E_{1/2}$ of 0.90 V and 0.81 V, respectively, with a slightly higher current density (4.43 mA cm^{-2}) and slightly lower by-product formation (11%), which corresponds to 3.8 electrons exchanged. Lastly, the physical mixture of the two monometallic samples (CNT_{Fe}/CNT_{Co_185H2}) displays the highest electroactivity of all bimetallic samples and an electrochemical performance very similar to the commercial Pt/C. The prepared sample presents E_{onset} and $E_{1/2}$ of 0.94 V and 0.88 V, respectively, and a very high current density at 0.4 V (5.36 mA cm^{-2} vs 5.42 mA cm^{-2} of Pt/C). The reaction is also taking place via the 4-electron mechanism like Pt/C (3.9 electrons for both CNT_{Fe}/CNT_{Co_185H2} and Pt/C) with a by-product formation of 5%. The comparison between CNT_{Fe}/CNT_{Co_185H2} and the current commercial ORR electrocatalyst demonstrates that they are nearly equivalent in every aspect. Nonetheless, the half-wave

potential of the developed bimetallic electrocatalyst is higher than that of Pt/C (0.88 V vs 0.83 V, respectively). Therefore, although CNT_{Fe}/CNT_{Co_185H2} presents a slightly lower OER performance than $CNT_{Fe_Co_185H2}$ and $CNT_{Co_185H2_Fe}$, it is much more electroactive towards the ORR, which is essential to obtain a high-efficient bifunctional oxygen electrocatalyst.

To further assess the performance of the electrocatalysts towards the ORR, stability measurements were carried out, as they can provide an interesting perspective of the catalysts' performance during their lifetime on the final device. These measurements were performed by chronoamperometry for 10000 s by applying a potential of 0.4 V (Figure 8.6a). The methanol tolerance of the most electroactive bimetallic sample towards the ORR (CNT_{Fe}/CNT_{Co_185H2}), CNT_{Fe} and the reference Pt/C, were also determined by the addition of pure methanol (1.5 mL) to the system at ca. 1000 s of the stability assessment (Figure 8.6b).

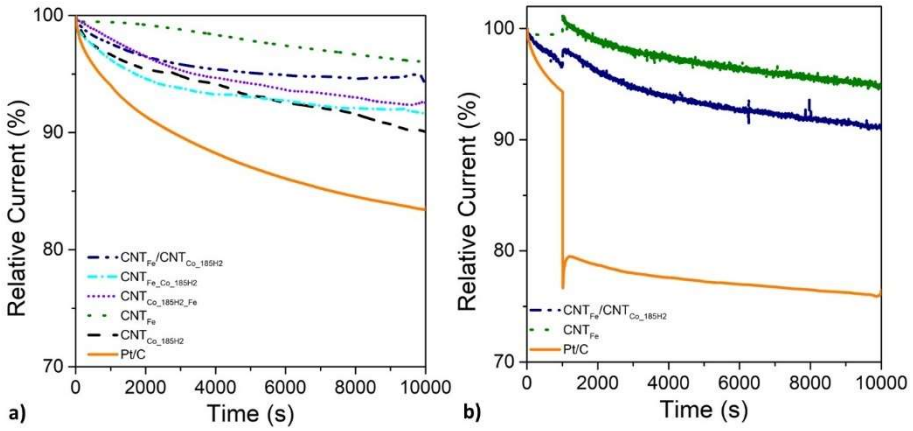


Figure 8.6 - Chronoamperometry assessments for the synthesized samples and Pt/C (a) and methanol resistance of samples CNT_{Fe}, CNT_{Fe}/CNT_{Co_185H2} and Pt/C (b) applying 0.4 V during 10000 s at 1600 rpm in an O_2-saturated 0.1 mol L^{-1} KOH electrolyte.

CNT_{Co_185H2} presents current density retention of 90% after 10000 s of reaction. On the other hand, CNT_{Fe} produces an outstanding 96% of its original current density after 10000 s. The bimetallic samples $CNT_{Fe_Co_185H2}$ and $CNT_{Co_185H2_Fe}$ also present a very good retention percentage (92% and 93%, respectively), which is higher than that of the commercial Pt/C (83%). Lastly, the physical mixture of the monometallic samples

(CNT_{Fe}/CNT_{Co_185H2}) displays a stability percentage of 94%, demonstrating that all prepared samples have exceptional long-term stabilities. Moreover, the analysis of the methanol tolerance demonstrates that the prepared electrocatalysts remark a slight increase in current density upon the addition of methanol that returns to its previous values (95% and 91% for CNT_{Fe} and CNT_{Fe}/CNT_{Co_185H2}, respectively) after the dispersion of the methanol on the electrolyte due to the electrode rotation at 1600 rpm. The slight current density increase may be explained by two different phenomena. The introduction of methanol on the reaction medium by applying a potential of 0.4 V (vs RHE) may result in its oxidation which will provide electrons for an even higher rate of oxygen reduction, and hence, to a temporary slight increase of current density. Moreover, the addition of methanol to the 0.1 mol L^{-1} KOH electrolyte slightly reduces the concentration of KOH in the final electrolyte composition. The oxygen solubility and diffusion coefficient increase with decreasing KOH concentration whereas the electrolyte viscosity decreases [57]. According to the Koutecký-Levich equation, these variations result in a higher theoretical limiting current density which is in agreement with slight increase of the current density. Nonetheless, both samples present very high methanol poisoning tolerance, especially in comparison to Pt/C. The commercial catalyst suffers a significant immediate loss of performance by adding methanol into the electrolyte (ca. 20%), which slightly recovers upon the complete dispersion of the methanol in the KOH. These results demonstrate that not only are the prepared carbon electrocatalysts able to perform at the level of the commercial catalyst for short (LSV) and long (chronoamperometry) periods, but they are also better suited to withstand poisoning of the final device, which is also a very important issue for scale-up applications.

8.3.2.3. Bifunctional oxygen electrocatalysis

The oxygen bifunctionality was assessed by the potential gap (ΔE), i.e. the difference between E_{10} and $E_{1/2}$. The values obtained for the prepared carbon and the benchmark electrocatalysts for each reaction (OER and ORR) are exhibited in Table 8.3. This parameter is essential to understand the overall oxygen electroactivity and bifunctionality.

Table 8.3 - $E_{1/2}$, $E_{10,}$ and ΔE for the prepared samples and benchmark electrocatalysts.

Sample	E_{10} (V)	$E_{1/2}$ (V)	ΔE (V)
CNT_{Fe}	1.79	0.88	0.91
CNT_{Co_185H2}	1.63	0.68	0.95
$CNT_{Fe_Co_185H2}$	1.63	0.73	0.90
$CNT_{Co_185H2_Fe}$	1.62	0.81	0.81
CNT_{Fe}/CNT_{Co_185H2}	1.64	0.88	0.76
Pt/C	1.87	0.83	1.04

The potentials observed towards the OER (E_{10}) for all bimetallic samples and CNT_{Co_185H2} are very similar (1.62-1.64 V). Consequently, the lowest ΔE should be achieved by obtaining the highest possible $E_{1/2}$ value for the ORR. From the set of bimetallic electrocatalysts shown in Table 8.3, CNT_{Fe}/CNT_{Co_185H2} exhibits the highest electroactivity towards the ORR, making it the bifunctional oxygen electrocatalyst with the highest electroactivity. Moreover, all bifunctional samples presented much lower potential gaps than the benchmark catalyst tested, hence are better-suited bifunctional oxygen electrocatalysts. Besides, the ΔE obtained is lower than those obtained for most published articles and only a few were able to achieve similar values (Table 8.4). Notwithstanding, the electrocatalysts prepared for this work present several advantages in comparison to most of the existing electrocatalysts in literature, such as: i) a very low number of production steps, ii) incorporation of a cheap precursor (cobalt nitrate), and iii) a very small amount of a very electroactive active center (FePc) towards the ORR (environmental and cost advantages), and iv) the procedure is easily scalable.

Table 8.4 - Δ*E* of the most electroactive sample prepared and some state-of-the-art electrocatalysts.

Sample	Δ*E* (V)	Ref.
$FeCo_2O_4$/hollow reduced graphene oxide spheres	0.96	[19]
Fe/N-CNT	0.90	[21]
Co/N-CNT	0.87	[17]
$CoFe_2O_4$ nanoparticles/rod-like ordered mesoporous carbon	0.84	[19]
FeCo-NPC-1100	0.81	[20]
Co,Fe,N-CNT	0.80	[16]
Co/N-CNT	0.78	[34]
$CoFe_2O_4$/CNT	0.76	[19]
CNT_{Fe}/CNT_{Co_185H2}	0.76	This work

8.4. Conclusions

CNT were used as bifunctional oxygen electrocatalysts after the incorporation of two different metal precursors onto the carbon matrix: cobalt nitrate and iron phthalocyanine. The cobalt precursor was incorporated by incipient wetness impregnation followed by thermal treatment at different temperatures and atmospheres to assess which conditions would provide a material with the highest electroactivity towards the OER. The results demonstrated that employing a low temperature (185 °C) and a H_2 atmosphere provided a high number of electroactive Co^{2+} sites that favored the oxygen evolution reaction. This interesting sample for the OER was further mixed with a sample of CNT-supporting iron phthalocyanine and tested as electrocatalysts for the ORR. The sample presented similar electrocatalytic performance and higher long-term stability and methanol poisoning tolerance in comparison to the commercial electrocatalyst (Pt/C). Besides, this bimetallic sample presented a low potential gap between both reactions (Δ*E* of 0.76 V) that is even lower than most of the best state-of-the-art published results for metal/heteroatom-doped carbon materials. Moreover, the use of cobalt nitrate instead of other complex cobalt precursors like cobalt phthalocyanine coupled with the use of a small amount of iron phthalocyanine allows for mass production of this electrocatalyst at low production costs,

making it a perfect candidate to replace noble metal-based electrocatalysts and for scale up testing using a gas-diffusion electrode, which in turn results in an electrocatalyst with a good up-scaling potential towards applying carbon materials for green energy applications.

8.5. Supplementary Information

8.5.1. Electrocatalysts characterization

In this section, the main textural and physico-chemical properties determined by X-ray spectroscopy (XPS), Raman spectroscopy and X-ray diffraction of the synthesized material are presented.

Table 8S.1 - Surface chemical composition determined by XPS.

	Composition				Co Region		
Sample	**C (wt%)**	**N (wt%)**	**O (wt%)**	**Co (wt%)**	**Co^{2+} (%)**	**Co^{3+} (%)**	**Co^{2+}/Co^{3+}**
CNT_{Co_150N2}	88.2	0.4	5.1	6.3	46.6	53.4	0.87
CNT_{Co_185N2}	85.6	n.d.	7.7	6.7	58.2	41.8	1.39
CNT_{Co_185H2}	87.9	n.d.	5.0	7.1	63.0	37.0	1.70
CNT_{Co_350N2}	94.0	n.d.	2.6	3.4	59.4	40.6	1.46
CNT_{Co_350H2}	96.1	n.d.	1.8	2.1	63.2	36.8	1.72
CNT_{Co_900N2}	95.3	n.d.	2.0	2.7	65.0	35.0	1.86
$CNT_{Co_185H2_Fe}$	88.1	0.2	5.2	6.5	57.5	42.5	1.35
$CNT_{Fe_Co_185H2}$	90.6	0.2	3.9	5.3	63.4	36.6	1.73
CNT_{Fe}/CNT_{Co_185H2}	94.4	0.6	2.0	3.0	62.9	37.1	1.69

n.d. – not detected

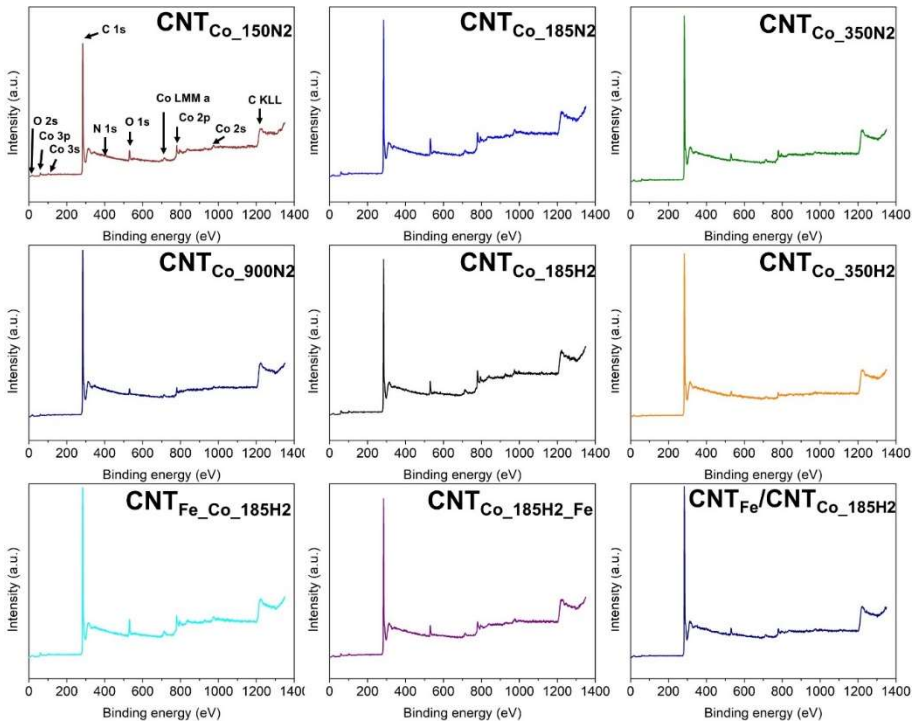


Figure 8S.1 - Survey spectra of the prepared electrocatalysts.

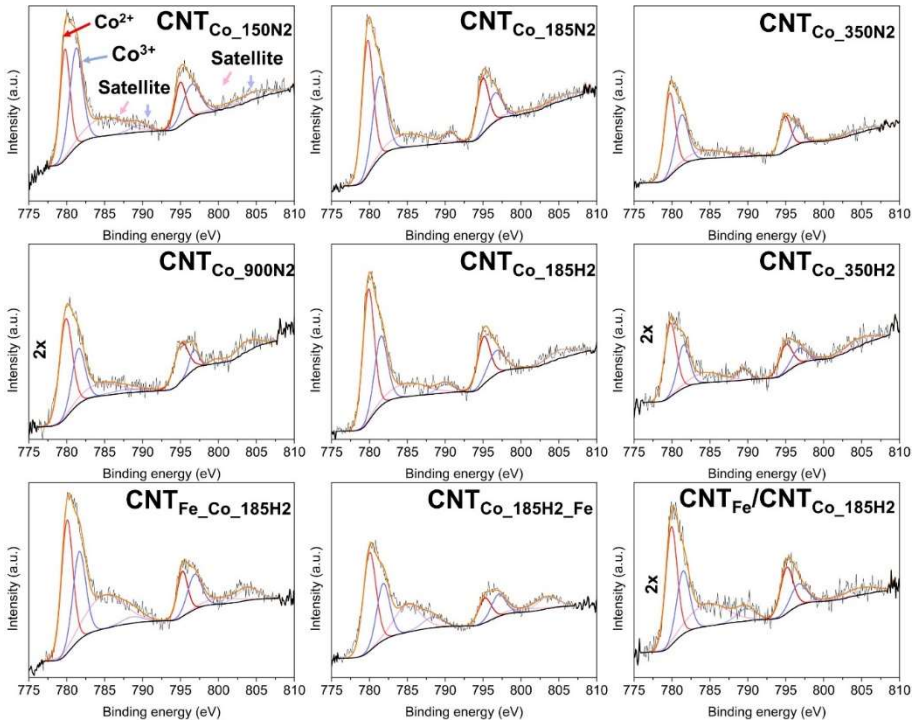


Figure 8S.2 - Deconvolution of the Co 2p X-ray photoelectron spectra of the prepared electrocatalysts.

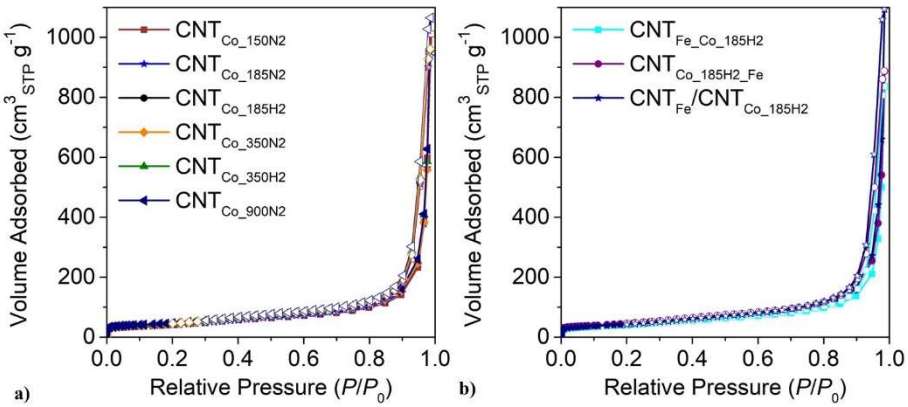


Figure 8S.3 - N_2 adsorption-desorption isotherms at -196 ºC of the monometallic (a) and bimetallic electrocatalysts (b).

Table 8S.2 - Ratio of the integrated D and G peaks obtained by Raman spectroscopy.

Sample	A_D/A_G
$\mathbf{CNT_{Co_150N2}}$	0.58
$\mathbf{CNT_{Co_185N2}}$	0.40
$\mathbf{CNT_{Co_185H2}}$	0.42
$\mathbf{CNT_{Co_350N2}}$	0.32
$\mathbf{CNT_{Co_350H2}}$	0.36
$\mathbf{CNT_{Co_900N2}}$	0.20
$\mathbf{CNT_{Co_185H2_Fe}}$	0.39
$\mathbf{CNT_{Fe_Co_185H2}}$	0.77
$\mathbf{CNT_{Fe}/CNT_{Co_185H2}}$	0.51

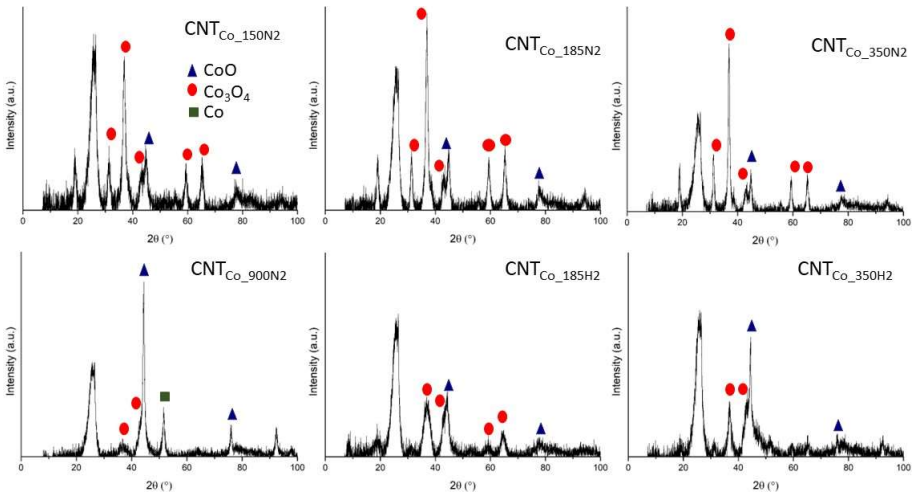


Figure 8S.4 - XRD patterns of the monometallic electrocatalysts.

One main carbon peak related to the graphitic structure of the CNT is detected at ca. 26° [58, 59], which is very sharp and strong in all samples analyzed. Additionally, two main cobalt-related peaks are detected on the XRD profiles: one at ca. 37° and another at ca. 44°, corresponding to Co_3O_4 and CoO, respectively [44]. The XRD profiles evolve from mainly Co_3O_4 to CoO species by increasing the temperature [44]. This effect is more evident in the sample treated at 900 ºC, in which the main cobalt peaks of the XRD pattern

are mainly attributed to CoO. Moreover, some metallic cobalt is also observed due to the presence of a significant peak at ca. 51° corresponding to Co [60]. On the other hand, the use of a H_2 atmosphere also favors the formation of CoO species [39], which is in agreement with XPS data. Overall, the XRD profiles follow the same trends observed for the XPS measurements due to the effect of temperature and gas. Moreover, the width of the peaks decreases by increasing the temperature from 150 °C to 350 °C, which is correlated by the Scherrer equation (Eq. S1) to an increase in the crystallite size from 58 nm to 130 nm [60, 61].

The Scherrer equation correlates the mean size of the crystalline domains with the line broadening at half the maximum intensity, Eq. 8S.1:

$$T = \frac{K\lambda}{\beta Cos\theta} \qquad (8S.1)$$

where T is the average crystallite size, K is the shape factor (0.94), λ is the X-ray radiation wavelength (1.5406 Å), β is the peak full width at half the maximum intensity and θ is the Bragg angle.

Nonetheless, at 900 °C the crystallite size decreases to 90 nm, probably due to a large variation of cobalt species on the sample and, consequently, a variation of the size of those species. The effect of the temperature is also observed in those samples treated under H_2 atmosphere, increasing the crystallite size with temperature (35 nm and 58 nm, at 185 °C and 350 °C, respectively).

8.5.2. Electrochemical assessments

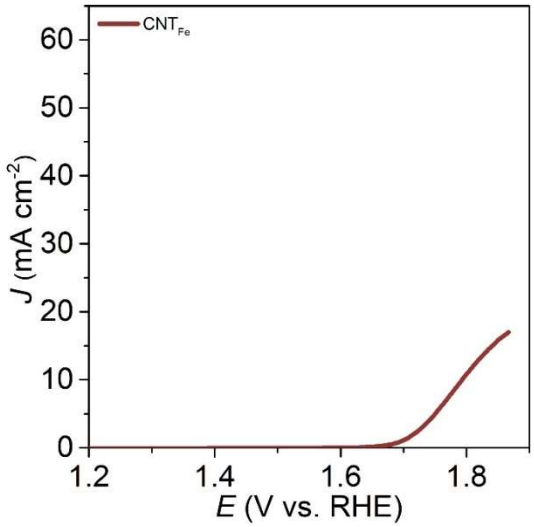


Figure 8S.5 - Linear sweep voltammetry curves recorded at 5 mV s^{-1} in a N_2-saturated 0.1 mol L^{-1} KOH electrolyte at 1600 rpm from 1.00 to 1.85 V for CNT_{Fe}.

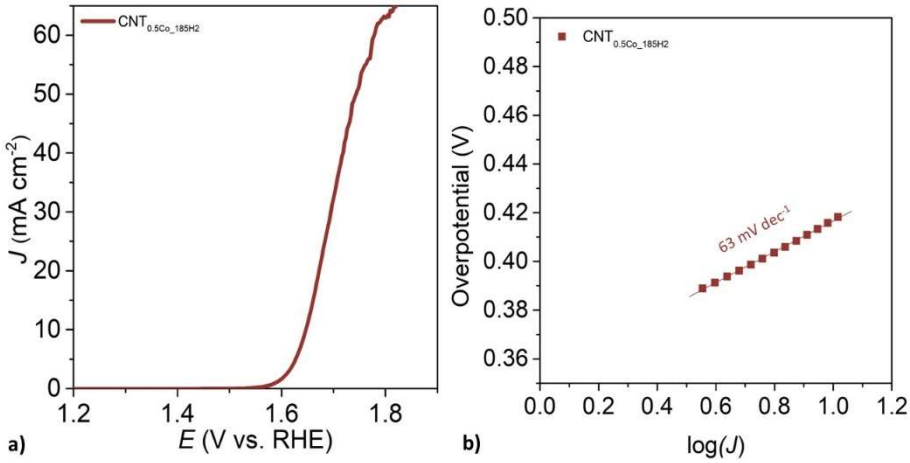


Figure 8S.6 - Linear sweep voltammetry curves recorded at 5 mV s^{-1} in a N_2-saturated 0.1 mol L^{-1} KOH electrolyte at 1600 rpm from 1.00 to 1.85 V for $CNT_{0.5Co_185H2}$.

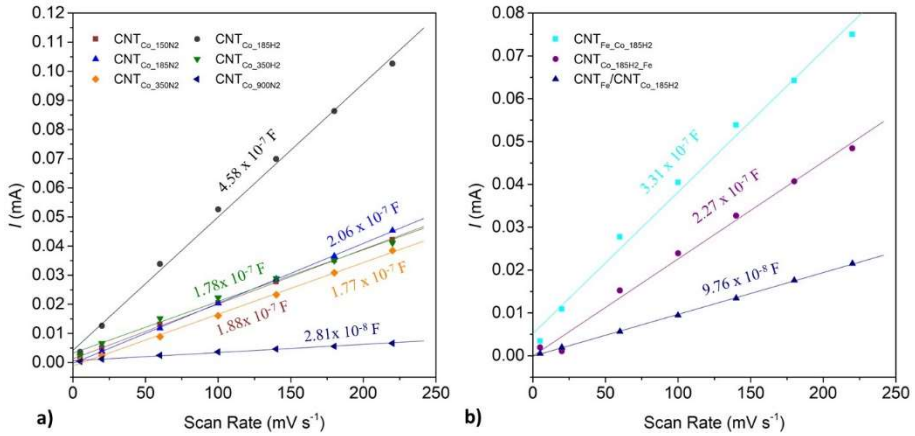


Figure 8S.7 - Linear fitting of capacitive currents at 0.75 V vs RHE plotted against the scan rate obtained from cyclic voltammograms of monometallic (a) and bimetallic (b) samples recorded at a scan rate range between 5 mV s^{-1} and 220 mV s^{-1} in N_2-saturated 0.1 mol L^{-1} KOH electrolyte.

8.6. References

[1] T.M. Gulotta, R. Salomone, F. Lanuzza, G. Saija, G. Mondello, G. Ioppolo, Life Cycle Assessment and Life Cycle Costing of unitized regenerative fuel cell: A systematic review, Environ. Impact Assess. Rev., 92 (2022) 106698.
[2] P. Gayen, S. Saha, X. Liu, K. Sharma, V.K. Ramani, High-performance AEM unitized regenerative fuel cell using Pt-pyrochlore as bifunctional oxygen electrocatalyst, Proc. Natl. Acad. Sci., 118 (2021) e2107205118.
[3] Q. Guo, H. Guo, F. Ye, L. Xing, C.F. Ma, A numerical study of dynamic behaviors of a unitized regenerative fuel cell during gas purging, Int. J. Hydrog. Energy, 47 (2022) 22203-22214.
[4] H. Guo, J. Song, F. Ye, M.A. Chong Fang, Dynamic response during mode switching of unitized regenerative fuel cells with orientational flow channels, Renew. Energy, 188 (2022) 698-710.
[5] G. Glenk, S. Reichelstein, Reversible Power-to-Gas systems for energy conversion and storage, Nat. Commun., 13 (2022) 2010.
[6] N. ul Hassan, P. Ganesan, A.A. Lando, W.E. Mustain, H.R. Colón-Mercado, Stable, high-performing bifunctional electrodes for anion exchange membrane-based unitized regenerative fuel cells, J. Power Sources, 541 (2022) 231599.
[7] J. Stacy, Y.N. Regmi, B. Leonard, M. Fan, The recent progress and future of oxygen reduction reaction catalysis: A review, Renew. Sust. Energ. Rev., 69 (2017) 401-414.
[8] A. Kirubakaran, S. Jain, R.K. Nema, A review on fuel cell technologies and power electronic interface, Renew. Sust. Energ. Rev., 13 (2009) 2430-2440.
[9] Y. Wang, D.Y.C. Leung, J. Xuan, H. Wang, A review on unitized regenerative fuel cell technologies, part-A: Unitized regenerative proton exchange membrane fuel cells, Renew. Sust. Energ. Rev., 65 (2016) 961-977.
[10] Y. Wang, D.Y.C. Leung, J. Xuan, H. Wang, A review on unitized regenerative fuel cell technologies, part B: Unitized regenerative alkaline fuel cell, solid oxide fuel cell, and microfluidic fuel cell, Renew. Sust. Energ. Rev., 75 (2017) 775-795.
[11] B. Paul, J. Andrews, PEM unitised reversible/regenerative hydrogen fuel cell systems: State of the art and technical challenges, Renew. Sust. Energ. Rev., 79 (2017) 585-599.
[12] M.M. Mohideen, Y. Liu, S. Ramakrishna, Recent progress of carbon dots and carbon nanotubes applied in oxygen reduction reaction of fuel cell for transportation, Appl. Energy, 257 (2020) 114027.
[13] W.E. Mustain, M. Chatenet, M. Page, Y.S. Kim, Durability challenges of anion exchange membrane fuel cells, Energy Environ. Sci., 13 (2020) 2805-2838.
[14] S. Gottesfeld, D.R. Dekel, M. Page, C. Bae, Y. Yan, P. Zelenay, Y.S. Kim, Anion exchange membrane fuel cells: Current status and remaining challenges, J. Power Sources, 375 (2018) 170-184.
[15] A. Sarapuu, E. Kibena-Põldsepp, M. Borghei, K. Tammeveski, Electrocatalysis of oxygen reduction on heteroatom-doped nanocarbons and transition metal–nitrogen–carbon catalysts for alkaline membrane fuel cells, J. Mater. Chem. A, 6 (2018) 776-804.
[16] R.G. Morais, N. Rey-Raap, J.L. Figueiredo, M.F.R. Pereira, Fe, Co, N-doped carbon nanotubes as bifunctional oxygen electrocatalysts, Appl. Surf. Sci., 572 (2022) 151459.
[17] L. Song, H. Fan, T. Wang, T. Xiang, M. Zhang, C. Hu, W. Zhou, J. He, Facile synthesis of Co, N enriched carbon nanotube and active site identifications for bifunctional oxygen reduction and evolution catalysis, Energy Storage Mater., 43 (2021) 365-374.
[18] J. Xia, K. Li, G.-L. Zhao, Electric Field Polarization To Increase Bifunctional Oxygen Electrocatalyst Performance of Nitrogen–Iron Functionalized Carbon Nanomaterials, ACS Appl. Energy Mater., 3 (2020) 1484-1495.
[19] X. Wu, C. Tang, Y. Cheng, X. Min, S.P. Jiang, S. Wang, Bifunctional Catalysts for Reversible Oxygen Evolution Reaction and Oxygen Reduction Reaction, Chem. Eur. J., 26 (2020) 3906-3929.

[20] B. Guo, Q. Ju, R. Ma, Z. Li, Q. Liu, F. Ai, M. Yang, S. Kaskel, J. Luo, T. Zhang, J. Wang, Mechanochemical synthesis of multi-site electrocatalysts as bifunctional zinc–air battery electrodes, J. Mater. Chem. A, 7 (2019) 19355-19363.
[21] L. Zhao, Q. Wang, X. Zhang, C. Deng, Z. Li, Y. Lei, M. Zhu, Combined Electron and Structure Manipulation on Fe-Containing N-Doped Carbon Nanotubes To Boost Bifunctional Oxygen Electrocatalysis, ACS Appl. Mater. Interfaces, 10 (2018) 35888-35895.
[22] H. Pan, X. Huang, Z. Lu, Z. Zhang, B. An, D. Wu, T. Wang, X. Chen, F. Cheng, Dual oxidation and sulfurization enabling hybrid Co/Co3O4@CoS in S/N-doped carbon matrix for bifunctional oxygen electrocatalysis and rechargeable Zn-air batteries, Chem. Eng. J., 419 (2021) 129619.
[23] R.G. Morais, N. Rey-Raap, J.L. Figueiredo, M.F.R. Pereira, Highly electroactive N–Fe hydrothermal carbons and carbon nanotubes for the oxygen reduction reaction, J. Energy Chem., 50 (2020) 260-270.
[24] J. Yang, J. Tao, T. Isomura, H. Yanagi, I. Moriguchi, N. Nakashima, A comparative study of iron phthalocyanine electrocatalysts supported on different nanocarbons for oxygen reduction reaction, Carbon, 145 (2019) 565-571.
[25] A. Morozan, S. Campidelli, A. Filoramo, B. Jousselme, S. Palacin, Catalytic activity of cobalt and iron phthalocyanines or porphyrins supported on different carbon nanotubes towards oxygen reduction reaction, Carbon, 49 (2011) 4839-4847.
[26] M. Canal-Rodríguez, N. Rey-Raap, J.Á. Menéndez, M.A. Montes-Morán, J.L. Figueiredo, M.F.R. Pereira, A. Arenillas, Effect of porous structure on doping and the catalytic performance of carbon xerogels towards the oxygen reduction reaction, Microporous Mesoporous Mater., 293 (2020) 109811.
[27] B. Mecheri, V.C.A. Ficca, M.A. Costa de Oliveira, A. D'Epifanio, E. Placidi, F. Arciprete, S. Licoccia, Facile synthesis of graphene-phthalocyanine composites as oxygen reduction electrocatalysts in microbial fuel cells, Appl. Catal. B-Environ., 237 (2018) 699-707.
[28] Y. Jiang, Y. Lu, X. Lv, D. Han, Q. Zhang, L. Niu, W. Chen, Enhanced Catalytic Performance of Pt-Free Iron Phthalocyanine by Graphene Support for Efficient Oxygen Reduction Reaction, ACS Catal., 3 (2013) 1263-1271.
[29] R. Jasinski, A New Fuel Cell Cathode Catalyst, Nature, 201 (1964) 1212-1213.
[30] R. Santhosh Kumar, S.C. Karthikeyan, S. Ramakrishnan, S. Vijayapradeep, A. Rhan Kim, J.-S. Kim, D. Jin Yoo, Anion dependency of spinel type cobalt catalysts for efficient overall water splitting in an acid medium, Chem. Eng. J., 451 (2023) 138471.
[31] H. Jin, R. Yu, C. Hu, P. Ji, Q. Ma, B. Liu, D. He, S. Mu, Size-controlled engineering of cobalt metal catalysts through a coordination effect for oxygen electrocatalysis, Appl. Catal. B-Environ., 317 (2022) 121766.
[32] M. Wu, G. Zhang, H. Tong, X. Liu, L. Du, N. Chen, J. Wang, T. Sun, T. Regier, S. Sun, Cobalt (II) oxide nanosheets with rich oxygen vacancies as highly efficient bifunctional catalysts for ultra-stable rechargeable Zn-air flow battery, Nano Energy, 79 (2021) 105409.
[33] Y. Tian, L. Xu, M. Li, D. Yuan, X. Liu, J. Qian, Y. Dou, J. Qiu, S. Zhang, Interface Engineering of CoS/CoO@N-Doped Graphene Nanocomposite for High-Performance Rechargeable Zn–Air Batteries, Nano-Micro Lett., 13 (2020) 3.
[34] Y. Liu, H. Jiang, Y. Zhu, X. Yang, C. Li, Transition metals (Fe, Co, and Ni) encapsulated in nitrogen-doped carbon nanotubes as bi-functional catalysts for oxygen electrode reactions, J. Mater. Chem. A, 4 (2016) 1694-1701.
[35] Y. Hao, Z. Lu, G. Zhang, Z. Chang, L. Luo, X. Sun, Cobalt-Embedded Nitrogen-Doped Carbon Nanotubes as High-Performance Bifunctional Oxygen Catalysts, Energy Technol., 5 (2017) 1265-1271.
[36] R.P. Forslund, W.G. Hardin, X. Rong, A.M. Abakumov, D. Filimonov, C.T. Alexander, J.T. Mefford, H. Iyer, A.M. Kolpak, K.P. Johnston, K.J. Stevenson, Exceptional electrocatalytic oxygen evolution via tunable charge transfer interactions in La0.5Sr1.5Ni1−xFexO4±δ Ruddlesden-Popper oxides, Nat. Commun., 9 (2018) 3150.

[37] A. Bonakdarpour, T. Dahn, R. Atanasoski, M. Debe, J. Dahn, H2O2 Release during Oxygen Reduction Reaction on Pt Nanoparticles, Electrochem. Solid-State Lett., 11 (2008) B208-B211.
[38] Y. Peng, J.-Y. Choi, T. Fürstenhaupt, K. Bai, Y. Zhang, D. Banham, New approach for rapidly determining Pt accessibility of Pt/C fuel cell catalysts, J. Mater. Chem. A, 9 (2021) 13471-13476.
[39] C. Ehrhardt, M. Gjikaj, W. Brockner, Thermal decomposition of cobalt nitrato compounds: Preparation of anhydrous cobalt(II)nitrate and its characterisation by Infrared and Raman spectra, Thermochim. Acta, 432 (2005) 36-40.
[40] A. Ashok, A. Kumar, F. Tarlochan, Surface Alloying in Silver-Cobalt through a Second Wave Solution Combustion Synthesis Technique, Nanomaterials, 8 (2018).
[41] J.F. Moulder, J. Chastain, Handbook of X-ray Photoelectron Spectroscopy: A Reference Book of Standard Spectra for Identification and Interpretation of XPS Data, Physical Electronics Division, Perkin-Elmer Corporation1992.
[42] Y. Ying, J.F. Godínez Salomón, L. Lartundo-Rojas, A. Moreno, R. Meyer, C.A. Damin, C.P. Rhodes, Hydrous cobalt–iridium oxide two-dimensional nanoframes: insights into activity and stability of bimetallic acidic oxygen evolution electrocatalysts, Nanoscale Adv., 3 (2021) 1976-1996.
[43] W. Brockner, C. Ehrhardt, M. Gjikaj, Thermal decomposition of nickel nitrate hexahydrate, Ni(NO3)2·6H2O, in comparison to Co(NO3)2·6H2O and Ca(NO3)2·4H2O, Thermochim. Acta, 456 (2007) 64-68.
[44] Y. Li, W. Qiu, F. Qin, H. Fang, V.G. Hadjiev, D. Litvinov, J. Bao, Identification of Cobalt Oxides with Raman Scattering and Fourier Transform Infrared Spectroscopy, J. Phys. Chem. C, 120 (2016) 4511-4516.
[45] R. Kecili, C.M. Hussain, Chapter 4 - Mechanism of Adsorption on Nanomaterials, in: C.M. Hussain (Ed.) Nanomaterials in Chromatography, Elsevier2018, pp. 89-115.
[46] E.N. Kaya, T. Basova, M. Polyakov, M. Durmuş, B. Kadem, A. Hassan, Hybrid materials of pyrene substituted phthalocyanines with single-walled carbon nanotubes: structure and sensing properties, RSC Adv., 5 (2015) 91855-91862.
[47] S.C. Petitto, E.M. Marsh, G.A. Carson, M.A. Langell, Cobalt oxide surface chemistry: The interaction of CoO(100), Co3O4(110) and Co3O4(111) with oxygen and water, J Mol Catal A Chem, 281 (2008) 49-58.
[48] T. Koczorowski, W. Szczolko, T. Goslinski, Physicochemical Properties and Catalytic Applications of Iron Porphyrazines and Phthalocyanines, in: M.M. Rahman, A.M. Asiri (Eds.) Recent Progress in Organometallic Chemistry, IntechOpen2017, pp. 101-121.
[49] H. Guo, Q. Feng, J. Zhu, J. Xu, Q. Li, S. Liu, K. Xu, C. Zhang, T. Liu, Cobalt nanoparticle-embedded nitrogen-doped carbon/carbon nanotube frameworks derived from a metal–organic framework for tri-functional ORR, OER and HER electrocatalysis, J. Mater. Chem. A, 7 (2019) 3664-3672.
[50] B. Martínez-Sánchez, D. Cazorla-Amorós, E. Morallón, P-functionalized carbon nanotubes promote highly stable electrocatalysts based on Fe-phthalocyanines for oxygen reduction: Experimental and computational studies, J. Energy Chem., 72 (2022) 276-290.
[51] N. Komba, G. Zhang, Q. Wei, X. Yang, J. Prakash, R. Chenitz, F. Rosei, S. Sun, Iron (II) phthalocyanine/N-doped graphene: A highly efficient non-precious metal catalyst for oxygen reduction, Int. J. Hydrog. Energy, 44 (2019) 18103-18114.
[52] Y. Liu, Y.-S. Fan, Z.-M. Liu, Pyrolysis of iron phthalocyanine on activated carbon as highly efficient non-noble metal oxygen reduction catalyst in microbial fuel cells, Chem. Eng. J., 361 (2019) 416-427.
[53] J. Yang, F. Toshimitsu, Z. Yang, T. Fujigaya, N. Nakashima, Pristine carbon nanotube/iron phthalocyanine hybrids with a well-defined nanostructure show excellent efficiency and durability for the oxygen reduction reaction, J. Mater. Chem. A, 5 (2017) 1184-1191.
[54] R. Venegas, F.J. Recio, C. Zuñiga, M. Viera, M.-P. Oyarzún, N. Silva, K. Neira, J.F. Marco, J.H. Zagal, F. Tasca, Comparison of the catalytic activity for O2 reduction of Fe and Co MN4

adsorbed on graphite electrodes and on carbon nanotubes, Phys. Chem. Chem. Phys., 19 (2017) 20441-20450.
[55] C.Z. Loyola, S. Ureta-Zañartu, J.H. Zagal, F. Tasca, Activity volcano plots for the oxygen reduction reaction using FeN4 complexes: From reported experimental data to the electrochemical meaning, Curr. Opin. Electrochem., 32 (2022) 100923.
[56] W. Orellana, C.Z. Loyola, J.F. Marco, F. Tasca, Evidence of carbon-supported porphyrins pyrolyzed for the oxygen reduction reaction keeping integrity, Sci. Rep., 12 (2022) 8072.
[57] J. Qiao, L. Xu, L. Ding, P. Shi, L. Zhang, R. Baker, J. Zhang, Effect of KOH concentration on the oxygen reduction kinetics catalyzed by heat-treated co-pyridine/C electrocatalysts, Int. J. Electrochem., 8 (2013) 1189-1208.
[58] R. Siddheswaran, D. Manikandan, R.E. Avila, C.E. Jeyanthi, R.V. Mangalaraja, Formation of Carbon Nanotube Forest over Spin-coated Fe2O3 Reduced Thin-film by Chemical Vapor Deposition, Fuller. Nanotub. Carbon Nanostructures, 23 (2015) 392-398.
[59] H. Soleimani, Synthesis of Carbon Nanotubes for Oil-water Interfacial Tension Reduction, Oil Gas Res., 1 (2015).
[60] X. Zhao, S. Veintemillas-Verdaguer, O. Bomatí-Miguel, M.d.P. Morales, H. Xu, Thermal history dependence of the crystal structure of Co fine particles, Phys. Rev. B, 71 (2005).
[61] D.T. Rahardjo, S. Budiawanti, Suharno, Y. Iriani, A. Supriyanto, B. Purnama, Temperature sintering dependence of crystalline structure in cobalt ferrite prepared by the sol-gel auto-combustion procedure, J. Phys. Conf. Ser., 1951 (2021) 012026.

Chapter 9

Gas diffusion electrode evaluation

Abstract

Bimetallic cobalt and iron catalysts supported on carbon nanotubes that displayed high electroactivities towards oxygen reduction and evolution reactions (ORR and OER, respectively) at a rotating ring disc electrode scale were tested as realistic fuel cell catalyst layers at relevant current densities. The upscaling of the measurements followed the same activity trends for ORR and OER, in which iron phthalocyanine (FePc) excels at oxygen reduction, whereas cobalt primarily catalyzes the OER. The monometallic iron electrocatalyst prepared by incorporation of FePc exhibited higher ORR electroactivities than state-of-the-art Fe-N-C electrodes. The incorporation of FePc on Co/CNT resulted in a sample with the highest ORR electroactivity after accelerated stability testing and the highest OER performance, hence it is the most electroactive bifunctional oxygen electrocatalyst at potentials close to those used in fuel cells. Thus, demonstrating this material's high potential as a substitute for noble metal electrocatalysts.

9.1. Introduction

Nowadays, the world is aiming to suppress its energetic needs using cleaner energy sources at the lowest possible price. To achieve this objective, the unitized regenerative fuel cell (URFC) presents itself as one of the most attractive electrochemical devices to be further optimized and plays a key role in the energetic panorama in the near future. This device aims to maximize the efficiency of an electrolyzer (EL) and a fuel cell (FC) by combining them in a single piece of equipment and achieving maximum energy efficiency [1-4]. Furthermore, the URFC can function as either EL or FC according to the specific energy requirements at the time of its usage. Moreover, the overall operation of the URFC is very friendly towards the environment as the only products resulting from it are H_2 and O_2, when operating in EL mode, or the generation of H_2O and heat as by-products of the generation of energy in FC mode [2, 5, 6]. A total of four different electrochemical reactions can take place in the URFC. Nonetheless, only two reactions can occur at each time depending on the operation mode: the oxygen evolution reaction (OER) and hydrogen evolution reaction (HER) - in EL mode – and the oxygen reduction reaction (ORR) and the hydrogen oxidation reaction (HOR) – in FC mode [7]. Due to the compartmentalization of the URFC, a single electrocatalyst is needed to catalyze the ORR/OER pair and the same, or another electrocatalyst, is required for the HOR/HER pair [8-10]. This need arises as one of the main challenges towards the upscaling and commercialization of the URFC, as the design of an efficient bifunctional electrocatalyst is still a great challenge for the scientific community. Moreover, the oxygen reaction pair presents more performance hindrances than the hydrogen pair, due to its much higher reaction losses and sluggish kinetics, hence the need to focus on improving the ORR/OER to avoid diminishing the overall URFC performance. The optimization of proton exchange membranes fuel cells (PEMFC) reached a mature state using noble metal catalysts that are already commercialized, which could also be applied in the URFC [8, 11-13]. Nonetheless, the use of noble metal catalysts increases the cost of production and represents a large portion of the overall device cost; hence, reducing these costs is one of the main actual objectives of the scientific community [4, 7, 14-16]. To reduce the costs associated with this problem, using an anion exchange membrane fuel cell (AEMFC) that works in basic media, may prove crucial for a world that relies on green energies at low

costs. The alkaline environment enables the use of a wider range of catalysts than PEMFC, especially widely available low-cost carbon materials [4]. Furthermore, the durability and the intrinsic activity of non-noble metal electrocatalysts are increased in basic medium [11, 17]. Carbon materials modified with heteroatoms and/or transition metals have been successfully tailored as bifunctional electrocatalysts towards the ORR and OER but are still not on par to be applied at large-scale [18-26]. Although thousands of ORR and OER studies are reported for different materials, there is still a lack of scientific research and knowledge about the electrocatalysts' performance in realistic commercial operating conditions. Therefore, this work focuses on investigating the performance of realistic fuel cell catalyst layers at relevant current densities of modified CNT that have already displayed excellent ORR and OER performance at the RDE level (samples from *Chapter 8*). The electrochemical performance of each catalyst was assessed using a gas diffusion electrode (GDE) and the results obtained were compared to those of the RDE setup to evaluate if the same trends and electroactivities were achieved.

9.2. Experimental

9.2.1. Catalyst ink and electrode preparation

The catalyst ink was prepared with 4 mg of each carbon material or commercial ORR/OER electrocatalysts and 4.85 mL of a solution containing purified water (produced by reverse osmose and capacitive deionization, VWR Chemicals), ultrapure ethanol (> 99.8%, Fischer Scientific) and Nafion (5 wt% in mixture of lower aliphatic alcohols and water, 45% water, Sigma-Aldrich) in a 178:146:1 volume ratio, respectively. The resulting ink was ultrasonicated in an ultrasonic processor until homogeneity was achieved before being loaded into the spray coating apparatus. The dispersion was then loaded onto the microporous layer side of the PTFE-coated gas diffusion layer (GDL, Sigracet 25 BC) by ultrasound spray coating at 125 °C, obtaining a final mass loading of ca. 0.5 ± 0.1 mg cm^{-2}.

9.2.2. GDE half-cell measurements

The electrochemical application of the synthesized materials was assessed in a three-electrode system composed of a reference electrode (RE), a counter electrode (CE), and a working electrode (WE). A Hg/HgO electrode filled with the electrolyte solution (2 mol L^{-1} KOH) was used as RE, whereas a commercial GDL bearing the electrocatalyst layer (CL) on its surface (gas diffusion electrode, GDE) was employed as WE for the ORR and OER. A titanium mesh coated with an Ir/Ta mixed oxide was employed as CE in the ORR testing, whereas the OER was performed using a Pt wire as CE. Before the analyzes, the reference electrode potential against reversible hydrogen electrode (RHE) was determined to correctly convert the measured potential to RHE.

Before the ORR measurements, all electrocatalyst layers underwent 200 activation cycles between 1.20 and 0.05 V (vs RHE) at 500 mV s^{-1}, whereas for OER measurements the catalyst layers underwent 50 activation cycles ranging from 1.65 V to 0.15 V (vs RHE) at 500 mV s^{-1}, both in N_2-saturated electrolyte. Both ORR and OER were then assessed by applying different galvanostatic steps and measuring the resulting potential for each step. The results obtained for each step were then used to plot the polarization curves of each material. Nonetheless, due to the varying uncompensated resistance (*iR* drop) at each step, several EIS were performed to determine such resistance and to properly perform a post-correction of all the measured potentials. The ORR galvanostatic procedure was performed in O_2-saturated electrolyte by applying a forward scan of negative current densities from -7.5 µA cm^{-2} to -2000 mA cm^{-2} followed by a backwards scan from -2000 mA cm^{-2} to -7.5 µA cm^{-2}. The OER galvanostatic procedure was very similar to the ORR measurements but applying only a forward scan of positive current densities (7.5 µA cm^{-2} to 2000 mA cm^{-2}). Prior to each step, an EIS was performed at the current density that was being applied using a frequency range of 10000 Hz to 10 Hz and an amplitude of 5% of the absolute value of the current density applied (e.g. for -100 mA cm^{-2} an amplitude of 5 mA was used whereas for -2000 mA cm^{-2} an amplitude of 100 mA was used). Additionally, the *iR* drop was determined for each EIS measurement by creating an equivalent system and determining the uncompensated resistance.

The long-term performance towards ORR of the materials was assessed by performing the full ORR procedure followed by an accelerated stability testing (AST) of 5000 CVs using a scan rate of 100 mV s^{-1} from 1.0 to 0.6 V (vs RHE) in O_2-saturated electrolyte followed by another full ORR procedure. The difference between the polarization curves from both procedures was the performance loss of each electrocatalyst. On the other hand, the stability of the materials towards OER was measured by chronopotentiometry by applying 10 mA cm^{-2} for 1 h after performing the catalyst layer activation procedure abovementioned (50 CVs ranging from 1.65 V to 0.15 V (vs RHE) at 500 mV s^{-1} in N_2-saturated electrolyte).

9.3. Results and discussion

9.3.1. Oxygen Reduction Reaction

The ORR activity of the most promising monometallic and bimetallic samples was measured by galvanostatic steps up to -2000 mA cm^{-2}. Besides these electrocatalysts, sample CNT was also assessed to further evaluate the electroactivity variation after the modification of their surface chemistry by the addition of metals, whereas Pt/C was studied as a benchmark for comparison with the prepared materials. The ORR polarization curves of CNT/monometallic and bimetallic samples are presented in Figure 9.1a and 9.1b, respectively. Table 9.1 presents the potential required for each electrocatalyst to achieve current densities from -500 to -2000 mA cm^{-2}.

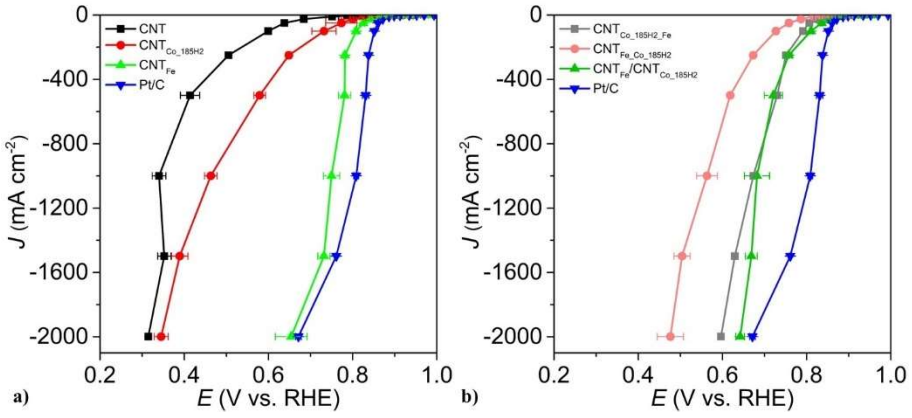


Figure 9.1 - ORR polarization curves of CNT and monometallic samples (a) and bimetallic samples (b) and Pt/C recorded in an O_2-saturated 2 mol L^{-1} KOH electrolyte.

Table 9.1 - Potentials required to achieve a determined current density during ORR assessments for the synthesized materials and Pt/C in an O_2-saturated 2 mol L^{-1} KOH electrolyte.

Sample	E_{-500} (V)	E_{-1000} (V)	E_{-1500} (V)	E_{-2000} (V)
CNT	0.414 ± 0.022	0.340 ± 0.016	0.352 ± 0.016	0.315 ± 0.019
CNT_{Co_185H2}	0.579 ± 0.014	0.463 ± 0.015	0.389 ± 0.019	0.345 ± 0.017
CNT_{Fe}	0.781 ± 0.015	0.750 ± 0.019	0.732 ± 0.015	0.654 ± 0.038
$CNT_{Fe_Co_185H2}$	0.618 ± 0.003	0.546 ± 0.005	0.494 ± 0.016	0.465 ± 0.033
$CNT_{Co_185H2_Fe}$	0.730 ± 0.001	0.673 ± 0.006	0.629 ± 0.006	0.597 ± 0.002
CNT_{Fe}/CNT_{Co_185H2}	0.721 ± 0.022	0.682 ± 0.030	0.669 ± 0.014	0.642 ± 0.010
Pt/C	0.831 ± 0.008	0.809 ± 0.006	0.761 ± 0.002	0.671 ± 0.007

Initially, the ORR performance of CNT and the monometallic electrocatalysts, samples CNT_{Co_185H2} and CNT_{Fe}, was evaluated. The CNT sample requires very high overpotentials to achieve current densities of -500 mA cm^{-2} or more. The incorporation of cobalt on the CNT enhances the electroactivity of the material towards ORR and requires a potential of 0.579 ± 0.014 V (vs RHE) to reach a current density of -500 mA cm^{-2} which gradually decreases to 0.345 ± 0.017 V (vs RHE) at -2000 mA cm^{-2}. The incorporation of FePc on the CNT greatly increases the ORR activity of the electrocatalyst and requires only a potential of 0.781 ± 0.014 V (vs RHE) to achieve -500 mA cm^{-2}. This result is a very close approximation to the performance of the commercial Pt/C electrocatalyst (50 mV difference). Further increasing the current density to -2000 mA cm^{-2} leads to a potential of 0.654 ± 0.038 V (vs RHE), which is still higher than state-of-the-art Fe-N-C cathodes (0.27 to 0.52 V vs RHE) that use triple the catalyst loading and higher activation times [27]. Regarding the bimetallic samples, their ORR electroactivity is lower than CNT_{Fe}. The incorporation of cobalt on CNT_{Fe} ($CNT_{Fe_Co_185H2}$) highly hinders the electrocatalyst's ORR performance, probably due to

the blockage of FePc sites and the lower ORR intrinsic activity of the cobalt sites in comparison to the FePc ones. The incorporation of FePc on CNT_{Co_185H2} ($CNT_{Co_185H2_Fe}$) leads to ORR electroactivities higher than $CNT_{Fe_Co_185H2}$, which may be attributed to a higher accessibility of the FePc active centers. Nonetheless, the potentials required to achieve high current densities (> -500 mA cm^{-2}) are still lower (51 to 103 mV) than those of CNT_{Fe}. The sample prepared by mixing both monometallic samples (CNT_{Fe}/CNT_{Co_185H2}) displays an ORR very similar to $CNT_{Co_185H2_Fe}$ up to -1000 mA cm^{-2}, which may be explained by both presenting exposed FePc centers. Moreover, at -1500 and -2000 mA cm^{-2}, CNT_{Fe}/CNT_{Co_185H2} displays higher potentials than $CNT_{Co_185H2_Fe}$, which suggests that the presence of cobalt centers may interact with iron, forming Co-Fe bonds which may hinder the overall electrocatalyst's performances at higher currents. Overall, the ORR performance of all materials follows the trend observed during RDE measurements: CNT_{Fe} > CNT_{Fe}/CNT_{Co_185H2} > $CNT_{Co_185H2_Fe}$ > $CNT_{Fe_Co_185H2}$ > CNT_{Co_185H2} > CNT.

After the initial ORR electrocatalytic evaluation, the durability of the electrocatalysts was assessed by accelerated stability testing (AST). The samples were initially tested towards ORR up to -2000 mA cm^2 and then subjected to a load cycling protocol under N_2-saturated electrolyte consisting of 5000 CVs between 1.0 and 0.6 V vs RHE using a scan rate of 100 mV s^{-1}. Afterwards, the electrocatalysts were retested towards their ORR electroactivity up to -2000 mA cm^2. The polarization curves before and after the AST protocol for monometallic and bimetallic samples are displayed in Figure 9.2a and 9.2b, respectively. Table 9.2 presents the potential difference for current densities from -500 to -2000 mA cm^{-2} for each of the analyzed materials.

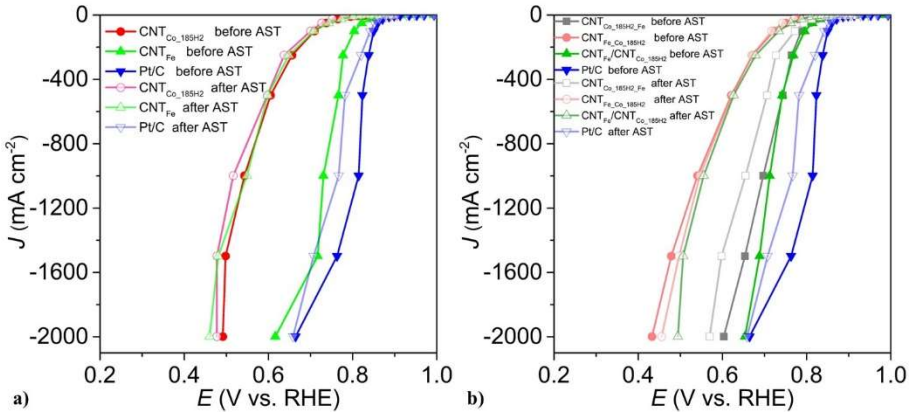


Figure 9.2 - ORR polarization curves before and after accelerated stability testing of the monometallic (a) and bimetallic samples (b) and Pt/C recorded in an O_2-saturated 2 mol L^{-1} KOH electrolyte.

Table 9.2 - Potential losses at different current densities during accelerated stability testing measurements for the synthesized materials and Pt/C in an O_2-saturated 2 mol L^{-1} KOH electrolyte.

Sample	ΔV_{-500} (mV)	ΔV_{-1000} (mV)	ΔV_{-1500} (mV)	ΔV_{-2000} (mV)
CNT_{Co_185H2}	8	27	20	14
CNT_{Fe}	168	182	236	156
$CNT_{Fe_Co_185H2}$	-3	-6	-19	-23
$CNT_{Co_185H2_Fe}$	38	42	56	34
CNT_{Fe}/CNT_{Co_185H2}	115	157	181	160
Pt/C	41	47	56	6

The stability testing exhibits clear differences between samples, especially due to their synthesis methods and composition. Samples CNT_{Fe} and CNT_{Fe}/CNT_{Co_185H2} display the highest ORR performance loss of all the tested electrocatalysts. These samples were prepared by incorporating FePc on CNT and, in the case of the bimetallic sample, the mixing of CNT_{Fe} with CNT_{Co_185H2}, which did not undergo another thermal treatment. Therefore, both samples' FePc active centers were solely bonded to the carbon structure. The deterioration of the FePc sites, which were the main ORR promoters, can explain the ORR electroactivity loss. The presence of O_2 in the alkaline electrolyte and consequent

oxygen reduction leads to a significant dissolution of the Fe species of the Fe-N-C molecules, which increases with the overpotential and/or current density [28]. The demetallation of the FePc macrocycle may then be the main reason for the electroactivity loss recorded for CNT_{Fe} and CNT_{Fe}/CNT_{Co_185H2}. Regarding CNT_{Co_185H2}, $CNT_{Co_185H2_Fe}$ and $CNT_{Fe_Co_185H2}$, interesting differences can be observed in their stability results. CNT_{Co_185H2} presents a lower performance loss than the commercial Pt/C, which indicates that the material's active sites are probably very stable and retain most of their activity. Nonetheless, their initial activity is much lower than that of Pt/C, and the ORR performance after AST is still subpar in comparison to Pt/C. $CNT_{Co_185H2_Fe}$ displays a lower degree of ORR performance loss in comparison to CNT_{Fe} and CNT_{Fe}/CNT_{Co_185H2} but higher than CNT_{Co_185H2} and $CNT_{Fe_Co_185H2}$. This difference may be explained by the structure of the sample. Although FePc is on the electrocatalyst's surface, it may have formed bonds with cobalt during the cobalt incorporation process and those bonds may be able to withstand dissolution/deactivation, providing higher long-term stability than that observed for CNT_{Fe} and CNT_{Fe}/CNT_{Co_185H2}. Nonetheless, some FePc on the matrix's surface is probably still being dissolved, even at a lower rate. Regarding sample $CNT_{Fe_Co_185H2}$, a slight increase in the ORR performance is observed after AST. This electroactivity enhancement is only observed for this sample and may be attributed to a deterioration of the electrocatalyst's surface that creates a higher exposure of the FePc sites that were under the cobalt species. Hence, FePc may be playing a bigger role in the oxygen reduction after AST on sample $CNT_{Fe_Co_185H2}$ due to its higher ORR intrinsic activity than that of Co species. Nonetheless, the activity of $CNT_{Fe_Co_185H2}$ is still lower than that of $CNT_{Co_185H2_Fe}$ after AST. Overall, $CNT_{Co_185H2_Fe}$ displays the highest ORR electroactivity after AST among all synthesized samples with a potential of 0.57 V vs RHE to achieve -2000 mA cm^{-2}. This result is very interesting and promising as the potential needed to achieve such a high current density is very close to the lower limit of the potential range at which a fuel cell under alkaline conditions operates (1.0 and 0.6 V vs RHE) [28].

9.3.2. Oxygen Evolution Reaction

The OER activity of the most promising monometallic and bimetallic samples was measured by galvanostatic steps up to 2000 mA cm^{-2}. It should be noted that at higher

currents more electrons are transferred and thus charge transfer resistance decreases. Nonetheless, at very high reaction rates, the charge transfer resistance gets close to zero and, upon determination of the circuit model of the Nyquist plot, the resistance of the 1st and 2nd resistors (R_1 and R_2) used are identical. Thus, at the highest current densities applied, the semicircle determined for the charge transfer resistance can be merely a cloud of points stemming from measurement artifacts and inductance around R_1, which difficult the determination of the *iR* drop. Moreover, this effect is different for each material; hence, at the same current density applied, some of the EIS measurements may be adapted to an equivalent circuit model only for some of the materials tested. At the current densities at which the *iR* drop can not be calculated, it is impossible to perform a post-correction of the measured potentials properly; thus, only the corrected potentials are used to plot the polarization curves. The OER polarization curves of monometallic and bimetallic samples are presented in Figure 9.3a and 9.3b, respectively. Table 9.3 presents the potential required for each electrocatalyst to achieve current densities from 500 to 1500 mA cm^{-2} and 10 mA cm^{-2}.

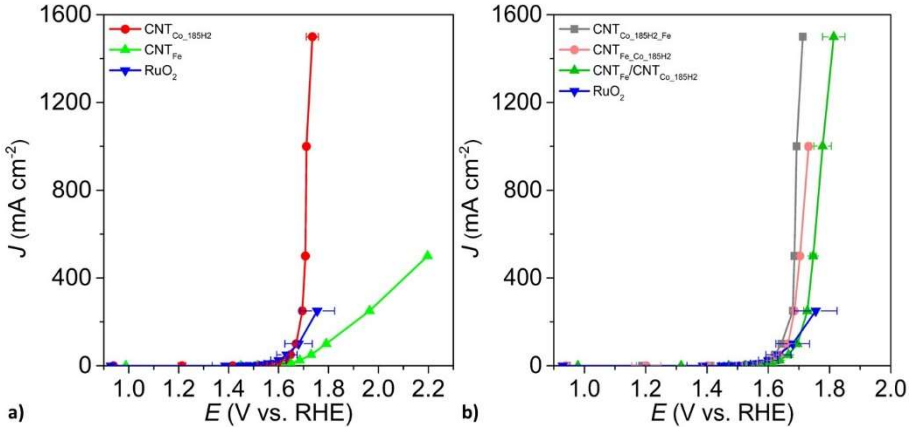


Figure 9.3 - OER polarization curves of the monometallic (a) and bimetallic samples (b) and RuO_2 recorded in an N_2-saturated 2 mol L^{-1} KOH electrolyte.

Table 9.3 - Potentials required to achieve a determined current density during OER assessments for the synthesized materials and RuO_2 in an N_2-saturated 2 mol L^{-1} KOH electrolyte.

Sample	E_{10} (V)	E_{500} (V)	E_{1000} (V)	E_{1500} (V)
CNT_{Co_185H2}	1.607 ± 0.001	1.708 ± 0.001	1.711 ± 0.001	1.736 ± 0.024
CNT_{Fe}	1.650	2.197	-	-
$CNT_{Fe_Co_185H2}$	1.591 ± 0.006	1.703 ± 0.002	1.732 ± 0.009	-
$CNT_{Co_185H2_Fe}$	1.582 ±0.004	1.686 ± 0.006	1.693 ± 0.005	1.713 ± 0.001
CNT_{Fe}/CNT_{Co_185H2}	1.614 ± 0.001	1.747 ± 0.010	1.777 ± 0.029	1.814 ± 0.036
RuO_2	1.565 ± 0.024	-	-	-

The incorporation of cobalt on CNT presents higher OER electroactivity than the incorporation of FePc across all current densities applied. These results follow the same trend observed for the RDE measurements in which cobalt outperforms iron species for the OER. Nonetheless, CNT_{Co_185H2} and CNT_{Fe} present a lower potential at 10 mA cm^{-2} (E_{10}) than that measured by RDE. CNT_{Co_185H2}'s E_{10} decreased from 1.63 V (cf. RDE values in *Chapter 8*) to 1.61 V vs RHE, whereas CNT_{Fe} presented an improvement of 140 mV from 1.79 V (cf. RDE values in *Chapter 8*) to 1.65 V, which is quite remarkable. Moreover, at higher current densities, the Co-doped CNT can reach high current densities (1500 mA cm^{-2}) at 1.736 ± 0.024 V, whereas the FePc-doped sample can only reach 500 mA cm^{-2} at 2.197 V. Therefore, CNT_{Fe} still needs further modifications to reach a more realistic scale.

Regarding bimetallic samples, the incorporation of both FePc and cobalt on the same CNT support results in very similar results at low current densities regardless of the incorporation order, whereas at higher current densities $CNT_{Co_185H2_Fe}$ presents higher OER electroactivities than $CNT_{Fe_Co_185H2}$. These results also replicate those of the RDE studies in which the presence of FePc on the outer surface of the electrocatalyst seems to be slightly synergizing with the cobalt sites and enhancing the performance towards the

OER. Moreover, as $CNT_{Co_185H2_Fe}$ requires a lower increase of overpotential to achieve a certain current density than $CNT_{Fe_Co_185H2}$, it also suggests that the reaction kinetics are faster for the former electrocatalyst, which is also in agreement with the RDE assessments. Additionally, regardless of the incorporation order, both samples present higher electroactivities than the monometallic samples and within the error of the commercial RuO_2 electrocatalyst up to 250 mA cm^{-2}. Sample CNT_{Fe}/CNT_{Co_185H2} presents an OER performance between both monometallic samples, which may be explained by presenting only half of each metal content of the other samples. This may play a key role towards the OER as more active centers may result in more H_2O molecules reacting, hence increasing the current density. Moreover, CNT_{Fe}/CNT_{Co_185H2} requires a higher increase of overpotential than the other bimetallic samples, which suggests that its reaction kinetics are not as fast as the other two samples ($CNT_{Co_185H2_Fe}$ and $CNT_{Fe_Co_185H2}$), which did not agree with the RDE measurements. This effect can be due to the electrochemical evaluation of the electrocatalysts using the GDE without systemic mass transport limitations and with high current densities that may be more influenced by the number of active centers. Thus, a performance difference between RDE and GDE for samples with different metallic contents may occur. Overall, the OER performance of all materials follows the trend observed during RDE measurements: $CNT_{Co_185H2_Fe} > CNT_{Co_185H2} = CNT_{Fe_Co_185H2} > CNT_{Fe}/CNT_{Co_185H2} > CNT_{Fe}$.

To further evaluate the electroactivity of the synthesized materials towards the OER, the stability of the electrocatalysts was analyzed. Chronopotentiometry measurements were performed by applying 10 mA cm^{-2} for 1 h and registering the variation of potential required to produce such current density. The results obtained are displayed in Figure 9.4.

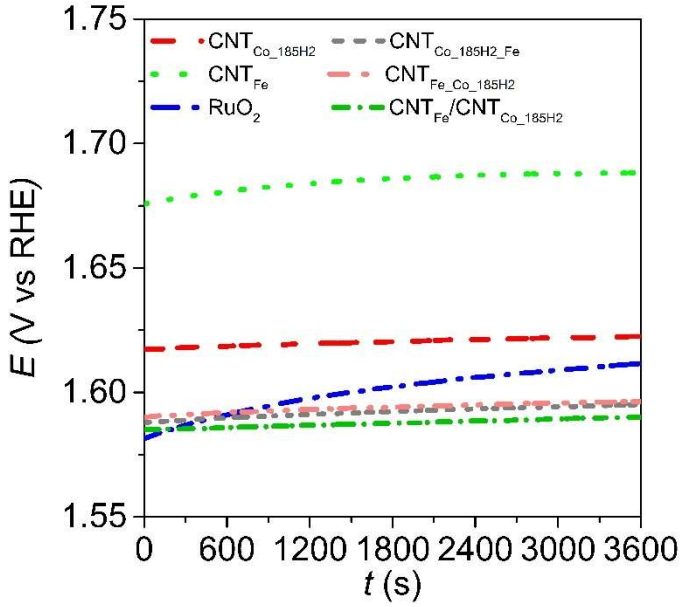


Figure 9.4 - Chronopotentiometry assessments for the synthesized samples and RuO_2 by applying 10 mA cm^{-2} for 1 h in an N_2-saturated 2 mol L^{-1} KOH electrolyte.

An EIS was performed before and after the chronopotentiometry measurements to ensure that the electrocatalysts' performance variation was not derived from an increase in the uncompensated resistance. The *iR* drop did not display significant differences before and after stability testing of the samples; hence, the performance variation was solely due to the electrocatalysts' degradation. The stability measurements exhibit small differences between samples. Samples CNT_{Co_185H2} and CNT_{Fe}/CNT_{Co_185H2} present an overpotential of 5 mV, whereas the overpotentials of $CNT_{Co_185H2_Fe}$ and $CNT_{Fe_Co_185H2}$ increase by 7 mV and 6 mV, respectively. Overall, all samples maintained their high OER electroactivity at 10 mA cm^{-2}. Nonetheless, sample CNT_{Fe} displayed an overpotential increase of 12 mV, another OER parameter in which it underperforms compared to the other materials prepared. Regarding the commercial RuO_2, its stability test demonstrates the highest overpotential increase of all samples (30 mV). Therefore, after just one hour of operation, three of the prepared samples (CNT_{Co_185H2}, $CNT_{Co_185H2_Fe}$ and $CNT_{Fe_Co_185H2}$) require a lower overpotential than RuO_2 to achieve the 10 mA cm^{-2} threshold that is so commonly used to evaluate an electrocatalyst's OER activity.

9.3.3. Bifunctional Oxygen Electrocatalysis

The oxygen bifunctionality was assessed by the ORR and OER performance of each electrocatalyst. Regarding the ORR, the following electroactivity was observed: CNT_{Fe} > CNT_{Fe}/CNT_{Co_185H2} > $CNT_{Co_185H2_Fe}$ > $CNT_{Fe_Co_185H2}$ > CNT_{Co_185H2}. Nonetheless, after the cycling protocol, CNT_{Fe} and CNT_{Fe}/CNT_{Co_185H2} displayed significant performance losses and $CNT_{Co_185H2_Fe}$ exhibited the most interesting ORR performance. Regarding the OER, the following electroactivity was observed: $CNT_{Co_185H2_Fe}$ > CNT_{Co_185H2} = $CNT_{Fe_Co_185H2}$ > CNT_{Fe}/CNT_{Co_185H2} > CNT_{Fe}. All samples presented very similar OER performance losses after the chronopotentiometry measurements, so their OER performance trend stayed the same. Therefore, $CNT_{Co_185H2_Fe}$ is the most promising bifunctional oxygen electrocatalyst synthesized closely followed by sample $CNT_{Fe_Co_185H2}$.

9.4. Conclusions

Rotating disk electrode measurements suggested that the incorporation of cobalt nitrate and iron phthalocyanine on CNT resulted in bifunctional oxygen electrocatalysts. The most promising materials determined by RDE assessments were tested as realistic fuel cell catalyst layers at relevant current densities. The ORR measurements demonstrated that the ORR electroactivity trend observed during RDE analyzes (CNT_{Fe} > CNT_{Fe}/CNT_{Co_185H2} > $CNT_{Co_185H2_Fe}$ > $CNT_{Fe_Co_185H2}$ > CNT_{Co_185H2}) was also followed during GDE measurements. Moreover, CNT_{Fe} achieved a current density of -2000 mA cm^{-2} at a potential very close to the commercial Pt/C (50 mV apart). This high ORR electroactivity is better than state-of-the-art Fe-N-C electrodes. Nonetheless, some leaching of the iron species to the electrolyte solution occurs, resulting in a demetallation of the electrocatalyst and loss of performance. On the other hand, $CNT_{Co_185H2_Fe}$ displays the highest ORR electroactivity after AST among the prepared samples with a potential of 0.57 V vs RHE to achieve -2000 mA cm^{-2}. This result suggests the importance of the presence of both metals and their interaction rather than simply mixing the two monometallic materials, which results in higher ORR electroactivity losses. Moreover, the potential determined to achieve such high current densities is very close to the operation potentials of a fuel cell (0.6 V). Regarding the OER, the trend observed during

RDE measurements ($CNT_{Co_185H2_Fe} > CNT_{Co_185H2} = CNT_{Fe_Co_185H2} > CNT_{Fe}/CNT_{Co_185H2} > CNT_{Fe}$) was also observed during GDE evaluation. All bimetallic samples displayed OER performances similar to the commercial RuO_2 to achieve the 10 mA cm^{-2} threshold, and lower performance losses during chronopotentiometry measurements than the noble metal. Overall, $CNT_{Co_185H2_Fe}$ displayed the highest ORR electroactivity after the accelerated stability tests and the highest OER performance of all samples. Thus, $CNT_{Co_185H2_Fe}$ was the most electroactive bifunctional oxygen electrocatalyst among all the samples tested and may be further modified to become an interesting commercial alternative to noble metals.

9.5. References

[1] Q. Guo, H. Guo, F. Ye, L. Xing, C.F. Ma, A numerical study of dynamic behaviors of a unitized regenerative fuel cell during gas purging, Int. J. Hydrog. Energy, 47 (2022) 22203-22214.
[2] H. Guo, J. Song, F. Ye, M.A. Chong Fang, Dynamic response during mode switching of unitized regenerative fuel cells with orientational flow channels, Renew. Energy, 188 (2022) 698-710.
[3] T.M. Gulotta, R. Salomone, F. Lanuzza, G. Saija, G. Mondello, G. Ioppolo, Life Cycle Assessment and Life Cycle Costing of unitized regenerative fuel cell: A systematic review, Environ. Impact Assess. Rev., 92 (2022) 106698.
[4] N. ul Hassan, P. Ganesan, A.A. Lando, W.E. Mustain, H.R. Colón-Mercado, Stable, high-performing bifunctional electrodes for anion exchange membrane-based unitized regenerative fuel cells, J. Power Sources, 541 (2022) 231599.
[5] J. Stacy, Y.N. Regmi, B. Leonard, M. Fan, The recent progress and future of oxygen reduction reaction catalysis: A review, Renew. Sust. Energ. Rev., 69 (2017) 401-414.
[6] A. Kirubakaran, S. Jain, R.K. Nema, A review on fuel cell technologies and power electronic interface, Renew. Sust. Energ. Rev., 13 (2009) 2430-2440.
[7] P. Gayen, S. Saha, X. Liu, K. Sharma, V.K. Ramani, High-performance AEM unitized regenerative fuel cell using Pt-pyrochlore as bifunctional oxygen electrocatalyst, Proc. Natl. Acad. Sci., 118 (2021) e2107205118.
[8] Y. Wang, D.Y.C. Leung, J. Xuan, H. Wang, A review on unitized regenerative fuel cell technologies, part-A: Unitized regenerative proton exchange membrane fuel cells, Renew. Sust. Energ. Rev., 65 (2016) 961-977.
[9] T. Sadhasivam, K. Dhanabalan, S.-H. Roh, T.-H. Kim, K.-W. Park, S. Jung, M. Kurkuri, H.-Y. Jung, A comprehensive review on unitized regenerative fuel cells: Crucial challenges and developments, 2016.
[10] K. Dutta, D. Rana, H.S. Han, P.P. Kundu, Unitized Regenerative Fuel Cells: A Review on Developed Catalyst Systems and Bipolar Plates, Fuel Cells, 17 (2017) 736-751.
[11] Y. Wang, D.Y.C. Leung, J. Xuan, H. Wang, A review on unitized regenerative fuel cell technologies, part B: Unitized regenerative alkaline fuel cell, solid oxide fuel cell, and microfluidic fuel cell, Renew. Sust. Energ. Rev., 75 (2017) 775-795.
[12] B. Paul, J. Andrews, PEM unitised reversible/regenerative hydrogen fuel cell systems: State of the art and technical challenges, Renew. Sust. Energ. Rev., 79 (2017) 585-599.
[13] M.M. Mohideen, Y. Liu, S. Ramakrishna, Recent progress of carbon dots and carbon nanotubes applied in oxygen reduction reaction of fuel cell for transportation, Appl. Energy, 257 (2020) 114027.
[14] W.E. Mustain, M. Chatenet, M. Page, Y.S. Kim, Durability challenges of anion exchange membrane fuel cells, Energy Environ. Sci., 13 (2020) 2805-2838.
[15] S. Gottesfeld, D.R. Dekel, M. Page, C. Bae, Y. Yan, P. Zelenay, Y.S. Kim, Anion exchange membrane fuel cells: Current status and remaining challenges, J. Power Sources, 375 (2018) 170-184.
[16] A. Sarapuu, E. Kibena-Põldsepp, M. Borghei, K. Tammeveski, Electrocatalysis of oxygen reduction on heteroatom-doped nanocarbons and transition metal–nitrogen–carbon catalysts for alkaline membrane fuel cells, J. Mater. Chem. A, 6 (2018) 776-804.
[17] Z.F. Pan, L. An, T.S. Zhao, Z.K. Tang, Advances and challenges in alkaline anion exchange membrane fuel cells, Progress in Energy and Combustion Science, 66 (2018) 141-175.
[18] H. Pan, X. Huang, Z. Lu, Z. Zhang, B. An, D. Wu, T. Wang, X. Chen, F. Cheng, Dual oxidation and sulfurization enabling hybrid Co/Co3O4@CoS in S/N-doped carbon matrix for bifunctional oxygen electrocatalysis and rechargeable Zn-air batteries, Chem. Eng. J., 419 (2021) 129619.
[19] R.G. Morais, N. Rey-Raap, J.L. Figueiredo, M.F.R. Pereira, Fe, Co, N-doped carbon nanotubes as bifunctional oxygen electrocatalysts, Appl. Surf. Sci., 572 (2022) 151459.

[20] J. Xia, K. Li, G.-L. Zhao, Electric Field Polarization To Increase Bifunctional Oxygen Electrocatalyst Performance of Nitrogen–Iron Functionalized Carbon Nanomaterials, ACS Appl. Energy Mater., 3 (2020) 1484-1495.
[21] A. Morozan, S. Campidelli, A. Filoramo, B. Jousselme, S. Palacin, Catalytic activity of cobalt and iron phthalocyanines or porphyrins supported on different carbon nanotubes towards oxygen reduction reaction, Carbon, 49 (2011) 4839-4847.
[22] M. Wu, G. Zhang, H. Tong, X. Liu, L. Du, N. Chen, J. Wang, T. Sun, T. Regier, S. Sun, Cobalt (II) oxide nanosheets with rich oxygen vacancies as highly efficient bifunctional catalysts for ultra-stable rechargeable Zn-air flow battery, Nano Energy, 79 (2021) 105409.
[23] Y. Tian, L. Xu, M. Li, D. Yuan, X. Liu, J. Qian, Y. Dou, J. Qiu, S. Zhang, Interface Engineering of CoS/CoO@N-Doped Graphene Nanocomposite for High-Performance Rechargeable Zn–Air Batteries, Nano-Micro Lett., 13 (2020) 3.
[24] Y. Liu, H. Jiang, Y. Zhu, X. Yang, C. Li, Transition metals (Fe, Co, and Ni) encapsulated in nitrogen-doped carbon nanotubes as bi-functional catalysts for oxygen electrode reactions, J. Mater. Chem. A, 4 (2016) 1694-1701.
[25] Y. Hao, Z. Lu, G. Zhang, Z. Chang, L. Luo, X. Sun, Cobalt-Embedded Nitrogen-Doped Carbon Nanotubes as High-Performance Bifunctional Oxygen Catalysts, Energy Technol., 5 (2017) 1265-1271.
[26] L. Song, H. Fan, T. Wang, T. Xiang, M. Zhang, C. Hu, W. Zhou, J. He, Facile synthesis of Co, N enriched carbon nanotube and active site identifications for bifunctional oxygen reduction and evolution catalysis, Energy Storage Mater., 43 (2021) 365-374.
[27] K. Ehelebe, T. Ashraf, S. Hager, D. Seeberger, S. Thiele, S. Cherevko, Fuel cell catalyst layer evaluation using a gas diffusion electrode half-cell: Oxygen reduction reaction on Fe-N-C in alkaline media, Electrochem. Commun., 116 (2020) 106761.
[28] Y.-P. Ku, K. Ehelebe, A. Hutzler, M. Bierling, T. Böhm, A. Zitolo, M. Vorokhta, N. Bibent, F.D. Speck, D. Seeberger, I. Khalakhan, K.J.J. Mayrhofer, S. Thiele, F. Jaouen, S. Cherevko, Oxygen Reduction Reaction in Alkaline Media Causes Iron Leaching from Fe–N–C Electrocatalysts, J. Am. Chem. Soc., 144 (2022) 9753-9763.

Chapter 10

Conclusions and Future Work

10.1. Main Conclusions

The main goal of this thesis was the development of highly electroactive bifunctional oxygen electrocatalysts (BOCs) and understanding the behavior of the materials' properties towards the oxygen reduction and evolution reactions (ORR and OER, respectively). For that, three different carbon materials were used to prepare the electrocatalysts: glucose-derived carbons, commercial carbon nanotubes (CNT), and glucose-derived carbon/CNT composites. The glucose-derived carbons present advantageous properties, specifically their high surface area, whereas CNT possess exceptional electrical conductivity; so their combination during the synthesis process results in a carbon composite with both individual properties. Moreover, the surface chemistry of all three carbon supports can be easily tailored allowing the incorporation of different heteroatoms and transition metals. The incorporation of nitrogen functionalities has been proved to be a promising strategy to achieve outstanding ORR and OER electrochemical performances due to the modification of the neighboring carbon atoms that favor the individual oxygen reaction steps. Additionally, the combination of transition metals can also lead to an electroactivity enhancement due to their different electronic and geometric properties that influence the ORR and/or OER. Therefore, this PhD thesis focuses on the evaluation of the effect of several catalysts' properties such as surface functionalities and transition metal combinations on their electrochemical performance to design and develop innovative and highly electroactive BOCs.

10.1.1. Oxygen Reduction Reaction electrocatalysts

The evaluation of the electrocatalysts towards the ORR started with the development of carbonized and activated glucose-derived carbons (CG and AG, respectively). It was observed that increasing activation times led to an increase in the microporosity of the carbon material, whereas carbonized samples present lower microporosity than AG samples. This textural property plays a major role in the ORR as samples with higher microporosity display slightly higher onset potentials (E_{onset}), probably due to their more graphitic structure generated during activation, and higher limiting current densities (J_L), which can be attributed to the more developed porous structure. Moreover,

electrochemical impedance spectroscopy (EIS) measurements showed a lower cell resistance and lower charge transfer resistance with increasing microporosity, which allows the ORR kinetics to increase and, consequently, achieve a higher E_{onset}. Furthermore, pores act as diffusion channels, hence wider pore sizes improved the electrolyte ion diffusion into the porous structure which was observed at the EIS's medium frequencies by the Warburg impedance. Thus, a higher value of J_L is achieved in structures with a higher degree of microporosity. In fact, a direct relationship between the BET surface area (S_{BET}) and the J_L was observed. On the other hand, the surface chemistry of the CG and AG samples was modified by the incorporation of nitrogen functionalities using different doping methods: ball milling (BM) and carbon/nitrogen precursor mixing. Both carbon supports were submitted to the BM procedures without adding the nitrogen precursor to understand the modifications produced during the milling and those due to the conjugation of BM and the nitrogen precursor. It was observed that BM i) created defects in the carbon matrix that interact with air, resulting in the incorporation of oxygen, and ii) decreased the materials' surface area and micropore volume. Regarding the incorporation of nitrogen functionalities, BM favored the incorporation of quaternary nitrogen (N-Q), due to the creation of defects during the mechanical process, and oxidized nitrogen (N-X) which was only present in ball milled samples. These nitrogen functionalities had an effect on the electrochemical performance as a higher N-6/N-Q ratio favored the onset potential, while a lower N-Q/N-6 ratio favored the number of electrons exchanged during the ORR. Furthermore, the correlation between J_L and the S_{BET} was also observed in the ball milled samples, although in N-doped samples played a less important role.

CNT display an intrinsically high electrical conductivity that is not present in porous carbons and can be crucial to enhance the catalyst's electroactivity. Therefore, a very small amount of CNT (2 wt% of the glucose used) were added during the hydrothermal carbonization (HTC) synthesis step. The presence of the CNT during the polymerization of glucose did not significantly change the microporosity of the material in comparison to CG. Nonetheless, the presence of oxidized CNT (CNT_O) during the HTC seemed to favor glucose polymerization, resulting in a material with lower microporosity. Moreover, the composite materials displayed higher S_{ext} than CG due to the presence of

CNT and CNT_O. The incorporation of CNT during the polymerization of glucose gave rise to an inhomogeneous material with two different carbon sphere size distributions, while the integration of CNT_O resulted in a homogenous material with small carbon spheres. This suggested that the presence of CNT could promote the formation of nucleation points that resulted in carbons with smaller spherical particles, and consequently, higher S_{ext}. The incorporation of nitrogen functionalities by BM gave rise to composites with different properties according to the type of CNT introduced during the polymerization. The BM process crushed some of the CNT and carbon spheres of the CG/CNT composite, resulting in a microporosity loss. Moreover, the decomposition of melamine by applying a thermal treatment after BM seemed to rearrange or merge the particles. On the other hand, the presence of CNT_O favored the formation of a more homogeneous structure with a larger degree of ordering and higher mechanical strength that partially prevented the crushing of the CNT and the carbon spheres during the BM, and hence, led to a carbon structure with enhanced electrical conductivity. The incorporation of nitrogen functionalities also resulted in a significant increase in the electrical conductivity, which seemed to be more influenced by the presence of N-Q groups that created donor electronic states near the Fermi level than the other functionalities. Regarding the electrocatalysts' ORR activity, an increase of 20% in the E_{onset} was observed due to the presence of CNT and nitrogen functionalities that act as active centers. Moreover, a linear relationship between the electrical conductivity and the J_L was established, whereas the presence of nitrogen shifted the reaction mechanism to a four-electron pathway and increased the electrocatalytic stability of the materials.

The incorporation of iron and iron/nitrogen on the CG and composites was evaluated towards the ORR. The incorporation of iron was achieved using an annealing treatment followed by reduction, whereas the incorporation of both Fe and N was achieved either by using a one-step method, in which iron and nitrogen were incorporated simultaneously, or a two-step approach, in which iron was first incorporated on the carbon material and, then, the nitrogen moieties. The incorporation of iron led to an increase in the S_{BET} and pore volume for both CG and CG/CNT_O which suggested that iron could be acting as an activating agent during the carbonization process. Moreover, the presence of Fe and N on the electrocatalysts' decreased the carbons' microporosity,

especially in samples prepared by the two-step method. In this approach, melamine was only treated for 2 h under N_2 atmosphere rather than 2 h in N_2 and 2 h under H_2 atmosphere used in the one-step process. Therefore, not only the time for the nitrogen precursor to decompose was increased but the decomposition of melamine may was also favored by the reaction with the H_2 carrier, which decreased the loss of microporosity during the simultaneous incorporation of Fe and N. The presence of CNT_O increased the graphitic domains of the composite due to its highly graphitic nature, while the solo incorporation of iron led to a more disordered matrix, probably due to the anchoring of some precursor nanoparticles on the carbon structure. The incorporation of nitrogen using the two-step approach increased the degree of order of the CG and Fe-doped CG sample. In contrast, the incorporation of Fe on the composite led to a higher amount of defects in the carbon's structure. On the other hand, the one-step method slightly increased the number of defects in the electrocatalysts'. Regarding the electrochemical characterization of the prepared materials, a direct relationship between two electrochemical parameters (E_{onset} and $J_{0.4}$) and the amount of iron present in the carbon's structure was found. Furthermore, the number of electrons exchanged during the ORR increased with the percentage of iron. Interesting differences were also observed between Fe,N-doped samples due to their incorporation method and/or carbon supports. The E_{onset} exhibited a higher increase in samples prepared using the two-step approach than a single-step method, probably due to the presence of a larger amount of N-6 functionalities on the former. Conversely, the reaction mechanism is closer to a direct oxygen reduction in samples prepared using a single-step functionalization, probably due to the presence of a large number of N-Q functionalities that seem to favor oxygen adsorption and dissociation. On the other hand, the $J_{0.4}$ appears to be more influenced by the type of carbon support used. CG samples prepared by the one-step method generated higher current densities, whereas a two-step method led to higher $J_{0.4}$ in composite samples, which may be related to a larger number of defects on the composite's carbon structure.

To further enhance the ORR electroactivity, three carbon supports (CG, AG and purified CNT) were functionalized with melamine and/or iron(II) phthalocyanine (FePc) following three different methodologies: i) functionalization with melamine via thermal treatment, ii) incorporation of FePc via incipient wetness impregnation (IWI) followed

by thermal treatment, and iii) functionalization with melamine followed by FePc incorporation. CG and AG were used to study the microporosity effect on the incorporation of the Fe-N_4 complex, whereas CNT was used as a carbon material without microporosity. The characterization of the samples suggested that the microporosity did not play a crucial role in the incorporation of nitrogen functionalities using melamine as a precursor. Conversely, the carbons' porosity exhibited a great influence in the incorporation of the iron complex. In samples with high microporosity (AG), the FePc was preferentially located inside the porous structure, whereas in materials with low (CG) or no microporosity (CNT) FePc was present on the surface. In addition, the incorporation of melamine before FePc led to the blockage of some pores of the AG, which modified the preferential location of the Fe-N_4 molecules to be closer to the surface. Regarding the ORR electroactivity, the iron complex was the main ORR active site and catalyzed the reaction through a four-electron mechanism. Additionally, its localization on the carbon structure was crucial for oxygen reduction. The FePc molecules located inside the porous structures were of more difficult access and, consequently, did not catalyze the ORR as much as those located on the carbons' surface, resulting in lower current densities and a small number of electrons exchanged. Nonetheless, the functionalization of AG with melamine before the incorporation of FePc led to an increase in the ORR electroactivity and shifted the reaction mechanism closer to a four-electron mechanism, in comparison to the AG sample doped only with FePc, due to a higher exposure of the FePc centers. The synergy between the highly electrical conductive CNT and the iron complex also gave rise to faster reaction kinetics and the reaction was achieved through the four-electron pathway. In fact, the incorporation of a very small amount of FePc on the CNT led to an ORR electroactivity with significantly better results than those obtained for the commercial catalyst (Pt/C), including higher $E_{1/2}$ (0.87 vs 0.83 V vs RHE), J_L (5.20 vs 4.46 mA cm^{-2}) and a similar reaction mechanism (4.0 electrons exchanged) and by-product formation (< 1%).

10.1.2. Bifunctional oxygen electrocatalysts

Considering the outstanding ORR electroactivity obtained using the CNT and FePc, CNT were then modified to provide high electroactivity towards both the ORR and OER. FePc and cobalt(II) phthalocyanine (CoPc) were incorporated into the CNT structure due to

the synergy between their π-π systems that are crucial to achieving higher electrocatalytic performances. Four different approaches were used to prepare bimetallic samples: i) incorporation of CoPc on the FePc-doped sample (CNT_{Fe_Co}), ii) incorporation of FePc on the CoPc-doped material (CNT_{Co_Fe}), iii) simultaneous incorporation of FePc and CoPc on the CNT (CNT_{CoFe}) and, iv) mixture of the monometallic CNT carbons (CNT_{Co} and CNT_{Fe}) using a 1:1 CNT_{Co}:CNT_{Fe} mass ratio ($50CNT_{Co}/50CNT_{Fe}$). An initial ORR/OER screening indicated that from these four approaches, the mixture of the monometallic materials produced the most interesting bifunctional oxygen electroactivity, even though it only presented half of the metallic content of the other three samples. Afterwards, 2 additional mixtures of the monometallic CNT (CNT_{Co} and CNT_{Fe}) were prepared using different CNT_{Co}:CNT_{Fe} mass ratios (3:1 – $75CNT_{Co}/25CNT_{Fe}$ and 1:3 - $25CNT_{Co}/75CNT_{Fe}$). The incorporation of CoPc and FePc in CNT did not modify the textural properties but increased the number of defects due to the presence of the metal phthalocyanines, achieving the maximum number of defects in the bimetallic sample prepared using a 1:1 CNT_{Co}:CNT_{Fe} mass ratio ($50CNT_{Co}/50CNT_{Fe}$). Regarding the ORR performance, it was observed that the electrocatalyst activity linearly increased with the contribution of FePc sites towards the total FePc/CoPc centers incorporated on the CNT. Moreover, FePc followed a direct oxygen reduction mechanism (4 electrons), whereas CoPc was closer to an indirect mechanism (2 electrons). Therefore, FePc was considered the main ORR active site of the two metallic complexes. Conversely, the OER catalytic performance followed a different trend. CNT_{Co} displayed a higher OER electroactivity than CNT_{Fe}, which suggested that CoPc was a more important active center towards OER than FePc. Nonetheless, their physical mixture ($50CNT_{Co}/50CNT_{Fe}$) led to a synergetic effect that significantly improved their electrochemical performance towards the OER. The electrocatalysts' bifunctional oxygen activity was evaluated by the potential gap (ΔE) between the OER (E_{10}) and the ORR ($E_{1/2}$) potentials. The $E_{1/2}$ of FePc-doped materials showed very slight differences, hence the E_{10} was the major factor to achieve the lowest oxygen overpotential. Considering the OER electrocatalytic performances, sample $50CNT_{Co}/50CNT_{Fe}$ displayed the lowest ΔE (0.81 V) of all prepared samples, which is a value even lower than that of the commercial catalysts (Pt/C – 1.04 V, and RuO_2 – 0.98 V).

Taking into account that the synthesized materials' ORR performance is already very similar to that of Pt/C, an enhancement of the OER electroactivity is crucial to decrease the overpotential difference between both reactions. To achieve this objective, a different cobalt precursor was incorporated into the CNT via incipient wetness impregnation instead of CoPc: cobalt(II) nitrate hexahydrate. After the impregnation, six different thermal treatment temperatures and/or atmospheres were employed. Four samples were prepared in N_2 atmosphere at 150 °C, 185 °C, 350 °C and 900 °C (CNT_{Co_150N2}, CNT_{Co_185N2}, $CNT_{Co_350N2,}$ and CNT_{Co_900N2}, respectively), and two additional samples were prepared by further treating CNT_{Co_185N2} and CNT_{Co_350N2} for 2 h in a H_2 atmosphere (CNT_{Co_185H2} and CNT_{Co_350H2}, respectively). These variations in temperature and/or atmosphere led to interesting differences in the materials' properties. A decrease in oxygen content and, consequently, an increase in the cobalt contribution to the global composition, as well as a reduction of Co^{3+} species to Co^{2+}, was observed by increasing the thermal treatment temperature and by using H_2 atmosphere rather than N_2. The textural properties of all samples were very similar, but the degree of graphitization increased with temperature. Moreover, at the same temperatures, the use of a H_2 atmosphere resulted in a material with a higher number of defects which suggested that the reduction of cobalt oxides generated defects in the carbon matrix. Regarding the OER performance of these materials, it was observed that the E_{10} decreased with temperature (1.69 to 1.66 V), probably due to an increase in the relative Co^{2+} content and Co^{2+}/Co^{3+} ratio on the surface. Moreover, samples treated under H_2 atmosphere displayed even lower values of E_{10} (1.63 V) due to their higher Co^{2+} content. Additionally, the presence of metallic Co (CNT_{Co_900N2}) seems to hinder the OER performance of the electrocatalyst, even though it has the highest percentage of Co^{2+}. Considering these results, different bimetallic samples were prepared using FePc and the cobalt precursor following three different approaches: i) incorporation of FePc on CNT_{Co_185H2} ($CNT_{Co_185H2_Fe}$), ii) incorporation of cobalt nitrate on CNT_{Fe} ($CNT_{Fe_Co_185H2}$), and iii) physical mixture of CNT_{Co_185H2} and CNT_{Fe} using a 1:1 mass ratio (CNT_{Fe}/CNT_{Co_185H2}). Contrarily to the CoPc,FePc-doped samples, the OER performance of all bimetallic electrocatalysts and CNT_{Co_185H2} was very similar, which may be explained by the high cobalt content in all samples (11.8-21.1 wt%) and their similarity in cobalt surface species (mainly Co^{2+}), which seems to command the OER. Nonetheless, several differences were observed

towards the ORR. Although CNT_{Co_185H2} displayed a reaction mechanism close to a four-electron pathway (3.7), it presented a low ORR electroactivity. Regarding bimetallic samples prepared by the incorporation of FePc and cobalt nitrate in two different steps, the incorporation of a large amount of cobalt on top of the few FePc sites available ($CNT_{Fe_Co_185H2}$) probably blocked part of them, hindering their exposure and resulting in an ORR performance similar to CNT_{Co_185H2}. Regarding $CNT_{Co_185H2_Fe}$, a significant increase of the E_{onset} and $E_{1/2}$ in comparison to CNT_{Co_185H2} was observed (100 mV and 130 mV, respectively). Nonetheless, the sample prepared by mixing both monometallic samples (CNT_{Fe}/CNT_{Co_185H2}) displayed the highest ORR electroactivity. This sample displayed a higher $E_{1/2}$ than the Pt/C catalyst (0.88 vs 0.83 V), and a very similar J_L and reaction mechanism. Regarding bifunctional oxygen electroactivity, most catalysts displayed similar E_{10}, hence the ΔE was mainly dictated by the ORR results. Thus, sample CNT_{Fe}/CNT_{Co_185H2} presented the lowest potential gap difference between oxygen reactions (0.76 V), which is an improvement in comparison to the previous Fe,Co-doped materials and a value lower than that of the commercial electrocatalysts (Pt/C – 1.04 V, and RuO_2 – 0.98 V). The E_{10}, E_3 and ΔE values obtained for the prepared bimetallic materials and the benchmark catalysts are presented in Table 10.1.

Table 10.1 - $E_{1/2}$, $E_{10,}$ and ΔE of the most promising prepared samples and benchmark electrocatalysts.

Sample	E_{10} (V)	$E_{1/2}$ (V)	ΔE (V)
CNT_{Co}	1.78	0.76	1.02
CNT_{Co_185H2}	1.63	0.68	0.95
CNT_{Fe}	1.79	0.88	0.91
$CNT_{Fe_Co_185H2}$	1.63	0.73	0.90
$25CNT_{Co}/75CNT_{Fe}$	1.75	0.86	0.89
$75CNT_{Co}/25CNT_{Fe}$	1.73	0.86	0.87
$50CNT_{Co}/50CNT_{Fe}$	1.67	0.86	0.81
$CNT_{Co_185H2_Fe}$	1.62	0.81	0.81
CNT_{Fe}/CNT_{Co_185H2}	1.64	0.88	0.76
Pt/C	1.87	0.83	1.04
RuO_2	1.58	0.60	0.98

Regarding both oxygen reactions, three main conclusions can be drawn at the RDE/RRDE scale from Table 10.1: i) the ORR performance of the benchmark catalyst (Pt/C) was surpassed by most of the prepared FePc-containing carbons, ii) the OER electroactivity of the prepared Co-doped samples using cobalt nitrate was very close to that of the benchmark catalyst (RuO_2) and iii) overall, the oxygen bifunctionality performance of all bimetallic materials outshined that of both noble-metal electrocatalysts, demonstrating the potential of the prepared materials to replace the noble metals-based electrocatalysts currently employed. Although there are Fe,Co-doped carbon materials reported in the literature with potential gaps similar to those presented in this work, it should be highlighted that all bimetallic samples prepared during this PhD thesis offer several advantages in comparison to most of the reported literature results, as these materials were prepared using a reduced number of synthesis steps, the incorporation of a very low amount of macrocycles, the use of low-cost precursors and an easily scalable procedure.

The most promising materials prepared using FePc and cobalt nitrate were then tested as realistic fuel cell catalyst layers at relevant current densities. The ORR measurements using a gas-diffusion electrode (GDE) demonstrated that the reaction's electroactivity trend observed during rotating disk electrode (RDE) analyzes was also followed: CNT_{Fe} > CNT_{Fe}/CNT_{Co_185H2} > $CNT_{Co_185H2_Fe}$ > $CNT_{Fe_Co_185H2}$ > CNT_{Co_185H2}. Furthermore, the FePc-doped CNT achieved high current densities (-2000 mA cm^{-2}), requiring only 50 mV more than the commercial Pt/C catalyst. The long-term performance of these samples was then assessed by accelerated stability testing (AST) and some leaching of the iron species to the electrolyte solution occurred, resulting in performance loss, especially for sample CNT_{Fe}. Nonetheless, $CNT_{Co_185H2_Fe}$ displayed a very interesting ORR electroactivity after AST with a potential of 0.57 V vs RHE to achieve -2000 mA cm^{-2}. This result suggested that the presence and interaction of iron and cobalt were crucial to increase the catalyst stability and protect the FePc active sites. Moreover, this result is very interesting and promising as the potential determined to achieve such high current densities is very close to the operating potential of a fuel cell (0.6 V). Regarding the OER, the measurements performed during the GDE evaluation also followed the same trend as the RDE assessments: $CNT_{Co_185H2_Fe}$ > CNT_{Co_185H2} = $CNT_{Fe_Co_185H2}$ >

$CNT_{Fe}/CNT_{Co_185H2} > CNT_{Fe}$. In this case, all bimetallic samples presented similar OER electroactivities to the commercial RuO_2 to achieve the 10 mA cm^{-2} threshold and lower performance losses during stability assessments than the noble metal. Overall, $CNT_{Co_185H2_Fe}$ displayed the highest ORR electroactivity after the accelerated stability tests and the highest OER performance. Thus, $CNT_{Co_185H2_Fe}$ was the most electroactive bifunctional oxygen electrocatalyst among all the samples tested and may be further modified to become an interesting commercial alternative to noble metals.

10.2. Future work

The work described in this PhD thesis demonstrated the high potential of properly designed carbon materials to replace noble metals as bifunctional oxygen electrocatalysts at a laboratory scale and relevant current densities. However, there is still plenty of room for improvement in these materials. The quest for carbon materials suitable for commercial applications is in high demand and should continue to be one of the most important global goals in the near future. Thus, the following suggestions for future work are proposed:

- Investigation of different carbon sources, particularly in the biomass field, and the use of waste materials and their valorization. Several biomass and waste sources are not only good carbon sources but may also already involve different heteroatoms. Thus, their use could be interesting to prepare heteroatom-doped carbons using, for example, a single thermal treatment and to reduce production costs.
- The exploration of other doping and functionalization methodologies involving the incorporation of sulfur and phosphorus heteroatoms on carbon materials. This may be an interesting strategy to obtain highly electroactive ORR/OER electrocatalysts, as S and P functionalities may provide different modifications to the carbons'/metals' properties as they can dislocate the charge of the material and improve oxygen adsorption, which may lead to an electrocatalytic performance enhancement.
- Incorporation of Ni species on carbon materials and optimization of the synthesis process to achieve highly electroactive Ni-doped catalysts towards the ORR and OER. Ni has been widely reported as a very electroactivity active center towards oxygen reactions and can, potentially, surpass the performances obtained by its cobalt counterpart.
- Preparation of bimetallic samples via incorporation of Ni and FePc on carbon materials. This would be an interesting approach as FePc-doped CNT has provided excellent ORR electrocatalytic activities at RDE and GDE scales and Ni could originate very electroactive OER centers, which would potentially result in a bifunctional oxygen electrocatalyst with very high electroactivities.
- Preparation of trimetallic carbon/N-doped carbon materials using Fe, Co, and Ni. This would be interesting as each metal provides crucial active centers and different synergies

that could potentially enhance the ORR/OER performances already obtained and increase the materials' electrochemical long-term stability.

- The loss of performance at high current densities is one of the main drawbacks of some materials prepared in this work. Therefore, a comprehensive study at relevant current densities using different electrolytes/electrolyte concentrations should be performed to determine their effect on the metallic centers' leaching.
- The evaluation of the performance of the most promising materials at the GDE level in a fuel cell and an electrolyzer. The topmost performing electrocatalysts could then be evaluated in a unitized regenerative fuel cell system as proof of concept.

Appendixes

Appendix A – Method's equations

The surface area of each material was calculated using the Brunauer-Emmett-Teller (BET) equation (Eq. A1.1):

$$\frac{\frac{P}{P_0}}{n^a(1-\frac{P}{P_0})} = \frac{1}{n_m^a c} + \frac{c-1}{n_m^a c}\left(\frac{P}{P_0}\right) \quad \text{(A1.1)}$$

Where n^a represents the amount of adsorbed gas (mol g^{-1}), P is the equilibrium pressure of the adsorbate, P_0 is the saturation pressure of the adsorbate, n_m^a is the monolayer adsorbed gas quantity (mol g^{-1}) and c is the BET constant, which is correlated to the adsorption energy of the first layer (E_1) and the condensation heat (E_L) and can be expressed by Eq. A1.2:

$$c = \exp\left(\frac{E_1 - E_L}{RT}\right) \quad \text{(A1.2)}$$

Where R is the gas constant (8.31 J K mol^{-1}), and T is the temperature of analysis. Representing $\frac{\frac{P}{P_0}}{n^a(1-\frac{P}{P_0})}$ in function of $\frac{P}{P_0}$ will result in a slope (α) corresponding to $\frac{c-1}{n_m^a c}$ and a y-axis interception (i) assigned to $\frac{1}{n_m^a c}$, which results in Eq. A1.3:

$$n_m^a = \frac{1}{\alpha + i} \quad \text{(A1.3)}$$

Considering that n_m^a covers the solid's surface with a monomolecular layer, the specific surface area of the material can be represented by:

$$S_{BET} = n_m^a \, N_A \, a_m \quad \text{(A1.4)}$$

Where N_A is Avogadro's number (6.02 x 10^{23} mol^{-1}) and a_m is the area occupied by each adsorbed molecule. This area can be calculated for any adsorbate chosen, nonetheless nitrogen is considered as standard and is the most used. Since the liquid nitrogen used for the measurements was at 77 K, the a_m value used in the equations was 0.162 nm^2.

The Dubinin-Radushkevich (DR) method is ascribed by the following equation:

$$W = W_0 \exp\left(-\left(\frac{RT ln\left(\frac{P_0}{P}\right)}{\beta E_0}\right)^2\right) \quad \text{(A1.5)}$$

Where W corresponds to the volume filled at a certain P/P_0, β is the affinity coefficient for carbon (0.35) and E_0 is the characteristic energy. The micropore volume can then be calculated by plotting the adsorption isotherm in logarithmic scale versus $\ln^2(P/P_0)$, in which the interception of the linear regression will represent V_{DR}.

During XRD measurements, θ can be calculated by the following sine function (Eq. A1.6).

$$\sin\theta = \frac{\lambda/2}{d} \quad \text{(A1.6)}$$

where θ is the Bragg's angle, λ is the X-ray radiation wavelength and d is the atomic plane distance. Further rearranging this equation results in the Bragg's Law equation:

$$n\lambda = 2d \sin\theta \quad \text{(A1.7)}$$

where n is the diffraction order.

The Scherrer equation correlates these sizes with the line broadening at half the maximum intensity [14] using Eq. A1.8:

$$\mathrm{T} = \frac{K\lambda}{\beta Cos\theta} \quad \text{(A1.8)}$$

where T is the average crystallite size, K is the shape factor (0.94) and β is the peak full width at half the maximum intensity.

The electrochemical active surface area can be calculated by:

$$\mathrm{ECSA} = \frac{C_{\mathrm{dl}}}{C_{\mathrm{S}}} \quad \text{(A1.9)}$$

where C_S is the specific capacitance of the catalyst's ideal flat surface. Nonetheless, due to the very similar chemical nature of the prepared carbon materials, it can be considered that they present the same C_S value. Therefore, the C_{dl} value is expected to be proportional to the ECSA.

The Levich equation is given by:

$$J_L = 0.62 n_e F C_0^* D^{2/3} \nu^{-1/6} \omega^{1/2} \quad \text{(A1.10)}$$

Where, J_L is the limiting current density, n_e is the number of electrons exchanged during the reaction, F is the Faraday constant (96485 C mol^{-1}), C_0^* is the bulk concentration of saturated O_2 in the electrolyte (1.15 x 10^{-3} mol L^{-1}), D is the diffusion coefficient of O_2 (1.95 × 10^{-5} cm^2 s^{-1}), ν is the kinematic viscosity of the electrolyte (0.008977 cm^2 s^{-1}, KOH 0.1 mol L^{-1}) and ω is the rotating speed (rad s^{-1}). The rotation speed applied to the electrode was in rpm, which slightly modifies the above equation into:

$$J_L = 0.20 n_e F C_0^* D^{2/3} \nu^{-1/6} \omega^{1/2} \quad \text{(A1.11)}$$

The Koutecký-Levich equation is described by:

$$\frac{1}{J} = \frac{1}{J_K} + \frac{1}{J_L} = \frac{1}{n_e F (k C_0^*)} + \frac{1}{0.20 n_e F C_0^* D^{2/3} \nu^{-1/6} \omega^{1/2}} \quad \text{(A1.12)}$$

where J is the measured current density and J_K is the kinetic current density.

Moreover, plotting $1/J$ as function of the square root of the rotation speed (rpm) at a determined potential will result in a slope and interception that can be used to calculate the number of electrons exchanged and kinetic current density using Eq. A.13 and A.14, respectively.

$$n_e = \frac{1}{\text{Slope} \times 0.20 F C_0^* D^{2/3} \nu^{-1/6}} \quad \text{(A1.13)}$$

$$J_K = \frac{1}{interception} \quad \text{(A1.14)}$$

The disk current density and the ring current density obtained by using a RRDE can be expressed by Eq. A1.15 and A1.16, respectively:

$$I_D = I_{4e} + I_{2e} + I_{2e'} \quad \text{(A1.15)}$$

$$I_R = N(I_{2e} - I_{2e'}) \quad \text{(A1.16)}$$

where I_D is the Faradaic current at the disk; I_{4e} is the Faradaic current related to the direct mechanism (reaction 1.1 and 1.2 in acidic and alkaline electrolyte, respectively); I_{2e} and $I_{2e'}$ are the Faradaic currents related to the indirect pathway shown in reactions 1.3-1.4

(acidic medium) and 1.5-1.6 (alkaline conditions), respectively; I_R is the Faradaic current at the ring and N is the collection coefficient at the ring (N = 0.249). This theoretical collection coefficient can be obtained by assuming that all disc products are detected at the ring after mass transport by Eq. A1.17:

$$N = \frac{A_R}{A_D} \tag{A1.17}$$

where A_R and A_D are the ring and disk areas, respectively. The diameter of the ring and disk are 6.268 mm and 5.000 mm, respectively. Both areas are distanced by a 0.375 mm gap. Hence:

$$N = \frac{\pi\,(\frac{6.268}{2})^2 - \pi\,(\frac{5.000 + 0.750}{2})^2}{\pi\,(\frac{5.000}{2})^2} = 0.249 \tag{A1.18}$$

The total number of electrons (n_e) detected by each oxygen molecule can be determined by:

$$n_e = \frac{N_e}{N_{O_2}} \tag{A1.19}$$

where N_e and N_{O2} are the total number of electrons transferred and the total number of oxygen molecules participating in the ORR, respectively. These two parameters can be expressed as:

$$N_e = \frac{N_A \Delta t}{F}\,(I_{4e} + I_{2e} + I_{2e'}) \tag{A1.20}$$

$$N_{O_2} = \frac{N_A \Delta t}{F}(\frac{I_{4e}}{4} + \frac{I_{2e}}{2}) \tag{A1.21}$$

where N_A is the constant of Avogrado and F is Faraday's constant.

Therefore, Eq. A1.19 can be expressed as:

$$n_e = \frac{N_e}{N_{O_2}} = \frac{\frac{N_A \Delta t}{F}\,(I_{4e} + I_{2e} + I_{2e'})}{\frac{N_A \Delta t}{F}(\frac{I_{4e}}{4} + \frac{I_{2e}}{2})} \tag{A1.22}$$

$$n_e = \frac{(I_{4e} + I_{2e} + I_{2e'})}{(\frac{I_{4e}}{4} + \frac{I_{2e}}{2})} \quad \text{(A1.23)}$$

The combination of Eq. A1.15, A1.16 and A1.23 results in:

$$n_e = \frac{4I_D}{I_D + (\frac{I_R}{N})} \quad \text{(A1.24)}$$

Similarly, the production of hydrogen peroxide can be expressed as the fraction between the number of hydrogen peroxide molecules formed and the total number of oxygen molecules participating in the ORR:

$$H_2O_2 = \frac{N_{H_2O_2}}{N_{O_2}} \quad \text{(A1.25)}$$

where N_{H2O2} is the total number of hydrogen peroxide molecules that can be expressed as:

$$N_{H_2O_2} = \frac{N_A \Delta t}{F}(\frac{I_{2e}}{2} - \frac{I_{2e'}}{2}) \quad \text{(A1.26)}$$

The combination of Eq. A1.25, A1.26, and A1.21 results in:

$$H_2O_2 = \frac{N_{H_2O_2}}{N_{O_2}} = \frac{\frac{N_A \Delta t}{F}(\frac{I_{2e}}{2} - \frac{I_{2e\prime}}{2})}{\frac{N_A \Delta t}{F}(\frac{I_{4e}}{4} + \frac{I_{2e}}{2})} \quad \text{(A1.27)}$$

$$H_2O_2 = \frac{2(I_{2e} - I_{2e\prime})}{I_{4e} + 2I_{2e}} \quad \text{(A1.28)}$$

Finally, the combination of Eq. A1.15, A1.16, and A1.28 results in:

$$H_2O_2 = \frac{2\left(\frac{I_R}{N}\right)}{I_D + \left(\frac{I_R}{N}\right)} \quad \text{(A1.29)}$$

The turnover frequency was calculated by:

$$TOF = \frac{J \times A}{4 \times F \times n} \quad \text{(A1.30)}$$

where J (mA cm^{-2}) is the current density at a selected overpotential, A is the area of the working electrode (cm^2), F is the Faraday constant (96 485 C mol^{-1}), and n is the number of moles of the active material. The TOF was calculated at a potential of 1.73 V, in which

all metallic samples present a significant current density, and by using the number of moles of the metallic active centers calculated from the ICP results instead of the nominal values or the XPS results, due to the low amount of metal employed which is more accurately assessed by ICP.

The resistance measured by electrochemical impedance spectroscopy in a resistor can be given by Ohm's Law:

$$V = I \times R \tag{A1.31}$$

$$\mathrm{R} = \frac{V}{I} \tag{A1.32}$$

where V is the voltage, I is the current, and R is the resistance. Further adjusting Ohm's Law to create a function to calculate the resistance at different input and output values according to the frequency applied, Eq. A1.33 is used:

$$\mathrm{Z_R} = \frac{V(f)}{I(f)} = R \tag{A1.33}$$

where $V(f)$ is the input voltage in function of the frequency applied, $I(f)$ is the output current in function of the frequency applied and Z_R is the impedance of the resistor which is equal to R.

The resistance of a capacitor (Z_C) is given by Eq. A1.34:

$$Z_{\mathrm{C}} = \frac{1}{i\omega C} \tag{A1.34}$$

where i is the intensity output, ω is the frequency and C is the capacitance. The use of a resistor and a capacitor in parallel results in an impedance calculated by Eq. A1.35:

$$Z = \frac{1}{\mathrm{Z_R}} + \frac{1}{\mathrm{Z_C}} = \frac{R}{1 + i\omega RC} \tag{A1.35}$$

The Warburg impedance is given by the following equation:

$$Z_{\mathrm{W}} = \sigma\omega^{-1/2} - i\sigma\omega^{-\frac{1}{2}} \tag{A1.36}$$

where σ is the Warburg coefficient, which is the diffusion coefficient of ions in solution, i is the intensity output and ω is the frequency.

Appendix B – Full agreement of the co-authors on the inclusion of the manuscripts







Co-authors authorization regarding the full agreement of the inclusion of manuscripts in the present thesis

José L. Figueiredo, Emeritus Professor at the Faculty of Engineering of the University of Porto (FEUP), M. Fernando R. Pereira, Full Professor at FEUP, Natalia Rey Raap, researcher at INCAR-CSIC, hereby authorize the PhD student Rafael Gomes Morais, from the FEUP Doctoral Program in Chemical and Biological Engineering, to include the following publication in his doctoral thesis entitled "Noble-metal free carbon-based materials for energy conversion":

R. G. Morais, N. Rey-Raap, J. L. Figueiredo, M. F.R. Pereira, Glucose-derived carbon materials with tailored properties as electrocatalysts for the oxygen reduction reaction, Beilstein J. Nanotechnol., 10 (2019) 1089-1102.

(José L. Figueiredo) (M. Fernando R. Pereira)

REY RAAP NATALIA - 20472933N Firmado digitalmente por REY RAAP NATALIA - 20472933N Fecha: 2023.05.26 15:35:35 +02'00'

(Natalia Rey Raap)

SRE CM LABORATORY OF SEPARATION AND REACTION ENGINEERING LABORATORY OF CATALYSIS AND MATERIALS

U.PORTO FEUP FACULDADE DE ENGENHARIA UNIVERSIDADE DO PORTO

ALiCE ASSOCIATE LABORATORY IN CHEMICAL ENGINEERING

LAQV requimte

U.PORTO FC FACULDADE DE CIÊNCIAS UNIVERSIDADE DO PORTO

IFIMUP Institute of Physics for Advanced Materials, Nanotechnology and Photonics

Co-authors authorization regarding the full agreement of the inclusion of manuscripts in the present thesis

José L. Figueiredo, Emeritus Professor at the Faculty of Engineering of the University of Porto (FEUP), M. Fernando R. Pereira, Full Professor at FEUP, Alexandra Guedes, Auxiliar Professor at the Faculty of Sciences of the University of Porto (FCUP), Natalia Rey Raap, researcher at INCAR-CSIC, Clara Pereira, researcher at LAQV-REQUIMTE, and Rui S. Costa, researcher at IFIMUP, hereby authorize the PhD student Rafael Gomes Morais, from the FEUP Doctoral Program in Chemical and Biological Engineering, to include the following publication in his doctoral thesis entitled "Noble-metal free carbon-based materials for energy conversion":

R. G. Morais, N. Rey-Raap, R. Costa, C. Pereira, A. Guedes, J. L. Figueiredo, M. F. R. Pereira, Hydrothermal Carbon/Carbon Nanotube Composites as Electrocatalysts for the Oxygen Reduction Reaction, J. Compos. Sci., 4 (2020) 1-14.

(José L. Figueiredo)

(M. Fernando R. Pereira)

Assinado por: **Maria Alexandra de Mascarenhas Guedes**
Num. de Identificação: 08084050
Data: 2023.05.24 13:14:59+01'00'
CHAVE MÓVEL

(Alexandra Guedes)

REY RAAP NATALIA - 20472933N
Firmado digitalmente por REY RAAP NATALIA - 20472933N
Fecha: 2023.05.26 15:33:53 +02'00'

(Natalia Rey Raap)

Assinado por: **Clara Isabel Barbosa Rodrigues Pereira**
Num. de Identificação: 11660538
Data: 2023.05.25 00:06:56+01'00'
CHAVE MÓVEL

(Clara Pereira)

(Rui S. Costa)

SRE CM LABORATORY OF SEPARATION AND REACTION ENGINEERING LABORATORY OF CATALYSIS AND MATERIALS

U.PORTO FEUP FACULDADE DE ENGENHARIA UNIVERSIDADE DO PORTO

ALiCE ASSOCIATE LABORATORY IN CHEMICAL ENGINEERING

Co-authors authorization regarding the full agreement of the inclusion of manuscripts in the present thesis

José L. Figueiredo, Emeritus Professor at the Faculty of Engineering of the University of Porto (FEUP), M. Fernando R. Pereira, Full Professor at FEUP, Natalia Rey Raap, researcher at INCAR-CSIC, hereby authorize the PhD student Rafael Gomes Morais, from the FEUP Doctoral Program in Chemical and Biological Engineering, to include the following publication in his doctoral thesis entitled "Noble-metal free carbon-based materials for energy conversion":

R.G. Morais, N. Rey-Raap, J.L. Figueiredo, M.F.R. Pereira, Highly electroactive N–Fe hydrothermal carbons and carbon nanotubes for the oxygen reduction reaction, J. Energy Chem., 50 (2020) 260-270.

(José L. Figueiredo)

(M. Fernando R. Pereira)

REY RAAP NATALIA - 20472933N

Firmado digitalmente por REY RAAP NATALIA - 20472933N
Fecha: 2023.05.26 15:37:24 +02'00'

(Natalia Rey Raap)

SRE CM LABORATORY OF SEPARATION AND REACTION ENGINEERING LABORATORY OF CATALYSIS AND MATERIALS

U.PORTO FEUP FACULDADE DE ENGENHARIA UNIVERSIDADE DO PORTO

ALiCE ASSOCIATE LABORATORY IN CHEMICAL ENGINEERING

Co-authors authorization regarding the full agreement of the inclusion of manuscripts in the present thesis

José L. Figueiredo, Emeritus Professor at the Faculty of Engineering of the University of Porto (FEUP), M. Fernando R. Pereira, Full Professor at FEUP, Natalia Rey Raap, researcher at INCAR-CSIC, hereby authorize the PhD student Rafael Gomes Morais, from the FEUP Doctoral Program in Chemical and Biological Engineering, to include the following publication in his doctoral thesis entitled "Noble-metal free carbon-based materials for energy conversion":

R.G. Morais, N. Rey-Raap, J.L. Figueiredo, M.F.R. Pereira, Fe, Co, N-doped carbon nanotubes as bifunctional oxygen electrocatalysts, Appl. Surf. Sci., 572 (2022) 151459.

(José L. Figueiredo)

(M. Fernando R. Pereira)

REY RAAP NATALIA - 20472933N

Firmado digitalmente por REY RAAP NATALIA - 20472933N
Fecha: 2023.05.26 15:36:49 +02'00'

(Natalia Rey Raap)

SRE CM LABORATORY OF SEPARATION AND REACTION ENGINEERING LABORATORY OF CATALYSIS AND MATERIALS

U.PORTO FEUP FACULDADE DE ENGENHARIA UNIVERSIDADE DO PORTO

ALiCE ASSOCIATE LABORATORY IN CHEMICAL ENGINEERING

Co-authors authorization regarding the full agreement of the inclusion of manuscripts in the present thesis

José L. Figueiredo, Emeritus Professor at the Faculty of Engineering of the University of Porto (FEUP), M. Fernando R. Pereira, Full Professor at FEUP, Natalia Rey Raap, researcher at INCAR-CSIC, hereby authorize the PhD student Rafael Gomes Morais, from the FEUP Doctoral Program in Chemical and Biological Engineering, to include the following publication in his doctoral thesis entitled "Noble-metal free carbon-based materials for energy conversion":

R.G. Morais, N. Rey-Raap, J.L. Figueiredo, M.F.R. Pereira, Optimization of cobalt on CNT towards the oxygen evolution reaction and its synergy with iron (II) phthalocyanine as bifunctional oxygen electrocatalyst, Catalysis Today, (2023) 114057.

(José L. Figueiredo)

(M. Fernando R. Pereira)

REY RAAP NATALIA - 20472933N

Firmado digitalmente por REY RAAP NATALIA - 20472933N
Fecha: 2023.05.26 15:34:51 +02'00'

(Natalia Rey Raap)

BEILSTEIN JOURNAL OF NANOTECHNOLOGY

Glucose-derived carbon materials with tailored properties as electrocatalysts for the oxygen reduction reaction

Rafael Gomes Morais, Natalia Rey-Raap*, José Luís Figueiredo and Manuel Fernando Ribeiro Pereira*

Full Research Paper

Open Access

Address:
Associate Laboratory LSRE-LCM, Departamento de Engenharia Química, Faculdade de Engenharia, Universidade do Porto, R. Dr. Roberto Frias s/n, 4200-465 Porto, Portugal

Email:
Natalia Rey-Raap* - nataliarey@fe.up.pt;
Manuel Fernando Ribeiro Pereira* - fpereira@fe.up.pt

* Corresponding author

Keywords:
electrocatalysts; microporosity; nitrogen-doped carbon materials; oxygen reduction reaction; surface chemistry

Beilstein J. Nanotechnol. **2019,** *10,* 1089–1102.
doi:10.3762/bjnano.10.109

Received: 14 February 2019
Accepted: 16 April 2019
Published: 21 May 2019

This article is part of the thematic issue "Carbon-based nanomaterials for energy applications".

Guest Editor: B. Etzold

© 2019 Morais et al.; licensee Beilstein-Institut.
License and terms: see end of document.

Abstract

Nitrogen-doped biomass-derived carbon materials were prepared by hydrothermal carbonization of glucose, and their textural and chemical properties were subsequently tailored to achieve materials with enhanced electrochemical performance towards the oxygen reduction reaction. Carbonization and physical activation were applied to modify the textural properties, while nitrogen functionalities were incorporated via different N-doping methodologies (ball milling and conventional methods) using melamine. A direct relationship between the microporosity of the activated carbons and the limiting current density was found, with the increase of microporosity leading to interesting improvements of the limiting current density. Regardless of the doping method used, similar amounts of nitrogen were incorporated into the carbon structures. However, significant differences were observed in the nitrogen functionalities according to the doping method applied: ball milling appeared to originate preferentially quaternary and oxidized nitrogen groups, while the formation of pyridinic and pyrrolic groups was favoured by conventional doping. The onset potential was improved and the two-electron mechanism of the original activated sample was shifted closer to a four-electron pathway due to the presence of nitrogen. Interestingly, the high pyridinic content related to a high ratio of pyridinic/quaternary nitrogen results in an increase of the onset potential, while a decrease in the quaternary/pyrrolic nitrogen ratio favors an increase in the number of electrons. Accordingly, the electrocatalyst with the highest performance was obtained from the activated sample doped with nitrogen by the conventional method, which combined the most appropriate textural and chemical properties: high microporosity and adequate proportion of the nitrogen functionalities.

Introduction

Due to the recent increase in interest for more sustainable, renewable and cheaper energy, multiple conversion devices are being developed using new and innovative materials. Fuel cells are outstanding conversion devices, as they convert chemical energy directly into electrical energy with high efficiency and low emission of pollutants (the by products are water and heat) [1,2]. Fuel cells offer the best advantages for use with engines, as they are able to function as long as there is fuel, and for batteries, as they have similar characteristics under load conditions [1]. The performance of a fuel cell is mainly controlled by the oxygen reduction reaction (ORR) that takes place at the cathode [2], specifically by the electrocatalyst used for the reaction. The most commonly used electrocatalyst to supply faster kinetics and a four-electron pathway are platinum-based materials [3,4], which are costly and may assume up to 50% of the total cost of a fuel cell [5].

Transition metals [6,7], metal oxides [8,9] and carbon materials [3,4] have been widely studied as electrocatalysts in ORR due to their attractive physical and electrochemical properties. Among these materials, metal-free carbon materials have received tremendous attention due to their versatility and lower price in comparison with metal-based materials [2]. The main advantage of carbon materials is the possibility of modifying their physical and chemical properties resulting in a more electroactive material [2,3,10], which is an especially important feature for the ORR. The incorporation of heteroatoms like nitrogen [11,12], oxygen [13], sulfur [14,15], phosphorous [16,17] and boron [18,19] has been proven to enhance the electroactivity of carbon materials. Nitrogen has been the most studied heteroatom in the context of the reaction mechanism, since nitrogen-doped materials can achieve a four-electron pathway towards ORR [20-22]. However, there is some controversy related to the effect of the different nitrogen functionalities in the process. Some investigations suggest that the reduction of oxygen is promoted by pyridinic groups [23], while other researchers reported that quaternary nitrogen groups are the most active sites [24,25], and some studies assume that both functionalities contribute to enhancing the performance of the materials towards ORR [20]. In addition, a recent study with carbon nanotubes (CNTs) reported that an increase of the pyridinic-N/quaternary-N and pyridinic-N/pyrrolic-N ratios increases the electroactivity and that decreasing the quaternary-N/pyrrolic-N ratio increases the number of electrons involved in the ORR [12]. The electron density movement due to the presence of quaternary nitrogen favors the O_2 dissociation, while the pyridinic nitrogen favors the bonding of oxygen to the neighboring carbon. Accordingly, the appropriate ratio between both nitrogen functionalities seems to be essential to improve the electroactivity of carbon materials. The differences reported on the influence of the nitrogen functionalities may be related to the nature and type of the carbon material employed, which in turn, depends on the precursors used and the method of synthesis applied.

Nitrogen-doped carbon materials have been synthesized by applying different doping methods to different types of materials, such as CNTs [12,23,26], graphene [20,25,27], carbon aerogels [15,28], carbon nanofibers [29], carbon nitrides [30], activated carbons [31] or mesoporous carbons [32,33]. Some of these materials are obtained from chemical compounds, fossil fuels or by complex and expensive synthesis procedures. In order to keep fuel cells as ecologically friendly as possible, the use of biomass as a carbon source appears to be an attractive alternative. In this context, hydrothermal carbonization (HTC) has appeared in recent years as an interesting strategy to obtain biomass-derived carbons due to its low cost and mild synthesis conditions, making the process environmentally friendly [34]. However, the main drawback of HTC is that the as-prepared hydrothermal carbon materials usually exhibit limited porosity and inadequate chemical properties for the ORR. To solve this problem, different strategies can be addressed: i) carbonization and activation methods to tailor the porosity and ii) the incorporation of heteroatoms to modify the surface chemistry, specifically by adding nitrogen functionalities. Biomass-derived carbons have been functionalized by applying thermal treatments in the presence of a gaseous or solid nitrogen precursor [35,36] or without any precursor in the case where the biomass already contains nitrogen in its constitution [11,37], and by in situ methods in which nitrogen precursors are introduced during the hydrothermal carbonization [38]. An additional strategy that can be applied to biomass processing is ball milling, which has been proposed as a green, cheap and easy method to incorporate nitrogen atoms and to modify the surface chemistry of carbon materials [39,40]. Some of these doping techniques have shown to provide materials with similar ORR performance as commercially available Pt/C electrocatalysts [39]. However, most of these studies have been focused only on the effect of nitrogen functionalities on the ORR, leaving aside the effect of porosity. In fact, although some studies suggest the importance of microporosity on the ORR [41], there is a lack of knowledge about its real effect on the ORR performance of nitrogen-doped porous carbon materials, and more specifically, of biomass-derived carbons.

Therefore, this study aims to prepare glucose-derived carbon materials with different textural and chemical properties and to correlate these properties with the performance towards ORR. Activated carbons with different microporosity were prepared by activating the samples at different times to determine the

relationship between the textural properties and the ORR performance. Moreover, different doping strategies were applied to assess the effect of such methods on the incorporation of nitrogen functionalities and to evaluate the influence of the different functional groups on the response of the electrocatalyst towards the oxygen reduction reaction.

Results and Discussion

Effect of microporosity

The nitrogen adsorption–desorption isotherms and the pore size distributions obtained by applying the quenched solid density functional theory (QSDFT) are presented in Figure 1a and 1b, respectively.

Activated carbons display isotherms of type I according to the International Union of Pure and Applied Chemistry (IUPAC) classification, attributed to microporous materials. As expected, the volume of nitrogen adsorbed at low relative pressure increases with the time of activation, resulting in materials with a larger volume of micropores (Supporting Information File 1, Table S1). This effect is due to the reverse Boudouard reaction, which extracts carbon atoms from the carbon structure, developing the porosity of the material [42]. Accordingly, a prolonged contact time between the carbon material and the activating agent results in materials with a more developed microporosity. In addition, the pore size of the samples is also broadened by increasing the contact time (Figure 1b). The reaction occurring during the physical activation of the samples removes carbon atoms, giving rise to larger voids inside the particles, and hence, to larger pore sizes.

Regarding the chemical composition, the activated samples are mainly composed of carbon, with a smaller percentage of oxygen in the range of 2–4 wt % (Supporting Information File 1, Table S2). Although these values are not too high, oxygen functionalities can modify the electroactivity of carbon materials [13], therefore the nature of these functional group has been analyzed by temperature programmed desorption (TPD) experiments to evaluate possible differences in the oxygen functionalities. The total amount of CO (anhydrides, phenols, carbonyls) and CO_2 (carboxylic acids, anhydrides, lactones) released was calculated from the corresponding TPD profiles, and the values obtained are compiled in Supporting Information File 1, Table S3. The CO_2 and CO desorption profiles, obtained for samples AG_{1h} and AG_{6h} are also shown in Supporting Information File 1, Figure S1. The TPD profiles show that the sample with the highest degree of activation (AG_{6h}) has a lower amount of phenols due to the longer time used for the activation. However, in general terms, the released CO and CO_2 and their ratio are quite similar, so it can be assumed that there are no significant differences between the chemical composition of the samples, and therefore, any difference in the ORR performance can be exclusively related to the microporosity and/or the degree of activation.

Linear sweep voltammograms (LSVs) recorded in an O_2-saturated basic electrolyte at 1600 rpm and the Nyquist plot obtained from electrochemical impedance spectroscopy measurements are shown in Figure 2a and 2b, respectively.

To evaluate the performance of the prepared electrocatalysts, cyclic voltammetry (CV) and linear sweep voltammetry (LSV) were performed. LSV curves of the activated samples show two main differences: i) the onset potential shifts to more positive values by increasing the time of activation, which can be related to the more graphitic structure that is generated during activa-

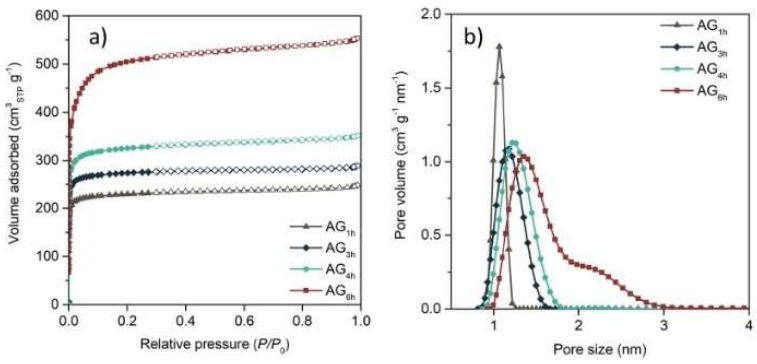


Figure 1: N_2 adsorption/desorption isotherms (a) and pore size distributions (b) of the activated carbons.

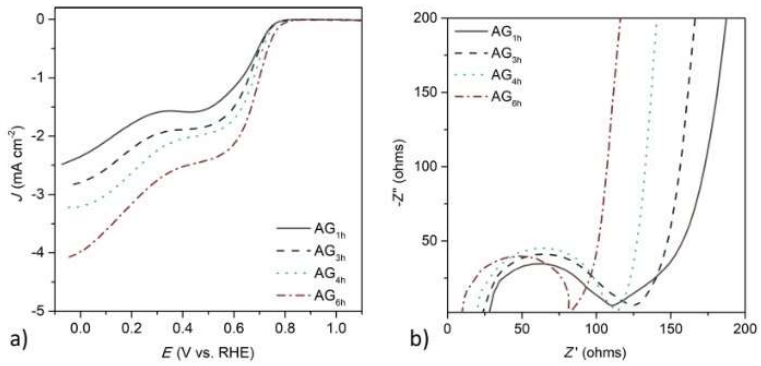


Figure 2: Linear sweep voltammetry recorded in an O_2-saturated 0.1 mol L^{-1} KOH electrolyte at 1600 rpm (a) and Nyquist plot obtained from electrochemical impedance spectroscopy (b).

tion; and ii) the value of the limiting current density increases with microporosity, which can be related to the more developed porous structure. These two effects can be confirmed by the electrochemical impedance spectroscopy measurements (Figure 2b). The Nyquist plot shows that a higher degree of activation results in a lower cell resistance and a smaller semicircle at high frequencies, indicating a lower charge transfer resistance, which allows the kinetics of the ORR to increase, and consequently, a higher onset potential is observed for sample AG_{6h} (the values of the onset potential are shown in Supporting Information File 1, Table S4). In addition, these results also suggest that a more developed microporous structure favors the electrolyte diffusion to the most electrochemically active pores, which also contributed to the ORR kinetics. Moreover, clear differences regarding ionic transportation are also observed at medium frequencies. Sample AG_{1h} shows a more defined Warburg impedance, indicating a higher resistance of the electrolyte ion diffusion into the porous structure, and hence, a lower value of limiting current density. These diffusion limitations are less evident for those samples with wider pore size, as pores act as diffusion channels favoring the kinetics of the ORR. In fact, a direct relationship was observed for microporosity and limiting current density for these carbon materials (Figure 3).

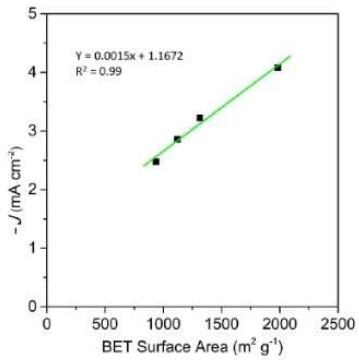


Figure 3: Relationship between BET surface area and the limiting current density of the activated samples.

However, regardless of the time used for the activation, all samples show a LSV curve with a similar shape. The reduction reaction occurs at two different potentials (0.75–0.78 V and 0.30–0.33 V), indicating that the ORR mechanism proceeds via the two-electron pathway. These results are corroborated by the experiments performed with a rotating ring disk electrode, from which the production of hydrogen peroxide was evaluated. More than 18% of hydrogen peroxide was produced with AG_{6h} (Supporting Information File 1, Figure S2), which is not desirable for the ORR. These results indicate that further modifications of this sample are needed to enhance the performance of the biomass-derived carbons towards ORR.

Effect of the surface chemistry

In order to improve the performance of glucose-derived activated carbons, the surface chemistry of the sample AG_{6h} (from now on simply named AG) was modified by applying different doping methods: ball milling and conventional mixing. In addition, such methods were also applied to a carbonized sample to evaluate the effect of the doping method according to the micro-

porosity generated from the initial thermal treatment. Both activated and carbonized samples also underwent the ball milling method without nitrogen precursor to discriminate among the modifications resulting from ball milling and those due to the conjugation of ball milling and the nitrogen precursor. The results obtained from the elemental analysis are presented in Table 1.

Table 1: Chemical composition determined by elemental analysis.

Sample	Carbon (wt %)	Nitrogen (wt %)	Oxygen (wt %)	Hydrogen (wt %)
AG	97.3	–	2.4	0.3
AG_{BM}	89.4	–	9.5	1.1
N-AG_{BM}	87.3	4.3	7.0	1.4
N-AG_C	90.1	4.1	4.9	0.9
CG	93.6	–	4.7	1.6
CG_M	85.5	–	12.3	2.2
N-CG_{BM}	82.9	6.9	8.8	1.4
N-CG_C	83.1	6.2	9.2	1.5

As expected, all samples are mainly composed of carbon, where the percentage is slightly higher for activated samples than for carbonized materials, due to the higher temperature used for activation (900 °C). The application of ball milling in both activated and carbonized samples results in a noticeable increase in the oxygen content. This phenomenon may be due to the defects created in the carbon structure during the milling process that react with air and incorporate oxygen. This effect is also observed for N-doped samples by ball milling. However, doped samples undergo a second thermal treatment that partially removes the oxygen incorporated during the ball milling process, resulting in lower oxygen content. Nevertheless, although the amount of oxygen in samples doped by ball milling is lower than in undoped samples, the percentage detected is still significant. As for conventionally doped samples, the oxygen content is twice the oxygen found in the original samples. Regardless of the degree of activation of the samples, the amount of nitrogen incorporated by the ball milling method is similar to that obtained by the conventional method. However, the incorporation of oxygen and nitrogen in the activated structures is lower than in carbonized samples. Activation at high temperature results in a structure with higher chemical stability and lower amount of defects in which heteroatoms can be incorporated, and so materials with a lower degree of functionalization are obtained.

Further understanding of the functionalities of the carbon materials was achieved by analyzing their surface composition by X-ray photoelectron spectroscopy (XPS). The XPS spectra in the C 1s, O 1s and N 1s regions were deconvoluted to identify the types of functionalities present in the surface of the carbon materials. The deconvolution of the C 1s spectra for undoped samples presents five main peaks (Supporting Information File 1, Figure S3), representing the following by increasing binding energy: i) carbon sp^2 (C=C, peak I) at 284.6 ± 0.1 eV; ii) carbon in phenol, alcohol, ether bonds (C–O, peak II) at 285.8 ± 0.2 eV; iii) carbonyl or quinone groups (C=O, peak III) at 287.2 ± 0.2 eV; iv) carboxyl groups (COOH, peak IV) at 288.9 eV ± 0.3; and v) the shake-up satellite due to π–π^* transitions in aromatic rings (peak V) at 290.6 ± 0.5 eV [43]. Carbon sp^2 (peak I) is an asymmetric peak consisting of a tail towards higher binding energies that represents ≈80% of surface carbon, which does not show significant differences for activated and carbonized samples. However, noticeable differences in the peaks attributed to carbon–oxygen bonds are observed due to the ball milling process and the doping methods applied. The peak attributed to carboxylic acids (peak IV) is significantly more pronounced for ball-milled samples (AG_{BM} and CG_{BM}), suggesting that the increase of oxygen detected by elemental analysis (Table 1) was due to the formation of a large number of carboxylic acids, which further reinforces the possible reaction between the defects generated on the sample during the ball milling process and air moisture. The XPS spectra for the C 1s region of the doped samples exhibit the same five peaks as those observed for the undoped samples. However, peak II and peak III also have contributions of C–N and C=N interactions, respectively [15]. These phenomena result in a significantly higher contribution of these two peaks than those observed for the undoped samples. Additionally, peak IV in conventionally doped materials (N-AG_C and N-CG_C) is more pronounced than that of their doped ball-milled counterparts. This peak can be assigned to sp^2-hybridized carbons in a triazine aromatic ring (N–C=N) [30], which may result from the polymerization of melamine during the subsequent thermal treatment. This effect is less obvious in the spectra of the activated sample, as its higher chemical stability results in a lower degree of functionalization and, therefore, a lower formation of the triazine aromatic ring.

The high-resolution N 1s spectra of doped samples was deconvoluted into three different peaks (Figure 4) representing the three major nitrogen groups, which are, by increasing binding energy: pyridinic at 398.4 ± 0.1 eV (N-6), pyrrolic at 400.0 ± 0.1 eV (N-5) and quaternary nitrogen at 401.4 ± 0.3 eV (N-Q) [12,26]. Additionally, another peak was observed at 403.2 ± 0.1 eV in samples N-AG_{BM} and N-CG_{BM}, attributed to oxidized nitrogen groups (N-X) [26], suggesting that the ball milling process is related to the appearance of oxidized groups, as this peak is not observed for conventionally doped samples (sample N-AG_C and N-CG_C). The ball milling method seems to

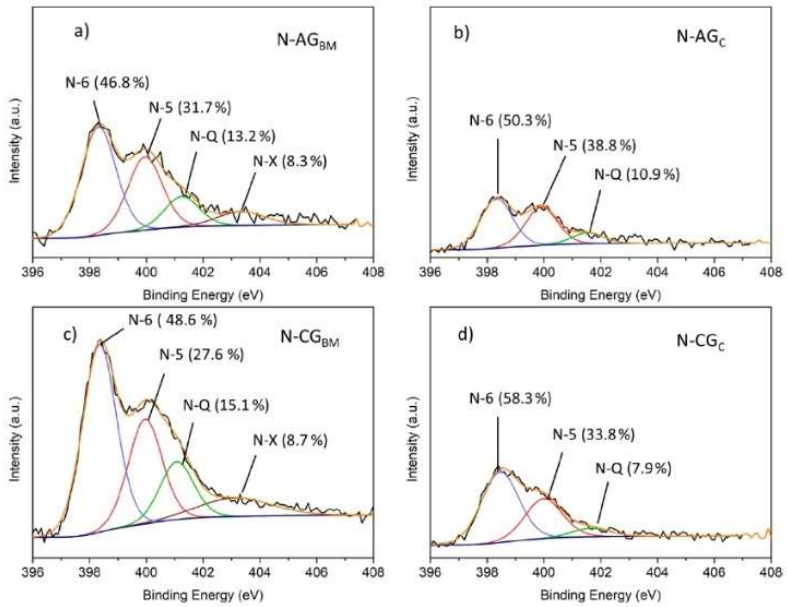


Figure 4: Deconvolution of the XPS N 1s spectra for N-AG$_{BM}$ (a) N-AG$_C$ (b), N-CG$_{BM}$ (c) and N-CG$_C$ (d).

modify the carbon structure promoting the contact between oxygen and nitrogen-containing species, which will react during the subsequent thermal treatment, oxidizing the nitrogen groups. In addition, differences in the contribution of each nitrogen group due to the doping method were also observed.

Samples doped via ball milling (Figure 4a and 4c) exhibit slightly lower percentages of pyridinic and pyrrolic groups than their conventionally doped counterparts (Figure 4b and 4d). Regarding quaternary nitrogen, significant differences were observed for both the doping method and the structure of the carbon. Activated samples exhibit similar contributions (13% and 11% for samples N-AG$_{BM}$ and N-AG$_C$, respectively), although ball milling seems to favor the incorporation of a slightly larger amount of N-Q. This effect is much more pronounced in carbonized samples that present larger differences as a function of the doping method: N-CG$_{BM}$ incorporated almost twice N-Q groups as N-CG$_C$. These results suggest that the ball milling process is more prone to incorporate quaternary groups as it creates defects in the activated and carbonized glucose structure, creating more sites to form quaternary structures inside the carbon matrix.

The XPS spectra in the O 1s region are shown in Supporting Information File 1, Figure S4. Three main oxygen peaks were identified, attributed to C=O bonds at 530.7 ± 0.3 eV (peak I), C–O groups at 532.0 ± 0.2 eV (peak II) and carboxylic acids at 533.3 ± 0.2 eV (peak III) [27]. Interesting differences are detected for N-doped carbons prepared by the ball milling method, as an additional peak is detected at higher binding energies corresponding to N–O–C bonds (peak IV), which is in agreement with the oxidized nitrogen peak also shown in the N 1s spectra. In addition, different contributions of the oxygen functionalities related to carbon bonds are presented, which is in agreement with those results obtained by the deconvolution of the C 1s spectra, especially for undoped ball-milled samples that exhibited a pronounced peak attributed to carboxylic acids. The O 1s spectra deconvolution does not clearly distinguish the contribution of the various surface groups due to overlaps in their binding energies. Therefore, the contribution of oxygen-containing surface groups in undoped samples was further analysed by TPD. The CO and CO_2 measurements obtained for undoped activated and carbonized samples are presented in Figure 5, while the deconvolution of the profiles is shown in Figures S5, S6, S7 and S8 in Supporting Information File 1.

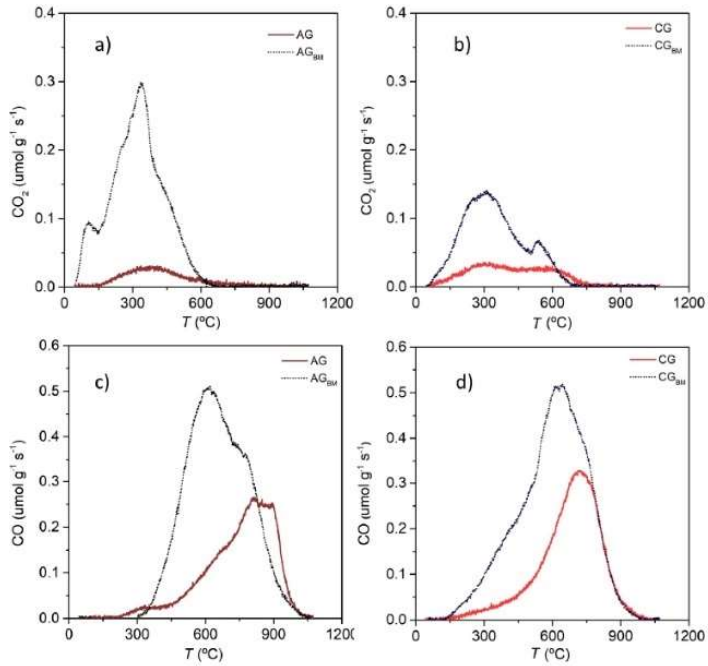


Figure 5: TPD profiles of CO_2 for activated samples (a) and carbonized samples (b) and CO profiles of activated samples (c) and carbonized samples (d).

The amount of CO_2 and CO released from ball-milled samples is significantly higher than that of their original counterparts. Analyzing the CO_2 profiles of activated samples three peaks can be observed (Supporting Information File 1, Figures S5a and S6a), which could be attributed to carboxylic acids, anhydride and lactone groups, respectively [26,44]. The peaks presented for the ball-milled activated sample are much more intense, especially the carboxylic acid peak, which is in agreement with the results obtained from XPS. The deconvolution of the CO profiles (Supporting Information File 1, Figures S5b, S6b, S7b and S8b) of all samples showed the presence of three main peaks corresponding to anhydrides, phenols and carbonyl/quinone groups [26,44]. Ball-milled samples present a much more significant contribution of phenols, corroborating the hypothesis that ball milling generates oxygen functional groups with weaker bonds due to reaction with air moisture. It should also be noted that the temperature at which oxygen groups are released as CO_2 and CO is higher for sample AG than for sample CG, confirming that the activated sample is more chemically stable.

The doping methods employed may also have an effect on the textural properties, which, as explained above, may modify the electroactive character of the biomass-derived carbons. Therefore, to evaluate the modifications caused to the textural properties due to the surface chemistry changes, nitrogen adsorption–desorption isotherms were obtained (Figure 6). The pore size distributions determined by applying the QSDFT are shown in Supporting Information File 1, Figure S9.

Like activated samples shown in Figure 1, modified activated and carbonized carbon materials display type I isotherms, characteristic of microporous materials. The application of ball milling and the different doping methods to both activated and carbonized samples led to a decrease in the volume of nitrogen adsorbed at low relative pressure, resulting in materials with a smaller volume of micropores (Supporting Information File 1, Table S5) and lower surface area (a decrease of ≈500 and 100 m^2 g^{-1} is observed after ball milling in the activated and carbonized samples, respectively). This decrease in microporosity suggests that the carbon material suffered changes in its

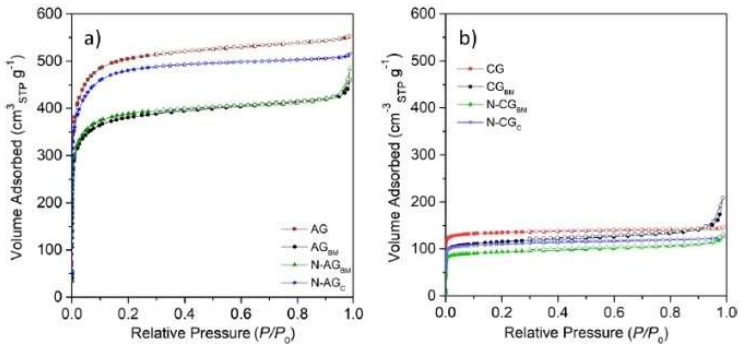


Figure 6: N_2 adsorption/desorption isotherms at −196 °C for activated carbons (a) and carbonized carbons (b).

structure due to the ball milling process, especially for the activated sample (Supporting Information File 1, Figure S10). This effect may be due to the loss of mass during the activation that results in materials with lower mechanical resistance than that of carbonized samples [45,46]. Moreover, ball-milled samples exhibit an increase of nitrogen adsorbed at high relative pressure ($P/P_0 > 0.9$), suggesting the formation of macropores. The addition of nitrogen by conventional mixing the carbon materials with melamine also results in a decrease in the surface area. In this case, the decrease is analogous for both activated and carbonized sample, suggesting that the N-groups introduced into the structure are blocking some pores, preventing the access of N_2 to the innermost pores of the carbon material during the isotherm measurements. The incorporation of nitrogen functionalities by using the ball milling process also modified the microporosity of the samples. However, differences are observed for the activated and carbonized sample. In the case of the activated sample, the incorporation of nitrogen does not seem to produce a noticeable blockage of the pores as previously observed for sample N-AG$_C$, resulting in a material with a BET surface area similar to that obtained for sample AG$_{BM}$, with ball milling being the predominant effect. In the case of sample N-CG$_{BM}$, the ball milling process and the incorporation of nitrogen seem to have a synergistic effect, resulting in a decrease of the S_{BET} almost equivalent to the sum of that observed for sample CG$_{BM}$ and N-CG$_C$.

Electrochemical measurements

Cyclic voltammograms recorded for activated samples and carbonized samples in a N_2- and O_2-saturated basic electrolyte at 5 mV s^{-1} are shown in Supporting Information File 1, Figure S11, while the LSV of activated and carbonized samples recorded in an O_2-saturated basic electrolyte at 1600 rpm are shown in Figure 7a and 7b, respectively.

Cyclic voltammograms measured in O_2-saturated electrolyte (Supporting Information File 1, Figure S11a) and LSV of activated samples show a reduction reaction peak starting at 0.78–0.82 V. This peak does not appear for N_2-saturated cyclic voltammograms (Supporting Information File 1, Figure S11c), thus confirming that the catalytic activity of the prepared electrocatalysts exists at the mentioned potentials. Table 2 summarizes the electrochemical results of the samples.

The onset potential of sample AG slightly shifts to more positive values from 0.78 V to 0.79 V by ball milling the sample (AG$_{BM}$) as shown in Figure 7a and Table 2. This increase may be due to the smaller particle size of the carbon powder obtained after ball milling, which could result in a material with higher electrical conductance, or due to the higher amount of oxygen [13]. The LSV of carbonized samples reveals that although sample CG$_{BM}$ presents a much higher oxygen content, CG and CG$_{BM}$ samples display the same onset potential (0.64 V), which suggests that the more positive onset potential of sample AG$_{BM}$ is due to its higher conductance. Moreover, samples AG and AG$_{BM}$ exhibit a second shoulder at more negative potentials, indicating that the ORR mechanism proceeds via the two-electron pathway producing hydrogen peroxide. This second reduction shoulder does not appear for the doped activated samples, suggesting that the mechanism of the reaction has shifted to the four-electron pathway. However, the incorporation of nitrogen atoms by ball milling the activated sample (N-AG$_{BM}$) does not modify the onset potential when compared to the undoped counterpart (AG$_{BM}$). This indicates that the simple incorporation of nitrogen atoms is not enough to increase the onset potential to more positive values for this type of carbon material. Contrary to activated samples, the incorporation of nitrogen atoms using the ball milling method in the carbonized sample (N-CG$_{BM}$) slightly

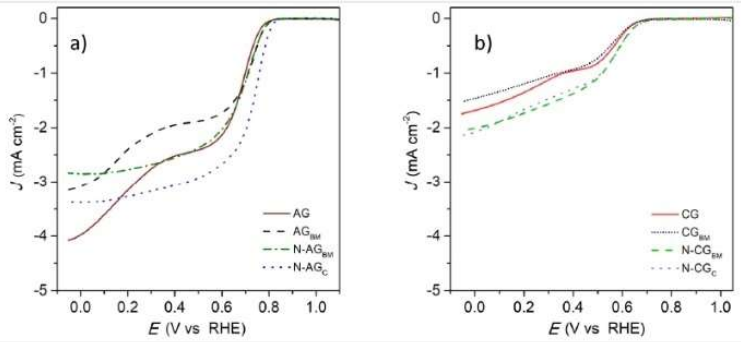


Figure 7: Linear sweep voltammetry recorded in an O_2-saturated 0.1 mol L^{-1} KOH electrolyte at 1600 rpm for activated (a) and carbonized (b) samples.

increases the onset potential regarding the undoped sample (CG_{BM}) from 0.64 V to 0.67 V. Like in activated samples, this is probably due to the smaller particle size obtained after ball milling, which could result in a material with higher electrical conductance.

The onset potential of sample N-AG_C is shifted to more positive values in relation to AG (from 0.78 V to 0.82 V). AG and N-AG_C do not present significant differences in the nature and amount of oxygen groups at their surface (Supporting Information File 1, Figure S4), which suggests that the increase in the onset potential is due to the incorporation of nitrogen. However, sample N-AG_{BM} and N-AG_C present similar nitrogen content (Table 1), but different values of onset potential are obtained, suggesting that the percentage of incorporated nitrogen is not the key factor, but the type of nitrogen functionality. Likewise, the addition of nitrogen using the conventional method (N-CG_C) also results in the same slight shift of the onset potential to more positive values in relation to CG and CG_{BM}.

In order to further understand the effect of nitrogen functionalities in the ORR, doped samples must be thoroughly compared. A difference in the content of pyridinic nitrogen is observed for doped activated samples (39% vs 32% for N-AG_C and N-AG_{BM}, respectively, Figure 4). Accordingly, the increase of the onset potential may be due to the presence of pyridinic nitrogen groups in the N-AG_C sample, which is in agreement with some studies in the literature [23]. The sample N-AG_C showed a higher value of the pyridinic-N/quaternary-N ratio than the sample N-AG_{BM} (3.6 vs 2.4, respectively) and a slightly higher value of the pyridinic-N/pyrrolic-N ratio (0.8 vs 0.7, respectively) which corroborates the theory that the increase of these two ratios is beneficial for the electrochemical activity of the prepared electrocatalysts [12]. This is not observed for carbonized samples as they do not present superior textural properties, compromising some of the effects that nitrogen could have on the carbon as a catalyst.

Information about the limiting current density can also be obtained from the LSV curves. As previously observed for acti-

Table 2: Electrochemical results of the synthesized samples.

Sample	Onset potential (V vs RHE)	Limiting current density (mA cm^{-2})	Electrons exchanged at 0.4 V vs RHE	H_2O_2 production (%)
AG	0.78	4.08	2.3	18
AG_{BM}	0.79	3.15	2.0	21
N-AG_{BM}	0.79	3.37	2.9	9
N-AG_C	0.82	2.83	3.2	7
CG	0.64	1.74	1.8	–
CG_{BM}	0.64	1.53	2.3	–
N-CG_{BM}	0.67	2.15	2.1	–
N-CG_C	0.67	2.05	2.1	–

vated samples at different times, there is a direct relationship between microporosity and the limiting current density (Figure 3). This trend is also observed for sample group AG, AG_{BM}, CG and CG_{BM} and for samples N-AG_C, N-AG_{BM}, CG_C and N-CG_{BM} (Figure 8).

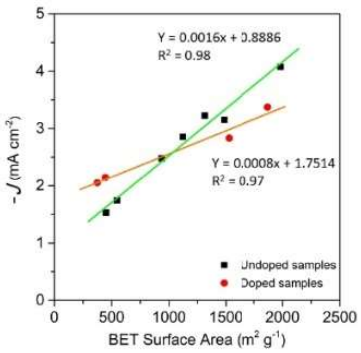


Figure 8: Relationship between BET surface area and limiting current density of undoped and doped samples.

These results indicate that the effect of microporosity cannot be compared between doped and undoped samples, suggesting that the limiting current density does not only depend on microporosity, but also on the surface chemistry of the samples.

Significant differences in the shape of the LSVs shown in Figure 7 are also observed due to the incorporation of nitrogen, which is related to the reaction mechanism. At lower potential, all activated samples present more than three electrons exchanged during the reduction reaction (Supporting Information File 1, Figure S12a). Regarding carbonized samples (Supporting Information File 1, Figure S12b), the number of electrons of CG and CG_{BM} represents a two-pathway mechanism at all potentials applied, unlike for the AG electrocatalysts. The electron exchange in the AG sample is reduced to two as the potential increases. The same effect was registered for the AG_{BM} sample that, even with a slightly inferior number of electrons exchanged at the lowest potential, the number of electrons also decreases to two as the potential applied increases. The incorporation of nitrogen atoms with the ball milling method (N-AG_{BM}) mitigated this effect, as the number of electrons exchanged during the oxygen reduction reaction stays at approximately three electrons, demonstrating that nitrogen incorporation helps to stabilize the number of electrons for a larger potential range. The conventionally doped sample (N-AG_C) shows the same pattern as the ball-milled doped sample, but its electron exchange stabilized slightly closer to the four-electron mechanism, probably due to the higher catalytic performance of pyridinic nitrogen groups, which maintains the reaction mechanism closer to a four-electron pathway. On the other hand, the decrease of the quaternary-N/pyrrolic-N ratio (from 0.28 to 0.22 for N-AG_{BM} and N-AG_C, respectively) resulted in an increase of the number of electrons involved, which is in agreement with recent studies [12]. Unlike in activated samples, the addition of nitrogen atoms through ball milling (N-CG_{BM}) does not result in an increase of electrons exchanged or in the stabilization of that number throughout the different applied potentials. This sample has a high quaternary-N/pyrrolic-N ratio (0.31), which does not favor the four-electron pathway.

Carbonized samples present a mechanism close to two-electrons throughout all potentials. Without a considerable number of electrons exchanged during the ORR, the nitrogen atoms do not seem to improve their stability to stay closer to a four-electron pathway. However, the conventionally doped sample (N-CG_C) displays a slight increase of electron exchange at low potentials, but still shifts to a two-electron pathway with increasing applied potential. The slight increase of the electrons may be related to the very low quaternary-N/pyrrolic-N ratio (0.13), which is reported to influence the number of electrons. The fact that the addition of nitrogen functionalities on carbonized samples does not seem to enhance the electroactivity as for activated samples indicates that it is fundamental to design both the surface chemistry and the textural proprieties of the carbon materials, as the modification of a single parameter is not enough to obtain acceptable electrocatalysts for ORR.

The approximation to a four-electron pathway with the modification of the surface chemistry is important to reduce the amount of hydrogen peroxide produced. The production of H_2O_2 was only determined for activated samples, since they have a mechanism closer to four-electron, whereas carbonized samples have a two-electron mechanism that would result in high amounts of this intermediate product. The improvement of the reaction mechanism of the modified activated carbon materials led to a decrease in the production of H_2O_2 from 18% with sample AG to 7% with N-AG_C (Supporting Information File 1, Figure S13). These results show that the proper combination of high microporosity associated with high pyridinic-N/quaternary-N ratio and low quaternary-N/pyrrolic-N ratio is essential to enhance the electrochemical performance of the developed electrocatalysts.

Conclusion

In this study, the effect of microporosity of glucose-derived carbon materials on the catalytic activity towards ORR was demonstrated. The increase of microporosity led to an increase

of the limiting current density and a slight increase of the onset potential, thus playing a key role in the ORR. The incorporation of nitrogen functionalities by employing different doping methods was also investigated. The amount of nitrogen incorporated was similar for all methods. The ball milling doping method led to a higher content of quaternary nitrogen and to the formation of oxidized nitrogen, while conventional doping favored the incorporation of pyridinic and pyrrolic functionalities. The results obtained reveal that the content of nitrogen is not as important as the type of functional groups incorporated for improving the performance of carbon materials towards ORR. In fact, a relationship between the nitrogen functionalities and the electroactivity of the biomass-derived carbons has been determined. It has been observed that a higher pyridinic-N/quaternary-N ratio favors the onset potential, while a lower quaternary-N/pyrrolic-N ratio favors the number of electrons exchanged during ORR. However, these results are only significant for highly microporous materials, demonstrating that the adequate combination of textural and chemical properties is essential for improving the electroactivity of biomass-derived carbons. In fact, the combination between high surface area, high pyridinic-N/quaternary-N ratio and low quaternary-N/pyrrolic-N ratio resulted in a material with an onset potential value of 0.82 V, a stable number of electrons involved in the reaction mechanism close to four throughout the studied potential range and a production of H_2O_2 lower than 7%.

Experimental

Preparation of carbon materials

Carbon materials were prepared from an initial solution of glucose (HiMedia, >99%) and deionized water (produced by filtration through inverse osmose by a Panice device) in a 1:6 ratio. The solutions were mixed and then closed in a teflon-lined stainless steel autoclave and hydrothermally carbonized during 12 h at 180 °C. The obtained material was washed with deionized water and dried at 100 °C overnight. The dried material was then activated under a CO_2 flow of 80 $cm^3\ min^{-1}\ g^{-1}$ at 900 °C for 1, 3, 4 and 6 h. The samples were labelled AG_X, where X is the hours used for activation.

The sample activated for 6 h was also doped with nitrogen by using melamine (≥99%, Sigma-Aldrich) as a precursor. Two different approaches were studied: i) the activated carbon material was mixed with melamine by ball milling and ii) the activated carbon material was manually mixed with melamine, henceforth referred to as the conventional method. The ball milling process was performed in an enclosed flask with two zirconia balls at 15 Hz frequency during 4 h using a Retsch MM200 device. Regardless of the doping method all samples underwent a subsequent thermal treatment under a N_2 atmosphere for 2 h at 700 °C to force the decomposition of melamine and to incorporate nitrogen atoms into the carbon structure. Additionally, a carbonized sample was prepared under a N_2 flow of 150 $cm^3\ min^{-1}$ at 700 °C for 2 h, to isolate the effect of functionalization with respect to the surface area. This sample also underwent the same two doping methods as the activated sample. All treatments were carried out in a vertical furnace with a fixed heating rate of 10 °C min^{-1}. The samples were labelled XG_Y and N-XG_Y for undoped and N-doped samples, respectively, where X can assume the form of A for activated samples and C for carbonized samples and Y is represented by BM for ball milled samples and C for conventionally doped samples. Activated and carbonized samples were also ball-milled in the absence of any precursor for comparison under the same conditions as in doped samples.

Materials characterization

The textural characterization was carried out by N_2 adsorption at −196 °C performed in a Quantachrome Autosorb iQ automated gas sorption analyzer. All samples were degassed under vacuum at 150 °C for 12 h before the analysis. The specific surface area (S_{BET}) was determined according to the Brunauer–Emmett–Teller (BET) equation, the total pore volume (V_p) was calculated as the volume of nitrogen adsorbed at the saturation point (relative pressure of 0.99) and the micropore volume (V_{DR}) was evaluated by the Dubinin–Radushkevich method.

The chemical composition of the samples was determined by elemental analysis. Carbon, hydrogen and nitrogen (C, H and N) were determined in a Vario micro cube analyzer (Elementar GmbH), by combustion of the sample at 1050 °C. The oxygen content was determined using a rapid oxy cube analyzer (Elementar GmbH) in which the sample underwent pyrolysis at 1450 °C. Each sample was analysed in triplicate. X-ray photoelectron spectroscopy (XPS) was employed to study the surface chemical composition of the samples. The analyses were carried out in a Kratos AXIS Ultra HAS spectrometer using monochromatic Al Kα radiation (1486.7 eV) at 15 kV (90 W), in fixed analyzer transmission mode, performing a pass energy of 80 eV for the general spectra and 40 eV for regions of interest. Temperature programmed desorption (TPD) was performed to determine and quantify the surface oxygenated groups of the samples by using an Altamira Instruments AMI-300 device. The samples were heated with a 10 °C min^{-1} ramp until 1050 °C. At the end of each analysis, a calibration of the CO and CO_2 content was carried out, allowing the quantification of the TPD profiles.

Electrochemical characterization

The electrochemical measurements were performed on a PGSTAT 302N potentiostat/galvanostat by using a three-elec-

trode cell configuration. Ag/AgCl (KCl 3 M) and a glassy carbon rod were used as reference and counter electrode, respectively. Working electrodes were prepared by depositing a suspension of the carbon samples on a glassy carbon rotating disk electrode (3 mm of diameter, Metrohm). These suspensions were prepared by dispersing 1 mg of the prepared samples in a solution containing 220 μL of ultrapure water (Millipore), 142 μL of ethanol (≥99%,Valente e Ribeiro) and 96 μL of nafion (5 wt %, Sigma-Aldrich). The suspension was sonicated for 30 min until a homogeneous dispersion was obtained. The mass loading of all samples was ≈0.1 mg cm^{-2}. A rotation speed controller allowed the rotation of the working electrode to be adjusted according to the assessments being done.

The experiments were carried out at room temperature in a 0.1 mol L^{-1} KOH solution saturated with N_2 or O_2 for 30 min before the cyclic voltammetry (CV) and linear sweep voltammetry (LSV) were performed. The CVs measurements were accomplished at a scan rate of 5, 20, 60 and 100 mV s^{-1} and the LSVs at a scan rate of 5 mV s^{-1} with a rotation speed range from 400 to 3000 rpm, both within a 1.2 V to −0.1 V potential range (vs RHE). The measured current was determined by subtracting the current obtained from the electrolyte saturated with N_2 from the current measured in the O_2-saturated electrolyte. Electrochemical impedance spectroscopy (EIS) was also applied to the fully discharged cell at 0 V in the frequency region of 10 kHz to 10 mHz with an AC amplitude of 10 mV. EIS was performed in the same type of cell, with N_2-saturated electrolyte (KOH 0.1 mol L^{-1}) and with no rotation.

The current density at the disk can be expressed by the Koutecký–Levich equation:

$$\frac{1}{j} = \frac{1}{j_L} + \frac{1}{j_k} = \frac{1}{B\omega^{1/2}} + \frac{1}{j_k}, \quad (1)$$

where j is the measured current density (mA·cm^{-2}), j_L is the O_2 diffusion-limited current density (mA cm^{-2}), j_k is the kinetic current density (mA cm^{-2}), ω is the electrode rotation rate (rpm) and B represents the Levich constant related to the diffusion limiting current density given by Equation 2.

$$B = 0.2nFD^{2/3}\nu^{-1/6}C \quad (2)$$

In Equation 2, F is the Faraday constant (96 486 C mol^{-1}), D is the diffusion coefficient of O_2 (1.95 × 10^{-5} cm^2 s^{-1}), ν is the kinematic viscosity of the electrolyte (0.008977 cm^2 s^{-1}) and C is the bulk concentration of O_2 (1.15 × 10^{-3} mol L^{-1}).

The number of electrons n was calculated at different potentials for each LSV recorded by applying Equation 1 and Equation 2.

The percentage of hydrogen peroxide (H_2O_2) produced during the ORR was also measured by using a rotating ring disk electrode (5 mm diameter, 24.9% collection efficiency, Methrom) as a working electrode, which was prepared by depositing a solution of the carbon sample on the disk area. The dispersions were prepared as detailed above and the mass loading was fixed at ≈0.1 mg cm^{-2}. The H_2O_2 percentage was calculated by Equation 3.

$$H_2O_2(\%) = 200 \times \frac{I_R / N}{I_D + I_R / N} \quad (3)$$

In Equation 3, I_R is the ring current density (mA cm^{-2}), I_N is the disk current density of the disk (mA cm^{-2}) and N is the collection efficiency (0.249).

Supporting Information

Supporting Information File 1

Characterization of the carbon materials, electrochemical assessments and relations resulting from this work.
[https://www.beilstein-journals.org/bjnano/content/supplementary/2190-4286-10-109-S1.pdf]

Acknowledgements

This work is a result of the projects "UniRCell", with the reference POCI-01-0145-FEDER-016422, Project POCI-01-0145-FEDER-006984 – Associate Laboratory LSRE-LCM funded by ERDF through COMPETE2020 - Programa Operacional Competitividade e Internacionalização (POCI), and by national funds through FCT - Fundação para a Ciência e a Tecnologia and PDEQB (PD9989). The authors are indebted to Dr. Carlos M. Sá (CEMUP) for assistance with XPS analyses.

ORCID® iDs

Rafael Gomes Morais - https://orcid.org/0000-0001-9046-5933
Natalia Rey-Raap - https://orcid.org/0000-0002-5003-0035
José Luís Figueiredo - https://orcid.org/0000-0002-0395-8199
Manuel Fernando Ribeiro Pereira - https://orcid.org/0000-0002-5447-2471

References

1. Kirubakaran, A.; Jain, S.; Nema, R. K. *Renewable Sustainable Energy Rev.* **2009,** *13,* 2430–2440. doi:10.1016/j.rser.2009.04.004
2. Stacy, J.; Regmi, Y. N.; Leonard, B.; Fan, M. *Renewable Sustainable Energy Rev.* **2017,** *69,* 401–414. doi:10.1016/j.rser.2016.09.135
3. Figueiredo, J. L. *Surf. Coat. Technol.* **2018,** *350,* 307–312. doi:10.1016/j.surfcoat.2018.07.033
4. Wu, Z.; Song, M.; Wang, J.; Liu, X. *Catalysts* **2018,** *8,* 196. doi:10.3390/catal8050196

5. Lee, K.; Zhang, L.; Lui, H.; Hui, R.; Shi, Z.; Zhang, J. *Electrochim. Acta* **2009,** *54,* 4704–4711. doi:10.1016/j.electacta.2009.03.081
6. Kobayashi, M.; Niwa, H.; Saito, M.; Harada, Y.; Oshima, M.; Ofuchi, H.; Terakura, K.; Ikeda, T.; Koshigoe, Y.; Ozaki, J.-i.; Miyata, S. *Electrochim. Acta* **2012,** *74,* 254–259. doi:10.1016/j.electacta.2012.04.075
7. Luo, J.; Tian, X.; Zeng, J.; Li, Y.; Song, H.; Liao, S. *ACS Catal.* **2016,** *6,* 6165–6174. doi:10.1021/acscatal.6b01618
8. Rezaei, B.; Taghipour Jahromi, A. R.; Ensafi, A. A. *Electrochim. Acta* **2018,** *283,* 1359–1365. doi:10.1016/j.electacta.2018.07.105
9. Xue, Y.; Sun, S.; Wang, Q.; Dong, Z.; Liu, Z. *J. Mater. Chem. A* **2018,** *6,* 10595–10626. doi:10.1039/c7ta10569j
10. Borghei, M.; Lehtonen, J.; Liu, L.; Rojas, O. J. *Adv. Mater. (Weinheim, Ger.)* **2018,** *30,* 1703691. doi:10.1002/adma.201703691
11. Huang, H.; Wei, X.; Gao, S. *Electrochim. Acta* **2016,** *220,* 427–435. doi:10.1016/j.electacta.2016.10.108
12. Rocha, I. M.; Soares, O. S. G. P.; Fernandes, D. M.; Freire, C.; Figueiredo, J. L.; Pereira, M. F. R. *ChemistrySelect* **2016,** *1,* 2522–2530. doi:10.1002/slct.201600615
13. Rocha, I. M.; Soares, O. S. G. P.; Figueiredo, J. L.; Freire, C.; Pereira, M. F. R. *Catal. Sci. Technol.* **2017,** *7,* 1868–1879. doi:10.1039/c7cy00020k
14. Wang, C.; Yang, F.; Xu, C.; Cao, Y.; Zhong, H.; Li, Y. *Mater. Lett.* **2018,** *214,* 209–212. doi:10.1016/j.matlet.2017.11.120
15. Wohlgemuth, S.-A.; White, R. J.; Willinger, M.-G.; Titirici, M.-M.; Antonietti, M. *Green Chem.* **2012,** *14,* 1515–1523. doi:10.1039/c2gc35309a
16. Wu, J.; Yang, Z.; Sun, Q.; Li, X.; Strasser, P.; Yang, R. *Electrochim. Acta* **2014,** *127,* 53–60. doi:10.1016/j.electacta.2014.02.016
17. Yang, D.-S.; Bhattacharjya, D.; Inamdar, S.; Park, J.; Yu, J.-S. *J. Am. Chem. Soc.* **2012,** *134,* 16127–16130. doi:10.1021/ja306376s
18. Cheng, Y.; Tian, Y.; Fan, X.; Liu, J.; Yan, C. *Electrochim. Acta* **2014,** *143,* 291–296. doi:10.1016/j.electacta.2014.08.001
19. Yang, L.; Jiang, S.; Zhao, Y.; Zhu, L.; Chen, S.; Wang, X.; Wu, Q.; Ma, J.; Ma, Y.; Hu, Z. *Angew. Chem., Int. Ed.* **2011,** *50,* 7132–7135. doi:10.1002/anie.201101287
20. Lai, L.; Potts, J. R.; Zhan, D.; Wang, L.; Poh, C. K.; Tang, C.; Gong, H.; Shen, Z.; Lin, J.; Ruoff, R. S. *Energy Environ. Sci.* **2012,** *5,* 7936–7942. doi:10.1039/c2ee21802j
21. Wei, W.; Liang, H.; Parvez, K.; Zhuang, X.; Feng, X.; Müllen, K. *Angew. Chem.* **2014,** *126,* 1596–1600. doi:10.1002/ange.201307319
22. Wei, Q.; Tong, X.; Zhang, G.; Qiao, J.; Gong, Q.; Sun, S. *Catalysts* **2015,** *5,* 1574–1602. doi:10.3390/catal5031574
23. Zheng, J.; Guo, C.; Chen, C.; Fan, M.; Gong, J.; Zhang, Y.; Zhao, T.; Sun, Y.; Xu, X.; Li, M.; Wang, R.; Luo, Z.; Chen, C. *Electrochim. Acta* **2015,** *168,* 386–393. doi:10.1016/j.electacta.2015.03.173
24. Niwa, H.; Horiba, K.; Harada, Y.; Oshima, M.; Ikeda, T.; Terakura, K.; Ozaki, J.-i.; Miyata, S. *J. Power Sources* **2009,** *187,* 93–97. doi:10.1016/j.jpowsour.2008.10.064
25. Geng, D.; Chen, Y.; Chen, Y.; Li, Y.; Li, R.; Sun, X.; Ye, S.; Knights, S. *Energy Environ. Sci.* **2011,** *4,* 760–764. doi:10.1039/c0ee00326c
26. Rocha, R.; Soares, O.; Figueiredo, J.; Pereira, M. *C* **2016,** *2,* 17. doi:10.3390/c2030017
27. Lei, Z.; Li, Y.; Zhang, I.; Li, D.-W.; Karpuzov, D.; Long, Y.-T. *Electrocatalytic Oxidation of NADH on Graphene Oxide and Reduced Graphene Oxide Modified Screen-Printed Electrode;* 2011; Vol. 6, pp 819–829.
28. Tian, X.; Zhou, M.; Tan, C.; Li, M.; Liang, L.; Li, K.; Su, P. *Chem. Eng. J.* **2018,** *348,* 775–785. doi:10.1016/j.cej.2018.05.007
29. Li, R.; Shao, X.; Li, S.; Cheng, P.; Hu, Z.; Yuan, D. *Nanotechnology* **2016,** *27,* 505402. doi:10.1088/0957-4484/27/50/505402
30. Fang, J.; Fan, H.; Li, M.; Long, C. *J. Mater. Chem. A* **2015,** *3,* 13819–13826. doi:10.1039/c5ta02257f
31. Zhang, B.; Wen, Z.; Ci, S.; Mao, S.; Chen, J.; He, Z. *ACS Appl. Mater. Interfaces* **2014,** *6,* 7464–7470. doi:10.1021/am5008547
32. Li, X.; Fang, Y.; Zhao, S.; Wu, J.; Li, F.; Tian, M.; Long, X.; Jin, J.; Ma, J. *J. Mater. Chem. A* **2016,** *4,* 13133–13141. doi:10.1039/c6ta04187f
33. Ferrero, G. A.; Fuertes, A. B.; Sevilla, M.; Titirici, M.-M. *Carbon* **2016,** *106,* 179–187. doi:10.1016/j.carbon.2016.04.080
34. Jain, A.; Balasubramanian, R.; Srinivasan, M. P. *Chem. Eng. J.* **2016,** *283,* 789–805. doi:10.1016/j.cej.2015.08.014
35. Gu, D.; Ma, R.; Zhou, Y.; Wang, F.; Yan, K.; Liu, Q.; Wang, J. *ACS Sustainable Chem. Eng.* **2017,** *5,* 11105–11116. doi:10.1021/acssuschemeng.7b03046
36. Baskar, S.; Murugesan, C.; Barpanda, P. *ECS Trans.* **2017,** *80* (10), 425–430. doi:10.1149/08010.0425ecst
37. Gu, D.; Zhou, Y.; Ma, R.; Wang, F.; Liu, Q.; Wang, J. *Nano-Micro Lett.* **2018,** *10,* 29. doi:10.1007/s40820-017-0181-1
38. Liu, F.; Peng, H.; You, C.; Fu, Z.; Huang, P.; Song, H.; Liao, S. *Electrochim. Acta* **2014,** *138,* 353–359. doi:10.1016/j.electacta.2014.06.098
39. Borghei, M.; Lehtonen, J.; Liu, L.; Rojas, O. J. *Adv. Mater. (Weinheim, Ger.)* **2018,** *30,* 1703691. doi:10.1002/adma.201703691
40. Sibul, R.; Kibena-Põldsepp, E.; Ratso, S.; Kook, M.; Käärik, M.; Merisalu, M.; Paiste, P.; Leis, J.; Sammelselg, V.; Tammeveski, K. *Electrochem. Commun.* **2018,** *93,* 39–43. doi:10.1016/j.elecom.2018.05.027
41. Lefevre, M.; Jaouen, F.; Dodelet, J.-P.; Li, X. H.; Chen, K.; Hay, A. *ECS Trans.* **2006,** *3* (1), 201–210. doi:10.1149/1.2356138
42. Marsh, H.; Rodríguez-Reinoso, F. Activation Processes (Thermal or Physical). In *Activated Carbon;* March, H.; Rodríguez-Reinoso, F., Eds.; Elsevier Science Ltd: Oxford, United Kingdom, 2006; pp 243–321. doi:10.1016/b978-008044463-5/50019-4
43. Zhou, J.-H.; Sui, Z.-J.; Zhu, J.; Li, P.; Chen, D.; Dai, Y.-C.; Yuan, W.-K. *Carbon* **2007,** *45,* 785–796. doi:10.1016/j.carbon.2006.11.019
44. Figueiredo, J. L.; Pereira, M. F. R.; Freitas, M. M. A.; Órfão, J. J. M. *Carbon* **1999,** *37,* 1379–1389. doi:10.1016/s0008-6223(98)00333-9
45. Prauchner, M. J.; Rodríguez-Reinoso, F. *Microporous Mesoporous Mater.* **2012,** *152,* 163–171. doi:10.1016/j.micromeso.2011.11.040
46. Amorós-Pérez, A.; Cano-Casanova, L.; Ouzzine, M.; Rufete-Beneite, M.; Romero-Anaya, A. J.; Lillo-Ródenas, M. Á.; Linares-Solano, Á. *Materials* **2018,** *11,* 770. doi:10.3390/ma11050770

License and Terms

This is an Open Access article under the terms of the Creative Commons Attribution License (http://creativecommons.org/licenses/by/4.0). Please note that the reuse, redistribution and reproduction in particular requires that the authors and source are credited.

The license is subject to the *Beilstein Journal of Nanotechnology* terms and conditions: (https://www.beilstein-journals.org/bjnano)

The definitive version of this article is the electronic one which can be found at: doi:10.3762/bjnano.10.109

Journal of
Composites Science

MDPI

Article

Hydrothermal Carbon/Carbon Nanotube Composites as Electrocatalysts for the Oxygen Reduction Reaction

Rafael G. Morais [1], Natalia Rey-Raap [1,*], Rui S. Costa [2], Clara Pereira [2], Alexandra Guedes [3], José L. Figueiredo [1] and M. Fernando R. Pereira [1]

1 Associate Laboratory LSRE-LCM, Departamento de Engenharia Química, Faculdade de Engenharia, Universidade do Porto, R. Dr Roberto Frias s/n, 4200-465 Porto, Portugal; rgm@fe.up.pt (R.G.M.); jlfig@fe.up.pt (J.L.F.); fpereira@fe.up.pt (M.F.R.P.)

2 REQUIMTE/LAQV, Departamento de Química e Bioquímica, Faculdade de Ciências, Universidade do Porto, 4169-007 Porto, Portugal; rucosta@fc.up.pt (R.S.C.); clara.pereira@fc.up.pt (C.P.)

3 Departamento de Geociências, Ambiente e Ordenamento do Território, Faculdade de Ciências, Universidade do Porto, 4169-007 Porto, Portugal; aguedes@fc.up.pt

* Correspondence: nataliarey@fe.up.pt; Tel.: +351-220-414-919

Received: 11 December 2019; Accepted: 10 February 2020; Published: 17 February 2020



Abstract: The oxygen reduction reaction is an essential reaction in several energy conversion devices such as fuel cells and batteries. So far, the best performance is obtained by using platinum-based electrocatalysts, which make the devices really expensive, and thus, new and more affordable materials should be designed. Biomass-derived carbons were prepared by hydrothermal carbonization in the presence of carbon nanotubes with different oxygen surface functionalities to evaluate their effect on the final properties. Additionally, nitrogen functional groups were also introduced by ball milling the carbon composite together with melamine. The oxygen groups on the surface of the carbon nanotubes favor their dispersion into the precursor mixture and the formation of a more homogenous carbon structure with higher mechanical strength. This type of structure partially avoids the crushing of the nanotubes and the carbon spheres during the ball milling, resulting in a carbon composite with enhanced electrical conductivity. Undoped and N-doped composites were used as electrocatalysts for the oxygen reduction reaction. The onset potential increases by 20% due to the incorporation of carbon nanotubes (CNTs) and nitrogen, which increases the number of active sites and improves the chemical reactivity, while the limiting current density increases by 47% due to the higher electrical conductivity.

Keywords: carbon nanotubes; hydrothermal carbons; nitrogen functionalization; oxygen reduction reaction; electrocatalysis

1. Introduction

In the last decades, researchers have focused on developing new innovative materials to enhance the performance of environmentally friendly energy conversion devices. In this context, fuel cells are considered an interesting alternative towards greener electrical energy conversion due to their high efficiency and low emission of pollutants [1,2]. However, the overall performance of these devices is limited by the sluggish kinetics of the oxygen reduction reaction (ORR) that takes place at the cathode [1,3]. Currently, the most efficient electrocatalyst towards the ORR is based on platinum [3,4], which is a scarce and expensive noble metal that extremely pushes up the cost of the fuel cell [5]. Consequently, extensive research efforts have been made to develop non-noble metal catalysts, or metal-free catalysts, exhibiting good catalytic activity towards ORR and excellent durability [1,3,4,6–8].

Carbon materials are a promising alternative to Pt-based electrocatalysts. Carbon nanotubes, carbon nanofibers, activated carbons, carbon xerogels, and graphene-based materials have been

widely studied as electrocatalysts [6,9–15]. Among them, activated carbons are interesting materials, as they can be obtained by low-cost and environmentally friendly routes [16]. In fact, the use of hydrothermal processes to prepare carbon materials from biomass has emerged recently as an interesting strategy [12,17–20]. Biomass is an abundant, low-cost, and environmental-friendly source [21], which makes hydrothermal carbons (HTCs) good candidates to replace Pt-based electrocatalysts [2,8,22]. HTCs are commonly made up of spherical particles, which size can be controlled by modifying the synthesis conditions: concentration and the type of saccharide precursor and temperature and time of the hydrothermal treatment [20]. Nevertheless, the chemical properties of HTCs need to be modified in order to approach the outstanding electrochemical performance of Pt-electrocatalyst reference materials [23,24]. These modifications can be achieved by the incorporation of heteroatoms like nitrogen, sulfur, phosphorus, or boron and/or advanced carbon materials like graphene oxide or carbon nanotubes (CNTs) [9,12,13,17,25–28]. Nitrogen is the most promising heteroatom for ORR, as pyridinic nitrogen favors the bonding of oxygen to the adjacent carbon, while the presence of quaternary nitrogen favors oxygen dissociation [7,29]. Therefore, the appropriate nitrogen functionalities seem to be essential to improve the electroactivity of the carbon materials towards the ORR. On the other hand, the use of CNT to prepare carbon composites is an interesting solution to stabilize the surface chemistry, to increase the graphitic domains and to accelerate electron transfer [30–32]. A recent publication has shown the benefits of adding CNT during the polymerization of glucose, ascertaining the optimum dose of CNT to maximize the performance of the composites in supercapacitor applications [31]. In the same line, carbide-derived carbons, graphene, chitosan, carbonized metal-organic frameworks (MOF), and activated carbons have been combined with CNT to obtained composites with improved performance towards the ORR [5,10,11,30,33–35]. Nonetheless, most of these carbon composites contain also metals to enhance the electroactivity of the carbons, which may somewhat hinder the real effects of the CNT on the properties of the composites.

Most of these published works are mainly focused on the preparation and application of carbon composites bearing CNT. However, little attention has been paid to the surface chemistry of the CNT, which can modify the final textural and chemical properties of the hydrothermal carbons, and hence, the effectiveness of the subsequent stages used to incorporate heteroatoms or metals. Accordingly, this work aims to study the isolated role of CNT during the hydrothermal carbonization of glucose by evaluating the modifications caused by the incorporation of CNT into the structure and electrochemical performance of the hydrothermal carbon/carbon nanotube composites. The composites were prepared by hydrothermal carbonization of glucose in the presence of multiwalled CNT and oxidized CNT. An attempt has been made to evaluate the effect of the surface chemistry of CNT in the polymerization of glucose and in the final properties of the composites. Besides, nitrogen functionalities were incorporated into the as-prepared composites. The effect of the structure of the composites, due to the presence of the CNT, on the functionalization process and on the nature of the nitrogen functionalities, has also been assessed. Electrochemical measurements were performed to fully characterize the electrocatalytic activity of the composites towards the oxygen reduction reaction. Interesting results regarding the electrochemical performance of the composites are detailed, showing the advantage of adding CNT during the hydrothermal polymerization of glucose to convert biomass into a high-value carbon composite.

2. Materials and Methods

2.1. Chemicals and Materials

The reagents used for the synthesis of the carbon materials were: D-glucose (Merck), multiwalled carbon nanotubes (Nanocyl NC3100 series, with average diameter of 9.5 nm, average length of 1.5 μm, and carbon purity higher than 95%), distilled water (from a Panice reverse osmosis water system), nitric acid (Fluka ≥65%), and melamine (Sigma-Aldrich, ≥99%). The reagents used for the preparation

of the electrode were: ultrapure water (Millipore), absolute ethanol (VWR Chemicals, ≥99.5%), and Nafion® (Sigma Aldrich, solution of 5 wt.% in a mixture of water (15–20%) and aliphatic alcohols).

2.2. Materials Preparation

The glucose-derived carbon/CNT composite (CG/CNT) was synthesized by hydrothermal polymerization of glucose in the presence of CNT. Briefly, glucose (15.0 wt.%) and CNT (0.3 wt.%) were dispersed in distilled water (84.7 wt.%) in an unsealed Teflon lined reactor chamber under sonication for 30 min at room temperature. After sonication, the Teflon lined reactor chamber was introduced into a stainless steel autoclave, sealed, and heated at 180 °C for 12 h. The autoclave was then cooled down naturally to room temperature, and the organic polymer obtained was filtered and washed with abundant distilled water. Finally, the sample was dried at 80 °C for 24 h and carbonized at 700 °C under a nitrogen flow of 150 cm^3 min^{-1}. The carbonization process was performed in a vertical furnace using a heating rate of 10 °C min^{-1} and 2 h as the residence time. In order to evaluate the effect of the surface chemistry of CNT on the polymerization of glucose, oxidized CNT were also employed to prepare the composite CG/CNT_{oxi}, following the methodology described above for sample CG/CNT. The oxidation of CNT was performed by the typical liquid-phase oxidation method. Briefly, 1 g of CNT was boiled with 75 mL of a 7 mol L^{-1} solution of nitric acid for 3 h. The oxidized material was then washed with abundant distilled water until neutral pH was reached and then dried at 80 °C for 24 h. The prepared materials (CG/CNT and CG/CNT_{oxi}) were functionalized with nitrogen by ball milling the carbon composite (60 wt.%) with melamine (40 wt.%). The ball milling process was performed in an enclosed flask with two zirconia balls at a 15 Hz frequency during 4 h using a Retsch MM200 mixer mill. Then, the samples were treated in a vertical furnace at 700 °C for 2 h under a nitrogen flow of 150 cm^3 min^{-1} to force the decomposition of melamine. The heating rate was fixed at 10 °C min^{-1}. Functionalized samples were labeled N-CG/CNT and N-CG/CNT_{oxi}. Additionally, a sample composed only by glucose (CG) was also prepared following the methodology described above for sample CG/CNT without the addition of CNT.

2.3. Physicochemical Characterization

The textural properties of all samples were determined by nitrogen adsorption–desorption isotherms performed at −196 °C. Before the analysis, the samples were degassed under vacuum at 150 °C overnight. The isotherms were obtained in a Quantachrome Autosorb iQ automated gas sorption analyzer. The specific surface area (S_{BET}) was estimated by applying the Brunauer–Emmett–Teller (BET) equation to the nitrogen adsorption branch of the isotherm. The micropore volume (V_{micro}) and the external surface area (S_{ext}) were determined by applying the t-plot method. The morphology of the composites was studied using a scanning electron microscope (Quanta FEG 400, FEI Company, Hillsboro, OR, USA). The composites were previously attached to an aluminum pin using conductive double-sided adhesive tape. A secondary electron detector Everhart-Thornley and an accelerating voltage of 15 kV were used in all the analyses. In addition, the surface chemistry of the HTC composites was evaluated by Fourier transform infrared spectroscopy (FTIR). FTIR spectra were recorded using a JASCO FT/IR 6800 spectrometer at a maximum resolution of 4 cm^{-1} over a range between 4000 and 400 cm^{-1}. The spectra were collected in attenuated total reflectance (ATR) mode over 256 scans. Raman spectra were measured directly on the carbon materials using a Jobin-Yvon XPLORA apparatus (Horiba Scientific, Kyoto, Japan) with a monochromatic wavelength laser of 532 nm. The chemical composition was determined by Elemental Analysis performed in a Vario Micro Cube analyzer from Elementar. This technique involves the combustion of the sample at a temperature close to 1000 °C in an oxygen-rich atmosphere. Analysis of the combustion products allows determining the contents of C, H, N, and S, while oxygen content is determined by the difference. The nitrogen surface functionalities of the N-doped composites were analyzed in a Kratos AXIS Ultra HSA X-ray photoelectron spectrometer (XPS). VISION and CASAXPS software were used for data acquisition and data analysis, respectively. The XPS measurements were performed with a monochromatic Al Ka

X-ray source (1486.7 eV), operating at 15 kV in hybrid mode, with a pass energy of 40 eV for regions of interest and 80 eV for the survey. The C 1s peak position was fixed at 284.6 eV and used as a reference to locate the other peaks. The fitting of the XPS in the N 1s region was performed by least squares using Shirley line as the background and Gaussian–Lorentzian peak shape. The electrical conductivity was measured by the four-point probe method applied to a disc-shaped piece of 1 cm diameter made of each carbon sample. The disc-shaped pieces were prepared by pressing at 8 t in a mold for 60 s. The four points were placed in contact with the carbon surface, and a potential between 0 and 2 V was applied. The current response was measured using a SourceMeter® unit instrument (Keithley 2400) and recorded with LabView software. A linear relationship between the potential applied and the current measured was obtained, following the Ohm Law, from which the resistivity of the samples, and in turn, the electrical conductivity, can be calculated.

2.4. Electrode Preparation

Each sample (1 mg) was first dispersed in 450 µL of a solution containing 20% of Nafion® and 80% of a liquid solution composed of ultrapure water and ethanol (1:1.5, v:v). The suspension was sonicated for 30 min until a homogeneous dispersion was obtained. Finally, the dispersion was deposited on a glassy carbon rotating ring-disk electrode (electrode from Metrohm that consists of a 5 mm disc of glassy carbon with a concentric platinum ring at a distance of 375 µm) to have a mass loading of 0.1 mg cm^{-2}.

2.5. Electrochemical Measurements

The electrochemical measurements were performed on a PGSTAT 302N potentiostat/galvanostat (Metrohm) by using a three-electrode cell configuration, which involves a beaker-type cell with three electrodes (working, counter, and reference) immersed in 0.1 mol L^{-1} KOH electrolyte solution. The rotating ring-disk electrode with the sample deposited on it was used as a working electrode, while an Ag/AgCl (KCl 3 mol L^{-1}) and a glassy carbon rod were used as reference and counter electrode, respectively. Initially, nitrogen gas was bubbled through the electrolyte for 30 min to remove all oxygen in the electrolyte solution. Cyclic voltammetry (CV) experiments were performed by changing the scan rates from 5 to 100 mV s^{-1} using a voltage window of 1.2 V (from 0.2 to −1.0 V vs the reference electrode). Linear sweep voltammetry (LSV) measurements were also performed in the same potential range at a scan rate of 5 mV s^{-1} with a disk rotation speed range from 400 to 3000 rpm. After the measurements with the electrolyte saturated in nitrogen, the electrolyte was saturated with oxygen for 30 min. Then, the CV and LSV experiments described above were performed to evaluate the performance of the materials towards the ORR. The current density measured at the ring and disk was calculated by subtracting the current obtained from the electrolyte saturated with N_2 from the current measured in the O_2-saturated electrolyte. The onset potential (E_{onset}) was determined from the LSV curve recorded at 1600 rpm for a current density of −0.1 mA cm^{-2} and converted to the reversible hydrogen electrode (RHE) scale according to the Nernst equation (Equation (S12) in the supporting information). The percentage of hydrogen peroxide (H_2O_2) produced during the ORR, and the number of electrons transferred were calculated from the current measured at the ring and disk following the Equations (S11) and (S7) shown in the supporting information. The chronoamperometric response was measured by applying 0.4 V vs RHE for 10000 s to compare the stability of the different electrocatalysts.

3. Results and Discussion

3.1. Textural, Morphological, and Chemical Properties

The changes in the textural properties due to the presence of CNT during the polymerization of glucose were evaluated by nitrogen adsorption at −196 °C. The shape of the isotherms is displayed in Figure 1, while the textural parameters are shown in Table 1. Sample CG exhibited a type I isotherm characteristic of exclusively microporous materials. The incorporation of CNT and oxidized CNT

(CNT_{oxi}) during the polymerization of glucose resulted in composites with different porous structures (CG/CNT and CG/CNT_{oxi}). The specific surface area of the composite CG/CNT was quite similar to that of the sample CG (Table 1), but interesting differences in the isotherm shape at medium and high relative pressure were observed (Figure 1b). The volume of nitrogen adsorbed remained constant at low-medium relative pressures (from 0.1 to 0.5), and then, abruptly increased at high relative pressure, which is characteristic of macroporous adsorbents. Besides, the isotherm of this composite exhibited a hysteresis loop at medium-high pressures produced by capillary condensation, which could be attributed to materials with mesopores corresponding to interparticle spaces, like carbon nanotubes (Figure S1).

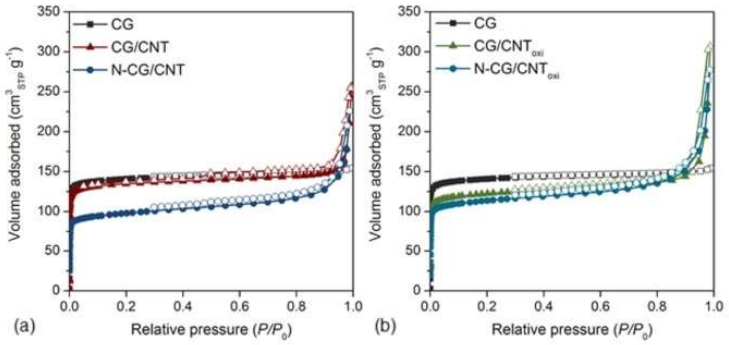


Figure 1. N_2 adsorption–desorption isotherms of carbonized glucose and undoped and N-doped carbon composites prepared by introducing a carbon nanotube (CNT; **a**) and oxidized CNT (**b**). Filled symbols: adsorption; open symbols: desorption.

Table 1. Textural properties of carbonized glucose and undoped and N-doped carbon composites.

Sample	S_{BET} (m^2 g^{-1})	V_{micro} (cm^3 g^{-1})	S_{ext} (m^2 g^{-1})
CG	574	0.22	15
CG/CNT	545	0.21	21
CG/CNT_{oxi}	489	0.20	37
N-CG/CNT	387	0.16	44
N-CG/CNT_{oxi}	451	0.19	57

On the other hand, the specific surface area of the composite CG/CNT_{oxi} was 15% and 10% lower than that of the sample CG and composite CG/CNT (Table 1), respectively. This result suggests that the presence of CNT_{oxi} had an effect on the polymerization of glucose or the carbonization process, resulting in a material with lower microporosity. The shape of the isotherm at medium-high relative pressure, assigned to the presence of CNT, was similar to that of the composite CG/CNT, indicating that the oxidation of the CNT did not alter the volume of pores of the composites. In fact, it was observed that CNT_{oxi} exhibited similar pore volume as the non-oxidized CNT (Figure S1). On the other hand, the external surface areas were also modified due to the presence of CNT and CNT_{oxi} during the polymerization of glucose. The external surface area of CNT and CNT_{oxi} was much higher than that of sample CG (Table S1), and hence, the composite exhibited a larger external surface area than sample CG, demonstrating the presence of CNT inside the structure. However, although the same amount of CNT and CNT_{oxi} was introduced for the preparation of the composites, differences in the external surface area were observed. This result indicates that the presence of CNT_{oxi} during the hydrothermal process modified the polymerization reaction, resulting in a material with a higher external surface area. So, to better understand the morphological changes resulting from the incorporation of CNT and CNT_{oxi} during the polymerization of glucose, the samples were examined by scanning electron microscopy

(SEM). Sample CG was composed of spheres of 0.69 ± 0.09 μm diameter (Figure 2a), which is a typical morphology of hydrothermal carbons [20,23]. The presence of CNT gave rise to an inhomogeneous material with two different carbon sphere size distributions (0.24 ± 0.03 μm and 0.40 ± 0.05 μm), while the incorporation of CNT_{oxi} resulted in a homogenous material with carbon spheres of 0.25 ± 0.04 μm.

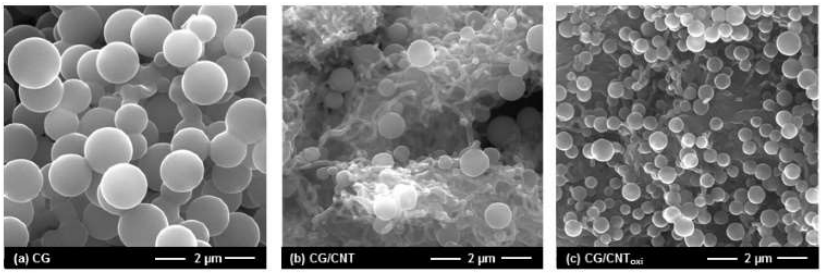


Figure 2. SEM micrographs of carbonized glucose (**a**) and carbon composites prepared by introducing CNT (**b**) and oxidized CNT (**c**).

It can be deduced from the SEM images that the chemical surface properties of the CNT had a noticeable effect on the formation of the carbon spheres. The growth mechanism of the spheres involves a complex set of simultaneous chemical reactions (isomerization, dehydration, condensation, or addition) that takes place during the polymerization of glucose [19,20]. Initially, the dehydration of glucose is promoted, giving rise to anions that react with each other via polymerization reactions [16]. Then, the aromatization of these molecules occurs, resulting in condensed furan rings bridged by aliphatic regions. These reactions proceed until the polymerized intermediates achieve a critical concentration, which produces the nucleation and growth of the particles forming a spherical-shaped structure [19,23]. The presence of CNT during the polymerization of glucose results in materials with smaller spheres, which suggests that CNT may promote the formation of nucleation points leading to a large number of small spherical particles, and hence, to a larger external surface area (Table 1) [31]. Besides, the oxygen groups on the surface of CNT_{oxi} also favor the dispersion of the CNT into the precursor mixture, and hence, the appearance of the nucleation points is more homogeneous. The assistance of CNT during the polymerization of glucose could be confirmed by FTIR spectroscopy (Figure 3a). The polymerized glucose obtained prior to carbonization (sample G) presented four main bands of interest: (i) an intense peak at 3400 cm^{-1}, which is attributed to O-H stretching vibration, (ii) a double-peak at 1600–1700 cm^{-1}, which is assigned to carbonyl groups, (iii) some peaks in the absorption region of 1200 cm^{-1} ascribed to C-O-C stretching groups, and (iv) some peaks in the absorption band ca. 800 cm^{-1} attributed to C-O-H bonds. These results demonstrated that the organic spheres obtained from the hydrothermal process exhibit a large amount of oxygen functional groups. The intensity of these peaks decreased by introducing CNT, being almost negligible for the composite prepared with CNT_{oxi}, especially the band assigned to -OH groups. These results suggest that the incorporation of CNT_{oxi} gives rise to materials with a lower concentration of oxygen functional groups (sample G/CNT_{oxi}), indicating a higher degree of polymerization compared to the sample that bears the pristine CNT (sample G/CNT) and the polymerized glucose (sample G).

These changes in the morphology due to the presence of CNT and CNT_{oxi} may also modify the effect of the ball milling process employed to incorporate nitrogen functionalities, as observed from the textural properties. The functionalization of CG/CNT with melamine gave rise to a material (N-CG/CNT) with a lower volume adsorbed at high relative pressure (Figure 1), which lost 29% of its BET surface area due to the functionalization process (Table 1). However, sample $N\text{-}CG/CNT_{oxi}$ remained almost identical to CG/CNT_{oxi}, as only a decrease of 8% was observed in the BET surface area. This difference could be due to the final morphology of the composites that could give rise

to a different behavior during the ball milling process. Some of the CNT and carbon spheres were crushed due to the ball milling (Figure S2), especially in the composite N-CG/CNT, which explains the significant loss in microporosity mentioned above. Besides, the thermal treatment applied to decompose melamine after ball milling seems to rearrange (or merge) the particles. These effects were less evident in the case of N-CG/CNT_{oxi}, although some loss of sphericity and some merged particles were also observed (Figure S2b). These differences between the N-doped composites might be due to the more heterogeneous structure obtained by the incorporation of CNT_{oxi} that probably resulted in a carbon structure with higher mechanical strength, and hence, the textural and morphological properties suffer fewer modifications during the functionalization process.

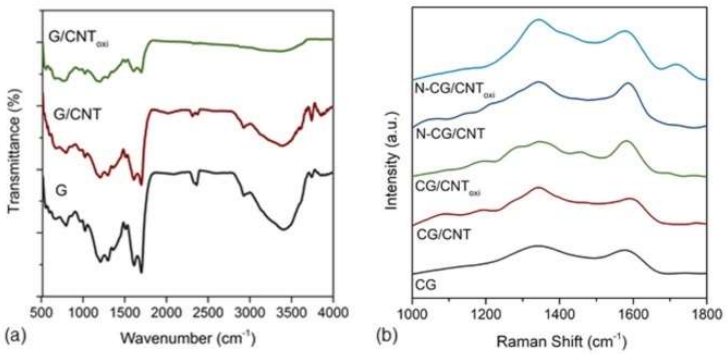


Figure 3. (**a**) FTIR spectra of hydrothermal glucose prepared without CNT (G) and in the presence of CNT (G/CNT) and CNT_{oxi} (G/CNT_{oxi}) and (**b**) Raman spectra of carbonized glucose and undoped and N-doped carbon composites prepared by introducing CNT and oxidized CNT.

As stated above, the surface chemistry of the CNT affected the polymerization of glucose, as the incorporation of CNT_{oxi} results in a material with a higher degree of polymerization. This modification in the polymerization reaction also resulted in differences in the ordering of the final carbon structure, which was evaluated by Raman spectroscopy. Figure 3b shows the Raman spectra for all undoped and doped carbons. The samples show a band at 1580 cm^{-1} ascribed to the graphitic domains (G band) and a second broad band centered at 1350 cm^{-1} (D band), which indicates disordered structures of turbostratic carbon layers. The intensity of both bands increased due to the addition of CNT and after the incorporation of nitrogen functionalities, especially for those samples prepared with oxidized CNT, suggesting a higher degree of ordering. The Raman spectra were further analyzed considering the splitting of the Raman features commonly employed for disordered carbonaceous materials [36]. The integrated areas of the main D and G bands were obtained from the deconvolution as a measure of relative disorder in carbon materials. The A_D/A_G ratio calculated from the integration of the peaks of the different spectra decreases by introducing CNT during the polymerization of glucose, especially by using CNT_{oxi} (Table S2). In addition, the relative decrease in the A_D/A_G ratio indicates the existence of a more ordered structure after the doping process. It should be highlighted that the A_D/A_G ratio usually increases after nitrogen functionalization due to the nitrogen replacing the carbon atoms, which increases the number of defects [15]. However, the degree of disorder of these samples is quite high, and hence, the Raman spectrum of N-CG/CNT_{oxi} is still attributed to a disordered carbonaceous material with a large number of defects.

Regarding the chemical composition, all samples were mainly composed of carbon (Table 2), with some contribution of hydrogen and oxygen. The differences in the amount of oxygen between CNT and CNT_{oxi} demonstrated that the CNT have been successfully oxidized. On the other hand, carbonized glucose (sample CG) exhibited a percentage of oxygen around 4.1%, which is within the

range typically observed in HTC carbon materials [23,31]. The amount of oxygen decreased due to the presence of CNT and CNT_{oxi}, which is in agreement with the hypothesis mentioned above about the higher degree of polymerization of these samples after the hydrothermal synthesis, as observed by FTIR. On the other hand, the amount of oxygen in the N-doped composites was doubled due to the ball milling process. This phenomenon may be due to the defects created, which then react with air, incorporating oxygen into the carbon structure [24]. Besides, the ball milling process allows the successful introduction of nitrogen, the incorporation of this heteroatom in the composite N-CG/CNT being higher. This effect is due to the lower degree of polymerization of the composite CG/CNT that allows a higher degree of functionalization.

Table 2. Chemical composition and electrical conductivity of carbonized glucose, undoped and N-doped carbon composites, carbon nanotubes, and oxidized carbon nanotubes.

Sample	C (wt.%)	H (wt.%)	O (wt.%)	N (wt.%)	K (S m^{-1})
CG	93.9	2.0	4.1	0.0	11
CG/CNT	94.3	2.1	3.6	0.0	150
CG/CNT_{oxi}	94.6	2.1	3.3	0.0	400
N-CG/CNT	85.1	1.7	6.4	6.8	280
$N\text{-}CG/CNT_{oxi}$	86.5	1.7	6.2	5.6	714
CNT	99.5	0.1	0.4	0.0	2500
CNT_{oxi}	95.3	0.9	3.8	0.0	1900

All these differences in the textural, morphological, and chemical properties result in materials with different electrical conductivities, as shown in Table 2. Carbon nanotubes exhibited a high electrical conductivity, which decreased up to 24% due to the presence of oxygen functionalities (CNT_{oxi}). On the other hand, the electrical conductivity of carbonized glucose was significantly low, but it could be increased up to 150 and 400 S m^{-1} due to the incorporation of CNT and CNT_{oxi}, respectively. It should be highlighted that the composite CG/CNT_{oxi} exhibited a higher electrical conductivity than CG/CNT, despite CNT_{oxi} having lower conductivity than the pristine CNT. It is well-known that oxygen functional groups decrease the electrical conductivity but increase the wettability of carbon materials [37]. In this case, CNT_{oxi} was used to assist the polymerization of glucose, so after the hydrothermal process and subsequent carbonization, the oxygen functional groups were no longer on the surface of the CNT_{oxi}. Consequently, both composites (CG/CNT and CG/CNT_{oxi}) exhibited similar chemical composition, as shown in Table 2. However, the use of CNT_{oxi} favored the formation of a more homogeneous structure with a larger degree of ordering and higher mechanical strength that partially prevents the crushing of the CNT and the carbon spheres, and hence, leads to a carbon structure with enhanced electrical conductivity. Besides, the addition of nitrogen functionalities also improves the electrical conductivity of the composites up to 87% and 78% for N-CG/CNT and $N\text{-}CG/CNT_{oxi}$, respectively. In this case, the increase is very similar for both composites, despite sample N-CG/CNT bearing a higher amount of nitrogen. This difference could be due to the type of nitrogen functional groups that have been identified by XPS (Figure 4). The high-resolution XPS spectra in the N 1s region were deconvoluted into the three main nitrogen contributions: pyridinic nitrogen (398.4 ± 0.1 eV), pyrrolic nitrogen (400.1 ± 0.1 eV) and quaternary nitrogen (401.3 ± 0.1 eV). The proportion of pyridinic nitrogen in the composite $N\text{-}CG/CNT_{oxi}$ was slightly lower, while the contribution of the peak attributed to quaternary nitrogen was 30% higher in comparison with N-CG/CNT. These quaternary groups may create donor electronic states near the Fermi level, enhancing the electrical conductivity [37]. Therefore, both the amount and type of nitrogen functional group are essential to increase the electrical conductivity of carbon materials.

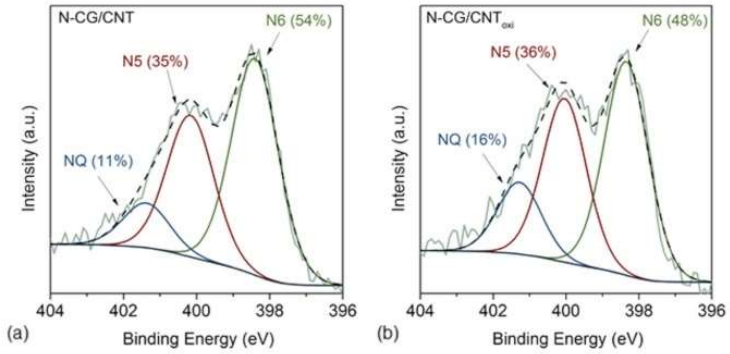


Figure 4. XPS spectra of N1s for N-doped composites N-CG/CNT (**a**) and N-CG/CNT$_{oxi}$ (**b**).

3.2. *Electrochemical Measurements*

The electrochemical activity of the carbon composites towards the oxygen reduction reaction (ORR) was determined by cyclic voltammetry (CV) in a rotating ring-disk electrode (RRDE). Featureless cyclic voltammograms were obtained from the measurement performed with the electrolyte saturated with N_2, demonstrating that the samples did not present any electrocatalytic activity under these conditions (Figure S3). Nonetheless, well-defined cathodic peaks were detected from the measurement performed with the electrolyte saturated with O_2, which indicates that all materials were electrochemically active towards the ORR (Figure S3). Similar results were observed for the N-doped composites (Figure S4). However, significant differences in the electroactivity could be found due to their distinct physico-chemical properties. Therefore, the performance of the carbon composites as electrocatalysts for the ORR was evaluated by linear sweep voltammetry (LSV) to elucidate the relationship between the electroactivity and the physico-chemical properties. The LSV recorded at 1600 rpm and the number of electrons transferred are plotted in Figure 5.

Two crucial parameters can be obtained from the LSV: the onset potential (V) and the limiting current density (mA cm^{-2}), their values being shown in Table 3. The onset potential increases by the formation of the composite (3%) and the incorporation of nitrogen (7%), probably due to the higher amount of active sites provided by the CNT and the nitrogen functionalities. Similar results were obtained for the composites prepared with CNT$_{oxi}$ (Figure 5b), increasing 6% the onset potential due to the introduction of CNT$_{oxi}$ and 13% more due to the nitrogen functionalities. So, the most remarkable enhancement was observed for the N-doped composite N-CG/CNT$_{oxi}$, shifting the onset potential from 0.66 (sample CG) to 0.79 V. This value is similar to those previously reported for biomass-derived carbons [24,38]. The limiting current density also followed the same trend. However, in this case, the increase could be attributed to the higher electrical conductivity of the samples, as a direct relationship has been found between the limiting current density and the electrical conductivity (Figure S5). These results demonstrate the importance of incorporating CNT into the hydrothermal carbon structures, especially CNT$_{oxi}$, and introducing nitrogen functionalities. Besides, the measurements performed using an RRDE allow evaluating the efficiency of the oxygen reduction process by calculating the production of sub-products during the reaction (Table 3), which is related to the mechanism of the reaction. Sample CG produced a considerable amount of sub-products that decreased due to the presence of CNT, and the drop was even more significant upon the incorporation of nitrogen functional groups. These results were correlated with the number of electrons transferred, a number of electrons transferred close to 4 indicating that the oxygen reduction was accomplished in a single step, while a number close to 2 corresponded to the production of sub-products. So, from the values shown in Figure 5c,d, it could be concluded that the incorporation of CNT and CNT$_{oxi}$ did not seem to produce any significant effect on the reaction mechanism, as the values obtained were quite similar to those

of the carbonized glucose (CG). However, the introduction of nitrogen functionalities results in a noticeable improvement in the efficiency of the oxygen reduction, as the N-doped composites shift the mechanism of the reaction towards the four-electron pathway (number of electrons transferred = 3.3, measured at −0.2 V). This value is higher than those previously shown for HTC [24,38]. This effect is due to the presence of nitrogen into the carbon structure that improves its electronic structure and chemical reactivity [15].

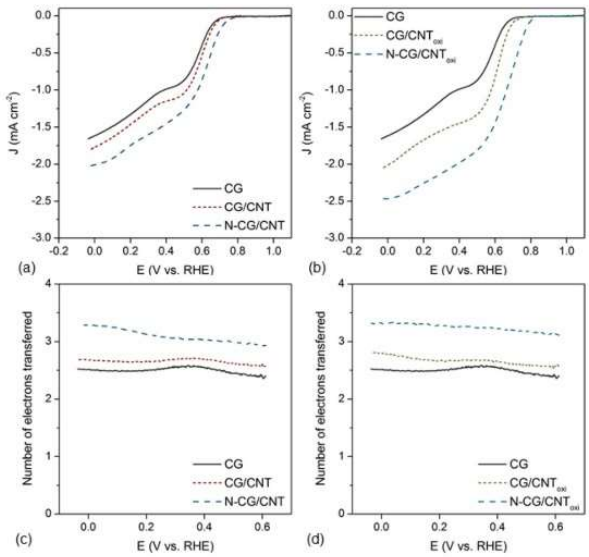


Figure 5. Linear sweep voltammograms (LSV) and the number of electrons transferred measured at 1600 rpm for the carbonized glucose and the undoped and N-doped carbon composites prepared by introducing CNT (**a**,**c**) and oxidized CNT (**b**,**d**).

Table 3. Electrochemical parameters obtained from linear sweep voltammetry measurements.

Sample	*E*onset (V) [1]	J_L (mA cm^{-2})	H_2O_2 (%) [2]	J_k (mA cm^{-2}) [3]
CG	0.66	1.7	75	1.3
CG/CNT	0.68	1.8	67	2.0
CG/CNT$_{oxi}$	0.70	2.1	67	3.1
N-CG/CNT	0.73	2.0	43	2.3
N-CG/CNT$_{oxi}$	0.79	2.5	36	5.7

[1] Onset potential measured at -0.1 mA cm^{-2}. [2] Production of hydrogen peroxide at 0.2 V vs RHE. [3] Kinetic current density measured at 0.4 V vs RHE.

Another important parameter that is commonly used to evaluate the activity of the electrocatalysts towards the ORR is the kinetic current density (J_k), which is calculated from the Koutecký–Levich equation (Equation (S13) shown in the supporting information). The J_k value calculated for N-CG/CNT$_{oxi}$ was higher than that of composite N-CG/CNT (Table 3) despite both having a similar nitrogen content, which suggests that the presence of nitrogen was not enough to enhance the reaction. This difference in the J_k values of the N-doped samples could be due to the type of nitrogen functionalities or to the modification produced by the incorporation of oxidized CNT. The comparison between composite N-CG/CNT and CG/CNT$_{oxi}$ (composites with similar onset potential and J_L) revealed that, in these samples, the improvement in the J_k value was due to the modification of the

physico-chemical properties produced by the introduction of CNT_{oxi} during the polymerization of the glucose, as CG/CNT_{oxi} exhibited a higher J_k value than N-CG/CNT. The long-term stability was another critical parameter to assess the performance of carbon materials as electrocatalysts towards the ORR. Therefore, the durability of all the samples was tested by chronoamperometry performed at 0.4 V vs RHE for 10000 s (Figure 6). It can be observed that the carbonized glucose sample lost 53% of its initial current density, which was already the lowest current density registered (Table 3). Nonetheless, the stability was highly increased by introducing CNT and CNT_{oxi} (13% and 27% more retention than CG, respectively) and was even further increased by the introduction of nitrogen. In fact, the N-doped composites exhibited a current density retention of more than 80%, especially composite $N\text{-}CG/CNT_{oxi}$. Therefore, taking into account all the important electrochemical parameters, composite $N\text{-}CG/CNT_{oxi}$ exhibited the highest electrocatalytic performance, which could be attributed to its high external surface area, its higher electrical conductivity, and the larger number of active sites offered by the quaternary and pyridinic nitrogen functional groups.

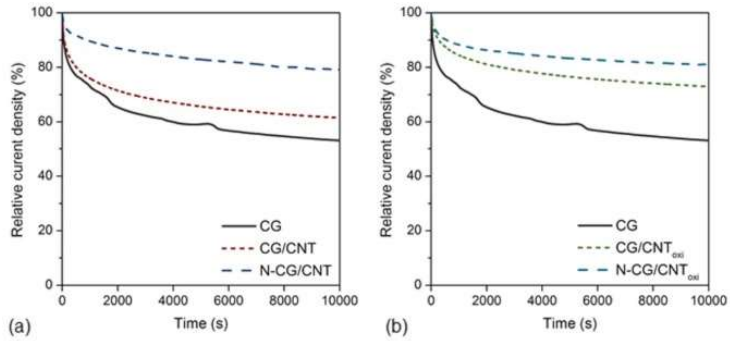


Figure 6. Chronoamperometry experiments measured at 0.4 V vs RHE for 10000 s for the carbonized glucose and the undoped and N-doped carbon composites prepared by introducing CNT (**a**) and oxidized CNT (**b**).

4. Conclusions

Biomass-derived carbon composites were prepared by hydrothermal carbonization in the presence of CNT and oxidized CNT (CNT_{oxi}) to evaluate the effect of the different oxygen functional groups on the hydrothermal polymerization of glucose and on the final physico-chemical properties. The presence of CNT during the polymerization of glucose promoted the formation of nucleation points that led to a large number of small spherical particles. The incorporation of CNT_{oxi} also favored the dispersion of the CNT into the precursor mixture, giving rise to a more homogenous carbon structure with a large number of small spheres (64% smaller than those of sample CG). Besides, the presence of CNT_{oxi} results in materials with a lower concentration of oxygen functional groups, suggesting a higher degree of polymerization compared to the sample that bears the pristine CNT. The efficiency of the ball milling employed to functionalize the composites was also modified due to these features provided by the CNT_{oxi}. The composite with the more homogeneous structure (CG/CNT_{oxi}) exhibited higher mechanical strength, and henceforth, the textural and morphological properties suffered fewer modifications during the functionalization process. In fact, a decrease of only 8% was observed in the BET surface area of sample $N\text{-}CG/CNT_{oxi}$, while this value rose to 29% for the composite N-CG/CNT. On the other hand, the ball milling process doubled the amount of oxygen and allows the successful introduction of nitrogen. However, differences between the incorporation of these heteroatoms were observed due to the final degree of polymerization of the samples. Lower incorporation of oxygen and nitrogen was detected for the composite with a higher degree of polymerization ($N\text{-}CG/CNT_{oxi}$).

Besides, the textural, morphological, and chemical properties obtained for the composite N-CG/CNT_{oxi} resulted in a material with enhanced electrical conductivity (from 11 to 714 S m^{-1}). Regarding the electrochemical performance, the onset potential increased by 20% due to the presence of CNT and nitrogen functional groups that act as active sites; the limiting current density increased linearly with the electrical conductivity, being improved by 47%; the production of sub-products decreased from 75% to 36% due to the incorporation of nitrogen, which shifted the mechanism of the reaction to the four-electron pathway; the kinetic current density increased from 1.3 to 3.1 mA cm^{-2} due to the addition of CNT_{oxi} during the polymerization of glucose and up to 5.7 mA cm^{-2} due to the presence of nitrogen functionalities; and the stability improved due to the nitrogen content, retaining almost 90% of the initial current density after 10000 s. Therefore, considering all the important electrochemical parameters, sample N-CG/CNT_{oxi} exhibited the highest electrocatalytic performance, which could be attributed to its high external surface area, its higher electrical conductivity, and the large number of active sites offered by the CNT and the nitrogen functional groups.

Supplementary Materials: The following are available online at http://www.mdpi.com/2504-477X/4/1/20/s1, Figure S1: N_2 adsorption-desorption isotherms of carbon nanotubes and oxidized carbon nanotubes, Table S1: Textural properties of carbon nanotubes and oxidized carbon nanotubes, Figure S2: SEM micrographs of N-doped composites with carbon nanotubes and with oxidized carbon nanotubes, Table S2: Integrated areas of the peaks D and G obtained by Raman spectroscopy, Figure S3: Cyclic Voltammograms measured at a scan rate of 5 mV s^{-1} in an electrolyte saturated with N_2 and O_2 for carbonized glucose (a), composite CG/CNT (b) and composite CG/CNT_{oxi} (c), Figure S4: Cyclic Voltammograms measured at a scan rate of 5 mV s^{-1} in an electrolyte saturated with N_2 and O_2 for N-doped composites prepared with CNT (a) and CNT_{oxi} (b), Figure S5: Relationship between the limiting current density and electrical conductivity, Equations (S1)-(S14) to calculate the electrochemical parameters.

Author Contributions: Conceptualization, N.R.-R., J.L.F. and M.F.R.P.; Investigation, R.G.M., R.S.C. and A.G.; Methodology, R.G.M. and N.R.-R.; Validation, R.G.M. and C.P.; Visualization, N.R.-R.; Writing—Original Draft Preparation, N.R.-R.; Writing—Review & Editing, J.L.F. and M.F.R.P.; Funding Acquisition, M.F.R.P. and C.P. All authors have read and agree to the published version of the manuscript.

Funding: This work was financially supported by Project UNIRCELL—POCI-01-0145-FEDER-016422—funded by European Structural and Investment Funds (FEEI) through—Programa Operacional Competitividade e Internacionalização—COMPETE2020 and by national funds through FCT—Fundaçã0 para a Ciência e a Tecnologia, I.P; and Associate Laboratory LSRE-LCM—UID/EQU/50020/2019—funded by national funds through FCT/MCTES (PIDDAC) and PDEQB (PD9989). R.S.C. thanks UniRCell Project for a MSc. grant. C.P. thanks FCT for the FCT Investigator contract IF/01080/2015.

Acknowledgments: The authors are indebted to Carlos M. Sá (CEMUP) and Rui Rocha (CEMUP) for their assistance with XPS and SEM analysis, respectively.

Conflicts of Interest: The authors declare no conflict of interest.

References

1. Mohideen, M.M.; Liu, Y.; Ramakrishna, S. Recent progress of carbon dots and carbon nanotubes applied in oxygen reduction reaction of fuel cell for transportation. *Appl. Energy* **2020**, *257*, 114027. [CrossRef]
2. Kaur, P.; Verma, G.; Sekhon, S.S. Biomass derived hierarchical porous carbon materials as oxygen reduction reaction electrocatalysts in fuel cells. *Prog. Mater. Sci.* **2019**, *102*, 1–71. [CrossRef]
3. Wu, Z.; Song, M.; Wang, J.; Liu, X. Recent Progress in Nitrogen-Doped Metal-Free Electrocatalysts for Oxygen Reduction Reaction. *Catalysts* **2018**, *8*, 196. [CrossRef]
4. Stacy, J.; Regmi, Y.N.; Leonard, B.; Fan, M. The recent progress and future of oxygen reduction reaction catalysis: A review. *Renew. Sustain. Energy Rev.* **2017**, *69*, 401–414. [CrossRef]
5. Zhang, Y.; Jiang, W.-J.; Zhang, X.; Guo, L.; Hu, J.-S.; Wei, Z.; Wan, L.-J. Engineering self-assembled N-doped graphene–carbon nanotube composites towards efficient oxygen reduction electrocatalysts. *Phys. Chem. Chem. Phys.* **2014**, *16*, 13605–13609. [CrossRef]
6. Sarapuu, A.; Kibena-Põldsepp, E.; Borghei, M.; Tammeveski, K. Electrocatalysis of oxygen reduction on heteroatom-doped nanocarbons and transition metal–nitrogen–carbon catalysts for alkaline membrane fuel cells. *J. Mater. Chem. A* **2018**, *6*, 776–804. [CrossRef]

7. Paul, R.; Dai, Q.; Hu, C.; Dai, L. Ten years of carbon-based metal-free electrocatalysts. *Carbon Energy* **2019**, *1*, 19–31. [CrossRef]
8. Paul, R.; Du, F.; Dai, L.; Ding, Y.; Wang, Z.L.; Wei, F.; Roy, A. 3D Heteroatom-Doped Carbon Nanomaterials as Multifunctional Metal-Free Catalysts for Integrated Energy Devices. *Adv. Mater.* **2019**, *31*, 1805598. [CrossRef]
9. Wu, D.; Zhu, C.; Shi, Y.; Jing, H.; Hu, J.; Song, X.; Si, D.; Liang, S.; Hao, C. Biomass-Derived Multilayer-Graphene-Encapsulated Cobalt Nanoparticles as Efficient Electrocatalyst for Versatile Renewable Energy Applications. *ACS Sustain. Chem. Eng.* **2019**, *7*, 1137–1145. [CrossRef]
10. Zheng, Y.; He, F.; Wu, J.; Ma, D.; Fan, H.; Zhu, S.; Li, X.; Lu, Y.; Liu, Q.; Hu, X. Nitrogen-Doped Carbon Nanotube-Graphene Frameworks with Encapsulated Fe/Fe3N Nanoparticles as Catalysts for Oxygen Reduction. *ACS Appl. Nano Mater.* **2019**, *2*, 3538–3547. [CrossRef]
11. Zhang, Y.; Lu, L.; Zhang, S.; Lv, Z.; Yang, D.; Liu, J.; Chen, Y.; Tian, X.; Jin, H.; Song, W. Biomass chitosan derived cobalt/nitrogen doped carbon nanotubes for the electrocatalytic oxygen reduction reaction. *J. Mater. Chem. A* **2018**, *6*, 5740–5745. [CrossRef]
12. Wütscher, A.; Eckhard, T.; Hiltrop, D.; Lotz, K.; Schuhmann, W.; Andronescu, C.; Muhler, M. Nitrogen-Doped Metal-Free Carbon Materials Derived from Cellulose as Electrocatalysts for the Oxygen Reduction Reaction. *ChemElectroChem* **2019**, *6*, 514–521. [CrossRef]
13. Huang, B.; Xia, M.; Qiu, J.; Xie, Z. Biomass Derived Graphene-Like Carbons for Electrocatalytic Oxygen Reduction Reaction. *ChemNanoMat* **2019**, *5*, 682–689. [CrossRef]
14. Gu, D.; Zhou, Y.; Ma, R.; Wang, F.; Liu, Q.; Wang, J. Facile Synthesis of N-Doped Graphene-Like Carbon Nanoflakes as Efficient and Stable Electrocatalysts for the Oxygen Reduction Reaction. *Nano Micro Lett.* **2018**, *10*, 29. [CrossRef]
15. Kumar, R.; da Silva, E.T.S.G.; Singh, R.K.; Savu, R.; Alaferdov, A.V.; Fonseca, L.C.; Carossi, L.C.; Singh, A.; Khandka, S.; Kar, K.K.; et al. Microwave-assisted synthesis of palladium nanoparticles intercalated nitrogen doped reduced graphene oxide and their electrocatalytic activity for direct-ethanol fuel cells. *J. Colloid Interface Sci.* **2018**, *515*, 160–171. [CrossRef] [PubMed]
16. Fang, Z.; Smith, R.L., Jr.; Kozinski, J.A.; Minowa, T.; Arai, K. Reaction of d-glucose in water at high temperatures (410 °C) and pressures (180 MPa) for the production of dyes and nano-particles. *J. Supercrit. Fluids* **2011**, *56*, 41–47. [CrossRef]
17. Sun, Y.; Zhong, R.; Zhang, H.; Huang, T.; Yu, J.; Fang, H.; Liang, D.; Guo, Z. Soybean milk derived carbon intercalated with reduced graphene oxide as high efficient electrocatalysts for oxygen reduction reaction. *Int. J. Hydrog. Energy* **2019**, *44*, 21790–21802. [CrossRef]
18. Shi, M.; Ma, J.; Yao, Z.; Li, Z.; Mi, H.; Xie, Y. Iron and nitrogen co-doped porous carbon derived from soybean dregs with enhanced catalytic performance for oxygen reduction. *J. Electroanal. Chem.* **2019**, *839*, 141–148. [CrossRef]
19. Titirici, M.M. Hydrothermal Carbons: Synthesis, Characterization, and Applications. In *Novel Carbon Adsorbents*; Elsevier Ltd.: Amsterdam, The Netherlands, 2012; pp. 351–399. [CrossRef]
20. Sevilla, M.; Fuertes, A.B. Chemical and Structural Properties of Carbonaceous Products Obtained by Hydrothermal Carbonization of Saccharides. *Chem. Eur. J.* **2009**, *15*, 4195–4203. [CrossRef]
21. Kumar, R.; Singh, R.K.; Singh, D.P. Natural and waste hydrocarbon precursors for the synthesis of carbon based nanomaterials: Graphene and CNTs. *Renew. Sustain. Energy Rev.* **2016**, *58*, 976–1006. [CrossRef]
22. Liu, L.; Zeng, G.; Chen, J.; Bi, L.; Dai, L.; Wen, Z. N-doped porous carbon nanosheets as pH-universal ORR electrocatalyst in various fuel cell devices. *Nano Energy* **2018**, *49*, 393–402. [CrossRef]
23. Falco, C.; Marco-Lozar, J.P.; Salinas-Torres, D.; Morallón, E.; Cazorla-Amorós, D.; Titirici, M.M.; Lozano-Castelló, D. Tailoring the porosity of chemically activated hydrothermal carbons: Influence of the precursor and hydrothermal carbonization temperature. *Carbon* **2013**, *62*, 346–355. [CrossRef]
24. Morais, R.G.; Rey-Raap, N.; Figueiredo, J.L.; Pereira, M.F.R. Glucose-derived carbon materials with tailored properties as electrocatalysts for the oxygen reduction reaction. *Beilstein J. Nanotechnol.* **2019**, *10*, 1089–1102. [CrossRef] [PubMed]
25. Xu, S.S.; Qiu, S.W.; Yuan, Z.Y.; Ren, T.Z.; Bandosz, T.J. Nitrogen-containing activated carbon of improved electrochemical performance derived from cotton stalks using indirect chemical activation. *J. Colloid Interface Sci.* **2019**, *540*, 285–294. [CrossRef]

26. Tran, T.N.; Song, M.Y.; Kang, T.H.; Samdani, J.; Park, H.Y.; Kim, H.; Jhung, S.H.; Yu, J.S. Iron Phosphide Incorporated into Iron-Treated Heteroatoms-Doped Porous Bio-Carbon as Efficient Electrocatalyst for the Oxygen Reduction Reaction. *ChemElectroChem* **2018**, *5*, 1944–1953. [CrossRef]
27. Kim, M.J.; Park, J.E.; Kim, S.; Lim, M.S.; Jin, A.; Kim, O.H.; Kim, M.J.; Lee, K.S.; Kim, J.; Kim, S.S.; et al. Biomass-Derived Air Cathode Materials: Pore-Controlled S,N-Co-doped Carbon for Fuel Cells and Metal-Air Batteries. *ACS Catal.* **2019**, *9*, 3389–3398. [CrossRef]
28. Li, X.; Guan, B.Y.; Gao, S.; Lou, X.W. A general dual-templating approach to biomass-derived hierarchically porous heteroatom-doped carbon materials for enhanced electrocatalytic oxygen reduction. *Energy Environ. Sci.* **2019**, *12*, 648–655. [CrossRef]
29. Quílez Bermejo, J.; Melle Franco, M.; San Fabián, E.; Morallon, E.; Cazorla-Amorós, D. Towards understanding of the active sites for ORR in N-doped carbon materials through a fine-tuning of nitrogen functionalities: An experimental and computational approach. *J. Mater. Chem. A* **2019**, *7*, 24239–24250. [CrossRef]
30. Ratso, S.; Käärik, M.; Kook, M.; Paiste, P.; Aruväli, J.; Vlassov, S.; Kisand, V.; Leis, J.; Kannan, A.M.; Tammeveski, K. High performance catalysts based on Fe/N co-doped carbide-derived carbon and carbon nanotube composites for oxygen reduction reaction in acid media. *Int. J. Hydrog. Energy* **2019**, *44*, 12636–12648. [CrossRef]
31. Rey-Raap, N.; Enterría, M.; Martins, J.I.; Pereira, M.F.R.; Figueiredo, J.L. Influence of Multiwalled Carbon Nanotubes as Additives in Biomass-Derived Carbons for Supercapacitor Applications. *ACS Appl. Mater. Interfaces* **2019**, *11*, 6066–6077. [CrossRef]
32. Borghei, M.; Lehtonen, J.; Liu, L.; Rojas, O.J. Advanced Biomass-Derived Electrocatalysts for the Oxygen Reduction Reaction. *Adv. Mater.* **2018**, *30*, 30. [CrossRef] [PubMed]
33. Wang, X.; Ma, Z.; Chai, L.; Xu, L.; Zhu, Z.; Hu, Y.; Qian, J.; Huang, S. MOF derived N-doped carbon coated CoP particle/carbon nanotube composite for efficient oxygen evolution reaction. *Carbon* **2019**, *141*, 643–651. [CrossRef]
34. Li, M.; Xiong, Y.; Liu, X.; Han, C.; Zhang, Y.; Bo, X.; Guo, L. Iron and nitrogen co-doped carbon nanotube@hollow carbon fibers derived from plant biomass as efficient catalysts for the oxygen reduction reaction. *J. Mater. Chem. A* **2015**, *3*, 9658–9667. [CrossRef]
35. Chung, H.T.; Won, J.H.; Zelenay, P. Active and stable carbon nanotube/nanoparticle composite electrocatalyst for oxygen reduction. *Nat. Commun.* **2013**, *4*, 1922. [CrossRef]
36. Rebelo, S.L.H.; Guedes, A.; Szefczyk, M.E.; Pereira, A.M.; Araújo, J.P.; Freire, C. Progress in the Raman spectra analysis of covalently functionalized multiwalled carbon nanotubes: Unraveling disorder in graphitic materials. *Phys. Chem. Chem. Phys.* **2016**, *18*, 12784–12796. [CrossRef]
37. Barroso Bogeat, A. Understanding and Tuning the Electrical Conductivity of Activated Carbon: A State-of-the-Art Review. *Crit. Rev. Solid State Mater. Sci.* **2019**, 1–37. [CrossRef]
38. Nunes, M.; Rocha, I.M.; Fernandes, D.M.; Mestre, A.S.; Moura, C.N.; Carvalho, A.P.; Pereira, M.F.R.; Freire, C. Sucrose-derived activated carbons: Electron transfer properties and application as oxygen reduction electrocatalysts. *RSC Adv.* **2015**, *5*, 102919–102931. [CrossRef]



© 2020 by the authors. Licensee MDPI, Basel, Switzerland. This article is an open access article distributed under the terms and conditions of the Creative Commons Attribution (CC BY) license (http://creativecommons.org/licenses/by/4.0/).

Journal of Energy Chemistry 50 (2020) 260–270

Contents lists available at ScienceDirect

Journal of Energy Chemistry

journal homepage: www.elsevier.com/locate/jechem

Highly electroactive N–Fe hydrothermal carbons and carbon nanotubes for the oxygen reduction reaction

R. G. Morais, N. Rey-Raap, J. L. Figueiredo*, M. F. R. Pereira

Associate Laboratory LSRE-LCM, Departamento de Engenharia Química, Faculdade de Engenharia, Universidade do Porto, R. Dr. Roberto Frias s/n, 4200-465 Porto, Portugal

ARTICLE INFO

Article history:
Received 30 January 2020
Revised 9 March 2020
Accepted 12 March 2020
Available online 8 April 2020

Keywords:
Iron(II) phthalocyanine
Hydrothermal carbons
Carbon nanotubes
Oxygen reduction reaction
Electrocatalysis

ABSTRACT

Glucose-derived carbons were prepared by hydrothermal carbonization of glucose followed by carbonization or activation to obtain carbon materials with different microporosities. These microporous carbons and carbon nanotubes (CNTs) were functionalized with melamine and/or iron(II) phthalocyanine (FePc) following three different methodologies: (i) Functionalization with melamine via thermal treatment, (ii) incorporation of the lowest amount of FePc reported in the literature via incipient wetness impregnation followed by thermal treatment and (iii) functionalization with melamine followed by FePc incorporation. The chemical and textural characterization of the prepared materials and their electrochemical assessment allowed to understand the role of microporosity in the incorporation of FePc and its effect on the oxygen reduction reaction (ORR). It was observed that FePc was preferentially incorporated inside the porous structure, especially in samples with more developed microporosity. However, functionalization with melamine modified the textural properties and the surface chemistry, favoring the incorporation of FePc on the surface. Regarding the electrochemical performance, the presence of FePc greatly enhanced the electroactivity of the microporous catalysts. An onset potential of 0.88 V and a four-electron pathway were obtained for glucose-derived carbons, whereas the limiting current densities and kinetic current densities rose by 126% and 222%, respectively, in comparison to the base sample. Notwithstanding, the highest electrochemical activity was observed for the sample prepared with CNTs, due to the synergy between the active metal centers and their highly graphitic carbon structure. The electrochemical parameters of CNT_{FePc} surpass the commercial Pt/C. The half-wave potential is 40 mV higher, the limiting current density increases by 17%, and a negligible production of by-products (< 1%) was observed.

© 2020 Science Press and Dalian Institute of Chemical Physics, Chinese Academy of Sciences. Published by Elsevier B.V. and Science Press. All rights reserved.

1. Introduction

The oxygen reduction reaction (ORR) takes place in several electrochemical systems such as fuel cells and metal-air batteries [1–7]. The main problem of this reaction is its slow kinetics, that hinders the overall performance of these electrochemical devices [2–5,7–10]. Platinum-derived electrocatalysts are commonly used to achieve faster reaction kinetics, overcoming these limitations. However, platinum is a scarce metal which represents very high costs towards the overall price of the electrochemical cell [2,6,8–10]. Therefore, it is urgent to develop new green and economical materials that optimize the ORR, paving the way towards a sustainable future. Carbon materials exhibit a high versatility and competitive price, which make them a serious contender to replace Pt. In fact, one of the major advantages of carbon materials is the possibility to tune their chemical and textural properties, enhancing their electroactivity towards the ORR [1,11–14].

One of the most frequently employed methods to tune the chemical properties of carbon materials is the incorporation of heteroatoms, which changes the surface chemistry and forms new active sites. Nitrogen is the most studied of such heteroatoms, as it promotes the mechanism of the reaction to the four-electron pathway, reducing oxygen directly without the generation of sub-products [12,15,16]. However, depending on the nature of the carbon material, the incorporation of nitrogen functionalities does not always result in a competitive material against Pt-based electrocatalysts. Therefore, further modifications such as the incorporation of transition metals (cobalt, manganese, nickel or iron) is crucial for the development of new electrocatalysts [8,10,16–19]. Iron offers interesting advantages due to its abundance, economic competitiveness and selectivity towards ORR compared to the other transition metals [8,10]. Although iron promotes the formation of more active sites and increases the electrical conductivity

* Corresponding author.
E-mail address: jlfig@fe.up.pt (J.L. Figueiredo).

https://doi.org/10.1016/j.jechem.2020.03.039
2095-4956/© 2020 Science Press and Dalian Institute of Chemical Physics, Chinese Academy of Sciences. Published by Elsevier B.V. and Science Press. All rights reserved.

of electrocatalysts towards ORR [20], the single incorporation of iron in a carbon matrix may result in materials with lower electrochemical performance than Pt/C. Therefore, the combination of heteroatoms and transition metals seems to be essential to improve the electrocatalytic activity of carbon materials. The combination of nitrogen and iron has been applied to different carbons supports such as activated carbons [21,22], porous carbons [23,24], carbon nanosheets [8,25], carbon black [24,26,27], graphene [2,28], carbon nanotubes [24,29–31] and black pearls [29,30]. The most commonly used methodologies to incorporate both nitrogen and iron use either two precursors, one that contains nitrogen and another that encloses iron [23,25], or one precursor that contains both elements [28,32–35]. Recently, the incorporation of Fe–N_4 complexes, such as porphyrins and metal-centered phthalocyanines (Pc), has emerged as an interesting strategy to achieve high electrochemical activities in ORR [3,17,21,36]. Among these complexes, iron Pcs are preferred due to their higher availability and lower costs in comparison to porphyrins [37]. Some studies have already been published focused on the incorporation of iron(II) phthalocyanine (FePc) into carbon structures and its effect on the electrochemical performance towards ORR; however, there are still some aspects that should be addressed, as most of these studies either use a large quantity of FePc for the preparation of the catalyst [21,22,28,29,32], or they apply a high number of steps to reach the final catalyst [26,29,30]. These two factors lead to high fabrication costs, which should be minimized in case of a scaled-up production. Furthermore, the effect of porosity regarding the incorporation of FePc in porous carbons and, consequently, its effect towards the ORR, has not been reported in the literature.

Herein, the main objective of this study is to prepare electrocatalysts from glucose-derived carbons and carbon nanotubes (CNTs) with high electrocatalytic activity towards ORR. Glucose-derived carbons were prepared by hydrothermal carbonization followed by carbonization or activation to obtain materials with different degrees of microporosity. Nitrogen functionalities and FePc were incorporated into the glucose-derived carbons and CNTs. A very low ratio of FePc:carbon material was used to minimize the electrocatalysts production cost. The influence of microporosity on the incorporation of FePc and the effect of the chemical properties on the ORR were studied. The incorporation of a small amount of FePc on the glucose-derived carbons and CNTs resulted in a remarkable improvement, showing the effectiveness of the functionalization method in converting green biomass-derived carbons into high-value electrocatalysts with outstanding electrochemical activities towards the ORR.

2. Experimental

2.1. Preparation of electrocatalysts

Different carbon supports were used for the preparation of the electrocatalysts: carbonized and activated glucose-derived carbon materials and purified carbon nanotubes. The carbonized and activated-glucose derived carbons were prepared from an initial mixture of glucose (HiMedia, >99%) and deionized water (produced by filtration through inverse osmose in a Panice equipment) in a 1:6 mass ratio. The mixture was sonicated for 30 min, closed in a Teflon-lined stainless steel autoclave and submitted to hydrothermal carbonization at 180 °C for 12 h. The prepared material was then washed with deionized water and dried at 80 °C overnight. The dried material was carbonized at 800 °C under N_2 atmosphere for 2 h or activated under a CO_2 flow of 80 $cm^3\ min^{-1}\ g^{-1}$ at 900 °C for 4 h. CNTs were purified following the methodology described elsewhere [38]. Briefly, CNTs were refluxed in a 1:1 ratio solution of sulfuric acid and distilled water at 140 °C for 4 h to remove impurities, washed with hot distilled water until neutral pH was achieved, and dried at 100 °C for 1 day.

The carbonized (CG) and activated (AG) hydrothermal carbons and the purified carbon nanotubes (CNT) were then modified by introducing nitrogen and/or iron into the carbon structure following three different methodologies: (i) nitrogen functionalization using melamine (Sigma-Aldrich, ≥ 99%) as nitrogen precursor, (ii) incorporation of iron(II) phthalocyanine (FePc, Sigma-Aldrich, 90%) into the carbon structure by the incipient wetness impregnation method, and (iii) nitrogen functionalization followed by the incorporation of FePc. The nitrogen functionalization was performed by mixing the carbon material with melamine (400 mg melamine per 600 mg carbon material), followed by subsequent thermal treatment under N_2 atmosphere at 600 °C for 2 h to decompose the nitrogen precursor and to incorporate the nitrogen atoms into the carbon structure. For the incipient wetness impregnation, a certain amount of FePc complex was dissolved in ethanol and added dropwise to the carbon material under sonication. The impregnated sample was kept under sonication for 30 min and dried at 80 °C overnight. The dried material underwent a subsequent thermal treatment in N_2 atmosphere at a selected temperature for 2 h. In order to assess the optimal amount of the FePc precursor and the temperature to be employed, different carbonized samples were prepared using two different quantities of FePc (incorporation of 50 mg and 100 mg of FePc into 1 g of carbon) and two different temperatures (500 °C and 800 °C). The optimum amount of FePc (50 mg) and temperature (500 °C) were selected according to the electrochemical results shown in the supporting information (Fig. S1). Samples doped with nitrogen were designated N–X, the samples with FePc were represented by X_{FePc} and samples prepared with both precursors were labeled N–X_{FePc}, where X can assume the form of CG for carbonized samples, AG for activated samples and CNT for carbon nanotubes.

2.2. Textural and chemical characterization

The textural characterization of the prepared materials was carried out by N_2 adsorption at −196 °C performed in a Quantachrome Autosorb iQ automated gas sorption analyzer. Prior to the analysis, all samples were degassed under vacuum for 12 h at 150 °C. The Brunauer–Emmett–Teller (BET) equation was used to calculate the specific surface area (S_{BET}), the total pore volume (V_p) was calculated as the volume of nitrogen adsorbed at the saturation point (relative pressure of 0.99), the micropore volume (V_{micro}) was determined by the t-plot method and the pore size distribution was obtained by applying the Quenched Solid Density Functional Theory (QSDFT). The chemical composition of the carbon materials was determined by elemental analysis. Carbon, hydrogen and nitrogen (C, H and N) contents were determined using a Vario Micro Cube analyzer (Elementar GmbH), in which the sample underwent combustion at 1050 °C, whereas the oxygen content was obtained in a Rapid Oxy Cube analyzer (Elementar GmbH), by pyrolysis at 1450 °C. The quantification of the metal loading was performed by inductively coupled plasma (ICP) emission spectrometry. The analyzes were carried out in a Perkin Elmer Optima 4300 using an optic with Echelle polychromator. The surface chemical composition of the samples was studied by X-ray photoelectron spectroscopy (XPS). The analyses were performed in a Kratos AXIS Ultra HAS spectrometer using a monochromatic Al K_α radiation (1486.7 eV) at 15 kV (90 W) in fixed analyzer transmission mode. The morphology of the samples and the elemental mapping distribution were evaluated by scanning electron microscopy (SEM) and energy-dispersive spectroscopy (EDS) using a Nova NanoSEM 200 (FEI Company). The samples, in powder form, were previously attached to an aluminum pin using conductive carbon double-sided adhesive tape. An Everhart-Thornley detector

was used as a secondary detector during SEM analysis and a Si(Li) detector was used for EDS and mapping analysis.

2.3. Electrochemical characterization

The electrochemical characterization was performed in a PGSTAT 302 N potentiostat/galvanostat using a three-electrode cell configuration. A glassy carbon rod and an Ag/AgCl (KCl 3 mol L^{-1}) electrode were used as counter and reference electrode, respectively. Working electrodes were prepared by deposition of a prepared suspension of the carbon samples on a glassy carbon rotating disk electrode (3 mm in diameter, Metrohm). These suspensions were obtained by dispersing 1 mg of the carbon sample in a solution containing 96 μL of Nafion (5 wt% in lower aliphatic alcohols and water, Sigma-Aldrich), 142 μL of ethanol (≥ 99.5%, VWR Chemicals) and 220 μL of ultrapure water (Milipore). The suspension was sonicated for at least 30 min until a homogeneous dispersion was obtained prior to deposition. The mass loading of all samples was ca. 0.1 mg cm^{-2}. The rotations of the working electrode were adjusted by a rotation speed controller, according to the assessment performed. All the electrochemical experiments were carried out at room temperature in a 0.1 mol L^{-1} KOH solution saturated with N_2 or O_2 for 30 min before performing cyclic voltammetry (CV) and linear sweep voltammetry (LSV) tests. The CV measurements were accomplished at a scan rate of 5, 20, 60 and 100 mV s^{-1} and the LSV at a scan rate of 5 mV s^{-1} with a rotation speed range from 400 to 3000 rpm, both within a −0.05 V to 1.1 V potential range (vs RHE). The experimental current was determined by subtracting the current obtained from the electrolyte saturated with N_2 from the current measured in the O_2-saturated electrolyte. Different electrochemical parameters were evaluated from the LSV data: onset potential (E_{onset}), half-wave potential ($E_{1/2}$), limiting current density (J_L) and kinetic current density (J_k). E_{onset} was determined at a current density of 0.1 mA cm^{-2}. $E_{1/2}$ was calculated from the derivative of the current-potential curve. The derivative curve, assuming an ideal sigmoid, exhibits a maximum value corresponding to half the diffusion-limited current, which is attributed to the $E_{1/2}$ [39]. J_L was considered as the current density measured in the linear sweep voltammograms at 0.15 V. J_k was calculated from the Koutecký–Levich equation:

$$\frac{1}{J} = \frac{1}{J_L} + \frac{1}{J_k} = \frac{1}{B\omega^{\frac{1}{2}}} + \frac{1}{J_k} \quad (1)$$

where J is the measured current density (mA cm^{-2}), J_L is the O_2 diffusion-limited current density (mA cm^{-2}), J_k is the kinetic current density (mA cm^{-2}), ω is the electrode rotation rate (rpm) and B represents the Levich constant related to the diffusion limiting current density given by Eq. (2):

$$B = 0.2nFD^{\frac{2}{3}}\nu^{-\frac{1}{6}}C \quad (2)$$

where n is the number of electrons exchanged, F is the Faraday constant (96 486 C mol^{-1}), D is the diffusion coefficient of O_2 (1.95×10^{-5} cm^2 s^{-1}), ν is the kinematic viscosity of the electrolyte (0.008977 cm^2 s^{-1}) and C is the bulk concentration of O_2 (1.15×10^{-3} mol L^{-1}).

The percentage of hydrogen peroxide (H_2O_2) produced and the number of electrons transferred during the ORR were measured by using a rotating ring-disk electrode (5 mm in diameter, 24.9% collection efficiency, Methrom) as the working electrode, which was prepared by depositing the suspension of the carbon samples on the disk area. The dispersion was prepared as detailed above and the mass loading was fixed at ca. 0.1 mg cm^{-2}. The H_2O_2 percentage and the number of electrons were calculated from the LSV recorded at 1600 rpm by Eqs. (3) and (4), respectively:

$$H_2O_2\ (\%) = 200 \times \frac{I_R/N}{I_D + I_R/N} \quad (3)$$

$$n = \frac{4I_D}{I_D + I_R/N} \quad (4)$$

where, I_R is the ring current density (mA cm^{-2}), I_D is the disk current density (mA cm^{-2}) and N is the collection efficiency (0.249).

Additionally, the stability of the prepared electrocatalyst was assessed by chronoamperometry, applying a potential of 0.4 V vs RHE for 10,000 s.

3. Results and discussion

3.1. Textural and morphological properties

The nitrogen adsorption–desorption isotherms obtained for the carbonized, activated and CNT samples are presented in Fig. 1(a–c), respectively. Table S1 shows a summary of the textural parameters obtained by the N_2 adsorption–desorption characterization of the carbon samples.

Carbonized and activated glucose-derived carbons display type I isotherms according to the International Union of Pure and Applied Chemistry (IUPAC) classification, characteristic of microporous materials, whereas carbon nanotube samples display type II isotherms, attributed to multi-layered materials [40]. Regardless of the nature of the carbon support, the functionalization process employed to introduce nitrogen functionalities in the porous materials led to a decrease of the amount of nitrogen adsorbed at low pressures, and hence, to a reduction of the surface area (S_{BET}, Table S1). However, noticeable differences in the loss of surface area are observed between the different carbon supports. In carbonized samples, a reduction of 85% was detected, whereas in activated samples, the surface area decreases 20% due to the incorporation of nitrogen functionalities. These results suggest that the functionalization process blocks some of the pores preventing the access of N_2 to the innermost part of the carbon structure. This effect may be due to the temperature employed to decompose melamine, that may lead to the formation of some carbon nitride clusters [41], which are located close to the pores. The pore size of the carbonized glucose is much smaller than that of the activated glucose, as shown in Fig. S2 (0.55 nm and 1.18 nm, respectively), and hence, the clusters formed are probably large enough to block some of the pores, inhibiting the passage of N_2 during the isotherm measurements and highly decreasing the S_{BET}. A schematic description of this hypothesis is presented in Fig. 2.

Similar to N-AG, N-CNT loses 28% of its S_{BET} due to the functionalization process. In this case, the decrease is probably due to the incorporation of nitrogen functional groups, which increases the electrostatic affinity between the CNT. This effect is confirmed by the decrease of the volume of N_2 adsorbed at high pressures ($P/P_0 > 0.9$), which suggests that the space within the CNT bundles decreases and corroborates the increase of affinity between the tubes. Similar but less marked trends are observed by the incorporation of FePc (X_{FePc} series). In the carbonized sample (CG_{FePc}), S_{BET} decreases 10%, which is a much lower value than that observed for N-CG (85%). Although some pore blockage occurs due to the incorporation of FePc, the quantity of iron precursor used was much lower than that of melamine (50 and 667 mg of FePc and melamine for 1 g of carbon material, respectively), which explains the lower impact in the pore blockage. Analogously, S_{BET} of the activated sample (AG_{FePc}) also suffers a smaller decrease (13%) than that observed for N-AG (20%), due to the incorporation of the iron precursor (Table S1). Similarly, S_{BET} of CNT_{FePc} decreases by 19%, which is also a lower value compared to the surface area of N-CNT (28%). This difference is, once again, due to the low amount of iron precursor used. The incorporation of FePc in N–X samples resulted in a synergetic effect, involving the effects observed for the N–X and X_{FePc} series. I.e., the surface area of NX_{FePc} is much lower than

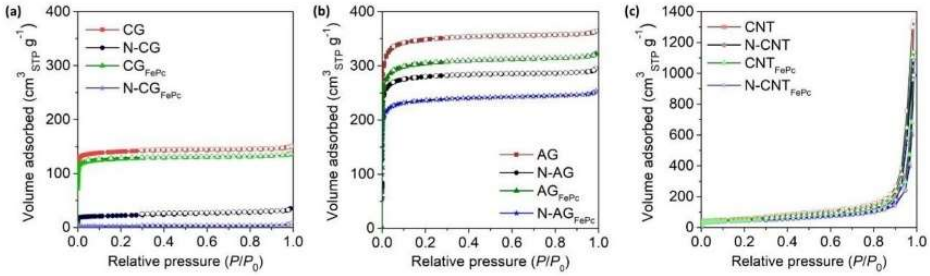


Fig. 1. N_2 adsorption–desorption isotherms of carbonized samples (a), activated samples (b) and carbon nanotube samples (c).

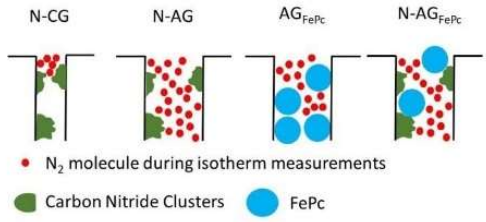


Fig. 2. Schematic illustration of the pore blockage and the effect on the incorporation of FePc.

that of samples N–X and X_{FePc}, which demonstrates that both precursors are responsible for the blockage of some pores, and hence, for the decrease of the microporosity.

To better understand the modifications caused by the incorporation of FePc, samples X_{FePc} and N–X_{FePc} were examined by scanning electron microscopy (SEM). The corresponding micrographs are displayed in Fig. 3.

Usually, the hydrothermal polymerization of glucose and its subsequent thermal treatment leads to the formation of carbon spheres [14,42]. The incorporation of FePc in CG and AG does not seem to modify the morphology of the samples, keeping the spherical shape of the particles (Fig. 3(a) and (b)). Similarly, the SEM micrograph of CNT_{FePc} (Fig. 3(c)) exhibits defined carbon nanotubes with no visible differences in the CNT structure. Therefore, the introduction of FePc does not affect the morphology of the samples. The mixing of melamine with the hydrothermal carbons and its subsequent thermal treatment resulted in the agglomeration of the carbon spheres, especially in the activated sample (Fig. 3(e)). The carbon spheres are almost undistinguishable in the micrograph of N-AG_{FePc}. On the other hand, functionalization with melamine and the subsequent incorporation of FePc does not modify the morphology of the CNT (Fig. 3(f)).

3.2. Chemical properties

The surface chemistry of each carbon support (carbonized and activated glucose-derived carbon and carbon nanotubes) was modified by applying different methodologies: (i) nitrogen functionalization, (ii) incorporation of iron(II) phthalocyanine (FePc) and iii) nitrogen functionalization followed by FePc incorporation. The bulk chemical composition obtained from the elemental analysis and inductively coupled plasma (ICP), and the surface composition determined by X-ray spectroscopy (XPS), are presented in Table 1.

Table 1. Chemical composition determined by elemental analysis, ICP and XPS.

Samples	Bulk composition (wt%)					Surface composition (wt%)			
	Elemental analysis				ICP	XPS			
	C	O	N	H	Fe	C	O	N	Fe
CG	94.4	4.0	–	1.6	–	89.4	10.6	–	–
N-CG	85.7	6.6	6.3	1.4	–	86.3	9.4	4.3	–
CG_{FePc}	93.0	4.6	0.8	1.2	0.4	81.8	13.7	2.9	1.6
N-CG_{FePc}	84.7	7.4	6.2	1.4	0.3	72.3	15.2	5.7	1.8
AG	95.0	3.9	–	1.1	–	84.7	15.3	–	–
N-AG	82.9	7.7	6.8	2.6	–	84.7	11.6	3.7	–
AG_{FePc}	94.0	3.5	1.1	0.9	0.5	88.1	11.9	–	–
N-AG_{FePc}	80.5	10.2	6.9	2.1	0.3	87.0	8.0	4.9	0.1
CNT	99.3	0.6	–	0.1	–	98.3	1.7	–	–
N-CNT	89.1	1.1	9.4	0.4	–	91.4	1.3	7.3	–
CNT_{FePc}	98.1	0.5	0.8	0.2	0.4	96.7	6.8	1.8	0.7
N-CNT_{FePc}	89.2	1.3	8.6	0.5	0.4	90.3	1.5	7.7	0.5

Samples CG and AG present very similar chemical compositions with a percentage of oxygen ca. 4 wt%, whereas the CNT exhibits a carbon content higher than 99 wt% with a very low amount of oxygen and hydrogen. As expected, the samples functionalized with nitrogen (N-CG, N-AG and N-CNT) show a noticeable content of nitrogen (6.3 wt%, 6.8 wt% and 9.4 wt%, respectively), demonstrating the successful functionalization of the samples. The amount of nitrogen incorporated is quite high in comparison to the values already reported in the literature for carbon materials functionalized by similar procedures [43,44]. This effect can be due to the decomposition of melamine into carbon nitrides that results in a high content of nitrogen. The incorporation of FePc in the initial samples results in materials with a low percentage of nitrogen and iron (CG_{FePc}, AG_{FePc} and CNT_{FePc}). These values are in agreement with the theoretical values (0.84 wt% and 0.42 wt% for nitrogen and iron, respectively), demonstrating the successful incorporation of the iron precursor into the different carbon materials. Lastly, the incorporation of FePc in N–X samples results in materials with similar nitrogen contents as those obtained by the functionalization only with melamine, as the amount of nitrogen incorporated due to FePc is really low in comparison with the amount of nitrogen introduced due to melamine. However, interesting differences in the percentage of iron are observed. The iron contents in the microporous samples N-CG_{FePc} and N-AG_{FePc} are lower than those registered for CG_{FePc} and AG_{FePc}, which could be explained by the previous functionalization process performed to incorporate nitrogen. Samples N-CG and N-AG exhibited lower microporosity (Fig. 1 and Table S1), and hence, a reduced number of pores. Therefore, the probability of incorporating FePc inside the porous structure is reduced and, consequently, FePc is preferentially located on the surface. However, the surface chemistry was

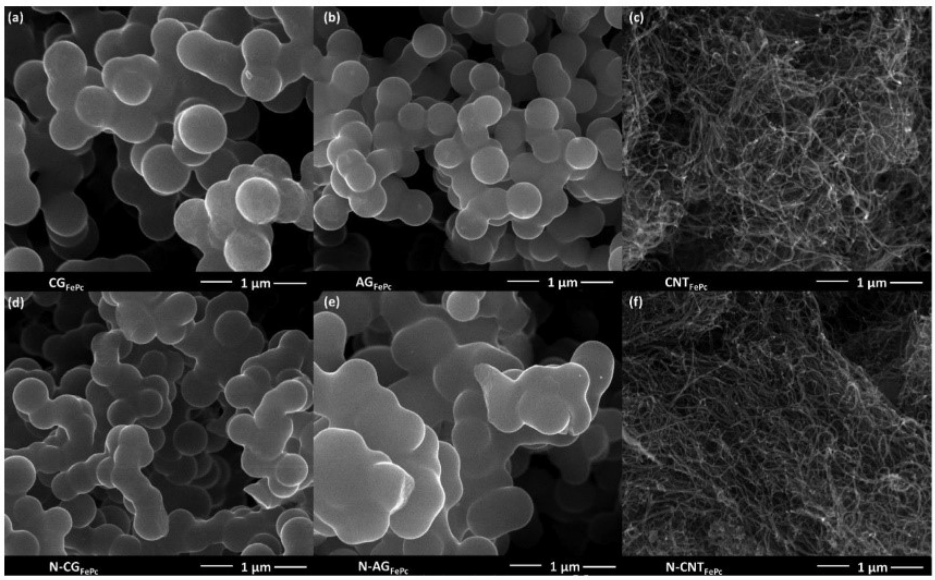


Fig. 3. SEM micrographs of CG_{FePc} (a), AG_{FePc} (b), CNT_{FePc} (c), N-CG_{FePc} (d), N-AG_{FePc} (e) and N-CNT_{FePc} (f).

also modified by the functionalization with nitrogen, which could have resulted in a lower affinity between FePc and the carbon structure, and therefore, a lower amount of precursor is incorporated. These differences are not observed between N-CNT_{FePc} and CNT_{FePc} due to the lack of microporosity, resulting in the incorporation of the same iron content (0.4 wt%). The surface chemistry of the prepared material was determined by X-ray spectroscopy (XPS) to evaluate this hypothesis. The results obtained from the surface composition of N–X samples suggest that the microporosity of glucose-derived carbons and the bundles of CNT favor the incorporation of the nitrogen functionalities in the bulk (HTC carbons) or in the free space of CNT bundles, as a decrease of 2 wt% of the nitrogen content (Table 1) is observed between the values obtained from elemental analysis and those obtained by XPS. In the case of the samples impregnated with FePc, notorious differences were observed due to the nature of the carbon support. The percentages of nitrogen and iron of samples CG_{FePc} (2.9 wt% and 1.6 wt%, respectively) and CNT_{FePc} (1.8 wt% and 0.7 wt%, respectively) suggest that the incorporation of FePc occurred mainly on the surface due to a higher content of both elements than the total theoretical content (0.84 wt% and 0.42 wt%, respectively). Conversely, AG_{FePc} presents neither nitrogen nor iron functionalities on the surface, despite ICP analysis confirming the presence of iron in the structure. These results suggest that the FePc precursor is incorporated inside the porous structure, which is corroborated by the decrease of S_{BET} (13%), and hence, it is not detected by XPS. On the other hand, N–X_{FePc} samples exhibit an increase of the nitrogen content in comparison to their N–X counterparts, which confirms the incorporation of FePc on the surface, even for sample N-AG_{FePc}. This effect could be due to the initial functionalization process, that blocks some of the pores of the activated sample, favoring the incorporation of FePc on the surface of the N-AG_{FePc} sample.

The high-resolution XPS spectra in the C 1*s*, N 1*s* and Fe 2*p* regions were deconvoluted to identify the different types of functionalities existing on the surface of the prepared electrocatalysts (Figs. S3, S4 and S5, respectively). The deconvolution of the C 1*s* spectra of the base samples (CG, AG and CNT) led to the following five main peaks: (i) carbon sp^2 (C=C, first peak) at 284.6 ± 0.1 eV, (ii) carbon present in ether, alcohol or phenol bonds (C–O) at 285.6 ± 0.2 eV (Peak II), (iii) quinone or carbonyl (C=O) 286.8 ± 0.2 eV (Peak III), (iv) carboxyl groups (COOH) at 289.0 ± 0.3 eV (Peak IV) and (v) the shake-up satellite due to π–π^* transitions in aromatic rings (Peak V) at binding energies higher than 290 eV. The appearance of Peaks II, III and IV in CG and AG demonstrates the presence of oxygen, which is in agreement with the results from elemental analysis. However, both samples presented a low contribution of Peak V, which suggests a low contribution of the π–π^* transitions. The C 1*s* spectrum of the CNT corroborates the low content of oxygen obtained by elemental analysis due to the lack of Peak IV and the small contribution of Peaks II and III. Besides, the large contribution of peak V suggests the presence of a high amount of π–π bonds in CNT. The deconvolution of the C 1*s* spectra of the N–X samples shows that the intensities of Peaks II and III increase due to the functionalization with nitrogen. These binding energies are also attributed to C–N and C=N bonds. Therefore, the higher intensity of these two peaks suggests the formation of C–N and C=N groups in the N–X samples. Furthermore, the formation of carbon nitrides during the decomposition of melamine may have led to the formation of N=C-(N_2) bonds detected at a binding energy of 288.7 eV, which is overlapped with the peak attributed to COOH (Peak IV). The low oxygen content of N-CNT suggests that the appearance of this peak is not due to formation of COOH, but due to the decomposition of melamine into carbon nitride, which corroborates the

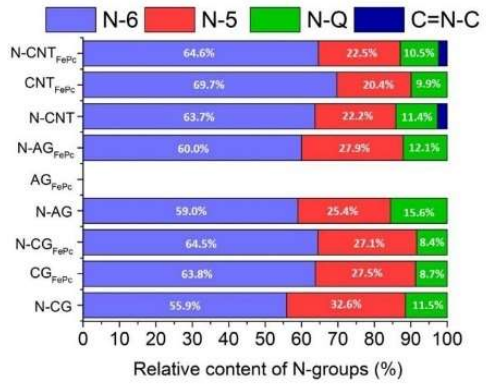


Fig. 4. Relative contents of the nitrogen functionalities in the carbon samples functionalized with melamine and/or that incorporated FePc.

assumption made in the elemental analysis about the carbon nanotubes presenting a high percentage of nitrogen due to the formation of carbon nitrides. In the case of the microporous samples, the contribution of this peak is hindered by the high contribution of oxygen functionalities. However, as the functionalization method applied was the same as in N-CNT, and high quantities of nitrogen were detected (Table 1), the contribution of the Peak IV is probably due to both COOH and N=C-(N_2).

The deconvolution of the N 1s region is crucial to further understand the functionalities of the prepared samples and their effect on the ORR mechanism (Fig. S4). Generally, the deconvolution of N-doped carbons presents three main peaks representing the following nitrogen functionalities: (i) pyridinic nitrogen (N-6) at 398.5 ± 0.2 eV, (ii) pyrrolic nitrogen (N-5) at 399.9 ± 0.2 eV and (iii) quaternary nitrogen (N-Q) at 401.0 ± 0.2 eV. The incorporation of nitrogen using melamine allows the formation of these three main functionalities. Furthermore, a fourth peak was observed at 405.0 ± 0.2 eV in samples N-CNT and N-CNT$_{FePc}$, corresponding to C=N–C in carbon nitrides, corroborating the previous hypothesis. Additionally, the peak corresponding to Fe–N_x bonds is ascribed to similar binding energy as that of the N-5 peak, which results in an overlap of both peaks [3,31]. Therefore, in the X_{FePc} and N–X_{FePc} series, the pyrrolic peak will also include the contribution of Fe–N_x bonds. The relative content of each nitrogen functionality is presented in Fig. 4.

The relative content of N-6 in N–X samples increases with the degree of graphitization of the initial sample (CG<AG<CNT). Besides, a low relative content of N–Q is observed, due to the low temperature employed for the functionalization [45,46]. The incorporation of FePc results in materials with different nitrogen functionalities. In CG$_{FePc}$ and CNT$_{FePc}$, the peaks attributed to N-6 and N-5 groups appear due to the presence of the FePc (the iron complex is mainly composed of 90.5% of N-6 and 9.5% of N-5, as shown in the deconvolution of the N 1*s* spectrum presented in Fig. S6). Besides, the iron precursor reacts with the carbon structure generating N–Q groups due to dehydrogenation of pyridinic nitrogen followed by an atomic rearrangement [47]. On the other hand, the nitrogen functionalities were not detected in sample AG$_{FePc}$. As explained before, FePc is probably located in the interior of the porous structure (Fig. 2) and, therefore, it is not detected by XPS. Similar to the samples functionalized with nitrogen (N–X series), the incorporation of FePc in N–X samples results in materials with the three nitrogen functionalities (N-6, N-5 and N–Q). Besides, the amount of the N-6 group is higher than that present in the N–X samples due to the presence of the nitrogen functionalities attributed to FePc.

The deconvolution of the Fe 2*p* spectra of samples CG$_{FePc}$ and N-CG$_{FePc}$ resulted in two different peaks and their respective spin-orbit splitting at + 13.1 eV: i) Fe^{2+} at 710.4 eV and ii) Fe^{3+} at 712.3 ± 0.1 eV (Fig. S5) [48]. These results demonstrate the co-existence of both Fe^{2+} and Fe^{3+} species in the carbon structure. Samples CNT$_{FePc}$ and N-CNT$_{FePc}$ exhibited the same two peaks but at lower binding energies, 709.1 eV and 711.0 eV, respectively, due to the different carbon structure of CNT. To further assess the successful incorporation of FePc in the carbon structures, EDS and elemental mapping measurements were performed. All samples containing FePc presented an iron content between 1.4 wt% and 1.9 wt%. Besides, the mapping images of N-CG$_{FePc}$ and N-CNT$_{FePc}$ (Fig. S7) demonstrate that iron is homogeneously dispersed across the mapping region.

3.3. Electrochemical assessment

The cyclic voltammograms (CV) of carbonized, activated and CNT samples recorded in an N_2-saturated 0.1 mol L^{-1} KOH electrolyte at 5 mV s^{-1} scan rate are displayed in Fig. 5(a–c).

The voltammograms of the carbonized (CG) and activated (AG) samples display similar intensities. However, interesting differences in the shape of the CV are observed, which could be due to the different textural properties between CG and AG. Sample CG has lower microporosity than AG, which results in a slower diffusion of the electrolyte, and consequently, in the appearance of a plateau at potentials lower than 0.35 V. Conversely, the voltammograms of the CNT series exhibit remarkably low current densities (Fig. 5(c)), indicating that the electrocatalytic activity is almost inexistent under these conditions. However, it should be noted in the voltammogram of sample CNT$_{FePc}$ (Fig. 5(c)) the appearance of two very small peaks, one reduction peak and one oxidation peak at 0.78 V and 0.83 V, respectively. In order to further evaluate these peaks, cyclic voltammetry tests at a higher scan rate (100 mV s^{-1}) were performed (Fig. S8). In this case, two reduction and two oxidation peaks are identified. The reduction peak at lower potentials (0.23 V) can be associated with the reduction processes within the Pc ring, whereas the reduction peak at higher potentials (0.78 V) may be caused by the redox pair Fe(III)/Fe(II) [4,34]. The appearance of these peaks only in the sample CNT$_{FePc}$ (the CV of CG$_{FePc}$ and AG$_{FePc}$ do not exhibit any similar peak, as shown in Fig. S8) can be explained by the different electron transport mechanism between glucose-derived carbons and CNT. Although FePc presents low electrical conductivity [24,49], the neighboring of the material in which the iron is incorporated is crucial to determine the electroactivity of the metal complex. FePc achieves high current densities in the presence of the π-electron systems in carbon materials, which are responsible for increasing the coupling of electrons around FePc [34]. Therefore, the low content of $\pi-\pi^*$ transitions in glucose-derived samples detected by XPS does not favor the electron coupling of FePc, and hence, the peaks attributed to the redox pair Fe(III)/Fe(II) are not detected. Conversely, in CNT$_{FePc}$, the highly graphitic carbon structure with a significant $\pi-\pi$ system favors the appearance of the redox reactions, and hence, the peaks attributed to the iron are observed. Notwithstanding, despite CNT showing these peaks attributed to the redox pair of iron, it can be concluded that, when the electrolyte was saturated with N_2, all the electrocatalysts prepared exhibited featureless profiles (Fig. 5). Therefore, in the case in which the electrolyte was saturated with O_2, the appearance of any significant peaks would be related to the oxygen reduction reaction (Fig. S9). In this case, all samples displayed one reduction peak that is not observed in N_2-saturated media, thus confirming

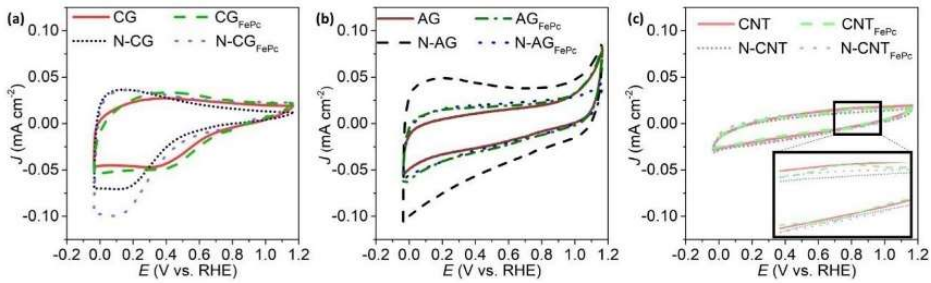


Fig. 5. N_2-saturated cyclic voltammograms for carbonized samples (a), activated samples (b) and CNTs (c) in 0.1 mol L^{-1} KOH electrolyte at 5 mV s^{-1}.

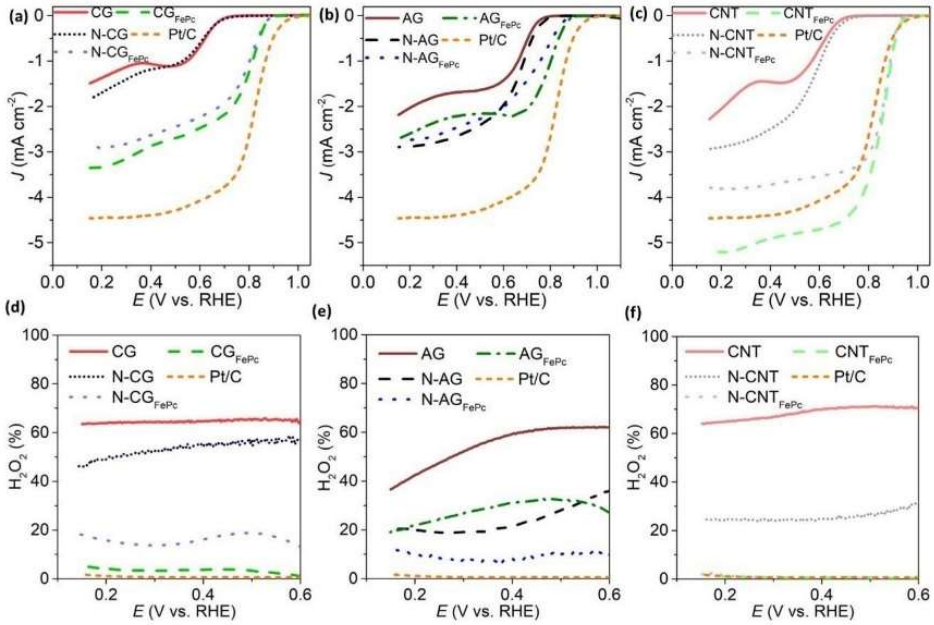


Fig. 6. Linear Sweep Voltammetry recorded in an O_2-saturated 0.1 mol L^{-1} KOH electrolyte at 1600 rpm for carbonized samples (a), activated samples (b) and CNTs (c), and the production of hydrogen peroxide for carbonized samples (d), activated samples (e) and CNTs (f).

the electrocatalytic activity of the electrocatalysts towards the ORR. To further assess the performance of the prepared carbon materials, linear sweep voltammetry was performed and the formation of H_2O_2 was determined. Linear sweep voltammograms of carbonized, activated and CNT samples recorded in an O_2-saturated 0.1 mol L^{-1} KOH electrolyte at 1600 rpm are represented in Fig. 6(a–c), respectively, whereas the formation of H_2O_2 is represented in Fig. 6(d–f), respectively. The onset potential, half-wave potential, limiting current density, kinetic current density, by-products formation and number of electrons exchanged for each electrocatalyst are presented in Table 2.

Activated glucose (AG) exhibited the highest electrocatalytic activity towards ORR (higher E_{onset}, $E_{1/2}$, J_L, and J_k (Table 2)) among the three base samples (CG, AG and CNT) due to the higher developed porous structure [15]. The electroactivity of base samples solely depends on the carbon structure and its properties. In undoped metal-free porous carbon materials, microporosity plays a crucial role in improving the kinetics of ORR [13,15]. Microporosity acts as actives centers during ORR due to the strong adsorption potential of O_2 molecules in the small pores, promoting the electrochemical reaction [13,15]. Therefore, AG exhibits higher electrochemical activity than CG. On the other hand, although CG and CNT present very similar E_{onset} and $E_{1/2}$, CNT provides a much higher J_L and J_k, which can be related to the more graphitic structure of CNT that favors the transportation of electrons, hence rising the current densities observed. The number of electrons exchanged in CG, AG and CNT is closer to 2 electrons than to 4 electrons. These results reveal that O_2 is first reduced to H_2O_2, and

Table 2. Onset potential (E_{onset}), half-wave potential ($E_{1/2}$), limiting current density (J_L), kinetic current density (J_K), hydrogen peroxide (H_2O_2) formation and the number of electrons exchanged (n) for the prepared electrocatalysts and the commercial Pt/C catalyst.

Samples	E_{onset} (V)	$E_{1/2}$ (V)	J_L (mA cm^{-2})	J_K (mA cm^{-2})[a]	H_2O_2 (%)[a]	Electrons exchanged (n)[a]
CG	0.68	0.61	1.49	1.84	65	2.7
N-CG	0.69	0.61	1.84	1.80	54	3.1
CG_{FePc}	0.88	0.82	3.36	5.92	4	3.9
$N\text{-}CG_{FePc}$	0.87	0.82	2.90	6.19	16	3.7
AG	0.80	0.73	2.62	9.07	59	2.8
N-AG	0.78	0.69	2.89	6.78	22	3.6
AG_{FePc}	0.88	0.81	2.71	5.46	31	3.4
$N\text{-}AG_{FePc}$	0.86	0.79	2.70	5.20	8	3.8
CNT	0.69	0.60	2.27	3.15	70	2.6
N-CNT	0.71	0.61	2.94	5.52	25	3.5
CNT_{FePc}	0.94	0.87	5.20	30.55	< 1	4.0
$N\text{-}CNT_{FePc}$	0.93	0.88	3.77	15.85	<1	4.0
Pt/C	0.96	0.83	4.46	17.43	<1	4.0

[a] Calculated at 0.4 V vs. RHE.

then, further reduced to H_2O, which is a two-step reaction (indirect mechanism). As a result, all the base samples exhibit a large formation of H_2O_2 as shown in Fig. 6(d–f). However, although AG produces a lower amount of H_2O_2 than CG and CNT, the production is not stable in all the potential ranges applied, whereas the by-product formation in CG and CNT is linear (Fig. 6(d) and (f), respectively). Although the results obtained for these three base samples are quite interesting, their electrochemical performance is still far from the performance achieved with the commercial Pt/C catalyst (Table 2). Therefore, their properties have been further tailored by the incorporation of nitrogen functionalities and iron.

The incorporation of nitrogen groups in carbon materials by decomposing melamine enhances their electrochemical performance. However, the nature of the carbon material plays a crucial role in the influence of the nitrogen functional groups. The onset potential of N-CG and N-CNT samples increased slightly and the half-wave potential remained almost invariable, whereas in N-AG both E_{onset} and $E_{1/2}$ decrease. These results suggest that not only nitrogen has a little influence over these parameters, but that the microporosity loss in N-AG results in a decrease of these electrochemical variables. Regarding the limiting current density, an increase was observed (23%, 10% and 30% in N-CG, N-AG and N-CNT, respectively), due to the presence of the nitrogen functional groups, that act as active centers towards O_2 reduction. Although the kinetic current density of N-CG remains unchanged in comparison to CG, a remarkable decrease of J_K is observed for N-AG (25%) compared to AG, which demonstrates the effect of microporosity on the reaction kinetics. The kinetic current density increased by 75% in N-CNT, which highlights the importance of nitrogen towards this electrochemical parameter. The number of electrons exchanged in N–X samples is higher than in CG, AG and CNT, due to the presence of the nitrogen functionalities. The presence of quaternary nitrogen results in an electron density movement that enhances O_2 dissociation, whereas N-6 intensifies the bonding of oxygen in nearby carbon atoms [15]. The increase of electrons exchanged to values closer to 4 electrons means that the reaction mechanism is produced via the direct reduction of O_2 to H_2O (a direct mechanism). Therefore, a decrease in the formation of H_2O_2 was observed in N–X samples (Fig. 6(d–f)). However, interesting differences were found in the magnitude of this decrease. The by-product formation of N-CG only decreased by 9% in comparison to CG, whereas the production of H_2O_2 decreased by 37% and 45% in N-AG and N-CNT, respectively, in comparison to their respective base samples. The lower decrease in N-CG can be explained by the lower electroactivity of CG and the lower incorporation of N-6 functionalities (55.9%), which has been reported to play a crucial role in ORR [50,51]. The higher amount of N-6 groups in N-AG and N-CNT (59.0% and 63.7%, respectively), gives rise to a lower amount of by-products. In addition, it should be highlighted that the reaction mechanism for N-AG and N-CNT is very close to the four-electron pathway and the formation of by-products is lower than 25%, which is quite close to the value obtained for the Pt/C electrocatalyst.

The incorporation of FePc in the base carbon materials greatly enhanced their electrochemical performance. However, although FePc complexes may act as active centers towards ORR [30,33], the nature of the carbon support played a crucial role in determining the overall effect of FePc during the electrochemical assessment. The incorporation of FePc in CG (CG_{FePc}) increased the onset potential and half-wave potential by 200 mV and 210 mV, respectively, in comparison to CG, and the limiting current density and kinetic current density by 126% and 222%, respectively. Additionally, the number of electrons exchanged is close to 4 (3.9 electrons) and the by-product formation is almost negligible (4%). Therefore, CG_{FePc} presents remarkable results with very impressive values of E_{onset} and $E_{1/2}$ and a reaction mechanism close to that of Pt/C. The incorporation of FePc in AG (AG_{FePc}) increased the onset potential and half-wave potential from 0.80 V and 0.73 V to 0.88 V and 0.81 V, respectively. Furthermore, the limiting current density increased by 3% and the kinetic current density decreased by 21% in comparison to AG. Additionally, the number of electrons exchanged is closer to 4 electrons (3.4 electrons) and the production of by-product is much lower (31%) than AG, demonstrating the beneficial effect of FePc to achieve a direct reaction mechanism. Although the incorporation of FePc into the glucose-derived carbons results in a significant enhancement of their electrochemical performances, some interesting differences are observed. Regardless of microporosity, samples CG_{FePc} and AG_{FePc} present very similar E_{onset} and $E_{1/2}$, which suggests that the increase of these parameters is due to the presence of FePc. However, J_L and J_K are higher in CG_{FePc}, and the reaction mechanism is also closer to the direct pathway. These results indicate that the incorporation of FePc inside the porous structure (AG_{FePc}) or on the surface (CG_{FePc}) of the carbon materials modifies their electrochemical activities. FePc located on the surface adsorbs O_2 and reduces oxygen in a direct pathway (4 electrons, as observed in CG_{FePc}), whereas FePc located in the bulk requires O_2 to diffuse into the pores to be adsorbed by FePc. This diffusion hinders the overall reduction of oxygen at the FePc active centers, which results in a reaction mechanism with contributions from the reduction of oxygen on the activated carbon surface (two-electron pathway) and from FePc (four-electron pathway), decreasing the values of J_L and J_K. This hypothesis is also corroborated by the number of electrons exchanged, which shows a value of 3.4 for sample AG_{FePc}, the average between the value obtained for AG (2.8 electrons) and the ideal 4 electrons. The incorporation of FePc in CNT (CNT_{FePc}) displayed similar but more marked trends than CG_{FePc}. The onset and half-wave potentials increased to 0.94 V and 0.87 V, respectively,

and J_L and J_k increased by 129% and 870%, respectively, in comparison to CNT. Similarly to the microporous samples, the onset potential of CNT_{FePc} increases due to the presence of FePc. Besides, J_k increases due to the FePc, as microporosity is not a determining factor in CNTs. The reaction mechanism in CNT_{FePc} shifted to the direct pathway, with negligible formation of by-products (< 1%). The lack of porosity favored the incorporation of FePc on the CNT surface leading to a higher number of available active sites. Therefore, the impressive electrocatalytic activity of CNT_{FePc} can be explained by the FePc active sites and the higher electrical conductivity of CNT in comparison to glucose-derived carbon materials [14]. Besides, CNT_{FePc} presents a $E_{1/2}$ 40 mV higher than Pt/C, and a higher limiting current density and kinetic current density (17% and 75%, respectively).

The incorporation of FePc in N–X samples also resulted in highly electrochemically active electrocatalysts. The incorporation of FePc in N-CG (N-CG_{FePc}) increased the E_{onset} and $E_{1/2}$ from 0.69 V to 0.87 V and from 0.61 V to 0.82 V, respectively, whereas J_L and J_K increased by 58% and 244%, respectively, in comparison to N-CG. Furthermore, the number of electrons exchanged is close to 4 (3.7 electrons) and the amount of H_2O_2 determined is 16%, indicating an almost completely direct mechanism. The E_{onset}, $E_{1/2}$ and number of electrons exchanged increased to values closer to those obtained for the Pt/C electrocatalyst, demonstrating that N-CG_{FePc} is a promising electrocatalyst for the ORR. The incorporation of FePc in N-AG (N-AG_{FePc}) increased the onset potential by 80 mV and the half-wave potential by 100 mV, in comparison to N-AG. The limiting current density and kinetic current density slightly decreased, due to a decrease of microporosity (Table S1), demonstrating the importance of keeping the microporosity to achieve high current densities in highly microporous materials. Besides, the reaction mechanism shifted to an almost entirely direct mechanism (3.8 electrons and 8% production of H_2O_2), due to the presence of FePc on the surface of the activated carbon, in comparison to AG_{FePc}. However, it should be highlighted that, in general terms, the electrochemical activities of N–X_{FePc} are lower than those of X_{FePc}. This can be explained by the fact that the functionalization with melamine in glucose-derived samples led to smaller incorporation of FePc, and hence, to a lower electroactivity. The incorporation of FePc in N-CNT led to an increase of E_{onset} and $E_{1/2}$ from 0.71 V to 0.93 V and from 0.61 V to 0.88 V, respectively, and an increase of the J_L and J_k of 28% and 187%, respectively, in comparison to N-CNT. The reaction pathway shifted to a direct mechanism with negligible formation of by-products (< 1%). These results suggest that the incorporation of FePc active sites on the surface of highly graphitic structures further enhances the electroactivity. However, it should be noted that the electroactivity of this sample (N-CNT_{FePc}) is lower than that of CNT_{FePc}. Although both samples exhibit similar iron contents, two very different active sites are present in N-CNT_{FePc}, those from N-groups and those from FePc. FePc is the most active of these two active centers; hence, the less efficient O_2 adsorption, dissociation and desorption over N active centers hinders the overall current densities, resulting in a material with lower J_L and J_k (N-CNT_{FePc}).

To further evaluate the electrochemical performance of the prepared carbon materials, chronoamperometry measurements were performed by applying a potential of 0.4 V (vs RHE) during 10,000 s. The results obtained are shown in Fig. 7. These experiments allow to determine the retention of the current density of each material over time at the selected potential, to assess the electrocatalysts stability. The stability tests performed for the base samples (CG, AG and CNT) demonstrated that CG and CNT have low stabilities (34.1% and 59.0%, respectively), whereas AG presents very high stability throughout the experiment (89.5%). These results can be related to the activation process that gave rise to a chemically stable material, which resists the possible attack of the basic medium [52]. In addition, AG showed higher stability in its current density than Pt/C (83.6%) at 0.4 V vs RHE, which reflects the electrocatalyst potential for high performances during long-term use.

The incorporation of nitrogen functional groups increases the stability of CG and CNT, with higher impact over the carbonized sample (increase by 37.6% and 11.9% for N-CG and N-CNT, respectively), whereas a slight decrease is observed for sample N-AG (2.6%). Nitrogen functionalities act as active sites in ORR, and therefore, are also pivotal to the stability of the electrocatalysts. In fact, the deterioration of these functional groups could result in a decrease in the measured current density over time. However, the use of an alkaline medium avoids the protonation of the N-6 functional groups [36], which results in the retention of N-6's activity. Furthermore, the existence of strong bonds in N–Q functional groups also favors the retention of the current density [23,36]. Therefore, the stability of samples N-CG and N-CNT is higher than that of CG and CNT. However, this effect is not observed for the activated sample. The decrease in the stability of the N-doped activated sample may be due to the high stability of the initial sample (AG), which could be caused by its high microporosity. Although nitrogen functionalities are important to achieve higher current densities and retention of current density over time, as observed in N-CG and N-CNT, the decrease of retention due to the loss of microporosity in N-AG overcomes the enhancements due to the presence of nitrogen functional groups. Nonetheless, N-AG presents higher retention of current density over time (86.9%) than the commercial catalyst (83.6%), demonstrating its potential for applications that require long operation times. The introduction of the FePc complex led to the same trend as that observed for the samples N–X. However, the use of different carbon supports resulted in stability modifications with different magnitudes. Although the stability of both CG and CNT increased with the incorporation of FePc (30.6% and 24.8%, respectively), an interesting difference is observed. The stability of CG approaches the 65% current density retention, whereas CNT_{FePc} is able to retain 83.6% of the initial current density. This difference of almost 20% may be explained by the higher affinity of FePc to the CNT structure (π electron system) than to the CG structure, resulting in stronger bonds. Additionally, the presence of strong N–Q bonds in CNT_{FePc} (Fig. 4) may play a crucial role in the stability enhancement. The incorporation of FePc in the activated sample (AG_{FePc}) led to a similar decrease of the current density retention (3.1%) as N-AG (2.6%), further corroborating that the highly stable activated structure due to microporosity plays a major role to achieve a high retention of the current density. Similarly to N-AG, AG_{FePc} also exhibits higher stability (86.4%) than Pt/C (83.6%), confirming the potential of this sample for long-term applications. The incorporation of FePc in the N–X series also led to an increase of the stability of N-CG_{FePc} and N-CNT_{FePc}, to 77.8% and 86.7%, respectively. The retention of current density displayed by N-CNT_{FePc} (Fig. 7) is much higher than that of Pt/C, which demonstrates the importance of combining nitrogen functionalities and iron particles to achieve higher stabilities (the stability of N-CNT_{FePc} is 2.9% higher than that of CNT_{FePc}). N-AG_{FePc} also showed a conjugation of the decreases observed in N-AG and AG_{FePc}, achieving stability of 80.5% after 10,000 s. This result further indicates the relevance of microporosity to achieve higher retention of current densities, as the gradual decrease of the surface area in the activated samples led to a decrease of the electrocatalysts stabilities. Therefore, these results suggest that the development of microporosity leads to higher retention of the current density over time and that the nitrogen functionalities act as actives sites, enhancing the stability of electrocatalysts with low performances.

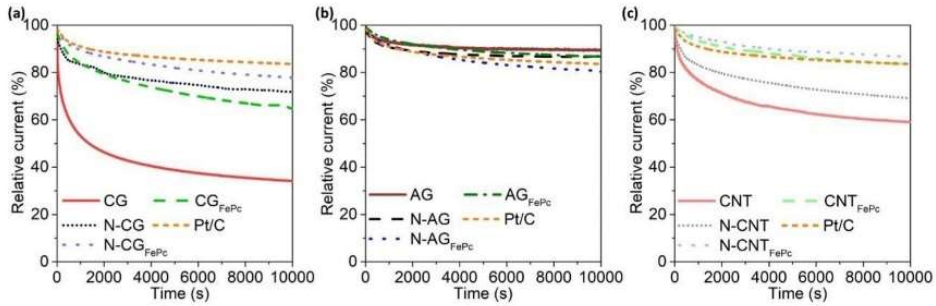


Fig. 7. Chronoamperimetry measurements for carbonized samples (a), activated samples (b) and CNTs (c) applying 0.4 V during 10,000 s at 1600 rpm in 0.1 mol L^{-1} KOH electrolyte.

4. Conclusions

Glucose-derived carbons were prepared by hydrothermal carbonization of glucose followed by carbonization or activation to prepare carbons with different porosities. In addition, commercial CNTs were also used as a carbon electrocatalyst without microporosity. The carbon materials were then doped with nitrogen, FePc and both nitrogen and FePc. Regardless of the microporosity, functionalization with melamine resulted in the incorporation of nitrogen functionalities on the surface of the carbons and the formation of carbon nitrides. Conversely, the incorporation of FePc was greatly influenced by the microporosity. In the highly microporous activated sample, FePc was located inside the porous structure, whereas in the carbonized sample FePc is deposited on the surface. However, functionalization with melamine before the incorporation of FePc modified the preferential location of the metal complex inside the activated sample, leading to the deposition of iron on the surface. Regarding the electrochemical characterization, the incorporation of FePc inside the porous carbon structure gave rise to slower reaction kinetics that hinders the reaction mechanism to achieve the four-electron pathway, while the previous functionalization with melamine shifted the mechanism of the reaction to the four-electron pathway. Regardless of the microporosity of the hydrothermal carbons, the incorporation of FePc resulted in similar onset (0.88 V) and half-wave potentials (0.82 V), demonstrating the crucial role of FePc. Besides, the incorporation of FePc in CNT resulted in an electrocatalyst with a high onset potential (0.94 V) and half-wave potential (0.87 V) with negligible formation of by-products (< 1%). These results are significantly better than those obtained for the commercial catalyst, which makes this sample a promising material to replace Pt/C. Moreover, the preparation of these electrocatalysts with outstanding performance was achieved using the lowest FePc:carbon ratio reported to date, which is an interesting starting point for future work towards optimization/industrialization of carbon materials to produce green energy.

Declaration of Competing Interest

The authors declare that they have no known competing financial interests or personal relationships that could have appeared to influence the work reported in this paper.

Acknowledgments

This work is a result of the projects: "UniRCell", with the reference POCI-01-0145-FEDER-016422; "AIProcMat@N2020 – Advanced Industrial Processes and Materials for a Sustainable Northern Region of Portugal 2020", with the reference NORTE-01-0145-FEDER-000006, supported by Norte Portugal Regional Operational Programme (NORTE 2020), under the Portugal 2020 Partnership Agreement, through the European Regional Development Fund (ERDF); Base Funding – UIDB/50020/2020 of the Associate Laboratory LSRE-LCM – funded by national funds through FCT/MCTES (PIDDAC); and PDEQB (PD9989). The authors are indebted to Dr. Carlos M. Sá (CEMUP) for assistance with XPS analyses and to Dr. Edith A. Avila (SEMAT) for assistance with SEM, EDS and elemental mapping.

Supplementary materials

Supplementary material associated with this article can be found, in the online version, at doi:10.1016/j.jechem.2020.03.039.

References

[1] R. Paul, Q. Dai, C. Hu, L. Dai, Carbon Energy 1 (2019) 19–31.
[2] N. Komba, G. Zhang, Q. Wei, X. Yang, J. Prakash, R. Chenitz, F. Rosei, S. Sun, Int. J. Hydrog. Energy 44 (2019) 18103–18114.
[3] S. Han, X. Hu, X. Fang, Y. Zhu, Adv. Energy Mater. (2018) 1800955.
[4] J. Yang, F. Toshimitsu, Z. Yang, T. Fujigaya, N. Nakashima, J. Mater. Chem. A 5 (2017) 1184–1191.
[5] S. Zhao, D.-W. Wang, R. Amal, L. Dai, Adv. Mater. 31 (2019) 1801526.
[6] K.-H. Wu, M. Allen-Ankins, Q. Zeng, B. Zhang, J. Pan, J. Zhang, D.-S. Su, I.R. Gentle, D.-W. Wang, ChemElectroChem 5 (2018) 1862–1867.
[7] J. Song, T. Liu, S. Ali, B. Li, D. Su, Chem. Phys. Lett. 677 (2017) 65–69.
[8] K. Hyun, T. Ueno, G. Panomsuwan, O.L. Li, N. Saito, Phys. Chem. Chem. Phys. 18 (2016) 10856–10863.
[9] H.T. Chung, D.A. Cullen, D. Higgins, B.T. Sneed, E.F. Holby, K.L. More, P. Zelenay, Science 357 (2017) 479.
[10] C. Goswami, K.K. Hazarika, P. Bharali, Mater. Sci. Energy Technol. 1 (2018) 117–128.
[11] P. Yan, B. Zhang, K.-H. Wu, D. Su, W. Qi, Carbon 143 (2019) 915–936.
[12] L. Yan, J. Yu, J. Houston, N. Flores, H. Luo, Green Energy Environ. 2 (2017) 84–99.
[13] D. Barrera, M. Florent, M. Kulko, T. Bandosz, J. Mater. Chem. A 7 (2019).
[14] R.G. Morais, N. Rey-Raap, R. Costa, C. Pereira, A. Guedes, J.L. Figueiredo, M.F.R. Pereira, J. Compos. Sci. 4 (2020) 1–14.
[15] R.G. Morais, N. Rey-Raap, J.L. Figueiredo, M.F.R. Pereira, Beilstein J. Nanotechnol. 10 (2019) 1089–1102.
[16] Y. Li, Q. Li, H. Wang, L. Zhang, D.P. Wilkinson, J. Zhang, Electrochem. Energy Rev. 2 (2019) 518–538.
[17] H.A. Miller, M. Bellini, W. Oberhauser, X. Deng, H. Chen, Q. He, M. Passaponti, M. Innocenti, R. Yang, F. Sun, Z. Jiang, F. Vizza, Phys. Chem. Chem. Phys. 18 (2016) 33142–33151.
[18] B. Jeong, D. Shin, M. Choun, S. Maurya, J. Baik, B.S. Mun, S.-H. Moon, D. Su, J. Lee, J. Phys. Chem. C 120 (2016) 7705–7714.
[19] K.H. Wu, W. Shi, D. Wang, J. Xu, Y. Ding, Y. Lin, W. Qi, B. Zhang, D. Su, Chem. Mater. 29 (2017) 4649–4653.
[20] D.-S. Yang, M.Y. Song, K.P. Singh, J.-S. Yu, Chem. Commun. 51 (2015) 2450–2453.
[21] Y. Liu, Y.-S. Fan, Z.-M. Liu, Chem. Eng. J. 361 (2018).
[22] B. Liang, S. Guo, Y. Zhao, I.U. Khan, X. Zhang, K. Li, C. Lv, J. Power Sour. 450 (2020) 227683.

[23] Z. Yan, C. Dai, M. Zhang, X. Lv, X. Zhao, J. Xie, Int. J. Hydrog. Energy 44 (2019) 4090–4101.
[24] J. Yang, J. Tao, T. Isomura, H. Yanagi, I. Moriguchi, N. Nakashima, Carbon 145 (2019) 565–571.
[25] Y. Liu, B. Huang, X. Zhang, X. Huang, Z. Xie, J. Power Sour. (2019) 125–133.
[26] Z. Zhang, M. Dou, J. Ji, F. Wang, Nano Energy 34 (2017) 338–343.
[27] Y. Zhu, B. Zhang, Z. Feng, D.S. Su, Catal. Today 260 (2016) 112–118.
[28] C. Zhang, R. Hao, H. Yin, F. Liu, Y. Hou, Nanoscale 4 (2012) 7326–7329.
[29] A. Iannaci, B. Mecheri, A. D'Epifanio, M.J.L. Elorri, S. Licoccia, Int. J. Hydrog. Energy 41 (2016) 19637–19644.
[30] C. Santoro, R. Gokhale, B. Mecheri, A. D'Epifanio, S. Licoccia, A. Serov, K. Artyushkova, P. Atanassov, ChemSusChem 10 (2017) 3243–3251.
[31] G. Dakai, S. Han, Y. Zhu, Appl. Surf. Sci. 434 (2017).
[32] Y. Liu, Y.S. Fan, Z.M. Liu, Chem. Eng. J. (2019) 416–427.
[33] A. Alsudairi, J. Li, N. Ramaswamy, S. Mukerjee, K.M. Abraham, Q. Jia, J. Phys. Chem. Lett. 8 (2017) 2881–2886.
[34] T. Koczorowski, W. Szczolko, T. Goslinski, Physicochemical properties and catalytic applications of iron porphyrazines and phthalocyanines, Recent Progress in Organometallic Chemistry, Intech Open, 2017.
[35] M. Canal-Rodríguez, N. Rey-Raap, J.Á. Menéndez, M.A. Montes-Morán, J.L. Figueiredo, M.F.R. Pereira, A. Arenillas, Microporous Mesoporous Mater. 293 (2020) 109811.
[36] G. Liu, X. Li, B. Popov, ECS Trans. 25 (2009).
[37] R.-M. Ion, Photosensit. Med. Environ. Secur. (2012) 315–349.
[38] A. Solhy, B.F. Machado, J. Beausoleil, Y. Kihn, F. Gonçalves, M.F.R. Pereira, J.J.M. Órfão, J.L. Figueiredo, J.L. Faria, P. Serp, Carbon 46 (2008) 1194–1207.
[39] A. Bonakdarpour, T. Dahn, R. Atanasoski, M. Debe, J. Dahn, Electrochem. Solid State Lett. 11 (2008).
[40] R. Kecili, C.M. Hussain, Chapter 4 – Mechanism of adsorption on nanomaterials, in: C.M. Hussain (Ed.), Nanomaterials in Chromatography, Elsevier, 2018, pp. 89–115.
[41] H.-S. Zhai, L. Cao, X.-H. Xia, Chin. Chem. Lett. 24 (2013) 103–106.
[42] N. Rey-Raap, M. Enterría, J.I. Martins, M.F.R. Pereira, J.L. Figueiredo, ACS Appl. Mater. Interfaces 11 (2019) 6066–6077.
[43] E.N. Gribov, A.N. Kuznetsov, V.A. Golovin, D.V. Krasnikov, V.I. Kuznetsov, Mater. Renew. Sustain. Energy 8 (2019) 7.
[44] Z.-H. Sheng, L. Shao, J.-J. Chen, W.-J. Bao, F.-B. Wang, X.-H. Xia, ACS Nano 5 (2011) 4350–4358.
[45] K. Stańczyk, R. Dziembaj, Z. Piwowarska, S. Witkowski, Carbon 33 (1995) 1383–1392.
[46] M. Xiao, J. Zhu, L. Ma, Z. Jin, J. Ge, X. Deng, Y. Hou, Q. He, J. Li, Q. Jia, S. Mukerjee, R. Yang, Z. Jiang, D. Su, C. Liu, W. Xing, ACS Catal. 8 (2018) 2824–2832.
[47] X.-F. Li, K.-Y. Lian, L. Liu, Y. Wu, Q. Qiu, J. Jiang, M. Deng, Y. Luo, Sci. Rep. 6 (2016) 23495.
[48] K. Moura, R. Lima, A. Coelho, E. Souza-Junior, J. Duque, C. Meneses, Nanoscale 6 (2013).
[49] T.A. Jones, B. Bott, Sens. Actuat. 9 (1986) 27–37.
[50] D. Guo, R. Shibuya, C. Akiba, S. Saji, T. Kondo, J. Nakamura, Science 351 (2016) 361.
[51] N. Zhou, N. Wang, Z. Wu, L. Li, Catalysts 8 (2018) 509.
[52] W.M.T.M. Reimerink, The use of activated carbon as catalyst and catalyst carrier in industrial applications, in: A. Dąbrowski (Ed.), Studies in Surface Science and Catalysis, Elsevier, 1999, pp. 751–769.

Applied Surface Science 572 (2022) 151459

Contents lists available at ScienceDirect

Applied Surface Science

journal homepage: www.elsevier.com/locate/apsusc

Full Length Article

Fe, Co, N-doped carbon nanotubes as bifunctional oxygen electrocatalysts

R.G. Morais [a], N. Rey-Raap [a,b,*], J.L. Figueiredo [a], M.F.R. Pereira [a,*]

[a] Laboratory of Separation and Reaction Engineering – Laboratory of Catalysis and Materials (LSRE LCM), Departamento de Engenharia Química, Faculdade de Engenharia, Universidade do Porto, R. Dr. Roberto Frias s/n, 4200 465 Porto, Portugal
[b] Department of Physical and Analytical Chemistry, Oviedo University-CINN, 33006, Oviedo, Spain

ARTICLE INFO

Keywords:
Phthalocyanine
Carbon Nanotube
Oxygen Reduction Reaction
Oxygen Evolution Reaction
Unitized Regenerative Fuel Cell

ABSTRACT

Carbon nanotubes were modified towards oxygen reduction and evolution reactions by incorporation of cobalt and/or iron phthalocyanines (CoPc and FePc, respectively). The obtained monometallic samples were physically mixed in different ratios to assess the importance of each phthalocyanine. The increase of FePc content enhanced the electroactivity towards the oxygen reduction reaction, especially the limiting current density and reaction mechanism, for which two relationships were found by varying the CoPc:FePc mass ratio. Samples with a mass ratio (FePc:CoPc) ≥ 1 surpassed the electroactivity of the current commercial electrocatalyst (Pt/C) and presented similarly high long-term durability (82–85%). Interestingly, a synergetic effect between both types of metallic active centers was observed for the oxygen evolution reaction. A 1:1 CoPc:FePc mass ratio provided the highest oxygen evolution reaction electroactivity, displaying a potential of 1.67 V at 10 mA cm $^{-2}$, higher than that of the commercial RuO_2 catalyst (1.58 V). This sample also presented the lowest potential gap (0.81 V), which is much lower than that of Pt/C (1.20 V) and RuO_2 (1.41 V), demonstrating the high potential of these materials as substitutes of noble metal electrocatalysts.

1. Introduction

The escalating world industrialization, population, and increasing use of portable electronic devices are leading to a significant increase in the global energy demand. Moreover, a transition from fossil fuels to renewable green energies is crucial for the planet's sustainability [1,2]. Nonetheless, due to the intermittency of renewable energies, there is a need to store energy when its production is higher than the demand and reconvert stored power into electrical energy when the demand is higher than its production. Therefore, the combination of conversion and storage devices is of utmost importance to achieve maximum energy efficiency. Regarding conversion devices, fuel cells are known to be environmentally friendly energy conversion systems with high efficiencies and non-polluting products [3,4]. Additionally, a coupled electrolyzer can use the low power inputs of the renewable energies to split water and generate the necessary fuels for the conversion device [5]. A compact system consisting of a fuel cell and an electrolyzer in a single electrochemical cell (the unitized regenerative fuel cell (URFC)) is one of the most promising devices regarding the future of green energy [1,5–8]. This device involves four different electrochemical reactions: the oxygen reduction reaction (ORR) and the hydrogen oxidation reaction (HOR) that take place in the fuel cell mode, and the oxygen evolution reaction (OER) and the hydrogen evolution reaction (HER) that take place in the electrolyzer mode. The most mature URFC technology is the proton-exchange membrane fuel cell (PEMFC) [1,5,9,10], which operates under acidic conditions, but the corresponding benchmark catalysts are based on noble metals which are scarce and increase the overall cost of the device [11]. To compete with PEMFC, a technology that has gained increased scientific interest as an alternative towards future energy sustainability is the use of anion-exchange membrane fuel cells (AEMFC), which operate under basic conditions [11–13]. Non-precious metal catalysts are reported to achieve high catalytic efficiencies and long-term stability in alkaline media [12]. Consequently, a basic medium opens the possibility to use a wider range of materials as electrocatalysts in comparison to acidic media that mostly favor noble metals and their oxides [1,5–7,9]. Nonetheless, the sluggish kinetics of the URFC's oxygen reactions (ORR and OER) hinders the round-trip efficiency of the device and requires further investigation to optimize the overall performance of the URFC without the use of noble-metals [1]. Carbon materials are an interesting alternative to the benchmark

* Corresponding authors at: Laboratory of Separation and Reaction Engineering – Laboratory of Catalysis and Materials (LSRE-LCM), Departamento de Engenharia Química, Faculdade de Engenharia, Universidade do Porto, R. Dr. Roberto Frias s/n, 4200-465 Porto, Portugal.
E-mail addresses: nataliarey@fe.up.pt (N. Rey-Raap), fpereira@fe.up.pt (M.F.R. Pereira).

https://doi.org/10.1016/j.apsusc.2021.151459
Received 30 July 2021; Received in revised form 14 September 2021; Accepted 27 September 2021
Available online 29 September 2021
0169-4332/© 2021 Elsevier B.V. All rights reserved.

catalysts, due to their lower costs and wider availability [14]. Moreover, the possibility to tune the properties of carbon materials is essential for the optimization of their electroactivity [15,16]. A wide variety of carbon materials such as porous carbons [17–19], carbon nanotubes [19–22], and graphene [21–24] have been studied as bifunctional electrocatalysts for ORR and OER, achieving interesting results. The introduction of different heteroatoms (nitrogen [17–21,23–27], phosphorus [18,24], and sulfur [21,22,28]) into the carbon structures is a common strategy used to modulate the catalyst's chemical properties. The incorporation of transition metals is also a much-studied subject to achieve bifunctional oxygen electrocatalysts [29–31]. Furthermore, the synergy between transition metals and heteroatoms, in particular nitrogen and sulfur, has been reported to highly increase the electroactivity of carbon materials [32–41]. Transition metals and heteroatoms can be found in a single precursor, especially by using macrocycles with both elements. The use of macrocycles can lead to a decrease in production costs, as it allows incorporating the metal and heteroatom in a single-step thermal treatment [42]. The most commonly used macrocycles are the metal-centered phthalocyanines (Pcs), particularly cobalt (II) phthalocyanine (CoPc) and iron(II) phthalocyanine (FePc). FePc has been widely studied towards the ORR [42–48]. These studies suggest that FePc is highly electroactive towards the ORR and favors the direct reduction of oxygen through the 4-electron mechanism [41,49]. Although CoPc is electroactive in ORR, this macrocycle presents lower current density than FePc and high formation of by-products, requiring further tailoring [44,50]. On the other hand, there is a lack of knowledge about the electrochemical behavior of these two Pcs (CoPc and FePc) when they are incorporated together on the same carbon surface, i.e., the synergy between them towards the ORR and OER. Moreover, despite the enhanced electrochemical performance of Pcs, major gaps still exist in the literature regarding the bifunctionality of these macrocycles. In fact, the combination of these phthalocyanines in a single carbon support as bifunctional oxygen electrocatalyst has not yet been reported.

This work aims to prepare carbon electrocatalysts with high electrocatalytic activity towards ORR and OER. Carbon nanotubes (CNTs) were used as carbon support due to the synergy of their π-π systems with phthalocyanines, which is important to enhance their electroactivity towards ORR and OER [42,51,52]. A very small amount of CoPc and/or FePc was incorporated on the CNTs to maintain a low production cost of the electrocatalysts. Furthermore, CoPc and FePc were added separately into the CNTs, to study the effect of each individual macrocycle on both reactions. Additionally, CoPc and FePc were incorporated simultaneously on the CNTs following different methodologies, achieving remarkable improvements compared to the incorporation of a single Pc.

2. Experimental

2.1. Preparation of electrocatalysts

Purified multi-walled carbon nanotubes (sample CNT) were used for the development of highly electroactive bifunctional ORR/OER electrocatalysts. Briefly, commercial CNTs (Nanocyl, > 95% C) underwent reflux at 140 °C for 4 h in a 1:1 (v/v) ratio solution of sulfuric acid (95%, VWR Chemicals) and distilled water (produced by filtration through inverse osmosis in a Panice equipment) to remove impurities. Afterwards, CNTs were washed with hot distilled water until a neutral pH was achieved and dried at 120 °C for 1 day. The purified CNTs were then tailored by incorporating two different Pcs: cobalt(II) phthalocyanine (CoPc, Sigma-Aldrich, 97%) and iron(II) phthalocyanine (FePc, Sigma-Aldrich, 90%). Pcs were incorporated by the incipient wetness impregnation method. Briefly, 50 mg of the selected macrocycle per g of CNT was dissolved in ethanol and added dropwise to CNT under sonication, maintained in the ultra-sonication bath for 30 min and dried overnight at 100 °C, followed by a thermal treatment in N_2 atmosphere at 500 °C for 2 h. This temperature was selected based on previously published research works, in which it was demonstrated that FePc suffers degradation at temperatures of 600 °C and higher [42,53]. Furthermore, these works demonstrate high electroactivity of FePc between 500 °C and 700 °C; therefore, 500 °C was the selected temperature. The introduction of cobalt and iron macrocycles led to samples CNT_{Co} and CNT_{Fe}, respectively.

Four different methodologies were studied to assess the optimal procedure to incorporate both molecules: i) incorporation of CoPc on the CNT_{Fe} sample ($CNT_{Fe\ Co}$); ii) incorporation of FePc on the CNT_{Co} sample ($CNT_{Co\ Fe}$), iii) incorporation of CoPc and FePc on the CNTs by a single-step impregnation process (CNT_{CoFe}), following the methodology described above for a single metal; and iv) sample CNT_{Co} and CNT_{Fe} were weighted using a 1:1 (m/m) ratio and physically mixed for a few minutes until a visually homogeneous mixture was obtained ($50CNT_{Co}$/$50CNT_{Fe}$). The sample obtained after mixing was used directly as catalyst without any further modification, hence avoiding the formation of a cobalt-iron alloy as no thermal treatment took place after mixing. It should be noted that the $50CNT_{Co}$/$50CNT_{Fe}$ sample presents only half of the total metal loading in comparison to CNT_{Fe_Co}, CNT_{Co_Fe}, and CNT_{CoFe}. These four materials were electrochemically characterized and the results obtained are shown in Fig. S1. The electrochemical measurements (Fig. S1) showed that the best procedure to achieve a bifunctional material was the physical mixture of CNT_{Fe} and CNT_{Co}, i.e. sample $50CNT_{Co}$/$50CNT_{Fe}$. To further optimize the electrocatalysts' preparation process, a sample following the same methodology as $50CNT_{Co}$/$50CNT_{Fe}$ was prepared by adding twice the amount of CoPc and FePc. This synthesized electrocatalyst ($50CNT_{2Co}$/$50CNT_{2Fe}$) was used to determine the best metal loading on the CNTs. The incorporation of twice the amount of macrocycle molecules did not result in a higher performance towards ORR/OER (Fig. S2). Therefore, the physical mixture using 50 mg of CoPc/FePc molecules per g of CNT ($50CNT_{Co}$/$50CNT_{Fe}$) was selected as the best procedure according to the electrochemical results displayed in the supporting information (Fig. S1 and Fig. S2). In addition, samples CNT_{Co} and CNT_{Fe} were physically mixed using two additional CNT_{Co}:CNT_{Fe} ratios, 3:1 (m/m) (sample $75CNT_{Co}$/$25CNT_{Fe}$) and 1:3 (m/m) (sample $25CNT_{Co}$/$75CNT_{Fe}$).

2.2. Textural and chemical characterization

The chemical composition of the prepared carbon materials was obtained by elemental analysis. A Vario Micro Cube analyzer (Elementar GmbH) was used to determine the carbon, hydrogen, and nitrogen (C, H, and N) contents by sample combustion at 1050 °C. A Rapid Oxy Cube analyzer (Elementar GmbH) was used to determine each sample's oxygen content by pyrolysis at 1450 °C. Each sample was analyzed in triplicate. The quantification of cobalt and/or iron loading on each sample was performed by inductively coupled plasma (ICP) emission spectrometry. The analyses were carried out in a Perkin Elmer Optima 4300 spectrometer using an optic with Echelle polychromator. Furthermore, the samples' surface chemical composition was determined by X-ray photoelectron spectroscopy (XPS). The analyses were performed in a Kratos AXIS Ultra HAS spectrometer using a monochromatic Al $K\alpha$ radiation (1486.7 eV) at 15 kV (90 W) in fixed analyzer transmission mode. To observe the morphology of the CNT samples and the elemental map distribution, a Nova NanoSEM 200 (FEI Company) was used to perform scanning electron microscopy (SEM) and energy dispersive spectroscopy (EDS). The samples, in powder form, were previously attached to an aluminum pin using conductive carbon double-sided adhesive tape. An Everhart-Thornley detector (ETD) and a backscattered electron detector (BSTD) were used as secondary detectors during SEM analyses, and a Si(Li) detector was used for EDS and mapping analyses. A JEOL 2200 FS apparatus was used to perform transmission electron microscopy (TEM). Raman spectra were measured directly on the carbon materials using an Alpha 300 apparatus (WiTec, Germany) with a monochromatic wavelength laser of 532 nm. The textural properties of the synthesized carbon materials were obtained by N_2 adsorption at −196 °C performed in a Quantachrome Autosorb iQ

automated gas sorption analyzer. All samples were degassed under vacuum at 150 °C for 12 h before the analyses. The Brunauer-Emmett-Teller (BET) equation was used to determine the specific surface area (S_{BET}), and the volume of nitrogen adsorbed at the saturation point (relative pressure of 0.99) was considered as the total pore volume (V_p).

2.3. Electrochemical characterization

The electrochemical characterization of the prepared carbon electrocatalysts was performed in a PGSTAT 302 N potentiostat/galvanostat using a three-electrode cell configuration. A glassy carbon rod and an Ag/AgCl (KCL 3 mol L^{-1}) electrode were used as counter and reference electrodes, respectively, for the ORR measurements, whereas a Pt foil was used as a counter electrode for the OER assessments. Working electrodes were prepared by deposition of a prepared suspension of the synthesized materials on a glassy carbon disk-platinum ring electrode (RRDE 5 mm in diameter, 24.9% collection efficiency, Methrom) for cyclic voltammetry (CV) and linear sweep voltammetry (LSV) during ORR measurements. A glassy carbon rotating disk electrode (RDE 3 mm in diameter, Metrohm) was used as a working electrode for ORR chronoamperometric tests, OER assessments, and for the CV performed to calculate the double-layer capacitance (C_{dl}).

The suspensions were obtained by dispersing 4 mg of the carbon sample in a solution containing 80 μL of Nafion (5 wt% in lower aliphatic alcohols and water, Sigma-Aldrich), 80 μL of ethanol (≥99.5%, VWR Chemicals), and 470 μL of ultrapure water (Millipore). The suspension was sonicated for at least 30 min until a homogeneous dispersion was obtained prior to deposition. The mass loading of all samples was ca. 0.8 mg cm^{-2}. The electrochemical measurements were carried out at room temperature in a 0.1 mol L^{-1} KOH solution saturated with N_2 or O_2 for 30 min before performing the specific electrochemical experiments. The ORR assessments consisted of CV and LSV experiments in both N_2 and O_2-saturated media. The CV measurements were accomplished at scan rates of 5, 20, 60, and 100 mV s^{-1}, and the LSV at a scan rate of 5 mV s^{-1} with a rotation speed ranging from 400 to 3000 rpm (applied to the working electrode by a rotation speed controller). The potential range employed for the CV and LSV was between 1.10 V and −0.05 V (vs RHE). The experimental current from LSV and CV was determined by subtracting the current obtained from the electrolyte saturated with N_2 from the current measured in the O_2-saturated medium. Different electrochemical parameters were obtained from the LSV data: (i) onset potential (E_{onset}), which value was considered at a current density of 0.1 mA cm^{-2}; (ii) half-wave potential ($E_{1/2}$), determined from the derivative of the current–potential curve, in which a maximum value, corresponding to half the diffusion-limited current, is ascribed to $E_{1/2}$ [54]; (iii) the potential at which a current density of 3 mA cm^{-2} was achieved (E_3); and iv) the limiting current density measured at 0.4 V vs RHE (J_L). Furthermore, the disk and ring currents obtained from the RRDE LSV were used to calculate the percentage of hydrogen peroxide (H_2O_2) produced and the number of electrons transferred during the ORR. The H_2O_2 percentage and the number of electrons were calculated from the LSV recorded at 1600 rpm by Eqs. (1) and (2), respectively:

$$H_2O_2\ (\%) = 200 \times \frac{\frac{I_R}{N}}{I_D + \frac{I_R}{N}} \quad (1)$$

$$n = \frac{4I_D}{I_D + \frac{I_R}{N}} \quad (2)$$

where I_R is the ring current (mA), I_D is the disk current (mA) and N is the collection efficiency (0.249).

Additionally, the stability of the prepared electrocatalyst during ORR was assessed by chronoamperometry, in which a potential of 0.4 V vs RHE was applied for 10000 s. Furthermore, the methanol tolerance was studied by adding 1.5 mL of methanol to the O_2-saturated electrolyte at 1000 s of the chronoamperometry measurement. Moreover, all the procedures performed for the prepared carbon materials were replicated for the ORR benchmark catalyst, Pt/C (20 wt%, Alfa Aesar), to be used as reference during the discussion of the results.

Regarding the OER, sample $25CNT_{Co}/75CNT_{Fe}$ was initially tested in both N_2- and O_2-saturated media to ensure that no significant differences would occur due to the selected saturation gas (Fig. S3). The obtained LSVs were identical and, consequently, it was concluded that, for these specific samples, the saturation gas does not affect the electrochemical OER measurements. Accordingly, the electrochemical assessments to evaluate the performance towards the OER consisted of LSV experiments in a N_2-saturated electrolyte.

The LSV measurements were obtained at a scan rate of 5 mV s^{-1} with a rotation speed of 1600 rpm within a 1.00 V to 1.85 V potential range (vs RHE). The obtained LSV was corrected using the E-*i*R relationship, where i is the obtained current and R is the uncompensated electrolyte ohmic resistance, which was obtained by the i-interrupt method [55]. The electrochemical parameters obtained from the abovementioned experiments were: i) the potential at which a current density of 10 mA cm^{-2} was achieved (E_{10}), ii) the Tafel slopes, calculated by plotting E vs log(J), and iii) the turnover frequency (TOF), obtained from Eq. (3) [56,57]:

$$\mathrm{TOF} = \frac{J \times A}{4 \times F \times n} \quad (3)$$

where J (mA cm^{-2}) is the current density at a selected overpotential, A is the area of the working electrode (cm^2), F is the Faraday constant (96,486 C mol^{-1}) and n is the number of moles of the active material. The TOF was calculated at a potential of 1.73 V, in which all metallic samples present a significant current density, and by using the number of moles of the metallic active centers calculated from the ICP results instead of the nominal values or the XPS results, due to the low amount of metal employed which is more accurately assessed by ICP. Additionally, the catalyst's stability towards OER was measured by performing 1000 LSV between 1.00 and 1.85 V and calculating the increase of the evolution overpotential between the first and last LSV.

Finally, the bifunctionality of the carbon samples was assessed by the potential gap (ΔE), which is considered as the difference between the OER threshold (E_{10}) and one of the potential parameters calculated for ORR (both $E_{1/2}$ or E_3 are commonly used in literature).

To further electrochemically characterize the prepared carbon materials, the double-layer capacitance (C_{dl}) was determined by cycling the loaded working electrodes at different scan rates. The CV measurements were performed under N_2-saturated media at a scan rate ranging from 5 mV s^{-1} to 220 mV s^{-1} within a potential range of 1.08 V and 1.18 V to ensure that no Faradic current is taking place [58]. The current intensity (I) recorded at a potential of 1.13 V for each CV was plotted vs. the employed scan rate. The C_{dl} value is the slope of the linear fit between I and the scan rate. The C_{dl} is a crucial parameter to calculate the electrochemical active surface area (ECSA), which is essential to understand the accessibility of the electrocatalyst's metal active centers [59]. The ECSA can be calculated by using Eq. (4):

$$\mathrm{ECSA} = \frac{C_{dl}}{C_S} \quad (4)$$

where C_S is the specific capacitance of the catalyst's ideal flat surface. Nonetheless, due to the very similar chemical nature of the prepared carbon materials, it can be considered that they present the same C_s value. Therefore, the C_{dl} value is expected to be proportional to the ECSA. Moreover, a recent study has reported a relationship between the C_{dl} and the accessibility of metallic active centers on carbon supports [59]. Hence, the C_{dl} can be helpful to compare how easily the main promoters of ORR and OER (active sites) can be reached by the O_2 and H_2O molecules, respectively.

3. Results and discussion

3.1. Chemical properties

The surface chemistry of the CNTs was chemically modified by the incorporation of CoPc or FePc molecules. The bulk chemical composition of each material, obtained from elemental analysis and ICP, is presented in Table 1.

The initial CNT sample displays a very high content of carbon (99.32 wt%) and very small amounts of oxygen and hydrogen. The incorporation of CoPc in the carbon nanotubes (CNT_{Co}) results in a material with low contents of nitrogen and cobalt, 0.95 wt% and 0.40 wt%, respectively. These values are in agreement with the theoretical values corresponding to the amount of CoPc added (0.90 wt% and 0.48 wt% for nitrogen and cobalt, respectively). Likewise, the incorporation of FePc into the base sample (CNT_{Fe}) also leads to low contents of nitrogen and iron (1.04 wt% and 0.35 wt%, respectively), which are also similar to the theoretical ones (0.84 wt% and 0.42 wt%, respectively). These results demonstrate that the Pcs were successfully introduced onto CNT. All the samples prepared by physical mixture of CNT_{Co} and CNT_{Fe} follow the expected pattern for their chemical composition based on the mixture ratio. CoPc and FePc present the same chemical structure, only differing in the central metallic atom. Therefore, the percentage of nitrogen revolves around the same values previously described for CNT_{Co} and CNT_{Fe}. On the other hand, the metal content observed represents each metal initially incorporated onto CNT, according to the mass ratio used. It should be noted that the small deviations observed for the ICP results may be due to the experimental error associated with the analysis, which is within 0.10 wt% of the theoretical value. Overall, these results suggest that all samples were successfully prepared.

The surface composition determined by X-ray photoelectron spectroscopy (XPS) and the survey spectra are presented in Table S1 and Fig. S4, respectively. The survey spectra confirm that only the elements discussed during the elemental/ICP analyses were detected on the catalysts' surface. The small amounts of Pcs employed in each sample lead to small amounts of the metallic elements on the surface of the CNTs (≤0.60 wt%), but the remarks made about the ICP results also apply at the surface chemical level. However, interesting differences between the bulk and the surface compositions were detected. Samples CNT_{Co} and $75CNT_{Co}/25CNT_{Fe}$ exhibit the same surface cobalt amount (0.60 wt%), which is slightly higher than that shown in Table 1. These results indicate that the CoPc molecules are preferentially located on the surface rather than in the bulk of the CNT bundles. Iron was not detected by XPS in $75CNT_{Co}/25CNT_{Fe}$ due to the low load of iron that did not reach the equipment detection threshold. Sample CNT_{Fe} exhibits a similar surface iron percentage as that observed by ICP, while sample $50CNT_{Co}/50CNT_{Fe}$ presents a slightly higher surface concentration of cobalt and a similar composition for iron (0.33 wt% and 0.17 wt%, respectively). These results suggest that FePc is homogeneously distributed on the CNT structure. The different behavior between CoPc and FePc may be attributed to the smaller particle size of the FePc molecule in comparison to the CoPc, which favors the incorporation of the iron species beyond the surface of the CNT bundles. Sample $25CNT_{Co}/75CNT_{Fe}$ presents similar amounts of both metallic elements on its surface, which differs from the percentage of each metal incorporated. Once again, this result demonstrates the cobalt's preference for attaching to the surface. The high-resolution XPS spectra of N *1s* and of Co *2p* and Fe *2p* regions are presented in Figs. 5 and S6, respectively. The N *1s* region was deconvoluted in three main peaks representing: (i) pyridinic nitrogen (N-6) at 398.9 ± 0.1 eV, (ii) pyrrolic nitrogen (N-5) at 399.9 ± 0.2 eV and (iii) quaternary nitrogen (N-Q) at 401.0 ± 0.2 eV [60]. Interesting differences are observed for the monometallic samples. CNT_{Co} presents three very well-defined peaks corresponding to the abovementioned nitrogen species, while CNT_{Fe} only presents the contribution of N-6 and N-5 functional groups. Phthalocyanines only present two types of nitrogen groups (N-6 and N-5) as corroborated by the XPS data (Fig. S5) and already reported in the literature [61]. Further comparison of the nitrogen spectra and nitrogen deconvolution of FePc and CNT_{Fe} leads to interesting findings. The incorporation of FePc on the CNT results in a decrease of N-6 contribution towards the total nitrogen content from 90.50% to 83.49% and an increase of the N-5 from 9.50% to 16.51% (Table S1). These results suggest that a slight decomposition of FePc takes place, and a FePc/CNT interaction occurs leading to the formation of N-5 functionalities. Nonetheless, the small nitrogen concentrations detected by XPS may be insufficient to assess the formation of N-Q on CNT_{Fe}, which has been detected in our previous publication [62]. Contrarily, the higher nitrogen surface content of CNT_{Co} allows a proper N *1s* deconvolution from which it can be observed that some nitrogen atoms separate from the macrocycle in sample CNT_{Co} and forms N-Q on the CNT surface as observed in the N *1s* deconvolution (Fig. S5). The nitrogen decomposition of CoPc may have occurred due to the temperature of the thermal treatment (500 °C) [62]. The N-Q contribution in the mixed samples decreases with the amount of CoPc. The Co *2p* region was deconvoluted in two different peaks and their respective spin–orbit splitting at 15.2 eV: i) Co^{3+} at 780.8 ± 0.1 eV and ii) Co^{2+} at 782.8 ± 0.2 eV (Fig. S6). These peaks were deconvoluted for all samples containing Co, except for sample $25CNT_{Co}/75CNT_{Fe}$, in which the percentage of Co is too low to allow deconvolution of the spin–orbit splits. Similarly, the low percentage of iron detected on the surface of the samples makes it difficult to deconvolute the high-resolution XPS spectrum of the Fe *2p* region and its respective peaks (Fig. S6). However, the Fe *2p* deconvolution of a sample similar to CNT_{Fe} was reported in our previous publication, from which the presence of two iron species (Fe^{2+} and Fe^{3+}) was confirmed [42].

Table 1
Chemical composition determined by elemental analyses and ICP.

Sample	C (wt %)	H (wt %)	N (wt %)	O (wt %)	Co (wt %)	Fe (wt %)
CNT	99.32	0.12	–	0.56	–	–
CNT_{Co}	98.37	0.14	0.95	0.14	0.40	–
CNT_{Fe}	97.99	0.15	1.04	0.47	–	0.35
$75CNT_{Co}/25CNT_{Fe}$	97.99	0.16	1.10	0.28	0.36	0.11
$50CNT_{Co}/50CNT_{Fe}$	98.22	0.16	0.92	0.33	0.23	0.14
$25CNT_{Co}/75CNT_{Fe}$	98.01	0.17	1.03	0.40	0.11	0.28

3.2. Morphological and textural properties

To analyze the presence of cobalt and iron, and possible modifications in the CNTs due to the impregnation method, samples CNT_{Co}, CNT_{Fe}, and $50CNT_{Co}/50CNT_{Fe}$ were examined by scanning electron microscopy (SEM). The corresponding micrographs using an Everhart-Thornley detector (ETD) are displayed in Fig. S7. The typical CNT morphology is observed for all samples, indicating that the incorporation of the Pcs does not modify the sample's morphology. The CNT morphology was also confirmed by transmission electron microscopy (TEM) performed on samples CNT_{Co} and $50CNT_{Co}/50CNT_{Fe}$ (Fig. S8). The presence of transition metals was not detected by TEM due to the small quantity of Pc incorporated. However, a Backscattered Electron detector (BSED) was employed to observe different levels of brightness between the CNTs and the metals. This technique was only effective to detect iron due to its high brightness during the analyses, whereas cobalt was not distinguishable from the CNTs. The absence of cobalt during analyses may be due to the high thermal stability of the cobalt atom within the CoPc molecule that did not transform into metallic cobalt, avoiding Co agglomerations. The BSED micrographs of sample CNT_{Fe} and $50CNT_{Co}/50CNT_{Fe}$ are displayed in Fig. 1a and b, respectively. The nanoscale of the iron macrocycle and the small amount supported onto the CNTs prevent the detection of isolated FePc molecules. However,

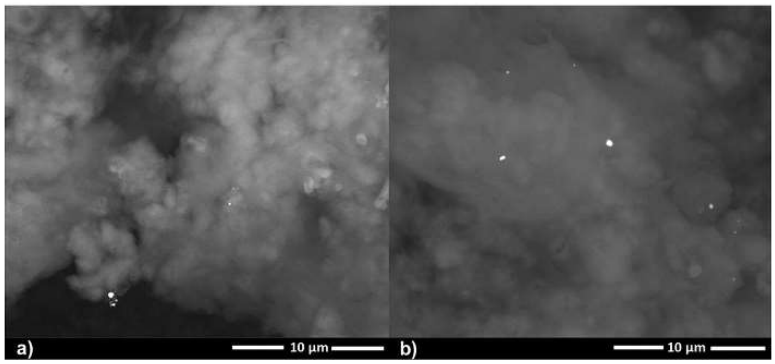


Fig. 1. SEM micrographs of CNT_{Fe} (a) and $50CNT_{Co}/50CNT_{Fe}$ (b).

some iron particles were detected in the SEM micrographs, which probably result from the agglomeration of iron during the thermal treatments.

Energy-dispersive spectroscopy (EDS) was performed to identify the metallic elements dispersion across CNT_{Co}, CNT_{Fe}, and $50CNT_{Co}/50CNT_{Fe}$ (Fig. S9). The elemental mapping of CNT_{Co} (Fig. S9b) and CNT_{Fe} (Fig. S9d) confirms the presence, and a large-scale dispersion, of cobalt and iron on the CNTs, which is favored by the low content of Co/Fe elements in these samples. The physical mixture of these two samples ($50CNT_{Co}/50CNT_{Fe}$) exhibits a slightly less intense color of the mapping images (Fig. S9f and S9g) in comparison to CNT_{Co} and CNT_{Fe}, since it only contains half of their metal contributions.

To further address the modifications attributed to the incorporation of the phthalocyanines, all samples were analyzed by Raman spectroscopy. The obtained spectra are presented in Fig. 2.

The samples exhibit a peak at ca. 1350 cm^{-1} (D band) ascribed to the basal plane defects of the carbon structure and a second peak at ca. 1580 cm^{-1} (G band), which is associated with the graphitic domains of the samples [15,60,63,64]. A third peak at higher shifts (ca. 2700 cm^{-1}) related to the π band in the electronic structure is also observed, which is characteristic of CNTs. The spectra were split into the Raman features commonly observed for carbon nanotube materials. The main D and G bands were deconvoluted, and the respective peak areas were integrated to provide additional information on the relative defects of the samples. The relative A_D/A_G ratio (Table S2) of CNT (0.39) increases with the incorporation of either CoPc (0.54) or FePc (0.42), which indicates an increase in the number of defects due to the presence of the metal phthalocyanines [65]. Regarding the bimetallic samples (Fig. 2b), the maximum number of defects is observed for the sample $50CNT_{Co}/50CNT_{Fe}$ (0.67), which could have been achieved by the coexistence of two different types of effects brought by each monometallic sample.

The textural properties of the synthesized carbon materials were studied by nitrogen adsorption–desorption isotherms, displayed in Fig. 3. The main textural parameters calculated from the isotherms are shown in Table S3.

All samples display type II isotherms, consistent with multi-layered materials such as carbon nanotubes [66]. The base CNT sample presents a S_{BET} of 218 $m^2\ g^{-1}$. The incorporation of CoPc and FePc on the CNT sample decreases the S_{BET} by 16% and 14%, respectively. The loss of S_{BET} is higher in CNT_{Co} than in CNT_{Fe}, probably due to the larger amount of CoPc detected on the CNT surface in comparison to the amount of FePc (Table S1). A decrease of V_p ($P/P_0 > 0.9$) upon the addition of CoPc or FePc is also observed, which may be caused by variations of the electrostatic charges between the CNTs upon the incorporation of the metallic complexes. Regardless of the ratio between the metals, the physical mixture of CNT_{Co} and CNT_{Fe} leads to very

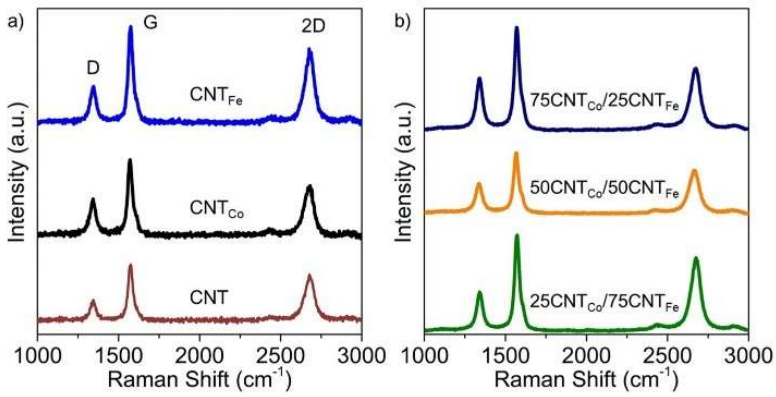


Fig. 2. Raman spectra of CNT and the monometallic electrocatalysts (a) and bimetallic electrocatalysts (b).

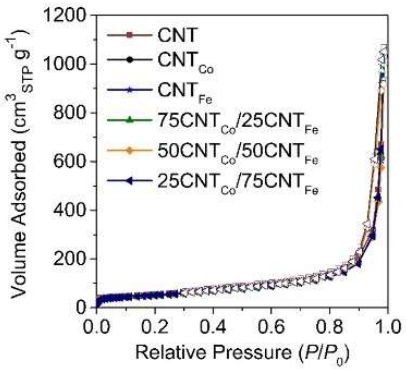


Fig. 3. N_2 adsorption–desorption isotherms at −196 °C of CNT, and the monometallic and bimetallic electrocatalysts.

similar values of S_{BET} (S_{BET} ranging from 181 to 184 $m^2\ g^{-1}$). These results indicate that the physical mixture of the samples does not modify their textural properties, as expected.

3.3. Electrochemical assessments

The ORR electroactivity of the prepared carbon samples was preliminarily assessed by CV measurements in both inert (N_2-saturated) and O_2-saturated media. Initially, N_2-saturated media voltammograms were recorded at 100 mV s^{-1} to identify the possible redox peaks. The obtained CVs are presented in Fig. 4.

CNT displays a featureless voltammogram in the N_2-saturated medium. The addition of CoPc (CNT_{Co}) results in the appearance of a reduction peak and its respective oxidation counterpart at low potentials (0.31 V and 0.40 V, respectively). These peaks are attributed to the redox reactions that occur on the Pc ring [42,52]. Similarly, the incorporation of FePc on CNT (CNT_{Fe}) also leads to the same two reduction and oxidation peaks but at slightly lower potentials (0.19 V and 0.36 V, respectively), which are attributed to the Pc ring around the iron atom

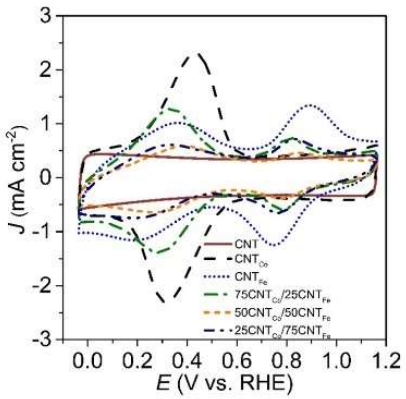


Fig. 4. Cyclic voltammograms recorded at 100 mV s^{-1} in N_2-saturated 0.1 mol L^{-1} KOH electrolyte from 1.10 to −0.05 V using a rotating ring-disk glassy carbon electrode with a Pt ring.

[67]. The CV of CNT_{Fe} also presents the appearance of peaks at ca. 0.75 V and 0.89 V attributed to the oxidation and reduction reaction of the redox couple Fe(III)/Fe(II), respectively [42,52]. Like in CNT_{Fe}, all mixed samples present the Pc-ring redox pair and the Fe(III)/Fe(II) redox pair. However, two interesting differences are observed for both pairs in the mixed samples: i) the Pc redox peaks appear in the potential range between the CNT_{Co} and CNT_{Fe} reduction and oxidation peaks; and ii) the reduction and oxidation peaks for the Fe(III)/Fe(II) species appear at higher and lower potentials than in CNT_{Fe}, respectively. This shift is probably due to the presence of CoPc that modifies the surface chemistry of the CNTs and, consequently, the potentials needed for the redox reactions.

CVs were also measured in a N_2- and O_2-saturated electrolyte at 5 mV s^{-1} (Fig. 5), which is the common scan rate employed for LSV. The redox peaks attributed to the Pc-ring and Fe(III)/Fe(II) redox pair are also observed despite the lower scan rate employed. The reduction and oxidation peaks observed at 5 mV s^{-1} appear at higher and lower potentials, respectively, compared to the CVs recorded at 100 mv s^{-1}. At low scan rates, the active species of the Pc and the electrolyte ions have enough residence time to interact, favoring the reduction and oxidation of the species, and hence, shifting the reduction and oxidation potentials to higher and lower values, respectively. The cyclic voltammograms recorded in the O_2-saturated electrolyte display the respective O_2 reduction peaks of the prepared samples. The voltammogram recorded in O_2-saturated medium in Fig. 5a shows that CNT displays a single reduction peak at 0.71 V, which is attributed to the ORR, since the N_2-saturated electrolyte voltammogram is featureless. CNT_{Co} displays the redox pair of the Pc ring previously observed in Fig. 4, and a peak at 0.80 V corresponding to the ORR. Regarding CNT_{Fe}, the peaks of the two redox pairs previously described still occur. Besides, the oxygen reduction peak is also observed, but at a higher onset potential (0.89 V) and with a much more significant current density. The simultaneous presence of the Fe(III)/Fe(II) reduction peak and the oxygen reduction peak may cause an overlap during the LSV assessments, which causes a modification in the shape of the curve after the ORR peak (Fig. 5c, d and f). The different combinations of CNT_{Co} and CNT_{Fe} present the redox peaks and the oxygen reduction peak (0.89 V) at the same potentials as CNT_{Fe}. Moreover, the current density observed for the O_2-saturated voltammogram also increases with the amount of FePc, due to its high electroactivity.

The disk current density, ring current, H_2O_2 formation, and number of electrons exchanged obtained from the LSV tests are displayed in Fig. 6a, b, c, and d, respectively. The main electrochemical parameters obtained for the electrocatalysts prepared and the reference material (Pt/C) are presented in Table 2. The base carbon sample (CNT) displays low E_{onset} and $E_{1/2}$ values (0.76 V and 0.65 V, respectively). Furthermore, CNT does not reach the 3 mA cm^{-2} threshold, usually considered for oxygen bifunctionality, and displays a current density of 1.91 mA cm^{-2} at 0.4 V. Additionally, the reaction follows a 2-electron ORR pathway and generates a high percentage of the undesired H_2O_2 (79%). Hence, the need to incorporate CoPc and FePc active centers to enhance the ORR electroactivity of the CNTs. The incorporation of CoPc (CNT_{Co}) results in a significant increase in the determined ORR parameters in comparison to CNT. The E_{onset} and $E_{1/2}$ increase by 90 mV and 110 mV, respectively, and a current density of 3 mA cm^{-2} is achieved at 0.6 V. At 0.4 V, the current density increases 96% in comparison to CNT and the formation of H_2O_2 is reduced by 21%. However, the number of electrons exchanged is 2.8, which means that the reaction mechanism of CNT_{Co} is still far from the desired 4-electron pathway. Conversely, the introduction of the FePc complex in the CNT sample leads to a much higher increase of electroactivity than that observed for CNT_{Co}, and the electrochemical parameters are comparable with the ORR benchmark catalyst, Pt/C. The E_{onset} increases from 0.76 V (CNT) to 0.96 V (CNT_{Fe}), whereas the $E_{1/2}$ rises from 0.65 V to 0.88 V, which is even higher than the Pt/C half-wave potential (0.81 V). Besides, the observed E_3 is 0.89 V, which is also higher than that observed for Pt/C (0.82 V). Regarding the

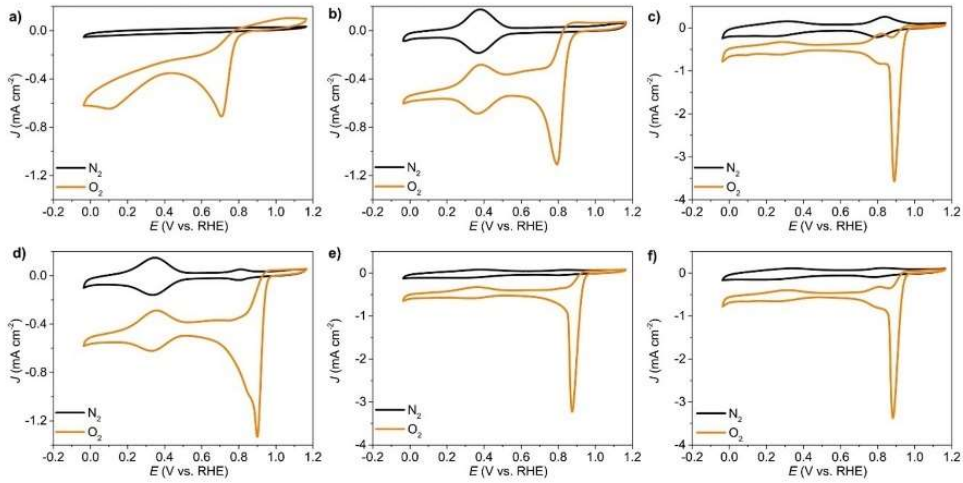


Fig. 5. Cyclic voltammograms recorded at 5 mV s^{-1} in N_2 (black) and O_2-saturated (orange) 0.1 mol L^{-1} KOH electrolytes from 1.10 to −0.05 V of CNT (a), CNT_{Co} (b), CNT_{Fe} (c), $75CNT_{Co}/25CNT_{Fe}$ (d), $50CNT_{Co}/50CNT_{Fe}$ (e) and $25CNT_{Co}/75CNT_{Fe}$ (f) using a rotating ring-disk glassy carbon electrode with a Pt ring.

current density at 0.4 V, J_f increases 279% compared to CNT. This value is also 35% higher than the current density measured for Pt/C at the same applied potential. The formation of H_2O_2 at 0.4 V is almost negligible (2%), and the number of electrons exchanged achieves a value of 4.0. Therefore, CNT_{Fe} exhibits a very similar ORR electroactivity as Pt/C, surpassing the benchmark electrocatalyst in almost all the electrochemical parameters. These results also suggest that the incorporation of FePc rather than CoPc greatly increases the ORR performance of the CNT. It should be noted that CNT_{Fe} presents a reduction current density higher than the theoretical diffusion-limited current density for ORR (ca. 6 mA cm^{-2}) [68], suggesting that a secondary reaction is also taking place during the ORR assessments. This secondary reaction is attributed to the presence of Fe(III) on the catalyst, generating a small peak at ca. 0.8 V in those samples with the highest concentration of FePc. This peak appears near the ORR, producing an overlap between the ORR current density and the Fe(III)/Fe(II) reduction peak [42,52]. Afterwards, both reduction reactions reach equilibrium, in which a current density is maintained throughout the plateau, giving rise to a current density higher than 6 mA cm^{-2}.

The differences in the onset potential and reaction mechanism between CoPc and FePc can be explained by the oxygen and H_2O_2 adsorption steps, respectively. The O_2 adsorption in Pcs occurs mainly on the central metal atom, and it is reported to have lower adsorption energy for FePc than for CoPc [50]. The lower value of binding energy for O_2 at the active site results in stronger adsorption of O_2 to the catalyst, which correlates with the higher E_{onset} of CNT_{Fe} shown in Table 2. On the other hand, the direct reduction pathway observed in CNT_{Fe} results from the adsorption of H_2O_2, in which both O atoms bind to the Fe atom, increasing the length of the O—O bond beyond the theoretical value (from 1.487 Å to 2.368 Å) [50], as shown in Fig. 7. This increase causes bond breakage between oxygen atoms, favoring the reaction through the 4-electron pathway. Conversely, the adsorption of H_2O_2 in CoPc assumes a different configuration, as shown in Fig. 7. The distance between oxygen atoms is similar to the equilibrium bond length, preventing bond breaking and leading to the indirect reaction mechanism [50].

The mixture of CNT_{Co} and CNT_{Fe} in a 3:1 ratio ($75CNT_{Co}/25CNT_{Fe}$) displays an increase in performance compared to the CNT_{Co} sample. The E_{onset} increases 90 mV in comparison to CNT_{Co}, whereas the $E_{1/2}$ increases by 110 mV. At 3 mA cm^{-2} a potential of 0.80 V is recorded, and a current density of 4.32 mA cm^{-2} is achieved at 0.4 V. The by-product formation decreases to 33%, corresponding to 3.3 electrons exchanged at 0.4 V. Moreover, sample $75CNT_{Co}/25CNT_{Fe}$ presents a higher half-wave potential than the commercial Pt/C. These results demonstrate that the incorporation of a small amount of FePc significantly improves the electroactivity of CNT_{Co} towards the ORR. Further tailoring was performed by increasing the percentage of CNT_{Fe} in the mixture. A CNT_{Co}:CNT_{Fe} ratio of 1:1 (sample $50CNT_{Co}/50CNT_{Fe}$) results in improved ORR electrochemical parameters (Table 2). The onset slightly increases (10 mV) in comparison to $75CNT_{Co}/25CNT_{Fe}$, whereas a small decrease of $E_{1/2}$ (10 mV) occurs. Nonetheless, a significant increase is observed for E_3 (70 mV), which is a key parameter towards oxygen bifunctionality. The current densities after reaching a plateau (potentials lower than 0.6 V) and at 0.4 V (5.28 mA cm^{-2}) overlap almost perfectly with the current densities obtained for Pt/C. The formation of by-products further decreases to 20% in comparison to $75CNT_{Co}/25CNT_{Fe}$, whereas the number of electrons exchanged increases to 3.6. These results suggest that the overall performance of CNT_{Co} can be improved by increasing the percentage of FePc. However, the E_{onset}, $E_{1/2}$, and E_3 recorded for sample $25CNT_{Co}/75CNT_{Fe}$ are very similar to those of $50CNT_{Co}/50CNT_{Fe}$, which suggests that after a 1:1 CNT_{Co}:CNT_{Fe} ratio, further addition of FePc does not significantly increase these electrochemical parameters. Nonetheless, an increase of 22% of current density upon reaching a plateau is observed in comparison to $50CNT_{Co}/50CNT_{Fe}$. The formation of by-products further decreases to 10% compared to the other mixtures, and the number of electrons transferred shifts to a value close to the direct mechanism (3.8 electrons). These results indicate that the ratio of CoPc:FePc active sites on the carbon structure plays a crucial role in the current density and the reaction mechanism. In fact, two interesting relationships were found between the FePc contribution calculated using the ICP values and the current densities at potentials where a plateau has been reached (Fig. 8a) and the number of electrons exchanged (Fig. 8b).

The current densities of the electrocatalysts increase with the percentage of FePc (Fig. 8a), due to the higher electroactivity of FePc centers towards oxygen reduction. FePc contributes more to the total

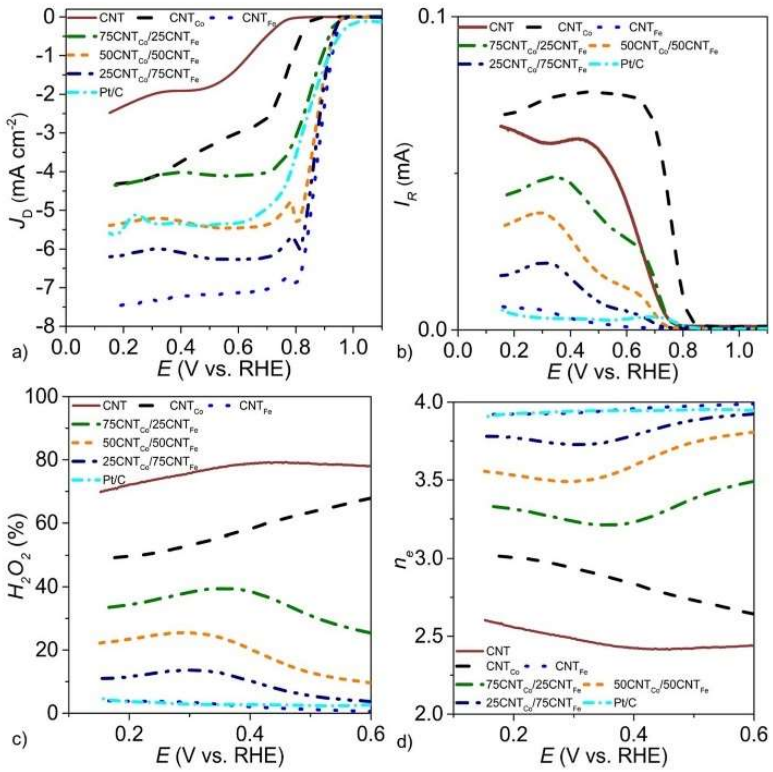


Fig. 6. Disk current density (a) and ring current (b) of the linear sweep voltammetry curves recorded at 5 mV s^{-1} in O_2-saturated 0.1 mol L^{-1} KOH electrolyte at 1600 rpm from 1.10 V to 0.15 V using a rotating ring-disk glassy carbon electrode with a Pt ring, production of hydrogen peroxide (c) and number of electrons exchanged (d) for the prepared samples.

Table 2
Onset potential (E_{onset}), half-wave potential ($E_{1/2}$), the potential at which a current density of 3 mA cm^{-2} is achieved (E_3), limiting current density (J_L), hydrogen peroxide (H_2O_2) formation, and the number of electrons exchanged (n_e) for the prepared electrocatalysts and the commercial Pt/C catalyst.

Sample	E_{onset} (V)	$E_{1/2}$ (V)	E_3 (V)	J_L (mA cm^{-2}) [a]	H_2O_2 (%)[a]	n_e[a]
CNT	0.76	0.65	–	1.91	79	2.4
CNT_{Co}	0.85	0.76	0.60	3.75	58	2.8
CNT_{Fe}	0.96	0.88	0.89	7.23	2	4.0
$75CNT_{Co}$/ $25CNT_{Fe}$	0.94	0.86	0.80	4.02	39	3.2
$50CNT_{Co}$/ $50CNT_{Fe}$	0.95	0.86	0.87	5.28	20	3.6
$25CNT_{Co}$/ $75CNT_{Fe}$	0.95	0.86	0.88	6.09	10	3.8
Pt/C	1.01	0.81	0.82	5.35	3	3.9

[a] Calculated at 0.4 V vs RHE.

current density than CoPc, indicating that more O_2 molecules are reduced at FePc actives centers than at CoPc sites. Therefore, increasing the percentage of FePc also shifts the reaction mechanism closer to the four-electron pathway, as experimentally confirmed (Fig. 8b). It should

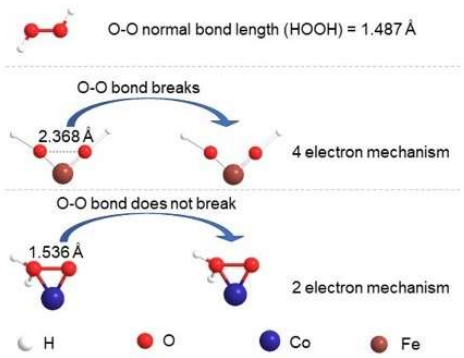


Fig. 7. Schematic illustration of H_2O_2 adsorption on iron and cobalt phthalocyanines and their respective reaction mechanisms.

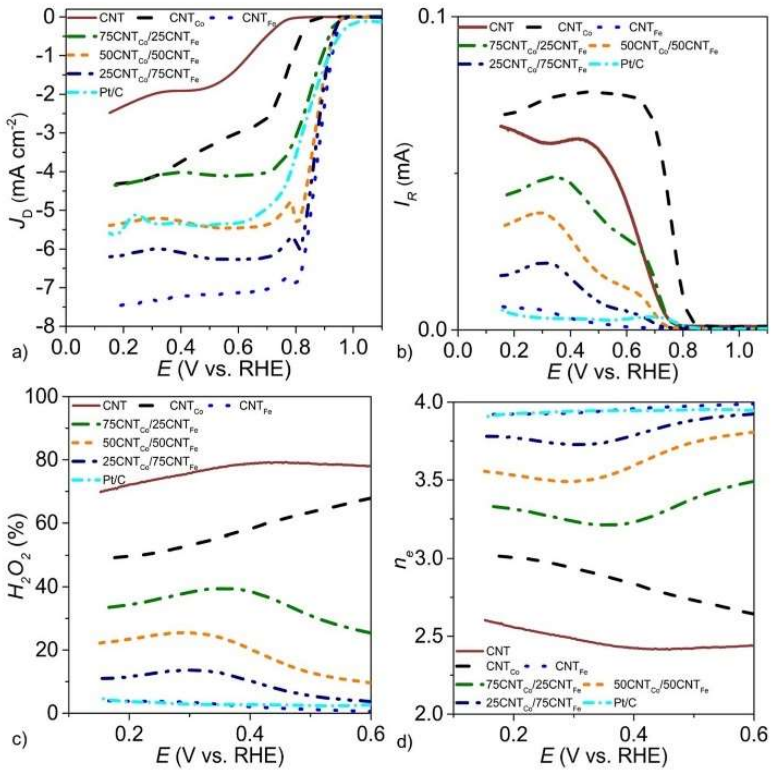


Fig. 6. Disk current density (a) and ring current (b) of the linear sweep voltammetry curves recorded at 5 mV s^{-1} in O_2-saturated 0.1 mol L^{-1} KOH electrolyte at 1600 rpm from 1.10 V to 0.15 V using a rotating ring-disk glassy carbon electrode with a Pt ring, production of hydrogen peroxide (c) and number of electrons exchanged (d) for the prepared samples.

Table 2
Onset potential (E_{onset}), half-wave potential ($E_{1/2}$), the potential at which a current density of 3 mA cm^{-2} is achieved (E_3), limiting current density (J_L), hydrogen peroxide (H_2O_2) formation, and the number of electrons exchanged (n_e) for the prepared electrocatalysts and the commercial Pt/C catalyst.

Sample	E_{onset} (V)	$E_{1/2}$ (V)	E_3 (V)	J_L (mA cm^{-2}) [a]	H_2O_2 (%)[a]	n_e[a]
CNT	0.76	0.65	–	1.91	79	2.4
CNT_{Co}	0.85	0.76	0.60	3.75	58	2.8
CNT_{Fe}	0.96	0.88	0.89	7.23	2	4.0
$75CNT_{Co}$/ $25CNT_{Fe}$	0.94	0.86	0.80	4.02	39	3.2
$50CNT_{Co}$/ $50CNT_{Fe}$	0.95	0.86	0.87	5.28	20	3.6
$25CNT_{Co}$/ $75CNT_{Fe}$	0.95	0.86	0.88	6.09	10	3.8
Pt/C	1.01	0.81	0.82	5.35	3	3.9

[a] Calculated at 0.4 V vs RHE.

current density than CoPc, indicating that more O_2 molecules are reduced at FePc actives centers than at CoPc sites. Therefore, increasing the percentage of FePc also shifts the reaction mechanism closer to the four-electron pathway, as experimentally confirmed (Fig. 8b). It should

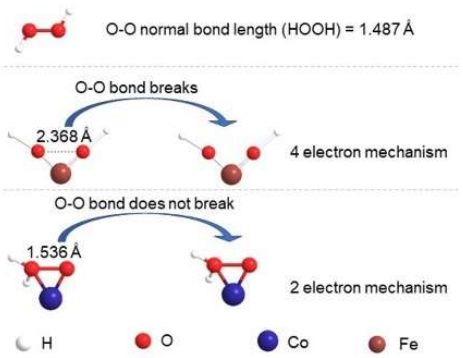


Fig. 7. Schematic illustration of H_2O_2 adsorption on iron and cobalt phthalocyanines and their respective reaction mechanisms.

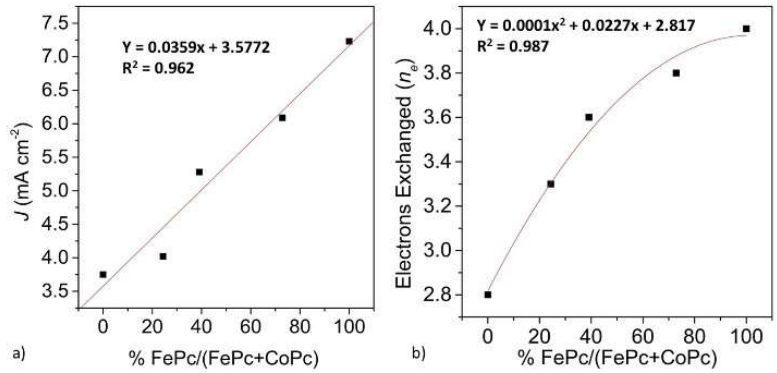


Fig. 8. Current density obtained from the linear sweep voltammetry curves of Fig. 6a (a) and the number of electrons exchanged obtained from Fig. 6d (b) at a potential of 0.4 V for the prepared samples versus the percentage of FePc against the total Pcs content calculated by ICP.

be noted that the sample with 25% FePc presents a lower current density (Fig. 8a), possibly due to the smaller number of defects in comparison to the sample without FePc and the other bimetallic samples, as observed in the Raman measurements.

Another key parameter to assess the performance of an electrocatalyst towards the ORR is its stability, which affects the lifetime of the final device. Therefore, the stabilities of the prepared carbon materials and the reference electrocatalyst were measured by RDE chronoamperometry, in which a potential of 0.4 V was applied over 10000 s. The methanol tolerance of sample $50CNT_{Co}/50CNT_{Fe}$ was also assessed by the addition of 1.5 mL of methanol at 1000 s during a chronoamperometry measurement. The stability and methanol tolerance results are presented in Fig. 9.

CNT exhibits stability of 58% during the chronoamperometric test, which is not ideal for long-term applications. The high formation of H_2O_2 during the electrochemical assessments may result in the oxidation of carbon through the byproduct's decomposition, which can lead to a weaker O_2-adsorption that hinders the ORR electrocatalysis [69]. The addition of CoPc and FePc active centers leads to a significant increase in current density retention (84% and 85% retention after 10000 s, respectively). It should be noted that CoPc and FePc molecules act as active sites towards the ORR, contributing to a large fraction of the measured current density and, consequently, to the overall catalyst's stability. However, it should be highlighted that FePc contributes more to keep a high current density than CoPc, as shown in Fig. 9a. Besides, CNT_{Fe} exhibits similar chronoamperometric results during the 10000 s test as Pt/C, while CNT_{Co} retains less relative current density than Pt/C during most of the analysis. Nonetheless, after reaching a relative current density of 84%, CNT_{Co} does not present further significant density losses. Overall, despite some differences between CNT_{Co} and the other two samples (CNT_{Fe} and Pt/C) during the early stages of the assessment, they all retain the same relative current density at the end of the stability test. Hence these electrocatalysts present the potential to achieve high performances during long-term use and to be promising candidates to replace Pt/C. Regarding the samples obtained by mixing CNT_{Co} and CNT_{Fe}, they all present the same level of retention (82% of their respective current densities after 10000 s). This high stability is a result of the very stable CoPc and FePc active centers that do not suffer significant degradation after the physical mixture of both base samples. Therefore, all the studied samples could be selected to replace the Pt/C commercial electrocatalyst. Additionally, it is shown in Fig. 9b that the addition of methanol to sample $50CNT_{Co}/50CNT_{Fe}$ during the chronoamperometric assessments increases momentarily the produced current density upon its addition. Moreover, the ORR current of $50CNT_{Co}/$

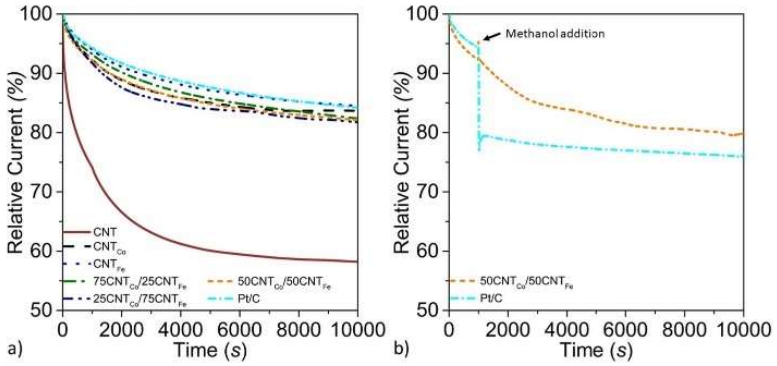


Fig. 9. Chronoamperometry measurements for the prepared samples (a) and methanol resistance of sample $50CNT_{Co}/50CNT_{Fe}$ (b) applying 0.4 V during 10000 s at 5 mV s^{-1} and 1600 rpm in an O_2-saturated 0.1 mol L^{-1} KOH electrolyte using a rotating disk glassy carbon electrode.

$50CNT_{Fe}$ remains almost unaffected after the addition of methanol, demonstrating its high methanol tolerance. This result is in agreement with existing literature that remarks the exceptional tolerance of metal-nitrogen-carbon electrocatalysts, in particular FeN_4 sites [70]. More importantly, the prepared catalyst does not suffer the significant performance loss that is recorded for the benchmark catalyst, which is another crucial advantage of these materials in comparison to Pt/C.

The prepared carbon electrocatalysts were also evaluated towards the OER to assess their potential bifunctionality. LSV performed in N_2-saturated medium at 5 mV s^{-1} and the Tafel slopes derived from the LSV are presented in Fig. 10a and 10b, respectively.

The CNT sample only starts catalyzing the OER near 1.70 V and does not reach the minimum 10 mA cm^{-2} threshold that is one of the most important parameters towards the OER [29]. The incorporation of CoPc (CNT_{Co}) increases the electroactivity of the carbon material, lowering the potential at which the reaction starts and achieving a E_{10} of 1.77 V. The introduction of the FePc molecules (CNT_{Fe}) enhances the performance of CNT towards OER due to the presence of FePc macrocycles resulting in a potential of 1.80 V at 10 mA cm^{-2}. Contrary to the electrochemical behavior towards the ORR, CNT_{Co} presents a slightly higher OER electroactivity than CNT_{Fe}. The physical mixture with a 3:1 CNT_{Co}:CNT_{Fe} ratio ($75CNT_{Co}/25CNT_{Fe}$) further increases the electroactivity of the material in comparison to CNT_{Co} and CNT_{Fe}, and an E_{10} of 1.73 V is achieved. It should be noted that, contrarily to the competition between both active sites observed towards the ORR, the coexistence of both species seems to provide a synergetic effect towards the electrocatalysis of the OER. The results obtained from the sample with the 1:1 ratio ($50CNT_{Co}/50CNT_{Fe}$) further corroborate this theory, as an additional increase of electroactivity is observed. The LSV of $50CNT_{Co}/50CNT_{Fe}$ displays an increase of current density at even lower potentials and provides the threshold current density at 1.67 V. This value is only 90 mV higher than the value reported for the benchmark RuO_2 electrocatalyst (1.58 V) [71]. Further increasing the percentage of CNT_{Fe} in the sample (sample $25CNT_{Co}/75CNT_{Fe}$) results in an increase of electroactivity in comparison to CNT_{Fe}, decreasing the E_{10} to 1.75 V. However, the electroactivity of $25CNT_{Co}/75CNT_{Fe}$ is lower than that of $50CNT_{Co}/50CNT_{Fe}$, which suggests that there is an optimal ratio of metallic macrocycles to achieve the best OER performance. Interestingly, comparison between $75CNT_{Co}/25CNT_{Fe}$ and $25CNT_{Co}/75CNT_{Fe}$ highlights the same trends observed for CNT_{Co} and CNT_{Fe}, in which an amount of CoPc larger than FePc seems to contribute slightly more to achieve high performances towards the OER. Although $75CNT_{Co}/25CNT_{Fe}$ presents a lower number of defects than $25CNT_{Co}/75CNT_{Fe}$ (Table S2), a higher content of CoPc results in higher OER performance, further corroborating the importance of the cobalt active centers. Sample $50CNT_{Co}/50CNT_{Fe}$ exhibits the best OER performance of all samples while displaying a similar degree of disorder/graphitization as $25CNT_{Co}/75CNT_{Fe}$. This demonstrates that an optimal ratio of CoPc and FePc is essential to enhance the CNT's OER activity. The presence of both molecules and their synergy is crucial to enhance the electroactivity of CNT as the performance of any mixture is higher than that of CNT_{Co} and CNT_{Fe}.

Another crucial parameter determined was the Tafel slope (Fig. 10b). CNT presents a Tafel slope of 117 mV/dec. The incorporation of CoPc leads to a decrease to 93 mV/dec, which indicates a faster initial step towards the OER. Similarly, the incorporation of FePc presents a decrease in the Tafel slope value (91 mV/dec), which can be explained by the presence of FePc active centers that may have led to faster kinetics due to the lower adsorption energy of H_2O compared to CoPc [50]. The use of a 3:1 CNT_{Co}:CNT_{Fe} ratio results in a sample with a slightly lower Tafel slope value (86 mV/dec) than that of CNT_{Fe}, which indicates that even though CoPc is the primary molecule of this sample, the synergetic effect of both macrocycles results in enhanced kinetics. Sample $50CNT_{Fe}/50CNT_{Co}$ further highlights this synergetic effect between the phthalocyanines by presenting the fastest kinetics with a Tafel slope value of 62 mV/dec. This value is lower than that reported for the benchmark catalyst RuO_2 (88 mV/dec) [72], which attests to the prepared electrocatalyst's fast kinetics. The calculated kinetics of $50CNT_{Fe}/50CNT_{Co}$ is also similar to some state-of-the-art CNT catalysts that support Co/N (53.7 and 62.0 mV/dec) [73]. Regarding sample $75CNT_{Fe}/25CNT_{Co}$, a similar value (84 mV/dec) as that observed in $25CNT_{Fe}/75CNT_{Co}$ is obtained. To further understand the kinetic differences and the improved OER electroactivity, the double-layer capacitance (C_{dl}) was calculated for each carbon material (Fig. S10). CNT presents a low value of C_{dl} (3.74×10^{-8} F). The incorporation of CoPc and FePc leads to a decrease of C_{dl} by 34% and 26%, respectively. It should be noted that the calculations used for the double-layer capacitance determination have been recently reported as part of a novel methodology to compare the metallic centers accessibility between catalysts where a metal species is supported on a carbon material [59]. This methodology suggests that a higher value of C_{dl} is correlated with a higher accessibility to the metallic active species present on the electrocatalyst tested. Therefore, the C_{dl} measurements of CNT_{Co} and CNT_{Fe} indicate that the incorporation of a single metal macrocycle presents a low accessibility to the metallic centers. Nonetheless, sample CNT must not be compared to the other samples prepared as it does not

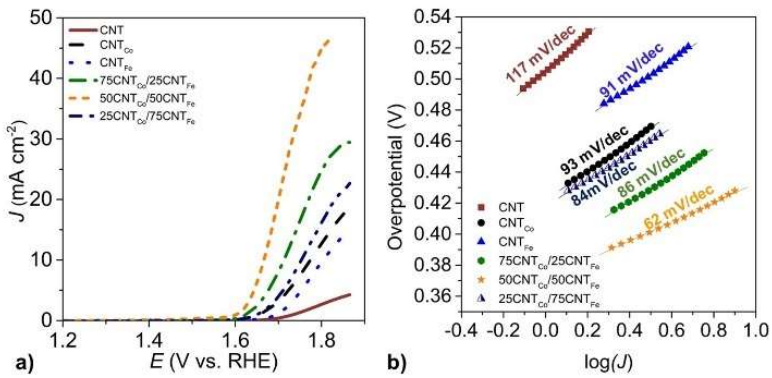


Fig. 10. Linear sweep voltammetry curves recorded at 5 mV s^{-1} in an N_2-saturated 0.1 mol L^{-1} KOH electrolyte at 1600 rpm from 1.00 to 1.85 V (a) and their corresponding Tafel plots (b) using a rotating disk glassy carbon electrode.

present metal active centers that are important to achieve faster kinetics and to apply this methodology. Furthermore, the comparison of the kinetics and C_{dl} of CNT_{Co} and CNT_{Fe} corroborates this methodology's hypothesis. The incorporation of FePc led to a higher value of C_{dl} than the incorporation of the CoPc molecules, which followed the same trend as the calculated kinetics, in which CNT_{Fe} presented the fastest one of the monometallic samples. A 3:1 CNT_{Co}:CNT_{Fe} mixture ratio leads to an increase of the C_{dl} to 23% more than the base CNT, and 87% and 67% higher than CNT_{Co} and CNT_{Fe}, respectively. This result indicates that the presence of two different types of active centers plays a crucial role to boost the capacity of the CNTs. Increasing the FePc contribution using a 1:1 CNT_{Co}:CNT_{Fe} ratio results in a very high increase of the calculated C_{dl} to 2.84×10^{-7} F. This value represents an increase of 401%, 660% and 578% in comparison to CNT, CNT_{Co}, and CNT_{Fe}, respectively. Moreover, the high C_{dl} of $50CNT_{Co}/50CNT_{Fe}$ is also coincident with the highest number of defects displayed in the Raman spectra, which could indicate that both the macrocycle molecules and the number of defects generated are important to increase the number of active sites. Further increasing the FePc contribution by preparing a sample with a 1:3 CNT_{Co}:CNT_{Fe} ratio leads to a decrease of the C_{dl} to values similar to those observed on $75CNT_{Co}/25CNT_{Fe}$. Therefore, the increasing order of C_{dl} is $CNT_{Co} < CNT_{Fe} < CNT < 75CNT_{Co}/25CNT_{Fe} < 25CNT_{Co}/75CNT_{Fe} < 50CNT_{Co}/50CNT_{Fe}$. These results suggest that the synergy between both metallic species increases the C_{dl}, and in turn, the metal sites accessibility of the electrocatalysts, which is crucial towards the adsorption of H_2O. The CNT_{Co} sample presents the lowest metal species accessibility, which results in a higher Tafel slope value than CNT_{Fe}. $75CNT_{Co}/25CNT_{Fe}$ presents lower C_{dl} than $25CNT_{Co}/75CNT_{Fe}$, which is also in agreement with the slower kinetics calculated. Furthermore, $50CNT_{Co}/50CNT_{Fe}$ has the highest metallic center accessibility, and hence, the fastest kinetics. This higher accessibility, in comparison to the other samples, indicates that the active centers are more easily reached by the H_2O molecules in the electrolyte and, consequently, facilitates their adsorption and subsequent evolution at the active centers. Therefore, the conjugation of higher accessibility of the catalyst's metal species and the metal active center's synergy towards the OER appears to explain the low Tafel slope value of $50CNT_{Co}/50CNT_{Fe}$.

The turnover-frequency (TOF) was also calculated from the LSV, which is another important parameter to assess the OER performance of an electrocatalyst, as it represents its intrinsic activity [57]. Samples CNT_{Co} and CNT_{Fe} present TOFs of 0.268 s^{-1} and 0.157 s^{-1}, respectively. Therefore, these initial results suggest that the cobalt macrocycle is more active towards the OER than the iron macrocycle. The mixture of both these samples in a 3:1 CNT_{Co}:CNT_{Fe} ratio increases the TOF to 0.519 s^{-1}, which represents increases of 94% and 231% in comparison to CNT_{Co} and CNT_{Fe}, respectively. Sample $50CNT_{Co}/50CNT_{Fe}$ achieved an even higher TOF reaching 1.480 s^{-1}, corresponding to increases of 353% and 843% compared to CNT_{Co} and CNT_{Fe}, respectively. Regarding the last mixture prepared ($25CNT_{Co}/75CNT_{Fe}$), the TOF value obtained is 0.336 s^{-1}, which is higher than that of the initial samples but lower than the values obtained for the 3:1 and 1:1 ratios. These results demonstrate that CoPc is more important towards OER than FePc, as the samples present improved performances when CoPc is the predominant active center. Nonetheless, a perfect balance between cobalt and iron molecules is necessary to achieve the highest electroactivity towards the OER, giving rise to the highest intrinsic activity for the sample with a mass ratio of 1:1. Stability tests for $50CNT_{Co}/50CNT_{Fe}$ were also carried out to investigate its durability towards OER. The results obtained are presented in Fig. 11.

As shown in Fig. 11, after 1000 LSVs, the overpotential of the electrocatalyst increased by 39 mV at a current density of 10 mA cm^{-2}, indicating that the bimetallic sample remains highly electroactive after long-term use. Overall, this catalyst presents high durability towards both oxygen reduction and evolution and an almost unchanged behavior towards methanol poisoning, which is important for scale-up applications.

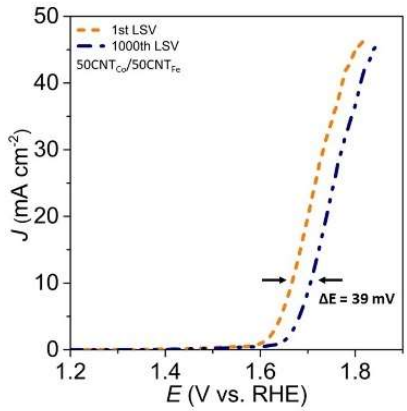


Fig. 11. Linear sweep voltammetry curves of $50CNT_{Co}/50CNT_{Fe}$ before and after the stability test.

The bifunctional activity, evaluated by the potential gap (ΔE) between E_{10} for the OER and $E_{1/2}$ or E_3 for the ORR, for the prepared carbon and the benchmark electrocatalysts, is presented in Table 3. This parameter is crucial to assess the overall oxygen activity.

The potentials observed towards the ORR ($E_{1/2}$) for the carbon samples containing iron reveal very slight differences, as shown in Table 3. Consequently, the major factor to achieve a low ΔE is to obtain the lowest possible E_{10} value for the OER. Therefore, the high OER electroactivity of $50CNT_{Co}/50CNT_{Fe}$ makes it the best-suited bifunctional electrocatalyst. Besides, all samples containing FePc are more suitable bifunctional electrocatalysts than the benchmark catalysts used nowadays, exhibiting much lower potential gaps. Furthermore, the results obtained are similar or better than some of the state-of-the-art metal/heteroatom-doped carbon materials already reported [57,72,74–78]. For instance, the incorporation of cobalt on carbon nanofibers has achieved a ΔE of 0.82 V [78], the use of cobalt and nitrogen on CNTs has been reported to achieve a potential gap of 0.78 V [75], whereas the incorporation of iron and nitrogen on CNTs accomplished a ΔE of 0.80 V [76], both very similar to $50CNT_{Co}/50CNT_{Fe}$. Moreover, $50CNT_{Co}/50CNT_{Fe}$ presents a slightly lower or identical ΔE (0.81 V) compared to reported state-of-the-art carbon materials with both metallic species such as $CoFe_2O_4$/CNTs (1.02 V) [77], $FeCo_2O_4$/hollow reduced graphene oxide spheres (0.96 V) [77], $CoFe_2O_4$ nanoparticles/rod-like ordered mesoporous carbon (0.84 V) [77], and FeCo-NPC-1100 (0.81 V) [72]. Notwithstanding, the electrocatalysts of the present study offer several advantages in comparison to most of those reported in the literature, such as: (i) a reduced number of synthesis steps, (ii) the incorporation of a very small amount of macrocycle molecules (environmentally and cost-wise), and (iii) an easily scalable

Table 3
$E_{1/2}$, E_3, E_{10} and ΔE for the prepared samples and benchmark catalysts.

Sample	$E_{1/2}$ (V)	E_3 (V)	E_{10} (V)	ΔE (V)[a]	ΔE (V)[b]
CNT_{Co}	0.76	0.60	1.78	1.02	1.18
CNT_{Fe}	0.88	0.89	1.80	0.92	0.91
$75CNT_{Co}/25CNT_{Fe}$	0.86	0.80	1.73	0.87	0.93
$50CNT_{Co}/50CNT_{Fe}$	0.86	0.87	1.67	0.81	0.80
$25CNT_{Co}/75CNT_{Fe}$	0.86	0.88	1.75	0.89	0.87
Pt/C	0.81	0.83 [71]	2.01 [71]	1.20	1.18
RuO_2	–	0.10 [71]	1.58 [71]	–	1.48

[a] $\Delta E = E_{10} - E_{1/2}$.
[b] $\Delta E = E_{10} - E_3$.

procedure.

4. Conclusions

Commercial CNTs were used as bifunctional oxygen electrocatalysts by incorporating two different metal macrocycles onto the carbon structure: CoPc (CNT_{Co}) and FePc (CNT_{Fe}). These two samples were then physically mixed using different CNT_{Co}:CNT_{Fe} mass ratios (3:1, 1:1, and 1:3). ICP analyses indicated the successful incorporation of the metal complexes, with percentages similar to the theoretical values. Regarding the ORR assessments, CNTs supporting FePc presented higher onsets (0.96 V) than those of CNTs with CoPc (0.85 V), and a reaction mechanism closer to the four-electron pathway due to the lower O_2 adsorption energy and longer O—O bonds formed in FePc active sites. This effect was also shown for the mixed samples, in which the electroactivity increased with the content of FePc, achieving electrochemical performances that surpassed that of Pt/C. Additionally, all CNT samples containing Pcs presented high capabilities to perform efficiently during long-term use with durabilities similar to the benchmark catalyst (Pt/C). Regarding the OER measurements, a totally different behavior was observed. Although CNT_{Co} and CNT_{Fe} presented low OER performances, the physical mixture of these samples led to a synergetic effect that significantly improved the electrochemical performance of CNTs towards the OER. The best OER electroactivity was observed when the mixture was prepared using the same amount of CNT_{Co} and CNT_{Fe} ($50CNT_{Co}$/$50CNT_{Fe}$), achieving a potential of 1.67 V at the 10 mA cm^{-2} threshold. This sample also exhibited the lowest potential gap (0.81 V), demonstrating its great potential as a bifunctional oxygen electrocatalyst. Besides, sample $50CNT_{Co}$/$50CNT_{Fe}$ was prepared using a minimal amount of macrocycle molecules, which may lead to low production costs and high up-scaling potential towards producing carbon material for green energy applications.

CRediT authorship contribution statement

R.G. Morais: Investigation, Methodology, Validation, Writing – original draft. **N. Rey-Raap:** Conceptualization, Methodology, Visualization, Writing – original draft, Writing – review & editing. **J.L. Figueiredo:** Conceptualization, Writing – review & editing. **M.F.R. Pereira:** Conceptualization, Writing – review & editing, Funding acquisition.

Declaration of Competing Interest

The authors declare that they have no known competing financial interests or personal relationships that could have appeared to influence the work reported in this paper.

Acknowledgments

This work was financially supported by: Project "UniRCell" - POCI-01-0145-FEDER-016422 - funded by European Structural and Investment Funds (FEEI) through - Programa Operacional Competitividade e Internacionalização - COMPETE2020 and by national funds through FCT - Fundação para a Ciência e a Tecnologia, I.P., Project "BiCat4Energy" with reference PTDC/EQU-EQU/1707/2020, Base-UIDB/50020/2020 and Programmatic-UIDP/50020/2020 funding of LSRE-LCM, funded by national funds through FCT/MCTES (PIDDAC), PDEQB (PD9989). RGM acknowledges the Research Grant from FCT (2020.06422.BD). The authors are indebted to CEMUP for assistance with XPS and SEM analyses.

Appendix A. Supplementary material

Supplementary data to this article can be found online at https://doi.org/10.1016/j.apsusc.2021.151459.

References

[1] Y. Wang, D.Y.C. Leung, J. Xuan, H. Wang, Renew. Sust. Energ. Rev. 65 (2016) 961–977, https://doi.org/10.1016/j.rser.2016.07.046.
[2] Y. Lv, C. Han, Y. Zhu, T. Zhang, S. Yao, Z. He, L. Dai, L. Wang, J. Mater. Sci. Technol. 75 (2021) 96–109, https://doi.org/10.1016/j.jmst.2020.09.042.
[3] J. Stacy, Y.N. Regmi, B. Leonard, M. Fan, Renew. Sust. Energ. Rev. 69 (2017) 401–414, https://doi.org/10.1016/j.rser.2016.09.135.
[4] A. Kirubakaran, S. Jain, R.K. Nema, Renew. Sust. Energ. Rev. 13 (2009) 2430–2440, https://doi.org/10.1016/j.rser.2009.04.004.
[5] B. Paul, J. Andrews, Renew. Sust. Energ. Rev. 79 (2017) 585–599, https://doi.org/10.1016/j.rser.2017.05.112.
[6] T. Sadhasivam, K. Dhanabalan, S.-H. Roh, T.-H. Kim, K.-W. Park, S. Jung, M. Kurkuri, H.-Y. Jung, Int. J. Hydrog. Energy 42 (2016) 1–19, https://doi.org/10.1016/j.ijhydene.2016.10.140.
[7] K. Dutta, D. Rana, H.S. Han, P.P. Kundu, Fuel Cells 17 (2017) 736–751, https://doi.org/10.1002/fuce.201700018.
[8] Z. Pu, G. Zhang, A. Hassanpour, D. Zheng, S. Wang, S. Liao, Z. Chen, S. Sun, Appl. Energy 283 (2021), 116376, https://doi.org/10.1016/j.apenergy.2020.116376.
[9] Y. Wang, D.Y.C. Leung, J. Xuan, H. Wang, Renew. Sust. Energ. Rev. 75 (2017) 775–795, https://doi.org/10.1016/j.rser.2016.11.054.
[10] M.M. Mohideen, Y. Liu, S. Ramakrishna, Appl. Energy 257 (2020), 114027, https://doi.org/10.1016/j.apenergy.2019.114027.
[11] S. Gottesfeld, D.R. Dekel, M. Page, C. Bae, Y. Yan, P. Zelenay, Y.S. Kim, J. Power Sources 375 (2018) 170–184, https://doi.org/10.1016/j.jpowsour.2017.08.010.
[12] W.E. Mustain, M. Chatenet, M. Page, Y.S. Kim, Energy Environ. Sci. 13 (2020) 2805–2838, https://doi.org/10.1039/D0EE01133A.
[13] A. Sarapuu, E. Kibena-Põldsepp, M. Borghei, K. Tammeveski, J. Mater. Chem. A 6 (2018) 776–804, https://doi.org/10.1039/C7TA08690C.
[14] Y. Qian, Z. Hu, X. Ge, S. Yang, Y. Peng, Z. Kang, Z. Liu, J.Y. Lee, D. Zhao, Carbon 111 (2017) 641–650, https://doi.org/10.1016/j.carbon.2016.10.046.
[15] R.G. Morais, N. Rey-Raap, R. Costa, C. Pereira, A. Guedes, J.L. Figueiredo, M.F. R. Pereira, J. Compos. Sci. 4 (2020) 1–14, https://doi.org/10.3390/jcs4010020.
[16] R.G. Morais, N. Rey-Raap, J.L. Figueiredo, M.F.R. Pereira, Beilstein J. Nanotechnol. 10 (2019) 1089–1102, https://doi.org/10.3762/bjnano.10.109.
[17] C. Sathiskumar, S. Ramakrishnan, M. Vinothkannan, A. Rhan Kim, S. Karthikeyan, D.J. Yoo, Nanomaterials 10 (2020) 1–17, https://doi.org/10.3390/nano10010076.
[18] Y. Xiao, S. Deng, M. Li, Q. Zhou, L. Xu, H. Zhang, D. Sun, Y. Tang, Front. Chem. 7 (2019) 1–13, https://doi.org/10.3389/fchem.2019.00523.
[19] T. Pan, H. Liu, G. Ren, Y. Li, X. Lu, Y. Zhu, Sci. Bull. 61 (2016) 889–896, https://doi.org/10.1007/s11434-016-1073-3.
[20] E.Y. Choi, D.E. Kim, S.Y. Lee, C.K. Kim, Carbon 166 (2020) 245–255, https://doi.org/10.1016/j.carbon.2020.05.034.
[21] J. Zhang, X. Song, P. Li, Z. Wu, Y. Wu, S. Wang, X. Liu, J. Taiwan Inst. Chem. Eng. 93 (2018) 336–341, https://doi.org/10.1016/j.jtice.2018.07.040.
[22] A.M. El Sawy, I.M. Mosa, D. Su, C.J. Guild, S. Khalid, R. Joesten, J.F. Rusling, S. L. Suib, Adv. Energy Mater. 6 (2016) 1501966, https://doi.org/10.1002/aenm.201501966.
[23] J. Zhang, Y. Sun, J. Zhu, Z. Gao, S. Li, S. Mu, Y. Huang, Adv. Sci. 5 (2018) 1801375, https://doi.org/10.1002/advs.201801375.
[24] R. Li, Z. Wei, X. Gou, ACS Catal. 5 (2015) 4133–4142, https://doi.org/10.1021/acscatal.5b00601.
[25] H. Shen, H. Peng, R. Cao, L. Yang, Y. Gao, A. Turak, T. Thomas, X. Guo, Y. Zhu, J. Wang, M. Yang, J. Phys. Chem. Lett. 12 (2021) 517–524, https://doi.org/10.1021/acs.jpclett.0c02812.
[26] D. Barrera, M. Florent, K. Sapag, T.J. Bandosz, A.C.S. Appl, Energy Mater. 2 (2019) 7412–7424, https://doi.org/10.1021/acsaem.9b01427.
[27] S.S. Sekhon, J. Lee, J.-S. Park, J. Energy Chem. 65 (2022) 149–172, https://doi.org/10.1016/j.jechem.2021.05.052.
[28] M. Seredych, K. László, E. Rodríguez-Castellón, T.J. Bandosz, J. Energy Chem. 25 (2016) 236–245, https://doi.org/10.1016/j.jechem.2016.01.005.
[29] H. Zhong, C.A. Campos-Roldán, Y. Zhao, S. Zhang, Y. Feng, N. Alonso-Vante, Catalysts 8 (2018) 1–43, https://doi.org/10.3390/catal8110559.
[30] K.B. Ibrahim, M.-C. Tsai, S.A. Chala, M.K. Berihun, A.W. Kahsay, T.A. Berhe, W.-N. Su, B. J. Hwang, J. Chin. Chem. Soc. 66 (2019) 829–865, https://doi.org/10.1002/jccs.201900001.
[31] H. Osgood, S.V. Devaguptapu, H. Xu, J. Cho, G. Wu, Nano Today 11 (2016) 601–625, https://doi.org/10.1016/j.nantod.2016.09.001.
[32] P. Ganesan, M. Prabu, J. Sanetuntikul, S. Shanmugam, ACS Catal. 5 (2015) 3625–3637, https://doi.org/10.1021/acscatal.5b00154.
[33] T. Oh, K. Kim, J. Kim, J. Energy Chem. 38 (2019) 60–67, https://doi.org/10.1016/j.jechem.2018.12.021.
[34] N. Li, Y. Nam, J.Y. Lee, Appl. Surf. Sci. 514 (2020), https://doi.org/10.1016/j.apsusc.2020.146073.
[35] K. Mamtani, D. Jain, A.C. Co, U.S. Ozkan, Energy Fuels 31 (2017) 6541–6547, https://doi.org/10.1021/acs.energyfuels.7b00242.
[36] C. Li, T. Huang, Z. Huang, J. Sun, C. Zong, J. Yang, W. Deng, F. Dai, Dalton Trans. 48 (2019) 17258–17265, https://doi.org/10.1039/C9DT03360B.
[37] L. Osmieri, R. Escudero-Cid, A.H.A. Monteverde Videla, P. Ocón, S. Specchia, Appl. Catal. B Environ. 201 (2017) 253–265, https://doi.org/10.1016/j.apcatb.2016.08.043.
[38] A. Arul, H. Pak, K.U. Moon, M. Christy, M.Y. Oh, K.S. Nahm, Appl. Catal. B Environ. 220 (2018) 488–496, https://doi.org/10.1016/j.apcatb.2017.08.064.
[39] X. Ge, A. Sumboja, D. Wuu, T. An, B. Li, F.W.T. Goh, T.S.A. Hor, Y. Zong, Z. Liu, ACS Catal. 5 (2015) 4643–4667, https://doi.org/10.1021/acscatal.5b00524.

[40] Y. Kumar, E. Kibena-Põldsepp, J. Kozlova, A. Kikas, M. Käärik, J. Aruväli, V. Kisand, J. Leis, A. Tamm, K. Tammeveski, ChemElectroChem 8 (2021) 2662–2670, https://doi.org/10.1002/celc.202100498.
[41] G. Abarca, M. Viera, C. Aliaga, J.F. Marco, W. Orellana, J.H. Zagal, F. Tasca, J. Mater. Chem. A 7 (2019) 24776–24783, https://doi.org/10.1039/C9TA09125D.
[42] R.G. Morais, N. Rey-Raap, J.L. Figueiredo, M.F.R. Pereira, J. Energy Chem. 50 (2020) 260–270, https://doi.org/10.1016/j.jechem.2020.03.039.
[43] J. Yang, J. Tao, T. Isonura, H. Yanagi, I. Moriguchi, N. Nakashima, Carbon 145 (2019) 565–571, https://doi.org/10.1016/j.carbon.2019.01.022.
[44] A. Morozan, S. Campidelli, A. Filoramo, B. Jousselme, S. Palacin, Carbon 49 (2011) 4839–4847, https://doi.org/10.1016/j.carbon.2011.07.004.
[45] M. Canal-Rodríguez, N. Rey-Raap, J.A. Menéndez, M.A. Montes-Morán, J. L. Figueiredo, M.F.R. Pereira, A. Arenillas, Microporous Mesoporous Mater. 293 (2020), 109811, https://doi.org/10.1016/j.micromeso.2019.109811.
[46] B. Mecheri, V.C.A. Ficca, M.A. Costa de Oliveira, A. D'Epifanio, E. Placidi, F. Arciprete, S. Licoccia, Appl. Catal. B-Environ. 237 (2018) 699–707, https://doi.org/10.1016/j.apcatb.2018.06.031.
[47] Y. Jiang, Y. Lu, X. Lv, D. Han, Q. Zhang, L. Niu, W. Chen, ACS Catal. 3 (2013) 1263–1271, https://doi.org/10.1021/cs4001927.
[48] R. Jasinski, Nature 201 (1964) 1212–1213, https://doi.org/10.1038/2011212a0.
[49] R. Venegas, F.J. Recio, J. Riquelme, K. Neira, J.F. Marco, I. Ponce, J.H. Zagal, F. Tasca, J. Mater. Chem. A 5 (2017) 12054–12059, https://doi.org/10.1039/C7TA02381B.
[50] R. Chen, H. Li, D. Chu, G. Wang, J. Phys. Chem. C 113 (2009) 20689–20697, https://doi.org/10.1021/jp906408y.
[51] R.-M. Ion, The use of phthalocyanines and related complexes in photodynamic therapy, in: T. Nyokong, V. Ahsen (Eds.), Photosensitizers in Medicine, Environment, and Security, Springer, Netherlands, 2012, pp. 315–349.
[52] T. Koczorowski, W. Szczolko, T. Goslinski, Physicochemical properties and catalytic applications of iron porphyrazines and phthalocyanines, in: M. M. Rahman, A.M. Asiri (Eds.), Recent Progress in Organometallic Chemistry, InTechOpen, 2017, pp. 101–121.
[53] H.A. Miller, M. Bellini, W. Oberhauser, X. Deng, H. Chen, Q. He, M. Passaponti, M. Innocenti, R. Yang, F. Sun, Z. Jiang, F. Vizza, Phys. Chem. Chem. Phys. 18 (2016) 33142–33151, https://doi.org/10.1039/C6CP06798K.
[54] A. Bonakdarpour, T. Dahn, R. Atanasoski, M. Debe, J. Dahn, Electrochem. Solid-State Lett. 11 (2008) B208–B211, https://doi.org/10.1149/1.2978090.
[55] R.P. Forslund, W.G. Hardin, X. Rong, A.M. Abakumov, D. Filimonov, C. T. Alexander, J.T. Mefford, H. Iyer, A.M. Kolpak, K.P. Johnston, K.J. Stevenson, Nat. Commun. 9 (2018) 3150, https://doi.org/10.1038/s41467-018-05600-y.
[56] M. Tahir, L. Pan, F. Idrees, X. Zhang, L. Wang, J.-J. Zou, Z.L. Wang, Nano Energy 37 (2017) 136–157, https://doi.org/10.1016/j.nanoen.2017.05.022.
[57] Z.-F. Huang, J. Wang, Y. Peng, C.-Y. Jung, A. Fisher, X. Wang, Adv. Energy Mater. 7 (2017) 1700544, https://doi.org/10.1002/aenm.201700544.
[58] Y.P. Zhu, Y. Jing, A. Vasileff, T. Heine, S. Z. Qiao, Adv. Energy Mater. 7 (2017) 1602928, https://doi.org/10.1002/aenm.201602928.
[59] Y. Peng, J.-Y. Choi, T. Fürstenhaupt, K. Bai, Y. Zhang, D. Banham, J. Mater. Chem. A 9 (2021) 13471–13476, https://doi.org/10.1039/D1TA01769A.
[60] Y. Jiang, M. Du, G. Cheng, P. Gao, T. Dong, J. Zhou, X. Feng, Z. He, Y. Li, L. Dai, W. Meng, L. Wang, J. Energy Chem. 59 (2021) 706–714, https://doi.org/10.1016/j.jechem.2020.12.013.
[61] P. Subramanian, A. Schechter, J. Electrochem. Soc. 163 (2016) F428–F436, https://doi.org/10.1149/2.117165jes.
[62] L.N. Ramavathu, K.K. Maniam, K. Gopalram, R. Chetty, J. Appl. Electrochem. 42 (2012) 945–951, https://doi.org/10.1007/s10800-012-0481-6.
[63] A. Jorio, R. Saito, J. Appl. Phys. 129 (2021), 021102, https://doi.org/10.1063/5.0030809.
[64] K. Zhang, C. Yan, A. Tang, Energy Storage Mater. 34 (2021) 301–310, https://doi.org/10.1016/j.ensm.2020.10.005.
[65] E.N. Kaya, T. Basova, M. Polyakov, M. Durmuş, B. Kadem, A. Hassan, RSC Adv. 5 (2015) (1862) 91855–91859, https://doi.org/10.1039/C5RA18697H.
[66] R. Kecili, C.M. Hussain, Chapter 4 – Mechanism of adsorption on nanomaterials, Nanomaterials in Chromatography Elsevier, 2018, pp. 89–115.
[67] J. Zagal, M. Páez, A.A. Tanaka, J.R. dos Santos, C.A. Linkous, J. Electroanal. Chem. 339 (1992) 13–30, https://doi.org/10.1016/0022-0728(92)80442-7.
[68] G. Zhong, S. Xu, L. Liu, C.Z. Zheng, J. Dou, F. Wang, X. Fu, W. Liao, H. Wang, ChemElectroChem 7 (2020) 1107–1114, https://doi.org/10.1002/celc.201902085.
[69] H. Singh, S. Zhuang, B. Ingis, B.B. Nunna, E.S. Lee, Carbon 151 (2019) 160–174, https://doi.org/10.1016/j.carbon.2019.05.075.
[70] Q. Shi, Y. He, X. Bai, M. Wang, D.A. Cullen, M. Lucero, X. Zhao, K.L. More, H. Zhou, Z. Feng, Y. Liu, G. Wu, Energy Environ. Sci. 13 (2020) 3544–3555, https://doi.org/10.1039/D0EE01968B.
[71] J. Xia, K. Li, G.-L. Zhao, A.C.S. Appl, Energy Mater. 3 (2020) 1484–1495, https://doi.org/10.1021/acsaem.9b01931.
[72] B. Guo, Q. Ju, R. Ma, Z. Li, Q. Liu, F. Ai, M. Yang, S. Kaskel, J. Luo, T. Zhang, J. Wang, J. Mater. Chem. A 7 (2019) 19355–19363, https://doi.org/10.1039/C9TA06411G.
[73] C. Huang, D. Wu, P. Qin, K. Ding, C. Pi, Q. Ruan, H. Song, B. Gao, H. Chen, P. K. Chu, Nano Energy 73 (2020), 104788, https://doi.org/10.1016/j.nanoen.2020.104788.
[74] D.U. Lee, P. Xu, Z.P. Cano, A.G. Kashkooli, M.G. Park, Z. Chen, J. Mater. Chem. A 4 (2016) 7107–7134, https://doi.org/10.1039/C6TA00173D.
[75] Y. Liu, H. Jiang, Y. Zhu, X. Yang, C. Li, J. Mater. Chem. A 4 (2016) 1694–1701, https://doi.org/10.1039/C5TA10551J.
[76] L. Zhao, Q. Wang, X. Zhang, C. Deng, Z. Li, Y. Lei, M. Zhu, A.C.S. Appl, Mater. Interfaces 10 (2018) 35888–35895, https://doi.org/10.1021/acsami.8b09197.
[77] X. Wu, C. Tang, Y. Cheng, X. Min, S.P. Jiang, S. Wang, Chem. Eur. J. 26 (2020) 3906–3929, https://doi.org/10.1002/chem.201905346.
[78] J. Yan, Y. Wang, Y. Zhang, S. Xia, J. Yu, B. Ding, Adv. Mater. 33 (2021) 2007525, https://doi.org/10.1002/adma.202007525.

Catalysis Today 418 (2023) 114057

Contents lists available at ScienceDirect

Catalysis Today

journal homepage: www.elsevier.com/locate/cattod

Optimization of cobalt on CNT towards the oxygen evolution reaction and its synergy with iron (II) phthalocyanine as bifunctional oxygen electrocatalyst

R.G. Morais [a,b], N. Rey-Raap [c,*], J.L. Figueiredo [a,b], M.F.R. Pereira [a,b,**]

[a] Laboratory of Separation and Reaction Engineering - Laboratory of Catalysis and Materials (LSRE LCM), Departamento de Engenharia Química, Faculdade de Engenharia, Universidade do Porto, R. Dr. Roberto Frias s/n, 4200-465 Porto, Portugal
[b] ALiCE - Associate Laboratory in Chemical Engineering, Faculdade de Engenharia, Universidade do Porto, R. Dr. Roberto Frias s/n, 4200-465 Porto, Portugal
[c] Instituto de Ciencia y Tecnología del Carbono, INCAR-CSIC, Francisco Pintado Fe 26, 33011 Oviedo, Spain

ARTICLE INFO

Keywords:
Carbon nanotube-supported electrocatalysts
Cobalt
Iron

ABSTRACT

Monometallic cobalt catalysts supported on carbon nanotubes (Co/CNT) were optimized for the oxygen evolution reaction (OER). The optimized Co/CNT catalyst was physically mixed with another catalyst composed of carbon nanotubes and iron phthalocyanine to achieve an electrocatalyst able to catalyse both the OER and the oxygen reduction reaction (ORR). A 1:1 mass ratio provided a similar OER electroactivity in comparison to the monometallic catalyst (1.64 V) and a high half-wave potential (0.88 V), which is much higher than that of the commercial Pt/C (0.83 V). This sample also produced the lowest potential gap (0.76 V), which is much lower than the commercial electrocatalysts and most state-of-the-art carbon-supported electrocatalysts.

1. Introduction

Nowadays, nations need to be energetically independent of fossil fuels and less reliant on other nations for their required energy supply. Furthermore, an energy transition from fossil fuels towards cleaner alternatives is of the greatest importance. The European Commission has proposed hydrogen as a strategy for a climate-neutral Europe [1]. One of the electrochemical devices that is quickly gaining attention from the scientific community is the unitized regenerative fuel cell (URFC). The URFC aims to achieve maximum energy efficiency by combining an electrolyzer and a fuel cell in a single device, producing non-polluting by-products and presenting several advantages in comparison to other systems, namely its portability and high durability [1–6]. The URFC is environmentally friendly, as the electrolyzer mode results in water splitting (H_2O) to generate the necessary fuels for the fuel cell (H_2 and O_2), whereas the generation of energy in the fuel cell mode does not generate polluting products, only H_2O and heat [4,7,8]. This device not only complies with the European strategy on adaptation to climate change but is also one of the most promising devices for the short and long-term future of green energy. The URFC involves four different electrochemical reactions: two reactions that take place while operating in the electrolyzer mode – the oxygen evolution reaction (OER) and the hydrogen evolution reaction (HER) - and another pair of reactions that take place in the fuel cell mode – the oxygen reduction reaction (ORR) and the hydrogen oxidation reaction (HOR) [2]. One of the main challenges in the development of this technology is the design of efficient bifunctional electrocatalysts, as they need to catalyse either ORR/OER or HOR/HER, due to the compartmentalization of the URFC device. Regarding both pairs of reactions, the oxygen pair presents much more sluggish kinetics and overall performance, hence needing further improvements to avoid hindering the overall URFC performance. Furthermore, the most developed URFC technology is based on the proton-exchange membrane fuel cell (PEMFC) [1,6,9–12], which operates under acidic conditions and requires the use of noble metals. In fact, the current benchmark catalysts for the oxygen reactions are Pt, Ir and Ru, which are scarce and very expensive, increasing the overall cost of the device and limiting its commercialization [6]. One of the main targets of the scientific community is to reduce these costs [2,6,13–15]. This can be achieved by changing the operating conditions to basic media, using an anion-exchange membrane fuel cell (AEMFC) while

* Corresponding author.
** Corresponding author at: Laboratory of Separation and Reaction Engineering - Laboratory of Catalysis and Materials (LSRE-LCM), Departamento de Engenharia Química, Faculdade de Engenharia, Universidade do Porto, R. Dr. Roberto Frias s/n, 4200–465 Porto, Portugal.
E-mail addresses: natalia.rey@incar.csic.es (N. Rey-Raap), fpereira@fe.up.pt (M.F.R. Pereira).

https://doi.org/10.1016/j.cattod.2023.114057
Received 19 December 2022; Received in revised form 11 February 2023; Accepted 23 February 2023
Available online 24 February 2023
0920-5861/© 2023 The Authors. Published by Elsevier B.V. This is an open access article under the CC BY-NC-ND license (http://creativecommons.org/licenses/by-nc-nd/4.0/).

maintaining high performance. This technology enables the use of a wider range of materials than PEMFC, especially the use of widely available and low-cost carbon materials [6]. These materials have been successfully tailored as bifunctional electrocatalysts towards ORR and OER [16–21], but still require further improvements before achieving large-scale production. The incorporation of different heteroatoms and transition metals, in particular cobalt and iron, is a commonly used methodology to modulate the electrocatalyst properties [16,18,22]. Regarding the ORR, iron(II) phthalocyanine (FePc) macrocycles containing both nitrogen and iron provide an interesting synergy between both elements and a constant 4-electron reaction pathway with high electroactivity [16,23–29]. Similarly, the use of the cobalt(II) phthalocyanine (CoPc) has also displayed interesting performances towards OER [16,25]. So, the combination of FePc and CoPc results in highly electroactive bifunctional materials [16,25]. Nonetheless, there is still room for improvement regarding both the electrochemical performances and the production costs. Cobalt has been widely reported as an interesting OER electrocatalyst [30,31] and can be incorporated into carbon supports using a large variety of methodologies and precursors. Moreover, carbon-based materials doped with cobalt species can also provide high bifunctional catalytic activity towards both ORR and OER [17,22,32–35]. Nonetheless, i) a comprehensive study of the evolution of cobalt species and their effect on the OER, ii) their synergy with FePc towards the ORR, and iii) their performance as bifunctional oxygen electrocatalysts are yet to be reported. Therefore, the focus of this work is to investigate the influence of cobalt species supported on carbon nanotubes (CNT) on the OER by incorporating a low-cost cobalt precursor. Furthermore, this study aims to synthesise carbon electrocatalysts with high electrocatalytic performance with regard to both oxygen reactions (OER and ORR) by mixing the optimized Co-doped CNT with a Fe-doped CNT with very high electroactivity towards the ORR. The use of cobalt nitrate as precursor resulted in low production costs due to its low price and the lower thermal treatment temperature needed to achieve the materials with the most promising OER performance. The synergy between both monometallic CNT-based electrocatalyst resulted in remarkable improvements towards bifunctionality, in comparison to the addition of only one metal species.

2. Experimental

2.1. Preparation of electrocatalysts

Highly electroactive bifunctional ORR/OER electrocatalysts were prepared using purified multi-walled carbon nanotubes. The purification process is explained elsewhere [16]. The CNT were then modified for the OER by addition of cobalt using cobalt (II) nitrate as a precursor. The cobalt precursor was added by the incipient wetness impregnation method. Briefly, 1.25 g of cobalt (II) nitrate hexahydrate (99%, Sigma Aldrich) per gram of purified CNT (Nanocyl, > 95%) was dissolved in ethanol and added dropwise to the CNT under sonication, maintained in the ultra-sonication bath for 30 min and dried overnight at 100 °C. After cobalt impregnation, 6 different samples were prepared using different thermal treatment temperatures and/or atmospheres. Four samples were prepared in a N_2 atmosphere at 150 °C, 185 °C, 350 °C, and 900 °C for 2 h (CNT_{Co_150N2}, CNT_{Co_185N2}, CNT_{Co_350N2}, and CNT_{Co_900N2}, respectively), and two additional samples were prepared by further treating CNT_{Co_185N2} and CNT_{Co_350N2} for 2 h in a H_2 atmosphere (CNT_{Co_185H2} and CNT_{Co_350H2}, respectively). Furthermore, three bifunctional samples were prepared by incorporating iron(II) phthalocyanine (FePc) into the electrocatalysts. Several methodologies were used to incorporate FePc: i) incorporation of FePc using a 1:20 mass ratio (FePc:Co-doped CNT) by incipient wetness impregnation and consequent thermal treatment in a N_2 atmosphere at 500 °C ($CNT_{Co\ 185H2\ Fe}$); ii) incorporation of FePc using a 1:20 mass ratio (FePc:CNT) and consequent thermal treatment in inert atmosphere at 500 °C (CNT_{Fe}) and subsequent incorporation of the cobalt nitrate as mentioned in the initial procedure for the sample CNT_{Co_185H2} ($CNT_{Fe_Co_185H2}$) and iii) physical mixture of sample $CNT_{Co\ 185H2}$ and CNT_{Fe} using a 1:1 mass ratio until a homogeneous mixture was obtained (CNT_{Fe}/CNT_{Co_185H2}). Besides, sample $CNT_{Fe}/CNT_{Co\ 185H2}$ presents only half of each metal compared to monometallic samples and other Fe,Co-doped materials prepared.

2.2. Chemical and textural characterization

Sample combustion at 1050 °C was performed to assess the content of carbon, hydrogen and nitrogen (C, H and N), whereas pyrolysis at 1450 °C was conducted to determine the oxygen content of each prepared material. C, H and N determination was done in a Vario Micro Cube equipment, whereas oxygen determination was performed using a Rapid Oxy Cube analyser, both from Elementar GmbH. Moreover, transition metal quantification (cobalt and iron) was determined using a polychromator Echelle in a Perkin Elmer Optima 4300 spectrometer by inductively coupled plasma (ICP) emission spectrometry. Additionally, the samples were analysed in a Kratos AXIS Ultra HAS spectrometer to determine their surface chemical composition by X-ray photoelectron spectroscopy (XPS). This was achieved using a fixed analyser transmission mode at 15 kV (90 W) and a monochromatic Al Kα radiation (1486.7 eV). Furthermore, N_2 adsorption-desorption isotherms were performed at − 196 °C for each material to determine their textural properties. The analyses took place in an automated gas sorption analyser (Quantachrome Autosorb iQ). Prior to analyses, degasification at 150 °C under vacuum conditions took place for 12 h. The specific surface area (S_{BET}) was determined by applying the Brunauer-Emmett-Teller equation. All materials were also analysed by Raman spectroscopy at a 532 nm monochromatic wavelength in an Alpha 300 equipment (WiTec, Germany). Lastly, selected materials were analysed by X-ray diffraction (XRD) to determine the composition of their crystalline phases. All XRD experiments took place at 45 kV and 40 mA on a X'Pert Pro diffractometer (PANalytical, Malvern, UK) composed by a PIXcel detector and employing a Cu Kα radiation with a wavelength of 1.541874 Å. The analyses were performed using a scan speed of 0.01° s^{-1} between 20° and 80° (2θ) through a Bragg-Brentano configuration.

2.3. Electrochemical characterization

All samples were electrochemically characterized using a three-electrode system with a reference (Ag/AgCl, KCL 3 mol L^{-1}) and a counter electrode (carbon rod). The working electrode was composed of a glassy carbon (GC) disk. Two different types of working electrodes were employed according to the data collection desired: i) a rotating disk electrode with a radius of 1.5 mm (RDE, Metrohm) for OER measurements and cyclic voltammetry (CV) that are crucial to determine the double-layer capacitance (C_{dl}), as well as stability tests towards the ORR and ii) a rotating ring-disk electrode (RRDE) with a 2.5 mm radius and a Pt ring (Methrom) that was used for linear sweep voltammetry (LSV) towards ORR assessments. The working electrode with each electrocatalyst was prepared by deposition of ca. 0.27 mg cm^{-2}, of a suspension containing the active material. Each suspension was prepared by sonication until homogeneity was achieved. The dispersion was prepared with 4 mg of each carbon material and a 1:1:6 solution ratio of Nafion (5 wt% in lower aliphatic alcohols and water, Sigma-Aldrich), ethanol (≥99.5%, VWR Chemicals) and ultrapure water (Milipore). All assessments were performed using a PGSTAT 302 N potentiostat/galvanostat and a 0.1 mol L^{-1} KOH medium at ambient temperature.

Regarding OER characterization, all samples were tested by performing LSV measurements at 1600 rpm and employing a scan rate of 5 mV s^{-1} up to a potential of 1.85 V (vs RHE). Prior to each LSV, the ohmic resistance (R) of each electrocatalyst in the electrolyte was determined using the i-interrupt method [36], which was then used to correct the LSVs obtained during the OER by using the E-iR equation, in which i corresponds to each current obtained during the electrochemical

characterization. After the LSVs, several important parameters used to compare samples worldwide were determined: i) the E_{10}, which is the potential necessary to replicate a 10% efficient conversion device that uses a solar-to-fuels technique (10 mA cm^{-2}) and ii) the Tafel slopes obtained from the LSVs through the E vs log (J) plots. Furthermore, the long-term performance of the materials was determined by performing 1000 LSVs between the initial potential applied (1.00 V) and the last point measured (1.85 V).

On the other hand, ORR testing (LSV) was achieved in an inert and O_2-saturated medium. Similarly to OER measurements, the scan rate employed for the LSVs was fixed at 5 mv s^{-1}, whereas different rotation speeds were recorded (400–3000 rpm). The rotation speeds were controlled by a rotation speed controller that applied each rotation selected to the working electrode. All ORR experiments took place by applying a potential between 1.10 V and 0.15 V (vs RHE). The final LSV current for each electrocatalyst was obtained by subtracting the current produced during the inert saturation assessments from that obtained in the KOH saturated with O_2. Furthermore, from the substracted LSV, several ORR parameters were determined: i) the onset potential (E_{onset}) at 0.1 mA cm^{-2}; ii) the half-wave potential ($E_{1/2}$), corresponding to the maximum value obtained by derivating the current-potential curve, which is equivalent to the potential at which the highest increase of J between two potentials occurs [37]; and iii) the limiting current density measured at 0.4 V vs RHE (J_L). Additionally, the by-product formation (H_2O_2) of each electrocatalyst and the respective reaction mechanism (electrons transferred), were determined by the disk and ring currents obtained from the LSVs measured using a RRDE. These last two parameters were obtained by applying Eqs. (1 and 2), respectively, to the LSVs measured at 1600 rpm:

$$H_2O_2(\%) = 200 \times \frac{\frac{I_R}{N}}{I_D + \frac{I_R}{N}} \quad (1)$$

$$n = \frac{4I_D}{I_D + \frac{I_R}{N}} \quad (2)$$

where I_R is the ring current (mA), I_D is the disk current (mA), and N is the collection efficiency (0.249).

The long-term durability of each carbon material towards the ORR was measured using a chronoamperometry procedure. The test was performed for 10000 s by employing a potential of 0.4 V vs RHE in O_2-saturated electrolyte. Additionally, to understand the poisoning tolerance of the electrocatalysts with the most interesting performances, methanol (1.5 mL) was added to the reaction medium during the chronoamperometry assessment at ca. 1000 s. Furthermore, each procedure was then replicated for Pt/C (20.2 wt%, 2.5 nm Pt particle size, Alfa Aesar), as a comparison standard for result discussion. Finally, the oxygen bifunctionality performance of the synthesised materials was determined by subtracting the main potential parameter of OER (E_{10}) from the value of $E_{1/2}$ obtained from the ORR assessments. This parameter is known as the potential gap (ΔE) between both reactions and is usually accepted as a good method to determine the bifunctionality of electrocatalysts.

The prepared carbon materials were also electrochemically characterized to determine the double-layer capacitance (C_{dl}) by performing CVs at several scan rates (5–220 mV s^{-1}). These assessments were performed in an inert saturated medium within a potential range in which no Faradic current is produced. Afterwards, the intensity is plotted vs the scan rate and fitted to a straight line. The value of the slope is considered the C_{dl} value. Furthermore, the electrochemical active surface area (ECSA) of each material, which is essential to gain some insight regarding the accessibility of the active centers [38], is calculated by dividing the C_{dl} by the specific capacitance (C_S) (Eq. 3):

$$ECSA = \frac{C_{dl}}{C_S} \quad (3)$$

Nonetheless, all samples prepared were synthesised using the same materials and very similar procedures, hence very few differences are expected in their chemical nature. Consequently, the ECSA can be considered to be proportional to the double-layer capacitance and can be directly correlated to the main active centers in both reactions.

3. Results and discussion

3.1. Chemical properties

The surface chemistry of the carbon support was tailored by the incorporation of cobalt nitrate and FePc molecules. The bulk chemical composition of each electrocatalyst obtained from elemental analysis and ICP is presented in Table 1.

The CNT_{Co_150N2} sample treated at the lowest temperature (150 °C) in the N_2 atmosphere displays the highest oxygen content (11.3 wt%) and the lowest cobalt content (19.6 wt%) of all monometallic cobalt-doped samples, and is the only one of those samples that present nitrogen due to the presence of some cobalt precursor that is not removed at 150 °C [39]. The oxygen content of the samples decreases by increasing the thermal treatment temperature (11.3 wt% > 9.4 wt% > 7.5 wt% > 2.7 wt%) and, consequently, the contribution of cobalt in the global composition increases (19.6 wt% < 20.6 wt% < 21.2 wt% < 22.4 wt%) as the absolute cobalt content remains the same whereas the sum of contributions of all elements decreases. The percentage of oxygen was further reduced after the thermal treatment under the H_2 atmosphere. This reduction is more significant at higher temperatures (350 °C), in which half of the initial oxygen content was lost (from 7.5 wt% to 3.7 wt%). Once again, an increase in the relative cobalt content is observed due to the decrease in oxygen. These results demonstrate that the cobalt precursor was successfully incorporated into the carbon support, although the different thermal treatment conditions resulted in materials with significantly different compositions. Regarding the bimetallic samples, interesting differences are observed. Sample $CNT_{Co\ 185H2\ Fe}$ presents a lower oxygen content than sample CNT_{Co_185H2} (6.9 wt% vs 8.0 wt%, respectively) due to the higher temperature applied during the incorporation of FePc (500 °C) compared to that used in the sample with only cobalt nitrate (185 °C). This result is in agreement with the conclusion drawn from the monometallic samples. Moreover, the cobalt content remains similar to that in CNT_{Co_185H2}. Sample $CNT_{Fe_Co_185H2}$ presents very similar oxygen and cobalt contents in comparison to CNT_{Co_185H2} due to the addition of the cobalt nitrate on the CNT_{Fe} sample, which resulted in a single thermal treatment applied to the cobalt nitrate equal to that applied in sample CNT_{Co_185H2}. In both samples ($CNT_{Co_185H2_Fe}$ and $CNT_{Fe_Co_185H2}$) the iron content is in agreement with the theoretical value (0.4 wt%). The content of FePc employed in these two bimetallic samples is too low, so nitrogen was not detected by elemental analysis, while ICP is a more suitable technique to determine low contents of target elements, allowing the detection of low iron amounts in the samples. The bimetallic sample CNT_{Fe}/CNT_{Co_185H2}

Table 1
Chemical composition determined by elemental analyses and ICP, and values of S_{BET} obtained from the N_2 adsorption-desorption isotherms.

Sample	C [wt %]	H [wt %]	N [wt %]	O [wt %]	Co [wt %]	Fe [wt %]	S_{BET} (m^2 g^{-1})
CNT_{Co_150N2}	68.0	0.3	0.8	11.3	19.6	0.0	148
CNT_{Co_185N2}	69.9	0.1	0.0	9.4	20.6	0.0	142
CNT_{Co_185H2}	70.7	0.2	0.0	8.0	21.1	0.0	158
CNT_{Co_350N2}	71.2	0.1	0.0	7.5	21.2	0.0	154
CNT_{Co_350H2}	73.2	0.1	0.0	3.7	23.0	0.0	156
CNT_{Co_900N2}	74.8	0.1	0.0	2.7	22.4	0.0	164
$CNT_{Co_185H2_Fe}$	72.5	0.1	0.0	6.9	20.1	0.4	157
$CNT_{Fe_Co_185H2}$	67.9	0.3	0.0	10.8	20.6	0.4	152
CNT_{Fe}/CNT_{Co_185H2}	82.7	0.1	0.5	4.7	11.8	0.2	149

presents around half of the oxygen, cobalt and iron contents of the monometallic samples, and nitrogen is detected derived from the FePc precursor, indicating that the mixture between samples was successful.

The surface composition determined by X-ray photoelectron spectroscopy (XPS) and the survey spectra are presented in Table S1 and Fig. S1, respectively. The survey spectra confirm the presence of all elements discussed during the elemental/ICP analysis except for iron. This absence is related to the much higher Co content than Fe, which results in the overlap of the Fe 2*p* region and the Co LMM region, from which only the Co peaks are perceptible. Regarding the overall composition of the samples, interesting differences are observed between XPS and elemental/ICP analyses. The surface oxygen and cobalt contents of all samples are lower than the overall values, indicating that the precursors incorporated are preferentially located in the CNT bundles rather than on their external surfaces. Furthermore, the effect of the temperature and gas composition employed in the thermal treatments is the same as that discussed for the elemental analysis and ICP, with two exceptions. The first exception is a slightly higher oxygen content on the surface of sample CNT_{Co_185N2}. Even though it has a lower overall oxygen content than its counterpart treated at 150 °C, the higher temperature employed may have dislocated some of the oxygen to the catalyst's surface. The second exception is the slightly lower surface cobalt content of CNT_{Co_350H2} in comparison to CNT_{Co_350N2}. This difference is not observed for the pair of samples treated at a lower temperature (185 °C), which indicates that the gas composition employed during the treatment does not have a significant effect. However, the temperature may have favored the precursor transition into the bulk of the CNT bundles, hence the lower Co surface content. These results demonstrate that temperature plays a key role in the location of the functional groups.

The high-resolution XPS spectra of the Co *2p* regions are presented in Fig. S2. The Co *2p* region displays two distinct sharp peaks at 780.0 ± 0.4 eV and at 795.2 ± 0.5 eV corresponding to Co $2p_{3/2}$ and Co $2p_{1/2}$, respectively [40], with a spin-orbit splitting of 15.2 eV [41]. The deconvolution of the Co $2p_{3/2}$ region demonstrates the presence and coexistence of Co^{2+} and Co^{3+}, which peaks appear at 779.9 ± 0.1 eV and 781.6 ± 0.3 eV, respectively. Furthermore, two shake-up satellite peaks are also detected at higher binding energies (784.7 ± 0.3 eV and 789.4 ± 1.2 eV), attributed to the presence of Co^{2+} and Co^{3+} species [42]. These four peaks present their corresponding spin-orbit splitting of 15.2 eV. Regardless of the atmosphere employed, the results of the deconvolution indicate an increase in Co^{2+} content and a decrease in Co^{3+} as the temperature increases (Table S1). These results are in agreement with the reaction mechanism ascribed to the thermal decomposition of the cobalt nitrate hexahydrate [43]. Briefly, after the dehydration of the cobalt precursor (150 °C), Co_2O_3 species are formed, in which the cobalt is in a Co^{3+} oxidation state. Afterwards, an increase in temperature from 150 °C up to 185 °C and 350 °C favors the conversion of Co_2O_3 into Co_3O_4, which presents a mix of Co^{2+} and Co^{3+} species instead of just Co^{3+}, hence increasing the relative content of Co^{2+}, as observed by XPS. Moreover, at temperatures above 700 °C, the formation of CoO also occurs [44], and, consequently, an increase of Co^{2+} is observed for the sample treated at 900 °C. Moreover, the subsequent thermal treatment under H_2 after the one in N_2 further reduces Co_3O_4 to CoO [39], further increasing the relative content of Co^{2+}, as observed by XPS. Regarding bimetallic samples, the deconvolution of the Co *2p* region of the sample $CNT_{Fe\ Co\ 185H2}$ presents a lower contribution of Co^{2+} in comparison to CNT_{Co_185H2}, which indicates that the previous incorporation of FePc hinders the effect of the H_2 atmosphere and, consequently, the formation of Co^{2+} species. On the other hand, $CNT_{Co\ 185H2\ Fe}$ shows an increase of Co^{2+} and a decrease of Co^{3+} species in comparison to CNT_{Co_185H2}, which follows the same trend as the monometallic samples due to the higher temperature applied during the second thermal treatment (500 °C). Lastly, the sample obtained by mixing both monometallic samples (CNT_{Fe}/CNT_{Co_185H2}) displays the same Co^{2+}/Co^{3+} ratio as $CNT_{Co\ 185H2}$ as no further thermal treatment nor significant mechanical modifications were performed on the bimetallic sample in comparison to the monometallic ones.

The nitrogen adsorption-desorption isotherms of the prepared carbon materials are displayed in Fig. S3 and the values of the BET surface area (S_{BET}) are presented in Table 1. All samples exhibit a type II isotherm, attributed to multi-layered adsorption commonly observed for carbon nanotubes [45]. Although different temperatures and atmospheres were employed during the thermal treatments, all samples display very similar textural properties. The S_{BET} of all prepared Co-doped materials varies from 142 to 164 $m^2\ g^{-1}$, which is lower than that of the purified CNT (217 $m^2\ g^{-1}$). This is due to the presence of cobalt in the carbon structure. Regarding bimetallic samples, all samples are within the same range as monometallic samples, ranging from 149 to 157 $m^2\ g^{-1}$, which is similar to the base Co-CNT sample prepared using similar conditions (CNT_{Co_185H2}). These results indicate that the methodology employed to incorporate the transition metals does not modify the textural properties.

To further study the changes assigned to the addition of the metallic precursors and/or the thermal treatments applied, all synthesised carbons were analysed by Raman spectroscopy. The obtained spectra are presented in Fig. 1.

All samples display two main peaks at ca. 1350 cm^{-1} (D band) associated with the basal plane defects of the carbon structure and a second peak at ca. 1580 cm^{-1} (G band), ascribed to graphitic domains, which are prevalent on CNT. Moreover, at higher shifts (ca. 2700 cm^{-1}), a third peak attributed to the π band in the electronic structure is also observed. To obtain additional information on the relative amount of defects, the peak areas of the respective D and G bands were integrated. The A_D/A_G ratio of all samples is presented in Table S2. The Co-doped CNT treated at the lowest temperature ($CNT_{Co\ 150N2}$) presents an A_D/A_G ratio of 0.58. The ratio decreases from 0.58 to 0.20 by increasing the temperature from 150 °C to 900 °C, suggesting the formation of a more graphitic structure with a smaller number of defects. Further treatment under H_2 atmosphere slightly increases the A_D/A_G ratio in comparison to their N_2 counterparts (0.40 vs 0.42 and 0.32 vs 0.36, at 185 °C and 350 °C, respectively). These differences suggest that the reduction of cobalt oxides due to the use of H_2 generates defects in the carbon structure.

Regarding the bimetallic samples, interesting differences are observed in comparison to Co-doped samples. Sample $CNT_{Co_185H2_Fe}$ presents an A_D/A_G ratio of 0.39, which is slightly lower than the base sample CNT_{Co_185H2} (0.42), probably due to the high temperature employed (500 °C). Nonetheless, both Co-doped samples treated at 350 °C present lower values than 0.39, indicating that the incorporation of FePc is probably generating defects in the carbon structure. This effect, due to the presence of FePc, has been previously reported in the literature [16,46]. Sample $CNT_{Fe_Co_185H2}$ exhibits an A_D/A_G ratio of 0.77, which is higher than either those of CNT_{Fe} (0.52) or $CNT_{Co\ 185H2}$ (0.42), which indicates that the incorporation of Co on the CNT_{Fe} sample is leading to the formation of additional defects on the carbon structure. Lastly, sample CNT_{Fe}/CNT_{Co_185H2} presents an A_D/A_G ratio of 0.51, which is in between the values of the monometallic samples employed in the mixture. This value was expected as this electrocatalyst was not subjected to any further thermal treatment.

To further understand the differences between the synthesized materials, the composition of the crystalline phases of the Co-doped CNTs was studied by X-ray diffraction (XRD). The obtained patterns are displayed in Fig. S4 and a detailed discussion is presented in the supplementary material. Briefly, from XRD patterns it can be inferred that using H_2 atmosphere and increasing the temperature of the thermal treatments favors the formation of CoO. In addition, the crystallite size increases from 58 nm to 130 nm by increasing the reduction temperature from 185 °C to 350 °C.

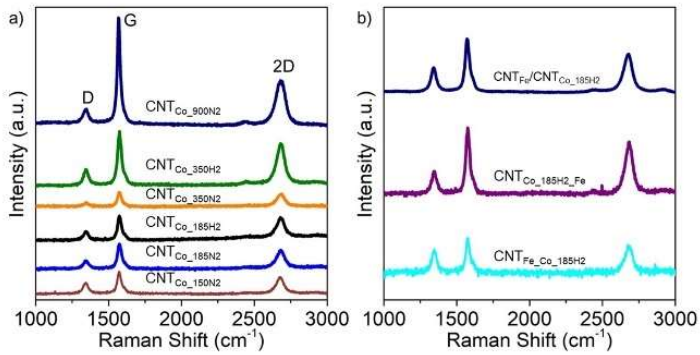


Fig. 1. Raman spectra of the Co-doped (a) and Co,Fe-doped electrocatalysts (b).

3.2. Electrochemical assessments

3.2.1. Oxygen evolution reaction

The OER electroactivity of the synthesised monometallic Co-doped carbon samples was measured by LSV in a N_2-saturated medium at a scan rate of 5 mV s^{-1} and 1600 rpm (Fig. 2a).

The E_{10} decreases with temperature from 1.69 V to 1.66 V (from 150 °C to 900 °C) which is likely due to the increase in the relative content of Co^{2+} and the Co^{2+}/Co^{3+} ratio on the surface (Table S1 – XPS). The formation of CoO species results in a very significant decrease of the unit cell length to almost half in comparison to Co_3O_4 [47], which may favor the adsorption and, consequently, the evolution of oxygen. Samples further treated under H_2 atmosphere display even lower values of E_{10} (1.63 V) due to the higher content of Co^{2+} in these samples. Nonetheless, $CNT_{Co\ 900N2}$ presents a higher Co^{2+} content than the other samples but not the highest electroactivity. This may be explained by the presence of metallic Co that hinders its performance. Accordingly, it is important to select the appropriate temperature and atmosphere to perform the reduction of cobalt species in order to obtain the highest percentage of Co^{2+} and not further reduced species. The reaction kinetics follow the same trend. The Tafel slope decreases (faster kinetics) with increasing temperature from 150 °C (104 mV dec^{-1}) to 350 °C (85 mV dec^{-1}), which is in agreement with the importance of Co^{2+} species towards the electrocatalyst performance. Nonetheless, at 900 °C, the reaction kinetics is slower (102 mV dec^{-1}) than that measured at 350 °C, which seems to be related to the presence of non-oxidized Co species. Regarding samples further treated in H_2, they present very similar Tafel slope values (Fig. 2b), with a slightly lower value for CNT_{Co_350H2}. This further corroborates the importance of Co species, as a higher relative Co^{2+} content leads to slightly faster reaction kinetics.

The bimetallic carbon materials were also tested as electrocatalysts in the OER. The LSV curves performed in a N_2-saturated medium at 5 mV s^{-1} are presented in Fig. 3a.

The sample $CNT_{Fe_Co_185H2}$ gives rise to a J of 10 mA cm^{-2} at 1.63 V (E_{10}), which is the same value as that obtained with sample $CNT_{Co\ 185H2}$. This result indicates that the incorporation of FePc on the carbon support does not provide a significant improvement in the OER activity. This effect may be due to the sample's preparation method and to the small amount of iron incorporated, which is 50 times smaller than that of cobalt. Consequently, the addition of a large amount of cobalt precursor on top of CNT_{Fe} and its very small amount of FePc may have led to the inhibition of iron active centers due to blocking by the cobalt species. Sample $CNT_{Co\ 185H2\ Fe}$ results in an E_{10} of 1.62 V, which is 10 mV lower than that of $CNT_{Co\ 185H2}$, suggesting that, despite cobalt species being the main active centers, the presence of FePc contributes to some extent to improve the electrocatalytic performance. This improvement is probably due to the preparation method that led to the presence of the iron active centers on the catalyst's surface avoiding the inhibition

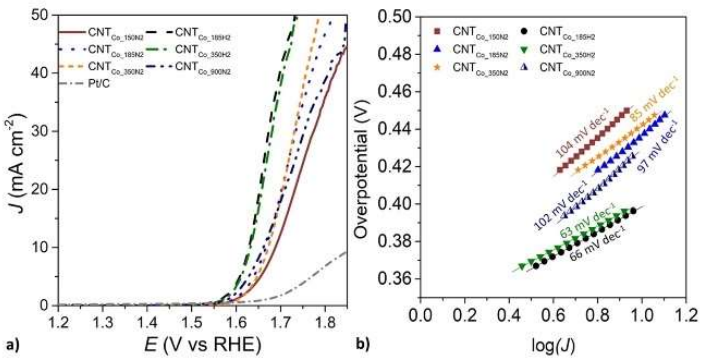


Fig. 2. Co-doped samples' (a) OER LSV curves recorded at 1600 rpm using a scan rate of 5 mV s^{-1} in a N_2-saturated 0.1 mol L^{-1} KOH electrolyte, and respective Tafel plots (b).

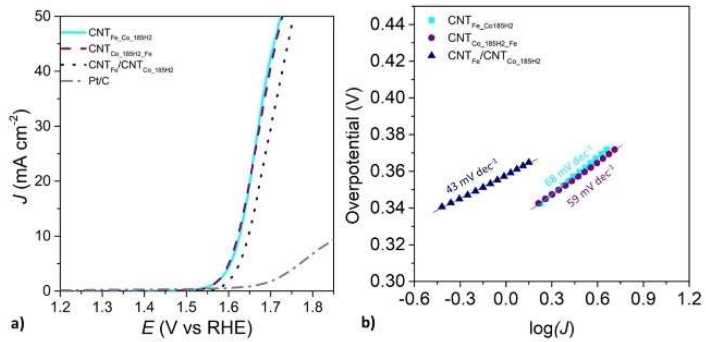


Fig. 3. Co_xFe-doped samples' (a) OER LSV curves recorded at 1600 rpm using a scan rate of 5 mV s^{-1} in a N_2-saturated 0.1 mol L^{-1} KOH electrolyte, and respective Tafel plots (b).

observed during the screening of $CNT_{Fe\ Co\ 185H2}$. Therefore, the order in which each metal is incorporated seems to play an important role in the material's electrochemical performance. The sample prepared from the physical mixture of two monometallic samples ($CNT_{Fe}/CNT_{Co\ 185H2}$) resulted in a slight increase in the E_{10} value in comparison to the abovementioned bimetallic electrocatalysts (1.64 V). This effect is probably due to the total content of cobalt. Although the cobalt content is reduced to half, the E_{10} only increases by 10 mV, which is a very low difference in comparison to sample $CNT_{Co\ 185H2}$. To further understand the interaction of both monometallic samples, CNT_{Fe} was tested towards the OER (Fig. S5) as well as a sample prepared using the same methodology as $CNT_{Co\ 185H2}$ but using only half of the cobalt precursor content ($CNT_{0.5Co_185H2}$, Fig. S6). It is possible to observe that CNT_{Fe} presents a low electroactivity towards OER (1.79 V), whereas $CNT_{0.5Co_185H2}$ presents a slight increase of E_{10} (1.65 V) in comparison to CNT_{Co_185H2} (1.63 V). The physical mixture of Fe-doped CNT and CNT_{Co_185H2} (CNT_{Fe}/CNT_{Co_185H2}) displays an E_{10} of 1.64 V, which, similarly to $CNT_{Co_185H2_Fe}$, exhibits a decrease of 10 mV in comparison to the Co-doped CNT with similar cobalt content ($CNT_{0.5Co_185H2}$). This result further infers that FePc contributes to improving the electrocatalyst's performance towards the OER. From these results, it should be highlighted that bimetallic samples present very close E_{10} values to those of the benchmark RuO_2 catalyst (1.58 V [18]).

The reaction kinetics of the bimetallic samples provide interesting insights into the OER performance. Firstly, sample $CNT_{Fe_Co_185H2}$ presents a very similar Tafel slope value (68 mV dec^{-1}) in comparison to the monometallic cobalt sample CNT_{Co_185H2}, which indicates that the cobalt active centers control the electrocatalyst performance. Nonetheless, the addition of FePc on the surface of CNT_{Co_185H2} (sample $CNT_{Co\ 185H2\ Fe}$) results in a Tafel slope of 59 mV dec^{-1}, which suggests that the presence of iron on the electrocatalyst surface has a positive outcome on the performance of the electrocatalyst. This effect is even more evident in the sample $CNT_{Fe}/CNT_{Co\ 185H2}$, in which both metals are incorporated into the CNT separately, favoring the synergy between the FePc and the CNT through their π-π systems [16,23,48], which enhances the electroactivity of the material and drops the Tafel slope to 43 mV dec^{-1}. Therefore, even though a slight performance loss is observed for CNT_{Fe}/CNT_{Co_185H2} due to the lower cobalt content, an impressive improvement in the reaction kinetics is achieved. The drop in the Tafel slope value of the mixed sample may be related to its ECSA. The analysis of the double-layer capacitance (C_{dl}) of the electrocatalysts (Fig. S7) suggests that CNT_{Fe}/CNT_{Co_185H2} has a much higher active area than the other samples, which may explain the enhanced reaction kinetics due to the larger amount of available active sites.

Stability tests for the bimetallic samples were also performed to understand their long-term use towards the OER. The LSVs obtained are displayed in Fig. 4.

As shown in Fig. 4, after 1000 LSVs, all samples remain highly electroactive towards the OER. Sample $CNT_{Fe\ Co\ 185H2}$ presents the lowest loss of electroactivity by increasing its overpotential by 33 mV, which is most likely caused by the deactivation of cobalt active sites since, in this sample, iron does not appear to be catalysing the OER, as previously discussed. Regarding $CNT_{Co\ 185H2\ Fe}$, the overpotential increases by 36 mV, which means that its stability is lower than that of $CNT_{Fe\ Co\ 185H2}$. This effect can be attributed to the degradation of FePc active sites that, in this sample, are crucial in the OER electroactivity. Lastly, $CNT_{Fe}/CNT_{Co\ 185H2}$ presents an increase of overpotential of 41 mV, which may be attributed to the lower amount of cobalt. Although this sample only presents half of the cobalt content in comparison to the other bimetallic samples, its reaction kinetics are faster, resulting in a higher turnover frequency of the active centers and, consequently, in their deactivation.

3.2.2. Oxygen reduction reaction

The prepared bimetallic electrocatalysts were tested in the ORR by

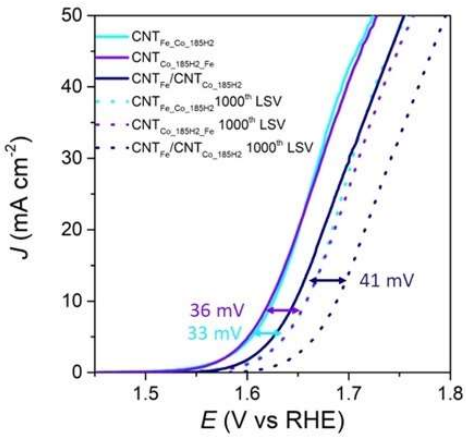


Fig. 4. 1st and 1000th OER LSV curves of bimetallic samples obtained in the stability test.

LSV, using a scan rate of 5 mV s^{-1} in a O_2-saturated 0.1 mol L^{-1} KOH electrolyte at 1600 rpm. Besides these electrocatalysts, samples CNT_{Co_185H2} and CNT_{Fe} were also assessed to further evaluate the modifications of each synthesis. Moreover, the ORR performance of Pt/C was also studied as a benchmark for comparisons with the prepared carbons. The disk current density and number of electrons exchanged are represented in Fig. 5a and b, respectively. ORR values determined for materials assessed and Pt/C are exhibited in Table 2.

Initially, samples $CNT_{Co\ 185H2}$ and CNT_{Fe} were analysed to evaluate their performance towards the ORR. $CNT_{Co\ 185H2}$ displays a low E_{onset} (0.80 V) and $E_{1/2}$ (0.68 V), and a limiting current density of 4.21 mA cm^{-2}. The electroactivity of this material is lower than state-of-the-art Co-doped carbons prepared specifically to catalyse the ORR [15, 49]. However, this sample presents an interesting reaction mechanism, almost achieving a 4-electron pathway (3.7 electrons) and a low by-product formation of 15%. Therefore, it is essential to further tailor its active centers to properly electrocatalyse both the OER and the ORR. The incorporation of FePc on the CNT results in a much higher electroactivity towards ORR in comparison to CNT_{Co_185H2}, a high current density, and an $E_{1/2}$ value higher than Pt/C (0.88 V vs 0.83 V, respectively). Moreover, this sample displays a 4-electron reaction mechanism with a negligible formation of H_2O_2. Furthermore, this sample presents higher current density and overall higher electrochemical performance than similar state-of-the-art $CNT_{Fe}Pc$, in which much higher contents of FePc were employed [50–53] and additional steps were needed to functionalize the material [50,52]. Moreover, the onset potentials obtained for CNT_{Fe} and $CNT_{Fe}/CNT_{Co\ 185H2}$ (0.96 V and 0.94 V vs RHE, respectively) were higher than the values previously reported in the state-of-the-art with similar materials such as CNT dopped with FePc prepared by also using low amounts of precursor and a similar number of steps (0.90 V vs RHE) [54] and (0.91 V vs RHE) [55]. In comparison to carbon materials doped with iron porphyrins, which are very similar to FePc, the onset potential obtained is also slightly higher than those reported in literature (0.93 V and 0.83 V vs RHE) [56]. Therefore, the methodology presented in this work is more suitable to produce an electrocatalyst for the ORR by cutting on raw material amount/costs and overall production costs.

This work aims to develop efficient bifunctional oxygen electrocatalysts, so, taking into consideration the results from the OER assessment using Co-doped CNT and the performance of CNT_{Co_185H2} and CNT_{Fe} towards the ORR, different combinations of these two materials (bimetallic samples) were tested. Regarding the incorporation of cobalt on CNT_{Fe} ($CNT_{Fe_Co_185H2}$), a decrease of 130 mV and 150 mV is observed for E_{onset} and $E_{1/2}$, respectively, in comparison to CNT_{Fe}.

Table 2
Main electrochemical ORR parameters: Onset potential (E_{onset}), half-wave potential ($E_{1/2}$), limiting current density (J_L), by-product (H_2O_2) production, and the number of electrons exchanged (n_e) for the synthesised electrocatalysts and Pt/C catalyst.

Sample	E_{onset} (V)	$E_{1/2}$ (V)	J_L (mA cm^{-2})[a]	H_2O_2 (%)[a]	n_e[a]
CNT_{Co_185H2}	0.80	0.68	4.21	15	3.7
CNT_{Fe}	0.96	0.88	6.10	< 1	4.0
$CNT_{Fe_Co_185H2}$	0.83	0.73	4.03	13	3.7
$CNT_{Co_185H2_Fe}$	0.90	0.81	4.43	11	3.8
CNT_{Fe}/CNT_{Co_185H2}	0.94	0.88	5.36	5	3.9
Pt/C	0.98	0.83	5.41	3	3.9

[a] Calculated at 0.4 V vs RHE.

Regarding the reaction mechanism, the blockage of FePc sites hinders the number of electrons exchanged, leading to the increase of by-products formed in comparison to CNT_{Fe}. Moreover, this mechanism is very similar to $CNT_{Co\ 185H2}$, which is probably due to the outer structure being very similar in both cases (cobalt treated at 185 °C in N_2 atmosphere followed by H_2 atmosphere), hence the same amount/type of active sites reducing O_2. Although $CNT_{Fe_Co_185H2}$ has a lower electrochemical performance than the monometallic iron sample, it is still more electroactive towards the ORR than CNT_{Co_185H2} and is very electroactive towards the OER, which is not the case for CNT_{Fe} (Fig. S5). The incorporation of FePc on CNT_{Co_185H2} ($CNT_{Co_185H2_Fe}$) results in a much higher electroactivity than the monometallic CNT_{Co_185H2} due to the presence of FePc on the outer layer of the electrocatalyst. The sample exhibits E_{onset} and $E_{1/2}$ of 0.90 V and 0.81 V, respectively, with a slightly higher current density (4.43 mA cm^{-2}) and slightly lower by-product formation (11%), which corresponds to 3.8 electrons exchanged. Lastly, the physical mixture of the two monometallic samples (CNT_{Fe}/$CNT_{Co\ 185H2}$) displays the highest electroactivity of all bimetallic samples and an electrochemical performance very similar to the commercial Pt/C. The prepared sample presents E_{onset} and $E_{1/2}$ of 0.94 V and 0.88 V, respectively, and a very high current density at 0.4 V (5.36 mA cm^{-2} vs 5.42 mA cm^{-2} of Pt/C). The reaction is also taking place via the 4-electron mechanism like Pt/C (3.9 electrons for both CNT_{Fe}/CNT_{Co_185H2} and Pt/C) with a by-product formation of 5%. The comparison between CNT_{Fe}/CNT_{Co_185H2} and the current commercial ORR electrocatalyst demonstrates that they are nearly equivalent in every aspect. Nonetheless, the half-wave potential of the developed bimetallic electrocatalyst is higher than that of Pt/C (0.88 V vs 0.83 V, respectively). Therefore, although CNT_{Fe}/CNT_{Co_185H2} presents a slightly lower OER performance than $CNT_{Fe_Co_185H2}$ and $CNT_{Co_185H2_Fe}$, it is much more electroactive towards the ORR, which is essential to obtain a high-efficient

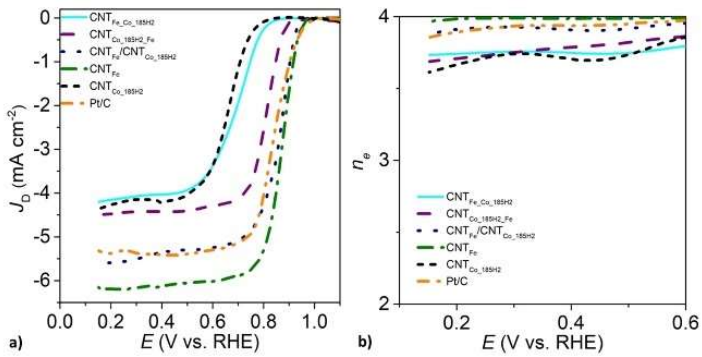


Fig. 5. Disk current density of the oxygen reduction reaction curves recorded at 1600 rpm and 5 mV s^{-1} in O_2-saturated 0.1 mol L^{-1} KOH electrolyte (a) and number of electrons exchanged (b).

bifunctional oxygen electrocatalyst.

To further assess the performance of the electrocatalysts towards the ORR, stability measurements were carried out, as they can provide an interesting perspective of the catalysts' performance during their lifetime on the final device. These measurements were performed by chronoamperometry for 10000 s by applying a potential of 0.4 V (Fig. 6a). The methanol tolerance of the most electroactive bimetallic sample towards the ORR ($CNT_{Fe}/CNT_{Co\ 185H2}$), CNT_{Fe} and the reference Pt/C, were also determined by the addition of pure methanol (1.5 mL) to the system at ca. 1000 s of the stability assessment (Fig. 6b).

$CNT_{Co\ 185H2}$ presents current density retention of 90% after 10000 s of reaction. On the other hand, CNT_{Fe} produces an outstanding 96% of its original current density after 10000 s. The bimetallic samples $CNT_{Fe_Co_185H2}$ and $CNT_{Co_185H2_Fe}$ also present a very good retention percentage (92% and 93%, respectively), which is higher than that of the commercial Pt/C (83%). Lastly, the physical mixture of the monometallic samples (CNT_{Fe}/CNT_{Co_185H2}) displays a stability percentage of 94%, demonstrating that all prepared samples have exceptional long-term stabilities. Moreover, the analysis of the methanol tolerance demonstrates that the prepared electrocatalysts remark a slight increase in current density upon the addition of methanol that returns to its previous values (95% and 91% for CNT_{Fe} and $CNT_{Fe}/CNT_{Co\ 185H2}$, respectively) after the dispersion of the methanol on the electrolyte due to the electrode rotation at 1600 rpm. The slight current density increase may be explained by two different phenomena. The introduction of methanol on the reaction medium by applying a potential of 0.4 V (vs RHE) may result in its oxidation which will provide electrons for an even higher rate of oxygen reduction, and hence, to a temporary slight increase of current density. Moreover, the addition of methanol to the 0.1 mol L^{-1} KOH electrolyte slightly reduces the concentration of KOH in the final electrolyte composition. The oxygen solubility and diffusion coefficient increase with decreasing KOH concentration whereas the electrolyte viscosity decreases [57]. According to the Koutecký-Levich equation, these variations result in a higher theoretical limiting current density which is in agreement with slight increase of the current density. Nonetheless, both samples present very high methanol poisoning tolerance, especially in comparison to Pt/C. The commercial catalyst suffers a significant immediate loss of performance by adding methanol into the electrolyte (ca. 20%), which slightly recovers upon the complete dispersion of the methanol in the KOH. These results demonstrate that not only are the prepared carbon electrocatalysts able to perform at the level of the commercial catalyst for short (LSV) and long (chronoamperometry) periods, but they are also better suited to withstand poisoning of the final device, which is also a very important issue for scale-up applications.

3.2.3. Bifunctional oxygen electrocatalysis

The oxygen bifunctionality was assessed by the potential gap (ΔE), i.e. the difference between E_{10} and $E_{1/2}$. The values obtained for the prepared carbon and the benchmark electrocatalysts for each reaction (OER and ORR) are exhibited in Table 3. This parameter is essential to understand the overall oxygen electroactivity and bifunctionality.

The potentials observed towards the OER (E_{10}) for all bimetallic samples and $CNT_{Co\ 185H2}$ are very similar (1.62–1.64 V). Consequently, the lowest ΔE should be achieved by obtaining the highest possible $E_{1/2}$ value for the ORR. From the set of bimetallic electrocatalysts shown in Table 3, $CNT_{Fe}/CNT_{Co\ 185H2}$ exhibits the highest electroactivity towards the ORR, making it the bifunctional oxygen electrocatalyst with the highest electroactivity. Moreover, all bifunctional samples presented much lower potential gaps than the benchmark catalyst tested, hence are better-suited bifunctional oxygen electrocatalysts. Besides, the ΔE obtained is lower than those obtained for most published articles and only a few were able to achieve similar values (Table 4). Notwithstanding, the electrocatalysts prepared for this work present several advantages in comparison to most of the existing electrocatalysts in literature, such as: i) a very low number of production steps, ii) incorporation of a cheap precursor (cobalt nitrate), and iii) a very small amount of a very electroactive active center (FePc) towards the ORR (environmental and cost advantages), and iv) the procedure is easily scalable.

4. Conclusions

CNT were used as bifunctional oxygen electrocatalysts after the incorporation of two different metal precursors onto the carbon matrix: cobalt nitrate and iron phthalocyanine. The cobalt precursor was incorporated by incipient wetness impregnation followed by thermal treatment at different temperatures and atmospheres to assess which conditions would provide a material with the highest electroactivity towards the OER. The results demonstrated that employing a low temperature (185 °C) and a H_2 atmosphere provided a high number of

Table 3
$E_{1/2}$, E_{10}, and ΔE for the prepared samples and benchmark electrocatalysts.

Sample	E_{10} (V)	$E_{1/2}$ (V)	ΔE (V)
CNT_{Fe}	1.79	0.88	0.91
$CNT_{Co\ 185H2}$	1.63	0.68	0.95
$CNT_{FePc\ Co\ 185H2}$	1.63	0.73	0.90
$CNT_{Co_185H2_FePc}$	1.62	0.81	0.81
$CNT_{FePc}/CNT_{Co_185H2}$	1.64	0.88	0.76
Pt/C	1.87	0.83	1.04

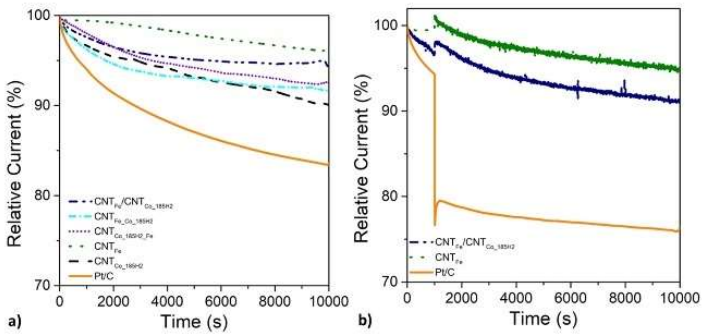


Fig. 6. Chronoamperometry assessments for the synthesised samples and Pt/C (a) and methanol resistance of samples CNT_{Fe}, CNT_{Fe}/CNT_{Co_185H2} and Pt/C (b) applying 0.4 V during 10000 s at 1600 rpm in an O_2-saturated 0.1 mol L^{-1} KOH electrolyte.

Table 4
ΔE of the most electroactive sample prepared and some state-of-the-art electrocatalysts.

Sample	ΔE (V)	Ref.
$FeCo_2O_4$/hollow reduced graphene oxide spheres	0.96	[19]
Fe/N-CNT	0.90	[21]
Co/N-CNT	0.87	[17]
$CoFe_2O_4$ nanoparticles/rod-like ordered mesoporous carbon	0.84	[19]
FeCo-NPC-1100	0.81	[20]
Co,Fe,N-CNT	0.80	[16]
Co/N-CNT	0.78	[34]
$CoFe_2O_4$/CNT	0.76	[19]
$CNT_{FePC}/CNT_{Co_185H2}$	0.76	This work

electroactive Co^{2+} sites that favored the oxygen evolution reaction. This interesting sample for the OER was further mixed with a sample of CNT-supporting iron phthalocyanine and tested as electrocatalysts for the ORR. The sample presented similar electrocatalytic performance and higher long-term stability and methanol poisoning tolerance in comparison to the commercial electrocatalyst (Pt/C). Besides, this bimetallic sample presented a low potential gap between both reactions (ΔE of 0.76 V) that is even lower than most of the best state-of-the-art published results for metal/heteroatom-doped carbon materials. Moreover, the use of cobalt nitrate instead of other complex cobalt precursors like cobalt phthalocyanine coupled with the use of a small amount of iron phthalocyanine allows for mass production of this electrocatalyst at low production costs, making it a perfect candidate to replace noble metal-based electrocatalysts and for up-scale testing using a gas-diffusion electrode, which in turn results in an electrocatalyst with a good up-scaling potential towards applying carbon materials for green energy applications.

CRediT authorship contribution statement

R.G. Morais: Conceptualization, Methodology, Investigation, Formal analysis, Visualization, Writing – original draft. **N. Rey-Raap:** Supervision, Conceptualization, Methodology, Writing – review & editing. **J.L. Figueiredo:** Conceptualization, Writing – review & editing. **M. Fernando R. Pereira:** Supervision, Conceptualization, Funding acquisition, Writing – review & editing.

Declaration of Competing Interest

The authors declare that they have no known competing financial interests or personal relationships that could have appeared to influence the work reported in this paper.

Data availability

Data will be made available on request.

Acknowledgments

This work was financially supported by Project "BiCat4Energy" with reference PTDC/EQU-EQU/1707/2020 and by LA/P/0045/2020 (ALiCE) and UIDB/50020/2020 - UIDP/50020/2020 (LSRE-LCM) funded by national funds through FCT/MCTES (PIDDAC). RGM acknowledges the research grant from FCT (2020.06422.BD). The authors are indebted to CEMUP for assistance with XPS.

Appendix A. Supporting information

Supplementary data associated with this article can be found in the online version at doi:10.1016/j.cattod.2023.114057.

References

[1] T.M. Gulotta, R. Salomone, F. Lanuzza, G. Saija, G. Mondello, G. Ioppolo, Life cycle assessment and life cycle costing of unitized regenerative fuel cells: a systematic review, Environ. Impact Assess. Rev. 92 (2022), 106698, https://doi.org/10.1016/j.eiar.2021.106698.
[2] P. Gayen, S. Saha, X. Liu, K. Sharma, V.K. Ramani, High-performance AEM unitized regenerative fuel cell using Pt-pyrochlore as bifunctional oxygen electrocatalyst, Proc. Natl. Acad. Sci. 118 (2021), e2107205118, https://doi.org/10.1073/pnas.2107205118.
[3] Q. Guo, H. Guo, F. Ye, L. Xing, C.F. Ma, A numerical study of dynamic behaviors of a unitized regenerative fuel cell during gas purging, Int. J. Hydrog. Energy 47 (2022) 22203–22214, https://doi.org/10.1016/j.ijhydene.2022.05.047.
[4] H. Guo, J. Song, F. Ye, M.A. Chong Fang, Dynamic response during mode switching of unitized regenerative fuel cells with orientational flow channels, Renew. Energy 188 (2022) 698–710, https://doi.org/10.1016/j.renene.2022.02.049.
[5] G. Glenk, S. Reichelstein, Reversible power to gas systems for energy conversion and storage, Nat. Commun. 13 (2022) 2010, https://doi.org/10.1038/s41467-022-29520-0.
[6] N. Ul Hassan, P. Ganesan, A.A. Lando, W.E. Mustain, H.R. Colón-Mercado, Stable, high-performing bifunctional electrodes for anion exchange membrane-based unitized regenerative fuel cells, J. Power Sources 541 (2022), 231599, https://doi.org/10.1016/j.jpowsour.2022.231599.
[7] J. Stacy, Y.N. Regmi, B. Leonard, M. Fan, The recent progress and future of oxygen reduction reaction catalysis: a review, Renew. Sust. Energ. Rev. 69 (2017) 401–414, https://doi.org/10.1016/j.rser.2016.09.135.
[8] A. Kirubakaran, S. Jain, R.K. Nema, A review on fuel cell technologies and power electronic interface, Renew. Sust. Energ. Rev. 13 (2009) 2430–2440, https://doi.org/10.1016/j.rser.2009.04.004.
[9] Y. Wang, D.Y.C. Leung, J. Xuan, H. Wang, A review on unitized regenerative fuel cell technologies, part A: unitized regenerative proton exchange membrane fuel cells, Renew. Sust. Energ. Rev. 65 (2016) 961–977, https://doi.org/10.1016/j.rser.2016.07.046.
[10] Y. Wang, D.Y.C. Leung, J. Xuan, H. Wang, A review on unitized regenerative fuel cell technologies, part B: unitized regenerative alkaline fuel cell, solid oxide fuel cell, and microfluidic fuel cell, Renew. Sust. Energ. Rev. 75 (2017) 775–795, https://doi.org/10.1016/j.rser.2016.11.054.
[11] B. Paul, J. Andrews, PEM unitised reversible/regenerative hydrogen fuel cell systems: state of the art and technical challenges, Renew. Sust. Energ. Rev. 79 (2017) 585–599, https://doi.org/10.1016/j.rser.2017.05.112.
[12] M.M. Mohideen, Y. Liu, S. Ramakrishna, Recent progress of carbon dots and carbon nanotubes applied in oxygen reduction reaction of fuel cell for transportation, Appl. Energy 257 (2020), 114027, https://doi.org/10.1016/j.apenergy.2019.114027.
[13] W.E. Mustain, M. Chatenet, M. Page, Y.S. Kim, Durability challenges of anion exchange membrane fuel cells, Energy Environ. Sci. 13 (2020) 2805–2838, https://doi.org/10.1039/D0EE01133A.
[14] S. Gottesfeld, D.R. Dekel, M. Page, C. Bae, Y. Yan, P. Zelenay, Y.S. Kim, Anion exchange membrane fuel cells: current status and remaining challenges, J. Power Sources 375 (2018) 170–184, https://doi.org/10.1016/j.jpowsour.2017.08.010.
[15] A. Sarapuu, E. Kibena-Põldsepp, M. Borghei, K. Tammeveski, Electrocatalysis of oxygen reduction on heteroatom-doped nanocarbons and transition metal–nitrogen–carbon catalysts for alkaline membrane fuel cells, J. Mater. Chem. A 6 (2018) 776–804, https://doi.org/10.1039/C7TA08690C.
[16] R.G. Morais, N. Rey-Raap, J.L. Figueiredo, M.F.R. Pereira, Fe, Co, N-doped carbon nanotubes as bifunctional oxygen electrocatalysts, Appl. Surf. Sci. 572 (2022), 151459, https://doi.org/10.1016/j.apsusc.2021.151459.
[17] L. Song, H. Fan, T. Wang, T. Xiang, M. Zhang, C. Hu, W. Zhou, J. He, Facile synthesis of Co, N enriched carbon nanotube and active site identifications for bifunctional oxygen reduction and evolution catalysis, Energy Storage Mater. 43 (2021) 365–374, https://doi.org/10.1016/j.ensm.2021.09.009.
[18] J. Xia, K. Li, G.-L. Zhao, Electric field polarization to increase bifunctional oxygen electrocatalyst performance of nitrogen–iron functionalized carbon nanomaterials, ACS Appl. Energy Mater. 3 (2020) 1484–1495, https://doi.org/10.1021/acsaem.9b01931.
[19] X. Wu, C. Tang, Y. Cheng, X. Min, S.P. Jiang, S. Wang, Bifunctional catalysts for reversible oxygen evolution reaction and oxygen reduction reaction, Chem. Eur. J. 26 (2020) 3906–3929, https://doi.org/10.1002/chem.201905346.
[20] B. Guo, Q. Ju, R. Ma, Z. Li, Q. Liu, F. Ai, M. Yang, S. Kaskel, J. Luo, T. Zhang, J. Wang, Mechanochemical synthesis of multi-site electrocatalysts as bifunctional zinc–air battery electrodes, J. Mater. Chem. A 7 (2019) 19355–19363, https://doi.org/10.1039/C9TA06411G.
[21] L. Zhao, Q. Wang, X. Zhang, C. Deng, Z. Li, Y. Lei, M. Zhu, Combined electron and structure manipulation on Fe-containing N-doped carbon nanotubes to boost bifunctional oxygen electrocatalysis, ACS Appl. Mater. Interfaces 10 (2018) 35888–35895, https://doi.org/10.1021/acsami.8b09197.
[22] H. Pan, X. Huang, Z. Lu, Z. Zhang, B. An, D. Wu, T. Wang, X. Chen, F. Cheng, Dual oxidation and sulfurization enabling hybrid Co/Co3O4@CoS in S/N-doped carbon matrix for bifunctional oxygen electrocatalysis and rechargeable Zn-air batteries, Chem. Eng. J. 419 (2021), 129619, https://doi.org/10.1016/j.cej.2021.129619.
[23] R.G. Morais, N. Rey-Raap, J.L. Figueiredo, M.F.R. Pereira, Highly electroactive N–Fe hydrothermal carbons and carbon nanotubes for the oxygen reduction reaction, J. Energy Chem. 50 (2020) 260–270, https://doi.org/10.1016/j.jechem.2020.03.039.
[24] J. Yang, J. Tao, T. Isomura, H. Yanagi, I. Moriguchi, N. Nakashima, A comparative study of iron phthalocyanine electrocatalysts supported on different nanocarbons

for oxygen reduction reaction, Carbon 145 (2019) 565–571, https://doi.org/10.1016/j.carbon.2019.01.022.
[25] A. Morozan, S. Campidelli, A. Filoramo, B. Jousselme, S. Palacin, Catalytic activity of cobalt and iron phthalocyanines or porphyrins supported on different carbon nanotubes towards oxygen reduction reaction, Carbon 49 (2011) 4839–4847, https://doi.org/10.1016/j.carbon.2011.07.004.
[26] M. Canal-Rodríguez, N. Rey-Raap, J.Á. Menéndez, M.A. Montes-Morán, J. L. Figueiredo, M.F.R. Pereira, A. Arenillas, Effect of porous structure on doping and the catalytic performance of carbon xerogels towards the oxygen reduction reaction, Microporous Mesoporous Mater. 293 (2020), 109811, https://doi.org/10.1016/j.micromeso.2019.109811.
[27] B. Mecheri, V.C.A. Ficca, M.A. Costa de Oliveira, A. D'Epifanio, E. Placidi, F. Arciprete, S. Licoccia, Facile synthesis of graphene-phthalocyanine composites as oxygen reduction electrocatalysts in microbial fuel cells, Appl. Catal. B-Environ. 237 (2018) 699–707, https://doi.org/10.1016/j.apcatb.2018.06.031.
[28] Y. Jiang, Y. Lu, X. Lv, D. Han, Q. Zhang, L. Niu, W. Chen, Enhanced catalytic performance of Pt-free iron phthalocyanine by graphene support for efficient oxygen reduction reaction, ACS Catal. 3 (2013) 1263–1271, https://doi.org/10.1021/cs4001927.
[29] R. Jasinski, A new fuel cell cathode catalyst, Nature 201 (1964) 1212–1213, https://doi.org/10.1038/2011212a0.
[30] R. Santhosh Kumar, S.C. Karthikeyan, S. Ramakrishnan, S. Vijayapradeep, A. Rhan Kim, J. S. Kim, D. Jin Yoo, Anion dependency of spinel type cobalt catalysts for efficient overall water splitting in an acid medium, Chem. Eng. J. 451 (2023), 138471, https://doi.org/10.1016/j.cej.2022.138471.
[31] H. Jin, R. Yu, C. Hu, P. Ji, Q. Ma, B. Liu, D. He, S. Mu, Size-controlled engineering of cobalt metal catalysts through a coordination effect for oxygen electrocatalysis, Appl. Catal. B-Environ. 317 (2022), 121766, https://doi.org/10.1016/j.apcatb.2022.121766.
[32] M. Wu, G. Zhang, H. Tong, X. Liu, L. Du, N. Chen, J. Wang, T. Sun, T. Regier, S. Sun, Cobalt (II) oxide nanosheets with rich oxygen vacancies as highly efficient bifunctional catalysts for ultra stable rechargeable Zn air flow battery, Nano Energy 79 (2021), 105409, https://doi.org/10.1016/j.nanoen.2020.105409.
[33] Y. Tian, L. Xu, M. Li, D. Yuan, X. Liu, J. Qian, Y. Dou, J. Qiu, S. Zhang, Interface Engineering of CoS/CoO@N-Doped Graphene Nanocomposite for High-Performance Rechargeable Zn–Air Batteries, Nano-Micro Lett. 13 (2020) 3, https://doi.org/10.1007/s40820-020-00526-x.
[34] Y. Liu, H. Jiang, Y. Zhu, X. Yang, C. Li, Transition metals (Fe, Co, and Ni) encapsulated in nitrogen-doped carbon nanotubes as bi-functional catalysts for oxygen electrode reactions, J. Mater. Chem. A 4 (2016) 1694–1701, https://doi.org/10.1039/C5TA10551J.
[35] Y. Hao, Z. Lu, G. Zhang, Z. Chang, L. Luo, X. Sun, Cobalt-embedded nitrogen-doped carbon nanotubes as high-performance bifunctional oxygen catalysts, Energy Technol. 5 (2017) 1265–1271, https://doi.org/10.1002/ente.201600559.
[36] R.P. Forslund, W.G. Hardin, X. Rong, A.M. Abakumov, D. Filimonov, C. T. Alexander, J.T. Mefford, H. Iyer, A.M. Kolpak, K.P. Johnston, K.J. Stevenson, Exceptional electrocatalytic oxygen evolution via tunable charge transfer interactions in La0.5Sr1.5Ni1−xFexO4±δ Ruddlesden Popper oxides, Nat. Commun. 9 (2018) 3150, https://doi.org/10.1038/s41467-018-05600-y.
[37] A. Bonakdarpour, T. Dahn, R. Atanasoski, M. Debe, J. Dahn, II2O2 release during oxygen reduction reaction on Pt nanoparticles, Electrochem. Solid-State Lett. 11 (2008) B208–B211, https://doi.org/10.1149/1.2978090.
[38] Y. Peng, J.-Y. Choi, T. Fürstenhaupt, K. Bai, Y. Zhang, D. Banham, New approach for rapidly determining Pt accessibility of Pt/C fuel cell catalysts, J. Mater. Chem. A 9 (2021) 13471–13476, https://doi.org/10.1039/D1TA01769A.
[39] C. Ehrhardt, M. Gjikaj, W. Brockner, Thermal decomposition of cobalt nitrato compounds: preparation of anhydrous cobalt(II)nitrate and its characterisation by Infrared and Raman spectra, Thermochim. Acta 432 (2005) 36–40, https://doi.org/10.1016/j.tca.2005.04.010.
[40] A. Ashok, A. Kumar, F. Tarlochan, Surface Alloying in Silver Cobalt through a Second Wave Solution Combustion Synthesis Technique, Nanomaterials 8 (2018), https://doi.org/10.3390/nano8080604.
[41] J.F. Moulder, J. Chastain, Handbook of X ray Photoelectron Spectroscopy: A Reference Book of Standard Spectra for Identification and Interpretation of XPS Data, Physical Electronics Division, Perkin-Elmer Corporation,, 1992.
[42] Y. Ying, J.F. Godínez Salomón, L. Lartundo-Rojas, A. Moreno, R. Meyer, C. A. Damin, C.P. Rhodes, Hydrous cobalt–iridium oxide two-dimensional nanoframes: insights into activity and stability of bimetallic acidic oxygen evolution electrocatalysts, Nanoscale Adv. 3 (2021) 1976–1996, https://doi.org/10.1039/D0NA00912A.
[43] W. Brockner, C. Ehrhardt, M. Gjikaj, Thermal decomposition of nickel nitrate hexahydrate, Ni(NO3)2·6H2O, in comparison to Co(NO3)2·6H2O and Ca(NO3)2·4H2O, Thermochim. Acta 456 (2007) 64–68, https://doi.org/10.1016/j.tca.2007.01.031.
[44] Y. Li, W. Qiu, F. Qin, H. Fang, V.G. Hadjiev, D. Litvinov, J. Bao, Identification of cobalt oxides with Raman scattering and fourier transform infrared spectroscopy, J. Phys. Chem. C. 120 (2016) 4511–4516, https://doi.org/10.1021/acs.jpcc.5b11185.
[45] R. Keeili, C.M. Hussain, Chapter 4 - Mechanism of Adsorption on Nanomaterials, in: C.M. Hussain (Ed.), Nanomaterials in Chromatography, Elsevier, 2018, pp. 89–115.
[46] E.N. Kaya, T. Basova, M. Polyakov, M. Durmuş, B. Kadem, A. Hassan, Hybrid materials of pyrene substituted phthalocyanines with single-walled carbon nanotubes: structure and sensing properties, RSC Adv. 5 (2015) 91855–91862, https://doi.org/10.1039/C5RA18697H.
[47] S.C. Petitto, E.M. Marsh, G.A. Carson, M.A. Langell, Cobalt oxide surface chemistry: the interaction of CoO(100), Co3O4(110) and Co3O4(111) with oxygen and water, J. Mol. Catal. A Chem. 281 (2008) 49–58, https://doi.org/10.1016/j.molcata.2007.08.023.
[48] T. Koczorowski, W. Szczolko, T. Goslinski, Physicochemical Properties and Catalytic Applications of Iron Porphyrazines and Phthalocyanines, in: M. M. Rahman, A.M. Asiri (Eds.), Recent Progress in Organometallic Chemistry, IntechOpen, 2017, pp. 101–121.
[49] H. Guo, Q. Feng, J. Zhu, J. Xu, Q. Li, S. Liu, K. Xu, C. Zhang, T. Liu, Cobalt nanoparticle-embedded nitrogen-doped carbon/carbon nanotube frameworks derived from a metal–organic framework for tri-functional ORR, OER and HER electrocatalysis, J. Mater. Chem. A 7 (2019) 3664–3672, https://doi.org/10.1039/C8TA11400F.
[50] B. Martínez Sánchez, D. Cazorla Amorós, E. Morallón, P functionalized carbon nanotubes promote highly stable electrocatalysts based on Fe phthalocyanines for oxygen reduction: Experimental and computational studies, J. Energy Chem. 72 (2022) 276–290, https://doi.org/10.1016/j.jechem.2022.05.024.
[51] N. Komba, G. Zhang, Q. Wei, X. Yang, J. Prakash, R. Chenitz, F. Rosei, S. Sun, Iron (II) phthalocyanine/N-doped graphene: a highly efficient non-precious metal catalyst for oxygen reduction, Int. J. Hydrog. Energy 44 (2019) 18103–18114, https://doi.org/10.1016/j.ijhydene.2019.05.032.
[52] Y. Liu, Y.-S. Fan, Z.-M. Liu, Pyrolysis of iron phthalocyanine on activated carbon as highly efficient non-noble metal oxygen reduction catalyst in microbial fuel cells, Chem. Eng. J. 361 (2019) 416–427, https://doi.org/10.1016/j.cej.2018.12.105.
[53] J. Yang, F. Toshimitsu, Z. Yang, T. Fujigaya, N. Nakashima, Pristine carbon nanotube/iron phthalocyanine hybrids with a well defined nanostructure show excellent efficiency and durability for the oxygen reduction reaction, J. Mater. Chem. A 5 (2017) 1184–1191, https://doi.org/10.1039/C6TA07882F.
[54] R. Venegas, F.J. Recio, C. Zuñiga, M. Viera, M. P. Oyarzún, N. Silva, K. Neira, J. F. Marco, J.H. Zagal, F. Tasca, Comparison of the catalytic activity for O2 reduction of Fe and Co MN4 adsorbed on graphite electrodes and on carbon nanotubes, Phys. Chem. Chem. Phys. 19 (2017) 20441–20450, https://doi.org/10.1039/C7CP03172F.
[55] C.Z. Loyola, S. Ureta-Zañartu, J.H. Zagal, F. Tasca, Activity volcano plots for the oxygen reduction reaction using FeN4 complexes: from reported experimental data to the electrochemical meaning, Curr. Opin. Electrochem. 32 (2022), 100923, https://doi.org/10.1016/j.coelec.2021.100923.
[56] W. Orellana, C.Z. Loyola, J.F. Marco, F. Tasca, Evidence of carbon-supported porphyrins pyrolyzed for the oxygen reduction reaction keeping integrity, Sci. Rep. 12 (2022) 8072, https://doi.org/10.1038/s41598-022-11820-6.
[57] J. Qiao, L. Xu, L. Ding, P. Shi, L. Zhang, R. Baker, J. Zhang, Effect of KOH concentration on the oxygen reduction kinetics catalyzed by heat treated co pyridine/C electrocatalysts, Int. J. Electrochem. 8 (2013) 1189–1208.